Springer Proceedings in Materials

Ivan A. Parinov
Shun-Hsyung Chang
Yun-Hae Kim
Nao-Aki Noda *Editors*

Physics and Mechanics of New Materials and Their Applications

Proceedings of the International Conference PHENMA 2020

Springer

Springer Proceedings in Materials

Volume 10

Springer Proceedings in Materials publishes the latest research in Materials Science and Engineering presented at high standard academic conferences and scientific meetings. It provides a platform for researchers, professionals and students to present their scientific findings and stay up-to-date with the development in Materials Science and Engineering. The scope is multidisciplinary and ranges from fundamental to applied research, including, but not limited to:

- Structural Materials
- Metallic Materials
- Magnetic, Optical and Electronic Materials
- Ceramics, Glass, Composites, Natural Materials
- Biomaterials
- Nanotechnology
- Characterization and Evaluation of Materials
- Energy Materials
- Materials Processing

To submit a proposal or request further information, please contact one of our Springer Publishing Editors according to your affiliation:

European countries: **Mayra Castro** (mayra.castro@springer.com)
India, South Asia and Middle East: **Priya Vyas** (priya.vyas@springer.com)
South Korea: **Smith Chae** (smith.chae@springer.com)
Southeast Asia, Australia and New Zealand: **Ramesh Nath Premnath** (ramesh.premnath@springernature.com)
The Americas: **Michael Luby** (michael.luby@springer.com)
China and all the other countries or regions: **Mengchu Huang** (mengchu.huang@springer.com)

More information about this series at http://www.springer.com/series/16157

Ivan A. Parinov · Shun-Hsyung Chang ·
Yun-Hae Kim · Nao-Aki Noda
Editors

Physics and Mechanics of New Materials and Their Applications

Proceedings of the International Conference PHENMA 2020

Springer

Editors
Ivan A. Parinov
I. I. Vorovich Mathematics, Mechanics and Computer Sciences Institute
Southern Federal University
Rostov-on-Don, Russia

Yun-Hae Kim
Department of Mechanical Engineering
Korea Maritime and Ocean University
Busan, Korea (Republic of)

Shun-Hsyung Chang
Department of Microelectronics Engineering
National Kaohsiung University of Science and Technology
Kaohsiung, Taiwan

Nao-Aki Noda
Department of Mechanical Engineering
Kyushu Institute of Technology
Kitakyushu, Japan

ISSN 2662-3161 ISSN 2662-317X (electronic)
Springer Proceedings in Materials
ISBN 978-3-030-76480-7 ISBN 978-3-030-76481-4 (eBook)
https://doi.org/10.1007/978-3-030-76481-4

This Springer imprint is published by the registered company Springer Nature Switzerland AG
The registered company address is: Gewerbestrasse 11, 6330 Cham, Switzerland

Preface

Today, the rapid development of advanced materials and composites determines the main achievements and successes in numerous areas of modern science and technique. These results very quickly find their application in industry and other areas. The improvement of structure-sensitive properties and also of many devices on their base is directly coupled with effective chemical, physical and mechanical investigations, modern numerical methods and approaches of mathematical modeling, computer simulation and natural experiment. Modern applications demonstrate growing interest in these results and determine promising directions of further development of science techniques and technologies. Industry requires the fabrication of devices, showing very high measurement accuracy, reliability, and durability, which could open wide horizons for operating the developed products by changing temperatures and pressures into wide ranges, and aggressive media, too. Moreover, the scientific and technical achievements should decide the sharp social problems of modern life (ecology, medicine, rehabilitation, etc.).

This collection of 50 chapters presents selected reports of the 2020 International Conference on "Physics, Mechanics of New Materials and Their Applications" (PHENMA-2020), which has taken place in Kitakyushu in Japan, 26–29 March, 2021 (http://www.phenma2020.sfedu.ru/). Due to the coronavirus pandemic, which began in the world in 2020, the PHENMA-2020 was postponed from 22–5 October, 2020 to the pointed date. The conference was sponsored by The Society of Materials Science, Kyushu Branch (Japan); Kitakyushu Convention and Visitors Association (Japan); The Korean Society for Composite Materials (South Korea); Ministry of Education and Science of Russian Federation; Russian Foundation for Basic Research; Ministry of Science and Technology of Taiwan; National Foundation for Science and Technology Development (Vietnam); Vietnam Union of Science and Technology Associations (VUSTA); Vietnam Association of Science Editing (VASE); South Scientific Center of Russian Academy of Science; New Century Education Foundation (Taiwan); Ocean and Underwater Technology Association (Taiwan); Unity Opto Technology Co. (Taiwan); Fair Well Fishery Co. (Taiwan); Woen Jinn Harbor Engineering Co. (Taiwan); Lorom Group (Taiwan); Longwell Co. (Taiwan);

Hanoi University of Science and Technology (Vietnam); Vietnam Maritime University (Vietnam); Vinh Long University of Technology Education (Vietnam); Hanoi University of Industry (Vietnam); Vietnamese-German University (Vietnam); Ho Chi Minh City University of Agriculture and Forestry (Vietnam); Research Institute of Agriculture Machinery (Vietnam); Don State Technical University (Russia); University of 17 Agustus 1945 Surabaya (Indonesia); Perkumpulan Ahli dan Dosen Republik Indonesia; University of Maarif Hasyim Latif, Sidoarjo (Indonesia); PDPM Indian Institute of Information Technology, Design and Manufacturing (India); and South Russian Regional Centre for Preparation and Implementation of International Projects.

The thematic of the PHENMA-2019 continued the ideas of previous international symposia and conferences: PMNM-2012 (Rostov-on-Don, Russia), PHENMA-2013 (Kaohsiung, Taiwan), PHENMA-2014 (Khon-Kaen, Thailand), PHENMA-2015 (Azov, Russia), PHENMA-2016 (Surabaya, Indonesia), PHENMA-2017 (Jabalpur, India), PHENMA-2018 (Busan, South Korea), and PHENMA-2019 (Hanoi, Vietnam), whose results have been published in the following edited books: "Physics and Mechanics of New Materials and Their Applications", Ivan A. Parinov, Shun Hsyung-Chang (Eds.), Nova Science Publishers, New York, 2013, 444 p., ISBN: 978-1-62618-535-7; "Advanced Materials—Physics, Mechanics and Applications", Springer Proceedings in Physics, Vol. 152, Shun-Hsyung Chang, Ivan A. Parinov, Vitaly Yu. Topolov (Eds.), Springer, Heidelberg, New York, Dordrecht, London, 2014, 380 p., ISBN: 978-3319037486; "Advanced Materials—Studies and Applications", Ivan A. Parinov, Shun-Hsyung Chang, Somnuk Theerakulpisut (Eds.), Nova Science Publishers, New York, 2015, 527 p., ISBN: 978-1-63463-749-7; "Advanced Materials—Manufacturing, Physics, Mechanics and Applications", Springer Proceedings in Physics, Vol. 175, Ivan A. Parinov, Shun-Hsyung Chang, Vitaly Yu. Topolov (Eds.), Heidelberg, New York, Dordrecht, London, Springer, Cham, 2016.—707 p., ISBN: 978-3319263229; Advanced Materials—Techniques, Physics, Mechanics and Applications, Springer Proceedings in Physics, Vol. 193, Ivan A. Parinov, Shun-Hsyung Chang, Muaffaq A. Jani (Eds.), Springer Nature, Cham, Switzerland, 2017.—627 p., ISBN: 978-3-319-56062-5; Advanced Materials—Proceedings of the International Conference on "Physics and Mechanics of New Materials and Their Applications", PHENMA-2017, Springer Proceedings in Physics, V. 207, Ivan A. Parinov, Shun-Hsyung Chang, Vijay K. Gupta (Eds.), Springer Nature, Cham, Switzerland, 2018.—640 p., ISBN: 978-3319789187; Advanced Materials—Proceedings of the International Conference on "Physics and Mechanics of New Materials and Their Applications", PHENMA-2018, Springer Proceedings in Physics, V. 224, Ivan A. Parinov, Shun-Hsyung Chang, Yun-Hae Kim (Eds.), Springer Nature, Cham, Switzerland, 2019.—666 p., ISBN: 978-3-030-19893-0; and Advanced Materials—Proceedings of the International Conference on "Physics and Mechanics of New Materials and Their Applications", PHENMA-2019, Springer Proceedings in Materials, V. 6, Ivan A. Parinov, Shun-Hsyung Chang, Banh Tien Long (Eds.), Springer Nature, Cham, Switzerland, 2020.—621 p., ISBN: 978-3-030-45119-6, respectively.

The papers of the PHENMA-2020 are divided into four scientific directions: (i) processing techniques of advanced materials, (ii) physics of advanced materials, (iii) mechanics of advanced materials, and (iv) applications of advanced materials.

Into the framework of the first direction, highly stable Pt/C catalysts with different mass fractions of Platinum are considered. Then, there are investigations of the activity of PtCuAu/C electrocatalysts in alcohols electrooxidation reaction in alkaline media, and also the influence of acid treatment on the functional characteristics of PtCu/C electrocatalysts is estimated. Moreover, carbon nanoparticles from graphite nitrate cointercalation compounds with carboxylic acids are studied and also sorption properties and obtaining carbon nanoparticles at the thermal expansion of graphite are studied. Then, subsequently, the fabrication of heteroepitaxial $BiFeO_3$ films on MgO(001) substrate and the effect of the preparation conditions on the catalytic activity of palladium in the salt K_2PdCl_4–C_2H_2–CH_3OH, subjected to preliminary mechanical activation, as well as the properties of solid solutions in a KNN-based system, are studied. Moreover, biocompatible plasma-sprayed coatings based on hydroxyapatite and $Al_2O_3$are manufactured. The first section is finished by the discussion of technological aspects of obtaining fuel composites based on fine-grained coal waste.

The physical topic is opened by constructing the statistical operator and density matrix for gamma quantum and deuterium, and also classic equation of dynamics follows from the quantum equation for the statistical operator. Then, the Riesz potential-type operator with a power-logarithmic kernel is studied in the generalized Hölder spaces on a sphere. The piezoelectric sensitivity and anisotropy in 1–3-type composites based on lead-free ferroelectrics are considered too. Crystal structure and dielectric properties of solid solutions $Bi_{3-x}Nd_xTiNbO_9$ and $Bi_7Ti_{4-x}Sn_xNbO_{21}$ are studied for change of parameter $0 \leq x \leq 1$. Synthesis and different properties of vacuum ion-plasma coatings based on carbon, as well as the properties of Au thin film deposited by pulsed laser sputtering on Si substrate and relaxation processes in organic anticorrosive films, are investigated. Finally, the functional possibilities of the optical interference meter of the surface displacements of control objects are estimated.

The section of mechanics is opened by the study of the Rayleigh waves propagation in structures with functionally graded piezoelectric material coatings. Then, simulation of elastic wave propagation in layered periodic elastomer composites is performed and asymptotics of displacements in back-reflected ultrasonic waves from a 3D defect located in an elastic material are defined. The oscillation problems for auxetic shells in liquid and non-axisymmetric shells are solved too. Moreover, it is considered that the contact interaction between parabolic punch and elastic strip bonded to poroelastic half-plane. The generative neural networks and nondestructive testing are developed for defect detection problems. The problem of the Fatigue Crack Growth Rate and Intrinsic Threshold Stress Intensity is studied theoretically and experimentally. The fatigue problems are considered for bolt nut connections and bimetallic work roll.

Analysis of the ultrasonic guided wave sensitivity to the bone structure for osteoporosis diagnostics opens the fourth section. Then, finite element modeling of a lensotome tip with piezoelectric drive is presented and the MRI image segmentation methods are discussed for radiation-induced brain edema after radiotherapy for patients with intracranial tumors as well as the reconstruction of the optical acoustic signal for visualization of biological tissues is discussed. Then, modeling the cantilever-type piezogenerator with proof mass and active pinching by using the porous piezoceramics is performed. The problems of piezoelectric energy harvesting and designing efficient harvesters using wind energy are considered together with the development of the control system for deformation of electromagnetoelastic actuator and surface acoustic wave current sensor with FeNi film. Monitoring of the medium state by using surface waves is performed. Underwater applications are connected with the study of nonlinear interaction of acoustic waves in underwater archeology and the development of underwater image communication technology. Finally, the parametric modeling of high-rise objects with complex configuration describing their external shaping and algorithmization of the system for geometric description of the 3D objects are performed.

The book will be interesting for students of different levels of education, scientists, and engineers in R&D of nanomaterials, nanostructures, piezoelectrics, and other promising materials and composites with structure-sensitive properties. The book also discusses theoretical and experimental problems, directed to designing modern devices based on advanced materials, which are available for a wide spectrum of scientific, technical, and technological applications. The book includes new research results in the fields of materials science, condensed matter physics, chemistry, mechanics, computational and physical modeling and experiment, manufacture of advanced materials and composites, mathematical processing test results, computational methods, and various applications.

This edited book was partially supported by the Russian Science Foundation (grant No. 21-19-00423).

Rostov-on-Don, Russia — Ivan A. Parinov
Kaohsiung, Taiwan — Shun-Hsyung Chang
Busan, Korea (Republic of) — Yun-Hae Kim
Kitakyushu, Japan — Nao-Aki Noda
April 2021

Contents

Contributors

K. G. Abdulvakhidov Southern Federal University, Rostov-on-Don, Russia

S. M. Afonin National Research University of Electronic Technology (MIET), Moscow, Russia

Anastasia Alekseenko Chemistry Department, Southern Federal University, Rostov-on-Don, Russia

Igor Andjikovich I. I. Vorovich Mathematics, Mechanics and Computer Sciences Institute, Southern Federal University, Rostov-on-Don, Russia

K. P. Andryushin Institute of Physics, Southern Federal University, Rostov-on-Don, Russia

Mohd Radzi Aridi Department of Mechanical Engineering, Kyushu Institute of Technology, Kitakyushu-shi, Fukuoka, Japan

S. V. Belenov Chemistry Department, Southern Federal University, Rostov-on-Don, Russia

T. I. Belyankova Southern Scientific Center of Russian Academy of Sciences, Rostov-on-Don, Russian Federation

Y. V. Berestneva Federal Scientific Centre of Agroecology Complex Melioration and Protective Afforestation of the Russian Academy of Sciences, Volgograd, Russia

Yuliya Berestneva Biotechnology Laboratory, Federal Scientific Centre of Agroecology, Complex Melioration and Protective Afforestation of the Russian Academy of Sciences, Volgograd, Russia

A. S. Bogatin Southern Federal University, Rostov-on-Don, Russia

Boris V. Bondarev Moscow Aviation Institute, Moscow, Russia

Christopher R. Bowen Department of Mechanical Engineering, University of Bath, Bath, UK

Nikolay V. Boyev Southern Federal University, Rostov-on-Don, Russian Federation

Y. A. Bulygin Department "International", Don State Technical University, Rostov-on-Don, Russia

Nina Buravchuk I.I. Vorovich Institute of Mathematics, Mechanics and Computer Science, Southern Federal University, Rostov-on-Don, Russia

Valerij Burchovetskij Department of High-Pressure Physics and Advanced Technologies, Donetsk Institute for Physics and Engineering Named After A.A. Galkin, Donetsk, Ukraine

Shun-Hsyung Chang Department of Microelectronic Engineering, National Kaohsuing University of Science and Technology, Kaohsuing, Taiwan, ROC

Pei-Ju Chao Department of Electronics Engineering, National Kaohsiung University of Science and Technology, Kaohsiung, Taiwan;
Medical Physics and Informatics Laboratory of Electronics Engineering, National Kaohsiung University of Science and Technology, Kaohsiung, Taiwan;
Department of Radiation Oncology, Kaohsiung Chang Gung Memorial Hospital, Chang Gung University College of Medicine, Kaohsiung, Taiwan

M. I. Chebakov I. I. Vorovich Mathematics, Mechanics and Computer Sciences Institute, Southern Federal University, Rostov-on-Don, Russia

Alexander Cherpakov I. I. Vorovich Mathematics, Mechanics and Computer Sciences Institute, Southern Federal University, Rostov-on-Don, Russia;
Department of Information Systems in Construction, Don State Technical University, Rostov-on-Don, Russia

A. V. Cherpakov Department of Information Systems in Construction, Don State Technical University, Rostov-on-Don, Russia;
I. I. Vorovich Mathematics, Mechanics, and Computer Science Institute, Southern Federal University, Rostov-on-Don, Russia

Chi-Ming Chou Department of Electronics Engineering, National Kaohsiung University of Science and Technology, Kaohsiung, Taiwan;
Medical Physics and Informatics Laboratory of Electronics Engineering, National Kaohsiung University of Science and Technology, Kaohsiung, Taiwan

Chih-Chin Chuang Department of Electrical Engineering, National Taiwan Ocean University, Keelung, Taiwan, ROC

A. A. Davydova L.M. Litvinenko Institute of Physical Organic and Coal Chemistry, Donetsk, Ukraine

Alina Davydova Department of Supramolecular Chemistry, L.M. Litvinenko Institute of Physical-Organic and Coal Chemistry, Donetsk, Ukraine

Alisa O. Denisova Department of Physics, Southern Federal University, Rostov-on-Don, Russia

Yuri Drobotov I. I. Vorovich Institute of Mathematics, Mechanics and Computer Science, Southern Federal University, Rostov-on-Don, Russia

Nguyen Duc-Toan School of Mechanical Engineering, Hanoi University of Science and Technology, Hanoi City, Vietnam

A. N. Epikhin Department of Ophthalmology, Rostov State Medical University, Rostov-on-Don, Russia

A. B. Eresko L.M. Litvinenko Institute of Physical Organic and Coal Chemistry, Donetsk, Ukraine

Olga Ermolenko Institute for Mathematics, Mechanics and Informatics, Kuban State University, Krasnodar, Russia

Sergey I. Fomenko Institute for Mathematics, Mechanics and Informatics, Kuban State University, Krasnodar, Russian Federation

Dmitry Fugarov Don State Technical University, Rostov-on-Don, Russia

Irina Gerasimova Chemistry Department, Southern Federal University, Rostov-on-Don, Russia

E. V. Glazunova Institute of Physics, Southern Federal University, Rostov-on-Don, Russia

V. A. Glazunova Donetsk Institute for Physics and Engineering Named After A.A. Galkin, Donetsk, Ukraine

Valentina Glazunova Department of High-Pressure Physics and Advanced Technologies, Donetsk Institute for Physics and Engineering Named After A.A. Galkin, Donetsk, Ukraine

N. I. Glushko Department of Theoretical and Applied Mechanics, Don State Technical University, Rostov-on-Don, Russia

Evgeny Glushkov Institute for Mathematics, Mechanics and Informatics, Kuban State University, Krasnodar, Russia

Natalia Glushkova Institute for Mathematics, Mechanics and Informatics, Kuban State University, Krasnodar, Russia

Viktoriya Gnatovskaya Department of Supramolecular Chemistry, L.M. Litvinenko Institute of Physical-Organic and Coal Chemistry, Donetsk, Ukraine

Mikhail V. Golub Institute for Mathematics, Mechanics and Informatics, Kuban State University, Krasnodar, Russian Federation

I. Yu. Golushko Research and Education Center “Materials”, Don State Technical University, Rostov-on-Don, Russia

Vijay K. Gupta Department of Mechanical Engineering, PDPM Indian Institute of Information Technology Design and Manufacturing, Jabalpur, India

Olga Guryanova I.I. Vorovich Institute of Mathematics, Mechanics and Computer Science, Southern Federal University, Rostov-on-Don, Russia

Rakesh Kumar Haldkar Southern Federal University, Rostov-on-Don, Russia

Hsuan-Chih Hsu Department of Radiation Oncology, Kaohsiung Chang Gung Memorial Hospital, Chang Gung University College of Medicine, Kaohsiung, Taiwan

Yu-Jie Huang Department of Radiation Oncology, Kaohsiung Chang Gung Memorial Hospital, Chang Gung University College of Medicine, Kaohsiung, Taiwan

Yuto Inui Mechanical Engineering Department, Kyusyu Institute of Technology, Kitakyushu, Fukuoka, Japan

Ashura N. Isaeva Department of Physics, Southern Federal University, Rostov-on-Don, Russia

E. M. Kaidashev Laboratory of Nanomaterials, Southern Federal University, Rostov-on-Don, Russia

V. V. Kalinchuk Southern Scientific Center of Russian Academy of Sciences, Rostov-on-Don, Russian Federation

Valery Kalinchuk Southern Scientific Center of Russian Academy of Sciences, Rostov-on-Don, Russia

V. A. Kalinin Scientific and Technical Center "Radio Engineering Devices and Systems" With Limited Liability, St. Petersburg, Russia

Chen-Lin Kang Department of Radiation Oncology, Kaohsiung Chang Gung Memorial Hospital, Chang Gung University College of Medicine, Kaohsiung, Taiwan

G. Ya. Karapetyan Laboratory of Nanomaterials, Southern Federal University, Rostov-on-Don, Russia

Ryo Kawano Mechanical Engineering Department, Kyusyu Institute of Technology, Kitakyushu, Fukuoka, Japan

Artur D. Khanazaryan Institute for Mathematics, Mechanics and Informatics, Kuban State University, Krasnodar, Russian Federation

I. A. Kirichenko Southern Federal University, Taganrog, Russia

L. I. Kiseleva Federal Research Centre the Southern Scientific Centre of the Russian Academy of Sciences, Rostov-on-Don, Russia

V. O. Kislitsin Scientific and Technical Center "Radio Engineering Devices and Systems" With Limited Liability, St. Petersburg, Russia

E. M. Kolosova I. I. Vorovich Mathematics, Mechanics and Computer Sciences Institute, Southern Federal University, Rostov-on-Don, Russia

S. A. Kovrigina Southern Federal University, Rostov-on-Don, Russia

D. V. Krasnov Department of Theoretical and Applied Mechanics, Don State Technical University, Rostov-on-Don, Russia

T. V. Krasnyakova Institute of Physical Organic and Coal Chemistry, Donetsk, Ukraine

Galina Kravchenko Department of Mechanical Engineering, Don State Technical University, Rostov-on-Don, Russia

Denis A. Kravchuk Southern Federal University, Taganrog, Russia

Oleg V. Kudryakov Department of Physical and Applied Material Science, Don State Technical University, Rostov-on-Don, Russia

M. E. Kutepov Laboratory of Nanomaterials, Southern Federal University, Rostov-on-Don, Russia

Tsair-Fwu Lee Department of Electronics Engineering, National Kaohsiung University of Science and Technology, Kaohsiung, Taiwan;
Medical Physics and Informatics Laboratory of Electronics Engineering, National Kaohsiung University of Science and Technology, Kaohsiung, Taiwan;
Biomedical Engineering, Kaohsiung Medical University, Kaohsiung, Taiwan

O. N. Lesnyak Department of Theoretical and Applied Mechanics, Don State Technical University, Rostov-on-Don, Russia

Chin-Feng Lin Department of Electrical Engineering, National Taiwan Ocean University, Keelung, Taiwan, ROC

Wei-Chun Lin Department of Orthopedic, Kaohsiung Municipal Min-Sheng Hospital, Kaohsiung, Taiwan

Xi Liu Mechanical Engineering Department, Kyusyu Institute of Technology, Kitakyushu, Fukuoka, Japan

A. V. Lyasnikova Don State Technical University, Rostov-on-Don, Russia

Risma Marleno Master of Civil Engineering, University of 17 Agustus 1945 Surabaya Indonesia, Surabaya, Indonesia

I. P. Melnikova Yu. A. Gagarin Saratov State Technical University, Saratov, Russia

Irina Michailova Southern Scientific Center of Russian Academy of Sciences, Rostov-on-Don, Russia

Yuri F. Migal The Southern Scientific Centre of the Russian Academy of Sciences, Rostov-on-Don, Russia

Igor P. Miroshnichenko Don State Technical University, Rostov-on-Don, Russia

S. A. Mitchenko Institute of Physical Organic and Coal Chemistry, Donetsk, Ukraine

Elizaveta Moguchikh Chemistry Department, Southern Federal University, Rostov-on-Don, Russia

A. V. Muratov L.M. Litvinenko Institute of Physical Organic and Coal Chemistry, Donetsk, Ukraine

A. V. Nagaenko Institute of High Technology and Piezo Technic, Southern Federal University, Rostov-on-Don, Russia

Tejkaran Narolia Department of Mechanical Engineering, PDPM Indian Institute of Information Technology Design and Manufacturing, Jabalpur, India

A. K. Nevelskaya Chemistry Department, Southern Federal University, Rostov-on-Don, Russia

D. V. Nikitenko Institute of Physical Organic and Coal Chemistry, Donetsk, Ukraine

A. L. Nikolaev Don State Technical University, Rostov-on-Don, Russia;
Research and Education Center "Materials", Don State Technical University, Rostov-on-Don, Russia

Aleksey Nikulin Chemistry Department, Southern Federal University, Rostov-on-Don, Russia

Alexey Nikulin Chemistry Department, Southern Federal University, Rostov-on-Don, Russia

Nao-Aki Noda Mechanical Engineering Department, Kyusyu Institute of Technology, Kitakyushu, Fukuoka, Japan;
Mechanical Engineering Department, Kyushu Institute of Technology, Tobata, Kitakyushu, Japan;
Department of Mechanical Engineering, Kyushu Institute of Technology, Kitakyushu-shi, Fukuoka, Japan

I. O. Nosatschev Southern Federal University, Rostov-on-Don, Russia

Eugeny S. Novikov Department of Theoretical Mechanics, Rostov State Transport University, Rostov-on-Don, Russia

O. N. Oskolkova L.M. Litvinenko Institute of Physical Organic and Coal Chemistry, Donetsk, Ukraine

Oksana Oskolkova Department of Supramolecular Chemistry, L.M. Litvinenko Institute of Physical-Organic and Coal Chemistry, Donetsk, Ukraine

Kirill Paperzh Chemistry Department, Southern Federal University, Rostov-on-Don, Russia

I. A. Parinov I. I. Vorovich Mathematics, Mechanics, and Computer Science Institute, Southern Federal University, Rostov-on-Don, Russia

Ivan Parinov I. I. Vorovich Mathematics, Mechanics and Computer Sciences Institute, Southern Federal University, Rostov-on-Don, Russia

Ivan A. Parinov Southern Federal University, Rostov-on-Don, Russia;
I. I. Vorovich Mathematics, Mechanics, and Computer Science Institute, Southern Federal University, Rostov-on-Don, Russia

A. V. Pavlenko Federal Research Centre the Southern Scientific Centre of the Russian Academy of Sciences, Rostov-on-Don, Russia

Angelina Pavlets Chemistry Department, Southern Federal University, Rostov-on-Don, Russia

Anna Poluyan Don State Technical University, Rostov-on-Don, Russia

Olga Purchina Don State Technical University, Rostov-on-Don, Russia

Erni Putri Department of Industrial Engineering, University of 17 Agustus, Surabaya, Indonesia

Rahimah Abdul Rafar Mechanical Engineering Department, Kyushu Institute of Technology, Tobata, Kitakyushu, Japan

E. V. Raksha L.M. Litvinenko Institute of Physical Organic and Coal Chemistry, Donetsk, Ukraine

Elena Raksha Department of Supramolecular Chemistry, L.M. Litvinenko Institute of Physical-Organic and Coal Chemistry, Donetsk, Ukraine

L. A. Reznichenko Institute of Physics, Southern Federal University, Rostov-on-Don, Russia

Fajar Romadhon Master of Civil Engineering, University of 17 Agustus 1945 Surabaya Indonesia, Surabaya, Indonesia

E. V. Sadyrin Research and Education Center "Materials", Don State Technical University, Rostov-on-Don, Russia

Yoshikazu Sano Mechanical Engineering Department, Kyusyu Institute of Technology, Kitakyushu, Fukuoka, Japan;
Mechanical Engineering Department, Kyushu Institute of Technology, Tobata, Kitakyushu, Japan;
Department of Mechanical Engineering, Kyushu Institute of Technology, Kitakyushu-shi, Fukuoka, Japan

Gede Sarya Master of Civil Engineering, University of 17 Agustus 1945 Surabaya Indonesia, Surabaya, Indonesia

M. V. Savoskin L.M. Litvinenko Institute of Physical Organic and Coal Chemistry, Donetsk, Ukraine

Michael Savoskin Department of Supramolecular Chemistry, L.M. Litvinenko Institute of Physical-Organic and Coal Chemistry, Donetsk, Ukraine

Andrey Sedov Southern Scientific Center of Russian Academy of Sciences, Rostov-on-Don, Russia

Alexander Senichev Department of Information Technologies, Don State Technical University, Rostov-on-Don, Russia

Sergey N. Shevtsov Aircraft Systems and Technologies Laboratory, South Center of Russian Academy of Science, Rostov-on-Don, Russia

Chin-Shiuh Shieh Department of Electronics Engineering, National Kaohsiung University of Science and Technology, Kaohsiung, Taiwan

L. A. Shilkina Institute of Physics, Southern Federal University, Rostov-on-Don, Russia

O. V. Shilyaeva Department of Information Systems in Construction, Don State Technical University, Rostov-on-Don, Russia

Ol'ga Shilyaeva Department of Information Systems in Construction, Don State Technical University, Rostov-on-Don, Russia

Alisa N. Shpak Institute for Mathematics, Mechanics and Informatics, Kuban State University, Krasnodar, Russian Federation

S. P. Shpanko Southern Federal University, Rostov-on-Don, Russia

Andrew V. Sidashov Department of Theoretical Mechanics, Rostov State Transport University, Rostov-on-Don, Russia

E. N. Sidorenko Southern Federal University, Rostov-on-Don, Russia

Bei -fen Siew Mechanical Engineering Department, Kyusyu Institute of Technology, Kitakyushu, Fukuoka, Japan

A. N. Soloviev Department of Theoretical and Applied Mechanics, Don State Technical University, Rostov-on-Don, Russia

Arkadiy Soloviev Department of Theoretical and Applied Mechanics, Don State Technical University, Rostov-on-Don, Russia;
I. I. Vorovich Mathematics, Mechanics and Computer Sciences Institute, Southern Federal University, Rostov-on-Don, Russia

A. A. Solovieva Department of Theoretical and Applied Mechanics, Don State Technical University, Rostov-on-Don, Russia

I. B. Starchenko Parametrika LCC, Taganrog, Russia

Irina B. Starchenko Parametrika LCC, Taganrog, Russia

D. V. Stryukov Federal Research Centre the Southern Scientific Centre of the Russian Academy of Sciences, Rostov-on-Don, Russia

Petr Sukhov Department of Supramolecular Chemistry, L.M. Litvinenko Institute of Physical-Organic and Coal Chemistry, Donetsk, Ukraine

R. Sunder BISS Division, ITW-India (P) Ltd, Bangalore, India

Hari Susanto Master of Civil Engineering, University of 17 Agustus 1945 Surabaya Indonesia, Surabaya, Indonesia

Yasushi Takase Mechanical Engineering Department, Kyushu Institute of Technology, Tobata, Kitakyushu, Japan

Kakeru Takata Department of Mechanical Engineering, Kyushu Institute of Technology, Kitakyushu-shi, Fukuoka, Japan

Alexey Tatarinov Riga Technical University, Riga, Latvia

Luyen The-Thanh Faculty of Mechanical Engineering, Hung Yen University of Technology and Education, Hung Yen, Vietnam

Mac Thi-Bich Faculty of Mechanical Engineering, Hung Yen University of Technology and Education, Hung Yen, Vietnam

Banh Tien-Long Faculty of Mechanical Engineering, Hung Yen University of Technology and Education, Hung Yen, Vietnam;
School of Mechanical Engineering, Hanoi University of Science and Technology, Hanoi City, Vietnam

G. N. Tolmachev Federal Research Centre the Southern Scientific Centre of the Russian Academy of Sciences, Rostov-on-Don, Russia

Vitaly Yu. Topolov Department of Physics, Southern Federal University, Rostov-on-Don, Russia

Elena Trufanova Department of Mechanical Engineering, Don State Technical University, Rostov-on-Don, Russia

Chin-Dar Tseng Department of Electronics Engineering, National Kaohsiung University of Science and Technology, Kaohsiung, Taiwan;
Medical Physics and Informatics Laboratory of Electronics Engineering, National Kaohsiung University of Science and Technology, Kaohsiung, Taiwan

Hiroyuki Tsurumaru Mechanical Engineering Department, Kyushu Institute of Technology, Tobata, Kitakyushu, Japan

O. M. Tukodova Don State Technical University, Rostov-on-Don, Russian Federation

Boris Vakulov I. I. Vorovich Institute of Mathematics, Mechanics and Computer Science, Southern Federal University, Rostov-on-Don, Russia

Valery N. Varavka Department of Physical and Applied Material Science, Don State Technical University, Rostov-on-Don, Russia

A. S. Vasiliev Research and Education Center "Materials", Don State Technical University, Rostov-on-Don, Russia

Pavel Vasiliev Department of Information Technologies, Don State Technical University, Rostov-on-Don, Russia

I. A. Verbenko Research Institute of Physics, Southern Federal University, Rostov-on-Don, Russia;
Institute of Physics, Southern Federal University, Rostov-on-Don, Russia

Iliya Verbenko Research Institute of Physics, Southern Federal University, Rostov-on-Don, Russia

A. A. Voitash L.M. Litvinenko Institute of Physical Organic and Coal Chemistry, Donetsk, Ukraine

Galina Volkova Department of High-Pressure Physics and Advanced Technologies, Donetsk Institute for Physics and Engineering Named After A.A. Galkin, Donetsk, Ukraine

E. I. Vorovich Don State Technical University, Rostov-on-Don, Russian Federation

Biao Wang Mechanical Engineering Department, Kyusyu Institute of Technology, Kitakyushu, Fukuoka, Japan

Chia-Chi Yen Department of Orthopedic, Kaohsiung Municipal Min-Sheng Hospital, Kaohsiung, Taiwan;
Department of Nutrition, Institute of Biomedical Nutrition, Hung-Kuang University, Taichung, Taiwan;
Department of Business Management, National Sun Yat-Sen University, Kaohsiung, Taiwan

A. S. Yudin I. I. Vorovich Institute of Mathematics, Mechanics and Computer Sciences, Southern Federal University, Rostov-on-Don, Russia

Igor Yu. Zabiyaka Department of Physical and Applied Material Science, Don State Technical University, Rostov-on-Don, Russia

Sun Zifeng Department of Mechanical Engineering, Kyushu Institute of Technology, Kitakyushu-shi, Fukuoka, Japan

S. V. Zubkov Research Institute of Physics, Southern Federal University, Rostov-on Don, Russia

Processing Techniques of Advanced Materials

Highly Stable Pt/C Catalysts with Different Mass Fraction of Platinum

Kirill Paperzh, Elizaveta Moguchikh, Aleksey Nikulin, and Irina Gerasimova

Abstract The stability of electrocatalysts for low-temperature fuel cells can be considered as one of the most important characteristics. The use of various carbon supports can affect the characteristics of electrocatalysts based on them. The article presents the preparation of Pt/C catalysts with a small platinum crystallite size, high specific characteristics, and increased stability in long-term stress testing.

Keywords Pt/c · Electrocatalysts · Nanoparticles (NPs) · Stability · Active surface area (ESA) · Carbon support · Stability · Oxygen reduction reaction (ORR)

1 Introduction

In recent years, promising alternative energy sources - low-temperature fuel cells (LFCs) , characterized by high power indicators and low operating temperatures and high efficiency have become of great importance [1–3].

The heart of each fuel cell is a membrane-electrode unit containing a proton-exchange membrane and two electrodes on which current-generating reactions are realized: oxygen reduction reaction (ORR), hydrogen or methanol oxidation [4–6]. The need to ensure that these reactions proceed at a high rate necessitates the use of platinum-containing catalysts [7].

Nanoparticles of platinum (NP) deposited on the surface of a carbon support are considered promising materials as electrocatalysts for low-temperature fuel cells [7, 8]. As supports for platinum-containing nanoparticles, highly dispersed carbon materials are used, which are characterized by a number of indicators: specific surface area; diameter, shape and volume of pores; hydrophobic-hydrophilic properties of the surface, etc. [9, 10]. The value of the surface area of the carbon material is determined by the ratio of the number of pores and their size. In the literature it is noted that metal nanoparticles located in pores of small diameter may be inaccessible for ORR [7, 8]. Thus, when producing platinum-containing electrocatalysts, it is necessary to

K. Paperzh (✉) · E. Moguchikh · A. Nikulin · I. Gerasimova
Chemistry Department, Southern Federal University, Rostov-on-Don, Russia
e-mail: kpaperzh@yandex.ru

I. A. Parinov et al. (eds.), *Physics and Mechanics of New Materials and Their Applications*, Springer Proceedings in Materials 10,
https://doi.org/10.1007/978-3-030-76481-4_1

select a carbon support with optimal characteristics. The most widely used carrier for the production of commercial catalysts is highly dispersed carbon Vulcan XC-72 with a surface area of 270–290 m^2/g and Ketjenblack with a surface area of 340–350 m^2/g.

Recently, there has been a growing interest of researchers in increasing the stability of "ordinary" dispersed carbon materials due to the doping their surface layers with heteroatoms N, B, P, S [11, 12]. To a large extent, these studies were initiated by the prospect of developing free-of-charge electrocatalysts for the oxygen electroreduction reaction in alkaline electrolytes. The active centers of catalysis in such materials can be groups containing heteroatoms, for example, nitrogen atoms linked to carbon by pyrrole and/or pyriridine bonds [13].

The main characteristics of platinum-containing catalysts are the mass fraction of platinum, the spatial distribution of nanoparticles over the surface of the carbon support, their shape and size. By controlling these parameters, it is possible to change the important electrochemical properties of the catalysts [14]. The value of the electrochemically active surface area (ESA) is one of the functional characteristics of catalysts [15]. This is the surface of platinum nanoparticles available for electrochemical reactions. By varying the size of nanoparticles, it is possible to increase the ESA values, but only in the absence of agglomeration. A change in the mass fraction of platinum and the size of nanoparticles also affects such an important property of the catalyst as stability.

Stability is the ability of materials to maintain their functional characteristics during the operation of PEMFC, to be one of the main functional characteristics of platinum-containing electrocatalysts [16]. The decrease in the activity of catalysts during the operation of PEMFC is associated with material degradation [16]. Resistance to degradation is associated with structural and morphological characteristics: the size of nanoparticles, their distribution over the surface, the strength of attachment, and the type of support.

Studies show that material degradation can be associated with dissolution of platinum-containing nanoparticles; with detachment of particles due to weak adsorption on the surface of the carbon carrier; agglomeration of particles on the surface of the carrier; oxidation of the carbon carrier; re-precipitation of metals and Ostwald ripening (a special case of re-precipitation, in which metal atoms are re-precipitated from smaller particles to larger ones) [16].

In recent literature, it has been described that the stability of Pt/C electrocatalysts increases with an increase in the average size of nanoparticles and the mass fraction of platinum in the catalyst [17]. In the course of fuel cell operation, the electrocatalyst containing large NPs will be more stable due to the almost complete absence of processes associated with the movement of NPs over the surface of the support, aggregation and dissolution of small platinum nanoparticles (less than 3 nm) due to their strong fixation on the carbon support and a higher thermodynamic stability of large particles. However, such materials are characterized by a small electrochemically active surface area.

It is important to note that by varying various structural parameters of Pt/C, such as the average crystallite size, mass fraction of Pt, distance between nanoparticles,

etc., one can control the set of electrochemical characteristics of catalysts. The aim of this work is to reveal the relationship between the structural characteristics of Pt/C catalysts and their stability during prolonged stress testing.

2 Experimental Part

Several Pt/C electrocatalysts with different mass fractions of platinum and the type of carbon carriers were obtained as the test materials by liquid-phase synthesis: Vulcan XC-72, Ketjenblack EC DJ-600, and N-doped Ketjenblack EC DJ-600-N. All obtained catalyst samples were compared with each other, as well as with the behavior of commercial Pt/C samples of JM.

2.1 Preparation of Pt/C Catalysts

A weighed portion of a carbon carrier (the corresponding support is indicated in Table 1) weighing 0.15 g was placed in the required amount of ethylene glycol (Superior grade, not less than 99.8%, GOST 19,710–83). The slurry was stirred on a magnetic stirrer and then homogenized (750 W, Cole-Parmer, Sonics Material). Then, with constant stirring, 6.64 ml of a solution of hydrochloric platinum acid with a concentration of 17.9 mg (Pt)/ml, and 5.5 ml of 0.5 M NaOH (n(OH)/n(Pt) = 12) were added. The mixture was transferred to a 100 ml round bottom flask. With constant stirring, a reducing agent, formaldehyde, was added (premium grade, 37.2%, GOST 1625–89). Then, in an inert atmosphere, the temperature was increased to 80 °C and the reaction mixture was kept under constant stirring for 2 h. After spontaneous cooling the suspension for 40 min, the product was filtered off by alternately repeatedly washing the filtrate with portions of bi-distilled water and isopropyl alcohol.

Table 1 Obtained Pt/C materials for research and commercial analogs

Sample	ω(Pt), %	D_{av}, nm	Support
Pt/C_{10}	9.5 ± 0.3	1.1	Vulcan XC-72
Pt/C_{15}	16.2 ± 0.5	1.1	Vulcan XC-72
Pt/C_{20}	20.5 ± 0.6	1.0	Vulcan XC-72
Pt/C_{30}	30.7 ± 0.9	1.1	Vulcan XC-72
Pt/C_{40}	39.5 ± 1.2	1.1	Vulcan XC-72
$Pt/C(1)_{20}$	22.0 ± 1.2	1.3	Ketjenblack EC DJ-600
$Pt/C(1)–N_{20}$	19.8 ± 0.6	1.5	N-doped Ketjenblack EC DJ-600-N
JM20	20 ± 0.6	2.0	–
TEC10V50E	45.8 ± 1.4	2.5	–

The catalysts were kept for 1 h in an oven at 80 °C, then 12 h in a desiccator over P_2O_5.

2.2 Characterization of the Catalysts Structure

The mass fraction of platinum in the studied samples was determined by the method of gravimetry. Ceramic crucibles were calcined to constant weight at 800–850 °C and weighed after complete cooling. Then, 0.02 g of Pt/C material was placed in crucibles, and weighed portions were burned in a muffle furnace at 800–850 °C for 40 min. The crucibles with a non-combustible residue were weighed after complete cooling. The change in weight was used to determine the content of metals in the sample.

To study the obtained materials, the powder diffraction method was used. An ARL X'TRA powder diffractometer with a Bragg–Brentano geometry (θ–θ), CuKα radiation ($\lambda = 0.154056$ nm) at room temperature was used to take X-ray diffraction patterns. X-ray diffraction patterns of the samples under study were recorded in the range of angles $5° \leq 2\theta \geq 90°$ by the step-by-step scanning method with a detector movement step of 0.02°. The X-ray diffraction patterns were processed by the SciDavis software for correct extraction of peak parameters, which is especially important when they overlap in the case of small particle sizes. The average crystallite size was estimated from the most intense reflection peak of the (111) face using the Scherrer equation [18].

2.3 Electrochemical Measurements

To carry out chemical measurements, an electro suspension of the catalytic ink of each of the samples was initially prepared. To do this, 900 μl of isopropyl alcohol and 100 μl of 0.5% aqueous emulsion of Nafion® polymer were added to 0.006 g of each sample. Then the suspension was dispersed with ultrasound. With stirring, an aliquot of "ink" with a volume of 6 μL was taken using a microdispenser and applied to the end face of a polished and degreased glassy carbon disk with an area of 0.196 cm^2, recording the exact weight of the drop. To fix the catalyst on top of the layer remaining on the electrode after drying the drop, 6 μL of 0.05% Nafion® emulsion was applied, and then dried in air for 15 min.

Before measuring the electrochemically active surface area of the catalyst, it was standardized the electrode. For this, the electrolyte was saturated with argon for 40 min. 100 cycles were recorded at potentials from minus 0.04 to plus 1.2 V relative to a reversible hydrogen electrode. The sweep speed is 200 mV/s.

Calculation of ESA was carried out by the amount of electricity spent on the electrochemical adsorption and desorption of atomic hydrogen, taking into account

the contribution of the charging currents of the double electric layer, as described in [19].

To assess the catalytic activity in the RVC, the electrolyte was saturated with oxygen for 1 h, after which a series of voltammograms was measured in the range from 0.12 to 1.19 V with a linear potential sweep at a rate of 20 mV/s at electrode rotation speeds of 400, 900, 1600, and 2500 rpm min. To take into account the contribution of the ohmic potential drop and processes not associated with ORR, the voltammograms, obtained when the potential is swept towards more positive values, were normalized according to generally accepted methods [20–22].

As methods for assessing the degree of degradation electrocatalysts, were selected the cyclic voltammetry methods in the potential range 0.6–1.0 V (RHE) with a sweep rate of 100 mV/s and 0.6–1.4 V (RHE) with a sweep rate of 100 mV/s. The cycling was carried out in a 0.1 M solution of $HClO_4$ saturated with argon at 25 °C; the number of cycles recorded was 5000 and 500, respectively. After every 500 or 100 cycles, two CVs were recorded at a potential sweep rate of 20 mV/s in the potential range from 0.04 V to 1.2 V (*vs* RHE). According to the second CV, ESA was calculated as described previously.

The stability was assessed by the relative change in the ESA of platinum before ($S_{ESA}{}^0$) and after ($S_{ESA}{}^j$) stress test by the formula:

$$\text{Stability} = \left(S_{ESA^j}/S_{ESA^0}\right) \times 100\% \quad (1)$$

where j is the number of potential sweep cycles carried out before a specific S_{ESA} measurement, $S_{ESA}{}^0$ is the initial area measured after standardization.

3 Results and Discussion

In the course of the study, a number of electrocatalysts were obtained containing various amounts of platinum from 9.5 to 39.5% (Table 1).

X-ray diffraction patterns of the catalysts under study have a form characteristic of supported Pt/C materials (Fig. 1). The presence of nanosized platinum crystallites causes broadening of the characteristic maxima of platinum, and with a decrease in the average crystallite size (D_{av}), this broadening increases. The results of calculating the values of D_{av} according to the Scherrer equation are shown in Table 1. All catalysts based on the Vulcan XC-72 carbon support are characterized by a similar crystallite size, namely 1.0–1.1 nm, regardless of the mass fraction of Pt in the samples (Table 1). The materials obtained on carbon supports Ketjenblack EC DJ-600 and N-doped Ketjenblack EC DJ-600-N are characterized by a higher average crystallite size of 1.3–1.5 nm. The high and narrow peak in the X-ray diffraction pattern of the commercial catalyst TEC10V50E indicates a relatively high Pt crystallite size of 2.5 nm compared to other materials.

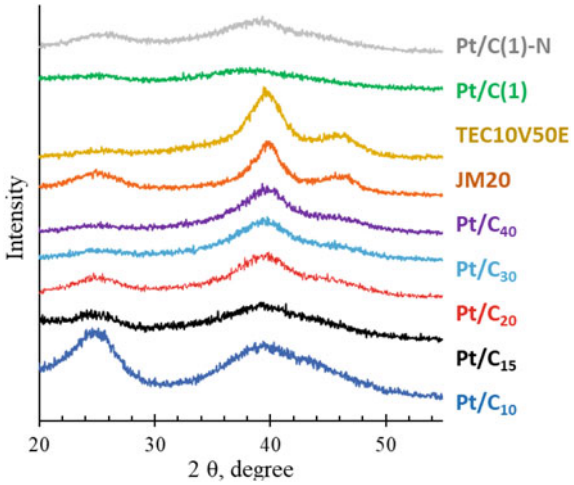

Fig. 1 XRD patterns of the Pt/C materials

Cyclic voltammograms of the studied platinum–carbon materials have a characteristic shape for nanosized platinum (Fig. 2). The electrochemically active surface area calculated from the half-sum of the amount of electricity consumed for adsorption and desorption of a monolayer of atomic hydrogen is shown in Table 2. An increase in ESA (from 9.5% to 35.5%), is observed, which may be associated with the possible agglomeration of NPs due to the large amount of Pt per unit area of the carbon support and, hence, the narrowing of the distance between particles (Tables 1, 2). The lowest degree of agglomeration is typical for the Pt/C_{10} sample due to the low metal content, as well as for materials on the original and modified Ketjenblack

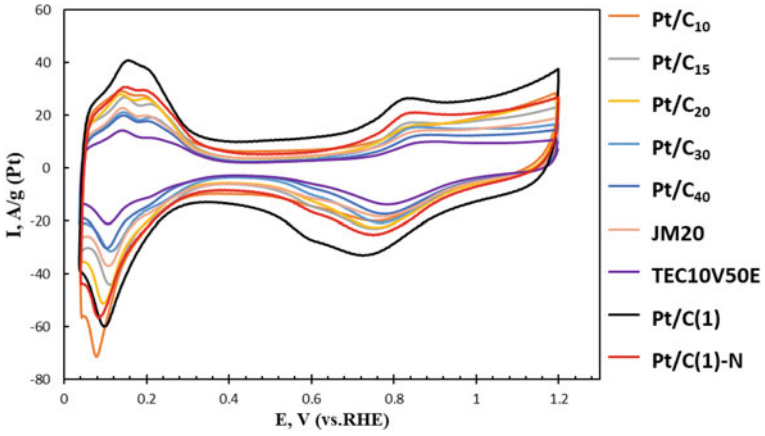

Fig. 2 Cyclic voltammograms of the metal–carbon catalysts; the sweep rate of the potential is 20 mV/s; 0.1 M $HClO_4$ solution is saturated by Ar at room temperature

Table 2 Electrochemical characteristics of the obtained and commercial samples of Pt/C catalysts

Образец	ESA^0, m^2/g (Pt)	$E_{1/2}$, V (RHE) (1600 rpm)	number ē	I_k, mA	I_{mass}, A/g (Pt)	Degree of aggregation
Pt/C_{10}	129 ± 13	0.89	4.4*	0.9*	287*	0.48
Pt/C_{15}	120 ± 12	0.92	3.6	1.4	230	0.56
Pt/C_{20}	118 ± 12	0.92	3.8	1.9	249	0.53
Pt/C_{30}	96 ± 10	0.92	4.1	2.1	206	0.61
Pt/C_{40}	83 ± 8	0.94	4.0	2.5	183	0.59
$Pt/C(1)_{20}$	114 ± 11	0.87	3.2	0.4	56	0.47
Pt/C(1) – N_{20}	110 ± 11	0.91	4.0	1.7	242	0.41
JM20	84 ± 8	0.91	3.9	1.3	180	0.25
TEC10V50E	62 ± 6	0.93	4.0	2.2	128	0.51

* – data at a potential of 0.85 V

support. In $Pt/C(1)_{20}$ and Pt/C(1) – N_{20} materials, nanoparticles are larger and less agglomerated.

The Pt/C_{10} material with a platinum content of 9.5% and a low degree of aggregation has the highest ESA value, and the commercial TEC10V50E catalyst with the largest nanoparticle size 2.5 nm and a high mass fraction of platinum of 45.8% is characterized by the lowest ESA values (Table 2).

The difference in the values of the experimentally determined ESA and the calculated geometric surface area of nanostructured materials is expressed in the indicator, namely the degree of aggregation (Table 2).

For each of the samples, the degree of aggregation was calculated using the equation:

$$\text{Degreeofaggregation} = 1 - \frac{\text{ESA}}{S\text{geom}} \tag{2}$$

where ESA is the electrochemically active surface area determined according to the CV data; S_{geom} is the geometric area calculated as

$$S_{\text{geom}} = \frac{61000}{D_{\text{NP}}(\text{Pt})} \tag{3}$$

where $\rho(\text{Pt}) = 21.4$ g/cm^3 is the platinum density; D_{NP} was calculated using the Scherrer equation on the base of X-ray analysis data.

Values over 0.5 may indicate a high proportion of nanoparticles stuck together into agglomerates. To a lesser extent, this effect is observed for commercial JM20 and Pt/C(1)–N_{20} material obtained on the base of an N-doped support. In the literature, many authors note that it is precisely the modification of the carbon support that

can contribute to an increase in active centers on the surface and a more uniform distribution of metal nanoparticles [23].

Investigation of the catalytic activity of the obtained materials in the RVC showed that the reaction proceeds according to the 4th electronic mechanism for all catalysts (Table 2). The half-wave potential increases with an increase in the mass fraction of the metal both for the samples on Vulcan XC-72 and for materials obtained on the basis of the original and modified Ketjenblack (Table 2). Predictably, the kinetic current for the obtained samples and commercial analogs increases with an increase in the platinum content from 9 to 39% and from 0.9 to 2.5 mA, respectively (Table 2). In this case, the mass activity in this series of catalysts decreases (Fig. 3, Table 2). A similar result is associated with the coarsening of platinum crystallites [17, 24]. The highest mass activity is characteristic of the Pt/C_{10} and $Pt/C(1)–N_{20}$ samples, which exceeds this parameter for commercial analogs several times (Table 2, Fig. 3). The mass activity in ORR increases with a decrease in the mass fraction of platinum in the obtained samples in the series $Pt/C_{40} < Pt/C_{30} < Pt/C_{20} < Pt/C(1)–N_{20}$. The Pt/C_{10} and Pt/C_{15} materials fall out of the general trend, most likely due to the low metal content.

The significant difference in currents in the diffusion region is associated with the different content of platinum in the samples (Fig. 3). The lowest value of the half-wave potential and low mass activity is characterized by $Pt/C(1)_{20}$, obtained on the basis of an undoped Ketjenblack carrier (Table 2, Fig. 3).

Long-term stress testing in the potential range of 0.6–1.0 V showed a high relative stability of more than 80% for all synthesized Pt/C materials on the Vulcan XC-72 carbon support (Table 3). The $Pt/C(1)_{20}$ sample obtained on the basis of the Ketjenblack support is characterized by the lowest stability value, while its N-doped one exhibits the highest stability among all studied catalysts (Table 3, Fig. 4b).

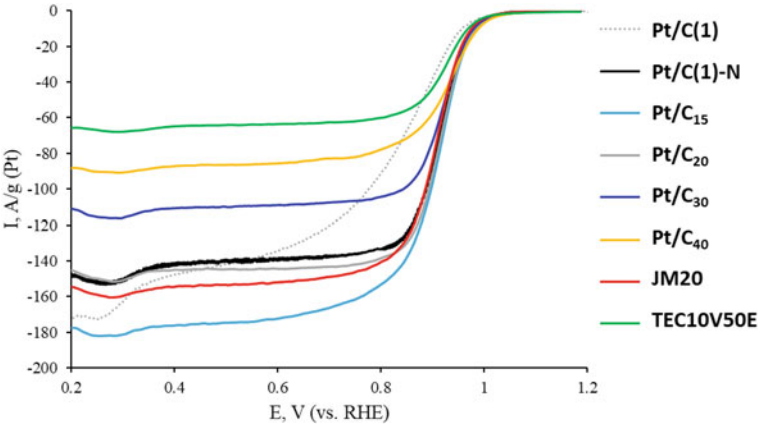

Fig. 3 Linear voltammograms of the ORR for the catalysts; the rotation speed of the disk is 1600 rpm

Table 3 Sample characteristics calculated after stress testing

Sample	ESA^{5000}, m^2/g (Pt)	Relative stability, %	I_{mass}, A/g (Pt)	$E_{1/2}$, V (RHE)
Pt/C_{10}	112	85	–	–
Pt/C_{15}	106	86	–	–
Pt/C_{20}	103	86	118	0.89
Pt/C_{30}	84	86	155	0.92
Pt/C_{40}	76	86	130	0.93
$Pt/C(1)_{20}$	66	58	12	0.76
$Pt/C(1)–N_{20}$	100	90	88	0.89
JM20	69	82	60	0.88
TEC10V50E	52	84	108	0.91

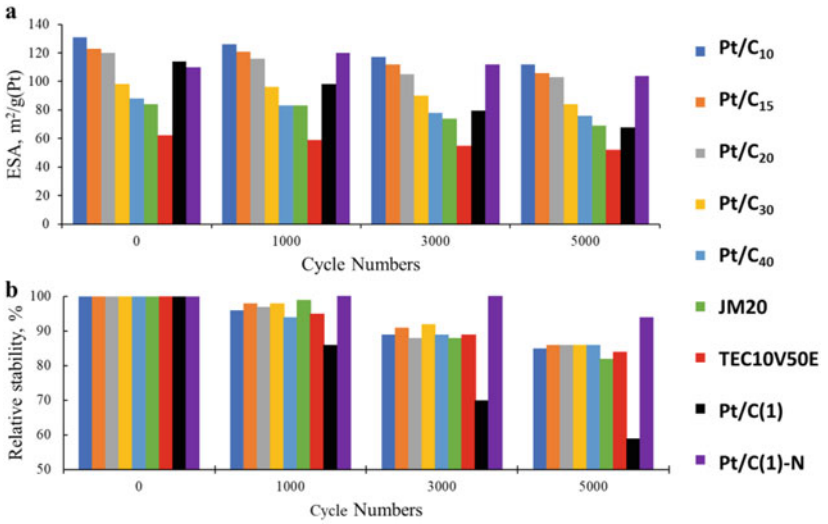

Fig. 4 Dependence of the ESA (a) and relative degree of degradation (b) on the number of cycles during cycling in the potential range 0.6–1.0 V

It is considered correct to carry out a comparative assessment not only by the value of relative stability, but also by the residual values of ESA and the value of activity. The highest residual ESA, characterizing the Pt/C_{10}, Pt/C_{10}, Pt/C_{10} and $Pt/C(1)–N_{20}$ samples is more than 100 m^2/g (Pt). Pt/C samples with a low platinum content (9–16%) are characterized by a decrease in activity during the stress test and, therefore, it is difficult to assess the behavior of these materials in ORR.

4 Conclusions

Pt/C catalysts containing from 9 to 39.9 wt% were obtained by synthesis methods in the liquid phase. platinum containing nanoparticles of small size (from 1.0 to 1.5 nm) on the carbon support Vulcan XC-72 and Ketjenblack. Due to the smaller size and higher ordering of the spatial distribution of nanoparticles, the Pt/C_n series catalysts are characterized by higher ESA values (from 129 to 83 m^2/g (Pt)) than the commercial Pt/C catalysts (84 and 62 m^2/g (Pt)) containing, respectively, 20 and 40% of the mass. platinum. Note that, despite the small size of platinum nanoparticles, all Pt/C_n catalysts are characterized by increased and close relative stability (more than 80%).

The Pt/C$(1)_{20}$ sample obtained using carbon, Ketjenblack, has low electrochemical characteristics compared to other samples. This is primarily due to the high dispersion that the inaccessible part of the nanoparticle carrier is paid for in the pores for ORR. The deposition of platinum nanoparticles on a nitrogen-doped carbon support leads to the production of the best catalyst in terms of high stability.

Acknowledgements This research was supported by the Russian Foundation for Basic Research (project No. 20-33-90135).

References

1. R. O'Hayre, S.-W. Cha, W. Colella, F. B. Prinz. *Fuel Cell Fundamentals*, 2nd edn. (Wiley, 2009), p. 57
2. C. Qin, J. Wang, D. Yang, B. Li, C. Zhang, Catalysts **6**(12), 197 (2016)
3. A. Kongkanand, M.F. Mathias, J. Phys. Chem. Lett. **7**, 1127 (2016)
4. G. Crawley. in *Fuel Cell Today*, vol. 1 (2006)
5. H. Lv, D. Li, D. Strmcnik, A.P. Paulikas, N.M. Markovic, V.R. Stamenkovic, Nano Energy **29**, 149 (2016)
6. Z. Yang, I.H. Hafez, M.R. Berber, N. Nakashima, ChemCatChem **7**, 808 (2015)
7. O.T. Holton, J.W. Stevenson, Platin. Met. Rev. **57**(4), 259 (2013)
8. D. Li, C. Wang, D.S. Strmcnik, D.V. Tripkovic, X. Sun, Y. Kang, M. Chi, J.D. Snyder, D. Van Der Vliet, Y. Tsai, V.R. Stamenkovic, S. Sun, N.M. Markovic, Energy Environ. Sci. **7**, 4061 (2014)
9. N. Ramaswamy, W. Gu, J.M. Ziegelbauer, S. Kumaraguru, J. Electrochem. Soc. **167**(6), 64 (2020)
10. R. Sharma, S. Ma Andersen *Applied Catalysis B: Environmental*, vol. 8. (2018), p.45
11. G.S. Harzer, A. Orfanidi, H. El-Sayed, P. Madkikar, H.A. Gasteiger, J. Electrochem. Soc. **165**(10), 770 (2017)
12. H. Schmies, E. Hornberger, B. Anke, T. Jurzinsky, H.N. Nong, F. Dionigi, P. Strasser, Chem. Mater. **30**(20), 7287 (2018)
13. J. Cao, Y. Chu, X. Tan, Mater. Chem. Phys. **144**(1–2), 17 (2014)
14. M. Koichi, Platinum Metals Rev. **54**, 223 (2010)
15. V.E. Guterman, Inorg. Mater. **52**, 23 (2016)
16. J.C. Meier, C. Galeano, I. Katsounaros, J. Witte, H.J. Bongard, A.A. Topalov, C. Baldizzone, S. Mezzavilla, F. Schüth, K.J.J. Mayrhofer, Beilstein J. Nanotechnol. **5**, 44 (2014)

17. Y. Zhang, J. Power Sources **273**, 62 (2015)
18. A.A. Alekseenko, Inorg. Mater. **51**, 1258 (2015)
19. A.A. Alekseenko, V.E. Guterman, S.V. Belenov, V.S. Menshikov, NYu. Tabachkova, O.I. Safronenko, E.A. Moguchikh, Int. J. of Hydrogen Energy **43**, 3676 (2018)
20. K. Shinozaki, J.W. Zack, S. Pylypenko, B.S. Pivovar, S.S. Kocha, J. Electrochem. Soc. **162**, 1384 (2015)
21. H.A. Gasteiger, Sh.S. Kocha, B. Sompalli, F.T. Wagner, Appl. Catal. B **56**, 9 (2005)
22. W.J. Khudhayer, N.N. Kariuki, X. Wang, D.J. Myers, A.U. Shaikh, T. Karabacak, J. Electrochem. Soc. **158**, 1029 (2011)
23. J. Cheng, Y. Li, X. Huang, Q. Wang, A. Meib, P.K. Shen, J. Mater. Chem. A **3**, 1492 (2015)
24. H. Yano, M. Watanabea, A. Iiyamaa, H. Uchida, Nano Energy **29**, 323 (2016)

Investigation of the Activity of PtCuAu/C Electrocatalysts in Alcohols Electrooxidation Reaction in Alkaline Media

A. K. Nevelskaya and S. V. Belenov

Abstract Platinum-based catalysts in some cases can improve the functional characteristics of the fuel cell. This study presents different methods for the synthesis of trimetallic catalysts with different architectures of nanoparticles for the reactions of methanol and ethanol electrooxidation in alkaline electrolytes. The catalysts were studied using powder diffraction, transmission electron microscopy, X-ray fluorescence analysis, and cyclic voltammetry. According to the results of chronoamperometry, the material obtained in one stage of synthesis shows higher initial values of the specific currents of oxidation of alcohols than the material obtained in two stages and commercial Pt/C. In ethanol oxidation reaction for the material obtained in one stage, this value is 1.2 and 2 times higher than the corresponding values of the material obtained in two stages and Pt/C catalyst, respectively. In the methanol oxidation reaction, the initial value of specific currents for this material is 1.5 times higher in comparison with other catalysts presented in the article.

Keywords Platinum-based catalysts · Trimetallic nanoparticles · Alloying · Ethanol oxidation reaction (EOR) · Methanol oxidation reaction (MOR) · Alkaline electrolytes · Transmission electron microscopy (TEM) · Cyclic voltammetry (CV)

1 Introduction

For the efficient operation of a fuel cell (FC) , various platinum-based catalysts are actively used today [1, 2]. In order to reduce the cost of such catalysts and increase their specific characteristics, scientists have proposed various approaches, one of which is the alloying of Pt with various *d*-metals to obtain bi- and trimetallic structures. Alloying with *d*-metals can increase the activity of both the oxygen electroreduction reaction and the alcohols electrooxidation reaction [3–5].

The most popular fuels of the direct alcohol fuel cells (DAFCs) are methanol and ethanol. It is known that the electrocatalytic activity during the oxidation of small

A. K. Nevelskaya (✉) · S. V. Belenov
Chemistry Department, Southern Federal University, Rostov-on-Don, Russia
e-mail: alya.nevelskaya@mail.ru

I. A. Parinov et al. (eds.), *Physics and Mechanics of New Materials and Their Applications*, Springer Proceedings in Materials 10,
https://doi.org/10.1007/978-3-030-76481-4_2

organic molecules in alkaline media is higher than in acidic media [6]. That is why it is promising to study the characteristics of catalysts that have shown high activity in acidic media.

The positive effect of Au atoms included in the composition of various catalysts studied in different media was revealed. Given that both Au and Pt are involved in the catalytic reaction, it is assumed that two factors are important: Au atoms surrounding Pt atom play an important role either in the removal of intermediate particles (such as CO, etc.), or in the providing of oxygen-containing particles in the process of methanol oxidation (Au is able to form such particles in alkaline electrolytes) [7]. It is also well-known that gold nanoparticles have a high catalytical activity for CO oxidation and in alkaline electrolytes gold forms oxygenated particles.

The structure and composition of platinum-based catalysts obviously affect its activity in the ethanol oxidation reaction [8] . Thus, according to the results of the authors [9] in alkaline media the Au@Pd/C catalyst exhibited the highest activity of the ethanol oxidation reaction (EOR) as compared to Pd/C and the $Au_{1-x}Pd_x$/C alloy. At 1.1 V, the catalytic activity of Au@Pd/C was twice as high and at 1.5 V it was almost three times higher than that of the Pd/C catalyst. It is also believed that catalysts based on Pt, in which the Pt component should be widely used, are suitable for the methanol oxidation reaction (MOR) in an alkaline medium [9]. It was also found that, in an acidic medium, precursor catalysts with different Cu content demonstrate an electrochemical activation process, which further affects the rearrangement of Pt/Au atoms on the surface of activated samples. The higher the Cu content in the precursor, the less residual hidden Cu atoms are retained after activation. On the one hand, the leaching of a large amount of copper triggers a rearrangement of Pt/Au atoms on the surface of metal nanoparticles, which allows the use of noble metals as much as possible. On the other hand, the contribution of a synergistic effect such as Cu depletion-induced geometric effect (lattice mismatch, deformation, defects and/or dislocations) and/or electronic modification effect should be another important factor for activated catalysts with high PtAu content [10].

1.1 Research Purpose

The aim of the chapter is to study the activity of PtCuAu/C catalysts with different nanoparticle architectures in the reaction of alcohol electrooxidation in an alkaline medium.

1.2 Research Scope

In this investigation, we consider the following frameworks of the problem:

(i) various methods for the synthesis of trimetallic catalysts and study of the architecture of the resulting nanoparticles;
(ii) the study of the structure effect of obtained PtCuAu/C catalysts on their activity in MOR and EOR.

2 Research Method

2.1 Synthesis of Catalysts

The synthesis of PtCuAu/C catalysts by the method of galvanic substitution and the method of simultaneous precipitation of precursors was carried out according to the procedure developed earlier [11].

The synthesis of PtCuAu/C catalysts by galvanic substitution was carried out in two stages. At the first stage, the PtCu/C material was synthesized by the method of simultaneous reduction of solutions of platinum and copper salts in a water-ethylene glycol suspension of a Vulcan XC72 carbon support. The second stage of the synthesis corresponds to the surface replacement of copper atoms by gold atoms.

The preparation of PtCuAu/C catalysts by the method of simultaneous reduction of precursors was carried out in one stage. The calculated amount of metal salts was added to the water-ethylene glycol suspension of the carbon support. An excess of an aqueous $NaBH_4$ solution was added to the resulting suspension. The initial composition of the catalysts is $PtCu_{0.55}Au_{0.1}$ and $PtCu_{0.52}Au_{0.1}$, obtained in two and one stage, respectively.

The material obtained in one stage was labeled as PtCuAu-1, and in two stages, respectively, as PtCuAu-2.

2.2 Powder X-ray

The phase composition of the materials and the size of the metal crystallites were determined by powder X-ray diffraction on an ARL X´TRA (CuKα) diffractometer, the angle interval 2θ from 15º to 55º with a step of 0.02º and a recording rate of 2º per minute. The average crystallite size was determined by the Scherrer formula:

$$D = K\lambda/(\mathrm{FWHM} \cdot \cos\theta), \tag{1}$$

where $K = 0.98$ is Scherrer's constant, λ is the wavelength of monochromatic radiation in Å, FWHM is the full width of the peak at half maximum (in radians), D is the average crystallite size, nm, θ is the angle of reflection in radians.

2.3 X-ray Fluorescence Analysis

The ratio of Cu:Pt:Au metals in the samples was determined by X-ray fluorescence analysis (XRF) on a spectrometer with complete external reflection of RFS-001 X-rays (Research Institute of Physics of Southern Federal University, Russia). Analysis conditions included: X-ray tube voltage of 50 kV, current of 150 μA, anode material of molybdenum, spectrum acquisition time of 300 s. Registration and processing of X-ray fluorescence spectra was carried out using the UniveRS software (Southern Federal University, Russia).

2.4 Transmission Electron Microscopy

Transmission electron microscopy (TEM) was performed on an FEI Tecnai G2 F20 transmission analytical electron microscope with an EMF attachment EDAX and a STEM detector. Samples for research were prepared by ultrasonic dispersion of a small amount of powder in distilled water for at least 5 min. Then, a few drops of the resulting solution were applied to an object grid with a carbon web. After drying, the dispersed nanoparticles were retained on the bridges of the carbon web, and the object grid was placed in the holder of a transmission electron microscope.

The samples presented were investigated by transmission electron microscopy (TEM) , high-resolution transmission electron microscopy (HRTEM) , and transmission scanning electron microscopy (STEM) using electron probe microprobe analysis of elemental composition (EDX). The studies were carried out at an accelerating voltage of the electron beam of 200 kV.

2.5 Electrochemical Characteristics

The electrochemical characteristics of the obtained catalysts were studied using a three-electrode cell on a rotating disk electrode. The catalytic ink was prepared according to the following procedure: 100 μL of a 0.5% Nafion solution and 900 μL of isopropyl alcohol were added to 0.006 g of the material. The suspension was sonicated for 15 min and mixed for 30 min. Then, 6 μL of the resulting suspension was applied to the work electrode with a pipette. A drop was dried at room temperature for 15 min, then, to fix the catalytic layer, 7 μl of 0.05% Nafion aqueous solution was dropped [12].

Cyclic voltammetry (CV) was performed first to standardize the surface in the potential range from 0.037 to 1.2 V at a potential sweep rate of 200 mV/s in 0.1 M KOH solution saturated with Ar for 30 min. Then, two CVs were registered in the same potential range with a potential sweep rate of 20 mV/s, and the electrochemical surface area (ESA) was measured. The ESA values were calculated from the average

value of the amount of electricity consumed for the adsorption and desorption of atomic hydrogen. All potentials in this work are given relative to the potential of a reversible hydrogen electrode (RHE); a silver chloride electrode was used as a reference electrode.

The activity of the obtained materials in the oxidation reaction of alcohols was studied by the CV method with the addition of 0.5 M CH_3OH / 0.5 M C_2H_5OH to electrolyte in the potential range from 0.175 to 1.375 V at a potential sweep rate of 20 mV/s. To assess the tolerance to intermediate oxidation products of methanol and ethanol, chronopotentiograms were recorded at a potential of 0.72 V for 30 min [9].

3 Results and Discussion

According to the powder diffraction data, the Pt peak 111 face for the synthesized materials is shifted towards large 2θ angles as compared to the peak for pure platinum (Fig. 1). This indicates the formation of a Pt-Cu solid solution. The crystallite sizes were calculated using the Scherrer equation and the crystal lattice parameter, 2, 2.6, and 3.8 nm, as well as 3.82, 3.83, and 3.92 Å for the PtCuAu-2, PtCuAu-1, and Pt/C catalysts, respectively. The X-ray diffraction pattern of the material obtained by the method of simultaneous reduction of the precursors of platinum, copper and gold in the liquid phase shows additional reflections corresponding to the gold phase about 15–20 nm in size. At the same time, no reflections corresponding to the gold phase are observed on the X-ray diffraction pattern of the material obtained in two stages, which does not exclude the presence of a certain amount of gold in the form of an amorphous phase.

According to the TEM results, the PtCuAu-1 catalyst has a narrower size distribution, as well as a lower average nanoparticle size compared to the PtCuAu-2 catalyst, 2.8 and 6.5 nm, respectively. It can be seen from the TEM photographs (Fig. 2) of the obtained catalysts that the trimetallic nanoparticles are fairly uniformly distributed over the carbon surface; however, a certain amount of agglomerates can also be noted .

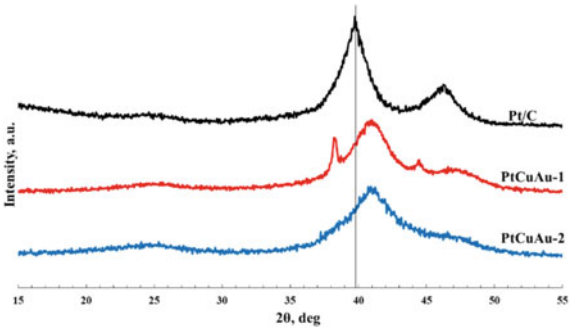

Fig. 1 X-ray diffraction patterns of synthesized materials and commercial Pt/C

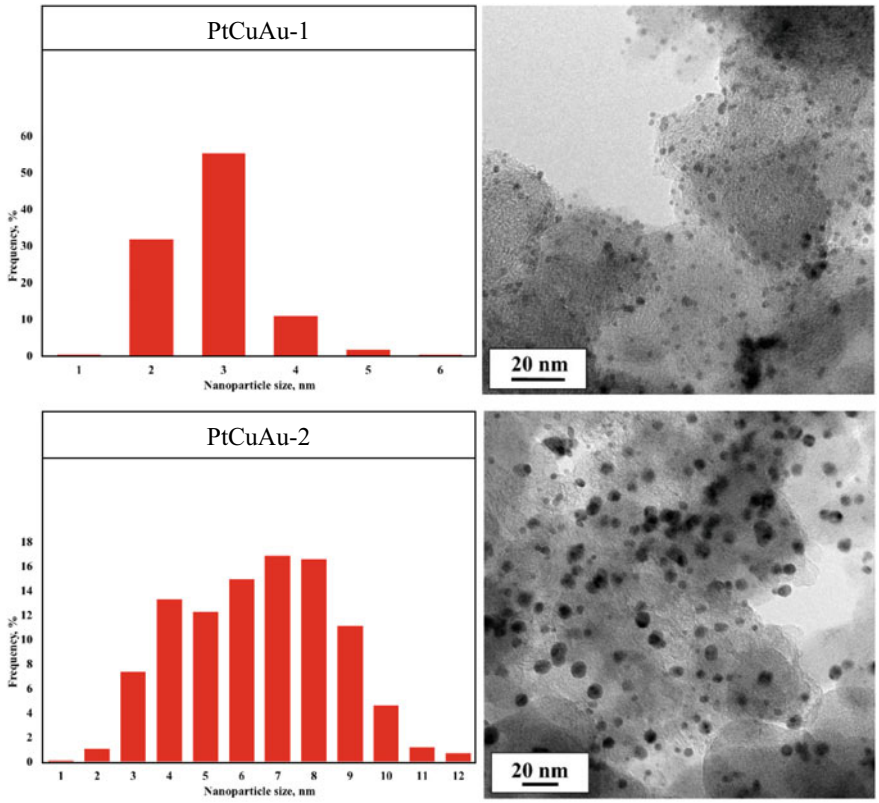

Fig. 2 Particle size distribution and TEM images of catalysts PtCuAu-1 and PtCuAu-2

The study of PtCuAu-1 and PtCuAu-2 materials by transmission scanning electron microscopy with elemental mapping of individual regions (Figs. 3, 4) showed the predominant formation of trimetallic nanoparticles containing gold, platinum and copper atoms on the surface of the carbon support. This fact confirms the formation of trimetallic nanoparticles in the obtained PtCuAu materials, rather than individual monometallic nanoparticles. Nevertheless, for the PtCuAu-2 material (Fig. 4), the presence of individual nanoparticles is noticeable, which practically do not contain platinum atoms, so in this case we can speak of the formation of individual CuAu nanoparticles on the surface of the carbon support. This fact can be associated with a two-stage method of obtaining this material, namely, with the deposition of copper ions that have passed into the solution in the process of galvanic substitution together with gold ions. Unfortunately, the spatial resolution of elemental mapping does not allow one to prove an increased content of gold atoms on the surface of trimetallic PtCuAu nanoparticles obtained by the method of galvanic substitution.

Based on the results of cyclic voltammetry, the ESA of the catalysts was calculated, equal to 43, 16, and 18 m^2/g (Pt) for the Pt/C, PtCuAu-2, and PtCuAu-1

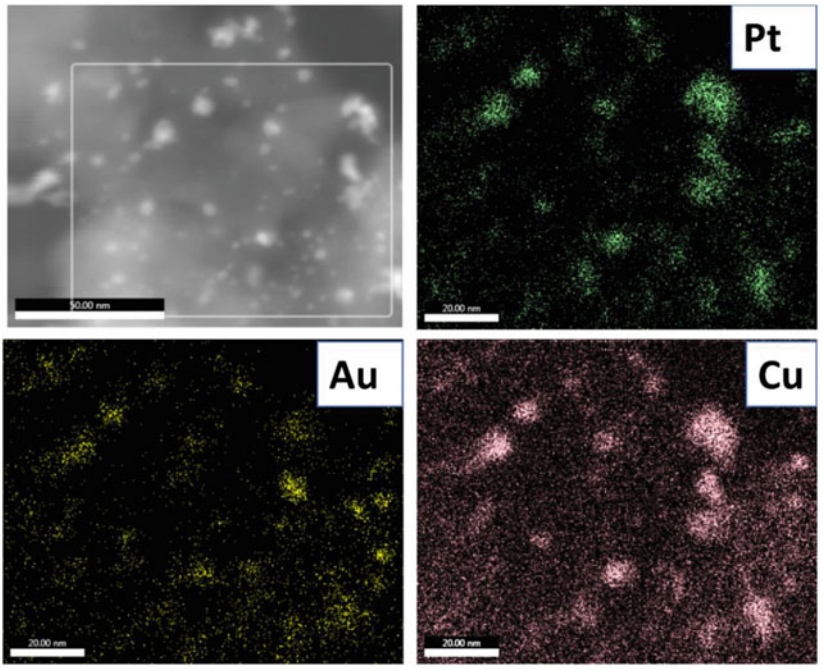

Fig. 3 The results of mapping the elemental and phase composition of the particles of the PtCuAu-1 sample: STEM image of the mapped area and a map of the distribution of chemical elements with a color scheme for matching elements

catalysts, respectively. This is due to the fact that catalysts based on Au exhibit weak adsorption of H_2 [13] in contrast to catalysts based on Pt or Pd, which exhibit stronger adsorption of H_2. The cyclic voltammogram for Pt/C-material (Fig. 5) has a typical shape characteristic of platinum-containing catalysts in an alkaline media. Materials PtCuAu-2 and PtCuAu-1 are characterized by almost identical CV shapes.

According to the results of CV in an electrolyte containing alcohols, the activity of the obtained catalysts in the reaction of ethanol electrooxidation is higher than that of the commercial Pt/C catalyst. This can be judged by the potential for the onset of ethanol oxidation (Fig. 6). For the synthesized materials, a shift in the potential of the onset of ethanol oxidation to the region of more negative potentials compared to the Pt/C catalyst was recorded (0.36 V, 0.40 V, and 0.50 V for PtCuAu-1, PtCuAu-2, and Pt/C, respectively). However, in the methanol electrooxidation reaction, the more active catalyst is PtCuAu/C obtained by the method of joint reduction of metal precursors (0.54 V, 0.58 V, and 0.56 V for PtCuAu-1, PtCuAu-2, and Pt/C, respectively).

The chronoamperometry results show that for the synthesized PtCuAu/C catalysts, a higher initial value of the specific current of ethanol oxidation (399 and 319 A/g (Pt) for PtCuAu-1 and PtCuAu-2, respectively) is observed in comparison with the Pt/C catalyst (197 A/g (Pt)) (Fig. 7b). However, in the methanol oxidation reaction, a

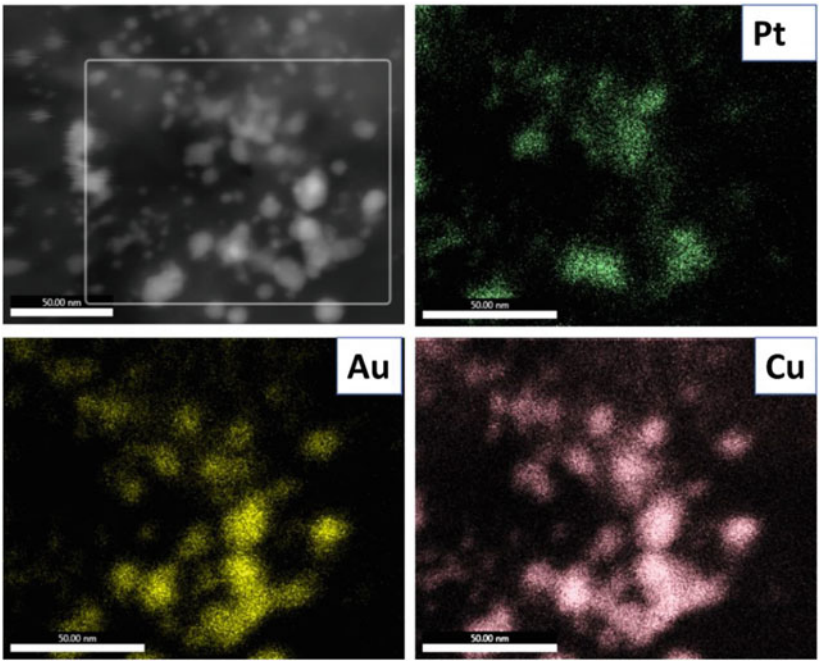

Fig. 4 The results of mapping the elemental and phase composition of the particles of the PtCuAu-2 sample: STEM image of the mapped area and a map of the distribution of chemical elements with a color scheme for matching elements

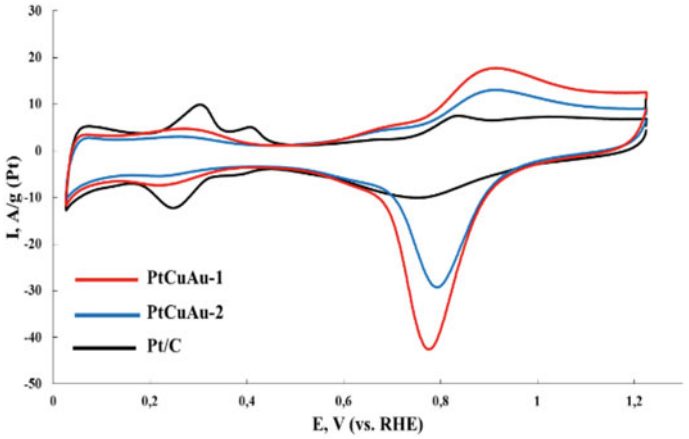

Fig. 5 Cyclic voltammograms in 0.1 M KOH (Ar) of the Pt/C, PtCuAu-2, and PtCuAu-1 catalysts

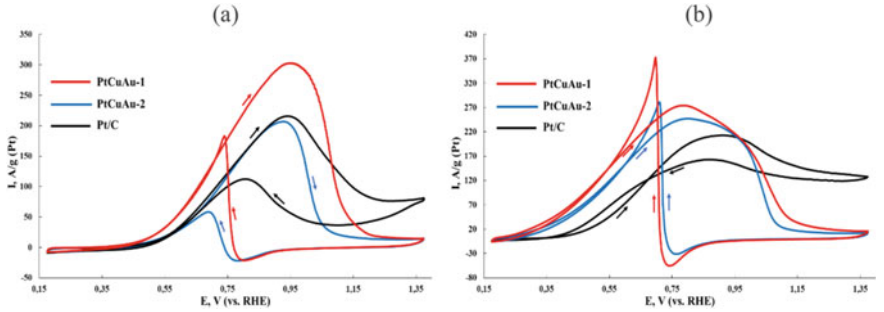

Fig. 6 Cyclic voltammograms of Pt/C, PtCuAu-2 and PtCuAu-1 catalysts **a** 0.1 M KOH (Ar) + 0.5 M CH_3OH, **b** 0.1 M KOH (Ar) + 0.5 M C_2H_5OH

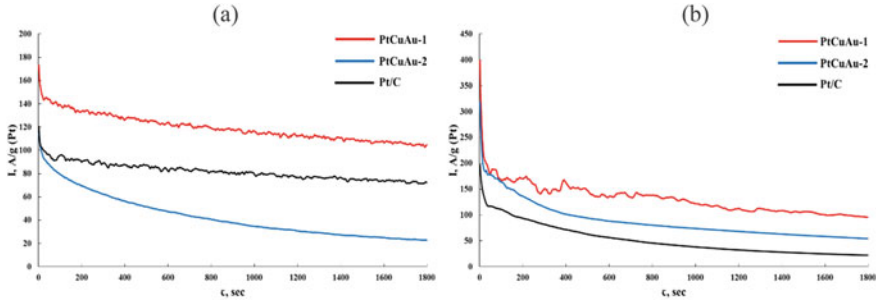

Fig. 7 Chronoamperograms of Pt/C, PtCuAu-2 and PtCuAu-1 catalysts **a** 0.1 M KOH (Ar) + 0.5 M CH_3OH, **b** 0.1 M KOH (Ar) + 0.5 M C_2H_5OH

higher initial value of the specific current of alcohol oxidation is characteristic only of the PtCuAu-1 material (173, 114, and 120 A/g (Pt) for PtCuAu-1, PtCuAu-2, and Pt/C, respectively). The result obtained correlates well with the data on the activity of materials obtained by the CV method.

4 Conclusion

I the result of the study, trimetallic catalysts with different nanoparticle architectures were studied. According to the results of the CV method with an electrolyte containing alcohols, in the oxidation of methanol and ethanol, PtCuAu-1 catalyst is the most active in comparison with PtCuAu-2 and Pt/C material. The results of chronoamperometry show that for the synthesized PtCuAu-1 and PtCuAu-2 catalysts, a higher initial value of the specific current of ethanol oxidation is observed

in comparison with the Pt/C catalyst. Thus, catalysts containing trimetallic nanoparticles can exhibit higher activity in the oxidation of ethanol in an alkaline media, regardless of the synthesis method.

Acknowledgements This research was financially supported by the Ministry of Science and Higher Education of the Russian Federation (State assignment in the field of scientific activity No 0852-2020-0019).

References

1. S.S. Siwal, S. Thakur, Q.B. Zhang, V.K. Thakur, Materials Today Chemistry **14**, 100182 (2019)
2. N. Jung, D.Y. Chung, J. Ryu, S.J. Yoo, Y.-E. Sung, Nano Today **9**(4), 433 (2014)
3. X. Wang, L. Zhang, H. Gong, Y. Zhu, H. Zhao, Y. Fu, Electrochim. Acta **212**, 277 (2016)
4. X. Cai, R. Lin, D.D. Shen, Y. Zhu, ACS Appl. Mater. Interfaces **11**, 29689 (2019)
5. G. Chen, X. Yang, Z. Xie, F. Zhao, Z. Zhou, Q. Yuan, J. Colloid Interface Sci. **562**, 244 (2019)
6. A. Santasalo-Aarnio, Y. Kwon, E. Ahlberg, K. Kontturi, T. Kallio, M.T.M. Koper, Electrochem. Commun. **13**(5), 466 (2011)
7. J. Luo, P.N. Njoki, Y. Lin, D. Mott, L. Wang, C.-J. Zhong, Langmuir **22**(6), 2892 (2006)
8. L.S.R. Silva, C.V.S. Almeida, C.T. Meneses, E.A. Batista, S.F. Santos, K.I.B. Eguiluz, G.R. Salazar-Banda, Appl. Catal. B **251**, 313 (2019)
9. J. Wang, N. Cheng, M.N. Banis, B. Xiao, A. Riese, X. Sun, Electrochim. Acta **185**, 267 (2015)
10. M. Wang, Y. He, R. Li, Z. Ma, Z. Zhang, X. Wang, Electrochim. Acta **178**, 259 (2015)
11. A.A. Alekseenko, V.E. Guterman, S.V. Belenov, V.S. Menshikov, NYu. Tabachkova, O.I. Safronenko, E.A. Moguchikh, Int. J. Hydrogen Energy. **43**(7), 3676 (2018)
12. S.V. Belenov, V.S. Men'shchikov, A.Y. Nikulin, N.M. Novikovskii. Russ. J. Electrochem. 56(8), 660 (2020)
13. Z. Zhang, L. Xin, J. Qi, D.J. Chadderdon, W. Li, Appl. Catal. B **136–137**, 29 (2013)

Influence of Acid Treatment on the Functional Characteristics of PtCu/C Electrocatalysts

Angelina Pavlets, Anastasia Alekseenko, and Alexey Nikulin

Abstract Two-component catalysts based on Pt-M bimetallic nanoparticles distributed on carbon support are very promising for use in low-temperature fuel cells with a proton-exchange membrane (PEM FC). At the first stage, it is necessary to obtain materials with high activity toward ORR and increased stability in stress test to use PtCu/C catalysts in PEM FC. At the second stage, it is necessary to carry out additional acid treatment of the catalysts in order to remove copper from the surface layer to minimize its selective dissolution, because it is known that Cu^{2+} cations can contaminate the polymer membrane, reducing its proton conductivity. In this work, we determined the structural parameters and composition, and also studied the electrochemical behavior of PtCu/C catalysts containing nanoparticles with a "gradient" structure in the initial state (as obtained) and after pretreatment in solutions of acid. Comparative determination of the activity of the catalysts showed that the pretreatment PtCu/C materials, which have a significantly higher stability compared to Pt/C, are not inferior to the latter in terms of their activity in the oxygen electroreduction reaction.

Keywords Pt/c · Electrocatalysts · Nanoparticles (NPs) · PtCu/C · Stability · Durability · Fuel cell (PEM FC) · Active surface area (ESA) · ORR

1 Introduction

The modern scientific community is actively developing clean and efficient energy conversion systems. The search for new resources in alternative energy has become necessary due to the serious energy crisis, as well as global environmental pollution, which have arisen in the result of excessive consumption of fossil fuels [1]. A low-temperature fuel cell with a proton exchange membrane is a promising device for converting the energy of chemical bonds into electric current with high efficiency [2].

A. Pavlets (✉) · A. Alekseenko · A. Nikulin
Chemistry Department, Southern Federal University, Rostov-on-Don, Russia
e-mail: angelina.pavlez@mail.ru

I. A. Parinov et al. (eds.), *Physics and Mechanics of New Materials and Their Applications*, Springer Proceedings in Materials 10,
https://doi.org/10.1007/978-3-030-76481-4_3

Composite materials based on platinum nanoparticles (NPs) are used as catalysts for PEM FC. It is known that Pt/C electrocatalysts are highly active in current-forming reactions such as the oxygen reduction reaction (ORR) [2, 3]. However, the widespread application of Pt catalysts is limited by the high price of the noble metal, low functional characteristics, and relatively low stability of such materials during operation [3].

To improve the functional characteristics of electrocatalysts, platinum is doped with less noble metals, such as copper, cobalt, nickel, iron, silver [4, 5]. There are numerous experimental data indicating a significant increase in the activity of bimetallic catalysts in ORR in comparison with standard Pt/C catalysts [4, 5].

The positive effect of the alloying component is due to a decrease in the interatomic distance in the crystal lattice of NPs, which facilitates the adsorption of oxygen molecules during the reaction [2, 6, 7]. Nørskov et al. showed that the use of PtM/C as ORR catalysts allows one to reduce the Pt-O bond energy, which increases the activity of such materials in comparison with composites based on pure platinum [7]. Bimetallic PtCu/C have been proven as highly active and highly stable ORR catalysts [8, 9]. Such systems are convenient to development new methods of synthesis, the study of electrochemical behavior and evolution of nanoparticles [9]. Varying the composition, controlling the architecture, size, dispersion and distribution of NPs over the support surface allows one to obtain catalysts with high electrochemical characteristics [8–10]

Materials containing bimetallic nanoparticles with *d*-metal are susceptible to selective dissolution of the alloying component, which may negatively affect the operation of the polymer membrane [5]. To solve this problem, as well as to increase the promoting effect of a less noble metal, an approach was proposed to obtain bimetallic NPs of the core (*M*)–shell (Pt) type. This method allows not only to reduce the content of expensive platinum, but also to significantly increase the efficiency of the catalyst in current-forming reactions and to reduce the tendency of the material to degrade during operation [8, 10, 11].

More novel and interesting is the approach to obtaining *M*@Pt systems with a gradient transition from a metal core to a platinum shell [12]. Layer-by-layer growth of an enriched platinum shell and smoothing of the transition between the crystal lattice of the *d*-metal and platinum, makes it possible to obtain a thermodynamically more stable system in comparison with the structure of a solid solution and pure platinum. Unfortunately, there are a number of problems associated with the obtaining of PtCu NPs of this type: (i) the formation of a copper core (oxidation of the copper surface, amorphous structure, large NPs size); (ii) deposition of precursors at subsequent stages on the formed nuclei; (iii) obtaining systems with reduced selective dissolution of copper.

Unfortunately, it is seemed impossible to apply a plurality of platinum-copper nanoparticles with a defect-free platinum shell to the surface of a carbon support and thereby prevent selective dissolution of copper. Earlier, we found that at the initial stage of electrochemical standardization of $PtCu_x$/C catalysts, an intense selective dissolution of copper occurs, while further, during stress test, the change in the Pt:Cu ratio is much less pronounced [13]. This made it possible to conditionally divide

the presented copper in the catalysts into "weak" (quickly and easily solved) and "strongly bound" (dissolves at a low rate under the conditions of subsequent stress test). We believe that the removal of "weakly bound" copper from two-component PtCu catalysts can be carried out not only electrochemically, but also by means of pretreatment in acid solutions, which opens the way for the further use of de-alloyed PtCu catalysts in PEM FC.

We have proposed a new approach to the preparation of PtCu/C electrocatalysts with a "gradient" nanoparticle structure by a multistage synthesis method. The acid treatment of the finished electrocatalyst is an additional stage of synthesis. Note that such pretreatment of PtM catalysts in acid is considered as a vital step in their preparation by various authors [8, 11, 14–17].

We believe that a bimetallic system with a gradient distribution of components is more efficient in ORR (and MOR), more quickly standardizes upon electrochemical activation (EA), and exhibits higher activity after stress tests compared to a commercial Pt/C catalyst. At the same time, the removed part of copper during acid treatment has no effect when the material is used in the MEA, and the catalysts will also have a more constant composition even during prolonged durability test.

1.1 Research Purpose

Structural and electrochemistry characteristic of PtCu/C catalysts with de-alloyed core–shell architecture is studied.

2 Experimental Part

2.1 Preparation of PtCu/C Catalysts

The method of synthesis is a modification of the method for obtaining "gradient" nanoparticles proposed earlier by A. Alekseenko et al. [12]. The synthesis of PtCu/C electrocatalysts was carried out by sequential multistage reduction of platinum ($H_2PtCl_6 \cdot 6H_2O$) and copper ($CuSO_4 \cdot 5H_2O$) precursors in an aqueous organic medium (water–ethylene glycol). Vulcan XC-72 graphitized carbon black was used as a support. The synthesis was carried out in an alkaline medium (NaOH, pH ~ 10); sodium borohydride ($NaBH_4$) was used as a reducing agent. Thus, three materials were obtained with different loading of Pt at the first stage of the synthesis, labeled as PtCu/C-1, PtCu/C-2, PtCu/C-3.

Then, the acid treatment of the obtained catalysts with 1 M nitric acid was carried out for 3 h with stirring, as a result of which three samples of PtCu/C-*n*-AC (where $n = 1, 2, 3$) were obtained.

2.2 Characterization of the Catalysts Structure

The atomic ratio of Pt: Cu metals in PtCu/C was determined by the X-ray fluorescence analysis (XRFlA) on a spectrometer with total external reflection of the X-ray radiation RFS-001 (Scientific Research Institute of Physics, Southern Federal University, Rostov-on-Don). Sample exposure time is 300 s. Registration and processing of the X-ray fluorescence spectra was carried out with the UniveRS software (Southern Federal University, Rostov-on-Don). The mass fractions of metals in the samples were determined by the gravimetric method of analysis taking into account the atomic ratio of metals.

To determine the average crystallite size, the X-ray phase analysis (XRD) was used. The X-ray diffractograms of PtCu/C materials were recorded in the angle range $2\theta = 15°–55°$ on an ARL X'TRA diffractometer (Thermo Fisher Scientific, Switzerland) using filtered CuKα radiation ($\lambda = 0.154056$ nm) at room temperature. The calculation of D_{av} was carried out for a characteristic reflection of 111 by the Scherrer formula for the most intense peak.

The microstructure of the samples was studied by transmission electron microscopy (TEM) . Photographs were taken with a JEM-2100 microscope (JEOL, Japan) at a voltage of 200 kV and a resolution of 0.2 nm.

2.3 Electrochemical Measurements

Electrochemical measurements of the catalysts were performed using an VersaSTAT 3 potentiostat in a standard three-electrode configuration at room temperature. A platinum wire was used as the counter electrode; a silver chloride electrode was used as the reference electrode. All reported potentials are relative to a reversible hydrogen electrode (RHE). A commercial catalyst was used as a standard Pt/C analog–JM20 (HiSPEC3000, Jonson Mattews, 20 wt.% Pt).

A thin film of the studied catalyst was deposited on a glassy carbon (GC) electrode to prepare the working electrode. The mixture of 900 μL of isopropanol and 100 μL of an aqueous emulsion of Nafion® 0.5% polymer was added to 6 mg of the catalyst to prepare catalytic ink. The suspension was thoroughly mixed and dispersed with ultrasound. The catalyst ink of 6 μl was then quantitatively put on the rotating disk electrode (RDE) by using a micropipette and dried in air atmosphere.

Electrochemical measurements were carried out in 0.1 M HClO4 in Ar (CV) and O_2 (LSV) atmospheres. Before electrochemical measuring each catalyst was electrochemically activated by 100 potential cycles in the potential range of 0.04–1.2 V at a scan rate of 200 mV/s. Then, two cycles were recorded with a scan rate of 20 mV/s in the potential range of 0.04–1.2 V to determine the electrochemically active surface area (ESA) . The ESA of catalyst was calculated by integrating the area in the hydrogen underpotential deposition (HUPD) region, taking into account

that the average charge density spent on the formation of one monolayer hydrogen atom on a polycrystalline of Pt electrode is 210 $\mu C/cm^2$.

The oxygen reduction reaction activity of the samples was evaluated by performing linear sweep voltammetry (LSV) in the potential range 0.1–1.2 V at a scan rate of 20 mV/s under a certain rotating speed (400, 900, 1600, 2500 rpm). The kinetic current at 0.9 V was calculated by using the Koutetsky–Levich equation: $1/j = 1/j_k + 1/j_d$, where j is the experimentally measured current, j_d is the diffusion current, and j_k is the kinetic current.

The durability test was investigated by repeated CV scanning cycles up to 5000 cycles between 0.6 V and 1.0 V at a sweep rate of 100 mV/s [17]. After 1000, 3000 and 5000 CV ESA was measured by the above method. The catalytic activity of the electrodes after the durability test was also studied and compared.

3 Results and Discussion

Initially, in the course of the study, a number of PtCu/C materials were obtained with a close mass fraction of Pt from 22.0 to 24.3 wt. % (Table 1). The obtained samples are characterized by a close atomic ratio of metals from $PtCu_{0.67}$ to $PtCu_{0.79}$ (Table 1). After acid treatment, the copper content in all samples is reduced by almost two times (Table 1).

All of PtCu/C samples are characterized by a small average crystallite size (less than 3 nm), which is calculated using the Scherrer equation (Table 1). A graphitized carbon peak (200) of $2\theta = 25$ is identified on diffractograms (Fig. 1). The most intense peak of the face (111) is shifted towards large angles of 2θ, which is a consequence of the alloying of Pt and Cu. Another evidence of alloying the components is the absence of peaks of the pure Pt and Cu. The fact that the peak of the face (111) is between the peaks of pure platinum and copper may be related to the effect of lattice deformation of the platinum shell caused by the Cu or Pt-Cu core [6].

Table 1 Structural characteristics of obtained PtCu/C electrocatalysts

Sample	Metals loading, wt. %	Pt loading, wt. %	Average crystallite size, nm (XRD)	Position of (111) maximum, 2θ, degrees	Composition
PtCu/C-1	27.9	22.2	2.7	41.3	$PtCu_{0.79}$
PtCu/C-1-AC	24.1	21.4	2.7	40.8	$PtCu_{0.39}$
PtCu/C-2	27.0	22.0	2.5	41.2	$PtCu_{0.70}$
PtCu/C-2-AC	23.2	20.9	2.7	41.0	$PtCu_{0.34}$
PtCu/C-3	29.6	24.3	2.7	41.4	$PtCu_{0.67}$
PtCu/C-3-AC	24.8	22.2	2.9	40.8	$PtCu_{0.36}$

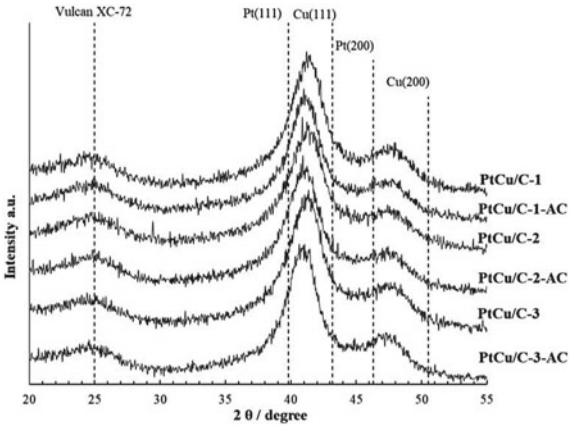

Fig. 1 XRD patterns of obtained PtCu/C materials

As expected, after forced leaching of copper, the peak of the face (111) shifts towards smaller angles of 2θ, which is due to the lower copper content in the PtCu/C-*n*-AC samples compared to PtCu/C-*n* (Fig. 1, Table 1). Also, in all XRD patterns, the peaks corresponding to CuO and Cu_2O are not identified, however, their absolute absence cannot be ruled out, since copper oxides can be in an amorphous state.

Transmission electron microscopy was performed on one of the PtCu/C samples and its corresponding acid-treated analog (Fig. 2). The initial catalyst is characterized by the presence of particles with a core–shell structure of small size of about 5 nm (Fig. 2a), which indicates the success of the applied synthesis method. After acid treatment, this structure is also retained, which may indicate leaching only of the surface copper (Fig. 2b). It is also worth noting that, after acid treatment, the presence of homogeneous nanoparticles of small size (no more than 2–3 nm) is observed in the sample; apparently, of pure Pt.

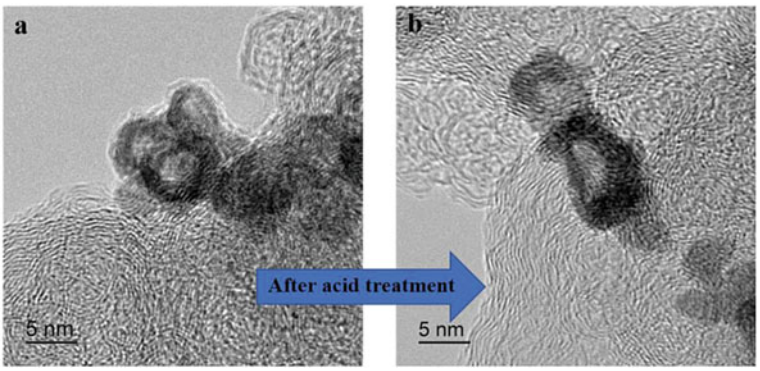

Fig. 2 TEM of the one of PtCu/C electrocatalysts before (**a**) and after (**b**) acid treatment

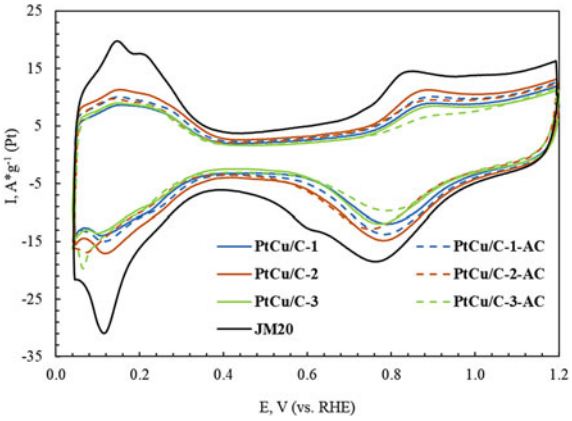

Fig. 3 Cyclic voltammograms of commercial Pt/C and PtCu/C electrodes after electrochemical activation, 0.1 M $HClO_4$, Ar atmosphere, scan rate is 20 $mV \cdot s^{-1}$

Figure 3 shows the cyclic voltammograms of the native and acid-treated PtCu/C samples, as well as the commercial Pt/C analog after electrochemical activation. The CV type is typical for Pt-polycrystalline electrode. Voltammograms show areas of hydrogen underpotential deposition (HUPD) between 0.05 and 0.4 V, as well as areas of formation and reduction of Pt-O in the range of 0.7–1.0 V. For PtCu/C samples, there are no features of Cu bulk dissolution (Fig. 3), which may indicate both the absence of copper on the nanoparticles surface and the possible chemical dissolution of Cu. With a cathodic sweep in the range of 0.7–1.2 V, all bimetallic catalysts (except for PtCu/C-2-AC) exhibit lower overpotential on the oxide reduction than the commercial analogue JM20 [15].

ESA determined by hydrogen adsorption/desorption on CV are close for PtCu/C and range from 41 to 52 m^2g^{-1} (Pt) (Table 2). It should be noted that acid treatment did not have a clear effect on the active surface area. Thus, for the PtCu/C-1-AC sample, ESA increases in comparison with the native sample, while the PtCu/C-2-AC sample loses 11 m^2g^{-1} (Pt) (Table 2). In this regard, it can be assumed that

Table 2 Electrochemical characteristics and composition of the PtCu/C and Pt/C electrocatalysts after electrochemical activation (EA)

Sample	Composition after EA	ESA, $A \cdot g^{-1}$ (Pt)	I_k, mA	I_{mass}, $A \cdot g^{-1}$ (Pt)	I_{sp}, $A \cdot m^{-2}$ (Pt)	Number of $\bar{e}$	$E_{1/2}$, V
PtCu/C-1	$PtCu_{0.32}$	43 ± 4	1.92	255	5.4	3.8	0.92
PtCu/C-1-AC	$PtCu_{0.26}$	50 ± 5	1.75	222	4.4	4.1	0.92
PtCu/C-2	$PtCu_{0.23}$	52 ± 5	2.50	317	8.9	4.1	0.93
PtCu/C-2-AC	$PtCu_{0.24}$	41 ± 4	1.66	222	5.4	4.4	0.91
PtCu/C-3	$PtCu_{0.26}$	52 ± 5	3.23	381	7.4	3.9	0.93
PtCu/C-3-AC	$PtCu_{0.27}$	48 ± 5	2.62	332	7.0	3.8	0.92
JM20	–	80 ± 8	1.37	180	2.2	3.8	0.92

during the chemical and electrochemical treatment of catalysts, the formation of super-porous structures does not occur for the Pt-Cu obtained systems [16].

Based on Table 2, the samples are characterized by close values of the metal ratio after electrochemical measurements. The advantage of acid treatment of PtCu/C electrocatalysts appears to be observed. For example, during the electrochemical activation, the copper content in the PtCu/C-2 sample decreases by a factor of 3, while for the PtCu/C-2-AC sample, this value is 1.4 times. Thus, during the preliminary acid treatment, the catalyst surface is standardized due to the dissolution of the alloying component unprotected by the platinum shell. It is also possible to estimate what amount of copper dissolves during the reorganization of the NPs surface during potential cycling. In general, the obtained results indicate a fairly high stability of the pretreated Pt-Cu nanoparticles.

Figure 4a shows the ORR polarization curves with potentials of the ORR onset (inset in Fig. 4a). As seen from Fig. 4a, the ORR curve of a commercial catalyst is shifted to lower potentials. Despite the fact that the surface area of the commercial Pt/C catalyst is still higher than for the PtCu/C samples, the latter are characterized by a higher activity in the oxygen reduction reaction (Table 2). So, according to the mass activity, the initial samples can be arranged in a row: PtCu/C-3 > PtCu/C-2 > PtCu/C-1 > JM20. The same situation is observed for acid-treated materials: PtCu/C-3-AC > PtCu/C-2-AC = PtCu/C-1 > JM20 (Table 2). According to the potential of the ORR onset, all electrocatalysts can be arranged as follows: PtCu/C-2 > PtCu/C-3 > PtCu/C-1-AC > PtCu/C-3-AC > PtCu/C-1 > PtCu/C-2-AC = JM20 (inset in Fig. 4a). As can be seen from the presented rows, bimetallic catalysts are characterized by better catalytic activity in ORR in comparison with commercial Pt/C.

Figure 4b shows straight lines in the Koutetsky–Levich coordinates. Based on the *y*-intercept coefficient of the line, it can be concluded that the PtCu/C samples are characterized by higher specific currents. High values of the correlation coefficients indicate the correctness and high accuracy of the measurements (Fig. 4b). Moreover, based on the equations of straight lines, the determined number of electrons in the reaction is close to 4 (Table 2), which indicates the minimum occurrence of side reactions.

After acid treatment, the mass and specific activity of PtCu/C-*n*-AC materials slightly decreases compared to the starting PtCu/C-*n* materials, but still remains higher than for the commercial analogue.

The stability of PtCu/C-1, PtCu/C-2, as well as their acid-treated analogs and commercial Pt/C, was evaluated by long-term stress test for 5000 voltampere cycles. The choice of these materials is due to the fact that the native PtCu/C samples are characterized by different mass activities, and their acid-treated analogs are similar in parameters.

The composition of the catalysts after the durability test changed insignificantly (Tables 2 and 3), which confirms the stability of the composition of bimetallic NPs. As can be seen from the histogram in Fig. 5a, the PtCu/C-2-AC sample is characterized by the highest stability equal to 94%, while the lowest value for commercial Pt/C material is 78%. It can also be seen from the histogram that the degradation rate of a commercial sample is higher than for Pt-Cu materials. The residual ESA value

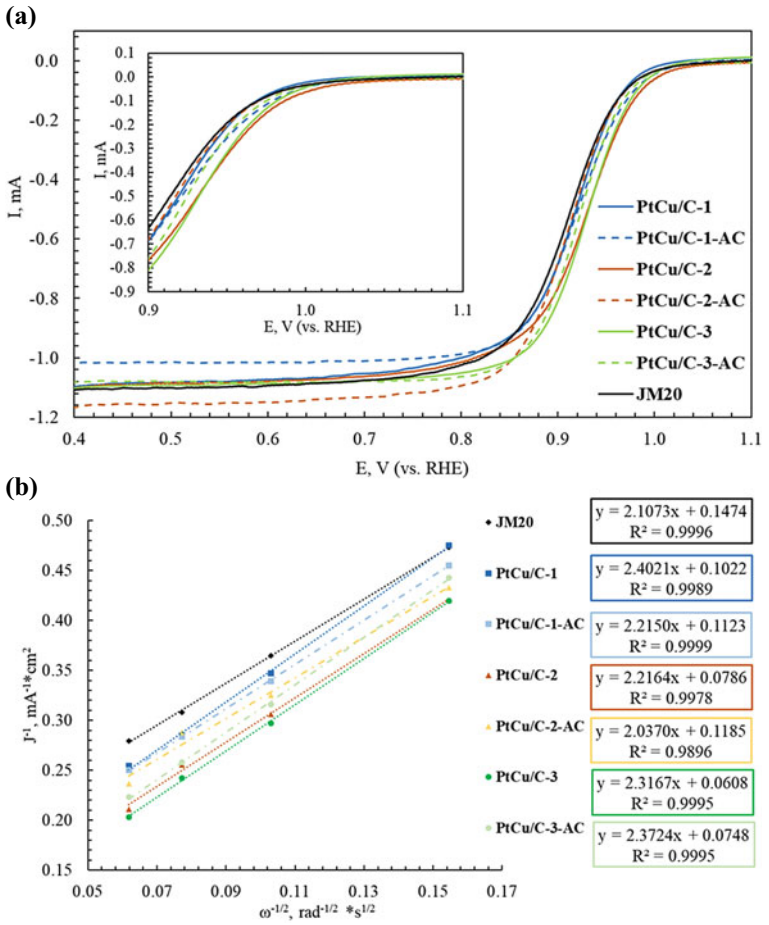

Fig. 4 **a** ORR polarization curves, 0.1 M $HClO_4$, O_2 atmosphere the rotation speed of the disk is 1600 rpm, scan rate is 20 mV·s^{-1}; **b** j^{-1}–$\omega^{-1/2}$ dependences at 0.90 V potential for obtained PtCu/C and Pt/C electrodes

Table 3 Electrochemical characteristics and composition of the PtCu/C and Pt/C electrocatalysts after stress test

Sample	Composition	ESA, A·g^{-1} (Pt)	I_{mass}, A·g^{-1} (Pt)	I_{sp}, A·m^{-2} (Pt)	Number of ē	$E_{1/2}$, V
PtCu/C-1	$PtCu_{0.29}$	37	300	8.0	3.9	0.92
PtCu/C-1-AC	$PtCu_{0.25}$	42	311	7.4	4.1	0.92
PtCu/C-2	$PtCu_{0.22}$	45	210	6.2	4.0	0.92
PtCu/C-2-AC	$PtCu_{0.21}$	45	340	9.4	4.4	0.91
JM20	–	62	59	1.0	4.1	0.89

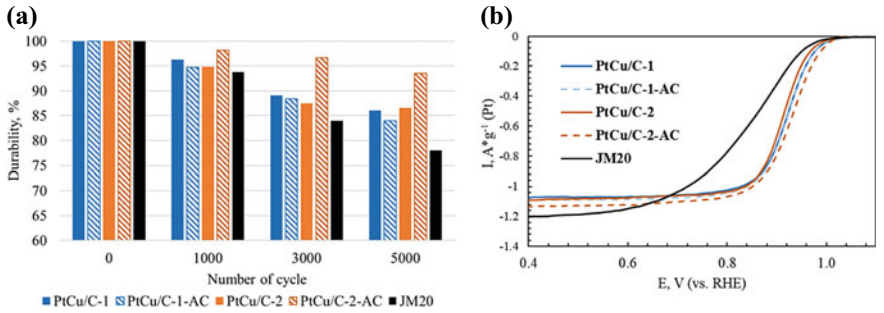

Fig. 5 **a** Relative ESA change during durability test and **b** ORR polarization curves of PtCu/C and Pt/C samples after durability test, 0.1 M $HClO_4$, O_2 atmosphere the rotation speed of the disk is 1600 rpm, scan rate is 20 $mV \cdot s^{-1}$

after stress test is the highest for PtCu/C-2 and PtCu/C-2-AC materials among all of obtained catalysts (Table 3). It should be noted that the PtCu/C-2-AC sample is characterized by the highest catalytic activity after the durability test: its mass activity exceeds that for the commercial one by 5.8 times, and the specific activity is 9.4 times higher (Table 3).

Figure 5b shows the polarization curves of the investigated materials after the durability test. The commercial analogue JM20 showed the greatest changes in the diffusion-kinetic region, which also indicates a high degradation of the material.

4 Conclusion

In this study, three PtCu/C materials were obtained, which were further treated with nitric acid. Comparison of performances showed that bimetallic catalysts are characterized by a small nanoparticle size (about 5 nm), a core–shell structure, and a high catalytic activity. Acid pretreatment of PtCu/C catalysts have shown some advantages: (i) it allows one to get rid of surface copper and stabilizes the NPs composition during measurements; (ii) it increases the stability of the electrocatalyst. The first advantage is a vital condition for the further use of bimetallic catalysts in real PEM FC.

Acknowledgements This research was supported by the Russian Science Foundation (grant No. 20-79-10211).

References

1. S. Chu, A. Majumdar, Nature **488**, 294 (2012)
2. M. Debe, Nature **486**, 43 (2012)
3. Y. Nie, L. Li, Z. Wei, Chem. Soc. Rev. **44**(8), 2168 (2015)
4. N. Jung, D.Y. Chung, J. Ryu, S.J. Yoo, Y.E. Sung, Nano Today **9**(4), 433 (2014)
5. V.E. Guterman, T.A. Lastovina, S.V. Belenov, N.Y. Tabachkova, V.G. Vlasenko, I.I. Khodos, E.N. Balakshina, J. Solid State Electrochem. **18**(5), 1307 (2013)
6. P. Strasser, S. Koh, T. Anniyev, J. Greeley, K. More, C. Yu, Z. Liu, S. Kaya, D. Nordlund, H. Ogasawara, M.F. Toney, A. Nilsson, Nature Chem **2**, 454 (2010)
7. J.K. Nørskov, J. Rossmeisl, A. Logadottir, L. Lindqvist, J.R. Kitchin, T. Bligaard, H. Jónsson, J. Phys. Chem. B **108**(46), 17886 (2004)
8. J. Garcia-Cardona, I. Sirés, F. Alcaide, E. Brillas, F. Centellas, P.L. Cabot, Int. J. Hydrogen Energy **45**(10), 20582 (2020)
9. N. Hodnik, M. Bele, A. Recnik, N.Z. Logar, M. Gaberšček, S. Hočevar, Energy Procedia **29**, 208 (2012)
10. N. Hodnik, C. Jeyabharathi, J.C. Meier, A. Kostka, K.L. Phani, A. Rečnik, M. Bele, S. Hočevar, M. Gaberšček, K.J.J. Mayrhofer, Phys. Chem. Chem. Phys. **16**(27), 13610 (2014)
11. M. Oezaslan, F. Hasché, P. Strasser, J. Phys. Chem. Lett. **4**(19), 3273 (2013)
12. A.A. Alekseenko, V.E. Guterman, S.V. Belenov, V.S. Menshikov, N.Yu. Tabachkova, O.I. Safronenko, E.A. Moguchikh, Int. J. Hydrogen Energy **43**(7), 3676 (2018)
13. A.A. Alekseenko, S.V. Belenov, V.S. Men'shchikov, V.E. Guterman, Russ. J. Electrochem. **54**, 415 (2018)
14. V.R. Stamenkovic, S.B. Mun, K.J.J. Mayrhofer, Ph.N. Ross, N.M. Markovic, J. Am. Chem. Soc. **128**, 8813 (2006)
15. Y. Sohn, J.H. Park, P. Kim, J.B. Joo, Curr. Appl. Phys. **15**(9), 993 (2015)
16. D. Wang, Y. Yu, H.L. Xin, R. Hovden, P. Ercius, J.A. Mundy, H. Chen, J.H. Richard, D.A. Muller, F.J. DiSalvo, H.D. Abruña, Nano Lett. **12**(10), 5230 (2012)
17. A.A. Alekseenko, E.A. Moguchikh, O.I. Safronenko, V.E. Guterman, Int. J. Hydrogen Energy **43**(51), 22885 (2018)

Carbon Nanoparticles from Graphite Nitrate Cointercalation Compounds with Carboxylic Acids

Elena Raksha, Alina Davydova, Oksana Oskolkova, Valentina Glazunova, Galina Volkova, Valerij Burchovetskij, Petr Sukhov, Viktoriya Gnatovskaya, Yuliya Berestneva, Iliya Verbenko, and Michael Savoskin

Abstract Liquid phase exfoliation of graphite nitrate (GN) and graphite nitrate cointercalation compounds (GNCCs) with carboxylic acids (acetic and formic) allows obtaining dispersions of carbon nanoparticles with various morphology – few-layer graphene, nanoscrolls as well as small graphene structural fragments. Treatment of as-prepared graphite nitrate with formic acid was revealed to be accompanied with its exfoliation and few-layer graphene formation. Few-layer graphenes and nanoscrolls have been prepared by exfoliation of the binary and triple GNCCs with carboxylic acids (formic and acetic) in ethanol assisted with sonication. The microstructure and morphology of obtained few-layer graphene and nanoscrolls were investigated by transmission electron microscopy (TEM) . Planar sizes of the as-prepared few-layer graphenes reached several tens of μm and their thickness was within 1 –10 atomic layers according to TEM data. It was found that acetic acid is more preferable cointercalant for carbon nanoparticles generation from GNCCs as compared to formic acid.

Keywords Liquid phase exfoliation · Graphite nitrate (GN) · Graphite nitrate cointercalation compounds (GNCCs) · Carbon nanoparticles · Few-layer graphene · Nanoscrolls · Sonication · Transmission electron microscopy (TEM)

E. Raksha (✉) · A. Davydova · O. Oskolkova · P. Sukhov · V. Gnatovskaya · M. Savoskin
Department of Supramolecular Chemistry, L.M. Litvinenko Institute of Physical-Organic and Coal Chemistry, Donetsk, Ukraine

V. Glazunova · G. Volkova · V. Burchovetskij
Department of High-Pressure Physics and Advanced Technologies, Donetsk Institute for Physics and Engineering Named After A.A. Galkin, Donetsk, Ukraine

Y. Berestneva
Biotechnology Laboratory, Federal Scientific Centre of Agroecology, Complex Melioration and Protective Afforestation of the Russian Academy of Sciences, Volgograd, Russia

I. Verbenko
Research Institute of Physics, Southern Federal University, Rostov-on-Don, Russia

I. A. Parinov et al. (eds.), *Physics and Mechanics of New Materials and Their Applications*, Springer Proceedings in Materials 10,
https://doi.org/10.1007/978-3-030-76481-4_4

1 Introduction

Liquid phase exfoliation of graphite via sonication as a method for producing carbon nanoparticles is currently one of the most widely used rout for producing graphene and few-layer graphene [1–5]. Typically, this process includes three stages: obtaining a dispersion of graphite in a solvent, exfoliation of graphite in a dispersion via sonication, and isolation or purification of graphene. The efficiency of the exfoliation process is influenced by the ultrasound power, the nature of the liquid medium, the duration of sonication, and the speed of centrifugation to remove exfoliation large particles of graphite from the dispersion [1, 6]. Prolonged sonication can induce significant morphological changes in graphene layers generated during the graphite exfoliation, which leads to the formation of nanoribbons, twisting of graphene and nanoribbons into nanoscrolls [7–10]. Also, sonication may result in destruction of graphene particles with the formation of small polyaromatic fragments, which in turn can condense to form nanofibers [11].

Graphite intercalation compounds (GICs) are also attractive precursors for the generation of graphene and graphene-like particles from the point of view of their structural organization. It has been shown that acceptor GICs (nitrate, fluoride, bisulfate) can be used to obtain dispersions of carbon nanoparticles, including graphene [12–14]. The synthesis, composition and properties of a broad range of binary and triple graphite nitrate cointercalation compounds containing different organic cointercalant species have been studied [15–18]. Additional modification of graphite nitrate with organic compounds leads to the stabilization of GICs and an increase in the distance between the nearest graphite layers due to the introduction of additional particles of organic cointercalants into the structure of graphite nitrate [15–19]. Such structural reorganization of graphite matrix is responsible for graphite nitrate intercalation compounds application as precursors of carbon nanoparticles generation in mild conditions [16–21].

This chapter presents the results on the production of few-layer graphene and nanoscrolls by liquid-phase exfoliation of graphite nitrate cointercalated with formic and acetic acids (GNCCs) . At this study, we consider the following frameworks of the problem:

(i) Synthesis and characterization of binary and triple GNCCs with formic and acetic acids as precursors for carbon nanoparticles obtaining;
(ii) Chemical exfoliation of graphite nitrate (GN) via treatment with formic acid;
(iii) Liquid phase exfoliation of binary and triple GNCCs with formic and acetic acids in ethanol via sonication.

2 Experimental

Graphite nitrate as well as graphite nitrate cointercalation compounds with acetic and formic acids were prepared as a starting material for the generation of carbon nanoparticles suspensions. GN and GNCCs were synthesized in a thermostatic reactor using

nitric acid with a density of 1.502 g·cm^{-3} (98%) and natural flake graphite GT-1 (Zavalie Graphite Works, Kirovograd region, Ukraine). A mixture of graphite (1 g) and HNO_3 (0.6 ml) was stirred for 10 min at 20°C to obtain a GN. Binary GNCCs were synthesized by treatment of as-prepared GN with organic co-intercalant (6 ml formic or acetic acid correspondingly). The reaction mixture was stirred again for 10 min. Triple GNCC with formic and acetic acids was obtained by treatment of as-prepared GN with mixture of acids (1 : 1 by volume) and reaction system was stirred for 10 min. Resulted GNCCs were separated by filtration and dried at 20°Cuntil the sample mass became constant.

The thermal expansion coefficients for obtained GNCCs were determined by heating of the samples within the thermal shock mode at 900 °C. Powder X-ray diffraction (XRD) measurements were performed on DRON 3 diffractometer (CuKα radiation, λ = 1.54181 Å). Only freshly prepared samples of graphite nitrate and GNCCs were used for XRD studies. Surface morphology of the synthesized GNCCs were estimated by scanning electron microscopy (SEM) using a complex analytical scanning electron microscope JSM 6490 LV (JEOL).

Dispersions of carbon nanoparticles were prepared by liquid phase exfoliation of the GN and GNCCs in various ways. The first one was the treatment of fresh as-prepared graphite nitrate with HCOOH, and the second way was the sonication of the GNCCs samples in ethanol (22 kHz and 470 W). The duration of the sonication was 1 h. Then, the samples were centrifuged (7 min, 3000 rpm). Morphology of the prepared nanoparticles was estimated by transmission electron microscopy (TEM) . The TEM images of the dispersions samples were obtained using JEOL JEM-200 transmission electronic microscope.

3 Results and Discussion

3.1 Graphite Nitrate Cointercalation Compounds with Carboxylic Acids as Precursors for Carbon Nanoparticles Dispersions

Binary nitrate graphite cointercalation compounds with carboxylic acids (formic and acetic) were used as precursors for carbon nanoparticles dispersions. GNCCs were synthesized by treatment of natural flake graphite with fuming nitric acid following by treatment of the formed graphite nitrate with cointercalant – carboxylic acid. General scheme of the GNCCs synthesis is provided in Fig. 1. Representative SEM images of initial graphite and discussed GNCCs are presented in Fig. 2. All samples demonstrate the layer structure, but GNCCs formation is accompanied with a reorganization of the graphite microstructure; moreover, by introducing of the cointercalants particles into interlayer space the delamination of flakes is observed.

Formation of binary GNCCs with organic compounds leads to additional stabilization of graphite nitrate as well as to enhancement of their ability to thermal expansion

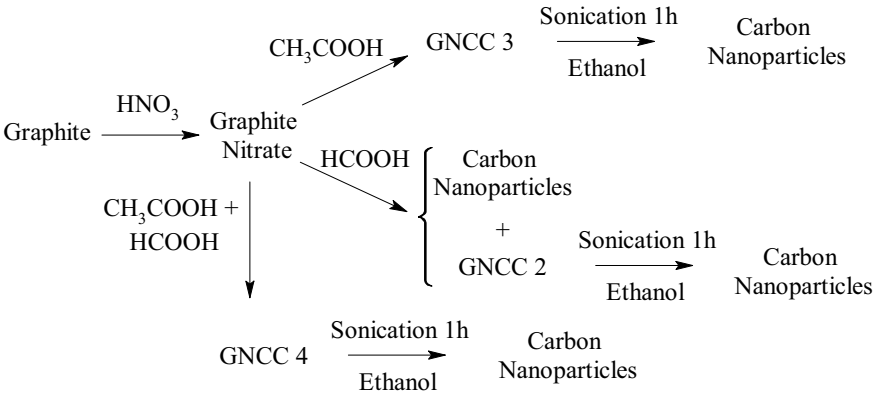

Fig. 1 Summarized scheme of carbon nanoparticles obtaining from GNCCs with carboxylic acids

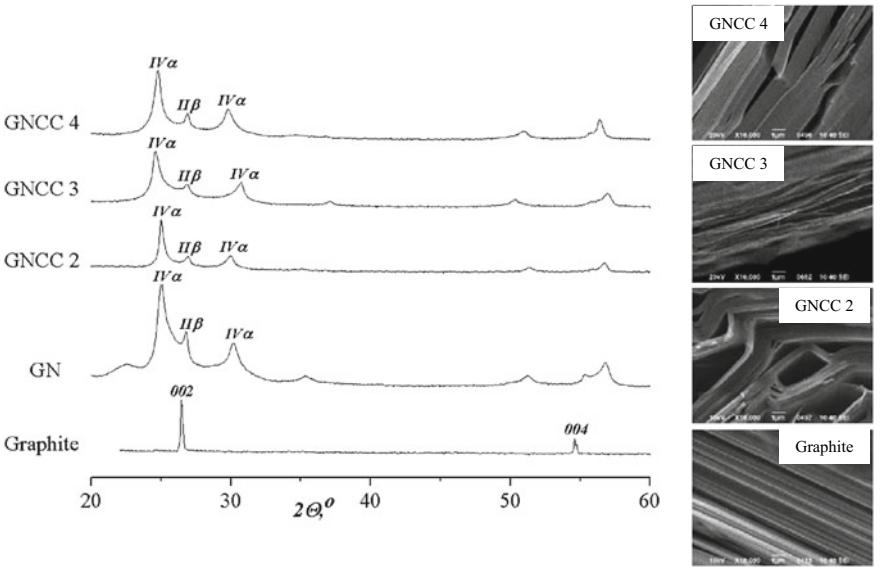

Fig. 2 X-ray diffraction patterns of graphite, graphite nitrate and GNCCs with formic acid (GNCC 2) , acetic acid (GNCC 3), formic and acetic acids (GNCC 4) and representative SEM images (side view) of graphite and GNCCs

[3–5, 9]. Coefficient of thermal expansion determined for studied GNCCs is within 249–380 $sm^3 \cdot g^{-1}$ and increases in the following row: GN < GNCC 2 < GNCC 3 < GNCC 4 (Table 1). Structure of the synthesized binary and triple GNCCs was characterized by X-ray diffraction method. Figure 2 demonstrates diffraction patterns of graphite, graphite nitrate and GNCCs in $I^{(0.5)} - 2\Theta$ coordinates. In obtained samples compounds of IV^{th} and II^{nd} stages of intercalation are presented. From the results

Table 1 Structural characteristics of the graphite nitrate and GNCCs with acetic and formic acids as well as coefficients of thermal expansion of the studied compounds

GNCC	Cointercalant	IV-α compound		II-β compound		K_V ($sm^3 \cdot g^{-1}$)
		2Θ (°)	d_i (Å)	2Θ (°)	d_i (Å)	
1	–	25.00	7.729	26.76	6.634	249
2	HCOOH	25.00	7.729	26.96	6.561	338
3	CH_3COOH	24.88	7.813	27.04	6.532	354
4	HCOOH + CH_3COOH	24.76	7.899	26.88	6.590	380

of X-ray diffraction analysis values of interplanar space filled with cointercalants species (d_i) were estimated for studied GN and GNCCs. The d_i values for GN and GNCCs with acids are increased up to 6.532–7.899 Å (Table 1) as compared with 3.359 Å for initial graphite. This structural reorganization of graphite matrix may be considered as a pre-organization process for few-layer and single-layer graphene formation. Thus studied GNCCs are perspective compounds for the liquid phase exfoliation and graphene-like particles generation.

3.2 Carbon Nanoparticles Obtaining by Treatment of the GN with HCOOH

It should be noted that treatment of intercalated graphite compounds with reductants like alcohols is used as a method of graphite matrix exfoliation without additional temperature influence [2, 8]. Thus treatment of fresh as-prepared graphite nitrate with HCOOH was considered as a way to produce the carbon nanoparticles dispersion. In this case, in addition to the formation of a binary cointercalation compound (GNCC 2) , HCOOH exothermically interacts with nitric acid adsorbed on the surface of particles, as well as located in the interlayer space of graphite nitrate with the release of a large amounts of gaseous products, namely CO_2 and NO_2 (Eq. 1). This process results in partial exfoliation of the GN and form GNCC 2 with formic acid as well as formation of the carbon nanoparticles dispersion in the HCOOH medium. This method was found to facilitate the few-layer graphenes formation. Representative TEM images of observed nanoparticles are shown in Fig. 3. The planar sizes of observed individual few-layer graphene particles reach 5–15 μm, and finer particles with planar sizes up to 500 nm are also present. The ratio of reflexes intensities of inner (I_1) and outer (I_2) circles at the microelectronogram (Fig. 3c) is $I_1/I_2 < 1$ indicating that observed particles are double-layer graphene structures.

$$HCOOH + 2HNO_3 \rightarrow CO_2 + 2NO_2 + 2H_2O \quad (1)$$

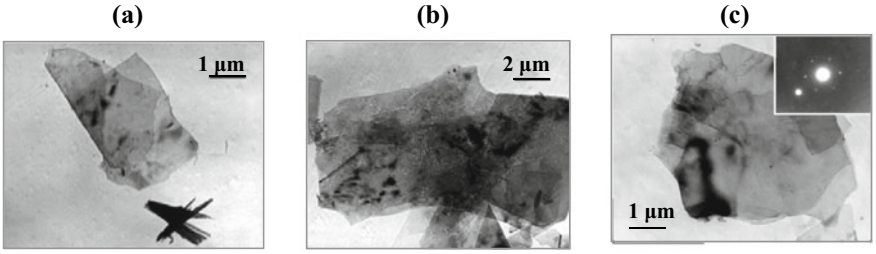

Fig. 3 Representative TEM images of carbon nanoparticles obtained by exfoliation of the graphite nitrate treated with formic acid

3.3 Carbon Nanoparticles Obtaining by the Sonication of GNCCs with Acetic and Formic Acids in Ethanol

Dispersions of carbon nanoparticles were also obtained by liquid-phase exfoliation of GNCCs with acetic or formic acid in ethanol assisted with sonication (22 kHz, 470 W, 1 h). The dispersions obtained were investigated by TEM method. Since our investigations were carried out mainly on the cointercalated compounds of the IV^{th} and II^{nd} intercalation stages it was difficult to expect a complete graphite lattice exfoliation into monolayer graphene particles.

An analysis of the dispersions obtained in ethanol by the TEM method revealed that carbon nanoparticles of various morphologies can be obtained by this technique. Most commonly, a mixture of particles is formed, which includes graphene-like particles of various sizes (both single-layer and few-layer), nanoscrolls, and small amorphous carbon nanoparticles. Morphology of the observed nanoparticles was revealed to depend on the nature of organic cointercalant used for the GNCC synthesis. Figure 4 shows representative TEM images of carbon nanoparticles obtained by GNCCs exfoliation in ethanol induced by ultrasound. In the case of GNCC with acetic acid, a mixture of few-layer graphene and nanoscrolls was observed (Fig. 4 a-c). The planar sizes of obtained individual few-layer graphene particles reach 5–6 μm. Nanoscrolls observed are characterized by straight stick-like shape, the length and diameter of this particles vary over a wide range: the former is from 0.2 to 2.5 μm, the latter is from 50 to 200 nm. Use of formic acid as a cointercalant for GNCC provides formation of a great number of structural defects of the particles surface. Dispersion obtained by sonication of such GNCC contained a mixture of particles including nanoscrolls (Fig. 4a-c) as well as amorphous particles, for which boiling under electrons beam of microscope was observed (Fig. 4f). It should be noted that in the case of this GNCC, an origin of nanoscrolls is the bulk incompletely exfoliated GNCC packages (Fig. 4g) but not single- or few-layer graphene. Thus nanoscrolls formed are characterized by irregular shape and warping. Their length is from 0.2 to 1 μm.

Thus, TEM results have shown that the obtained dispersions contain a mixture of particles: few-layer graphenes, nanoscrolls, as well as smaller fragments formed in

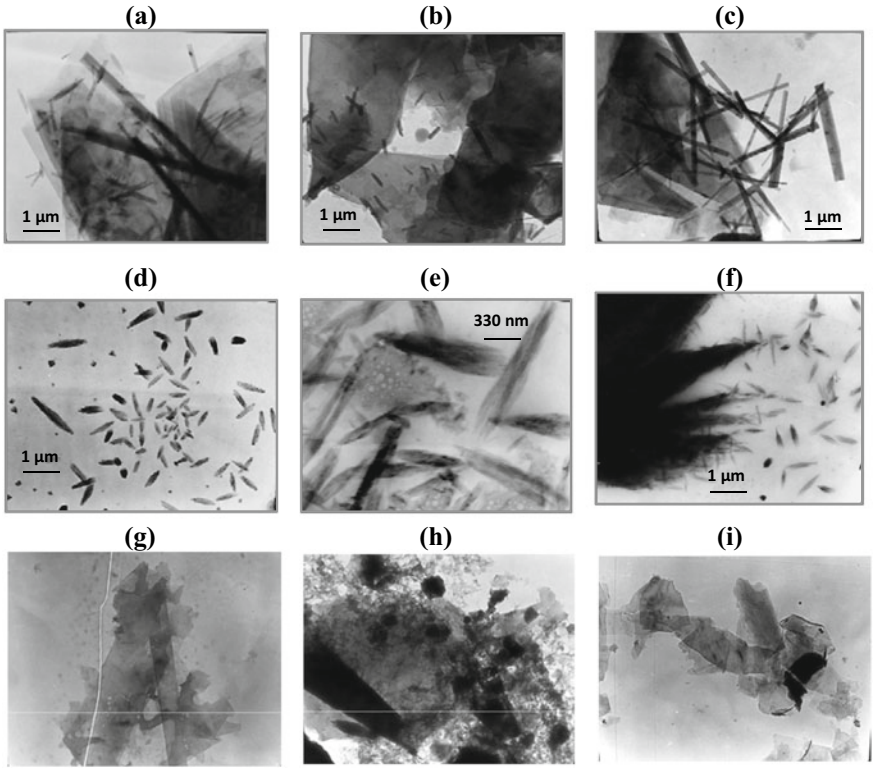

Fig. 4 Representative TEM images of carbon nanoparticles obtained in ethyl alcohol by sonication of the binary GNCCs with acetic acid (**a–c**), formic acid (**d–f**), and triple GNCC with acetic and formic acids (**g–i**)

the result of the destruction of graphene sheets or graphite nanoplates. The use of sonication promotes the exfoliation of the graphite matrix, however leads to twisting or deformation of the resulting few-layer graphenes. The destruction of nanoparticles with the formation of small amorphous polyaromatic fragments can be caused by the participation of a cointercalants in radical-chain reactions occurring in cavitation cavities when the system is treated with ultrasound.

4 Conclusion

The product formed during the interaction of graphite nitrate with carboxylic acids is a mixture of compounds of the IInd (β-form) and IVth (α-form) stages of intercalation. The layered structure of GNCC is pre-organized for the formation of few-layer graphene particles. The presence of carbon nanoparticles (few-layer graphene and

nanoscrolls) in the exfoliation products of binary and triple graphite nitrate cointercalation compounds with formic and acetic acids in ethanol medium has been established by the transmission electron microscopy method. It was shown that varying the cointercalant nature as well as exfoliation technique makes it possible to obtain different types of carbon nanoparticles. Graphene-like particles with planar sizes up to several micrometers were formed from GNCC with formic acid in the cointercalant media. Sonication contributes to a significant increase in the number of defects and fragmentation of graphene planes formed by this GNCC exfoliation in ethanol. Exfoliation of the GNCCs with acetic and formic acids in ethanol leads to the few-layer graphene and nanoscrolls generation.

The presented results revealed graphite nitrate cointercalation compounds to be a promising source of carbon nanoparticles. Exfoliation of GNCCs in liquid media by sonication can be simple and effective route for obtaining carbon nanoparticles under mild conditions at large scales.

References

1. Y. Xu, H. Cao, Y. Xue, B. Li, W. Cai, Nanomaterials **8**(11), 942 (2018)
2. Y. Arao, F. Mori, M. Kubouchi, Carbon **118**, 18 (2017)
3. J. Chen, W. Shi, Y. Chen, Q. Yang, M. Wang, B. Liu, Z. Tang, M. Jiang, De Fang, C. Xiong. Appl. Phys. Lett. vol. 108(7), 073105 (2016)
4. M. Berktas, L.H. Hezarkhani, B.S. Poudeh, Okan. Graphene Technol. **5**, 59 (2020)
5. P. Szirmai, B.G. Markus, J.C. Chacon-Torres, P. Eckerlein, K. Edelthalhammer, J.M. Englert, U. Mundloch, A. Hirsch, F. Hauke, B. Náfrádi, L. Forró, C. Kramberger, T. Pichler, F. Simon, Sci. Rep. **9**(1), 19480 (2019)
6. S. Pavlova, E.A. Obraztsova, A.V. Belkin, C. Monat, P. Rojo-Romeo, E.D. Obraztsova, J. Nanophotonics **10**(1), 012525 (2016)
7. J.I. Tapia, M. Quintana, in *Handbook of Carbon Nanomaterials*: *Graphene – Fundamental Properties*, vol. 5, (World Scientific Publishing 2014), p. 186
8. L.M. Viculis, J.J. Mack, R.B. Kaner, Science **299**(5611), 1361 (2003)
9. J.H. Bang, K.S. Suslick, Adv. Mater. **22**(10), 1039 (2010)
10. A. Sidorov, D. Mudd, G. Sumanasekera P. J. Ouseph, C. S. Jayanthi, S.-Y. Wu. Nanotechnology. **20**(5), 055611 (2009)
11. S. Wang, J. Am. Chem. Soc. **131**, 16832 (2009)
12. T. Liu, X. Zhang, M. Liu, W. Wu, K. Liu, Y. Liu, Y. Gu, R. Zhang, J. Mater. Chem. C. **6**, 8343 (2018)
13. M.V. Savoskin, V.N. Mochalin, A.P. Yaroshenko, N.I. Lazareva, T.E. Konstantinova, I.V. Barsukov, I.G. Prokofiev, Carbon **45**(14), 2797 (2007)
14. N.A. Nebogatikova, I.A. Antonova, A.I. Ivanov, V.A. Demin, D.G. Kvashnin, A. Olejniczak, A.K. Gutakovskii, K.A. Kornieieva, P.L.J. Renault, V.A. Skuratov, L.A. Chernozatonskii, Nanotechnology **31**(29), 295602 (2020)
15. M.V. Savoskin, A.P. Yaroshenko, G.E. Whyman, R.D. Mysyk, J. Phys. Chem. Sol. **67**(5–6), 1127 (2006)
16. M. V. Savoskin, A. N. Vdovichenko, E. V. Raksha, Yu. V. Berestneva, V. Yu. Vishnevskij, O. M. Padun, I. A. Verbenko, Yu. I. Yurasov, in *Physics, Mechanics of New Materials and Their Applications*, ed. by I. A. Parinov, S. H. Chang, M. A. Jani (Nova Science Publishers, New York, 2017), p. 115

17. M. V. Savoskin, A. N. Vdovichenko, E. V. Raksha, Yu. V. Berestneva, V. Yu. Vishnevskij, A. P. Prudchenko, V. A. Glazunova, K. P. Andryushin, Yu. I. Yurasov, in *Physics, Mechanics of New Materials and Their Applications*, ed. by I. A. Parinov, Sh. H. Chang, V. K. Gupta (Nova Science Publishers, New York, 2018), p. 7
18. E. V. Raksha, Yu. V. Berestneva, O. M. Padun, A. N. Vdovichenko, M. V. Savoskin, G. E. Zaikov, in *Innovations in Chemical Physics and Mesoscopy. Nanoscience and Nanoengineering. Novel Applications*, ed. by V. E. Dement′ev, A. K. Haghi, V. I. Kodolov (Apple Academic Press, Oakville, 2019), p. 297
19. G. Bepete, E. Anglaret, L. Ortolani, V. Morandi, K. Huang, A. Penicaud, K. Drummond, Nature Chem. **9**, 347 (2017)
20. W. Sirisaksoontorn, A.A. Adenuga, V.T. Remcho, M.M. Lerner, J. Am. Chem. Soc. **133**, 12436 (2011)
21. E. V. Raksha, A. A. Davydova, Yu. V. Berestneva, M. V. Savoskin, V. A. Glazunova, A. N. Vdovichenko, O. N. Oskolkova, P. V. Sukhov, V. V. Gnatovskaya, I. A. Verbenko, Yu. I. Yurasov, in *Advanced Materials, Proceedings of the International Conference on "Physics and Mechanics of New Materials and Their Applications", PHENMA2019,* vol. 6, ed. by I. A. Parinov, S. H. Chang, B. T. Long (Springer Proceedings in Materials. Springer Nature Switzerland AG, 2020), p. 41

Thermally Expanded Graphite: Sorption Properties and Carbon Nanoparticles Obtaining

A. A. Voitash, E. V. Raksha, A. A. Davydova, O. N. Oskolkova, Y. V. Berestneva, A. V. Muratov, A. B. Eresko, V. A. Glazunova, M. V. Savoskin, I. A. Verbenko, and Y. I. Yurasov

Abstract This paper presents the results of complex investigations of structural and physicochemical properties of thermally expanded graphite (TEG) based on graphite nitrate, cointercalated with formic and acetic acids. Consideration was given to possibility of obtaining of graphene nanoparticles by liquid phase exfoliation of the TEG. Adsorption properties of the TEG for bioactive compounds such as 1,10-phenanthroline and benzofuro[2,3-*d*][1,2]diazepines were estimated.

Keywords Thermally expanded graphite (TEG) · Adsorption · Graphite nitrate cointercalation compound · Carbon nanoparticles · Few-layer graphene · Benzofuro[2,3-d][1,2]diazepines (BFDs) · 1,10-Phenanthroline (Phen)

1 Introduction

Thermally expanded graphite (TEG) is a highly porous material with an exceptional combination of properties like high porosity, low bulk density and well-developed specific surface. TEG has a variety of applications such as water purification [1, 2], manufacturing of heat-resistant foils and sealants [3]. Adsorption properties of TEG also allow its using in chemical synthesis and as a substrate for supported catalyst

A. A. Voitash · E. V. Raksha (✉) · A. A. Davydova · O. N. Oskolkova · A. V. Muratov · A. B. Eresko · M. V. Savoskin
L.M. Litvinenko Institute of Physical Organic and Coal Chemistry, Donetsk 83114, Ukraine

Y. V. Berestneva
Federal Scientific Centre of Agroecology Complex Melioration and Protective Afforestation of the Russian Academy of Sciences, Volgograd 400062, Russia

V. A. Glazunova
Donetsk Institute for Physics and Engineering Named After A.A. Galkin, Donetsk 83114, Ukraine

I. A. Verbenko · Y. I. Yurasov
Research Institute of Physics, Southern Federal University, Rostov-on-Don 344090, Russia

Y. I. Yurasov
South Scientific Centre RAS, Rostov-on-Don 344006, Russia

I. A. Parinov et al. (eds.), *Physics and Mechanics of New Materials and Their Applications*, Springer Proceedings in Materials 10,
https://doi.org/10.1007/978-3-030-76481-4_5

[7] as well as a matrix for mass spectrometry [4]. It also known that liquid phase exfoliation of TEG is a promising simple, low-cost method for the preparation of few-layer graphenes [5].

Acceptor graphite intercalation compounds (GICs) are widely used for TEG obtaining due to their ability to volume multiple increasing during heat treatment. Recent investigations show that introduction of additional intercalants into the GIC structure leads to changes in their reactivity and often improves their ability to thermal expansion [6]. Binary graphite nitrate cointercalation compounds have shown to demonstrate high thermal expansion coefficients [6], thus they are promising precursors for TEG production. From this viewpoint additional information is needed about macro- and microstructure of TEG produced from graphite nitrate cointercalation compounds.

2 Experimental

The thermally expanded graphite (TEG) was obtained as described elsewhere [7] via two steps including synthesis of the triple graphite nitrate cointercalation compound (TGCC) and heating of the TGCC in thermal shock mode. The TGCC was prepared by sequential treatment of natural flake graphite GT-1 (Zavalie Graphite Works, Kirovograd Region, Ukraine) with nitric acid (98%) and organic cointercalants: acetic and formic acids. The consumptions of nitric acid and the cointercalants were 0.6 and 6 cm^3 per 1 g of graphite, respectively. Resulted TGCC was expanded in a preheated muffle furnace at 900 °C.

The adsorption capacity of TEG for benzofuro[2,3-*d*][1,2]diazepines (BFDs) and 1,10-phenanthroline (Phen) was investigated in static regime. Experiments were performed in a reaction flask to determine the adsorption of a single concentration of the sorbates. The solutions of BFDs in chloroform with concentrations of (3.3–4.1) $\times$ 10^{-4} g/L and Phen in 1: 1 mixture of water and ethanol with concentration of 5.5 $\times$ 10^{-3} g/L were prepared. The pre-weighted quantities of TEG in amount of 3.5 g /L were added to each flask. These flasks were kept for 24 h. The equilibrium BFDs and Phen concentrations were measured using the Helios Gamma UV–vis spectrophotometer at the maximum absorbance wavelength value for each compound. The equilibrium adsorption capacity of investigated compounds (q, g/g TEG) was estimated by the following equation:

$$q = \frac{V \cdot (C - C_e)}{m}, \tag{1}$$

where C and C_e are the initial and the equilibrium concentration of the sorbate, respectively, g/L; V is the volume of sorbate solution, L; m is the adsorbent weight, g.

Dispersions of carbon nanoparticles were prepared by liquid phase exfoliation of the TEG by sonication in *tert*-butanol (22 kHz and 470 W, 1 h) with subsequent centrifugal separation.

Morphology of the prepared nanoparticles was estimated by transmission electron microscopy (TEM) . The TEM images of the dispersion samples were obtained using JEOL JEM-200 transmission electronic microscope. X-ray diffraction (XRD) measurements were performed on DRON 3 diffractometer (CuK_α radiation, $\lambda = 1.54181$ Å). Freshly prepared sample of TGCC was used for XRD studies. Surface morphology of the TGCC and TEG was estimated by scanning electron microscopy (SEM) using a complex analytical scanning electron microscope JSM 6490 LV (JEOL).

3 Results and Discussion

The TEG as a precursor for carbon nanoparticles was obtained from the TGCC with acetic and formic acids. Formation of binary and triple graphite nitrate cointercalation compounds with organic compounds leads to additional stabilization of graphite nitrate as well as to enhancement of their ability to thermal expansion as it was demonstrated earlier [6, 8, 9]. Obtained TGCC demonstrates good thermal expansion ability: thermal expansion coefficient obtained for considered TGCC sample is 380 $sm^3 \cdot g^{-1}$.

Structural reorganization of graphite after treatment with nitric acid and cointercalants as well as thermal expansion were characterized by X-ray diffraction method. Figure 1 demonstrates diffraction patterns of graphite, TGCC and TEG in $I^{(0.5)}$–2Θ coordinates. In the TGCC sample, the compounds of II^{nd} and IV^{th} stages of intercalation are presented, that is consistent to previous investigations [6–10].

Reflexes, which are typical for the graphite phase, are observed on the X-ray diffraction pattern of TEG obtained from the TGCC (Fig. 1a, c) while reflexes from initial TGCC are absent. Broadening and shift of the reflexes *002, 004* towards lesser angles and appearing of reflexes *100*, *101* on the TEG X-ray diffraction pattern indicates an increase of interplanar space and lesser organization of graphite layers of the TEG (Fig. 1c).

The microstructure and morphology of initial graphite, TGCC and thermally expanded graphite obtained were investigated by SEM method. Both graphite macrostructure and microstructure undergo a number of changes during the formation of TGCC and its expansion. Intercalation of initial graphite with the formation of TGCC with acetic and formic acids leads to some delamination of graphite particles (Fig. 1). The expansion of TGCC leads to formation of cell structure in obtaining TEG. Visible pore width in the structure varies from 1.0 to 20 μm. Therefore, TEG based on TGCC demonstrates pre-organized structure for few-layer graphenes generation.

The large specific surface of the TEG causes its high sorption properties. The sorption capacity of the TEG for bioactive compounds was estimated on the

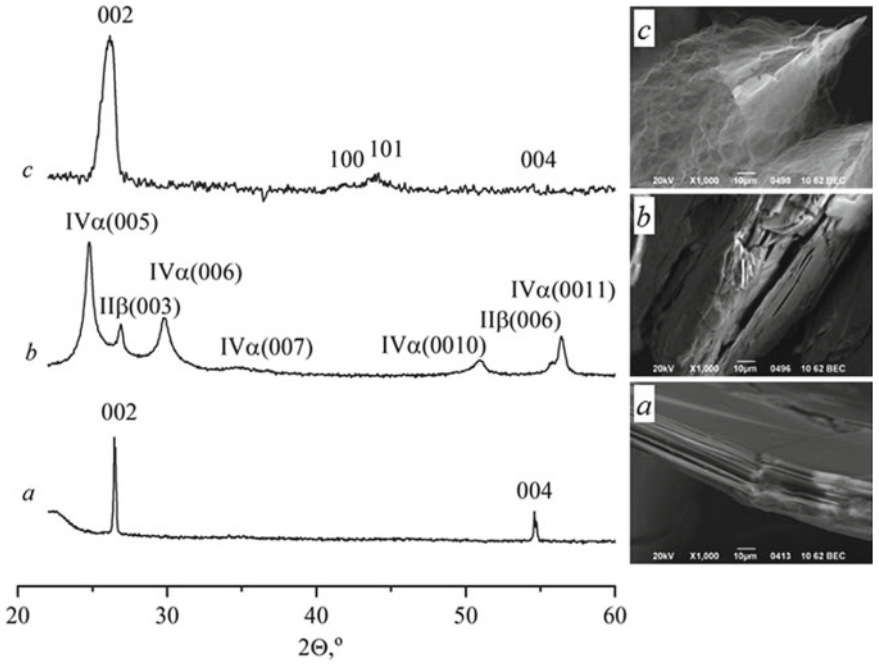

Fig. 1 X-ray diffraction patterns and representative SEM images (side view) of graphite (***a***), TGCC (***b***) and TEG (***c***)

example of 1,10-phenanthroline (Phen) and 1-R-4-(4-chlorophenyl)-7-methyl-5H-[1]benzofuro[2,3-*d*][1,2]diazepines (BFDs) , obtained by the Bischler-Napieralski reaction as described elsewhere [11]. The structures of these compounds are shown in Fig. 2. The values of sorption capacities (q) determined for TEG are presented in Table 1. Estimated q values increase in the following order: BFD2 < BFD1 = BFD3 < Phen.

Dispersions of carbon nanoparticles were obtained by exfoliation of TEG in *tert*-buthanol assisted with sonication (22 kHz, 470 W, 1 h). The morphology of nanoparticles was investigated by TEM method. Representative TEM images (Fig. 3) demonstrate thin and homogeneous graphene particles with smooth and slightly twisted edges. The planar sizes of obtained individual few-layer graphene particles reach 6 μm.

The ratio of reflexes intensities of inner (I_1) and outer (I_2) circles at the TEM images can be used for nanoparticle width estimation [12, 13]. The ratio of intensities is $I_1/I_2 > 1$ for single-layer nanoparticles, $I_1/I_2 < 1$ for double-layer, and $I_1/I_2 = 1$ for particles containing three or more graphene layers. Selected area electron diffraction (SAED) patterns of investigated sample show bright hexagon spots with matching intensities of inner and outer circles, indicating formation of few-layer graphene structures. There also are duplicated reflexes that indicate a disorientation of overlapping graphene nanoparticles.

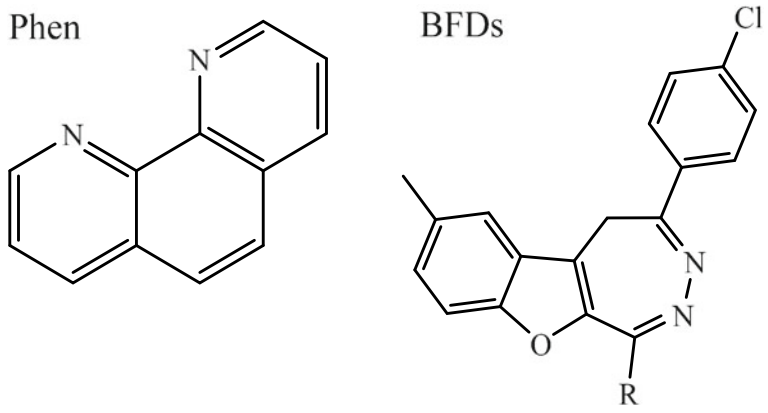

Fig. 2 Structure of 1,10-phenanthroline (Phen) and 1-R-4-(4-chlorophenyl)-7-methyl-5H-[1]benzofuro[2,3-d][1,2]diazepines: R = 3-thienyl (BFD1), 4-O-Me-C_6H_4 (BFD2), 4-NO_2-C_6H_4 (BFD3)

Table 1 Sorption capacities of TEG for bioactive compounds

Compound	*q*, g/g TEG
Phen	0.020
BFD1	0.014
BFD2	0.007
BFD3	0.014

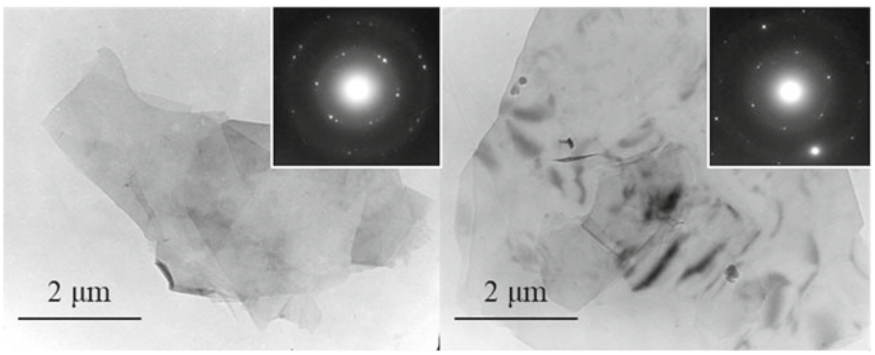

Fig. 3 Representative TEM images and SAED patterns of carbon nanoparticles obtained in *tert*-buthanol by sonication of the TEG

4 Conclusion

The TEG was obtained from the triple graphite cointercalation compound with carboxylic (formic and acetic) acids and characterized by powder X-ray diffraction as well as SEM methods. It was shown that studied TEG is appropriate starting material for the few-layer graphenes generation. Dispersion of few-layer graphenes up to 6 μm length has been obtained by the TEG liquid phase exfoliation in *tert*-buthanol with sonication. Adsorption properties of the TEG for bioactive compounds (benzofuro[2,3-*d*][1,2]diazepines and phenanthroline) were estimated. Sorption capacity value is within 0.007–0.020 g/g TEG for studied compounds.

References

1. M.V. Savos'kin, A.P. Yaroshenko, V.N. Mochalin, B.V. Panchenko, Russ. J. Appl. Chem. **76**, 906 (2003)
2. M. Inagaki, F. Kang, M. Toyoda, Chem. Phys. Carbon **29**, 1 (2004)
3. I.H. Jung, D.A. Dikin, R. Piner, R. Ruoff, Nano Lett. **8**, 4283 (2008)
4. S.V. Snegir, G.P. Prihod'ko, Yu.I. Sementsov, V.A. Pokrovsky, I.O. Fritsky, Surface **13**, 201 (2007)
5. A.A. Voitash, V.Yu. Vishnevsky, Yu.V. Berestneva et al., Appl. Aspects Nano-Physics and Nano-Engineering **1**, 25 (2019)
6. M.V. Savoskin, A.P. Yaroshenko, G.E. Whyman, R.D. Mysyk, J. Phys. Chem. Solids **67**, 1127 (2006)
7. A.A. Davydova, A.A. Voitash, Yu.V. Berestneva et al., Chem. Saf. Sci. **3**, 39 (2019)
8. E.V. Raksha, Yu.V. Berestneva, O.M. Padun, et al., in *Innovations in Chemical Physics and Mesoscopy*, ed. by V.E. Dement′ev, A.K. Haghi, V.I. Kodolov. Nanoscience and Nanoengineering. Novel Applications. (Apple Academic Press, 2019), p. 297
9. E.V. Raksha, A.A. Davydova, Yu.V. Berestneva, et al., in *Advanced Materials - Proceedings of the International Conference on "Physics and Mechanics of New Materials and Their Applications"*, ed. by I.A. Parinov, Sh.-H. Chang, B.-T. Long. PHENMA 2019. Springer Proceedings in Materials. vol. 6 (Springer Nature, Cham, Switzerland, 2020), p. 41
10. A.A. Davydova, E.V. Raksha, O.N. Oskolkova et al., Physical and chemical aspects of the study of clusters. Nanostruct. Nanomaterials **12**, 580 (2020)
11. A.V. Muratov, S.A. Grebenyuk, A.B. Eresko, Russ. J. Org. Chem. **54**, 861 (2018)
12. A.B. Bourlinos, V. Georgakilas, R. Zboril et al., Small **5**(16), 1841 (2009)
13. Y. Hernandez, V. Nicolosi, M. Lotya et al., Nat. Nanotechnol. **3**(9), 563 (2008)

Heteroepitaxial $BiFeO_3$ Films Fabricated on MgO(001) and $Sr_{0.61}Ba_{0.39}Nb_2O_6$/MgO(001)

D. V. Stryukov, A. V. Pavlenko, L. I. Kiseleva, and G. N. Tolmachev

Abstract $BiFeO_3$/MgO(001) and $BiFeO_3/Sr_{0.61}Ba_{0.39}Nb_2O_6$/MgO(001) heterostructures were deposited by a one-stage technique of RF-cathode sputtering of a stoichiometric composition ceramic target in an oxygen atmosphere. The films were studied by X-ray diffraction and scanning electron microscopy at room temperature. It is shown that the heterostructures have high crystal perfection and a low number of structural defects. It was found that the bismuth ferrite unit cell has monoclinic symmetry in the $BiFeO_3$/MgO(001) heterostructure. There is only a slight unit cell strain in both heterostructures. The presence of the $Sr_{0.61}Ba_{0.39}Nb_2O_6$ between $BiFeO_3$ and MgO does not break the parallel of their crystallographic axes.

Keywords Thin film · Heterostructure · X-ray diffraction · Bismuth ferrite · Strontium-barium niobate

1 Introduction

In modern terminology, materials in which two or more types of orderings coexist simultaneously (ferroelectric, magnetic, and ferroelastic) are commonly termed as multiferroics. Interest in them continues to this day due to the wide range of their possible applications in multifunctional devices [1]. The greatest attention is drawn to the relationship between different order parameters, which can lead to new physical effects, such as, for example, the control of magnetic properties by electric field or vice versa. One of the important criteria for the use of multiferroics is the room temperature ordering [2]. However, there are very few single-phase multiferroics that satisfy this condition, among which the most famous is bismuth ferrite $BiFeO_3$ (BFO), a multiferroic with a perovskite structure, in which ferroelectric and antiferromagnetic orderings are realized. Bulk BFO has a rhombohedral unit cell with the R3c space group. The temperatures of both phase transitions are significantly higher than

D. V. Stryukov (✉) · A. V. Pavlenko · L. I. Kiseleva · G. N. Tolmachev
Federal Research Centre the Southern Scientific Centre of the Russian Academy of Sciences, Rostov-on-Don 344006, Russia
e-mail: strdl@mail.ru

I. A. Parinov et al. (eds.), *Physics and Mechanics of New Materials and Their Applications*, Springer Proceedings in Materials 10,
https://doi.org/10.1007/978-3-030-76481-4_6

room temperature (T_C ~ 1100 K; T_N ~ 640 K) [1–5], and the remanent polarization along the [111] polar direction sufficiently high for ferroelectric materials (P_r ~ 100 μC/cm^2) [3, 4]. All the above makes bismuth ferrite a promising candidate for use in high-density ferroelectric memory devices. Moreover, many other effects have been found in BFO, such as magnetoelectric, magnetodielectric and photovoltaic effects, and birefringence.

To date, BFO thin films have already been fabricated by various deposition technologies: pulsed laser deposition [6, 7], sol–gel [8], magnetron sputtering [9]. Due to the presence of a large number of impurity phases arising in the process of BFO synthesis, additional annealing after synthesis [7, 8] or preliminary deposition of sublayers [6, 9] are often used in the technological cycle of fabricating heterostructures based on it. The use of an additional layer based on functional materials can not only prevent the appearance of impurities but it is also one of the most promising steps towards the creation of new microelectronic devices, where interactions between different orderings of functional layers can occur. As an additional layer, the strontium-barium niobate $Sr_xBa_{1-x}Nb_2O_6$ was chosen. $Sr_xBa_{1-x}Nb_2O_6$ solid solution is a uniaxial ferroelectric relaxor with the structure of unfilled tetragonal potassium-tungsten bronze. Interest in them is due to the high electro-optical and pyroelectric coefficients [10], that can be used in MEMS, electro-optical elements, and pyroelectric sensors.

2 Problem Formulation

It has been studied by X-ray diffraction analysis and SEM microscopy the structure of BFO thin films grown with and without a $Sr_{0.61}Ba_{0.39}Nb_2O_6$ sublayer on MgO (001) substrate by a one-stage gas-discharge RF-cathode sputtering in an oxygen atmosphere.

2.1 Objects and Methods

The deposition of $BiFeO_3$ (BFO) and $Sr_{0.61}Ba_{0.39}Nb_2O_6$ (SBN) thin films was carried out by RF-cathode sputtering technique on a “Plasma 50 SE” system (Center for Collective Use of the SSC RAS) in an oxygen atmosphere using the intermittent deposition technology. As a substrate MgO(001) monocrystalline plates of 0.5 mm thick were used, the initial temperature of the substrate was 400 °C and the working gas pressure was 0.5–0.6 Torr.

The structural perfection of the films, the unit cell parameters and the orientation relationships between film and substrate were performed by X-ray diffraction on a DRON-4–07 diffractometer (CuKα–radiation).

Microscopic studies of the heterostructures were carried out on an FE-SEM Zeiss SUPRA 25 scanning electron microscope.

2.2 Experimental Results and Discussion

The X-ray diffraction studies of the BFO/MgO(001) and BFO/SBN/MgO(001) heterostructures do not show any traces of impurity phases and on the diffraction patterns, only reflections from the heterostructure layers and the substrate were registered (Fig. 1). It should be noted that during the searching for optimal conditions for the heterostructure synthesis of both SBN and BFO, lines of impurity phases were founded, but due to the weakness of reflections, it was unable to establish a type of impurities.

The BFO film grows oriented relative to the substrate axes in both cases. The φ-scans (Fig. 2) of the (113) BFO thin film reflection confirm epitaxial growth, with the orientation of all crystallographic axes of the BFO parallel to the axes of the substrate in both heterostructures. The SBN layer is also fabricated epitaxially. Moreover, the parallel orientation of BFO is observed even in the presence of an SBN layer, which, similarly to [11], have two types of orientation domains with an in-plane rotation of the axes by + 18.4° and –18.4°.

At the precision θ-2θ-scanning of (00l) reflections (Fig. 3) of the two-layer BFO/SBN/MgO(001) heterostructure, a splitting of the reflections corresponding to separate scattering by each layer is observed. From the analysis of the angular positions of the (00l) reflections, taking into account the $K_{\alpha 1}$ and $K_{\alpha 2}$ components in the obtained X-ray diffraction patterns, the out-of-plane unit cell parameters are $c_{BFO} = 3.964 \pm 0.001$ Å for BFO/MgO(001) and $c_{BFO} = 3.960 \pm 0.001$ Å, $c_{SBN} = 3.972 \pm 0.001$ Å for BFO/SBN/MgO(001). The addition of the SBN layer results in a slight decrease in the BFO unit cell parameter, corresponding to –0.1% additional unit cell strain.

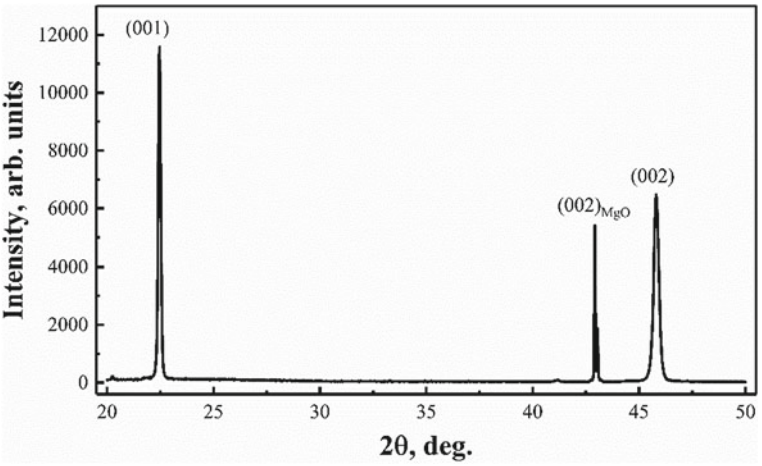

Fig. 1 θ-2θ diffraction pattern of BFO/MgO(001)

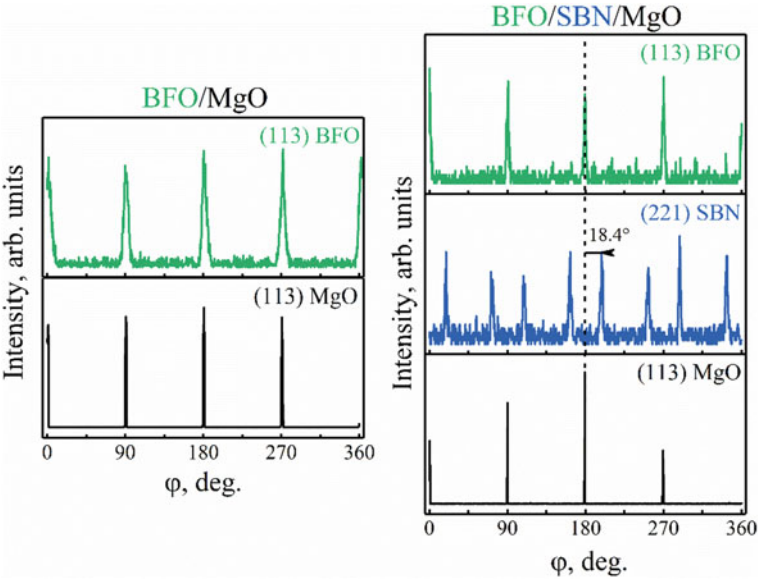

Fig. 2 φ-scans of (113) BFO, (221) SBN and (113) MgO reflections for BFO/MgO(001) and BFO/SBN/MgO(001) heterostructures

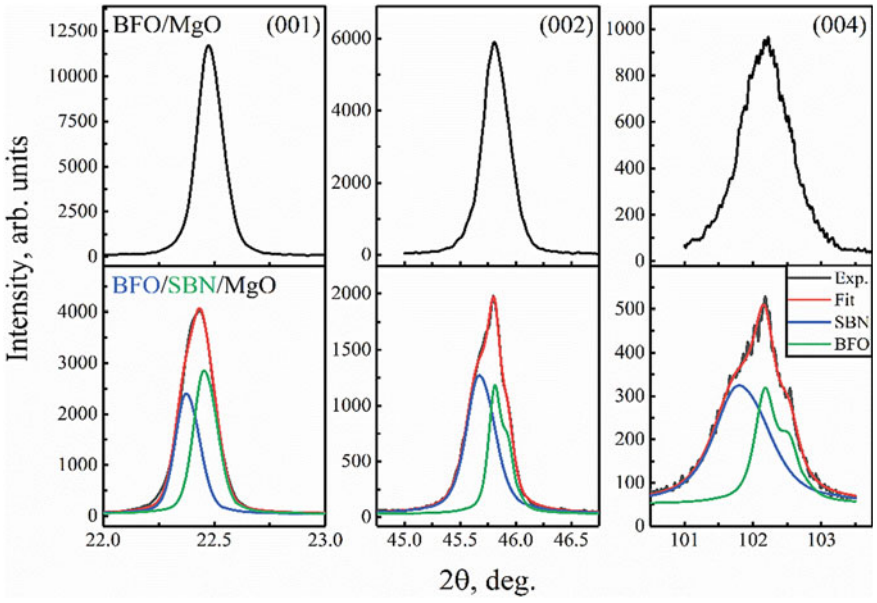

Fig. 3 Precision θ-2θ-scanning of (00l) reflections for BFO/MgO(001) (top) and BFO/SBN/MgO(001) (bottom) heterostructures

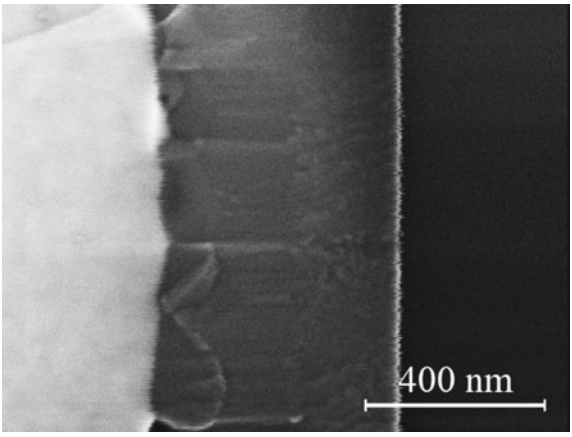

Fig. 4 SEM image of mechanical cross-cut of BFO/SBN/MgO(001) heterostructure

To determine the in-plane unit cell parameters a series of (113) and (103) reflections of the BFO/MgO(001) heterostructure in an asymmetric geometry were obtained. Within the accuracy of the obtained X-ray diffraction data, for BFO the most probable is the following monoclinic unit cell $a = b = c = 3.964$ nm, $\alpha = \beta = 89.75°$, $\gamma = 90°$. Comparing the obtained parameters with the parameters of bulk BFO ($a = 3.965$ Å; $\alpha = 89.45°$), it can be seen that the unit cell strain is insignificant.

The films have high crystal perfection and a low number of structural defects, which appear in narrow reflections on the θ-2θ and φ scans. The misorientations of the crystallographic axes are insignificant and do not exceed 0.7°. The high crystalline perfection, homogeneity and absence of impurities were also approved by SEM cross-cut studies of BFO/SBN/MgO(001) heterostructure (Fig. 4). Each layer of the two-layer heterostructure differs in texture and color, which is due to both different compositions and different electrical properties, while the interface is fairly uniform. Pores, cavities, inclusions of impurity phases have not been found.

3 Conclusion

BFO epitaxial films on MgO (001) substrates with and without an SBN epitaxial layer were obtained by the RF-cathodic sputtering technique. By deposition a sufficiently thick film, it was possible to achieve almost complete relaxation of the unit cell strain. It was found that the deposition of an intermediate SBN layer does not lead to a significant change in the unit cell parameters. It was shown that the presence of two types of orientational domains in the SBN layer (± 18.4º) does not lead to a rotation of the BFO unit cell.

Acknowledgements This study was performed within a government contract for the Southern Scientific Center of the Russian Academy of Sciences (project no. 0120-1354-247) and supported by grant No. MK-678.2020.2 of the President of the Russian Federation.

References

1. J.F. Scott, J. Mater. Chem. **22**, 4567 (2012)
2. N.A. Hill, J. Phys. Chem. B. **104**(29), 6694 (2000)
3. R.R. Das, D.M. Kim, S.H. Baek, C.B. Eom, F. Zavaliche, S.Y. Yang, R. Ramesh, Y.B. Chen, X.Q. Pan, X. Ke, M.S. Rzchowski, S.K. Streiffer, Appl. Phys. Lett. **88**, 242904 (2006)
4. J. Li, J. Wang, M. Wuttig, R. Ramesh, N. Wang, B. Ruette, A.P. Pyatakov, A.K. Zvezdin, D. Viehland, Appl. Phys. Lett. **84**, 5261 (2004)
5. J. Wang, J.B. Neaton, H. Zheng, V. Nagarajan, S.B. Ogale, B. Liu, D. Viehland, V. Vaithyanathan, D.G. Schlom, U.V. Waghmare, N.A. Spaldin, K.M. Rabe, M. Wuttig, R. Ramesh, Science **299**, 1719 (2003)
6. C.-Y. Kuo, Z. Hu, J.C. Yang, S.-C. Liao, Y.L. Huang, R.K. Vasudevan, M.B. Okatan, S. Jesse, S.V. Kalinin, L. Li, H.J. Liu, C.-H. Lai, T.W. Pi, S. Agrestini, K. Chen, P. Ohresser, A. Tanaka, L.H. Tjeng, Y.H. Chu, Nat. Commun. **7**, 12712 (2016)
7. F. Aziz, P. Pandey, M. Chandra, A. Khare, D.S. Rana, K.R. Mavani, J. Magn. Magn. Mater. **356**, 98 (2014)
8. M. Tyagi, R. Chatterjee, P. Sharma, J. Mater. Sci.: Mater. Electron. **26**, 1987 (2015)
9. Y.-H. Lee, C.-C. Lee, Z.-X. Liu, C.-S. Liang, J.-M. Wu, Electrochem. Solid-State Lett. **9**(5), F38 (2006)
10. Yu S Kuz'minov, *Ferroelectric Crystals for Control of Laser Radiation* (Nauka, Moscow, 1982), p. 400 (In Russian)
11. A.V. Pavlenko, L.I. Ivleva, D.V. Stryukov, A.P. Kovtun, A.S. Anokhin, P.A. Lykov, Phys. Solid State **61**, 244 (2019)

The Effect of the Preparation Conditions on the Catalytic Activity of Palladium in the System of Mechanically Pre-activated Salt K_2PdCl_4–C_2H_2–CH_3OH

T. V. Krasnyakova, D. V. Nikitenko, I. A. Verbenko, and S. A. Mitchenko

Abstract Preliminary mechanochemical activation of the K_2PdCl_4 salt forms a heterogeneous catalyst for the reaction of acetylene with methanol to form 1,1-dimethoxyethane and vinyl chloride. An increase in the duration of the palladium salt pre-treatment is accompanied by: (i) an increase in the surface concentration of active sites of the prepared catalyst, which leads to a rise in its catalytic activity; (ii) a monotonic increase in vinyl chloride selectivity. An increase in the reaction temperature has a beneficial effect on the selectivity of the reaction with respect to both observed products.

Keywords Heterogeneous catalyst · Mechanochemical activation (MA) · Catalyst surface · Acetylene · Methanol

1 Introduction

The new materials formation is one of the central problems of modern engineering and technology development. Engineering, materials science, medicine and other industries require the production of materials with special electrical, magnetic, temperature-dependent, chemical and other properties. One of the methods for obtaining of such materials is mechanochemical activation, which is a combination of uniaxial loading and shear deformation of a substance in various dispersion media [1]. Methods of mechanochemical activation make it possible to obtain nano- and submicrocrystalline materials with special physicochemical characteristics, which differ significantly from the properties of the initial polycrystalline sample. Specific properties are often determined by the nanocrystalline structure, a high degree of defectiveness, and the presence of amorphous, quasicrystalline, and metastable phases.

T. V. Krasnyakova (✉) · D. V. Nikitenko · S. A. Mitchenko
Institute of Physical Organic and Coal Chemistry, Donetsk, Ukraine
e-mail: ktv_@list.ru

I. A. Verbenko
Research Institute of Physics, Southern Federal University, Rostov-on-Don, Russia

I. A. Parinov et al. (eds.), *Physics and Mechanics of New Materials and Their Applications*, Springer Proceedings in Materials 10,
https://doi.org/10.1007/978-3-030-76481-4_7

The creating localized on the surface defects of a crystal structure (active sites of heterogeneous catalysts) by mechanochemical grinding opens up wide possibilities for using this method in heterogeneous catalysis [2].

Previously we have found [3, 4], that mechanical treatment in an atmosphere of unsaturated hydrocarbons of a palladium salt K_2PdCl_4 leads to the formation on the surface of coordinatively unsaturated complexes $[PdCl_3*]^-$. Such states are active sites of a heterogeneous catalyst for the hydrochlorination of acetylene with gaseous HCl [5, 6]. If the halogen in the hydrochloride molecule is replaced by the methoxy group OMe, then it can be assumed that the addition of methanol to acetylene will proceed in a similar way. Indeed [7], in the absence of continuous mechanical treatment, the pre-activated in acetylene K_2PdCl_4 salt catalyzes the reaction of methanol with acetylene to form 1,1-dimethoxyethane. Vinyl chloride is released in parallel.

1.1 Research Purpose

The aim of this work is to determine the effect of the reaction conditions in the system of mechanically pre-activated salt K_2PdCl_4–C_2H_2–CH_3OH on the regularities of its course.

1.2 Research Scope

In this study, we consider the following frameworks of the problem:

(i) The impact of the mechanical energy absorbed by the palladium salt during its MA on the rate and selectivity of the reaction over the formed catalyst.
(ii) The effect of temperature on the rate and selectivity of the reaction.

2 Research Method

2.1 Preparation of Heterogeneous Catalysts

The salt K_2PtCl_4 was synthesized via a standard procedure [8] and was dried at 120–140 °C for 3 days. Increasing the drying time did not significantly affect the reaction kinetics. The reactions were carried out in a closed reactor. The reactor was sealed with a replaceable rubber gasket.

To prepare the active catalysts, dry palladium salt (0.25 g) was mechanochemically activated for a certain time in an acetylene atmosphere in a ~ 14 ml glass reactor using a MMVE-0.005 vibratory mill (Hephaestus, Russia) at a specific power input

of ~ 15W/kg. Acetylene was obtained from calcium carbide using a standard procedure [9]. The resulting gases were dried over calcined $CaCl_2$. The specific dose of mechanical energy absorbed by the K_2PdCl_4 powder was determined according to the relation [10]:

$$D_{\text{sp.}} = It, \tag{1}$$

where t is the time of the MA of the salt. The specific surface area of the resultant catalysts was determined by the BET method from argon desorption.

2.2 Chromatographic Studies

Gas mixture analyzed by GLC using an LKhM-8-MD chromatograph with a flame-ionization detector and equipped with data acquisition system MultiChrom Ampersand. The components of the mixture were separated on a 2 m column filled with an adsorbent Silochrome S-120. Reagents and reaction products were identified by retention time. The relative content of acetylene and vinyl chloride in the gas phase of the reactor was determined as the ratio of the areas of the corresponding chromatographic peaks to the peak area of ethane used as an internal standard. The amount of compound was calculated using calibration curves for acetylene or vinyl chloride. The amount of vinyl chloride liberated was determined taking account of the difference in sensitivity of the flame ionization detector relative to C_2H_2 and C_2H_3Cl by a factor of 1.26.

2.3 Kinetics Studies

The mechanochemically pre-activated catalyst was purged with a flow of dry argon for 15 min to remove foreign gases. Then the reactor was sealed and the required amount of methanol, acetylene and ethane (methane) as an internal standard were introduced through a rubber gasket using a microsyringe. The reactor containing the catalyst and the gas mixture was placed in a thermostat. Probes of the gas phase from the closed reactor were taken without breaking the tightness at regular intervals using a syringe with a fixed volume of 0.121 ml.

The kinetics of acetylene consumption and vinyl chloride accumulation was studied in the temperature range of 30–100 °C. Selectivity to vinyl chloride was determined chromatographically as the ratio of the amount of the released product to the amount of consumed acetylene.

The yield of the reaction products was determined independently by NMR spectrometry. After the reaction, 1 ml of deuterated chloroform was introduced into the reactor, and 1 μl of HMDS was added to the resulting suspension as an internal

standard. The contents of the reactor were transferred to a centrifuge tube, the precipitate was separated by centrifugation, and the solution was transferred to an NMR ampoule. NMR spectra of the reaction products $H_3C–CH(OCH_3)_2$ and $H_2C = CHCl$ were recorded on a Bruker AVANCE-II-400 instrument (Bruker BioSpin GmbH) with an operating frequency of 400 MHz, the software for which allowed integrating the signals.

3 Results and Discussion

3.1 Catalytic Reaction of Acetylene with Methanol

For the formation of the active form of the catalyst, MA of the salt is required, since the reaction does not proceed on the catalyst surface without preliminary treatment. The kinetics of acetylene consumption under conditions of excess methanol corresponds to a first-order equation.

The amount of palladium salt loaded with a mass of $m = 0.25$ g corresponds to 767 μmol. Taking into account the lattice parameters of the crystal structure of K_2PdCl_4 ($a = b = 7.05$ Å and $c = 4.1$ Å [11]) and the specific surface area of the salt ($S_{sp} \approx 6.7$ m^2/g [4]), we can evaluate the upper limit of the amount of palladium complex anions located on the surface:

$$N = \frac{S_{sp} \cdot m}{a \cdot c} \tag{2}$$

which is ~ 6×10^{18} anions and corresponds to ~ 10 μmol of Pd on the surface. In our experiments, the maximum amount of acetylene consumed over one catalyst load was at least 1.7 mmol, and catalytic activity did not significantly decrease. Thus, the minimum number of catalytic cycles for palladium complexes located on the surface of the salt is ~ 170, which corresponds to ~ 2.2 cycles based on bulk palladium.

With an excess of methyl alcohol, the acetylene consumption from the gas phase of a closed reactor corresponds to the first-order kinetic law, as in the case of acetylene hydrochlorination [6]. The first order in acetylene can be explained by the fact that Pd(II) does not give stable π-complexes [4, 12]. Their amount on the surface is determined by the partial pressure of acetylene in the gas phase, and the change in the amount of methanol adsorbed on the surface under the above conditions can be neglected.

3.2 Dependence of Catalyst Activity on the Time of Its MA

On the surface of a nonactivated salt, acetylene is not consumed at a noticeable rate. An increase in the pre-activation time of the K_2PdCl_4 powder leads to a monotonic increase in the catalyst activity (Table 1).

The specific surface area of the catalyst also growths monotonically with an increase in the salt pre-activation time (Table 2) [4].

The dependence of the specific surface area S_{sp} of the catalyst on the dose of mechanical energy D_{sp} absorbed by the powder has the form of a curve with saturation (Fig. 1) and corresponds to the equation:

$$S_{sp} = S_0 + S^*_{sp}\left(1 - e^{-\eta_S D_{sp}}\right), \tag{3}$$

where S_0 is the specific surface area of the initial K_2PdCl_4 powder, $(S_0 + S^*_{sp})$ is the limiting value of the increase in the specific surface area due to MA, and η_s is the constant characterizing the efficiency of new surface formation (quantity inverse to the specific work of surface formation).

Table 1 Dependence of the observed rate constant (k_{ef}) of acetylene consumption in the reaction of acetylene and methanol on the duration (t) of the pre-treatment of the K_2PdCl_4 salt

t, min	$k_{ef} \times 10^4$, s^{-1}
0	0
10	0.32 ± 0.01
15	0.65 ± 0.01
20	0.60 ± 0.01
30	0.70 ± 0.01
40	1.30 ± 0.02
60	1.70 ± 0.10
67	1.90 ± 0.10
90	3.10 ± 0.10
120	4.30 ± 0.20
180	4.30 ± 0.20
240	5.20 ± 0.10

Table 2 Effect of the time (t) of the catalyst MA on the specific surface area (S_{sp}) of the K_2PdCl_4 salt [4]

t, min	S_{sp}, m^2/g
0	~ 0.02
15	4.7 ± 0.50
30	6.0 ± 0.60
60	5.9 ± 0.60
90	6.9 ± 0.70
120	7.2 ± 0.70

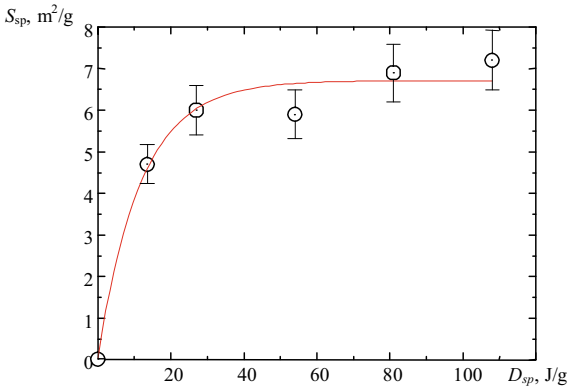

Fig. 1 Dependence of the specific surface area S_{sp} of the K_2PdCl_4 powder on the absorbed specific dose D_{sp} of mechanical energy. The points are experimental S_{sp} values, and the curve represents the data calculated using (3) for $(S_0 + S^*_{sp}) = (6.7 \pm 0.7)$ m^2/g and $\eta_s = (8 \pm 2) \times 10^{-2}$ g/J [6]

The increase in catalytic activity with an increase in the MA time can be due to two factors, namely, an increase in the specific surface area of the salt and an increase in the surface concentration of active sites. We exclude the impact of the first factor on the observed rate constant of acetylene consumption by considering the rate constant k^* per unit catalyst surface area:

$$k^* = k_{ef}\left(S_{sp}m\right)^{-1} \tag{4}$$

The dependence of parameter k^* on the specific dose D_{sp} of mechanical energy absorbed by the powder also has the form of a curve with saturation (Fig. 2) and obeys the equation:

$$k^* = k^*_{max}\left(1 - e^{-\eta D_{sp}}\right), \tag{5}$$

where k^*_{max} is the limiting value of k^*,

and η is the constant characterizing the efficiency of the formation of active sites in the catalyst under MA (quantity inverse to the specific work of formation of active sites in the catalyst).

The selectivity of the reaction for vinyl chloride $Y = \frac{\nu(C_2H_3Cl)}{\nu(C_2H_2)}$ increases with an increase in the duration of the pretreatment of the palladium salt (Table 3).

The dependence of selectivity of the reaction to vinyl chloride Y_{VCM} on the specific dose D_{sp} of mechanical energy absorbed by the powder also appears as a curve with saturation (Fig. 3) and obeys the equation:

$$Y = Y_\infty\left(1 - e^{-\eta_Y D_{sp}}\right) \tag{6}$$

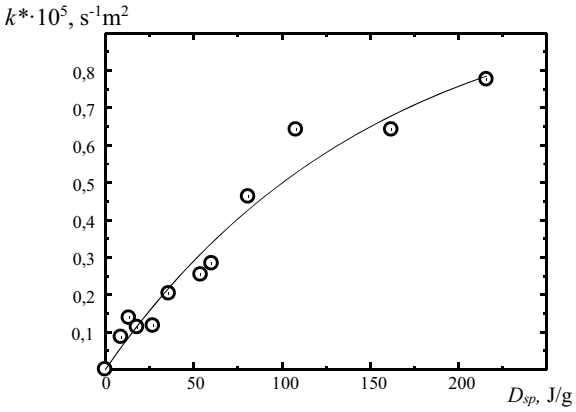

Fig. 2 Dependence of the apparent rate constant k^* of acetylene consumption per unit area of the catalyst surface on the specific dose D_{sp} of mechanical energy absorbed by the K_2PdCl_4 powder. The points are experimental k^* values, and the curve represents the data calculated using (5) for $k^*_{max} = (1.04 \pm 0.17) \times 10^{-5}$ s^{-1} m^{-2} and $\eta = (0.7 \pm 0.2) \times 10^{-2}$ g/J

Table 3 Selectivity of the reaction to vinyl chloride (Y), depending on the time (t) of MA of the K_2PdCl_4 salt

t, min	Y, %
10	0
20	4.4 ± 0.3
40	5.2 ± 0.2
60	8.2 ± 0.3
67	14.2 ± 1.7
120	15.6 ± 0.8
180	14.0 ± 1.0
240	15.4 ± 2.0

where Y_∞ is the limiting value of selectivity of the reaction to vinyl chloride, η_Y is constant, characterizing the efficiency of formation of active sites of the catalyst for vinyl chloride production.

The significant difference of the parameter η_s from η and η_Y (Table 4) obviously means that the surface growth and the formation of active sites of the catalyst are not related. The close values of η and η_Y suggest that 1,1-dimethoxyethane and vinyl chloride are formed at the same active sites. The surface concentration of the active sites of the catalyst increases with a rise of the pre-activation time of the salt, as evidenced by the monotonic increase in the observed rate constant of acetylene consumption reduced to a unit surface area of the catalyst.

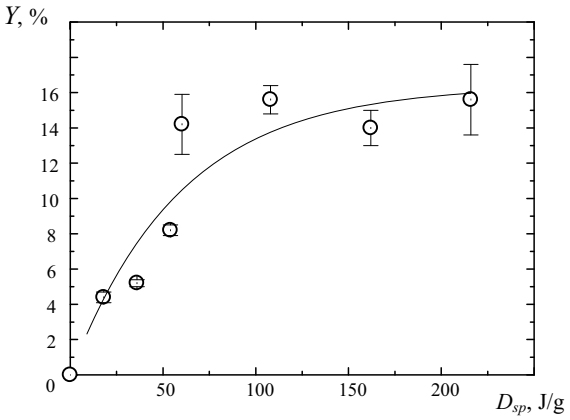

Fig. 3 Dependence of the selectivity Y of the reaction to vinyl chloride on the specific dose D_{sp} of mechanical energy absorbed by the K_2PdCl_4 powder during MA. The points are experimental Y values, and the curve represents the data, calculated using (6) for $Y_\infty = (16.4 \pm 2.2)$ % and $\eta_Y = (1.7 \pm 0.6) \times 10^{-2}$ g/J

Table 4 Parameters in (3, 5, 6)

η_Y,10^{-2} g/J	η,10^{-2} g/J	η_s, 10^{-2} g/J
1.7 ± 0.6	0.7 ± 0.2	8 ± 2

3.3 Temperature Dependence of Catalyst Activity and Selectivity

The values of the observed rate constants of acetylene consumption and product yields at different temperatures given in Table 5. As can be seen, an increase in temperature has a beneficial effect on the selectivity of the reaction with respect to both observed products, especially for the vinyl chloride monomer.

Table 5 Values of the observed rate constant k_{ef} of acetylene consumption and the selectivity of the reaction to vinyl chloride (Y) and 1,1-dimethoxyethane (Y_{DME}); duration of MA 1 h

T, °C	k_{ef}, 10^{-4} c^{-1}	Y, %	Y_{DME}, %
30	1.5 ± 0.1	5 ± 1	15 ± 2
50	2.1 ± 0.1	11 ± 1	27 ± 3
80	3.7 ± 0.1	20 ± 1	28 ± 3
103	7.9 ± 0.2	30 ± 2	27 ± 2

4 Conclusion

For K_2PdCl_4 salt, we have showed:

(i) salt without preliminary MA is inactive for the reaction of methyl alcohol with acetylene;
(ii) the active sites of the catalyst are formed upon mechanically activation of the salt in an acetylene atmosphere;
(iii) an increase in duration of MA of the salt results in a growth of its catalytic activity due to an increase in the surface concentration of active sites and is accompanied by a rise of the yield of vinyl chloride by-product;
(iv) the selectivity for both products increases with raising temperature.

Acknowledgements Research was financially supported by the Ministry of Science and Higher Education of the Russian Federation (State assignment in the field of scientific activity, Southern Federal University, 2020).

References

1. G. Heinicke, *Tribochemistry* (Akademie-Verlag, Berlin, 1984)
2. S.A. Mitchenko, Theoret. Exp. Chem. **43**(4), 199 (2007)
3. S.A. Mitchenko, T.V. Krasnyakova, I.V. Zhikharev, Theoret. Exp. Chem. **46**(1), 32 (2010)
4. T.V. Krasnyakova, I.V. Zhikharev, R.S. Mitchenko, V.I. Burkhovetski, A.M. Korduban, T.V. Kryshchuk, S.A. Mitchenko, J. Catal. **288**, 33 (2012)
5. S.A. Mitchenko, T.V. Krasnyakova, I.V. Zhikharev, Theoret. Exp. Chem. **44**(5), 306 (2008)
6. S.A. Mitchenko, T.V. Krasnyakova, I.V. Zhikharev, Kinet. Catal. **50**(5), 764 (2009)
7. T.V. Krasnyakova, D.V. Nikitenko, O.V. Khazipov, S.A. Mitchenko, Kinet. Catal. **61**(6), 940 (2020)
8. *Synthesis of Platinum Metal Complex Compounds*, ed. by I.N. Chernyaev. Handbook, (Nauka, Moscow, 1964). (In Russian)
9. F.M. Rapoport, A.A. Il'inskaya, *Laboratory Methods for Pure Gases Receiving* (Goskhimizdat, Moscow, 1963). ((In Russian))
10. PYu. Butyagin, A.R. Kuznetsov, I.K. Pavlychev, Instruments and Technique of Experiment **6**, 201 (1986). ((In Russian))
11. *JCPDS*: International Centre for Diffraction Data, No. 12–412
12. M. Herberhold. *Metal π-Complexes. V. II. Complexes with mono-olefinic ligands.* (Elsevier, Amsterdam, London, N.-Y., 1972)

Phase Formation and Optimisation of the Properties of Solid Solutions in a KNN-Based System for Hydroacoustics Devices

E. V. Glazunova, I. A. Verbenko, L. A. Shilkina, K. P. Andryushin, A. V. Nagaenko, and L. A. Reznichenko

Abstract Following bans on the use of toxic substances in electrical and electronic equipment, since 2003, special attention has been paid to the development and production of lead-free materials based on sodium-potassium niobate systems. This study reports the results of optimising the ferro-piezoelectric properties of $Li_aK_bNaNb_dTa_mSb_nO_3$ solid solutions using technological systems and doping. The influence of the ratio of components and dopants on the structure and piezoelectric properties of solid solutions is established. The promising compositions, which may be the basis for producing functional materials that can be used in hydroacoustic devices, were selected by analysing the dielectric and piezoelectric characteristics.

Keywords Lead-free piezoelectric ceramics · Sodium–potassium niobate (KNN) · Hydroacoustic devices

1 Introduction

Responsibly managing ocean resources is important globally because they provide many food products. The sustainable economic use of aquatic biological resources requires constant, objective, and regularly renewable quantitative control of populations in the aquatic environment. Modern hydroacoustic devices, such as hydrophones, fish finders, and trawl probes, are applied globally. Since the 1960s, most industrial piezoceramic materials used in the hydroacoustic industry and other fields are solid solutions based on lead zirconate titanate systems (PZT) [1]. However, these compounds have many negative properties. First, lead is an extremely toxic

E. V. Glazunova (✉) · I. A. Verbenko · L. A. Shilkina · K. P. Andryushin · L. A. Reznichenko
Institute of Physics, Southern Federal University, Rostov-on-Don 344090, Russia
e-mail: kate93g@mail.ru

A. V. Nagaenko
Institute of High Technology and Piezo Technic, Southern Federal University, Rostov-on-Don 344090, Russia

I. A. Parinov et al. (eds.), *Physics and Mechanics of New Materials and Their Applications*, Springer Proceedings in Materials 10,
https://doi.org/10.1007/978-3-030-76481-4_8

element. Its cumulative effects can seriously harm the environment, so its use in environmental projects is limited (RoHS 2011/65/EU) [2, 3]. Second, piezoceramic materials' industrial parameters vary widely and are associated with low production manufacturability and the properties of the compounds themselves (high chemical activity in aqueous media and aging effects). Third, the low-frequency selectivity of modern piezoelectric transducers necessitates applying complex electronics to suppress false oscillations to extract and enhance the necessary target signals. Finally, piezoceramic transducers currently used to produce antennas have extremely complex structures and piezoceramics are very fragile materials, so increasing their material strength requires considerable effort. Providing high-quality hydroacoustic signal reception and reducing structural interference on the media side are also challenging. Compensating for interference is possible only with high-performance piezoceramic sensors. Moreover, the electromechanical conversion parameters of acoustic oscillations in piezoelectric materials based on PZT systems depend on changes in static pressure and temperature. These parameters are associated with significantly nonlinear properties of these materials due to the proximity of morphotropic and polymorphic phase boundaries. Currently used piezoelectric materials are characterised by markedly reduced electromechanical signal efficiency in the infrasound regions, which is most important from a hydroacoustic perspective. A serious obstacle to the introduction of these materials is low-performance piezoelectric elements. In piezoceramics based on PZT systems, their performance fluctuates from 10–30% [4]. Based on their characteristics, applying materials based on PZT systems to hydroacoustic devices operating in their reception mode is limited based on current data. To solve these problems and reduce the weight and size of hydroacoustic complexes, creating new lead-free piezoelectric materials with targeted piezoelectric characteristics is required for hydroacoustic applications [5, 6] suitable for controlling and managing aquatic environments and their biological resources. Lead-free materials are attractive systems based on alkali metal niobates that have been thoroughly studied. To date, considerable research has been devoted to investigating ceramics based on $K_{1-x}Na_xNbO_3$ (KNN) systems.

Solid solutions with KNN-based systems have advantages over other lead-free piezoelectric due to their higher dielectric constants caused by the morphotropic boundary's proximity to the line of ferroelectric phase transitions, high manufacturability, and Curie temperature ($T_C > 400$ K), and are suitable for practical applications [7–11]. Prior studies [12–14] demonstrated that solid solutions with KNN systems near the morphotropic boundary $x \approx 0.50$ exhibited piezoelectric characteristics that are the closest to PZT compositions: piezoelectric module $d_{33} \sim 80$ pC/N and electromechanical coupling coefficient of the planar oscillation mode $K_p \sim 0.36$. These compositions have very promising research prospects. Solid KNN $(Li_{0.05}Na_{0.52}K_{0.42})NbO_3$ solutions modified with lithium have an insufficient dielectric constant $\varepsilon_{33}{}^{T}/\varepsilon_0 = 930$ but high piezoelectric activity ($K_p = 0.45$, $|d_{31}| = 82$ pC/N). The piezoelectric activity is even better in $(1–x)Na_{1/2}K_{1/2}NbO_3–xLiSbO_3$ systems: $d_{33} > 150$ pC/N and $K_p = 0.46$ at a Curie temperature $T_C = 630$ K [15], which significantly overlaps the room temperature range.

A literature analysis [16] demonstrated that materials used in hydroacoustic fishing should have an average relative polarised permittivity of $\varepsilon_{33}{}^{T}/\varepsilon_0 = 1200$, a high electromechanical coupling coefficient in the planar oscillation mode $K_p > 0.40$ and a low mechanical quality factor $Q_M < 200$ at room temperature.

An analysis of the related literature (RU 2,580,538, RU 2,571,465, US 2013/0162109, and KR 2013/0029476) demonstrated that the most promising hydroacoustic industry materials have $Li_aK_bNa_cNb_dTa_mSb_nO_3$ chemical compositions. When various modifiers are added to these solid solutions, for example, NiO and B_2O_3 (RU 2,580,538, RU 2,571,465), it is possible to achieve an average polarised ceramics $\varepsilon_{33}{}^{T}/\varepsilon_0 \approx 1200$, a sufficiently high piezoelectric module $|d_{31}| \approx 60$ pC/N, and an electromechanical coupling coefficient in the planar oscillation mode $K_p \approx 0.30$ and low $Q_M \approx 80$. However, for these applications, the material has insufficient piezoelectric activity (K_p). By doping Bi_2O_3 and Fe_2O_3 oxides into the system (RU 2015/2542009), the piezoelectric activity can be significantly increased to $K_p \sim 0.50$, but simultaneously, $\varepsilon_{33}{}^{T}/\varepsilon_0$ decreases to ~ 600, which is two times lower than the required value. Adding ZrO_2, MnO, and SiO_2 to the system (US 2013/0162109) provides high values of $K_p \sim 0.40$, $|d_{31}| \approx 80$ pC/N values, but a low value of $\varepsilon_{33}{}^{T}/\varepsilon_0 \approx 900$.

Several crystal-chemical and technological difficulties hinder the introduction of ceramics based on industrial KNN systems caused by the starting materials' high chemical activity [17] and the critical dependence of the objects' properties on the thermodynamic history (manufacturing conditions). In many cases, reducing the influence of these properties can be achieved by introducing modifiers, such as various Cu-containing additives. Introducing dopants significantly decreases the optimal sintering temperatures, the conservation of a given stoichiometric composition, and increasing in the relative density of ceramic samples [18, 19]. Thus, the complex modification of the $Li_aK_bNa_cNb_dTa_mSb_nO_3$ system using Bi_2O_3 and Fe_2O_3 oxides and $CuNb_2O_6$ obtains high-density ceramics with properties that can be used in the hydroacoustic industry.

1.1 Research Purpose

The goal of this study was to establish phase formation laws and produce optimally targeted electrophysical properties of solid solution multicomponent systems based on sodium-potassium niobate modified by Bi_2O_3, Fe_2O_3, and $CuNb_2O_6$ oxides to develop new piezoelectric materials for hydroacoustic equipment.

2 Research Method

$Li_aK_bNa_cNb_dTa_mSb_nO_3$, modified ($Fe_2O_3 + Bi_2O_3$), and $CuNb_2O_6$ systems were the subjects of this study. The raw powders were $NaHCO_3$ (99%), $KHCO_3$ (98%),

Li_2CO_3 (98%), Nb_2O_5 (98%), Ta_2O_5 (99%), Sb_2O_5 (99%), Fe_2O_3 (98%), Bi_2O_3 (99%), and CuO (99.9%). The solid solutions were prepared using a two-stage solid-state reaction at $T_1 = 1273$ K for 6 h and $T_2 = 1373$ K for 6 h followed by sintering using conventional ceramic technology (CCT) at $T_{sin.} = 1468$ K for 2 h with variable temperatures during each stage of the production process. Three solid solution superstoichiometric modification methods were used in this study: 0.5 wt.% (Fe_2O_3 + Bi_2O_3) and $CuNb_2O_6$ (SS-1), 1.5 wt.% (Fe_2O_3 + Bi_2O_3) and $CuNb_2O_6$ (SS-2), and 2.0 wt.% (Fe_2O_3 + Bi_2O_3) and $CuNb_2O_6$ (SS-3).

The synthesis and sintering conditions were selected for the experimental samples based on the results of X-ray (XRD) measurements of the ceramic samples' relative density. X-ray diffraction was conducted using a DRON 3.0 diffractometer (using CoK_α radiation with Bragg–Brentano focusing). The microstructure was observed using scanning electron microscopy (SEM) with a JSM –6390L microscope. The samples were polarised in oil in a chamber with PES 5 K at 3.0–3.5 kV. The electrophysical parameters were measured using Agilent 4980A and Wayne Kerr 6500B precision LCR meters via the resonance–antiresonance method [20, 21] at room temperature. The piezo-modules were measured using APC International, Ltd.Piezo d33Test System. The temperature dependence $\varepsilon/\varepsilon_0$ was measured in a temperature range $T = 300$–900 K at frequencies of 75 kHz–1 MHz.

3 Results and Discussion

An X-ray phase analysis of the $Li_aK_bNa_cNb_dTa_mSb_nO_3$ system showed that all of the solid solutions had perovskite-type structures. An XR analysis demonstrated that two impurity phases formed as a result of the synthesis: pyrochlore and $LiSbO_3$.

An X-ray phase analysis also showed (Fig. 1) that the second modification method is optimal from the technological point of view (were produced the pure solid solutions after synthesis).

The solid solution obtained using the second modification method (1.5 wt.% Fe_2O_3 + Bi_2O_3 and 1.5 wt.% $CuNb_2O_6$) after the synthesis was pure. The X-ray phase analysis also demonstrated that at all of the sintering temperatures, the solid solutions had $Li_2K_3Ta_5O_{15}$ impurity phases.

Data of the relative density of the solid solutions are shown in Table 1. The experimental samples had the highest density (greater than 95%) at $T_{sint.} = 1468$ K after 2 h of exposure.

To select the optimal concentration of the modifiers, the $\rho_{\text{rel.}}$ and the evolution of the grain structure with different content of additives were investigated (Fig. 2).

The preparation of solid solutions with the combined modifiers leads to the following effects: a sharp increase in large grains to a size of ~ 10 μm in SS-2; the transition from stochastic placement in SS-1 to the formation of certain ensembles in SS-2 (highlighted in Fig. 2b by dashed lines); reducing their size in SS-3; transformation of habit from anisotropic "plates" in SS-2 to almost cubic crystallites in SS-3 with the formation of dense regions characterized by the coalescence of

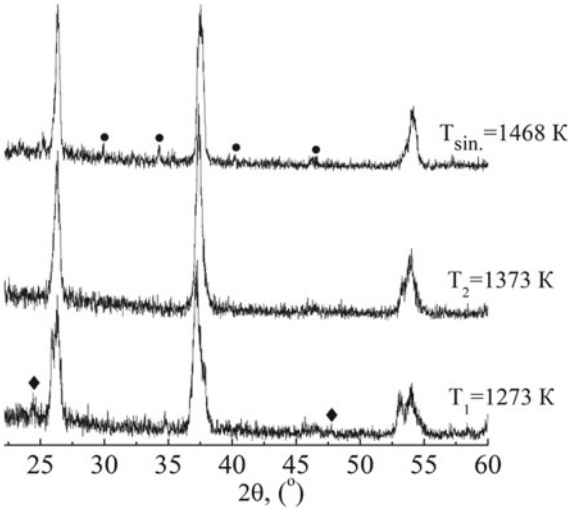

Fig. 1 X-ray diffraction peaks of the solid solutions in the $Li_dK_bNa_cNb_dTa_mSb_nO_3$ systems with 1.5 wt.% ($Fe_2O_3 + Bi_2O_3$) and 1.5 wt.% $CuNb_2O_6$ under optimal conditions (the $LiSbO_3$ peaks are marked by diamonds and the $Li_2K_3Ta_5O_{15}$ peaks are marked by circles)

Table 1 Experimental and relative density of the solid solutions

Technology	ρ, g/cm^3	$\rho_{rel.}$, %
SS-1	3.94	80.6
SS-2	4.67	95.5
SS-3	4.62	94.5

such grains (Fig. 2c by dashed lines). It is undoubtedly related to the qualitative and quantitative composition of modifiers containing low-melting Bi- and Cu-containing components, which are sources of liquid phases [22, 23].

There is the heterogeneity of the grain landscape where crystallites have a form of either parallelepiped ("plates") (larger grains) or close to cubic form (small grains), as shown in Fig. 2. Wherein the size of large and small grains can differ several times (Fig. 2b). The packing of grains is chaotic in places is loose (Fig. 2a).

The presence of these components leads to recrystallization (secondary discontinuous recrystallization type) [24], in which the selective growth of large grains occurs similar growing of single crystals, but not due to the movement of boundaries. Wherein the grains become a certain growth shape and a regular cut, identical to the habit of single crystals growing from a molten solution.

Based on the data obtained, the optimal quantitative composition of the modifier was selected, which ensures sufficient compaction of crystallites and, as a consequence, a higher $\rho_{rel.}$ (95.5%) of the samples.

The temperature dependence of the ceramics' dielectric constant $\varepsilon/\varepsilon_0$ and loss tanδ is shown in Fig. 3. The analyses of the dependence demonstrated anomalies in the 500–600 K region, corresponding to a ferroelectric phase transition between the cubic and tetragonal phases. Moreover, the maximum $\varepsilon/\varepsilon_0$ shifted to higher temperatures and the frequency dispersion decreased.

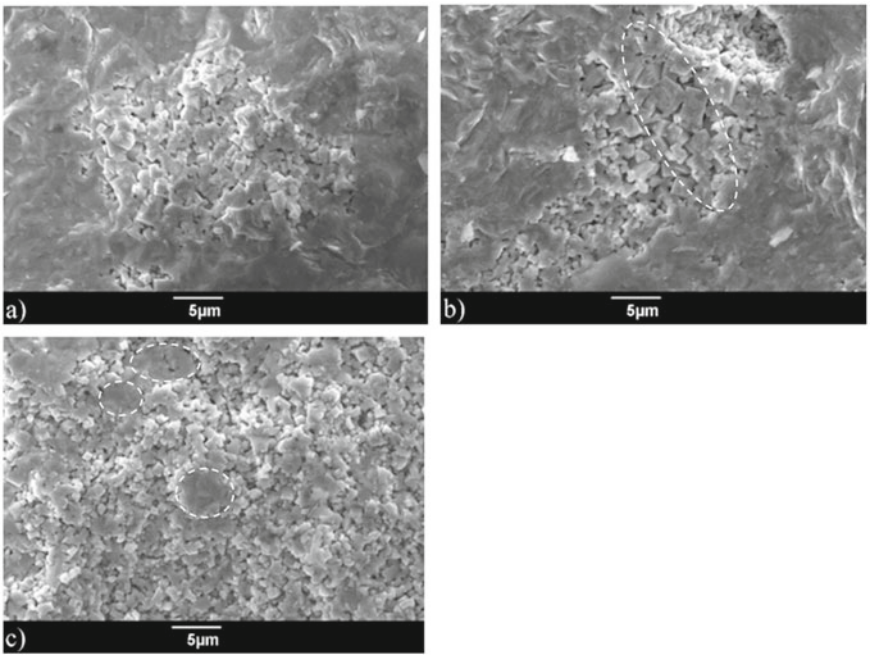

Fig. 2 SEM images of $Li_aK_bNa_cNb_dTa_mSb_nO_3$ modified: **a** SS-1, **b** SS-2, and **c** SS-3

The maximum $\varepsilon/\varepsilon_0$ value ($\varepsilon/\varepsilon_0 > 3000$) occurred at dopant concentrations of ($Fe_2O_3 + Bi_2O_3$) 1.5 wt.% and $CuNb_2O_6$ 1.5 wt.%. However, tanδ in the ferroelectric phase transition region did not exceed 0.02.

The piezoelectric characteristics of previous research on this topic obtained from related reports in the literature (see Table 2) are also provided for comparison.

Compared with the material modified with $CuNb_2O_6$ [RU 2561439], our material exhibited a higher $\varepsilon_{33}{}^T/\varepsilon_0$ and piezoelectric coefficients, and a low Q_M value. It also significantly exceeded the $\varepsilon_{33}{}^T/\varepsilon_0$ value in contrast to the material modified with Fe_2O_3 and Bi_2O_3 [RU 2542009].

The materials produced using a complex combined modification of Fe_2O_3, Bi_2O_3, and $CuNb_2O_6$ oxides were superior to materials found in the literature due to a significant decrease in Q_M and increase in $\varepsilon_{33}{}^T/\varepsilon_0$ to 1135 while maintaining high K_p, and $|d_{31}|$, 0.42, and 52 pC/N, respectively, as listed in Table 2.

Thus, we assumed that the formation of the piezoelectric and electromechanical properties of ferroelectric ceramics, in this case, is influenced by two mechanisms. First, the incorporation of Fe^{3+} and Bi^{3+} ions into the B sublattice of KNN leads to a lack of oxygen and following oxygen vacancies [25, 26]. In the result of the pinning effect, the ferroelectric hard of ceramics increases (an increase in K_p and a slight decrease in dielectric parameters) [27]. Second, when Cu^{2+} is introduced into the KNN system during sintering, intermediate Cu-containing compounds with a low melting point can be formed [17, 28], which are associated with the formation of

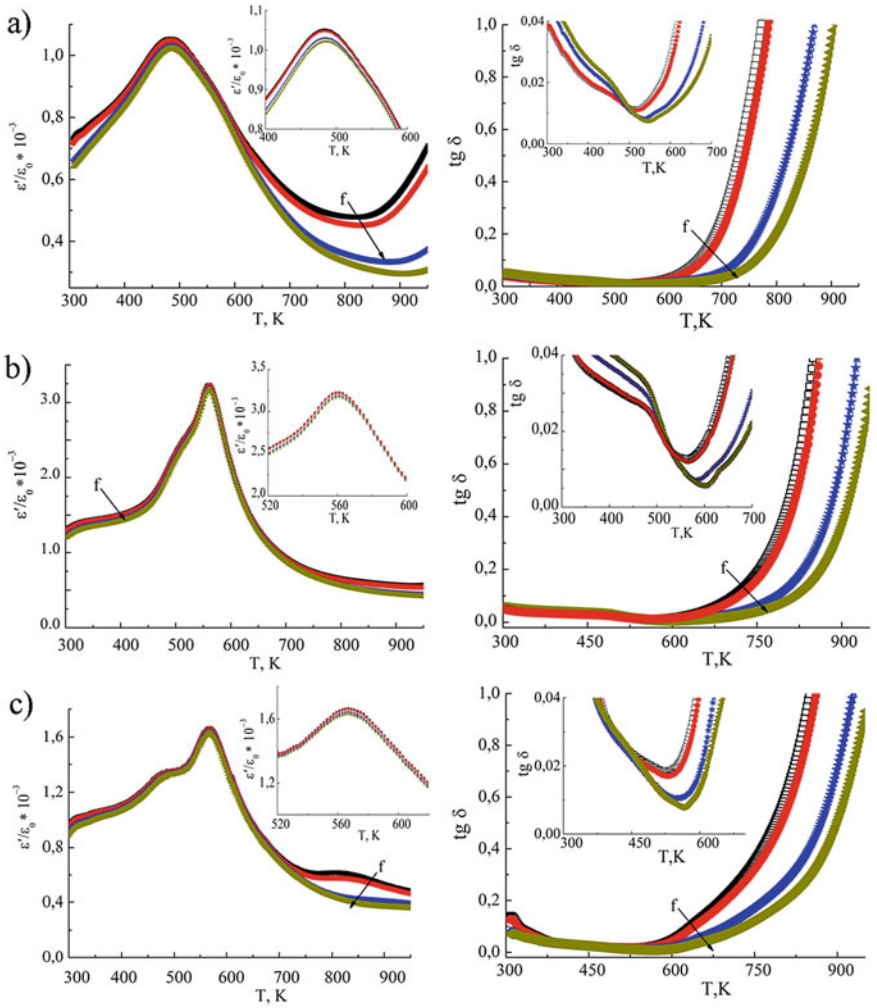

Fig. 3 Temperature dependence of the dielectric constant $\varepsilon/\varepsilon_0$ and loss tanδ of $Li_aK_bNa_cNb_dTa_mSb_nO_3$ modified with: **a** SS-1, **b** SS-2, and **c** SS-3 at frequencies of 75 kHz–1 MHz (in color)

liquid phases that promote the obtaining of a perfect grain structure. In this case, the area of grain boundaries, which are centers of "pinched" of domain walls, decreases. The increased $\varepsilon_{33}{}^{T}/\varepsilon_0$, while maintaining piezoelectric activity and reducing Q_M was likely associated with the sintering processes due to the formation of liquid phases with the participation of Bi_2O_3 and $CuNb_2O_6$ [22, 23, 28]. Thus, depending on which of these two processes will prevail and determines the properties of the material.

Thus, we see that due to the introduction of combined heterovalent additives (additional of the compounds Li_2O, Ta_2O_5, Sb_2O_5, Nb_2O_5, Fe_2O_3, Bi_2O_3, and $CuNb_2O_6$

Table 2 Dielectric, piezoelectric, and ferroelastic characteristics of the $Li_aK_bNa_cNb_dTa_mSb_nO_3$ with 1.5 wt. % ($Fe_2O_3 + Bi_2O_3$) and 1.5 wt. % $CuNb_2O_6$

Technology	ρ, g/cm^3	$\rho_{rel.}$, %	$\varepsilon_{33}{}^T/\varepsilon_0$	K_p	$\lvert d_{31}\rvert$, pC/N	d_{33}, pC/N	Q_M	$V_1{}^E \times 10^3$, km/s
RU 2,561,439 ($CuNb_2O_6$)	4.30	87.9	345	0.32	30.0	90	500	4.745
RU 2,542,009 ($Fe_2O_3 + Bi_2O_3$)	4.10	83.8	603	0.51	63.0	160	115	4.150
CCT (SS-2)	4.67	95.5	1135	0.42	52.0	85	35.4	4.446

into KNN, we managed to increase K_p, which determines the high efficiency of converters in the modes of reception and emission. Low values of Q_M improve the quality signal and suppress false oscillations, which are necessary when using the material in devices operating in the receiving mode (for example, in hydrophones). High values of the speed of sound in the obtained material allow reducing the required thickness of the piezoelectric element in the working hydroacoustic device.

4 Conclusion

Lead-free multicomponent solid solutions based on KNN with $Li_aK_bNa_cNb_dTa_mSb_nO_3$ + 1.5 wt.% ($Fe_2O_3 + Bi_2O_3$) and 1.5 wt.% $CuNb_2O_6$ compositions were produced. These ceramics are effective for use in hydroacoustic devices due to their high $K_p = 0.42$, $d_{31} = 52$ pC/N, average $\varepsilon_{33}{}^T/\varepsilon_0 \sim 1135$, low $Q_M = 35.4$, and environmental friendliness.

The piezomaterials developed in this study can be used in ultrasonic devices to receive hydroacoustic signals (sonar) to convert acoustic signals into electrical signals.

Acknowledgements The study was carried out with the financial support of the Ministry of Science and Higher Education of the Russian Federation (State task in the field of scientific activity, scientific project No (0852-2020-0032)/(BAZ0110/20-3-07IF).

References

1. D. Kajewski, P. Zajdel, A. Soszyński, J. Koperski, I. Lazar, K. Roleder, Ceram. Int. **45**(8), 9871 (2019)
2. Directive 2002/95/EC of the European Parliament and of the Council of 27 January 2003 on the restriction of the use of certain hazardous substances in electrical and electronic equipment. Official J. Eur. Union. **13**, 10 (2003)

3. Directive 2011/65/EU of the European Parliament and of the Council of 8 June 2011 on the restriction of the use of certain hazardous substances in electrical and electronic equipment. Official J. Eur. Union. *L 174*, **54**, 88 (2011)
4. R.J. Bobber, *Hydroacoustic Measurements*, (Moscow, World, 1974), p. 361
5. J. Varghese, R.W. Whatmore, J.D. Holmes, J. Mater. Chem. C. **1**, 2618 (2013)
6. J.J. Zhou, J.F. Li, X.W. Zhang, J. Eur. Ceram. Soc. **32**, 267 (2012)
7. Y. Saito, H. Takao, T. Tani, T. Nonoyama, K. Takatori, T. Homma, T. Nagaya, M. Nature **432**, 84 (2004)
8. X. Chen, X. Yan, X. Li, G. Liu, Xu. Jie Sun, H.Z. Li, J. Alloy. Compd. **762**, 697 (2018)
9. M.-K. Lee, S.-A. Yang, J.-J. Park, G.-J. Lee, Sci. Rep. **9**(1), 4195 (2019)
10. J.G. Wu, D.Q. Xiao, J.G. Zhu, Chem. Rev **115**, 2559 (2015)
11. J.B. Lim, Y.H. Jeong, M.H. Kim, D. Suvorov, J.H. Jeon, Ceram Int. **38**, 2605 (2012)
12. M. Ahtee, A.M. Glazer, Acta Crystallogr. A **32**, 434 (1976)
13. I.P. Raevskii, L.A. Reznichenko, O.I. Prokopalo, Izv. Akad. Nauk. SSSR **15**, 872 (1979)
14. S. Singh, J. Negi, N.S. Panwar, J. Phys. Chem. Solids **123**, 311 (2018)
15. D. Lin, K. W. Kwok, K. H. Lam, H. L. W. Chan, J. Appl. Phys. **101**, 074111 (2007)
16. Ya. S. Karlik, Yu. V. Marapulets, *Fishing Hydroacoustic Branch*, (2004), p. 262
17. V. P. Sakhnenko, N.V. Dergunova, L.A. Reznichenko. *Energy Crystal Chemistry of Solid Solutions Oxygen Octahedral Type and Modeling Piezoceramic Materials,* (Rostov-on-Don, Rostov State University Press, 1999), p. 321
18. M.-R. Yang, S.-Y. Chu, I.-H. Chan, et al. J. Alloys. Compd. **522**(1–5), 094103 (2012)
19. X. Tan, H. Fan, S. Ke et al., Mater. Res. Bull **47**, 4472 (2012)
20. *IEEE Standard on Piezoelectricity ANSI/IEEE Std 176*, New-York. DOI: https://doi.org/10.1109/IEEESTD.1988.79638 (1988)
21. A.A. Pavelko, L.A. Reznichenko, LFPM-2018. Rostov-on-Don **2**, 221 (2018)
22. I. Narai-Sabo. *Inorganic Crystal Chemistry*, (Budapest, 1969), p. 504
23. M.V. Talanov, L.A. Shilkina, L.A. Reznichenko, Inorg. Mater. **52**(10), 1134 (2016)
24. L.A. Reznichenko, V.A. Alyoshin, A.N. Klevtsov, O.N. Razumovskaya, L.A. Shilkina, Ferroelectrics **247**(1–3), 95 (2000)
25. J. Minhong, L. Xinyu, C. Guohua, Scripta Mater. **60**, 909 (2009)
26. E. Erunal, P. Jakes, S. Korbel et al. *Phys. Rev. B.* **84**(1–11), 184113 (2011)
27. E. Li, H. Kakemoto, S. Wada, IEEE Transact. Ultrasonics, Ferroelectrics, and Frequency Control **55**, 980 (2008)
28. M. Matsubara, T. Yamaguchi, W. Sakamoto, K Kikuta, T. Yogo, S.-I. Hirano, J. Am. Ceram. Soc. **88**(5), 1190 (2005)

Improving the Osseointegration Properties of Biocompatible Plasma-Sprayed Coatings Based on Hydroxyapatite and Al_2O_3

I. P. Melnikova, A. L. Nikolaev, and A. V. Lyasnikova

Abstract A new technique of biocompatible coatings spraying on the surface of implants was developed. This technique is based on a special preparation of powders before plasma spraying, namely, the use of immobilization techniques and thermomechanical processing (TMP) of powders. We investigated coatings based on Al_2O_3 and Hydroxyapatite (HAp) obtained with different parameters of TMP. Compression tests and thermal cycling tests have shown that Al_2O_3 powders subjected to TMP at 1200–1250 ºC have the highest resistance to mechanical and thermal influences. It was also shown that coatings obtained from HAp powders subjected to TMP at 800 ºC have a more uniform morphology. At the same time, coatings based on powders obtained with TMP at 1000 °C are more crystalline. The roughness and average size of the open pore channel on these coatings is greater than on coatings obtained with other TMP temperatures. XRD and IR-spectroscopy showed the formation of a new phase of β-tricalcium phosphate, β-$Ca_3(PO_4)_2$, in HAp powders obtained using TMP at 1000 °C. The results achieved in this work will help to obtain biocompatible coatings based on Al_2O_3 and HAp, which will increase the osseointegration properties of implants.

Keywords Hydroxyapatite (HAp) · Al_2O_3 · Plasma spraying · Thermomechanical processing (TMP) · Coatings

1 Introduction

Modern dentistry and traumatology widely uses biocompatible materials based on Al_2O_3 and calcium phosphate ceramics to replace bone tissue with defects of various etiology. The main limitation of these implants is low mechanical stability. One of the

I. P. Melnikova
Yu. A. Gagarin Saratov State Technical University, Saratov, Russia

A. L. Nikolaev (✉) · A. V. Lyasnikova
Don State Technical University, Rostov-on-Don, Russia
e-mail: andreynicolaev@eurosites.ru

I. A. Parinov et al. (eds.), *Physics and Mechanics of New Materials and Their Applications*, Springer Proceedings in Materials 10,
https://doi.org/10.1007/978-3-030-76481-4_9

solutions to the problem is plasma spraying of Al_2O_3 powder and calcium phosphate materials used for the formation of ceramic coatings on the surface of implants. The coatings should have specific mechanical, physicochemical and biochemical properties to interact with the environment of the host organism. It is well known that size of the pores in the porous scaffold is associated with the size of the constituent particles [1].

We have developed and applied a new technology of plasma spraying of ceramic coatings on intraosseous titan implants with porous titan sublayer formed by particles 250 μm. To achieve high homogeneity of the porous structure of the coatings and sufficient pore size for the effective growth of blood vessels and bone tissue into an implant, we use biocompatible powder with the particle size of 40–100 μm [2]. HAp powder has binding properties complicating its sifting, which makes usage of smaller particles inefficient due to significant material losses.

This work is aimed at the development of functional characteristics of biocompatible plasma-sprayed coatings, in particular, improvement of their mechanical properties by homogenization of the porous structure and stabilization of the crystalline structure.

2 Experimental Details

We have developed a method of assessment of processing quality for Al_2O_3 powder. The main criterion of the quality is compressive strength of test tablets formed from the powder. Tablets of 8 mm size are formed from Al_2O_3 powders and their mixtures with plasticizers (2% of the tablet mass) in press forms under 0.32 GPa pressure. Tablets are sintered in hydrogen furnaces of continuous pushing-type with temperature controlled by optical pyrometer LOP-72 at 1750 ºC for 10 min. Finally they are tested by compression on tensile machine. We used the "BV-22" as a plasticizer.

During the experiments, aluminum oxide coarse powders with 40–60 μm particles of spherical form and electrovacuum Al_2O_3 powders with 1–3 μm particles were mixed in ¼ proportion in ceramic evaporation chamber for 15–20 min. Loosely packed mixtures of Al_2O_3 powders were annealed at 1100–1500 ºC in hydrogen for 3 h, and then grinded in a ceramic mortar for 20 min. Thermal cycling was carried out by sintering mixtures of Al_2O_3 powders in hydrogen atmosphere at 1750 ºC for 10 min. Testing was carried out in glass vacuum diodes (in vacuum of 3×10^{-7} mmHg or higher) in cycles ($U_N = 9$ V for 3 min on 7 min off) at 1470 ºC.

Obtained powder was plasma-sprayed onto samples of BT1-00 titan with sublayer of titan powder (particle size is 250 μm). Metallographic and fractographic analysis of the coating, performed with microscopes "MBS-10", "MIM 8 M" and profilometer "model 170,623". X-ray and phase analysis of powders was carried using diffractometer "DRON-3". Morphology of the plasma-sprayed coatings and structure of the layers was carried out using scanning electron microscope (SEM) MIRA II LMU TESCAN (Czech Republic) at accelerating voltage in range of 20–30 kV. Samples

were covered by gold coating (10–20 nm) by magnetron deposition. The microstructure and open pore size of the coatings were demonstrated using an atomic force microscope (AFM) Nanoeducator (NT-MDT, Russia).

3 Results and Discussion

A widely used method to improve powder granulometric composition, that eliminates ultra dispersed and fine dispersed, is based on thermomechanical processing (TMP) with prolonged annealing followed by light milling [3]. During the annealing, the smallest and the most active particles of the processed powder attach to each other and to larger particles. These conglomerates withstand the light milling. Larger, less active conglomerates (60–70 μm) are fractioned into smaller particles during milling. Thus, pre-annealed and milled powder becomes less polydisperse which allows one to form porous scaffolds with more homogeneous structure.

During spraying, small particles (below 40 μm) are strongly heated, however, they have relatively low kinetic energy. The particles deform insignificantly when hitting the substrate, which results in their weaker adhesion. Above this size limit, increased mass allows them to gain sufficient kinetic energy, which results in stronger deformations, leading to increased contact area, and thus increased coating adhesion to the substrate.

Considering the abovementioned mechanisms, the newly developed TMP method for the powders of biocompatible materials, based on the synthesis of combined particles of source powder through spraying of small particles (40 μm) on larger ones, also leads to higher adhesion of the coating to the titanium scaffold with sublayer of titanium powder [4].

During plasma spraying in high praying in a high-temperature jet, heat transfer from smaller particles to larger ones prevents a fraction of smaller particles from full melting. When hitting the substrate, combined particle is fractioned into larger single particle and a couple of smaller ones [5, 6]. One can speculate that smaller particles, having speed compatible to a larger one, will fraction into nanometer-sized particles. Introduction of the ceramic nanoparticles to the structure of biocompatible material improves its functional characteristics by increasing the contact area between implants and bones.

We have tested a method for the stabilization of aluminum oxide properties. It relies on homogenization of distribution of various size particles in the volume of material by prolonged thermal processing of Al_2O_3 powders and their mixtures, followed up by milling.

The results of the compression tests of the samples, shown in Table 1, prove that their strength increased after TMO. Maximal strength was reached for the samples of Al_2O_3 powders annealed at 1200–1250 ºC, which indicates the most optimal [7] and homogeneous packing [8] of particles (Table 1).

Pre-annealed, grinded mixture of Al_2O_3 powders becomes more homogeneous in granulometric composition. It is associated with elimination of ultra dispersed

Table 1 Testing results of samples from mixtures of Al_2O_3 powders, annealed at various temperature

Mixture annealing temperature, T °C	Compressive strength, σ_v, kg/mm^2
No annealing	17.4
1100	22.2
1200	35.5
1250	35.4
1300	28.5
1400	25.6
1500	24.8

fraction (1 μm and less) [9], which is fixed on microgranules, after the powder mixture processing (Fig. 1).

We performed additional mechanical strength and durability tests of Al_2O_3 powder mixtures by thermocycling. Then we coated the surface of the vacuum diodes with these suspensions and annealed them at 1750 ºC in hydrogen atmosphere. Measurements were carried out in a high vacuum at 1470 ºC. The experimental results are present in Table 2. To do that we prepared a suspension and subjected it to heating (Table 2).

Comparing the results of testing samples for compression and thermal cycling (Tables 1 and 2), one can see that usage of homogeneously structured mixtures of Al_2O_3 powders, which is achieved by their thermal processing at 1250 ºC, corresponds to maximal durability of coating formed from these mixtures, as well as their increased mechanical strength in cyclic tests. Thus, thermomechanical processing of Al_2O_3 powders at 1200–1250 ºC leads to the homogenization of the granulometric composition, which improves functional characteristics of the biocompatible material of plasma-sprayed coatings by corresponding homogenization of their porous structure.

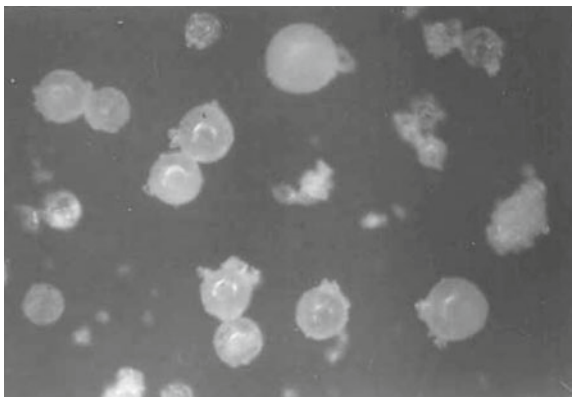

Fig. 1 Mixture of Al_2O_3 powders of different grain size composition after TMP. The image was obtained using optical microscopy

Table 2 Thermal cycling results for Al_2O_3 films of different grain size composition, annealed at different temperatures

Annealing temperature of Al_2O_3 powders, T, °C	Number of cycles (N)		
	Shrinking	Destruction	
		Cracks	Delamination
Without burning	450	1500	–
1200	800	–	4100
1250	790	–	4200
1300	150	–	3500
1500	100	Burnt out after 250 cycles	

The developed method of thermomechanical processing of Al_2O_3 powders may be applied for the preparation of calcium phosphate ceramic biocompatible powders prior to their plasma spraying. Thermomechanical processing of polydisperse HAp powders prior to plasma spraying, performed for homogenization of the granulometric composition, was carried out at 800–1000 ºC. Powders were annealed in furnace for 3 h. Then they were grinded in a ceramic mortar for 20 min. Temperature was controlled by the thermocouple. Metallographic and fractographic analysis of coatings from powders obtained by this method showed that thermomechanical processing at 800, 900 and 1000 ºC lead to the formation of more homogeneous structure with larger pores (Fig. 2). The size of the pores increases with the increase of annealing temperature in accordance with variation of the surface morphology (Table 3).

With the increase of the TMO annealing temperature, increase of the particle size, characteristic of TMO, leads to the more developed surface morphology of the coating and increase of the open pore channel size (Table 4). The size of open pore channels and the value of the surface roughness of the sprayed coatings can be estimated from Fig. 3.

We also performed studies of the influence of TMO annealing temperature on the structure of GA powders, their structure, crystallinity, phase composition, binding properties by X-ray diffractometric and electron microscopic analysis (Figs. 4, 6). The crystallinity was determined from the ratio of the XRD reflections area to the total area of the reflections and the background in the 2θ angle range from 39° to 44°.

TMP of HAp powders at temperature in the range of 800–900 ºC does not change phase composition of powders but changes its crystallinity and lowers inner stress (Table 5). In initial state, HAp is amorphous and its structure is unstable. During annealing between 800 and 1000 ºC, it crystalizes and reliefs stress. Annealing at 1000 ºC results in the formation of new phase of β-$Ca_3(PO_4)_2$ (β-tricalcium phosphate) [10], which is reflected by the new line in the XRD of HAp (Fig. 4). Moreover, a change in the character of absorption lines in the IR-spectra indicates the appearance of β-tricalcium phosphate (Fig. 5) [11].

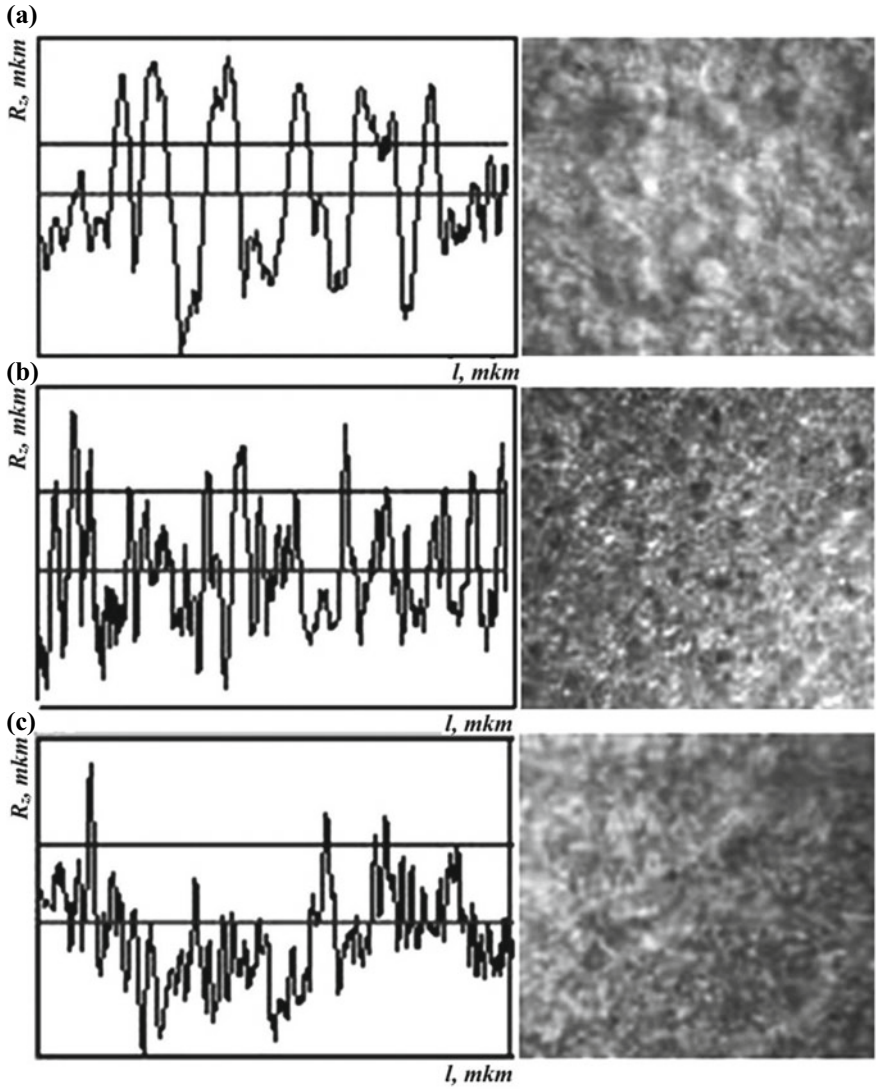

Fig. 2 Image and profile of the surface of a plasma-sprayed coating made of HAp on titanium with a sublayer of titanium powder after TMP at 1000 °C (**a**); 800 °C (**b**); and without TMP (**c**)

Substantial increase of the particle size of biocompatible HAp-based material at TMP annealing temperature of 1000 ºC, leads to the decrease of the spraying quality due to the formation of large open pore channels (Table 4) and consequently substantial uncoated areas of the sublayer. Thus, recommended temperatures for

Table 3 Influence of the annealing temperature of HAp-powder on roughness of plasma sprayed coatings

Annealing temperature of TMP T, °C	Roughness parameters, μm			
	R_a	R_z	R_{max}	S_m
Without TMP	5.5	45.8	54.9	58.7
800	5.9	49.9	62.6	121
1000	16.7	104	125	237

Table 4 Influence of the TMP annealing temperature of source powder on the size of the open pore channel in HAp-based coatings

Powder composition	Annealing temperature of powder, °C	Size of open pore channel, μm
HAp (40–100 μm)	Without TMP	5–7
HAp (40–100 μm) + HAp (< 40 μm)	800	7.8–19.6
HAp (40–100 μm) + HAp (< 40 μm)	1000	39.2

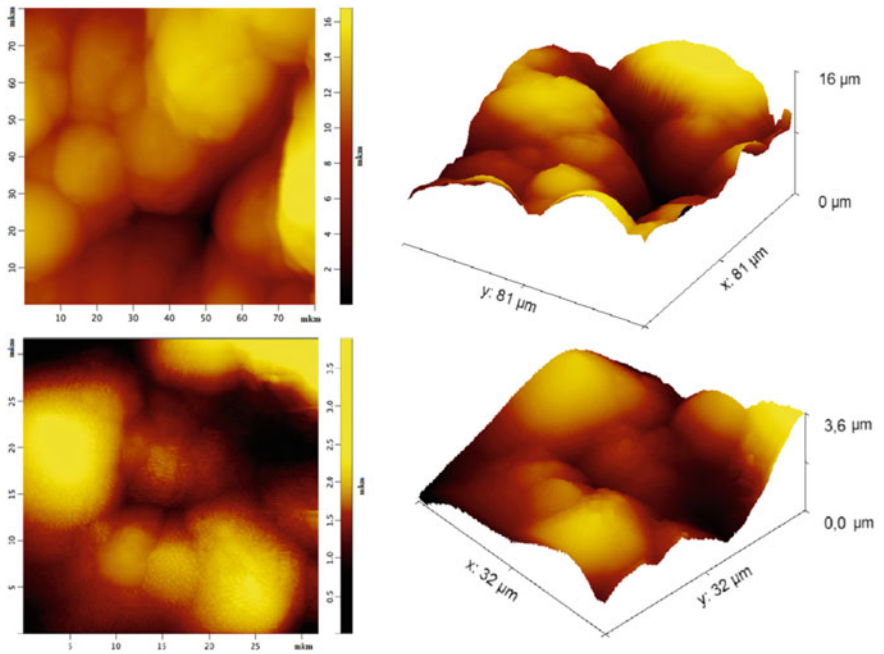

Fig. 3 AFM of the surface of a plasma-sprayed HAp coating from a powder obtained using TMP at 800 °C

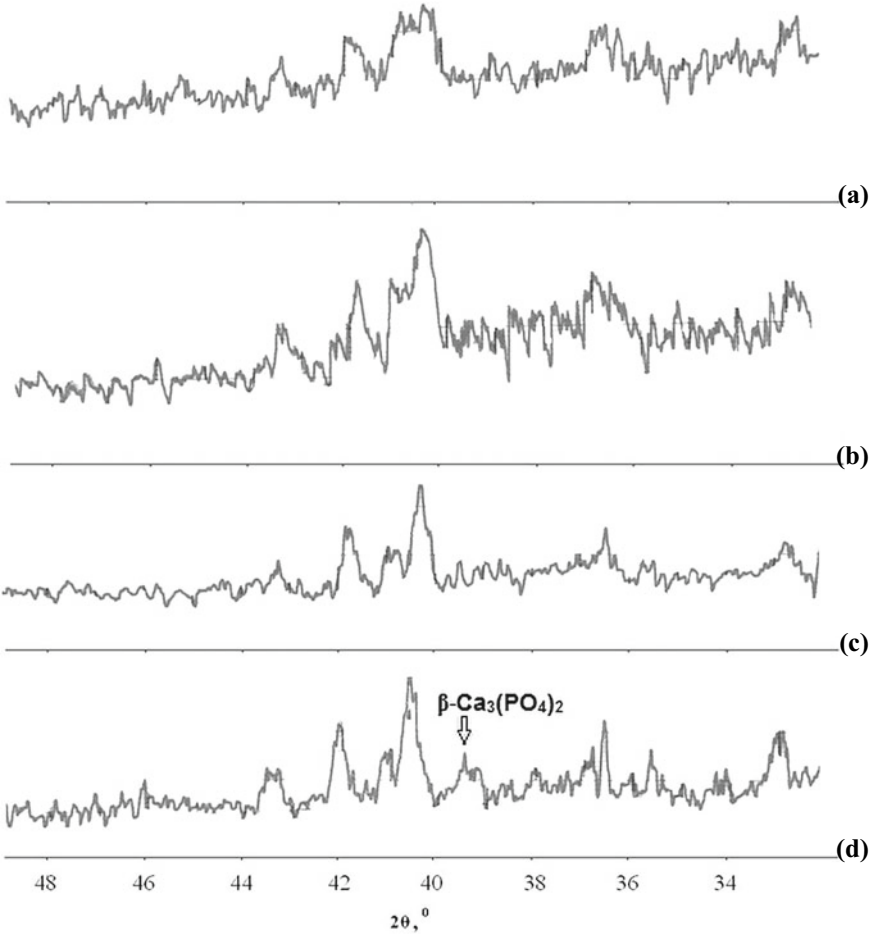

Fig. 4 XRD spectra of HAp powders obtained without TMP (**a**) and with TMP at 800 °C (**b**); 900 °C (**c**); 1000 °C (**d**)

Table 5 Influence of TMP temperature on HAp properties

TMP temperature, T, °C	Binding properties (adhesion of powders to the pestle)	Crystallinity, %	Presence of β-$Ca_3(PO_4)_2$ line with $d = 2.88$ Å ($2\theta = 39.5°$)
Without TMP	yes	33	–
800	yes	39	–
900	yes	45	–
1000	no (crumbly)	57	+

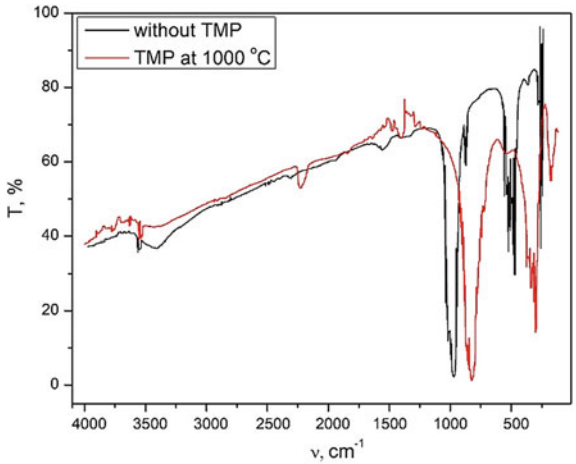

Fig. 5 IR-spectra of HAp powders without TMP (black line) and with TMP at 1000 °C (red line)

TMO powder annealing are 800–900 ºC. Homogenization of the HAp coating structure after TMP at 800 ºC is also confirmed by electron microscopy (Fig. 6 a, b) [12].

Figure 4 shows marks on the large particles, caused by the detachment of immobilized by TMP smaller particles in the moment of the collision with substrate. As a result, the structure of HAp coating contains not only 180 nm nanoparticles, whose size is defined by the fracture of the HAp particles on deposition, but also specific smaller 40–60 nm nanoparticles (Fig. 6, d). Fracture of HAp particles, prior subjected to TMP, is likely facilitated by their more crystallinity [13, 14].

4 Conclusion

A new method for the processing of biocompatible aluminum oxide powders and HAp powders has been developed. It is based on their prolonged annealing followed by milling, which eliminates fine fraction of polydisperse powders, increases average particle size, and, as a result, an average size of the pore as well as homogeneity of porous structure. It has been demonstrated that the new method for homogenization of the structure increases strength and durability of coatings from biocompatible material aluminum oxide. It has been shown that TMO of HAp powder leads to the homogenization of the porous structure and formation of the stable crystalline structure of plasma-sprayed coating, which in turn improves its functional characteristics. To improve the functionality of biocompatible coatings based on Al_2O_3 and HAp, it is advisable to use the TMP process of powders to perform the process of immobilization of microparticles of Al_2O_3 and HAp on granules of these materials. This contributes to the nanostructuring of coatings during plasma spraying, as well as the improvement of the structural characteristics of the porous structure and the

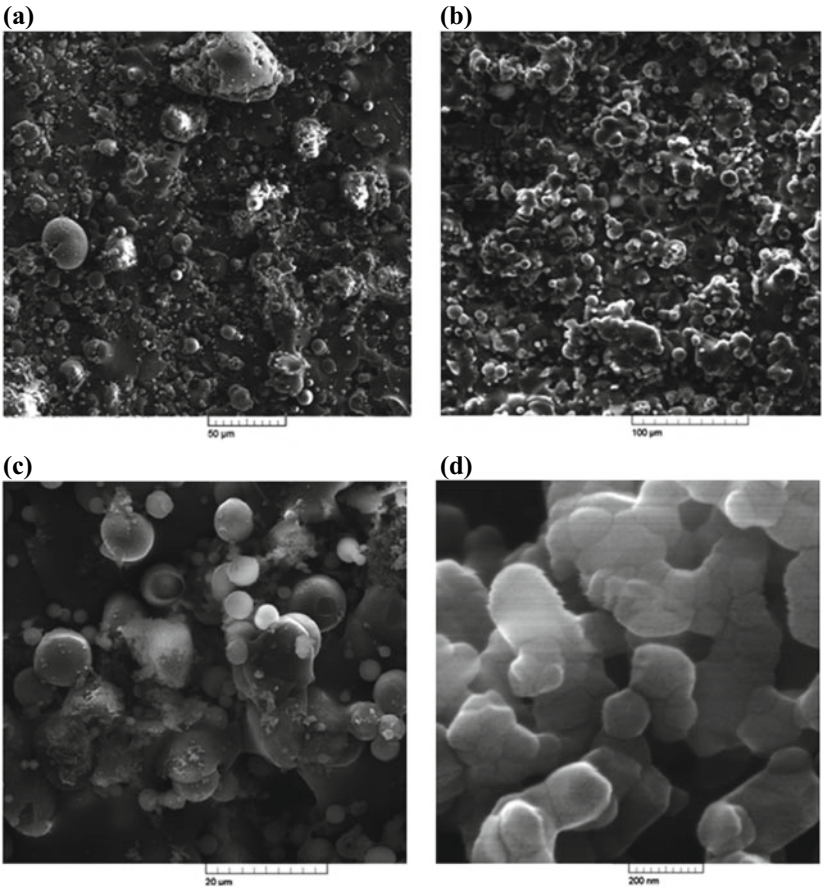

Fig. 6 SEM image of the plasma-sprayed HAp coating without TMP (**a**) and after TMP with annealing at 800 °C (**b–d**)

morphology of the implant surface. It is shown that the optimal temperature of TMP for immobilization of small particles of Al_2O_3 on Al_2O_3 macrogranules is 1200–1250 °C. Annealing of HAp powders during TMP in the temperature range from 800 to 1000 °C leads to the enlargement of particles without a significant change in the ratio of amorphous and crystalline phases. At a TMP temperature of 1000 °C and higher, the HAp crystallinity increases (by more than 50%) and β-Ca_3 $(PO_4)_2$ forms. Application of the results obtained will significantly increase the osseointegration properties of implants with coatings based on HAp and Al_2O_3.

Acknowledgements This research was performed into framework of financing RFBR grant number 20-07-00637_A.

References

1. A.V. Lyasnikova, O.A. Markelova, O.A. Dudareva, V.N. Lyasnikov, A.P. Barabash, S.P. Shpinyak, Powder Metall. Met. Ceram. **55**(5), 328 (2016)
2. I. P. Mel'nikova, A. V. Lyasnikova, V. N. Lyasnikov. *Russ. Phys. J.* **56**(10), 1190 (2014).
3. V.A. Koshuro, G.G. Nechaev, Tech. Phys. **59**(10), 1570 (2014)
4. F. Sharifianjazi, A.H. Pakseresht, M.S. Asl, A. Esmaeilkhanian, H.W. Jang, M. Shokouhimehr, J. Compos. Compd. **2**(2), 26 (2020)
5. D. Arcos, M. Vallet-Regí, J. Mater. Chem. B **8**(9), 1781 (2020)
6. S. Ferraris, S. Yamaguchi, N. Barbani, M. Cazzola, C. Cristallini, M. Miola, S. Spriano, Acta Biomater. **102**, 468 (2020)
7. F.S. Alvar, M. Heydari, A. Kazemzadeh, M.R. Vaezi, L. Nikzad, Ceram. Int. **46**(4), 4215 (2020)
8. A. Asimakopoulou, I. Gkekas, G. Kastrinaki, A. Prigione, V.T. Zaspalis, S. Petrakis, J. Functional biomaterials **11**(3), 65 (2020)
9. R. Ahmadi, A. Afshar. *Surface and Coatings Technology*, **405**, 126594 (2021)
10. A. L. Nikolaev, B. I. Mitrin, E. V. Sadyrin, V. B. Zelentsov, A. R. Aguiar, S. M. Aizikovich. in *Modeling, Synthesis and Fracture of Advanced Materials for Industrial and Medical Applications*, (Springer, Cham, 2020), p. 137
11. D. A. Zhilin, N. V. Lyanguzov, V. I. Pushkariov, et al., in *Advanced Material–Studies and Applications*, ed. by I. A. Parinov, S. H. Chang, S. Theerakulpisut (Nova Science Publishers, New York, 2015), p. 57
12. V.N. Lyasnikov, A.V. Lyasnikova, A.V. Pivovarov, I.N. Antonov, V.A. Papshev, Biomed. Eng. **45**(4), 119 (2011)
13. V. I. Pushkariov, A. L. Nikolaev, E. M. Kaidashev. Synthesis and characterization of ZnO nanorods obtained by catalyst-free thermal technique. *J. Phys.: Conf. Ser. IOP Publishing.* **541**(1), 012031 (2014)
14. A. L. Nikolaev, E. M. Kaidashev, A. S. Kamencev. in *Advanced Materials-Proceedings of the International Conference on "Physics and Mechanics of New Materials and Their Applications", PHENMA 2018*, Springer Proceedings in Physics, vol. 224, ed. by Ivan A. Parinov, Shun-Hsyung Chang, Yun-Hae Kim (Springer Nature, Cham, Switzerland,2019) p. 103

Technological Aspects of Obtaining Fuel Composites Based on Fine-Grained Coal Waste

Nina Buravchuk, Olga Guryanova, and Erni Putri

Abstract The results of experimental research on the selection of binders for briquetting anthracite mines, coal and coke breeze, coal sludge, available in coal-mining regions are presented. It is developed an inexpensive, affordable binder for briquetting fine-grained coal waste. The influence of granulometric composition of coal components, binder content, moisture content of coal components, specific pressing pressure on the technical properties of fuel briquettes has been investigated. Methods of increasing moisture resistance and water resistance of fuel composites are proposed. The technical analysis of an experimental batch of fuel briquettes is presented. The mechanism of strengthening and formation of the structure and properties of fuel composites is considered.

Keywords Anthracite fines · Coal sludge · Fine coal and coke · Coal waste · Binder · Molasses · Carbide sludge · Bottoms of organic synthesis cracking · Briquetting · Fuel composite · Fuel briquette · Moisture resistance · Water resistance

1 Introduction

Significant amounts of coal waste have been accumulated in the coal-industrial regions: anthracite fines, fine coal and coke, coal sludge. The stocks of fine-grained coal materials are huge, and unused waste from the coal mining stored is dumps. They have a negative impact on the environment. The reserves of fine-grained coal

N. Buravchuk (✉) · O. Guryanova
I.I. Vorovich Institute of Mathematics, Mechanics and Computer Science, Southern Federal University, Rostov-on-Don, Russia
e-mail: nburavchuk@sfedu.ru

O. Guryanova
e-mail: oguranova@sfedu.ru

E. Putri
Department of Industrial Engineering, University of 17 Agustus, Surabaya 1945 (UNTAG), Indonesia

I. A. Parinov et al. (eds.), *Physics and Mechanics of New Materials and Their Applications*, Springer Proceedings in Materials 10,
https://doi.org/10.1007/978-3-030-76481-4_10

materials are enormous. The study of such qualitative characteristics of these raw materials as ash content, sulfur content, heat of combustion, and the release of volatile substances made it possible to establish their prospects for use as a full-fledged household fuel after appropriate processing. This is a valuable carbon-containing raw material, but its use in a finely dispersed state is not effective due to the obstruction of transportation, dusting, and incomplete combustion. At the same time, due to the reduction in the output of high-quality coals for household needs and industrial energy, there is a need for additional types of solid fuel.

The problem of using screenings of coal and anthracite is increasingly attracting the attention of many researchers [1–6] in connection with the need to utilize coal fines and obtain additional conditioned fuel. Therefore, in the presence of a huge reserve of unused coal resources, it becomes necessary to develop a technology that ensures the efficient production of fuel products with specified quality indicators. It is possible to obtain a product with the required properties from substandard, but having a certain energy potential, raw materials, using the briquetting technology. The most reasonable technological direction, which can ensure the production of fuel with satisfactory consumer characteristics, is the briquetting of substandard carbon-containing waste with binders. This is a versatile way to obtain fuel briquettes from almost any material. This is especially true for anthracite fines, screenings and coal fines. Anthracite fines, coke, coal fines have a certain hardness and their mixtures are rigid, not plastic. A fuel briquette based on such carbon components can be obtained either with binders or with a very high compaction pressure. As follows from the analysis of the available domestic and foreign experience in the manufacture of briquettes, the most common binders are oil bitumen and coal tar pitch. However, these binders are classified as substances with increased carcinogenic properties. It is well-known the using inorganic binders such as lime, cement, water glass, gypsum. However, these binders increase ash content, impair combustion and the cost of briquettes. There are very few inexpensive, non-scarce binders that ensure the environmental safety of fuel briquettes, the manufacturability of their production process and the required quality indicators of briquettes. These are the main reasons why the production of briquettes from anthracite fines and coal fines has not received large-scale development.

Fuel briquettes are rightfully considered the fuel of the XXI century, the number of its consumers in various countries of the world is growing every year. The demand for solid fuel is steadily increasing, the fuel market is practically empty. Using the energy potential of substandard products by briquetting them and turning them into refined fuel will not only replenish the coal-raw material base, but also involve waste in production, and reduce the technogenic load on the environment.

1.1 Purpose of the Study

The purpose of this study is to develop a technology for briquetting fine-grained and fine-dispersed coal-containing waste with binders. When developing the technology,

the following principles of constructing technological processes for producing coal composite materials were taken as a basis:

(i) selection of an adsorbent based on a set of properties that meet the requirements for finished products;
(ii) introduction of additional components into the composition of coal compositions to impart new consumer properties to the entire composition;
(iii) performing the necessary technological operations to obtain products with the specified technical quality indicators.

1.2 Research Objectives

The fuel briquette is a dispersed-granular composite consisting of a carbon-containing component and a binder. When forming the structure of the composite, it is necessary to create conditions for creating a structure that is most effective and optimal in terms of resistance to atmospheric influences during storage and thermal and mechanical loads during their use. The solution to this problem involves:

(i) to justify the requirements for the grain size composition of the carbon-containing component (large-scale composite structure criterion);
(ii) to determine the optimum moisture content of the carbon-containing component;
(iii) to establish the optimal ratio of the solid component and a binder;
(iv) to determine the optimal compaction force of the composition;
(v) to set the hardening mode of the dispersed-granular composite.

2 Research Methods

Analytical and laboratory studies were carried out in order to obtain information on the technical properties and composition of the initial components for briquetting. The research results make it possible to determine the main technological aspects of coal waste briquetting. Further technological studies were carried out, according to which a complete assessment of the quality of raw materials was given in accordance with the requirements of regulatory and technical documentation. Rational combinations of research methods make it possible to develop optimal parameters for briquetting fine-grained coal waste and obtain efficient fuel composites.

The main technological operations during briquetting included preliminary preparation of coal raw materials: crushing and classification. Next, the prepared components: anthracite fines, coal sludge and coke fine, taken in a certain ratio, were thoroughly mixed until the components were evenly distributed (visual assessment). A binder was previously prepared. The solid components were mixed with a certain amount of binder. The mixture was thoroughly mixed until a homogeneous mass was obtained. Briquettes were manufactured on a hydraulic press in a cylindrical matrix

with a lenticular shape of the upper and lower working surfaces of the punches with a pressing load of 25–40 MPa. Testing of briquettes for compressive strength was carried out on specimens-cylinders with a height and a diameter of 50 mm. The hardening of briquettes took place, as a rule, during natural drying.

3 Results and Discussion

Environmental stress in the coal-mining regions of the country is largely determined by the high level of waste from coal mining and processing. In terms of its quality characteristics, coal waste is not inferior to mined coals, but it is almost impossible to use their energy potential due to their fine dispersion and dustiness. The objects of the study were coal-containing raw materials from coal-processing factories of the Rostov region. Binders were made from wastes from the sugar-beet industry of the Krasnodar region and wastes from chemical industries in the Rostov region.

The following components were used as raw coal for research:

(i) anthracite fines are the anthracite screenings and waste from coal preparation plants, with a fraction of 0-6 mm; carbon content in organic matter is 93.0–95.0% and density is 1.4–1.8 g/cm^3.
(ii) coal fines are the coal screenings and waste from coal preparation plants; carbon content is 76–90%; density is 1.2–1.8 g/cm^3.
(iii) coal sludge are the wastes from coal preparation plants, fine grades of anthracite and coal with particle size of 0 – 1 mm.
(iv) coke fine is the coke screenings, contains 82–88% carbon, density is 1.4–1.95 g/cm^3.

The technical characteristics of the coal components are given in Table 1.

Molasses, a by-product of sugar beet production, was used as the basis of the binder for briquetting the carbonaceous raw materials. Refers to the group of disaccharides. The molasses contains up to 45–50% beet sugar $C_{12}H_{22}O_{11}$. Soluble polysaccharides easily swell in water and form viscous colloidal solutions in it. Molasses is a thick,

Table 1 Technical properties of coal technogenic raw materials

Type of raw material	Indicators				
	Ash content, %	Sulfur content, %	Volatile matter release, %	Humidity, %	Calorific value, MJ/kg
Anthracite fines	5.0–30.0	0.9−1.2	3.0–9.0	9.0–12.0	18.8–33.2
Coal fines	14.6–32.0	1.4–1.8	11.0–43.5	4.0–12.8	12.4–17.2
Coal sludge	26.0–45.0	1.2 −1.7	5.0–9.0	8.0–28.0	14.9–18.5
Coke fine	10.0–12.0	2.1−2.4	21.0–28.0	4.0–16.0	15.2–36.4

syrupy, opaque, viscous liquid from brown to dark brown in color. Molasses has a specific smell from sucrose caramelization products and a sweet taste with a bitter aftertaste. Its relative density, depending on the content of dry substances, is 1.30–1.52 g/cm^3. The chemical composition of molasses is very complex. In its most general form, molasses contains up to 20% water, 45–50% sugar, 20–25% organic matter, and 10% non-sugar mineral substances.

Molasses is a concentrated solution of various organic and mineral substances, some of which are in a colloidal state. The colloids contained in the molasses have significant surface activity and therefore are well adsorbed on the surface of the particles to be glued.

The molasses is delivered to the place of use by road transport in tank trucks or metal closed containers. Molasses is stored in closed metal tanks. The guaranteed shelf life of molasses is at least 9 months from the date of acceptance of the molasses by the consumer. The storage time of molasses does not affect its adhesive (binding) ability.

Carbide sludge is used as a structuring additive for molasses. It is a lime containing product. Formed as a waste product in the production of acetylene from calcium carbide. According to the state of aggregation, carbide sludge is a finely dispersed gray-blue paste. This is lime of the 2nd grade, bluish tint. Mass fraction of calcium hydroxide [Ca $(OH)_2$] is not less than 35%. Carbide sludge is not a scarce product, accumulates in dumps of chemical plants, has a low cost.

As a hydrophobizing additive to molasses, we used the bottoms of organic synthesis cracking, namely wastes of synthetic products factories with a melting temperature of 35–38 °C, a pour point of 46–48 °C and an ash content of 0.016–0.018%.

The ability of coals to be briquetted depends on the coal belonging to one class or another. There are no strict criteria for evaluating the briquetting of coal and carbonaceous materials. As a rule, the ability to briquetting is associated with the ability of coal to plastically deform when it is pressed under certain conditions [7, 8]. A qualitative rapid assessment of the briquetting capacity of coal can be the simplest way: determination of the briquetting capacity of the charge by establishing the minimum amount of binder that is required to be introduced into the charge, for obtaining a mechanically strong briquette with a minimum pressing pressure. The main criterion for the formability of the coal-containing charge is the strength of the raw briquette. Evaluation of the briquetting ability of coal waste and the quality of the resulting product was determined by the strength of the briquettes for dropping and compression.

The efficiency of coal briquetting can be increased by activating the surface of the coal particles. One of the activation methods is grinding or mechanical activation. During crushing and grinding under the influence of mechanical forces, physico-chemical processes are intensified, leading to a change in the reactivity of coal. Under the influence of shock loads or friction, various structural defects accumulate in coal particles: cracks, roughness, unevenness. On the solid surface of the coal particles, the number of active centers increases, and the adsorption activity of the coal component in relation to the binder increases. The reactivity of coal changes.

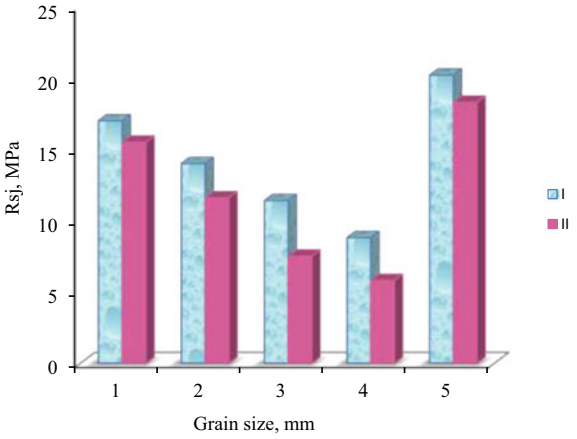

Fig. 1 Effect of coal grain size on the strength of fuel briquettes: (1) 0–1 mm; (2) 0–3 mm; (3) 1–3 mm; (4) 3–6 mm; (5) optimal grain size composition; I - binder: molasses; II - binder: molasses + carbide sludge

The processed material is stored with free energy. Moreover, mechanical fixation of the binder occurs on a rough surface.

One of the factors affecting the briquette ability and quality of fuel composites is the granulometric composition of the briquetted material. The granulometric composition of the briquetted material characterizes the ratio of particles of different sizes in the charge and affects the packing density of the particles. Polydisperse systems have a high specific surface area characterized by an excess of surface energy. This causes the particles to converge, i.e. transition of the system to a stable thermodynamic state. Such a system forms a denser packing of particles and a high briquette strength. Studies on the influence of the size of the initial carbon-containing raw material on the strength properties of briquettes have shown that the greatest value of the compressive strength was obtained in samples containing waste coal with a fraction of 0–1 mm (Fig. 1). This is due to the fact that fine coal particles on a solid surface have more active centers interacting with a binder. However, with such a grain size composition, the specific surface area of the particles increases and, accordingly, the consumption of the binder grows. Position 5 in Fig. 1 reflects the strength of briquettes with an optimal particle size distribution of the charge. With an optimal grain size composition of the charge, the time and energy consumption for brittle and elastic deformations of the composite during pressing decreases, and the share of energy and time for useful plastic deformations increases.

It has been experimentally established that when anthracite fines with a size of 0–6 mm are included in the briquette, their particle size distribution should be following: (i) 5–7% > 6 mm; (ii) 25–30% with sizes of 3–6 mm; (iii) 30–33% with sizes of 1-3 mm; (iv) 35–45% with sizes of 0 – 1 mm. In the result of the studies performed, the optimal granulometric composition of the charge for briquetting was determined: the content of the 6 mm class is 2–3%; 3 – 6 mm is 24–28%; 1–3 mm is 27–35%; 0 – 1 mm is 38 – 45%.

To increase the plasticity, manufacturability and improve the grain size composition of the charge, finely dispersed coal sludge was introduced. In the grain composition of coal sludge with a particle size of 0–3 mm, the content of fractions was 1–3 and for 0–1 mm, it was 40–45% each, for particles over 3 mm, it was no more than 10%. Dusty fractions of coal sludge fill the voids of the frame, which creates larger fractions. The stabilization of large particles by small ones is based on the ability of the latter to be fixed due to long-range intermolecular forces near large particles. This provides a tighter packing of the dispersed phase particles. This particle packing is characterized by a large grain contact area. This provides the briquettes with sufficient strength to resist external destructive influences to which the briquettes are exposed during storage, loading and transportation.

Both the strength of the raw briquette and the final technical characteristics of the fuel composition significantly depend on the initial moisture content of the coal waste intended for briquetting. A change in the moisture content in coal waste affects the adhesion forces between particles [9]. The presence of a water film allows particles to bind at distances greater than the van der Waals radius of interaction of two particles in the absence of a liquid phase and favors the mobility of particles relative to each other when the specific pressing pressure is applied. The increased moisture content in coal is accompanied by a thickening of water films, accompanied by the separation of solid particles from each other and a decrease in the action of molecular forces. From domestic and foreign experience, it follows that the optimal moisture content of fine coal, intended for briquetting, is estimated as 2–3% [10].

With such a moisture content of the anthracite fines, it is possible to obtain a strong raw briquette with a minimum consumption of binder. Satisfactory results can also be obtained when the initial moisture of anthracite fines the 5–6% [11]. The strength properties of the raw briquette are influenced by the moisture content of the charge. With a lack of moisture, a continuous hydration film on the surface of the particles is not provided, that affects the adhesive strength of the binder with the carbon component. There are no conditions for maximum manifestation of adhesion forces. With an excess of moisture, the thickness of the hydration film increases, preventing the adsorption contact of the particles, the wetting ability of the binder decreases and the strength of the briquette composition decreases.

Figure 2 shows the effect of the moisture content of the charge for briquetting on the strength of fuel briquettes at various consumptions of molasses. It follows from the figure that the nature of the dependence is approximately identical for all consumption of the binder.

With an increase in the moisture content of the charge, the strength of the raw briquette decreases. It follows from the experiment carried out, which shows the lower the binder content, the narrower the range of moisture content of the charge to obtain sufficient strength of the raw briquette. The optimum value of the moisture content of the charge is established from the values of the compressive strength of the specimens at the minimum and maximum pressing load. The highest values of strength are noted with a binder content of 6–10% in the range of moisture content of the charge 4–7%. This conclusion is also confirmed by the experimental data presented in Fig. 3. It has been found that at a molasses consumption from 6 to 7%, the

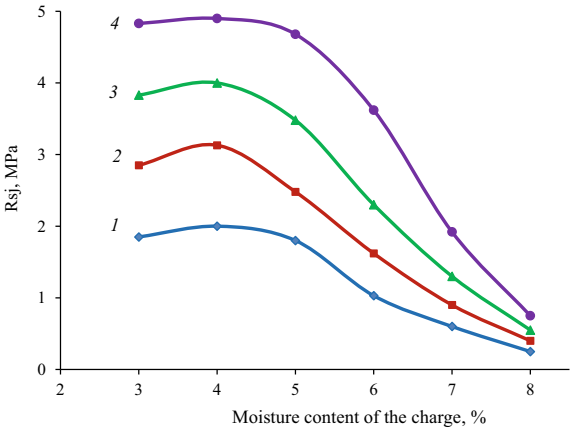

Fig. 2 Dependence of the strength of the raw briquette on the moisture content of the charge; binder consumption (%): (1) 4.0; (2) 6.0; (3) 8.0; (4) 10.0

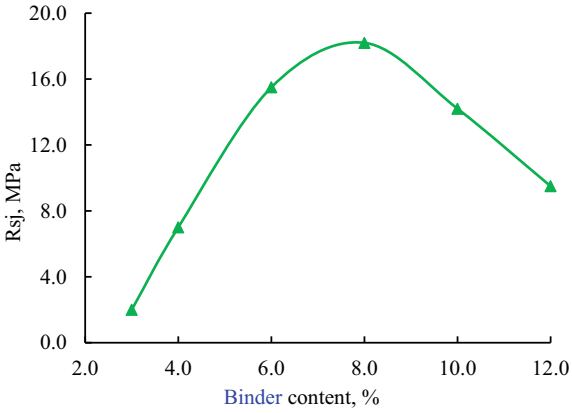

Fig. 3 Dependence of the strength of fuel briquettes on the consumption of the binder

molded briquettes have a strength sufficient to prevent the briquette from collapsing during transportation to the place of strengthening and storage. Low binder content does not provide the required strength of the fuel briquette. Excess binder is squeezed out of the mold during pressing. For a specific consumption of molasses, there is an optimum moisture content of the initial components, at which the maximum strength of the raw briquette is achieved. By forming a fuel composite, it is necessary to create a structure that is stable in terms of resistance to weathering. One of the important characteristics of the quality of fuel briquettes is the indicator of their mechanical strength. Moisture resistance of briquettes is the ability not to collapse under the influence of high humidity. This property of briquettes can be estimated by the residual mechanical strength. Under high humidity conditions, structural bonds in molasses-based fuel briquettes can be weakened to the point of destruction. This is due to the hygroscopicity of molasses.

At constant parameters of temperature and relative humidity of the environment, the system undergoes structural changes to a lesser extent. In natural climatic conditions, when the temperature and humidity of the environment change cyclically and repeatedly, additional factors of destruction appear, expressed in the weakening of structural bonds under the action of repeated heating–cooling, humidification-drying, freezing–thawing. The resulting shrinkage and swelling deformations lead to the appearance of cracks in the samples, which turns out to be a very strong factor in the process of structure formation, contributing to the destruction of the composite.

To stabilize the structure of neoplasms and prevent a decrease in the strength of briquettes during storage under high humidity conditions due to the hygroscopicity of compounds based on molasses, various methods were used. For example, a special additive–hardener was introduced into fuel composition to block the sugars contained in molasses and negatively affect the properties of briquettes during long-term storage in high humidity conditions. Of the tested substances, the greatest effect is achieved when using finely dispersed carbide sludge. The action of this component in the composition is multifunctional. Carbide sludge is used as a structuring agent and activator in a system containing hard coal particles and molasses. The advantage of using this waste is that it does not require preliminary preparation, is mixed with molasses in any ratio, and lowers the viscosity of molasses. The resulting mixing mixture is evenly distributed on the surface of the particles, enveloping all the components, gives plasticity to the molded charge and ensures good formability and high strength of the raw briquette after pressing. Carbide sludge contributes to the formation of calcium saccharates, resistant to moisture changes.

The assessment of the moisture resistance of briquettes containing carbide sludge as an additive to molasses was carried out according to the strength and moisture content of the samples stored for a year in a climatic chamber at a humidity of 98% and a temperature of 20 °C. The moisture content and strength were monitored monthly.

As follows from the data obtained, when the briquettes are found during the year under high humidity conditions, their strength decreases within 2.6–9.3%, the increase in moisture in the briquettes was 3.3–4.7%. A slight decrease in strength and an increase in moisture content did not affect the quality of the briquettes. This is confirmed by a drop test of briquettes according to the standard method [12]. The dumping strength of briquettes kept in a climatic chamber under conditions of high humidity is 85–92%. Thus, the addition of carbide sludge stabilizes the strength of briquettes in high humidity conditions.

Another technique for stabilizing the structure of the fuel composition is heat treatment. Thus, the manufactured briquettes were subjected to heat treatment at various temperature and time conditions. Figure 4 shows the nature of the change in the strength of the samples depending on the temperature and time of treatment. The highest strength is observed in the samples hardening at elevated temperatures (170, 200 °C). At such temperatures, the largest number of irreversible bonds is formed, which give the composition water resistance and moisture resistance.

In the result of testing the properties of heat-treated fuel briquettes, the following was established. During heat treatment, physicochemical transformations occur in the

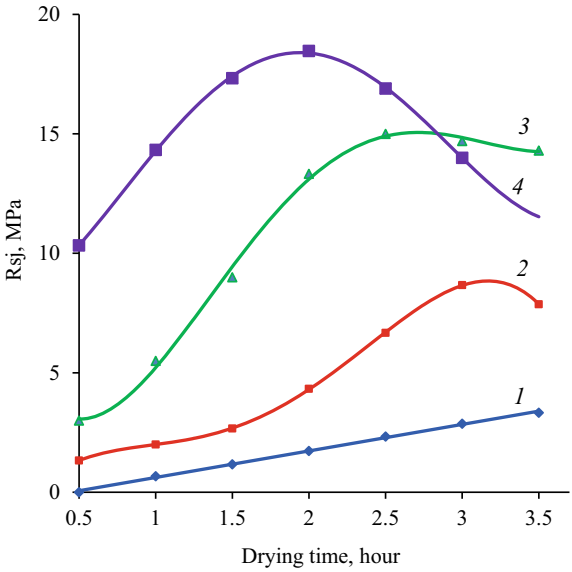

Fig. 4 Dependence of the strength of fuel composites on the temperature and duration of heat treatment: (1) 130 °C; (2) 150 °C; (3) 170 °C; (4) 200 °C

structure of the fuel composition, which entail a change in the structure of the material, the appearance of bonds of the condensation-crystallization type, forming insoluble solidification products and imparting water resistance and moisture resistance to the composition. However, at high processing temperatures, dehydration of neoplasms occurs, the probability of destructive changes increases, the density decreases and the porosity of the material structure increases. These factors reduce the water resistance and moisture resistance of briquettes. It has been experimentally established that briquettes that have undergone treatment at temperatures of 150 and 170 °C for at least 60 min can withstand tests for water resistance and moisture resistance. From an economic viewpoint, the optimal mode is heat treatment at 150 °C for 60 min.

According to the results of the studies carried out, it can be stated that for imparting moisture resistance to fuel briquettes, from an economic viewpoint, it is more attractive to use carbide sludge as a binder component. In this case, energy consumption for the manufacture of briquettes is significantly reduced, and material costs are also reduced: carbide sludge does not require costs for its extraction and the price of this waste is low.

To increase the water resistance of the fuel briquettes, a hydrophobizator (bottoms of thermal cracking of paraffins) was introduced. It was experimentally found that it is more expedient to mix the hydrophobizator with molasses at a temperature of 45–50 °C. Distillation residues combine well with molasses, forming a homogeneous solution. Distillation residues play not only the role of a hydrophobizing, but also a plasticizing additive. This mixture is a complex binder. The results of the study of water absorption of briquettes depending on the content of bottoms at different consumption of molasses, presented in Fig. 5, make it possible to determine the most

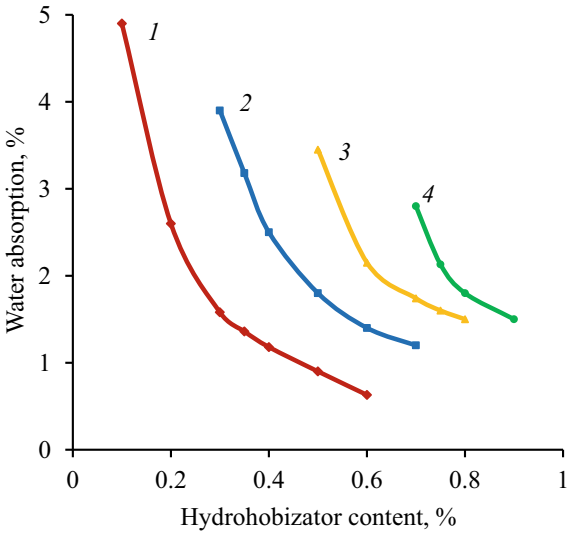

Fig. 5 Change in water absorption of briquettes from the content of hydrophobizator and molasses; molasses consumption: (1) 4.0%; (2) 6.0%; (3) 8.0%; (4) 10.0%

optimal range of consumption of molasses (6–8%) and water repellent (0.6–0.8%) to obtain briquettes with water absorption of no more than 2.0%.

The manufacture of briquettes using the bottoms of organic cracking of paraffins is as follows. The setting mixture (binder) is being prepared. For this, distillation residues are introduced into the heated to a fluid state, the mixture is heated (to the softening temperature of the distillation residues) and stirred until a homogeneous mass is obtained. The mixture prepared in this way is mixed with a heated carbon-containing component, namely anthracite waste and sludge, or coke fines. Stirring is carried out until the coal fines are completely wetted and a homogeneous mass is obtained. Briquettes are molded from a charge having a temperature of 40–45 °C, and a pressing load of 25–40 MPa, depending on the composition and moisture content of the charge. The molded samples have sufficient strength to be transported to the storage site. Hardening of briquettes is possible both under natural hardening conditions at an ambient temperature of 18–20 °C and a relative humidity of 55–60%, as well as with forced drying. When drying briquettes under the influence of molecular-surface forces, their structure changes. Natural drying makes it possible to obtain briquettes with a minimum number of defects, since this slows down the material. However, the intensity of the processes of structure formation and the number of crystalline phases that affect the properties of briquettes increase with their temperature treatment. Optimal heat treatment mode is a temperature of 105–110 °C, a holding time of 0.5 h and air cooling.

In the conditions of a coal chemical laboratory, an experimental comparative combustion of an experimental batch of fuel briquettes and raw coal was carried out. The compositions of the fuel composites are shown in Table 2. The obtained results of combustion are presented in Table 3. The nature of combustion of fuel briquettes on a binder of molasses with additives and high-quality coal of AM grade is almost

Table 2 Compositions of a pilot batch of fuel briquettes, wt. %

Composition number	Anthracite fines	Coal sludge	Fine coal	Molasses	Carbide sludge
1	71.3	14.0	–	6.7	8.0
2	68.2	–	20.0	6.8	5.0

Table 3 Results of comparative combustion of fuel briquettes and coal

Type of fuel	Ash content, %	Mass moisture of working fuel, %	Total sulfur content, %	Volatile matter release, %	Amount of unburned fuel, %
Briquette composition 1	17.9	4.4	1.14	4.7	27.6
Briquette composition 2	16.8	4.7	1.16	6.8	27.9
Coal, grade AM	13.7	4.2	1.12	7.1	24.8

identical. Fuel briquettes were ignited by burning wood (like ordinary coal of large grades). Combustion of briquettes is good, it was not accompanied by cracking, sparks. After a day, the briquettes are red-hot, no cakes are formed, the ash residue is not caked, and is dusty in structure. Briquettes do not crumble during combustion, retain their shape, and withstand mechanical stress during combustion.

The heat resistance of the briquettes is characterized as "good". Experimental combustion of fuel briquettes has shown: the permeability of the bulk layer is better than that of ordinary coal. The ash residue during unloading does not generate dust, there is no caking in the layer, combustion proceeds without emitting odor. The combustion processes of briquettes of different composition and manufacture are almost identical.

Determination of the quality indicators of fuel briquettes was carried out according to the technical specifications and state standards for assessing the quality of coal [12]. Table 4 shows the quality indicators of briquettes intended for use as fuel in the domestic market, as an alternative to raw coal.

The theoretical basis of the complex method of strengthening the fuel composition is the principles of physical and chemical mechanics of dispersed systems [13, 14]. These principles are based on the creation of conditions for directed structure formation and the formation of desired properties of solidified compositions, namely fuel briquettes. The strength properties of the fuel dispersed-granular composite are largely determined by the structure of the contact between the carbonaceous material and the binder. Immediately after the binder has wetted the solid surface of the coal particles, complex processes of a different nature occur, the activity of which largely determines the quality of the fuel briquettes. One of the most important processes that determine the physical and mechanical properties of briquettes is the selective adsorption of the components of a complex binder on a solid surface of a

Table 4 Technical characteristics of pilot batches of fuel briquettes

Indicator	Indicator value
Drop mechanical strength (R_{sb}), %	99.5 – 100
Total moisture ($W_t{}^r$), %	4.0 – 4.7
Ash content ($A_t{}^d$), %	8.9 – 28.0
Mass fraction of total sulfur ($S_t{}^d$), %	0.9 – 1.34
Volatile matter release (V^{daf}), %	4.3 – 19.0
Net calorific value ($Q_i{}^r$), MJ/kg	21.87 – 27.81
Higher calorific value ($Q_s{}^{daf}$), MJ/kg	26.44 – 33,93
Chlorine mass fraction (Cl^d), %	0.027 – 0.031
Mass fraction of arsenic (As^d), %	0.0013 – 0.0015

carbon-containing material, which largely depends on the nature of the adsorbent, the chemical composition of the binder and subsequent technological operations that provide the required quality indicators of briquettes.

According to the results of studies [15], anthracites are inert, since their structural basis consists of aromatic compounds of a high degree of condensation. The interaction of anthracites with binders is carried out through strong van der Waals bonds. A change in the surface of the coal particles affects the nature of the interaction with the binder. Thus, according to [16], grinding coal to 0–3 mm promotes an increase in the relative adhesion of long-flame coals by 59.0%, gas coals by 60.8%, lean coals by 63.7%, anthracites by 71.2%. According to [17], to improve the adsorption properties of the inactive surface, its modification is carried out, which promotes the hydrophilization of the surface. For this, surfactants are used. Improvement of wettability upon contact of a hydrophobic material with an aqueous surfactant solution is associated with hydrophilization of the material surface in the result of adsorption of surfactant molecules and water and with a decrease in surface tension at the liquid–gas interface. As the main binder in the developed technology, it is recommended to use colloidal-dispersed solutions of molasses, namely a by-product of sugar beet production. As follows, from the results of experimental works [18], molasses exhibits the properties of an anionic surfactant. The adsorption of molasses on the active centers of the low-polarity [15] coal surface changes its properties, contributing to the hydrophilization of the surface. On the positively charged surface of anthracite [19], the adsorption of the anionic surfactant (molasses) occurs according to the ion exchange mechanism [20]. Thus, the plasticizing effect of molasses in the composition for briquetting is associated with the hydrophilization of the surface, an increase in its potential, which occurs due to the adsorption of surfactants, which is predominantly ion-exchange in nature.

Under the influence of the processes occurring at the interface between the binder and the surface of the adsorbent, structuring layers are formed around the granular carbon-containing component, which determine the strength and other technical characteristics of fuel briquettes. To ensure a strong and stable adhesion of the binder to the surface of the coal particles, the latter should cover the surface of the coal

particles with a continuous thin layer [21]. The adsorbed binder layer, depending on the shape of the particles, forms a film of different thickness on their surface. The presence of such a film favors the mobility of particles relative to each other when pressing load is applied, and an increase in the contact area of the particles. At the optimal thickness of the film layer, the maximum manifestation of capillary forces and an increase in the adhesive interaction between the particles and the binder take place. In thin layers (of the order of angstroms), the action of unsaturated molecular forces of the surface is manifested, contributing to the manifestation of physical adsorption processes, accompanied by an increase in the cohesion of the binder in this layer. The bond strength reaches its maximum when the adhesive layers at the contact points become equal to the thickness of the adsorption layer.

The added calcium-containing additives intensify the hardening process, block sugars and form compounds with molasses, which contribute to the compaction and hardening of the structure, the creation of the most durable bonds that are resistant to fluctuations in the humidity and temperature conditions of the environment. An increase in the number and area of contacts between the particles and the intensity of their adhesion increases with the application of pressing load, when there is maximum contact and the manifestation of the adhesive-cohesive properties of the binder to the surface of the particles of the constituent components of the charge. At the initial stage of structure formation, the strength of the system is associated with the appearance of dispersed structures of the coagulation structure. Further strengthening under conditions of normal humidity and ambient temperature is accompanied by the transformation of coagulation structures into condensation-crystallization structures, which provide the mechanical strength of the fuel compositions.

4 Conclusion

Fuel composites (fuel briquettes) are an economical, high-calorie, transportable and easy-to-use lump fuel for the needs of the population and industrial enterprises. According to studies [22], it was found that when burning in the same furnace of raw coal with a high content of fines, its coefficient efficiency is 0.467, coal concentrate with a particle size of more than 13 mm is 0.625, and aggregate fuel is 0.75.

The developed technology for briquetting fine-grained carbon-containing waste provides high uniformity and stability of quality indicators of fuel briquettes. This type of fuel in all respects is one of the most demanded materials. The scale of solving the problems of utilization of wastes with a certain energy potential and a shortage of coal makes it possible to recommend the developed technology for briquetting fine-grained carbon-containing materials and products based on them for widespread development in production and use in power plants for industrial and domestic purposes. The need for refined fuel is high, its production is promising.

Composite fuel from potentially combustible waste will replenish the coal-raw material base, reduce the shortage of solid fuel, and can be exported. The proposed briquetting technology can be used to produce fuel briquettes with high consumer properties, competitive in the domestic and world markets.

From an economic point of view, it is attractive to create briquette production at an existing processing plant or mine, with the maximum use of existing engineering structures and communications. In [23], the authors, taking into account modern technical solutions for briquetting, set out the basic principles of an approach to organizing the production of briquettes from coal fines and sludge. It is advisable to locate such an enterprise in close proximity to the places of accumulation of coal waste in order to reduce material costs for the delivery of raw materials with energy potential to the briquette manufacturing enterprise.

Acknowledgements This work was supported by the Southern Federal University, 2020 (Ministry of Science and Higher Education of the Russian Federation) under the project VNGr-07/2020-04-IM.

References

1. T.N. Alexandrova, A.V. Rasskazova, Notes Mining Inst. **220**, 573 (2016)
2. V.S. Solodov, A.V. Papin, V.I. Kosintsev, N.S. Ossovskaya. *Bulletin of the Kuzbass State Technical University*. **3**(97), 110 (2013) (In Russian)
3. A.S. Maloletnev, O.A. Maznev, K.I. Naumov, Solid Fuel Chem. **2**, 47 (2012)
4. L.A. Petrova, V.G. Latyshev, Oil and Gas Bus. **1**, 49 (2007). ((In Russian))
5. L.A. Nikolaev. V.G. Latyshev, O. N. Burenina, *Solid Fuel Chem.* **2**, 55 (2009)
6. N.I. Buravchuk, O.V. Guryanova, E.P. Okorokov, L.N. Pavlova, News of Universities North Caucasian Region. Tech. Sci. **4**, 99 (2002). ((In Russian))
7. M.P. Volarovich, N.I. Gamayunov, O.A. Tseplakov, *Physicochemical Mechanics of Dispersed Structures*, (Moscow, Science, 1966), p. 265 (In Russian)
8. A.T. Elishevich, *Mineral Product Briquetting*, (Moscow, Nedra, 1989), p. 300 (In Russian)
9. N.I. Buravchuk, O.V. Guryanova, Solid Fuel Chem. **4**, 49 (2014)
10. I. Ya. Kalendarev *Influence of Physical and Mechanical Properties of Coals on the Compressibility and Conditions for Obtaining Briquettes and Formed Sorbents*. PhD thesis (Chemistry). (Tashkent, 1984), p. 27 (In Russian)
11. Yu.V. Shuvalov, Yu.D. Tarasov, Mining Information Bulletin **8**, 243 (2011). ((In Russian))
12. E.M. Taits, A.I. Andreeva, *Coal Analysis and Testing Methods,* (Moscow, Nedra, 1983), p. 301 (In Russian)
13. P.A. Rebinder, *Selected Works*, (Moscow, Science, 1978), p. 196 (In Russian)
14. P.A. Rebinder, *Surface Phenomena in Dispersed Systems. Physical and Chemical Mechanics.* Selected Works. (Moscow, Nauka, 1979), p. 384 (In Russian)
15. G.I. Petrova, T.V. Moskalenko, A.M. Leonov A. M, *Mining Inf. Anal. Bull. (Sci. Tech. J.).* **7**, 366 (2010) (In Russian)
16. A.T. Elishevich, Solid Fuel Chem. **6**, 60 (1978)
17. S.I. Surinov, A.N. Polushkin, Solid Fuel Chem. **4**, 13 (1987)
18. V.N. Vorobiev, P.S. Leshchenko, L.K. Klimov, Solid Fuel Chem. **2**, 81 (1997)
19. A.S. Makarov, T.D. Degtyarenko, E.P. Olofinsky, Solid Fuel Chem. **3**, 26 (1987)

20. G. Parfit, K. Rochester. *Adsorption from Solutions on the Surface of Solids.* (Moscow, Mir., 1986), p. 488 (In Russian)
21. ShZh. Kurmankulov, A.T. Elishevich, Solid Fuel Chem. **3**, 106 (1986)
22. G.S. Golovin, I.P. Krapchin, Solid Fuel Chem. **2**, 21 (1998)
23. A.I. Seregin, E.G. Gorlov, Mining Inf. Anal. Bull. (Sci. Tech. J.) **10**, 416 (2009). ((In Russian))

Physics of Advanced Materials

Statistical Operator and Density Matrix for Gamma Quantum and Deuterium

Boris V. Bondarev

Abstract In this chapter, we study the problem of how to use the statistical operator $\hat{\varrho}$ to describe the nuclear reaction of the death of deuterium D, when it is irradiated with a gamma quantum:

$$\gamma + D \rightarrow p + n,$$

as a result, deuterium decays into a proton p and a neutron n. Gamma quantum with a frequency ω is identified with that part of the light wave that is traveling in space at the speed of light and occupies the volume of a cylinder with a length $L = 1/k$, where k is the modulus of the wave vector $\boldsymbol{k}$, and directed along this vector. This part of the wave has the energy W, which is possessed by the γ-quantum, and transfers the energy $W^{(S)}$ through the surface of the cylinder perpendicular to the vector $\boldsymbol{k}$ during the passage of the distance L by the wave.

This chapter begins with an equation for the statistical operator $\hat{\varrho}$, which was written by the Swedish scientist Lindblad. The main result of his work is the operator $\widehat{D}$, which describes the effect of the thermostat R on the quantum system S. This operator is given in the most general form and cannot tell what happens with the system S. The author of this chapter wrote down two dissipative diffusion and attenuation operators that specify the operator$\widehat{D}$. Next, we need to know the potential energy of the system S to write the Hamiltonian. To do this, we use the assumption that the proton and neutron have potential energy inversely proportional to the distance between them. This assumption made it possible to write an equation for the statistical operator, in which the energies of the γ-quantum W and $W^{(S)}$ stand. This equation splits into two equations. In the first equation, the statistical operator describes the motion of proton and neutron around their center of mass. In the second equation, the statistical operator describes the motion of the center of mass, and in this case, calculating the average values of the coordinate and momentum make it possible to tell which path deuterium traveled during the fall of the gamma quantum on it and what speed it acquires after that. Then we returned to the first equation and

B. V. Bondarev (✉)
Moscow Aviation Institute, Moscow, Russia
e-mail: bondarev.b@mail.ru

I. A. Parinov et al. (eds.), *Physics and Mechanics of New Materials and Their Applications*, Springer Proceedings in Materials 10,
https://doi.org/10.1007/978-3-030-76481-4_11

began to solve how the gamma-ray quantum causes the displacement of deuterium in the perpendicular direction. When, at the end of the life of a gamma-ray quantum, it is absorbed by deuterium and its displacement becomes zero, the proton and neutron are released from the binding force and fly in different directions at the calculated speeds.

Keywords Statistical operator · Density matrix · Gamma quantum · Deuterium · Proton · Neutron · Photon · Lindblad equation · Hamiltonian

1 Introduction

We can only see light if photon or electromagnetic waves hit our eyes or our body. In the first case, we literally see the light. In the second, we feel the body heat or even burn. In life, we see light only when it illuminates the objects around us. If the light passes by us, we do not notice it. It seems that it is very simple.

In quantum physics, the main tools are the statistical operator $\hat{\varrho}$ and its equivalent density matrix $\varrho = \varrho\left(t, \boldsymbol{r}, \boldsymbol{r}'\right)$. Take, for example, deuterium is a particle that consists of a proton and a neutron. Here at once there are difficulties. How do we write, an equation for the statistical operator of a system consisting of only two particles, namely a proton and a neutron? However, this task is solved very simply. It is necessary to substitute the dissipative operator, the potential energy of the proton and neutron, and the force in the Lindblad equation. Now let us look at how the gamma quantum interacts with deuterium. It is known that some gamma-rays, falling into deuterium, destroy it and it decays into a proton and a neutron. However, how this happens is a mystery. What is a gamma quantum? This is a high-energy wave particle. It is possible to record the mechanical conservation laws. However, they do not solve the problem as it happens. In this chapter, we will solve this problem.

In quantum physics, a photon is considered as a wave particle with energy:

$$\varepsilon = \hbar\omega \tag{1}$$

and momentum

$$\boldsymbol{p} = \hbar\boldsymbol{k}. \tag{2}$$

Here ω and $\boldsymbol{k}$ are the frequency and the wave vector. They are related by the relation: $k = \omega/c$, where k is the modulus of the wave vector, and c is the speed of light. So that you can write:

$$cp = \hbar\omega. \tag{3}$$

If the vector $\boldsymbol{p}$ coincides in the direction with one of the coordinate axes, for example with the x-axis, then instead of the formula (4) we can write:

$$cp_x = \hbar\omega. \tag{4}$$

In classical physics, the electromagnetic field, described by the vectors of electric $\boldsymbol{E} = \boldsymbol{E}(t, \boldsymbol{r})$ and magnetic $\boldsymbol{H} = \boldsymbol{H}(t, \boldsymbol{r})$ fields, is characterized by a volume energy density:

$$w = 1/2\left(\varepsilon_0 \boldsymbol{E}^2 + \mu_0 \boldsymbol{H}^2\right), \tag{5}$$

where $\varepsilon_0\ \mu_0 = 1/c^2$ and the Umov—Poiting vector:

$$\boldsymbol{S} = [\boldsymbol{E}\boldsymbol{H}]. \tag{6}$$

These values satisfy the equation:

$$\partial w/\partial t = -\boldsymbol{j}E - \mathrm{div}\boldsymbol{S}, \tag{7}$$

which expresses the law of conservation of energy of the electromagnetic field. Here $\boldsymbol{j}$ is the electric current density. In the future, we will assume that $\boldsymbol{j} = 0$.

The differential Eq. (6) corresponds to the integral equation:

$$\mathrm{d}W/\mathrm{d}t = -\int \boldsymbol{S}\boldsymbol{n}\,\mathrm{d}S, \tag{8}$$

where

$$W = \int w\mathrm{d}V \tag{9}$$

is the energy of the electromagnetic field in the volume V, $\boldsymbol{n}$ is the external normal to the surface S, which limits this volume. The flow of the vector $\boldsymbol{S}$ through the surface S is the energy of the electromagnetic field that flows from the volume V per unit time.

In the future, we will be interested in a flat light wave. For an electromagnetic wave that propagates along the x-axis, the electric intensity $\boldsymbol{E}$ will be described in the special case by the formulae:

$$E_x = 0,\ E_y = E_0\cos(\omega t - kx),\ E_z = 0; \tag{10}$$

and the magnetic field strength $\boldsymbol{H}$ will be $H_x = 0$, $H_y = 0$, $H_z = H_0\cos(\omega t - kx)$.

This wave in the void is characterized by a volumetric energy density

$$w = \varepsilon_0 E_0^2 \cos^2(\omega t - kx), \tag{11}$$

and the vector $\boldsymbol{S}$, whose projections on the coordinate axis will be equal to

$$S_x = \sqrt{\varepsilon_0/\mu_0} E_0^2 \cos^2(\omega t - kx),\ S_y = 0,\ S_z = 0. \tag{12}$$

2 Photon and Part of Light Wave

Let us make a connection of formulae that describe a photon and a light wave. To do this, we construct a cylinder that has a cross-sectional area $\boldsymbol{S}$ and a length L. The cylinder itself is directed by its generatrix along the x-axis. Since the volume of the cylinder is equal to $S\,L$, the energy of the electromagnetic field inside the cylinder will be equal to:

$$W = wV = wSL = \varepsilon_0 SLE_0^2 \cos^2(\omega t - kx). \tag{13}$$

Put it here: $\omega t - kx = 0$. On this condition, we have $W_0 = \varepsilon_0\, S\, L\, E_0^2$.

If we recall the formula (1), we get $W_0 = \hbar\omega$.

Substituting this value in the function (13), we have

$$W = \hbar\omega \cos^2(\omega t - kx). \tag{14}$$

Looking at this function, we begin to understand that a photon is a part of a plane light wave that fits into a cylinder of $S\,L$ volume.

Now consider the vector $\boldsymbol{S}$, which is directed along the x-axis. In order to write an expression for energy, we will write d $W^{(S)} = S_x\, S\, \mathrm{d}t$. This is the energy transmitted by radiation through the area S during the time dt. For the time from zero to an arbitrary $t \le \tau$, where $= L/c$, the time, which is taken for a gamma quantum to travel the path L, the energy transmitted by radiation through the area S during this time will be equal to:

$$W^{(S)} = \hbar\omega c/L \int_0^t \cos^2(\omega t - kx)\mathrm{d}t, \tag{15}$$

where the previously obtained ratio was used $\sqrt{\varepsilon_0/\mu_0} S\, E_0^2 = \hbar\omega\, c/L$, or

$$W^{(S)} = cp_x c/L \int_0^t \cos^2(\omega t - kx)\mathrm{d}t, \tag{16}$$

where the ratio (4) was used; $c\ p_x = \hbar\,\omega$.

Now, until we find an approximate expression for the energy $W^{(S)}$, we will write it as

$$W^{(S)} = W^{(S)}(t, kx). \tag{17}$$

3 Lindblad Equations for the Statistical Operator

It cannot be said that the quantum system S in the void is not affected by any other systems. System S is not a "closed" system. On the contrary, it constantly interacts with its environment, which is called the R thermostat. The only property that characterizes a thermostat is its temperature T.

Swedish scientist Lindblad wrote down an equation that describes an "open" quantum system [1]:

$$\mathrm{i}\hbar\partial\hat{\varrho}/\partial t = [\hat{H}\hat{\varrho}] + \mathrm{i}\hbar\hat{D}, \tag{18}$$

where $\hat{\varrho}$ is a statistical operator;

$$\hat{H} = \hat{\boldsymbol{p}}^2/(2m) + \hat{U}(\hat{\boldsymbol{r}}) \tag{19}$$

is a Hamiltonian;$\hat{\boldsymbol{r}}$, $\hat{\boldsymbol{p}}$ and $\widehat{U}$ are operators of coordinates, momentum and potential energy, respectively; $\widehat{D}$ is a dissipative operator written by Lindblad and equal to:

$$\hat{D} = \sum_{jk} C_{jk}\left\{2\hat{a}_j\hat{\varrho}\hat{a}_k^+ - \hat{a}_k^+\hat{a}_j\hat{\varrho} - \hat{\varrho}\hat{a}_k^+\hat{a}_j\right\}, \tag{20}$$

where C_{jk} are unknown coefficients, and $\hat{a}_j$ are unknown operators. The statistical operator satisfies the normalization condition:

$$\mathrm{Tr}\hat{\varrho} = 1. \tag{21}$$

4 Dissipative Diffusion and Attenuation Operators

Let us write the following operators [2]:

$$\hat{\boldsymbol{a}} = \hat{\boldsymbol{p}} + \mathrm{i}\hbar\beta\widehat{\boldsymbol{F}}/4, \hat{\boldsymbol{b}} = \hat{\boldsymbol{r}} + \mathrm{i}\hbar\beta\hat{\boldsymbol{p}}/(4m), \tag{22}$$

where $\beta = 1/(k_{\mathrm{B}}T)$. There is an inverse temperature, called dissipative diffusion and attenuation operators. Being substituted into the Lindblad equations after a series of transformations and the derivation of the Wigner equation, it turned out that this equation coincides with the Fokker—Planck equation. Moreover, substituting these operators in the Lindblad equation introduces temperature into the quantum equation.

Let us substitute the formulae (22) into the Lindblad equation (18). We will have a new equation:

$$\begin{aligned}\mathrm{i}\hbar\partial\hat{\varrho}/\partial t = [\hat{H}\hat{\varrho}]+ \\ + \mathrm{i}D/\hbar\Big\{2\hat{\boldsymbol{a}}\hat{\varrho}\hat{\boldsymbol{a}}^{+} - \Big[\hat{\boldsymbol{a}}^{+}\hat{\boldsymbol{a}}, \hat{\varrho}\Big]_{+}\Big\} + \mathrm{i}\gamma/\hbar\Big\{2\hat{\boldsymbol{b}}\hat{\varrho}\hat{\boldsymbol{b}}^{+} - \Big[\hat{\boldsymbol{b}}^{+}\hat{\boldsymbol{b}}, \hat{\varrho}\Big]_{+}\Big\},\end{aligned} \tag{23}$$

where D is the diffusion coefficient, $\alpha = \beta\,\gamma$ is the coefficient of friction.

To make this equation simpler, we introduce more operators:

$$\hat{\boldsymbol{a}}_1 = \hat{\boldsymbol{p}}, \hat{\boldsymbol{a}}_2 = \mathrm{i}\hbar\beta\widehat{\boldsymbol{F}}/4, \hat{\boldsymbol{b}}_1 = \hat{\boldsymbol{r}}, \hat{\boldsymbol{b}}_2 = \mathrm{i}\hbar\beta\hat{\boldsymbol{p}}/(4\,m). \tag{24}$$

Then the equation takes the form:

$$\begin{aligned}\mathrm{i}\hbar\partial\hat{\varrho}/\partial t = \Big[\hat{\boldsymbol{p}}^2/(2\,m) + \hat{U}(\hat{\boldsymbol{r}}), \hat{\varrho}\Big]+ \\ + D\beta/2\Big[\hat{\boldsymbol{p}}[\widehat{\boldsymbol{F}}\hat{\varrho}]_{+}\Big] + \alpha/(2m)\big[\hat{\boldsymbol{r}}[\hat{\boldsymbol{p}}\hat{\varrho}]_{+}\big].\end{aligned} \tag{25}$$

In order to solve the equation, we must first substitute potential energy and force into it.

As for the coefficient β, which characterizes the effect of the thermostat on the quantum system, it is clear that when the temperature approaches zero, this effect increases to infinity. To avoid this absurdity, we add another quantum energy $\hbar\omega$ to the energy $k_{\mathrm{B}}T$, where the frequency ω characterizes the quantum effect of the thermostat on the quantum system in the form of electromagnetic waves and other massless particles:

$$\beta = 1/(\hbar\omega + k_{\mathrm{B}}T). \tag{26}$$

5 Statistical Operator of Deuterium

In [3] , we used the assumption that nucleons have a potential energy $U(\boldsymbol{r})$ during their interaction, knowing which we find the strength of their interaction, $\boldsymbol{F} = -\nabla U$.

Deuterium consists of a proton and a neutron, which have potential energy:

$$U(\boldsymbol{r}_p - \boldsymbol{r}_n) = \kappa^2/|\boldsymbol{r}_p - \boldsymbol{r}_n|, \tag{27}$$

where $\boldsymbol{r}_p$ and $\boldsymbol{r}_n$ are the radius-vectors of the proton and neutron. It has been proposed that a proton has a positive nucleon charge of $(+\kappa)$, and a neutron has a negative charge of $(-\kappa)$. In this case, the proton and neutron are attracted to each other by the forces:

$$\boldsymbol{F}_p(\boldsymbol{r}_p - \boldsymbol{r}_n) = -\kappa^2(\boldsymbol{r}_p - \boldsymbol{r}_n)/|\boldsymbol{r}_p - \boldsymbol{r}_n|^3, \boldsymbol{F}_n = -\boldsymbol{F}_p. \tag{28}$$

Let us denote in Eq. (25):

$$\begin{aligned} &m = m_p + m_n, \\ &\hat{\boldsymbol{r}} = \hat{\boldsymbol{r}}_p - \hat{\boldsymbol{r}}_n, \hat{\boldsymbol{p}} = \hat{\boldsymbol{p}}_p - \hat{\boldsymbol{p}}_n \\ &\hat{U}(\hat{\boldsymbol{r}}) = U_{pn}(\hat{\boldsymbol{r}}_p - \hat{\boldsymbol{r}}_n), \hat{\boldsymbol{F}}(\hat{\boldsymbol{r}}) = \hat{\boldsymbol{F}}_{pn}(\hat{\boldsymbol{r}}_p - \hat{\boldsymbol{r}}_n). \end{aligned}$$

Thus, all the operators in Eq. (25) are defined and this equation can now be solved.

Equation (25) describes the state of deuterium, when the center of mass is at the origin. If we want to write a more general equation, we will write the momentum operator $\hat{\boldsymbol{p}}_c$ of the center of mass. Here is the equation we are looking for

$$\begin{aligned} \mathrm{i}\hbar\partial\hat{\varrho}/\partial t = 1/(2m)\left[\left(\hat{\boldsymbol{p}}_c^2 + \hat{\boldsymbol{p}}^2\right)\hat{\varrho}\right] + [\hat{U}(\hat{\boldsymbol{r}})\hat{\varrho}] + \\ + D\beta/2\left[\hat{\boldsymbol{p}}[\hat{\boldsymbol{F}}\hat{\varrho}]_+\right] + \alpha/(2m)\left[\hat{\boldsymbol{r}}[\hat{\boldsymbol{p}}\hat{\varrho}]_+\right]. \end{aligned} \tag{29}$$

The center of mass is by definition equal to $\hat{\boldsymbol{r}}_c = (m_p\hat{\boldsymbol{r}}_p + m_n\hat{\boldsymbol{r}}_n)/(m_p + m_n)$.

Then the center of mass momentum operator will be $\hat{\boldsymbol{p}}_c = (m_p\hat{\boldsymbol{p}}_p + m_n\hat{\boldsymbol{p}}_n)/(m_p + m_n)$.

The solution of Eq. (29) is equal to the product of two functions:

$$\hat{\varrho} = \hat{\varrho}^{(D)}\hat{\varrho}^{(c)}. \tag{30}$$

The first function $\hat{\varrho}^{(D)}$ describes the motion of proton and neutron around their center of mass. the second function $\hat{\varrho}^{(c)}$ describes the motion of the center of mass and satisfies the equation:

$$\mathrm{i}\hbar\partial\hat{\varrho}^{(c)}/\partial t = 1/(2\,m)\Big[\widehat{\boldsymbol{p}}_c^2\hat{\varrho}^{(c)}\Big]. \tag{31}$$

This corresponds to the Liouville—von Neumann equation, which describes the motion of a free particle in a void when there are no other particles around it and there is no thermostat.

6 Statistical Operator for Deuterium and Gamma-Ray Incident on It

The equation for the statistical operator, when a photon falls on deuterium during the time from zero to τ, will look as

$$\begin{aligned}\mathrm{i}\hbar\partial\hat{\varrho}/\partial t = 1/(2m)\Big[\widehat{\boldsymbol{p}}_c^2\hat{\varrho}\Big] + \Big[\hat{W}^{(S)}\hat{\varrho}\Big] + 1/(2m)\Big[\widehat{\boldsymbol{p}}^2\hat{\varrho}\Big] + [\hat{U}(\widehat{\boldsymbol{r}}) + \hat{W}, \hat{\varrho}]+ \\ + D\beta/2\Big[\widehat{\boldsymbol{p}}[\widehat{\boldsymbol{F}}\hat{\varrho}]_+\Big] + \alpha/(2m)\big[\hat{\boldsymbol{r}}[\widehat{\boldsymbol{p}}\hat{\varrho}]_+\big],\end{aligned} \tag{32}$$

where

$$\hat{W} = cp_y\cos^2\Big(\omega t\hat{I} - \hat{k}_x\hat{x}\Big). \tag{33}$$

$$\hat{W}^{(S)} = \hat{W}^{(S)}\Big(t\hat{I}, \hat{k}_x\hat{x}\Big), \tag{34}$$

$\hat{I}$ is a single operator. This equation splits into two equations. Substituting the function (30) leads to two equations:

$$\mathrm{i}\hbar\partial\hat{\varrho}^{(c)}/\partial t = 1/(2m)\Big[\widehat{\boldsymbol{p}}_c^2\hat{\varrho}^{(c)}\Big] + \Big[\hat{W}^{(s)}\hat{\varrho}^{(c)}\Big], \tag{35}$$

$$\begin{aligned}\mathrm{i}\hbar\partial\hat{\varrho}^{(D)}/\partial t = 1/(2m)\Big[\widehat{\boldsymbol{p}}^2\hat{\varrho}^{(D)}\Big] + \Big[\hat{U}(\widehat{\boldsymbol{r}}) + \hat{W}, \hat{\varrho}^{(D)}\Big]+ \\ + D\beta/2\Big[\widehat{\boldsymbol{p}}\Big[\widehat{\boldsymbol{F}}\hat{\varrho}^{(D)}\Big]_+\Big] + \alpha/(2m)\Big[\hat{\boldsymbol{r}}\big[\widehat{\boldsymbol{p}}\hat{\varrho}^{(D)}\big]_+\Big].\end{aligned} \tag{36}$$

The first equation describes the motion of the center of mass under the action of a light wave, and the second equation describes the change in the state of deuterium under the action of a wave, in which the vector $\boldsymbol{E}$ is directed along the y-axis.

7 The Motion of a Free Particle

Let us consider Eq. (35) without taking into account the action of the electromagnetic wave:

$$\mathrm{i}\hbar\partial\hat{\varrho}^{(c)}/\partial t = 1/(2m)\left[\widehat{\boldsymbol{p}}_c^2\hat{\varrho}^{(c)}\right]. \tag{37}$$

For simplicity, we omit the index indicating that the operators $\hat{\varrho}$ and $\widehat{\boldsymbol{p}}$ belong to the center of mass, and write this equation in the coordinate representation, where $\hat{\boldsymbol{r}} = \boldsymbol{r}$, $\widehat{\boldsymbol{p}} = -\mathrm{i}\,\hbar\,\nabla$.

We get the equation:

$$\mathrm{i}\hbar\partial\varrho/\partial t = -\hbar^2/(2m)\left(\nabla^2 - \nabla'^2\right)\varrho. \tag{38}$$

The resulting equation has the solution [4]:

$$\varrho\left(t, \mathbf{r}, \mathbf{r}'\right) = (\alpha/\pi)^{3/2}\exp\left\{-\alpha\left[\left(\boldsymbol{r} + \boldsymbol{r}'\right)/2 - \boldsymbol{r}_0 - \boldsymbol{v}_0 t\right]^2\right\}\cdot$$
$$\cdot\exp\left\{-\mathrm{i}m\boldsymbol{v}_0\left(\boldsymbol{r} - \boldsymbol{r}'\right)/\hbar\right\}. \tag{39}$$

This solution says that at time $= t0$, the particle was at the point $\boldsymbol{r}_0$ and then it moved at a constant speed $\boldsymbol{v}_0$.

8 Movement of Mass Center of Deuterium Under the Influence of Gamma-Ray Incident on It

Let us consider Eq. (35) and write it in a simpler form:

$$\mathrm{i}\hbar\partial\hat{\varrho}/\partial t = 1/(2m)\left[\widehat{\boldsymbol{p}}^2\hat{\varrho}\right] + \left[\hat{W}^{(S)}\left(t\hat{I}, \hat{k}_x\hat{x}\right)\hat{\varrho}\right], \tag{40}$$

where $\hat{\varrho} = \hat{\varrho}^{(c)}$, $\widehat{\boldsymbol{p}} = \widehat{\boldsymbol{p}}_c$; $\widehat{W}^{(S)}$ is defined by formula (34). There is a problem. We will not be able to quickly calculate the trace Tr, where there is an operator that depends on the operators standing by the sign of the trigonometric function.

Since the coordinate $x = x(t)$ of the point, with deuterium located is unknown, it is easiest to assume that deuterium remains in place at all while the gamma quantum falls on it, i.e., let us put $x = 0$. So that the energy (16) will now be

$$W^{(S)} = cp_x c/L\int_0^t \cos^2(\omega t)\mathrm{d}t. \tag{41}$$

Let us look at formulae (4) and (15). We see that the length of the cylinder is equal to the inversely opposite modulus of the wave vector $\boldsymbol{k}$:

$$L = 1/k \tag{42}$$

and $c/L = c\,k = \omega$.

Now we write the formula (41) as follows

$$\hat{W}^{(S)} = c\varphi(t)\hat{p}_x, \tag{43}$$

where $\varphi(t) = \omega \int_0^t \cos^2(\omega t)\mathrm{d}t = 1/2\{\omega t + 1/2\sin(2\omega t)\}$.

Now we calculate how the average values of $\langle\hat{x}\rangle$ and $\langle\hat{p}_x\rangle$ change over time t. Other average values of $\langle\hat{y}\rangle$ and $\langle\hat{z}\rangle$ are already known to us, since the movement occurs only along the x-axis. The average value of $\langle\hat{x}\rangle$ is by definition equal to:

$$\langle\hat{x}\rangle = \mathrm{Tr}(\hat{x}\hat{\varrho}), \tag{44}$$

and the change over time will be found by the formula:

$$\mathrm{d}\langle\hat{x}\rangle/\mathrm{d}t = \mathrm{Tr}(\hat{x}\partial\hat{\varrho}/\partial t) = -\mathrm{i}/\hbar\mathrm{Tr}\big(\hat{x}\big\{1/(2m)\big[\hat{p}_x^2\hat{\varrho}\big] + c\varphi(t)\big[\hat{p}_x\hat{\varrho}\big]\big\}\big). \tag{45}$$

Now we calculate the trace Tr of the following two operators: $\mathrm{Tr}(\widehat{x}[\,\widehat{p}_x^{\,2}\,\widehat{\varrho}])$ and $\mathrm{Tr}(\widehat{x}[\,\widehat{p}_x\widehat{\varrho}])$:

(1) Calculate at first $\mathrm{Tr}\big(\hat{x}\big[\hat{p}_x^2\hat{\varrho}\big]\big) = \mathrm{Tr}\big(\hat{x}\hat{p}_x^2\hat{\varrho} - \hat{x}\hat{\varrho}\hat{p}_x^2\big)$.

Let us use the property:

$$\mathrm{Tr}(\hat{a}\hat{b}) = \mathrm{Tr}(\hat{b}\hat{a}). \tag{46}$$

We will have $\mathrm{Tr}\big(\hat{x}\big[\hat{p}_x^2\hat{\varrho}\big]\big) = \mathrm{Tr}\big(\hat{x}\hat{p}_x^2\hat{\varrho} - \hat{p}_x^2\hat{x}\hat{\varrho}\big) = \mathrm{Tr}\big\{\big(\hat{x}\hat{p}_x\big)\hat{p}_x\hat{\varrho} - \hat{p}_x\big(\hat{p}_x\hat{x}\big)\hat{\varrho}\big\}$.

Now let us use the formula:

$$\hat{x}\hat{p}_x - \hat{p}_x\hat{x} = \mathrm{i}\hbar. \tag{47}$$

We obtain

$$\begin{aligned}\mathrm{Tr}\big(\hat{x}\big[\hat{p}_x^2\hat{\varrho}\big]\big) &= \mathrm{Tr}\big\{\big(\hat{p}_x\hat{x} + \mathrm{I}\hbar\big)\hat{p}_x\hat{\varrho} - \hat{p}_x\big(\hat{x}\hat{p}_x - \mathrm{I}\hbar\big)\hat{\varrho}\big\} = \\ &= \mathrm{Tr}\big\{\mathrm{i}\hbar\hat{p}_x\hat{\varrho} + \hat{p}_x\mathrm{i}\hbar\hat{\varrho}\big\} = 2\mathrm{i}\hbar\langle\hat{p}_x\rangle.\end{aligned} \tag{48}$$

(2) Now we calculate $\mathrm{Tr}\big(\hat{x}\big[\hat{p}_x\hat{\rho}\big]\big) = \mathrm{Tr}\big(\hat{x}\hat{p}_x\hat{\rho} - \hat{x}\hat{\varrho}\hat{p}_x\big)$.

Applying the formulae (46) and (47), we obtain

$$\mathrm{Tr}\left(\hat{x}\left[\hat{p}_x\hat{\varrho}\right]\right) = -\mathrm{i}\hbar, \tag{49}$$

where the normalization condition (21) was used.

Substitute the calculated formulae (48) and (49) in Eq. (45):

$$\mathrm{d}\langle\hat{x}\rangle/\mathrm{d}t = \left\langle\hat{p}_x\right\rangle/m + c\varphi(t). \tag{50}$$

It is obvious that: Tr ($\widehat{p}_x[\,\widehat{p}_x^2\,\widehat{\varrho}]) = 0$, Tr ($\widehat{p}_x[\,\widehat{p}_x\widehat{\varrho}]) = 0$ and $\mathrm{d}\langle\widehat{p}_x\rangle/\mathrm{d}t = 0$.

Let us find the solution of Eq. (50) under the initial conditions:

$$\begin{cases} \langle\hat{x}\rangle(0) = 0, \\ \left\langle\hat{p}_x\right\rangle(0) = 0, \end{cases}$$

The solution of (50) is:

$$\begin{aligned} \langle\hat{x}\rangle(t) &= c\int_0^t \varphi(t)\mathrm{d}t = c/2\int_0^t \{\omega t + 1/2\sin(2\omega t)\}\mathrm{d}t = \\ &= c/4\left\{\omega t^2 + 1/(2\omega)\cos(2\omega t)\right\}. \end{aligned} \tag{51}$$

For the entire time of the fall of the gamma quantum on deuterium, it will shift from zero by a distance of

$$\langle\hat{x}\rangle(\tau) = c/4\left\{\omega\tau^2 + 1/(2\omega)\cos(2\omega\tau)\right\} \tag{52}$$

and gains speed

$$v_x(\tau) = c\varphi(\tau) = c/2\{\omega\tau + 1/2\sin(2\omega\tau)\}. \tag{53}$$

In another, slightly more complex calculation, we should decompose the cosine in a series of powers of x and leave only the first degree:$\cos^2(\omega t - kx) \approx \cos^2(\omega t) + kx\sin(2\omega t)$.

Then we get $W^{(S)} = \hbar\omega c/L\int_0^t \left\{\cos^2(\omega t) + kx\sin(2\omega t)\right\}\mathrm{d}t = c\{\varphi(t)p_x + k\psi(t)p_x x\}$, where $\psi(t) = 1/2\cos(2\omega t)$.

Now this formula for the operator $\widehat{W}^{(S)}$ will have the form:

$$\hat{W}^{(S)}\left(t\hat{I}, \hat{k}_x\hat{x}\right) = c\left\{\varphi(t)\hat{p}_x + k\psi(t)\hat{p}_x\hat{x}\right\}. \tag{54}$$

Let us write Eq. (45) by adding another term to it:

$$\mathrm{d}\langle\hat{x}\rangle/\mathrm{d}t = -\mathrm{i}/\hbar\mathrm{Tr}\big(\hat{x}\big\{\ldots + ck\psi(t)\big[\hat{p}_x\hat{x},\hat{\varrho}\big]\big\}\big) \tag{55}$$

and calculate the trace $\mathrm{Tr}\big(\hat{x}\big[\hat{p}_x\hat{x},\hat{\varrho}\big]\big) = \mathrm{Tr}\big(\hat{x}\hat{p}_x\hat{x}\hat{\varrho} - \hat{x}\hat{\varrho}\hat{p}_x\hat{x}\big)$.

First, we apply formula (46).

We will have $\mathrm{Tr}\big(\hat{x}\big[\hat{p}_x\hat{x},\hat{\varrho}\big]\big) = \mathrm{Tr}\big(\hat{x}\hat{p}_x\hat{x}\hat{\varrho} - \hat{p}_x\hat{x}\hat{x}\hat{\varrho}\big) = \mathrm{Tr}\big\{\hat{x}\hat{p}_x\hat{x}\hat{\varrho} - \big(\hat{p}_x\hat{x}\big)\hat{x}\hat{\varrho}\big\}$.

Now we use formula (47). We get

$$\mathrm{Tr}\big(\hat{x}\big[\hat{p}_x\hat{x},\hat{\varrho}\big]\big) = \mathrm{Tr}\big\{\hat{x}\hat{p}_x\hat{x}\hat{\varrho} - \big(\hat{x}\hat{p}_x - \mathrm{i}\hbar\big)\hat{x}\hat{\varrho}\big\} = \mathrm{i}\hbar\mathrm{Tr}(\hat{x}\hat{\varrho}) = \mathrm{i}\hbar\langle\hat{x}\rangle. \tag{56}$$

Substitute the calculated formula (56) into Eq. (55):

$$\mathrm{d}\langle\hat{x}\rangle/\mathrm{d}t = \big\langle\hat{p}_x\big\rangle/m - c\varphi(t) + c\psi(t)\hbar k\langle\hat{x}\rangle.. \tag{57}$$

We write down the equation for the change in the mean value of the pulse over time:

$$\mathrm{d}\big\langle\hat{p}_x\big\rangle/\mathrm{d}t = \mathrm{Tr}\big(\hat{p}_x\partial\hat{\varrho}/\partial t\big) = -\mathrm{i}/\hbar\mathrm{Tr}\big(\hat{p}_x\big\{\ldots + ck\psi(t)\big[\hat{p}_x\hat{x}_2\hat{\varrho}\big]\big\}\big). \tag{58}$$

Now we calculate the trace: $\mathrm{Tr}\,(\,\widehat{p}_x[\widehat{p}_x\widehat{x},\widehat{\varrho}]) = \mathrm{Tr}\,(\,\widehat{p}_x\widehat{p}_x\widehat{x}\widehat{\varrho} - \widehat{p}_x\,\widehat{\varrho}\widehat{p}_x\widehat{x})$.

Applying the formulae (46) and (47), we have

$$\begin{aligned}&\mathrm{Tr}\big(\hat{p}_x\big[\hat{p}_x\hat{x},\hat{\varrho}\big]\big) = \mathrm{Tr}\big(\hat{p}_x\hat{p}_x\hat{x}\hat{\varrho} - \hat{p}_x\hat{x}\hat{p}_x\hat{\varrho}\big) = \mathrm{Tr}\big(\hat{p}_x\big(\hat{p}_x\hat{x}\big)\hat{\varrho} - \hat{p}_x\hat{x}\hat{p}_x\hat{\varrho}\big) =\\ &\mathrm{Tr}\big(\hat{p}_x\big(\hat{x}\hat{p}_x - i\hbar\big)\hat{\varrho} - \hat{p}_x\hat{x}\hat{p}_x\hat{\varrho}\big) = -i\hbar\mathrm{Tr}\big(\hat{p}_x\hat{\varrho}\big) = -i\hbar\big\langle\hat{p}_x\big\rangle.\end{aligned} \tag{59}$$

Substituting this formula into (58) gives

$$\mathrm{d}\big\langle\hat{p}_x\big\rangle/\mathrm{d}t = -ck\psi(t)\big\langle\hat{p}_x\big\rangle. \tag{60}$$

We got two equations:

$$\begin{cases}\mathrm{d}\langle\hat{x}\rangle/\mathrm{d}t = \big\langle\hat{p}_x\big\rangle/m - c\varphi(t) + c\psi(t)\hbar k\langle\hat{x}\rangle,\\ \mathrm{d}\big\langle\hat{p}_x\big\rangle/\mathrm{d}t = -ck\psi(t)\big\langle\hat{p}_x\big\rangle.\end{cases}$$

9 Average Value of Deuterium Energy

We write down an analogue of the Schrodinger equation for deuterium:

$$\mathrm{i}\hbar\partial\psi/\partial t = \Big\{1/(2m)\widehat{\boldsymbol{p}}^2 + U(\boldsymbol{r})\Big\},\psi, \tag{61}$$

where $\psi = \psi(t, \boldsymbol{r})$ is the wave function, $\boldsymbol{r}$ is the radius-vector that starts at the center of mass of the proton and neutron, $U(\boldsymbol{r})$ is their potential energy, which has the form:

$$U(\boldsymbol{r}) = -\kappa^2/r, \tag{62}$$

where κ is the charge of the nucleon for a proton, it is considered positive, and for a neutron, it is considered negative.

Equation (61) has the same solutions as the solutions of the Schrodinger equation for the hydrogen atom. For the ground state, the wave function will be

$$\psi(t, \boldsymbol{r}) = \exp(-\mathrm{i}E_\mathrm{o}t/\hbar)\varphi(\boldsymbol{r}), \tag{63}$$

where E_o is the lowest energy of deuterium. The ground state of a proton and neutron pair, which describes their position in space around the center of mass, is given by the function:

$$\varphi(\boldsymbol{r}) = A\exp(-\alpha r), \tag{64}$$

where A and α are constants. Using the normalization condition, we find $A = \alpha/2\sqrt{\alpha/(2\pi)}$.

With the help of wave function$\varphi(\boldsymbol{r})$ we write the probability density $w = w(r)$, which allows us to find the probability of proton and neutron located at a distance from the center of mass in $[\, r, r + \mathrm{d}r]$:

$$w(r) = |A\exp(-\alpha r)|^2 4\pi r^2 \mathrm{d}r. \tag{65}$$

The greatest probability of finding these particles at a distance of r_o is

$$r_0 = 1/\alpha. \tag{66}$$

Let us find how the energy E_0 of deuterium is related to the distance r_0. Suppose that the proton and neutron rotate around the center of mass on a circle of radius r. Following Bohr's calculation, we write down the quantization postulate:

$$mvr = n\hbar, \tag{67}$$

where v is the modulus of the proton and neutron velocities in a circular orbit, the integer $n = 1, 2, \ldots$ is called a quantum number. The force acting between the nucleons will be equal to:

$$F = \kappa^2/r^2. \tag{68}$$

Let us write down Newton's second law:

$$mv^2/r = F, \tag{69}$$

which, together with Bohr's postulate (67), forms a system of two equations with two unknowns v and r:

$$\begin{cases} mv^2/r = \kappa^2/r^2, \\ mvr - n\hbar. \end{cases} \tag{70}$$

Let us find these unknowns:

$$v = \kappa^2/(n\hbar) \text{ and } r = (n\hbar)^2/\left(m\kappa^2\right). \tag{71}$$

For $n = 1$ we get:

$$r_0 = \hbar^2/\left(m\kappa^2\right). \tag{72}$$

The internal energy E of deuterium is mechanical and potential energy:

$$E = mv^2/2 - \kappa^2/r. \tag{73}$$

From Newton's law we find that $mv^2 = \kappa^2/r$. Therefore, the energy will be equal to.
$E = -\,m\,v^2/2$ or

$$E = -\kappa^2/(2r). \tag{74}$$

From the first formula, after substituting $v = \kappa^2/(n\hbar)$ into it, the deuterium energy will be:

$$E = -m\kappa^4/\left(2\hbar^2 n^2\right). \tag{75}$$

Thus, the lowest energy E_o of deuterium at $n = 1$ is equal to

$$E_0 = -m\kappa^4/\left(2\hbar^2\right), \tag{76}$$

and the formula (74) gives:

$$E_0 = -\kappa^2/(2r_0). \tag{77}$$

10 Equation of Change in the State of Deuterium Under the Influence of the Gamma Quantum

We write Eq. (36) for the statistical operator $\hat{\varrho}^{(D)}$, dropping the dissipative diffusion operator from it and substituting the Gamma quantum energy $\widehat{W}$, defined by the formula (14). Since the electric $\boldsymbol{E}$ vector is directed along the y-axis, we replace, using the formula (4), the quantum energy $\hbar\,\omega$ with the energy p_y:

$$\hbar\omega = cp_y. \tag{78}$$

We get the equation:

$$\begin{aligned} \mathrm{i}\hbar\partial\hat{\varrho}^{(D)}/\partial t = 1/(2m)\Big[\widehat{\boldsymbol{p}}^2\hat{\varrho}^{(D)}\Big] + \Big[\hat{U}(\widehat{\boldsymbol{r}}) + cp_y\cos^2(\omega t - kx), \hat{\varrho}^{(D)}\Big] + \\ + \alpha/(2m)\Big[\widehat{\boldsymbol{r}}\big[\widehat{\boldsymbol{p}}\hat{\varrho}^{(D)}\big]_+\Big]. \end{aligned} \tag{79}$$

So that this equation can be used in the problem, we replace the true potential energy with the potential energy:

$$\hat{U}(\widehat{\boldsymbol{r}}) = \mathrm{const} + K\widehat{\boldsymbol{r}}^2. \tag{80}$$

Now Eq. (79) takes the form:

$$\begin{aligned} \mathrm{i}\hbar\partial\hat{\varrho}/\partial t = 1/(2m)\Big[\widehat{\boldsymbol{p}}^2\hat{\varrho}\Big] + \Big[K\widehat{\boldsymbol{r}}^2 + cp_y\cos^2(\omega t - kx), \hat{\varrho}\Big] + \\ + \alpha/(2m)\big[\widehat{\boldsymbol{r}}[\widehat{\boldsymbol{p}}\hat{\varrho}]_+\big], \end{aligned} \tag{81}$$

where $\hat{\varrho} = \hat{\varrho}^{(D)}$.

To determine what happens to deuterium under the influence of the gamma quantum, it is necessary to find the average values of the coordinates $\langle\widehat{\boldsymbol{r}}\rangle$ and the momentum $\langle\widehat{\boldsymbol{p}}\rangle$ and their changes over time. The average values of these values are equal to

$$\langle\widehat{\boldsymbol{r}}\rangle = \mathrm{Tr}(\widehat{\boldsymbol{r}}\hat{\varrho}),\ \langle\widehat{\boldsymbol{p}}\rangle = \mathrm{Tr}(\widehat{\boldsymbol{p}}\hat{\varrho}). \tag{82}$$

The change in values over time is obtained by the formulae:

$$\mathrm{d}\langle\widehat{\boldsymbol{r}}\rangle/\mathrm{d}t = \mathrm{Tr}(\widehat{\boldsymbol{r}}\partial\hat{\varrho}/\partial t),\ \partial\langle\widehat{\boldsymbol{p}}\rangle/\partial t = \mathrm{Tr}(\widehat{\boldsymbol{p}}\partial\hat{\varrho}/\partial t).$$

First, we find the change in the average value of $\langle\widehat{\boldsymbol{r}}\rangle$ over time:

$$\mathrm{d}\langle\hat{\boldsymbol{r}}\rangle/\mathrm{d}t = -\mathrm{i}/\hbar\mathrm{Tr}\Big(\hat{\boldsymbol{r}}\Big\{1/(2m)\Big[\widehat{\boldsymbol{p}}^2\hat{\varrho}\Big] + \Big[K\widehat{\boldsymbol{r}}^2 + cp_y\cos^2(\omega t - kx)_y, \hat{\varrho}\Big] + \\ + \alpha/(2m)\big[\hat{\boldsymbol{r}}[\widehat{\boldsymbol{p}}\hat{\varrho}]_+\big]\Big\}\Big)\cdot \tag{83}$$

Now we will have to calculate four quantities [5]: $\mathrm{Tr}\Big(\hat{\boldsymbol{r}}\Big[\widehat{\boldsymbol{p}}^2\hat{\varrho}\Big]\Big)$, $\mathrm{Tr}\Big(\hat{\boldsymbol{r}}\Big[\widehat{\boldsymbol{r}}^2\hat{\varrho}\Big]\Big)$, $\mathrm{Tr}\big(\hat{\boldsymbol{r}}\big[p_y\hat{\varrho}\big]\big)$ and $\mathrm{Tr}\big(\hat{\boldsymbol{r}}\big[\hat{\boldsymbol{r}}[\widehat{\boldsymbol{p}}\hat{\varrho}]_+\big]\big)$.

(1) Calculate the value: $\mathrm{Tr}\Big(\hat{\boldsymbol{r}}\Big[\widehat{\boldsymbol{p}}^2\hat{\varrho}\Big]\Big) = \mathrm{Tr}\Big\{\hat{\boldsymbol{r}}\Big(\widehat{\boldsymbol{p}}^2\hat{\varrho} - \hat{\varrho}\widehat{\boldsymbol{p}}^2\Big)\Big\} = \mathrm{Tr}\Big(\hat{\boldsymbol{r}}\widehat{\boldsymbol{p}}^2\hat{\varrho} - \hat{\boldsymbol{r}}\hat{\varrho}\widehat{\boldsymbol{p}}^2\Big)$.

Now we will use the formula:

$$\mathrm{Tr}(\hat{a}\hat{b}) = \mathrm{Tr}(\hat{b}\hat{a}). \tag{84}$$

We get: $\mathrm{Tr}\Big(\hat{\boldsymbol{r}}\Big[\widehat{\boldsymbol{p}}^2\hat{\varrho}\Big]\Big) = \mathrm{Tr}\Big(\hat{\boldsymbol{r}}\widehat{\boldsymbol{p}}^2\hat{\varrho} - \widehat{\boldsymbol{p}}^2\hat{\boldsymbol{r}}\hat{\varrho}\Big) = \mathrm{Tr}\{(\hat{\boldsymbol{r}}\widehat{\boldsymbol{p}})\widehat{\boldsymbol{p}}\hat{\varrho} - \widehat{\boldsymbol{p}}(\widehat{\boldsymbol{p}}\hat{\boldsymbol{r}})\hat{\varrho}\}$.

Let us use the formula:

$$\widehat{\boldsymbol{r}}\widehat{\boldsymbol{p}} - \widehat{\boldsymbol{p}}\widehat{\boldsymbol{r}} = \mathrm{i}\hbar\delta_{kl}. \tag{85}$$

We will have

$$\mathrm{Tr}\Big(\hat{\boldsymbol{r}}\Big[\widehat{\boldsymbol{p}}^2\hat{\varrho}\Big]\Big) = \mathrm{Tr}\big\{\big(\mathrm{i}\hbar\delta_{kl} + \widehat{\boldsymbol{p}}\hat{\boldsymbol{r}}\big)\widehat{\boldsymbol{p}}\hat{\varrho} - \widehat{\boldsymbol{p}}\big(\hat{\boldsymbol{r}}\widehat{\boldsymbol{p}} - \mathrm{i}\hbar\delta_{kl}\big)\hat{\varrho}\big\} = \\ = 2\mathrm{i}\hbar\delta_{kl}\mathrm{Tr}(\widehat{\boldsymbol{p}}\hat{\varrho}) = 2\mathrm{i}\hbar\langle\boldsymbol{p}\rangle. \tag{86}$$

(2) Consider the following term: $\mathrm{Tr}\Big(\hat{\boldsymbol{r}}\Big[\hat{\boldsymbol{r}}^2\hat{\varrho}\Big]\Big) = \mathrm{Tr}\Big(\hat{\boldsymbol{r}}^3\hat{\varrho} - \hat{\boldsymbol{r}}\hat{\varrho}\hat{\boldsymbol{r}}^2\Big)$.

According to the formula (84), we will have:

$$\mathrm{Tr}\big(\hat{\boldsymbol{r}}\big[p_y\hat{\varrho}\big]\big) = \mathrm{Tr}\Big(\hat{\boldsymbol{r}}\Big[\hat{\boldsymbol{r}}^2\hat{\varrho}\Big]\Big) = 0. \tag{87}$$

(3) Now we calculate: $\mathrm{Tr}\big(\hat{\boldsymbol{r}}\big[p_y\hat{\varrho}\big]\big) = \mathrm{Tr}\big\{\hat{\boldsymbol{r}}\big(p_y\hat{\varrho} - \hat{\varrho}p_y\big)\big\} = \mathrm{Tr}\big\{\hat{\boldsymbol{r}}p_y\hat{\varrho} - \hat{\boldsymbol{r}}\hat{\varrho}p_y\big\}$.

Applying the formulas (84) and (85), we have:

$$\mathrm{Tr}\big(\hat{\boldsymbol{r}}\big[p_y\hat{\varrho}\big]\big) = \mathrm{Tr}\{\hat{\boldsymbol{r}}p_y\hat{\varrho} - p_y\hat{\boldsymbol{r}}\hat{\varrho}) = \mathrm{i}\hbar\mathrm{Tr}\hat{\varrho}\boldsymbol{j} = \mathrm{i}\hbar\boldsymbol{j}, \tag{88}$$

where $\boldsymbol{j}$ is a unit vector directed along the y-axis.

(4) Finally, the last member:

$$\begin{aligned}\mathrm{Tr}\left(\hat{\boldsymbol{r}}\left[\hat{\boldsymbol{r}}[\hat{\boldsymbol{p}}\hat{\varrho}]_+\right]\right) &= \mathrm{Tr}(\hat{\boldsymbol{r}}[\hat{\boldsymbol{r}}(\hat{\boldsymbol{p}}\hat{\varrho}+\hat{\varrho}\hat{\boldsymbol{p}})]) \\ &= \mathrm{Tr}\left(\hat{\boldsymbol{r}}^2(\hat{\boldsymbol{p}}\hat{\varrho}+\hat{\varrho}\hat{\boldsymbol{p}})-\hat{\boldsymbol{r}}(\hat{\boldsymbol{p}}\hat{\varrho}+\hat{\varrho}\hat{\boldsymbol{p}})\hat{\boldsymbol{r}}\right)= \\ &= \mathrm{Tr}\left(\hat{\boldsymbol{r}}^2\hat{\boldsymbol{p}}\hat{\varrho}+\hat{\boldsymbol{r}}^2\hat{\varrho}\hat{\boldsymbol{p}}-\hat{\boldsymbol{r}}\hat{\boldsymbol{p}}\hat{\varrho}\hat{\boldsymbol{r}}-\hat{\boldsymbol{r}}\hat{\varrho}\hat{\boldsymbol{p}}\hat{\boldsymbol{r}}\right) \\ &= \mathrm{Tr}\left(\hat{\boldsymbol{r}}^2\hat{\boldsymbol{p}}\hat{\varrho}+\hat{\boldsymbol{p}}\hat{\boldsymbol{r}}^2\hat{\varrho}-\hat{\boldsymbol{r}}^2\hat{\boldsymbol{p}}\hat{\varrho}-\hat{\boldsymbol{p}}\hat{\boldsymbol{r}}^2\hat{\varrho}\right)=0. \qquad (89)\end{aligned}$$

Substituting formulae (86) and (88) into formula (83), we obtain:

$$\mathrm{d}\langle\hat{\boldsymbol{r}}\rangle/\mathrm{d}t = \langle\hat{\boldsymbol{p}}\rangle/M + c\boldsymbol{j}\cos^2\{\omega t - kx(t)\}. \qquad (90)$$

Here $x = x(t)$ is the coordinate of deuteriumv, i.e. the distance by which it will shift during the fall of the gamma quantum on it from zero to the current moment t.

Find the change in time of the average value of the pulse $\langle\boldsymbol{p}\rangle$:

$$\begin{aligned}\mathrm{d}\langle\hat{\boldsymbol{p}}\rangle/\mathrm{d}t = -\mathrm{i}/\hbar\mathrm{Tr}\Big(\hat{\boldsymbol{p}}\Big\{1/(2m)\Big[\hat{\boldsymbol{p}}^2\hat{\varrho}\Big]+\Big[K\hat{\boldsymbol{r}}^2+cp_y\cos^2\{\omega t-kx(t)\},\hat{\varrho}\Big] \\ +\alpha/(2m)\big[\hat{\boldsymbol{r}}[\hat{\boldsymbol{p}}\hat{\varrho}]_+\big]. \qquad (91)\end{aligned}$$

Now we will calculate four quantities: $\mathrm{Tr}\left(\hat{\boldsymbol{p}}\left[\hat{\boldsymbol{p}}^2\hat{\varrho}\right]\right)$, $\mathrm{Tr}\left(\hat{\boldsymbol{p}}\left[\hat{\boldsymbol{r}}^2\hat{\varrho}\right]\right)$, $\mathrm{Tr}\big(\hat{\boldsymbol{p}}\big[p_y\hat{\varrho}\big]\big)$ and $\mathrm{Tr}\big(\hat{\boldsymbol{p}}\big[\hat{\boldsymbol{r}}[\hat{\boldsymbol{p}}\hat{\varrho}]_+\big]\big)$.

(1) Calculate the following value:

$$\mathrm{Tr}\left(\hat{\boldsymbol{p}}\left[\hat{\boldsymbol{p}}^2\hat{\varrho}\right]\right)=0. \qquad (92)$$

(2) Consider the following term: $\mathrm{Tr}\left(\hat{\boldsymbol{p}}\left[\hat{\boldsymbol{r}}^2\hat{\varrho}\right]\right)=\mathrm{Tr}\left(\hat{\boldsymbol{p}}\hat{\boldsymbol{r}}^2\hat{\varrho}-\hat{\boldsymbol{p}}\hat{\varrho}\hat{\boldsymbol{r}}^2\right)$.
According to the formula (84) we will have: $\mathrm{Tr}\left(\hat{\boldsymbol{p}}\left[\hat{\boldsymbol{r}}^2\hat{\varrho}\right]\right) = \mathrm{Tr}\left(\hat{\boldsymbol{p}}\hat{\boldsymbol{r}}^2\hat{\varrho}-\hat{\boldsymbol{r}}^2\hat{\boldsymbol{p}}\hat{\varrho}\right)$.
Now we apply the formula (85). We get:

(3) Now calculate the term:

$$\mathrm{Tr}\big(\hat{\boldsymbol{p}}\big[p_y\hat{\varrho}\big]\big)=\mathrm{Tr}\big\{\hat{\boldsymbol{p}}\big(p_y\hat{\varrho}-\hat{\varrho}p_y\big)\big\}=\mathrm{Tr}\{\hat{\boldsymbol{p}}p_y\hat{\varrho}-\hat{\boldsymbol{p}}\hat{\varrho}p_y)\big\}=0. \qquad (94)$$

(4) Finally, the last term:

$$\begin{aligned}&\mathrm{Tr}\big(\hat{\boldsymbol{p}}\big[\hat{\boldsymbol{r}}[\hat{\boldsymbol{p}}\hat{\varrho}]_+\big]\big)=\mathrm{Tr}(\hat{\boldsymbol{p}}[\hat{\boldsymbol{r}}(\hat{\boldsymbol{p}}\hat{\varrho}+\hat{\varrho}\hat{\boldsymbol{p}})])=\mathrm{Tr}(\hat{\boldsymbol{p}}\hat{\boldsymbol{r}}(\hat{\boldsymbol{p}}\hat{\varrho}+\hat{\varrho}\hat{\boldsymbol{p}})-\hat{\boldsymbol{p}}(\hat{\boldsymbol{p}}\hat{\varrho}+\hat{\varrho}\hat{\boldsymbol{p}})\hat{\boldsymbol{r}})= \\ &\mathrm{Tr}(\hat{\boldsymbol{p}}\hat{\boldsymbol{r}}\hat{\boldsymbol{p}}\hat{\varrho}+\hat{\boldsymbol{p}}\hat{\boldsymbol{r}}\hat{\varrho}\hat{\boldsymbol{p}}-\hat{\boldsymbol{p}}\hat{\boldsymbol{p}}\hat{\varrho}\hat{\boldsymbol{r}}-\hat{\boldsymbol{p}}\hat{\varrho}\hat{\boldsymbol{p}}\hat{\boldsymbol{r}})=\mathrm{Tr}(\hat{\boldsymbol{p}}\hat{\boldsymbol{r}}\hat{\boldsymbol{p}}\hat{\varrho}+\hat{\boldsymbol{p}}\hat{\boldsymbol{p}}\hat{\boldsymbol{r}}\hat{\varrho}-\hat{\boldsymbol{r}}\hat{\boldsymbol{p}}\hat{\boldsymbol{p}}\hat{\varrho}-\hat{\boldsymbol{p}}\hat{\boldsymbol{r}}\hat{\boldsymbol{p}}\hat{\varrho})= \\ &\mathrm{Tr}(\hat{\boldsymbol{p}}(\hat{\boldsymbol{p}}\hat{\boldsymbol{r}})\hat{\varrho}-(\hat{\boldsymbol{r}}\hat{\boldsymbol{p}})\hat{\boldsymbol{p}}\hat{\varrho}).\end{aligned}$$

Apply formula (85):

$$\begin{aligned}\mathrm{Tr}\big(\widehat{\boldsymbol{p}}\big[\hat{\boldsymbol{r}}[\widehat{\boldsymbol{p}}\hat{\varrho}]_+\big]\big) &= \mathrm{Tr}\big(\widehat{\boldsymbol{p}}\big(\hat{\boldsymbol{r}}\widehat{\boldsymbol{p}} - \mathrm{i}\hbar\delta_{kl}\big)\hat{\varrho} - \big(\widehat{\boldsymbol{p}}\hat{\boldsymbol{r}} + \mathrm{i}\hbar\delta_{kl}\big)\widehat{\boldsymbol{p}}\hat{\varrho}\big) = \\ &= -2\mathrm{i}\hbar\mathrm{Tr}(\widehat{\boldsymbol{p}}\hat{\varrho}) = -2\mathrm{i}\hbar\langle\boldsymbol{p}\rangle. \end{aligned} \tag{95}$$

Substituting formulae (10.16) and (95) into formula (91), we obtain:

$$\mathrm{d}\langle\widehat{\boldsymbol{p}}\rangle/\mathrm{d}t = -2K\langle\boldsymbol{r}\rangle - \alpha/m\langle\boldsymbol{p}\rangle. \tag{96}$$

Thus, we have a system of two equations:

$$\begin{cases} \mathrm{d}\langle\hat{\boldsymbol{r}}\rangle/\mathrm{d}t = \langle\widehat{\boldsymbol{p}}\rangle/m + c\boldsymbol{j}\cos^2\{\omega t - kx(t)\}, \\ \mathrm{d}\langle\widehat{\boldsymbol{p}}\rangle/\mathrm{d}t = -2K\langle\hat{\boldsymbol{r}}\rangle - \alpha/m\langle\widehat{\boldsymbol{p}}\rangle. \end{cases} \tag{97}$$

The gamma quantum affects only the coordinate and momentum along the y-axis. Let us write these equations for the x-axis:

$$\begin{cases} \mathrm{d}\langle\hat{x}\rangle/\mathrm{d}t = \langle\hat{p}_x\rangle/m, \\ \mathrm{d}\langle\hat{p}_x\rangle/\mathrm{d}t = -2K\langle\hat{x}\rangle - \alpha/m\langle\hat{p}_x\rangle. \end{cases} \tag{98}$$

From this system, we derive the equation: $m\mathrm{d}^2\langle\hat{x}\rangle/\mathrm{d}t^2 + \alpha\mathrm{d}\langle\hat{x}\rangle/\mathrm{d}t + 2K\langle\hat{x}\rangle = 0$.

All solutions to this equation tend to zero over time:

$$\lim_{t\to\infty}\langle\hat{x}\rangle(t) = 0. \tag{99}$$

The same applies to the function $z = \langle\hat{z}\rangle(t)$.

11 Displacement of Deuterium Coordinate and Momentum Under Action of Gamma-Ray Quantum

Now let us write down the system of Eqs. (97) for the y-axis:

$$\begin{cases} \mathrm{d}\langle\hat{y}\rangle/\mathrm{d}t = \langle\hat{p}_y\rangle/m + c\cos^2\{\omega t - kx(t)\}, \\ \mathrm{d}\langle\hat{p}_y\rangle/\mathrm{d}t = -2K\langle\hat{y}\rangle - \alpha/m\langle\hat{p}_y\rangle. \end{cases} \tag{100}$$

We derive the equation for the mean value of the coordinate $\langle\hat{y}\rangle$. First, from the first equation, we find the second derivative of this function:

$$\mathrm{d}^2\langle\hat{y}\rangle/\mathrm{d}t^2 = 1/m\mathrm{d}\left\langle\hat{p}_y\right\rangle/\mathrm{d}t + c\omega\phi(t), \tag{101}$$

where

$$\phi(t) = \{1 - v(t)/c\}\sin\{2[\omega t - kx(t)]\}. \tag{102}$$

Here from formulae (51) and (53) we will have:

$$x(t) = c/4\left\{\omega t^2 + 1/(2\omega)\cos(2\omega t)\right\}, \tag{103}$$

$$v_x(t) = c\varphi(t) = c/2\{\omega t + 1/2\sin(2\omega t)\}. \tag{104}$$

Now we substitute the derivative $\mathrm{d}\langle\hat{p}_y\rangle/\mathrm{d}t$ from the second Eq. (100) into Eq. (101): $m\mathrm{d}^2\langle\hat{y}\rangle/\mathrm{d}t^2 = -2K\langle\hat{y}\rangle - \alpha\left\langle\hat{p}_y\right\rangle + c\omega m\phi(t)$.

Substituting into this equation $\langle\hat{p}_y\rangle$ from the first equation of the system (100), we have the desired equation:

$$\begin{aligned} &m\mathrm{d}^2\langle\hat{y}\rangle/\mathrm{d}t^2 + \alpha\mathrm{d}\langle\hat{y}\rangle/\mathrm{d}t + 2K\langle\hat{y}\rangle = \\ &= \alpha cm\cos^2\{\omega t - kx(t)\} + c\omega m\phi(t). \end{aligned} \tag{105}$$

This is Newton's second law. The expression: $-\alpha\mathrm{d}\langle\hat{y}\rangle/\mathrm{d}t$ is the friction force with which the thermostat R acts on the proton and neutron; and the expression : $-2K\langle\hat{y}\rangle$ is the force of attraction between proton and neutron, which occurs due to a fictitious potential; on the right side there is the force due to the action of the gamma quantum on deuterium.

In the new notation, Eq. (105) will look as

$$\mathrm{d}^2y/\mathrm{d}t^2 + 2a\mathrm{d}y/\mathrm{d}t + \Omega^2y = f(t), \tag{106}$$

where

$$y = \langle\hat{y}\rangle,\ 2a = \alpha/m,\ \Omega^2 = 2K/m,\ f(t) = c\omega\phi(t). \tag{107}$$

In the last notation, the first term is discarded in view of its smallness, since $\ll \omega$.

Equation (106) is a linear inhomogeneous equation. Let us start to solve a homogeneous equation:

$$\mathrm{d}^2y/\mathrm{d}t^2 + 2a\mathrm{d}y/\mathrm{d}t + \Omega^2y = 0. \tag{108}$$

We will look for its solution in the form:

$$y(t) = \mathrm{e}^{\lambda t}, \tag{109}$$

Substituting this function into the equation results in the equation: $\lambda^2 + 2a\lambda + \Omega^2 = 0$, which has two roots: $\lambda_{12} = -a \pm \mathrm{i}\sqrt{\Omega^2 - a^2}$. Thus, a homogeneous equation will have a solution of the form: $y(t) = \left\{B_1 \exp\left(-\mathrm{i}\sqrt{\Omega^2 - a^2}t\right) + B_2 \exp\left(\mathrm{i}\sqrt{\Omega^2 - a^2}t\right)\right\}\mathrm{e}^{-at}$,

where B_1 and B_2 is the constant of integration. We assume that $\Omega \gg a$.

Then $y(t) = \{B_1 \exp(-\mathrm{i}\Omega t) + B_2 \exp(\mathrm{i}\Omega t)\}\mathrm{e}^{-at}$.

Let us use Euler's formula: $\exp(\mathrm{i}\Omega t) = \cos(\Omega t) + \mathrm{i}\sin(\Omega t)$.

We get: $y(t) = \{(B_1 + B_2)\cos(\Omega t) + (-B_1 + B_2)\mathrm{i}\sin(\Omega t)\}\mathrm{e}^{-at}$.

Now let us introduce new constants: $C_1 = B_1 + B_2$, $C_2 = (-B_1 + B_2)\mathrm{i}$.

Then homogeneous equation has the solution:

$$y(t) = \{C_1 \cos(\Omega t) + C_2 \sin(\Omega t)\}\mathrm{e}^{-at}. \tag{110}$$

This solution tends to zero. Therefore, we will be interested in solving an inhomogeneous equation.

Find the function $f(t)$ by substituting the function (102):

$$f(t) = c\omega\{1 - v(t)/c\}\sin\{2[\omega t - kx(t)]\}. \tag{111}$$

This is a fairly complex dependency. To solve Eqs. (106) and (101), we need to use a computer. We simplify the solution of the problem by putting the functions $x(t)$ and $v\ (t)$ approximately equal to their largest values:

$$f(t) \approx c\omega\{1 - v(\tau)/c\}\sin\{2[\omega t - kx(\tau)]\}, \tag{112}$$

that is, we assumed that $x(t) \approx x(\tau)$ and $v(t) \approx v(\tau)$.

Now let us go back to Eq. (106). We will search a solution of this equation that is proportional to the function $f(t)$. We decompose this function using the trigonometric formula.

$\sin(\alpha - \beta) = \sin\alpha\cos\beta - \cos\alpha\sin\beta$ and obtain:

$$f(t) = c\omega\{1 - v(\tau)/c\}\{\sin(2\omega t)\cos[kx(\tau)] - \cos(2\omega t)\sin[kx(\tau)]\}. \tag{113}$$

Therefore, we will search a solution in the form:

$$y(t) = A\sin(2\omega t + \alpha). \tag{114}$$

To determine the amplitude A and the initial phase α of the forced oscillations, we substitute the value and derivatives of the function $y(t)$ in Eq. (106). Since this is the desired solution of the equation, we must obtain the identity. The derivatives are equal to:

$$dy/dt = 2\omega A\cos(2\omega t+\alpha),\ d^2y/dt^2 = -4\omega^2 A\sin(2\omega t+\alpha).$$

Substituting them into the equation gives:

$$-4\omega^2 A\sin(2\omega t+\alpha)+2a\{2\omega A\cos(2\omega t+\alpha)\}+\Omega^2\{A\sin(2\omega t+\alpha)\}=f(t).$$

The group of the terms on the left side of this equation:

$$\left\{-4\omega^2 A+\Omega^2 A\right\}\sin(2\omega t+\alpha)+4a\omega A\cos(2\omega t+\alpha)=f(t).$$

Decompose the sine and cosine of the sum into its component parts:

$$\left\{-4\omega^2 A+\Omega^2 A\right\}\{\sin(2\omega t)\cos\alpha+\cos(2\omega t)\sin\alpha\}+4a\omega A\{\cos(2\omega t)\cos\alpha- \sin(2\omega t)\sin\alpha\}=f(t).$$

Now select the coefficients for sin(2 ωt) and cos (2 ωt) and substitute the function $f(t)$, we get the identity: $\left\{\left(\Omega^2-4\omega^2\right)A\cos\alpha-4a\omega A\sin\alpha\right\}\sin(2\omega t)+$
$+\left\{\left(\Omega^2-4\omega^2\right)A\sin\alpha+4a\omega A\cos\alpha\right\}\cos(2\omega t)=$
$=c\omega\{1-v(\tau)/c\}\{\sin(2\omega t)\cos[kx(\tau)]-\cos(2\omega t)\sin[kx(\tau)]\}$.
We equate the coefficients for sin(2 ω t) in the left and right parts of this equation:

$$\left(\Omega^2-4\omega^2\right)A\cos\alpha-4a\omega A\sin\alpha=c\omega\{1-v(\tau)/c\}\cos[kx(\tau)]. \quad (115)$$

Then we get another equation:

$$\left(\Omega^2-4\omega^2\right)A\sin\alpha+4a\omega A\cos\alpha=-c\omega\{1-v(\tau)/c\}\sin[kx(\tau)]. \quad (116)$$

We obtain a system of two Eqs. (115) and (116) with two unknowns A and α. The second unknown is assumed to be equal to $\sin\alpha = 4\,a\,\omega/\left(\Omega^2-4\omega^2\right)\cos\alpha$.

Together with the equation: $\sin^2\alpha+\cos^2\alpha=1$, it forms a system from which we will find:

$$\sin\alpha = 4a\omega/\sqrt{\left(\Omega^2-4\omega^2\right)^2+(4a\omega)^2},$$
$$\cos\alpha = \left(\Omega^2-4\omega^2\right)/\sqrt{\left(\Omega^2-4\omega^2\right)^2+(4a\omega)^2},\ \mathrm{tg}\alpha = 4a\omega/\left(\Omega^2-4\omega^2\right).$$

Now we square each Eq. (115) and (116) and add:

$$A^2\left\{\left(\Omega^2-4\omega^2\right)^2\cos^2\alpha-2\left(\Omega^2-4\omega^2\right)\cos\alpha 4a\omega\sin\alpha+(4a\omega\sin\alpha)^2\right\}=$$
$$=\{c\omega[1-v(\tau)/c]\cos[kx(\tau)]\}^2$$
$$A^2\left\{\left(\Omega^2-4\omega^2\right)^2\sin^2\alpha+2\left(\Omega^2-4\omega^2\right)\cos\alpha 4a\omega\sin\alpha+(4a\omega\cos\alpha)^2\right\}=$$
$$=\{c\omega[1-v(\tau)/c]\sin[kx(\tau)]\}^2$$

After addition, we get: $A^2\left\{\left(\Omega^2-4\omega^2\right)^2+(4a\omega)^2\right\}=\{c\omega[1-v(\tau)/c]\}^2$.

As a result, we will have:

$$A=c\omega[1-v(\tau)/c]/\sqrt{\left\{\left(\Omega^2-4\omega^2\right)^2+(4a\omega)^2\right\}}. \tag{117}$$

Thus, the solution (114) is found.

However, if there is a break in the bond between proton and neutron, then the displacement function $y=\langle\hat{y}\rangle(t)$ of deuterium must satisfy the boundary conditions:

$$\langle\hat{y}\rangle(0)=0 \tag{118}$$

$$\langle\hat{y}\rangle(\tau)=0, \tag{119}$$

that is, at the beginning and end of the life of the gamma quantum, the deuterium shift should be zero. At least the second condition must be met. if it is violated and

$$\langle\hat{y}\rangle(\tau)\neq 0, \tag{120}$$

this means that the decay of deuterium into proton and neutron does not occur and it continues to move, flying at an angle in one direction, and the quantum – in the other.

What will be the function $y=y(t)$ instead of the formula (114)? Let us look at the function $f=f(t)$ in the formula (113), which is on the right side of Eq. (106). It becomes clear that the function should be as

$$y(t)=A\sin(2\omega t+\alpha)+B\cos(2\omega t+\beta). \tag{121}$$

To set the constants B and β, we use condition (118) to this function: $A\sin\alpha+B\cos\beta=0$.

This condition must be met automatically in all cases, for example if: $B=A$ and $\beta=\pi/2-\alpha$.

Since $\cos(2\omega t+\pi/2-\alpha)=\sin(2\omega t-\alpha)$, the function (121) takes the form:

$$y(t) = A\{\sin(2\omega t + \alpha) + \sin(2\omega t - \alpha)\}. \tag{122}$$

12 Gamma Quantum Absorbed by Deuterium

Consider the case when a gamma-ray quantum is absorbed by deuterium and it decays into proton and neutron. This happens when the condition (119) is met. Using the function (122), we write this condition as follows:

$$\sin(2\omega\tau + \alpha) + \sin(2\omega\tau - \alpha) = 0. \tag{123}$$

Now we find the solution of the second equation of the system (100):

$$\mathrm{d}\langle\hat{p}_y\rangle/\mathrm{d}t = -2K\langle\hat{y}\rangle - \alpha/m\langle\hat{p}_y\rangle.$$

Let us introduce the notations: $mv = \langle\hat{p}_y\rangle$, $y = \langle\hat{y}\rangle$, $2\,a = \alpha/m$, $\Omega^2 = 2K/m$ and obtain:

$$\mathrm{d}v/\mathrm{d}t = -\Omega^2 y(t) - 2av. \tag{124}$$

This is a linear inhomogeneous equation. The homogeneous equation: $\mathrm{d}v/\mathrm{d}t = -2av$ has a solution: $v(t) = C\exp(-2at)$, which tends to zero. Therefore, we will search a solution to the inhomogeneous equation as

$$v(t) = C(t)\exp(-2at). \tag{125}$$

Substituting this function into (124) gives: $\exp(-2at)\mathrm{d}C/\mathrm{d}t = -\Omega^2 y(t)C(t)\exp(-2at)$.

Using the function (122) on the right side of this equation, leads it to the form:

$$\mathrm{d}C/\mathrm{d}t = -\Omega^2 C(t)A\{\sin(2\omega t + \alpha) + \sin(2\omega t - \alpha)\}. \tag{126}$$

Integrating Eq. (126), we obtain: $\ln C(t) = \text{const} - \Omega^2 A\int_0^t \{\sin(2\omega t + \alpha) + \sin(2\omega t - \alpha)\}\mathrm{d}t = \text{const} + \Omega^2 A/(2\omega)\ \{\cos(2\omega t + \alpha) + \cos(2\omega t - \alpha)\}|_0^t == \text{const} + \Omega^2 A/(2\omega)\{\cos(2\omega t + \alpha) + \cos(2\omega t - \alpha) - 2\cos\alpha\}$.

Now we will have: $C(t) = C\exp\left\{\Omega^2 A/(2\omega)[\cos(2\omega t + \alpha) + \cos(2\omega t - \alpha) - 2\cos\alpha]\right\}$.

Substituting this expression into (125) gives:

$$v(t) = v_\circ \exp\left\{\Omega^2 A/(2\omega)[\cos(2\omega t + \alpha) + \right.$$
$$\left. + \cos(2\omega t - \alpha) - 2\cos\alpha]\right\}\exp\{-2a(t - \tau)\}, \tag{127}$$

where $v_0 = C\exp(-2a\tau)$.

Let us look again at what happens to the electric wave function during its fall on deuterium from zero to τ. At the very beginning of this process, when $t = 0$, the offset (122) is also zero: $y(0) = 0$. At the end of the process, when $t = \tau$, according to the formula (123), the offset will again be zero. So by this time the electric wave function will cease to exist. The function $W = W(t)$, which describes this wave, changes from the value:

$$W(0) = \hbar\omega\cos^2(\omega t - kx)\big|_{t=0} = \hbar\omega\cos^2(kx) \text{ to } W(\tau) = 0. \tag{128}$$

What does this mean? In the language of the gamma quantum, this means that it is absorbed by deuterium, and in the language of the electric wave function, the absorption process takes place over time τ.

What is left at the end of this process? There is still deuterium, which by the time $t = \tau$ has picked up speed:

$$v(\tau) = v_0\exp\left\{\Omega^2 A/(2\omega)[\cos(2\omega\tau + \alpha) + \cos(2\omega\tau - \alpha) - 2\cos\alpha]\right\}. \tag{129}$$

What will happen next when time t is greater than time $\tau : t > \tau$? Then deuterium decays into proton and neutron. How this decay occurs we will talk about this later.

Now we will write what velocities $\boldsymbol{v}_1$ and $\boldsymbol{v}_2$ receive proton and neutron after the decay of deuterium immediately at time $t > \tau$ and how these velocities are related to the deuterium velocity (128). On the x-axis, these vectors give zero:

$$v_{1x} = v_{2x} = 0. \tag{130}$$

Here the projections of these velocities on the y-axis will be equal:

$$v_{1y}(t > \tau) = v_{1y} = v_\circ\exp\left\{\Omega^2 A/(2\omega)[\cos(2\omega\tau + \alpha) - \cos\alpha]\right\}, \tag{131}$$

$$v_{2y}(t > \tau) = v_{2y} = -v_\circ\exp\left\{\Omega^2 A/(2\omega)[\cos(2\omega\tau + \alpha) - \cos\alpha]\right\}. \tag{132}$$

The relationship between the deuterium velocity $v(\tau)$ and the velocity projections $\boldsymbol{v}_1$ and $\boldsymbol{v}_2$ on the y-axis is very simple:

$$v(\tau) = v_{1y} - v_{2y},\ v_{1y} + v_{2y} = 0. \tag{133}$$

In order to solve the relatively simple Eq. (81), the true potential energy was replaced by a more convenient energy for solving the problem: $U(r) = \text{const} + K\,r_0^2$.

The true potential energy is $U(r) = -\kappa^2/r$.

Its value at $r = r_\text{o}$ will be equal to the lowest value of the deuterium energy:

$$U(r_0) = -E_0. \tag{134}$$

At time $t = \tau$, the electric wave function becomes zero, as indicated by formula (128), and completely disappears. It had the energy $\hbar\,\omega$ and where did it go with its disappearance? The answer is simple. It gave the energy to deuterium: $\hbar\omega = E_0$. However, at the same time, the potential energy $U(r)$ of deuterium will tend to zero and the force of attraction between the proton and neutron also becomes zero: $\lim\limits_{r\to\infty} U(r) = 0$, $\lim\limits_{r\to\infty} F(r) = 0$. Both the proton and neutron quietly leave the place, where they were bound by the nuclear force.

13 Gamma-Ray Scattering on Deuterium

When condition (123) is not met and $\sin(2\omega\tau + \alpha) + \sin(2\omega\tau - \alpha) \neq 0$, then everything that happened under that condition cannot happen. Now deuterium, while maintaining its structure, simply deviates at a certain angle to the direction of the gamma-ray quantum incident on it, which itself deviates in different directions at a different angle. We will solve this problem in the next article.

14 Laws of Conservation of Momentum and Energy

For the reaction: $\gamma + D \to p + n$, the laws of conservation of momentum and energy are fulfilled:

$$\boldsymbol{p}_\gamma + \boldsymbol{p}_D = \boldsymbol{p}_p + \boldsymbol{p}_n,\ E_\gamma + E_D = E_p + E_n, \tag{135}$$

For a gamma-quantum, the momentum and energy are equal: $\boldsymbol{p}_\gamma = \hbar\boldsymbol{k}, E_\gamma = \hbar\omega$.

For deuterium, which was at rest before the gamma ray hit it, the momentum and energy will be equal: $\boldsymbol{p}_D = 0$, $E_D = Mc^2$, where M is the mass of deuterium, which is less than the sum of the masses of the proton and neutron: $M < m$.

The impulses and energies of the proton and neutron, which are relativistic particles here, will be equal to: $\boldsymbol{p}_i = m_i\boldsymbol{v}_i/\sqrt{1 - v_i^2/c^2}$, $E_p = m_i c^2/\sqrt{1 - v_i^2/c^2}$, where $i = p, n$.

The laws of conservation of momentum and energy are powerful tools of mechanics. However, they do not take into account all the subtle questions of quantum physics. In the problem that was solved in this article, the influence of electromagnetic radiation on deuterium was considered. Its motion was described as the most important and only tools of quantum physics, namely the statistical operator and the density matrix were used. The entire process of interaction of radiation with deuterium was considered from the beginning of the fall of radiation on deuterium

to its end. The conservation laws do not consider this process at all, compressing its duration to zero.

15 Conclusion

Here are the main results of this work. For the entire time of the fall of the gamma quantum on deuterium from zero to the end of its action, it moves along the x-axis by a distance:

$$x(\tau) = c/4\left\{\omega\tau^2 + 1/(2\omega)\cos(2\omega\tau)\right\} \tag{136}$$

and gains a speed:

$$v_x(\tau) = c/2\{\omega\tau + 1/2\sin(2\omega\tau)\}. \tag{137}$$

Under the action of an electric field, deuterium is displaced along the y-axis by a distance:

$$y(t) = A\{\sin(2\omega t + \alpha) + \sin(2\omega t - \alpha)\}, \tag{138}$$

where $A = c\omega[1 - v_x(\tau)/c]/\sqrt{\left\{\left(\Omega^2 - 4\omega^2\right)^2 + (4a\omega)^2\right\}}$.

When the condition:

$$\sin(2\omega\tau + \alpha) + \sin(2\omega\tau - \alpha) = 0, \tag{139}$$

is fulfilled, then it serves as a criterion, in the result of which the decay of deuterium into proton and neutron occurs. The projections of the decay product velocities have the forms:

$$v_{1y} = v_0 \exp\left\{\Omega^2 A/(2\omega)[\cos(2\omega\tau + \alpha) - \cos\alpha]\right\}, \tag{140}$$

$$v_{2y} = -v_0 \exp\left\{\Omega^2 A/(2\omega)[\cos(2\omega\tau + \alpha) - \cos\alpha]\right\}. \tag{141}$$

This criterion allows one to write the ratio:

$$M + E_0/c^2 = m. \tag{142}$$

To make momentum and energy relativistic, one simply adds to Eq. (29) the operator $\hat{c} = c(v/c)\ \hat{I}$, where I is the unit operator.

References

1. G. Lindblad, Commun. Math. Phys. **48**, 119 (1976)
2. B.V. Bondarev, Phys. A **176**(2), 366 (1991)
3. B.V. Bondarev, Sci. Disc. **46**(1), 34 (2020)
4. B.V. Bondarev, Sci. Disc. **47**(1), 23 (2020)
5. B.V. Bondarev, *Density Matrix Theories in Quantum Physics*. Bentham, p. 393 (2020)

New Relativistic Equation for Statistical Operator

Boris V. Bondarev

Abstract In this paper, we derive a covariant quantum equation for the statistical operator $\hat{\varrho}$. This equation is written for a free particle and for a hydrogen atom.

Keywords Lorentz transformation · Momentum and energy of relativistic particle · Statistical operator · Dissipative operators · Relativistic equation

1 Introduction

The Klein—Gordon—Fock equation and the Dirac equation were written shortly after the discovery of the Schrodinger equation

$$i\,\hbar\,\partial\psi/\partial t \;=\; \widehat{H}\;\psi,$$

where $\psi = \psi(t, \boldsymbol{r})$ is the wave function, $\widehat{H}$ is the Hamiltonian. Relativistic equations were derived for the wave function $\psi = \psi(t, \boldsymbol{r})$.

Then the physicist von Neumann wrote down his equation

$$i\,\hbar\,\partial\hat{\varrho}/\partial t \;=\; [\widehat{H}\;\hat{\varrho}],$$

in which the statistical operator $\hat{\varrho}$ appeared.

In quantum physics, the main tool is the statistical operator $\hat{\varrho}$. But a covariant quantum equation for this operator has not yet been written, i.e. an equation that does not change under the action of the Lorentz transformation.

Consider two coordinate systems that move at a constant speed $\boldsymbol{V}$ relative to each other [1]. You can always direct the coordinate axes so that they are directed parallel to each other, and the vector $\boldsymbol{V}$ is directed along the x axis. In addition, we will

B. V. Bondarev (✉)
Moscow Aviation Institute, Moscow, Russia
e-mail: bondarev.b@mail.ru

I. A. Parinov et al. (eds.), *Physics and Mechanics of New Materials and Their Applications*, Springer Proceedings in Materials 10,
https://doi.org/10.1007/978-3-030-76481-4_12

assume that the speed of light in these two systems is the same. In this case, the coordinates x, y, z and time t in one coordinate system will be associated with the same values x', y', z' and t' of the other system by the Lorentz transformation [1]

$$\begin{cases} x = \gamma\,(x' + Vt'), \\ y = y', \quad z = z', \\ t = \gamma\,(Vx'/c^2 + t'), \end{cases} \tag{1}$$

where

$$\gamma = (1 - V^2/c^2)^{-1/2}, \tag{2}$$

$V = x/t = \text{const}$ by $x' = 0$.

An equation that has the same form in these coordinate systems is called covariant. In other words, we can say that the covariant equation is invariant with respect to the Lorentz transformation.

Now consider the motion of a single relativistic particle.

The momentum and energy of this particle will be equal

$$\boldsymbol{p}_{\text{relativ}} = \lambda\, m\, v, \quad E_{\text{relativ}} = \lambda\, m\, c^2, \tag{3}$$

where

$$\boldsymbol{v} = \mathrm{d}\boldsymbol{r}/\mathrm{d}t \tag{4}$$

is the velocity of the particle, $\boldsymbol{r} = \boldsymbol{r}(t)$ is its radius vector, m is the mass of the particle,

$$\lambda = (1 - v^2/c^2)^{-1/2}. \tag{5}$$

The dynamics of a relativistic particle obeys the equation

$$m\,\mathrm{d}(\lambda \boldsymbol{v})/\mathrm{d}t = \boldsymbol{F}, \tag{6}$$

where $\boldsymbol{F}$ is the force. This equation follows from the equation

$$m\,(\mathrm{d}^2\boldsymbol{r})/(\mathrm{d}\tau^2) = \lambda \boldsymbol{F},$$

where $\mathrm{d}\tau = \mathrm{d}t/\lambda$.

Let's write down another equation

$$m\,c^2 \mathrm{d}\lambda/\mathrm{d}t \;=\; P, \tag{7}$$

where $P = \boldsymbol{F}\,\boldsymbol{v}$ is the power.

Using formula (4) and applying formulas (6) and (7), we obtain a system of two equations for the functions $\boldsymbol{r} = \boldsymbol{r}(t)$ and $\boldsymbol{v} = \boldsymbol{v}(t)$:

$$\begin{cases} \mathrm{d}\boldsymbol{r}/\mathrm{d}t \;=\; \boldsymbol{v}, \\ \lambda(v)\,m\;\mathrm{d}\boldsymbol{v}/\mathrm{d}t \;=\; \boldsymbol{F} \;-\; (\boldsymbol{F}\boldsymbol{v})\;v/c^2\;\boldsymbol{v}. \end{cases} \tag{8}$$

2 The Lindblad Equations

The equation for the statistical operator was derived by the author of this paper from the Lindblad Eq. [2]

$$\mathrm{i}\,\hbar\,\partial\widehat{\varrho}/\partial t \;=\; [\widehat{H}\widehat{\varrho}] \;+\; \mathrm{i}\,\hbar\,\widehat{D}, \tag{9}$$

where $\widehat{\varrho}$ is the statistical operator, $\widehat{H}$ is the Hamiltonian, D is the dissipative operator, which was written by Lindblad and which is equal to

$$\widehat{D} = \sum_{jk} C_{jk}\{2\hat{a}_j\widehat{\varrho}\,\hat{a}_k^{+} - \hat{a}_k^{+}\hat{a}_j\widehat{\varrho} - \widehat{\varrho}\hat{a}_k^{+}\hat{a}_j\}, \tag{10}$$

where C_{jk} is the unknown coefficients, and $\hat{a}_j$ is the unknown operators that still need to be found.

3 Dissipative Operators

The author of this article wrote the dissipative diffusion and attenuation operators in the form [3, 4]

$$\hat{\boldsymbol{a}} \;=\; \hat{\boldsymbol{p}} \;+\; \mathrm{i}\,\hbar\,\beta\,\widehat{\boldsymbol{F}}/4, \quad \hat{\boldsymbol{b}} \;=\; \hat{\boldsymbol{r}} \;+\; \mathrm{i}\,\hbar\;\beta\hat{\boldsymbol{p}}/(4\;\mathrm{m}), \tag{11}$$

where $\hat{\boldsymbol{r}}$ and $\hat{\boldsymbol{p}}$ are the operators of the coordinates and momentum of the particle, $\boldsymbol{F}$ is the operator of the force that acts on it,

$$\beta \;=\; 1/(k_B T).$$

4 New Equation for Statistical Operator

We substitute formulas (11) in the Lindblad Eq. (9). We will have a new equation

$$\begin{aligned} &\mathrm{i}\,\hbar\,\partial\hat{\varrho}/\partial t \;=\; [\widehat{H}\hat{\varrho}] \\ &+\,\mathrm{i}\;D/\hbar\{[\hat{\boldsymbol{p}}[\hat{\boldsymbol{p}}\,\hat{\varrho}]] + \mathrm{i}\,\hbar\,\beta/2[\hat{\boldsymbol{p}}[\widehat{\boldsymbol{F}}\hat{\varrho}]_+]\} \\ &-\,\mathrm{i}\;\gamma/\hbar\{[\hat{\boldsymbol{r}}[\hat{\boldsymbol{r}}\,\hat{\varrho}]] - \mathrm{i}\,\hbar\,\beta/(2\,m)\,[\hat{\boldsymbol{r}}[\hat{\boldsymbol{p}}\,\hat{\varrho}]_+]\}, \end{aligned} \tag{12}$$

here D and γ are the diffusion and attenuation coefficients. In this equation, the terms that will contain β^2 are discarded.

The coefficient β increases to infinity at $T \to 0$. To avoid this absurdity, we add to the energy $k_{\mathrm{B}}T$ another quantum energy $\hbar\omega$, where the frequency ω characterizes the quantum effect of the thermostat on the quantum system in the form of electromagnetic waves and other massless particles:

$$\beta \;=\; 1/(\hbar\,\omega \;+ k_B T). \tag{13}$$

5 Non-relativistic Equation for Statistical Operator of Free Particle

For a free particle, the Hamiltonian is equal to the kinetic energy operator

$$\widehat{H} \;=\; \hat{\boldsymbol{p}}^2/(2\,m), \tag{14}$$

and the diffusion coefficients D are set to zero. So that the non-relativistic equation for the statistical operator of a free particle will have the form

$$\begin{aligned} &\mathrm{i}\,\hbar\,\partial\hat{\varrho}/\partial t \;=\; [\hat{\boldsymbol{p}}^2/(2m)\hat{\varrho}] \\ &-\,\mathrm{i}\,\gamma/\hbar\{[\hat{\boldsymbol{r}}[\hat{\boldsymbol{r}}\,\hat{\varrho}]] \;+\; \mathrm{i}\,\hbar\,\beta/(2\,m)\;[\hat{\boldsymbol{r}}\,[\hat{\boldsymbol{p}}\hat{\varrho}]_+]\}. \end{aligned} \tag{15}$$

6 Covariant Equation for Free Particle Statistical Operator

We write down the momentum and kinetic energy operators of a relativistic particle

$$\hat{\boldsymbol{p}}_{\mathrm{relativ}} \;=\; \hat{\lambda}\,\hat{\boldsymbol{p}},\;\; \widehat{E}_{relativ} \;=\; \hat{\lambda}\,m\,c^2, \tag{16}$$

where

$$\widehat{\boldsymbol{p}} \;=\; \boldsymbol{m}\,\widehat{\boldsymbol{v}}, \quad \widehat{\lambda} \;=\; (1-\widehat{v}^2/c^2)^{-1/2}. \tag{17}$$

Using the formula $\widehat{\boldsymbol{p}} \;=\; m\,\widehat{\boldsymbol{v}}$, we express the particle velocity operator $\widehat{\boldsymbol{v}}$ in terms of the momentum operator

$$\widehat{\boldsymbol{v}} \;=\; \widehat{\boldsymbol{p}}/m. \tag{18}$$

Thus, we get

$$\widehat{\lambda} = \lambda(\widehat{p}) = \{1-\widehat{p}^2/(m^2c^2)\}^{(-1/2)}. \tag{19}$$

So we will have the equation [5]

$$\begin{aligned} &\mathrm{i}\hbar\,\partial\widehat{\varrho}/\partial t = mc^2[\lambda(\widehat{p})\widehat{\varrho}] \\ &-\mathrm{i}\,\gamma/\hbar\{\,[\widehat{\boldsymbol{r}}\;[\widehat{\boldsymbol{r}}\;\;\widehat{\varrho}]\,] \;+\; \mathrm{i}\;\hbar\beta/(2m)\;[\widehat{\boldsymbol{r}}\;[\;\lambda(\widehat{p})\;\widehat{\boldsymbol{p}}\;\;\widehat{\varrho}]_+\}. \end{aligned} \tag{20}$$

This equation is a covariant quantum equation for the statistical operator of a free particle.

We simplify the function (19) by applying the notation

$$\xi = \widehat{p}^2/(m^2c^2). \tag{21}$$

In this case, the function takes the form

$$\lambda(\xi) \;=\; (1\;-\;\xi)^{-1/2}. \tag{22}$$

We decompose this function into a Taylor series

$$\lambda(\xi) \;=\; \lambda(0) \;+\; \lambda'(0)\,\xi \;+\; 1/2\,\lambda''(0)\xi^2 \;+\;\ldots$$

The derived functions are equal to

$$\begin{aligned} \lambda'(\xi) \;&=\; \mathrm{d}(1-\xi)^{-1/2}/\mathrm{d}\,\xi \\ &= 1/2(1-\xi)^{-3/2}, \end{aligned}$$

$$\begin{aligned} \lambda''(\xi) \;&=\; -1/2d(1-\xi)^{-3/2}/\mathrm{d}\,\xi \\ &= -3/4(1-\xi)^{-5/2},\ldots \end{aligned}$$

Thus we get,

$$\lambda(\xi) \;=\; 1 + \; 1/2\,\xi \;=\; 3/4\xi^2 \;+\; \ldots$$

Substituting the value (21) here leads to the result

$$\lambda(\widehat{p}) = 1 + \widehat{p}^2/(2m^2c^2) - 3\widehat{p}^4/(2m^2c^2)^2 \;+\; \ldots \tag{23}$$

We substitute this operator in Eq. (20). We get

$$\begin{aligned} &\mathrm{i}\,\hbar\,\partial\,\widehat{\varrho}/\partial t \;\cong mc^2[1 + \widehat{p}^2/2m^2c^2) - 3\widehat{p}^4/(2m^2c^2)^2, \widehat{\varrho}] \\ &- \mathrm{i}\,\gamma/\hbar\,\{[\widehat{\boldsymbol{r}}\,[\widehat{\boldsymbol{r}}\,\widehat{\varrho}]] \;+\; \mathrm{i}\,\hbar\,\beta/(2m)\,[\widehat{\boldsymbol{r}}\,[\{1 + \widehat{p}^2/(2\,m^2\,c^2)\}\widehat{\boldsymbol{p}}\,\widehat{\varrho}]_+\,]\,\}. \end{aligned}$$

Transform the first term on the right side of this equation

$$\begin{aligned} &m\,c^2\,[1 + \widehat{p}^2/(2m^2c^2) - 3\widehat{p}^4/(2m^2c^2)^2, \widehat{\varrho}] \\ &= [\widehat{p}^2/(2\,m) \;-\; 3/(4m^3c^2)\;\widehat{p}^4,\; \widehat{\varrho}]. \end{aligned}$$

Now the equation takes the form

$$\begin{aligned} &\mathrm{i}\,\hbar\,\partial\widehat{\varrho}/\partial t \;\cong\; [\widehat{p}^2/(2m) - 3/(4m^3c^2)\widehat{p}^4,\; \widehat{\varrho}] \;-\; \mathrm{i}\,\gamma/\hbar\{[\widehat{\boldsymbol{r}}[\widehat{\boldsymbol{r}}\widehat{\varrho}]] \\ &+\mathrm{i}\,\hbar\,\beta/(2m)\,[\widehat{\boldsymbol{r}}[\{1 + \;\widehat{p}^2/(2m^2c^2)\;\widehat{\boldsymbol{p}},\; \widehat{\varrho}]_+]\}. \end{aligned} \tag{24}$$

Look closely at this equation. You will see that the operators $\widehat{\boldsymbol{r}}$ and $\widehat{p}$ occur here only as products of $\widehat{\boldsymbol{p}}^2,\ \widehat{\boldsymbol{p}}^4,\ \widehat{\boldsymbol{r}}^2,\ \widehat{\boldsymbol{r}}^2\ \widehat{p}$ *and* $\widehat{\boldsymbol{r}}^2\ \widehat{p}^3$. This makes it possible to find the average value of the coordinates $\langle\widehat{\boldsymbol{r}}\rangle$ of the particle and its momentum $\langle\widehat{\boldsymbol{p}}\rangle$. And then find the changes in these values over time:

$$\mathrm{d}\langle\widehat{\boldsymbol{r}}\rangle/\mathrm{d}t \;=\; \mathrm{Tr}\,(\widehat{\boldsymbol{r}}\;\partial\widehat{\varrho}/\partial t),\quad \mathrm{d}\langle\widehat{\boldsymbol{p}}\rangle/\mathrm{d}t \;=\; \mathrm{Tr}\,(\;\widehat{\boldsymbol{p}}\;\partial\widehat{\varrho}/\partial t).$$

As a result, you will have a system

$$\begin{cases} \mathrm{d}\langle\widehat{\boldsymbol{r}}\rangle/\mathrm{d}t \;=\; \langle\widehat{\boldsymbol{p}}\rangle/m, \\ \mathrm{d}\langle\widehat{\boldsymbol{p}}\rangle/\mathrm{d}t \;=\; -\alpha/m\langle\widehat{\boldsymbol{p}}\rangle \;+\; \alpha/(m^3c^2)\widehat{p}^2\langle\widehat{\boldsymbol{p}}\rangle, \end{cases} \tag{25}$$

where $\alpha = \beta\ \gamma$. It is natural to assume that $\langle\widehat{\boldsymbol{r}}\rangle \;\equiv\; \boldsymbol{r}$ and $\langle\widehat{\boldsymbol{p}}\rangle \;\equiv\; \boldsymbol{p}$. If we also denote the force $\boldsymbol{F} \;=\; -\alpha\boldsymbol{v}$, then after a series of elementary transformations we will teach the system (8).

7 Covariant Quantum Equation for Statistical Operator of Hydrogen Atom

Now we write down a covariant quantum equation for the statistical operator of the hydrogen atom. There are two particles in this atom. This is an electron and a proton, which carry electric charges – e and + e. Therefore, they have potential energy

$$U_{ep}(\boldsymbol{r}_e - \boldsymbol{r}_p) = -e^2/\left|\boldsymbol{r}_e - \boldsymbol{r}_p\right|, \tag{26}$$

where $\boldsymbol{r}_e$ and $\boldsymbol{r}_p$ are the radius vectors of the electron and proton.

The Hamiltonian of the atom will be equal to

$$\widehat{H} = \widehat{\boldsymbol{p}}_e^2/(2m_e) + \widehat{\boldsymbol{p}}_p^2/(2m_p) + U_{ep}(\boldsymbol{r}_e - \boldsymbol{r}_p), \tag{27}$$

where $\widehat{\boldsymbol{p}}_e$ and $\boldsymbol{p}_p$ are the electron and proton pulses, and m_e and m_p are their masses.

We take the dissipative operators to be equal

$$\begin{aligned} \mathrm{i}\,\hbar\,\widehat{D} = &-\mathrm{i}\,\gamma/\hbar\{[\boldsymbol{r}_e - \boldsymbol{r}_p[(\boldsymbol{r}_e - \boldsymbol{r}_p)\,\widehat{\varrho}]]\} \\ &+ \mathrm{i}\,\hbar\,\beta\,(2\,m_e)\,[\boldsymbol{r}_e - \boldsymbol{r}_p[(\widehat{\boldsymbol{p}}_e - \widehat{\boldsymbol{p}}_p)\,\widehat{\varrho}]_+]. \end{aligned} \tag{28}$$

Now we write down the non-relativistic equation

$$\mathrm{i}\,\hbar\,\partial\,\widehat{\varrho}/\partial\ t = [\widehat{H}\,\widehat{\varrho}] + \mathrm{i}\,\hbar\,\widehat{D}.$$

In relativistic physics, the formulas are known

$$\widehat{\boldsymbol{p}}^{(e)}_{\text{relativ}} = \widehat{\lambda}_e\,\widehat{\boldsymbol{p}}_e,\ \ldots\,\widehat{E}^{(e)}_{\text{relativ}}\,\widehat{\lambda}_e\,m^e\,c^2, \tag{29}$$

where

$$\widehat{\lambda}_e = \lambda(\widehat{\boldsymbol{p}}_e/m_e) = \{1 - \widehat{\boldsymbol{p}}_e^2/(m_e^2\,c^2)\}^{-1/2} \tag{30}$$

for the electron;

$$\widehat{\boldsymbol{p}}^{(p)}_{\text{relativ}} = \widehat{\lambda}_p\widehat{\boldsymbol{p}}_p,\ldots\ \widehat{E}^{(p)}_{\text{relativ}} = \widehat{\lambda}_p m_p\,c^2, \tag{31}$$

where

$$\hat{\lambda}_{\boldsymbol{p}} \;=\; \lambda(\hat{\boldsymbol{p}}_{\boldsymbol{p}}/m_{\boldsymbol{p}}) \;=\; \{1 \,-\, \hat{\boldsymbol{p}}_{\boldsymbol{p}}^2/m_{\boldsymbol{p}}^2)\}^{-1/2} \tag{32}$$

for the proton.

Now we write down a covariant quantum equation for the statistical operator of the hydrogen atom

$$\begin{gathered}
\mathrm{i}\,\hbar\,\partial\,\hat{\varrho}/\partial t \\
=\; [\lambda\hat{\boldsymbol{p}}_e/m_e]m_e\,c^2 \;+\; \lambda(\hat{\boldsymbol{p}}_{\boldsymbol{p}}/m_{\boldsymbol{p}})m_{\boldsymbol{p}}\,c^2 \\
+\,U_{ep}(\boldsymbol{r}_e-\boldsymbol{r}_p),\;\hat{\varrho}] \\
-\mathrm{i}\,\gamma/\hbar\{[(\boldsymbol{r}_e-\boldsymbol{r}_p)[(\boldsymbol{r}_e-\boldsymbol{r}_p)\,\hat{\varrho}\,]]\} \\
+\mathrm{i}\,\hbar\,\beta/(2m_e)[(\boldsymbol{r}_e-\boldsymbol{r}_p) \\
[\lambda(\hat{\boldsymbol{p}}_e/m_e)\hat{\boldsymbol{p}}_e \;-\; \lambda(\hat{\boldsymbol{p}}_p/m_p)\hat{\boldsymbol{p}}_p,\;\hat{\varrho}]_+].
\end{gathered} \tag{33}$$

8 Conclusion

We have not forgotten that almost all microscopic particles have spins. Since the statistical operator $\hat{\varrho}$ is the main characteristic of particles in quantum theory, it must also take into account spins.

Consider the operator $\hat{\varrho}$ of a single particle. Like any other particle, its state is described by four operators, one of which is the spin operator $\hat{\sigma}$. For example, in the coordinate representation, the operator $\hat{\varrho}$ depends on three coordinates $\hat{x},\ \hat{y},\ \hat{z}$ and the spin operator $\hat{\sigma}$:

$$\hat{\varrho} \;=\; \hat{\varrho}(\hat{x},\ \hat{y},\ \hat{z},\ \hat{\sigma}).$$

Spin manifests itself only when a term that describes the effect of spin appears in the equation for the operator $\hat{\varrho}$. Otherwise, the spin is not visible. Here is the simplest example.

An electron in a magnetic field has energy

$$E_{\text{магнит}} \;=\; -\,\mu_{\text{B}}\,\sigma\;\mathcal{H}\,,$$

where $\mu_B \;=\; e\,\hbar/(2\,m)$—Bora magneton, $\sigma = \pm\,1/2$ − electron spin,

$$\mathcal{H} = \mathcal{H}(t,\boldsymbol{r})$$

is a modulus of the magnetic field strength. Now in the equation for the operator $\hat{\varrho}$ we can write the term

$$-\mu_{\mathrm{B}}\left[\hat{\sigma}\,\widehat{\mathcal{H}}\,\hat{\varrho}\right].$$

References

1. B.V. Bondarev, Course of general physics. Moscow. Sputnik+ (2015), p. 420
2. G. Lindblad, On the generators of quantum dynamical semigroups. Commun. Math. Phys. **48**, 119–130 (1976)
3. B.V. Bondarev, Quantum Markovian master equation for a system of identical particles interacting with a heat reservoir. Phys. A **176**(2), 366–386 (1991)
4. B.V. Bondarev, Density matrix theories in quantum physics. Bentham (2020), p. 393
5. B.V. Bondarev, Covariant quantum equation for statistical operator. Sci. Disc. **1**(54), 17–20 (2021)

The Riesz Potential Type Operator with a Power-Logarithmic Kernel in the Generalized Hölder Spaces on a Sphere

Boris Vakulov and Yuri Drobotov

Abstract Marcel Riesz kernels include the ones of the classical theory as special and limiting cases. Therefore, and due to their link with the fractional powers of the Laplace operator, Riesz potential type operators are of significant interest. Along with hypersingular integrals they form a valuable toolkit for considering various problems of mathematical physics. Riesz fractional integro-differentiation is studied in connection with fractal media, that can be, for instance, a porous material or a polymer. When researching integral equations on their solvability and the sustainability of the solutions, the issue on a relationship between the integrability of a pre-image and the integral operator's smoothness is essential. For a spherical convolution operator, such a study can be based on two approaches: the Fourier—Laplace multipliers theory, and Zygmund type estimates, which are used to describe the behavior of the continuity modulus. In this chapter, both are applied to consider the Riesz potential type operator with a power-logarithmic kernel on a sphere.

Keywords Riesz potential type operator · Spherical convolution · Fourier–laplace multiplier · Zygmund type estimate · Inverse operator · Boundedness theorem · Integrable function · Generalized hölder space · Smoothness · Fractional calculus

1 Introduction

An integral operator considered here is the Riesz potential type operator with a power-logarithmic kernel, defined as

$$(K^{\alpha} f)(x) = \int\limits_{S^{n-1}} \frac{f(\sigma)}{|x-\sigma|^{n-1-\alpha}} \ln^{\nu} \frac{r}{|x-\sigma|} d\sigma, \; x \in S^{n-1}, \tag{1}$$

B. Vakulov · Y. Drobotov (✉)
I. I. Vorovich Institute of Mathematics, Mechanics and Computer Science, Southern Federal University, Rostov-on-Don, Russia
e-mail: yu.e.drobotov@yandex.ru

I. A. Parinov et al. (eds.), *Physics and Mechanics of New Materials and Their Applications*, Springer Proceedings in Materials 10,
https://doi.org/10.1007/978-3-030-76481-4_13

where α, ν and r are the real parameters, and S^{n-1} is a sphere in the Euclidean space R^n, $n \geq 3$, defined below. We shall omit details accompanying the introduction of such operators in favor of using clearer notation, which has already become classical. Nevertheless, according to the common definition of a potential operator given, for instance, in [1, p. 43], for each region G in R^n, coincident with R^n, a kernel $K(x, \sigma)$ is considered as a real function defined on $G \times G$, and μ is assumed to be a signed measure with support in G. For a μ-measurable domain $\Omega(\mu)$ the following expression is called the K-potential of the signed measure μ:

$$U_K^{\mu}(x) = \int\limits_{\Omega(\mu)} K(x, \sigma) d\mu(\sigma).$$

By fixing the measure μ, we shall study the properties of the reflection by (1), based on researching the function:

$$k_{\alpha,\nu}(x, \sigma) = |x - \sigma|^{\alpha - n + 1} \ln^{\nu} \frac{r}{|x - \sigma|}, \tag{2}$$

which we shall call the power-logarithmic kernel to use this term hereinafter.

With $\nu = 0$, (2) is the Marcel Riesz kernel, classically written as [2, p. 492]

$$k_{\alpha}(x) = \frac{1}{\gamma_n(\alpha)} \begin{cases} |x|^{\alpha - n}, & \alpha - n \neq 0, 2, 4, 6, ..., \\ |x|^{\alpha - n} \ln \frac{1}{|x|}, & \alpha - n = 0, 2, 4, 6, ..., \end{cases}$$

where the constant $\gamma_n(\alpha)$ is equal to

$$\gamma_n = \begin{cases} 2^{\alpha} \pi^{n/2} \Gamma\left(\frac{\alpha}{2}\right) \Big/ \Gamma\left(\frac{n-\alpha}{2}\right), & \alpha \neq n + 2k, \ \alpha \neq -2k, \\ 1, & \alpha = -2k \\ (-1)^{(n-\alpha)/2} \pi^{n/2} 2^{\alpha - 1} \left(\frac{\alpha - n}{2}\right)! \, \Gamma\left(\frac{\alpha}{2}\right), & \alpha = n + 2k. \end{cases}$$

The Riesz potential is defined for all α, $\mathrm{Re}\alpha > 0$, as the following convolution:

$$(I^{\alpha} \varphi)(x) = \int\limits_{R^n} k_{\alpha}(x - y) \, \varphi(y) \, dy, \ x \in R^n, \tag{3}$$

For mathematical physics and applications, this potential is remarkable as it implements the negative fractional powers $(-\Delta)^{\alpha/2}$ of the Laplace operator. In general, fractional calculus serves for analysis on fractal sets, having been developed into a new branch of mathematics [3].

If $\nu = 0$ in (1), the latter becomes an operator similar to (3), and we shall call it the Riesz potential type operator on a sphere. It is studied quite fully for various function spaces. In particular, the following fundamental result about the expected form of the inverse operator holds [4, p. 160]:

Theorem 1. *The operator* $(I^{\alpha})^{-1}$ *inverse to the spherical potential* I^{α} *is expected to be.*

$$(I^{\alpha})^{-1} = c_{\alpha}\, E + D^{\alpha},\ c_{\alpha} = \Gamma\left(\tfrac{n-1+\alpha}{2}\right)\Big/\Gamma\left(\tfrac{n-1-\alpha}{2}\right),$$

where E *is the identity operator:* $E\, f = f$, $\Gamma(z)$*is the Euler gamma-function, and* D^{α} *is a spherical hypersingular integral, defined for* $0 < \mathrm{Re}\alpha < 1$ *and sufficiently "nice" functions as*

$$(D^{\alpha} f)(x) = \tfrac{1}{A(n,-\alpha)} \int\limits_{\mathrm{S}^{n-1}} \tfrac{f(\sigma)-f(x)}{|x-\sigma|^{n-1+\alpha}}\, d\sigma,\ x \in \mathrm{S}^{n-1}, \tag{4}$$

and for $0 < \mathrm{Re}\alpha < 2$ *and a sufficiently smooth function* $f(x)$*as the limit of the truncated hypersingular operator:*

$$(D^{\alpha} f)(x) = \tfrac{1}{A(n,-\alpha)} \lim_{\varepsilon\to\infty} \int\limits_{\mathrm{S}_{\varepsilon}^{n-1}(x)} \tfrac{f(\sigma)-f(x)}{|x-\sigma|^{n-1+\alpha}}\, d\sigma,\ x \in \mathrm{S}^{n-1}, \tag{5}$$

where $S_{\varepsilon}^{n-1}(x) = \left\{\sigma \in S^{n-1} : |\sigma - x| > \varepsilon\right\}$.

The hölderian properties of $K^{\alpha,0}$ were studied in the papers [5, 6], and [6] also considered the case of $\alpha > 0$. For $\nu \neq 0$, the inversion of an operator similar to (4) was obtained in [7] for the first time. Namely, the result was carried out for the integral operator on a finite segment $[a, b]$ of the real axis. One cannot fail to mention the paper [8], where the Noetherian properties of such operators was investigated.

In the multidimensional case, the operators (4) were studied in [7], where the conditions for them bounded in the generalized Hölder spaces were considered. These conditions on the characteristics $\omega(h)$ of the spaces were provided in the terms of a generalized Zygmund—Bary—Stechki class.

1.1 Research Purpose

Conditions for the spherical convolution operator with a power-logarithmic kernel to be a bounded reflection between the L^p, $1 \le p \le \infty$, space of integrable functions to a generalized Hölder space H^{ω} are studied.

1.2 Research Scope

The following two general approaches are used here:

(i) The Fourier—Laplace multipliers theory for considering particular cases;
(ii) Zygmund type estimates for carrying out the boundedness theorem.

2 Research Method

2.1 Preliminaries

Let the symbol R^n, $n \geq 3$, stand for the set of all vectors $x = (x_1, x_2, ..., x_n)$ with real coordinates. Being supplied with a metric:

$$|x - \sigma| = \sqrt{(x_1 - \sigma_1)^2 + ... + (x_n - \sigma_n)^2},\ |x| = |x - 0|,$$

R^n is the Euclidean space with an inner product defined as $x \cdot \sigma = x_1\sigma_1 + ... + x_n\sigma_n$, or, due to the parallelogram identity,

$$x \cdot \sigma = \frac{1}{2}\big(|x + \sigma|^2 - |x|^2 - |\sigma|^2\big).$$

This allows one to express the metric through the inner product:

$$|x - \sigma| = \sqrt{|x|^2 + |\sigma|^2 - 2\,x \cdot \sigma} \tag{6}$$

The unit sphere (or a hypersphere, for the greater dimensions) S^{n-1} in R^n is considered as a set of points, equidistant from the origin by a distance of one, that is $S^{n-1} := \{\sigma \in R^n : |\sigma| = 1\}$.

For $x, \sigma \in S^{n-1}$, the relation (4) becomes:

$$|x - \sigma| = \sqrt{2}\sqrt{1 - x \cdot \sigma}, \tag{7}$$

which allows one to consider (1) as a spherical convolution operator:

$$(K\,f)(x) = \int\limits_{S^{n-1}} k(x \cdot \sigma) f(\sigma) d\sigma,\ x \in S^{n-1}. \tag{8}$$

2.2 The Fourier—Laplace Multipliers Theory

Spherical harmonics Y_m are the eigenfunctions of any operator of the form (8):

$$K\,Y_m = k_m\,Y_m,$$

which follows from a Funk—Hecke formula [4, p. 10]. A spherical harmonic $Y_m(\sigma)$, $\sigma \in \mathrm{S}^{n-1}$, of order m is, in fact, the restriction to the unit sphere S^{n-1} of a homogeneous of degree m polynomial Y_m, satisfying the equation $\Delta Y_m = 0$. Its explicit representation is:

$$Y_m(x) = \sum_{|j|=m} p_j \, x^j,$$

where $p_j = p_{j_1,\ldots j_n}$ are constants, $|j| = j_1 + \ldots + j_n$, and $x^j = x_1^{j_1} \ldots x_n^{j_n}$. Every term of the sequence $\{k_m\}_{m=0}^{\infty}$ is calculated as

$$k_m = \frac{2\,\pi^{\frac{n-1}{2}}}{\Gamma((n-1)/2)} \int\limits_{-1}^{1} k(t)\, P_m(t)\big(1-t^2\big)^{\frac{n-3}{2}} dt,$$

where $P_m(t)$ are the generalized Legendre polynomials.

By considering the orthonormal system of spherical harmonics $Y_{m\mu}(x)$,$\mu = 1, 2, \ldots, d(m)$,

$$d(m) = (n+2m-2)(n+m-3)!\big/(m!\,(n-2)!),\ m = 0, 1, \ldots,$$

one can define the operator (6) as $(K\,f)(x) = \sum\limits_{m,\,\mu} k_m\, f_{m\mu}\, Y_{m\mu}(x)$,

where $f_{m\,\mu}$ are the coefficients of decomposing $f(x)$ through the complete orthonormal system of spherical harmonics $Y_{m\,\mu}(x)$:

$$f(x) = \sum_{m=0}^{\infty} \sum_{\mu=1}^{d_n(m)} f_{m\,\mu}\, Y_{m\,\mu}(x),\ x \in \mathrm{S}^{n-1}.$$

The spectrum $\{k_m\}_{m=0}^{\infty}$ is called the Fourier—Laplace multiplier generating the operator (8). For instance, the Riesz potential type operator on a sphere is generated by the Fourier—Laplace multiplier [9]:

$$k_m = \frac{\Gamma\big(m + (n-1)/2 - \alpha/2\big)}{\Gamma\big(m + (n-1)/2 + \alpha/2\big)}. \tag{9}$$

Expressed in the terms of the Jacobi polynomials, The Fourier—Laplace multiplier of the operator (1) is calculated as

$$k_m = -\frac{2\,\pi^{\frac{n-1}{2}}\, K_m(n)}{\Gamma((n-1)/2)} \int\limits_{-1}^{1} (1-t)^{\frac{\alpha}{2}-1}(1+t)^{\frac{n-3}{2}} \ln^{\nu} \tfrac{1-t}{r}\, P_m^{(\lambda,\lambda)}(t)dt,\ \lambda = \tfrac{n-3}{2}, \tag{10}$$

The latter can be used for studying the properties of (1) in particular cases. Moreover, in numerical computations, the following evaluation for a $2r$-differentiable function $f(x)$ may be useful [4, p. 15]:

$$\left|f_{m\mu}\right| \leq \frac{M}{m^{2r}},\ M = \sqrt{\int\limits_{\mathbf{S}^{n-1}} |(\delta^r f)(\sigma)|^2\, d\sigma},$$

where δ is the Beltrami—Laplace operator: $\delta f = |x|^2\, \Delta f$.

The Laplace operator Δ is acting here on the continuation $f\left(x/|x|\right)$ of $f(x)$.

2.3 Considered Function Spaces

By the symbol $L^p(\Omega)$, $\Omega \subset \mathrm{R}^n$, we shall denote the space of p-integrable functions, defined by the norm:

$$\|f\|_{L^p(\Omega)} = \left\{\int\limits_{\Omega} |f(x)|^p\, dx\right\}^{\frac{1}{p}},\ 1 \leq p < \infty,$$
$$\|f\|_{L^\infty(\Omega)} = \operatorname*{ess\,sup}_{x\in\Omega} |f(x)|.$$

Let it be noticed, that, due to the corresponding property of the Lebesgue integral, if $\Omega_0 \subset \Omega$, then $L^p(\Omega_0) \subset L^p(\Omega)$. We shall use this property implicitly.

Let the continuity modulus of a function $f(x)$ on a sphere be denoted as

$$M(f,t) = \sup_{\substack{|x-y| \leq t \\ x,\, y \,\in\, \mathrm{S}^{n-1}}} |f(x) - f(y)|.$$

Consider the class W of functions $\omega(t)$, $t \in [0, l]$, continuous and almost increasing, and satisfying the condition: $\omega(0) = 0$; $\omega(t) > 0$, $t > 0$..

Let $H^\omega\left(\mathrm{S}^{n-1}\right)$ denotes the generalized Hölder space whose elements are continuous functions $f(x)$, such that

$$M(f,h) \leq C\,\omega(h),\ 0 < C < \infty. \tag{11}$$

$H^\omega\left(\mathrm{S}^{n-1}\right)$ is a Banach space with respect to the norm:

$$\|f\|_{H^\omega(\mathrm{S}^{n-1})} = \|f\|_{C(\mathrm{S}^{n-1})} + \sup_{t>0} \frac{M(f,t)}{\omega(t)},$$

where $\|f\|_{C(\mathrm{S}^{n-1})}$ is the norm of $f(x)$ in the space of continuous functions.

The theory of the generalized Hölder spaces is currently relevant as, inter alia, it provides sufficiently convenient terms for defining and studying the concept of smoothness. Thus, even if the "usual" smoothness (i.e., the integer order differentiability) on a sphere is considered, it is essential to clarify this concept. It can be defined through two, fundamentally different, groups of terms: the ones, connected with the Laplace–Beltrami operator, and the terms, which relate to differentiation in Cartesian coordinates [10]. Both ways lead to, in general, equivalent Hölderian classes $H^{\lambda}(S^n)$ with non-integer λ and to certainly different ones with integer $\lambda \geq 1$.

Along with studying the Fourier—Laplace multiplier (10), the mapping of (1) to the space $H^{\omega}\left(S^{n-1}\right)$ can be considered in the scope of constructing the evaluation (11). Inequalities involving the continuity modulus $M(f, t)$ are called Zygmund type estimates.

3 Results and Discussion

3.1 Inverse Operator

For $\nu = 1$, the multiplier (10) calculated in [11] and turned out was expressed in the terms of (7), which allowed one to base on Theorem 1 and prove a similar theorem:

Theorem 2. *The inverse operator for K^{α} is expected to be a composition of the spherical hypersingular integral D^{α}, defined by (4), (5), and a spherical convolution operator A with the specific multiplier, i.e.*

$$\left(K^{\alpha,1}\right)^{-1} = (c_{\alpha}\, E + D^{\alpha})\, A,$$

where

$$c_{\alpha} = \Gamma\left(\frac{n-1+\alpha}{2}\right) \Big/ \Gamma\left(\frac{n-1-\alpha}{2}\right),$$

and

$$(A\, f)(x) = \int\limits_{S^{n-1}} a(x \cdot \sigma) f(\sigma) d\sigma, \quad x \in S^{n-1},$$

$$a(x \cdot \sigma) = \frac{1}{4}\, \pi^{-\frac{n}{2}}\, \Gamma\left(\frac{n-2}{2}\right) \sum_{m=0}^{\infty} (2m + n - 2)\; l_m^{-1}\; C_m^{\frac{n-2}{2}}\, (x \cdot \sigma)$$

is a spherical convolution operator, generated by the Fourier—Laplace multiplier $\left\{l_m^{-1}\right\}_{m=0}^{\infty}$ *with*

$$l_m = -2^{\frac{n+\alpha-1}{2}}\pi^{\frac{n-1}{2}}\left(\begin{array}{c} m \\ m+n-3 \end{array}\right)^{-1}\frac{(n-2)}{m((n-1)/2)_m}\left(m+\frac{n-\alpha-1}{2}\right)$$
$$\Gamma\left(\frac{\alpha}{2}\right)B^{-1}\left(\frac{n-1}{2},m\right)\times\Gamma^{-1}\left(\frac{n-\alpha+1}{2}\right)$$
$$\left\{1+1n\frac{2}{r}\left[\psi\left(\frac{\alpha-n+3}{2}\right)+\psi\left(\frac{\alpha}{2}\right)-\psi\left(\frac{\alpha-n+3}{2}-m\right)-\psi\left(\frac{\alpha+n-1}{2}+m\right)\right].\right\}$$

Here, the following relations are used:

$$\mathrm{B}(z,w)=\frac{\Gamma(z)\,\Gamma(w)}{\Gamma(z+w)},\ \psi(z)=\frac{\Gamma'(z)}{\Gamma(z)}=\frac{d}{d\,z}\ \ln\ \Gamma(z),$$

$$(m)_k=m\cdot(m+1)\cdot\ldots\cdot(m+k-1),\ k=1,2,3,\ldots;\ \left(\begin{array}{c} m \\ k \end{array}\right)=\frac{(m)_k}{k!}.$$

The results on boundedness of $K^{\alpha,0}$ and D^{α} in the generalized Hölder spaces were carried out in [5]. The latter were defined as

$$H_k^{\omega}\left(\mathrm{S}^{n-1}\right)=\left\{f\in C\left(\mathrm{S}^{n-1}\right):M\left(\mathrm{D}^k f,h\right)\le c\omega(h)\right\}$$

where D^{α} was a spherical convolution operator with a multiplier from $W_{\alpha,[(n+1)/2]}$, while $W_{k,N}$ was used to denote the class of multipliers $\{k_m\}_{m=0}^{\infty}$ through the spherical harmonics, $|k_m|<\infty$, which allow the following asymptotic:

$$k_m=\sum_{j=0}^{N}c_j m^{\lambda-j}+O\left(m^{\lambda-N-\varepsilon}\right),\ m\to\infty,$$

with $c_0\neq 0$, $0<\varepsilon<1$, $\lambda\in\mathrm{R}$ and $N=0,1,\ldots$. They were used there to prove the isomorphism:

$$K^{\alpha,0}\left(H_k^{\omega}\left(\mathrm{S}^{n-1}\right)\right)=H_{k+[\alpha]}^{\omega_\alpha}\left(\mathrm{S}^{n-1}\right),\ \omega_\alpha(h)=h^{\alpha-[\alpha]}\,\omega(h),$$

where $\omega(h)$ belongs to the Zygmund—Bary—Stechkin class $\Phi^0_{1-\alpha+[\alpha]}$.

From Theorem 2 and the results of [5], it follows that $K^{\alpha,1}$ is an isomorphism between the generalized Hölder spaces $H_k^{\omega}\left(\mathrm{S}^{n-1}\right)$. The results of [6] allow us to wide this statement for specific weighted analogs of $H_k^{\omega}\left(\mathrm{S}^{n-1}\right)$.

3.2 Boundedness Theorem

Let Hölder's inequality be recalled, as it is widely used in the proof of the main result. For $1 \le p \le \infty$, $p' = p/(p-1)$, and $f \in L^p(\Omega)$, $g \in L^{p'}(\Omega)$, the following estimation holds:

$$\int\limits_{\Omega} |f(x)\, g(x)|\, dx \le \|f\|_{L^p(\Omega)}\, \|g\|_{L^{p'}(\Omega)},\ \Omega \subset \mathrm{R}^n.$$

Together with it, the following three lemmas are to be applied to evaluate the resulting integrals:

Lemma 1. *Let $n \ge 3$ and $0 \le a < b \le 2$. Then*

$$J(a,b) = \int\limits_{a<|x-\sigma|<b} g(|x-\sigma|)\, d\sigma \le c_n \int\limits_a^b g(u)\, u^{n-2}\, du,\ 0 < c_n < \infty, \tag{12}$$

$$\int\limits_{a<|x-\sigma|<b} g(|x-\sigma|)\, d\sigma = \int\limits_{a<|y-\sigma|<b} g(|y-\sigma|)\, d\sigma,\ x, y \in \mathrm{S}^{n-1}. \tag{13}$$

The statement of the lemma follows from the expression [12]:

$$J(a,b) = 2^{3-n}\, c_n \int\limits_a^b g(u)\, u^{n-2} \left(4-u^2\right)^{(n-3)/2} du,$$

with the right side independent on $x \in \mathrm{S}^{n-1}$, which is similar to the Catalan's formula [4, p. 13].

Lemma 2. *Let $\beta > 0$ and $\nu \in \mathrm{R}^1$. The following estimations hold:*

$$\int\limits_0^h u^{\beta-1}\, \ln^{\nu} \tfrac{r}{u}\, du \le c\, h^{\beta}\, \ln^{\nu} \tfrac{r}{h},\ \int\limits_h^2 u^{-\beta-1}\, \ln^{\nu} \tfrac{r}{u}\, du \le c\, h^{-\beta}\, \ln^{\nu} \tfrac{r}{h},\ 0 < c < \infty. \tag{14}$$

Lemma 3. *Let $x, y, \sigma \in \mathrm{S}^{n-1}$ and $|x-\sigma| \ge 2\,|x-y|$. For $\gamma \ge 0$ and $\nu \in \mathrm{R}^1$, the following inequality holds:*

$$\left| |x-\sigma|^{-\gamma}\, \ln^{\nu} \tfrac{r}{|x-\sigma|} - |y-\sigma|^{-\gamma}\, \ln^{\nu} \tfrac{r}{|y-\sigma|} \right| \le \tfrac{c\,|x-y|}{|x-\sigma|^{\gamma+1}}\, \ln^{\nu} \tfrac{r_0}{|x-\sigma|},\ r_0 > 2, \tag{15}$$

where $0 < c < \infty$.

The proofs of Lemmas 2 and 3 are known from the paper [12]. They are specific for studying of integral operators in the Hölder spaces. Now, we shall use them to prove the main result of the presented research:

Theorem 3. *Let $n \geq 3$ and $\nu \in \mathrm{R}^1$. If*

$$\alpha > \tfrac{n-1}{p},\ 1 \leq p \leq \infty, \tag{16}$$

then there exists $m > 2$ such that $K^{\alpha,\nu}$ is bounded from $L^p\big(\mathrm{S}^{n-1}\big)$ to $H^{\omega}\big(\mathrm{S}^{n-1}\big)$ with

$$\omega(h) = h^{\alpha - \frac{n-1}{p}} \ln^{\nu} \frac{m}{h}. \tag{17}$$

Proof. Let $x, y \in \mathrm{S}^{n-1}$ satisfy the following assumptions:

$$0 < |x - y| \leq \frac{h}{2} < 1. \tag{18}$$

Consider the absolute difference:

$$\begin{aligned} |(K^{\alpha,\nu} f)(x) - (K^{\alpha,\nu} f)(y)| = \Bigg| & \int\limits_{\mathrm{S}^{n-1}_{<}(x,h)} k_{\alpha,\nu}(x,\sigma)\, f(\sigma)\, d\sigma \\ & + \int\limits_{\mathrm{S}^{n-1}_{\geq}(x,h)} k_{\alpha,\nu}(x,\sigma)\, f(\sigma)\, d\sigma - \\ & - \int\limits_{\mathrm{S}^{n-1}_{<}(x,h)} k_{\alpha,\nu}(y,\sigma)\, f(\sigma)\, d\sigma \\ & - \int\limits_{\mathrm{S}^{n-1}_{\geq}(x,h)} k_{\alpha,\nu}(y,\sigma)\, f(\sigma)\, d\sigma \Bigg| \leq |I_1| + |I_2| + |I_3|, \end{aligned}$$

where

$$\begin{aligned} \mathrm{S}^{n-1}_{<}(x,h) &:= \big\{\sigma \in \mathrm{S}^{n-1} :\ 0 < |x - \sigma| < h\big\}, \\ \mathrm{S}^{n-1}_{\geq}(x,h) &:= \big\{\sigma \in \mathrm{S}^{n-1} :\ h \leq |x - \sigma| < 2\big\}, \end{aligned} \tag{19}$$

with the integrals defined as

$$I_1 := \int\limits_{S_<^{n-1}(x,h)} \frac{f(\sigma)}{|x-\sigma|^{n-1-\alpha}} \ln^{\nu} \frac{r}{|x-\sigma|} d\sigma,\ I_2 := \int\limits_{S_<^{n-1}(x,h)} \frac{f(\sigma)}{|y-\sigma|^{n-1-\alpha}} \ln^{\nu} \frac{r}{|y-\sigma|} d\sigma,$$
$$I_3 := \int\limits_{S_\geq^{n-1}(x,h)} \frac{f(\sigma)}{|x-\sigma|^{n-1-\alpha}} \ln^{\nu} \frac{r}{|x-\sigma|} d\sigma - \int\limits_{S_\geq^{n-1}(x,h)} \frac{f(\sigma)}{|y-\sigma|^{n-1-\alpha}} \ln^{\nu} \frac{r}{|y-\sigma|} d\sigma.$$

Evaluation of I_1. After applying Hölder's inequality, (12) is used, namely:

$$|I_1| \leq \|f\|_{L^p} \left\{ \int\limits_{x-\sigma<h} |x-\sigma|^{p'(\alpha-n+1)} \ln^{\nu p'} \frac{r}{x-\sigma} d\sigma \right\}^{\frac{1}{p'}}$$
$$\leq c\|f\|_{L_p} \left\{ \int\limits_0^h u^{p'(\alpha-n+1)+n-2} \ln^{\nu p'} \frac{r}{u} du \right\}^{\frac{1}{p'}}.$$

Due to the first estimate in (14), the final majorant of $|I_1|$ is equal to

$$|I_1| \leq c\, h^{\alpha-\frac{n-1}{p}} \ln^{\nu} \frac{r}{h}. \tag{20}$$

Evaluation of I_2. Let it be noticed, that $\{\sigma : |x-\sigma| < h\} \subset \{\sigma : |y-\sigma| < 2h\}$, thus

$$|I_2| \leq \int\limits_{S_<^{n-1}(y,2h)} \left| k_{\alpha,\nu}(y,\sigma)\, f(\sigma) \right| d\sigma,$$

and this case is reduced to the previous one due to the relation (13). Considering the constants' being arbitrary in the context of the context of the study, we shall write:

$$|I_2| \leq c\, h^{\alpha-\frac{n-1}{p}} \ln^{\nu} \frac{r}{h}. \tag{21}$$

Evaluation of I_3. Applying the evaluation (15), we write the following majorant:

$$|I_3| \leq \|f\|_{L^p} \left\{ \int\limits_{|x-\sigma|\geq h} \left| |x-\sigma|^{\alpha-n+1} \ln^{\nu} \frac{r}{|x-\sigma|} - |y-\sigma|^{\alpha-n+1} \ln^{\nu} \frac{r}{|y-\sigma|} \right|^{p'} d\sigma \right\}^{\frac{1}{p'}}$$
$$\leq c\,\|f\|_{L^p}\, |x-y| \left\{ \int\limits_{|x-\sigma|\geq h} |x-\sigma|^{(n-\alpha)p'} \ln^{\nu p'} \frac{r_0}{|x-\sigma|} d\sigma \right\}^{\frac{1}{p'}}.$$

Now, with using (12) and (14), and considering the assumptions (18), the following evaluation is provided:

$$|I_3| \le c\|f\|_{L^p} h \left\{ \int_h^2 u^{(n-\alpha)p'+n-2} \ln^{\nu p'} \frac{r_0}{u} du \right\}^{\frac{1}{p'}} \le c \|f\|_{L^p} h^{\alpha - \frac{n-1}{p}} \ln^{\nu} \frac{r_0}{h}. \tag{22}$$

Finally, due to the natural logarithm function being strictly increasing, we shall take the maximum of the two values r and r_0 as m to obtain (17) with the condition (16) satisfied.

Q. E. D.

4 Conclusion

The inverse operator for the Riesz potential type operator with a logarithmic kernel is constructed with application of the Fourier—Laplace multipliers theory. It allows one to discover homeomorphisms between the generalized Hölder spaces, as well as between the ones and the spaces of integrable functions. However, in the general case of a power-logarithmic kernel, the latter does not provide with comprehensible expressions, so the Zygmund type estimates are applied for investigating the boundedness of the operator, which means its continuity in the considered function spaces. The presented results are of interest in the context of mathematical physics on fractal sets, in terms of which materials with complex properties can be considered.

Acknowledgements Research was financially supported by Southern Federal University, grant No. VnGr-07/2020–04-IM (Ministry of Science and Higher Education of the Russian Federation).

References

1. N.S. Landkof, *Foundations of Modern Potential Theory* (Springer, Providence, RI, 1973).
2. S.G. Samko, A.A. Marichev, O.I. Kilbas, *Fractional Integrals and Derivatives: Theory and Applications* (Gordon and Breach Science Publishers, Philadelphia, PA, 1993).
3. V.E. Tarasov, *Fractional Dynamics: Applications of Fractional Calculus to Dynamics of Particles, Fields and Media* (Springer, Berlin, Germany, 2010).
4. S.G. Samko, *Hypersingular Integrals and Their Applications* (Taylor & Francis, London and New York, 2002).
5. B.G. Vakulov, Soviet Mathematics (Izvestiya VUZ. Matematika), **30**(11), 90 (1986) (In Russian)
6. B.G. Vakulov, Izvestiya Vuzov. Severo-Kavkazskii Region. Nat. Sci. **4**, 5 (1999). ((In Russian))
7. V. Volterra, Atti. Accad. Naz. Lineei Rend. cl. sci. fis. mat. e natur, fasc. **11**(5), 167 (1916)
8. A.A. Kilbas, Soviet Mathematics (Izvestiya VUZ. Matematika), **23**(1), 22 (1979) (In Russian)
9. S.G. Samko, Soviet Mathematics (Izvestiya VUZ. Matematika), **27**(4), 35 (1983) (In Russian)
10. B.G. Vakulov, S.G. Samko, Soviet Mathematics (Izvestiya VUZ. Matematika), **31**(12), 90 (1987) (In Russian)

11. B.G. Vakulov, Yu. E. Drobotov, in *Recent Applications of Financial Risk Modelling and Portfolio Management*, ed. by T. Škrinjarić, M. Čižmešija, B. Christiansen. IGI Global, 275 (2021)
12. B.G. Vakulov, N.K. Karapetyants, L.D. Shankishvili, Russian Mathematics (Izvestiya VUZ. Matematika). **47**(2), 1 (2003) (In Russian)

Piezoelectric Sensitivity and Anisotropy in 1–3-Type Composites Based on Lead-Free Ferroelectrics

Vitaly Yu. Topolov, Ashura N. Isaeva, Christopher R. Bowen, and Alisa O. Denisova

Abstract The piezoelectric effect in novel 1–3-type composites with lead-free components is studied in terms of the effective piezoelectric coefficients d_{3j}^* and g_{3j}^*, electromechanical coupling factors k_{3j}^* and anisotropy factors d_{33}^* / d_{31}^* and k_{33}^* / k_{31}^*. The piezoelectric component is either a domain-engineered [001]-poled single crystal or a poled ceramic, and both the single crystal and ceramic are based on ferroelectric alkali-niobate—alkali-tantalate solid solutions. In the studied composites this component represents a system of long rods that are oriented parallel to the poling axis OX_3, and the rods are surrounded by a large piezo-passive polymer matrix that can be either monolithic (in 1–3 composites) or porous (in 1–3–0 composites). The high level of piezoelectric sensitivity of the lead-free 1–3 and 1–3–0 composites is noted due to the longitudinal piezoelectric coefficient $g_{33}^* \sim 10^2$–10^3 mV·m / N. Conditions for a large anisotropy $d_{33}^* / | d_{31}^* | = g_{33}^* / | g_{31}^* | \geq 5$ and $k_{33}^* / | k_{31}^* | \geq 5$ are valid in specific volume-fraction ranges of the ferroelectric component and porosity in the polymer component. The important role of the pore shape in achieving the large anisotropy of d_{3j}^* and k_{3j}^* of the 1–3–0 composite is discussed. The studied 1–3-type composites are of interest for the selection of advanced piezoelectric materials for transducer, sensor and related applications, with additional respect to the environment due to the lead-free nature of the composite components.

Keywords Lead-free · Piezoelectric coefficient · Piezoelectric sensitivity · Anisotropy factor · Composite

V. Yu. Topolov (✉) · A. N. Isaeva · A. O. Denisova
Department of Physics, Southern Federal University, 344090 Rostov-on-Don, Russia
e-mail: vutopolov@sfedu.ru

C. R. Bowen
Department of Mechanical Engineering, University of Bath, Bath BA2 7AY, UK

I. A. Parinov et al. (eds.), *Physics and Mechanics of New Materials and Their Applications*, Springer Proceedings in Materials 10,
https://doi.org/10.1007/978-3-030-76481-4_14

1 Introduction

An interest in 1–3-type composites based on lead-free ferroelectrics (either domain-engineered single crystals (SCs) [1–3] or poled ferroelectric ceramics (FCs) [4, 5]) originates from the piezoelectric properties, their anisotropy and other parameters which are important for piezotechnical and energy-harvesting applications [6–9]. The 1–3-type composites are characterised as a system of long piezoelectric rods arranged in a large matrix, as seen in Fig. 1. The rods are often oriented parallel to the poling axis and continuously distributed along one co-ordinate axis (represented by the index '1' in the 1–3 connectivity notation according to work [10]) and surrounded by a large matrix (represented by the index '3' in the 1–3 connectivity notation).

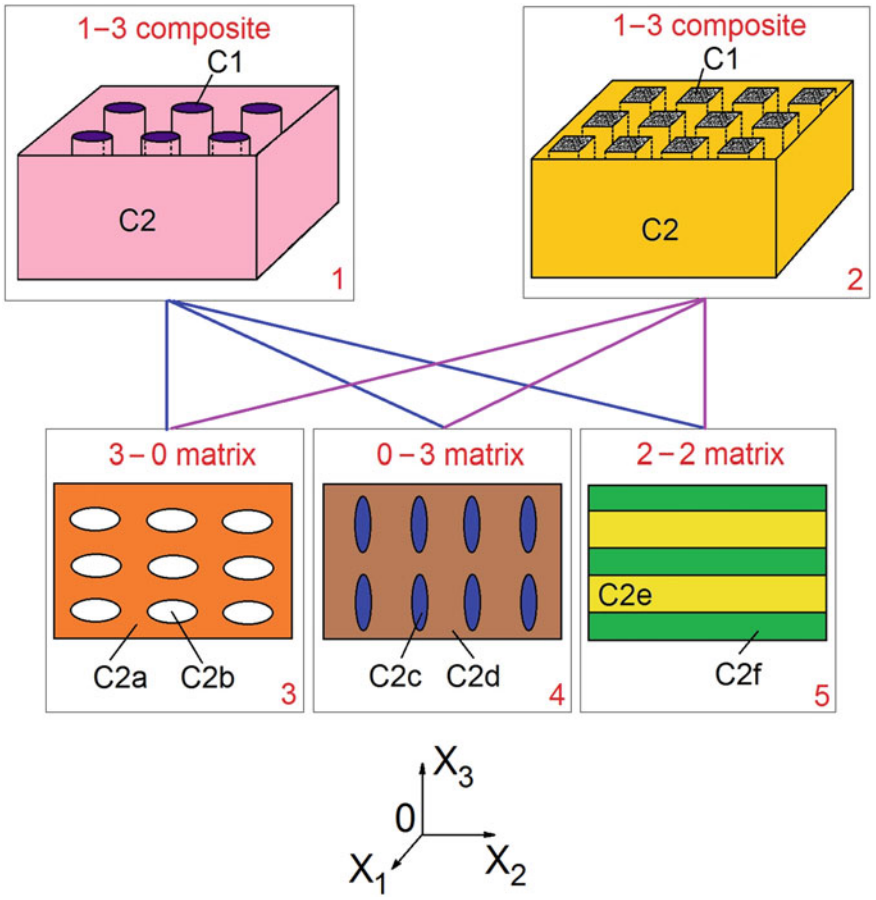

Fig. 1 Schematic of 1–3 composite (insets 1 and 2) and matrix (insets 3–5). C1, C2, C2a, C2b, C2c, C2d, C2e, and C2f are components of the 1–3-type composites. ($X_1X_2X_3$) is the rectangular co-ordinate system (reprinted from paper by Bowen et al. [7], with permission from Wiley–VCH)

This matrix can be either piezo-passive or piezoelectric [1–4, 11]. As a rule, the physical properties of the rod strongly differ from the properties of the matrix, and the matrix can be made of a wide variety of materials as a polymer or cement [6, 12]. The polymer matrix can be monolithic (see insets 1 and 2 in Fig. 1), auxetic [13] or porous (see work [3, 6, 13] and inset 3 in Fig. 1). Moreover, the matrix of the composite can be heterogeneous [2, 14], for instance, reinforced by inclusions with specific properties (see inset 4 in Fig. 1) or laminar (see inset 5 in Fig. 1). In each case the matrix surrounding the rods in the 1–3-type composite influences its electromechanical coupling, piezoelectric properties [2, 6, 7, 12, 14], figures of merit [6, 7, 11–15], hydrostatic and other parameters [6, 11–15]. The use of a lead-free ferroelectric component (rods) with large piezoelectric coefficients d_{3j} [1–3] and additional changes in the microgeometry and properties of the composite matrix [2, 7, 12, 14, 15] lead to unique sets of effective parameters that allow the properties of the piezo-active composites to be tailored for specific applications [6, 8, 16].

Undoubtedly, the piezo-active 1–3-type composites are advanced dielectric materials that are of interest for studies on the relationships in the fundamental triangle 'composition—structure—properties' [17]. These studies cannot be restricted, for instance, by a framework of physics or materials science only. In the context of modern composites [17] the term 'composition' means not only the chemical contents of the components, but also their volume fraction within the composite sample. The term 'structure' is considered not only as a composite structure but also describes the microgeometrical features, inclusion shapes, and specifics of the arrangement of components [7, 12, 14]. The term 'properties' is related to the composite as a heterogeneous medium that exhibits effective, or homogenised, properties [12, 17]. In the present chapter we describe the influence of components in the 1–3-type composites on their effective piezoelectric coefficients $d_{3j}{}^{*}$ and $g_{3j}{}^{*}$, electromechanical coupling factors (ECFs) $k_{3j}{}^{*}$ and related anisotropy factors, where $j = 1$ and 3.

2 Model Concepts, Effective Electromechanical Properties and Components of Composites

2.1 Model of the 1–3-type Composite

The 1–3-type composite contains a system of the piezoelectric rods (C1 in Fig. 1) in a large polymer matrix (C2 in Fig. 1). The rods are in the form of rectangular parallelepipeds (see inset 2 in Fig. 1) and are continuous in the OX_3 direction, which is the poling direction of the composite sample as a whole. Each rod has a square base, and the centres of the rod bases form a simple square lattice in the (X_1OX_2) plane. Hereafter we consider two kinds of composites, namely composites containing a system of ferroelectric SC rods and composites containing a system of FC rods. The main crystallographic axes X, Y and Z of each SC rod are parallel to the co-ordinate axes as follows: $X \parallel OX_1$, $Y \parallel OX_2$ and $Z \parallel OX_3$. Each SC rod is characterised by a

spontaneous polarisation vector $\boldsymbol{P_s}^{(1)} \uparrow\uparrow OX_3$. For the composite based on FC, we assume that the remanent polarisation of each FC rod is $\boldsymbol{P_r}^{(1)} \uparrow\uparrow OX_3$. The OX_3 axis is regarded as a poling axis of the studied 1–3-type composites, irrespective of their ferroelectric components. The volume fraction of the C1 component (rods in inset 2 in Fig. 1) equals m, and the volume fraction of the C2 component (matrix in inset 2 in Fig. 1) is $1 - m$.

The matrix of the aforementioned composites can be either monolithic or porous. The porous matrix contains spheroidal air pores, see inset 3 in Fig. 1. The shape of each pore is described by the equation:

$$\left(x_1/a_{1p}\right)^2 + \left(x_2/a_{2p}\right)^2 + \left(x_3/a_{3p}\right)^2 = 1 \tag{1}$$

in the axes of the co-ordinate system $(X_1X_2X_3)$, and semiaxes of the spheroid from Eq. (1) are a_{1p}, $a_{2p} = a_{1p}$ and a_{3p}. The shape of each pore is characterised by an aspect ratio $\rho_p = a_{1p} / a_{3p}$. The porous matrix is characterised by 3–0 connectivity (in terms of work [10]) owing to the isolated pores in the continuous medium, and the composite with the porous matrix can be described by 1–3–0 connectivity. It is assumed that the centres of each pore occupy sites of a simple tetragonal lattice. The largest semiaxis of each pore is much smaller than the side length of the square that is the cross section of the rod by the (X_1OX_2) plane. Due to this assumption, we consider the 1–3–0 composite on analogy with the conventional 1–3 composite [6, 7, 17], but by taking into account the effective (or homogenised) properties of the porous matrix [18]. It should be added that the porous polymer matrix can be produced, for instance, by means of additive manufacturing (3D printing) [19].

2.2 *Effective Electromechanical Properties and Parameters of the 1–3-type Composite*

Effective elastic, piezoelectric and dielectric (i.e., electromechanical) properties of the 1–3–0 composite are evaluated in two stages. In the first stage, the properties of the porous polymer matrix with 3–0 connectivity are determined in terms of work [18]. These properties depend on the volume fraction of the pores (i.e., porosity of the matrix) m_p and on the aspect ratio of the pore ρ_p. The calculation procedure is based on Eshelby's concept on spheroidal inclusions in heterogeneous solids [20]. The effective electromechanical properties of the porous medium are given by [18]

$$\left\| C^{(3)} \right\| = \left\| C^{(2)} \right\| \left[\| I \| - m_p \left(\| I \| - (1 - m_p) \| S \| \right)^{-1} \right] \tag{2}$$

In Eq. (2), $\| \boldsymbol{C^{(2)}} \|$ is the 9×9 matrix of the properties of monolithic polymer, $\| \boldsymbol{I} \|$ is the 9×9 identity matrix, and $\| \boldsymbol{S} \|$ is the 9×9 matrix that comprises components of the electroelastic Eshelby tensor [21]. The components of $\| \boldsymbol{S} \|$ from Eq. (2) depend on the aspect ratio ρ_p of the pore and on the properties of monolithic polymer. Its

properties are represented by

$$\left\| C^{(2)} \right\| = \begin{pmatrix} \left\| C^{(2),E} \right\| & \left\| e^{(2)} \right\|^t \\ \left\| e^{(2)} \right\| & -\left\| \varepsilon^{(2),\xi} \right\| \end{pmatrix}, \tag{3}$$

where $\| \boldsymbol{c}^{(2),E} \|$ is the 6 × 6 matrix of elastic moduli at electric field $E = \text{const}$, $\| \boldsymbol{e}^{(2)} \|$ is the 3 × 6 matrix of piezoelectric coefficients, $\| \boldsymbol{\varepsilon}^{(2),\xi} \|$ is the 3 × 3 matrix of dielectric permittivities at mechanical strain $\xi = \text{const}$, and superscript "t" refers to the transposed matrix. It should be added that $\| \boldsymbol{C}^{(3)} \|$ from Eq. (2) and $\| \boldsymbol{C}^{(2)} \|$ from Eq. (3) have the similar structure, and in a limiting case of $m_p = 0$ (i.e., for the monolithic polymer matrix), according to Eq. (2), we obtain $\| \boldsymbol{C}^{(3)} \| = \| \boldsymbol{C}^{(2)} \|$.

In the second stage of our evaluation, the effective electromechanical properties of the composite with parallelepiped-shaped rods (see inset 2 in Fig. 1) are evaluated by means of the matrix method [2, 3, 12, 17]. In the matrix method an electromechanical interaction between the piezoelectric rods is taken into account, and internal fields of $\boldsymbol{E}$ and σ_{qr} are assumed to be homogeneous within the rod and surrounding matrix. The matrix of the effective properties of the 1–3-type composite is written as

$$\left\| C^* \right\| = \left\| C^{(1)} \right\| \cdot \| M \| \, m + \left\| C^{(3)} \right\| (1 - m) \cdot [\| M \| m + \| I \| \, (1 - m)]^{-1}, \tag{4}$$

where $\| \boldsymbol{C}^{(1)} \|$ characterises the properties of the rod, $\| \boldsymbol{C}^{(3)} \|$ characterises the properties of the matrix of the composite, and $\| \boldsymbol{M} \|$ contains components of the 'concentration tensor' in accordance with boundary conditions for electric and mechanical fields on the lateral faces of each rod [12, 17]. The $\| \boldsymbol{M} \|$ elements are expressed in terms of the $\| \boldsymbol{C}^{(1)} \|$ and $\| \boldsymbol{C}^{(3)} \|$ elements [12, 17]. The effective properties of the composite [see Eq. (4)] are determined in the long-wave approximation [6, 12, 17], assuming that a wavelength of an external field is much longer than the size of the rod in the composite sample (Fig. 1). The $\| \boldsymbol{C}^* \|$ matrix from Eq. (4) has the general form:

$$\left\| C^* \right\| = \begin{pmatrix} \left\| s^{*E} \right\| & \| d^* \|^t \\ \| d^* \| & \| \varepsilon^{*\sigma} \| \end{pmatrix}, \tag{5}$$

and its elements depend on the volume fraction of the C1 component (rods) m, aspect ratio of pores ρ_p and porosity m_p in the C2 component (matrix of the composite, see insets 2 and 3 in Fig. 1). In Eq. (5), $\| \boldsymbol{s}^{*E} \|$ is the 6 × 6 matrix of elastic compliances at $E = \text{const}$, $\| \boldsymbol{d}^* \|$ is the 3 × 6 matrix of piezoelectric coefficients, $\| \boldsymbol{\varepsilon}^{*\sigma} \|$ is the 3 × 3 matrix of dielectric permittivities at mechanical stress $\sigma = \text{const}$, and 't' denotes transposition. The $\| \boldsymbol{C}^{(1)} \|$ and $\| \boldsymbol{C}^{(3)} \|$ matrices from Eq. (4) have the structure of $\| \boldsymbol{C}^* \|$ shown in Eq. (5). A transition from the set of electromechanical constants involved in $\| \boldsymbol{c}^{(2),E} \|$, $\| \boldsymbol{e}^{(2)} \|$ and $\| \boldsymbol{\varepsilon}^{(2),\xi} \|$ from Eq. (3) to the set of ${s_{ab}}^{(2),E}$, ${d_{ij}}^{(2)}$ and ${\varepsilon_{pp}}^{(2),\sigma}$ is carried out using conventional formulae [22] for a piezoelectric medium. The full set of constants ${s_{ab}}^{(2),E}$, ${d_{ij}}^{(2)}$ and ${\varepsilon_{pp}}^{(2),\sigma}$ is involved in the $\| \boldsymbol{C}^{(3)} \|$ matrix

from Eq. (4) and is to be taken into consideration to find the $\| \boldsymbol{M} \|$ matrix [12, 17] from Eq. (4). It should be noted that numerous results obtained by using the matrix method have been compared to evaluations within the framework of the finite element method [3, 12, 15], where good agreement between results is observed for piezo-active 1–3-type composites [11, 23].

Based on the evaluated $\| \boldsymbol{C}^* \|$ matrix from Eq. (4), we analyse the volume-fraction (m) behaviour of the following effective parameters of the lead-free 1–3-type composites:

(i) piezoelectric coefficients d^*_{3j} and g^*_{3j}, which are linked in accordance with the formula [22]

$$d^*_{3j} = \varepsilon^{*\sigma}_{3f} g^*_{fj}, \tag{6}$$

(ii) ECFs

$$k^*_{3j} = d^*_{3j} \,/\, (\varepsilon^{*\sigma}_{33} s^{*E}_{jj})^{1/2}. \tag{7}$$

and

(iii) anisotropy factors

$$\zeta^*_d = d^*_{33} \,/\, d^*_{31} \; and \; \zeta^*_k = k^*_{33} \,/\, k^*_{31}. \tag{8}$$

The piezoelectric coefficients d^*_{3j} and g^*_{3j} from Eq. (6) are used to characterise the piezoelectric sensitivity of a material [6, 12, 18, 22], $j = 1$ is related to the transverse piezoelectric effect, and $j = 3$ is related to the longitudinal piezoelectric effect. Both d^*_{3j} and g^*_{3j} from Eq. (6) form traditional (or squared) figures of merit $d^*_{3j} g^*_{3j}$ [6, 7, 11–15] that are important for energy-harvesting applications. Knowledge of the ECFs k^*_{3j} from Eq. (7) is important to evaluate the effectiveness of the conversion of electric energy into mechanical energy and vice versa [6, 7, 12, 18]. The anisotropy factors ${\zeta_d}^*$ and ${\zeta_k}^*$ from Eqs. (8) are to be taken into account in piezoelectric devices with ultrasonic antennae based on pulse-echo principles and control of its preferred direction, and exploitation of sensors and transducers operating at the longitudinal oscillation mode etc. [2, 7, 17].

2.3 Components of Composites

The full sets of electromechanical constants of the components of the studied composites are shown in Table 1. Among the lead-free ferroelectric components to be of interest, we consider the [001]-poled domain-engineered KNNTL-Mn [24] and KNN-T SCs [25] and high-performance KNNS–BNZH FC studied recently [26]. As follows from Table 1, the piezoelectric coefficients d_{ij} of the KNNS–BNZH FC occupy an intermediate position between the d_{ij} values of the KNNTL-Mn and

Table 1 Room-temperature elastic compliances $s_{ab}{}^{E}$ (in 10^{-12} Pa^{-1}), piezoelectric coefficients d_{ij} (in pC / N) and dielectric permittivity $\varepsilon_{pp}^{\sigma}$ of [001]-poled domain-engineered SCs (4*mm* symmetry), poled FC (∞mm symmetry) and isotropic polymers

Electromechanical constants	KNNTL-Mn[a] SC [24]	KNN-T[b] SC [25]	KNNS–BNZH[c] FC [26]	Araldite [12, 27]	Polyurethane [12, 28]	Polyethylene (high-density) [12]
s_{11}^{E}	33.4	11.9	1.37	216	405	1540
s_{12}^{E}	−7.36	−4.30	−0.63	−78	−151	−517
s_{13}^{E}	−25.8	−5.60	−0.50	−78	−151	−517
s_{33}^{E}	57.7	15.5	1.68	216	405	1540
s_{44}^{E}	12.8	12.0	4.39	588	1110	4110
s_{66}^{E}	13.5	10.7	4.00	588	1110	4110
d_{15}	66	45.0	690	0	0	0
d_{31}	−260	−77	−140	0	0	0
d_{33}	545	162	380	0	0	0
$\varepsilon_{11}^{\sigma}/\varepsilon_0$	400	291	2190	4.0	3.5	2.3
$\varepsilon_{33}^{\sigma}/\varepsilon_0$	650	267	2000	4.0	3.5	2.3

[a] $[Li_x(K_{1-y}Na_y)_{1-x}](Nb_{1-z}Ta_z)O_3$:Mn, where $x = 0.06$, $y = 0.1$–0.3, $z = 0.07$–0.17, and the level of Mn doping is 0.25 mol. %, Ref. [24]

[b] $(K_{0.562}Na_{0.438})(Nb_{0.768}Ta_{0.232})O_3$, Ref. [25]

[c] $0.965(K_{0.48}Na_{0.52})(Nb_{0.96}Sb_{0.04})O_3$–$0.035Bi_{0.5}Na_{0.5}Zr_{0.15}Hf_{0.75}O_3$, Ref. [26]

KNN-T SCs. The KNNTL-Mn SC and KNNS–BNZH FC exhibit the piezoelectric coefficients d_{ij} that are larger than the similar parameters of such conventional lead-containing FCs as, for instance, PZT-4, PZT-5 or PZT-5A [17, 26]. The piezo-passive polymer components listed in Table 1 are characterised by elastic properties [12, 27, 28] that differ markedly. For instance, the elastic compliance s_{33}^E of araldite is approximately two times smaller than s_{33}^E of polyurethane and ca. 7.1 times smaller than s_{33}^E of polyethylene. In contrast to these values, the s_{33}^E / s_{13}^E ratio related to polymers from Table 1 varies within a narrow range, from ca. –2.7 to –3. Such a choice of polymers is important to enable an analysis of the influence of the rod and matrix properties on the piezoelectric sensitivity, electromechanical coupling and anisotropy factors of 1–3-type composites.

3 Piezoelectric Sensitivity and Anisotropy Factors of Composites

In Sect. 3 we analyse particular volume-fraction (m) dependences of the effective parameters (6)–(8), which are evaluated for 1–3 and 1–3–0 composites with components listed in Table 1. We also consider examples of a large anisotropy of the effective parameters concerned with the piezoelectric response and electromechanical coupling of the composite. By analogy with work [2] we introduce conditions for the large piezoelectric anisotropy:

$$\left|\zeta_d^*\right| \geq 5 \tag{9}$$

and for the large anisotropy of ECFs from Eq. (7)

$$\left|\zeta_k^*\right| \geq 5 \tag{10}$$

Taking into account Eq. (6), we note that condition (9) is also valid to describe the large piezoelectric anisotropy of the piezoelectric coefficients

$$g_{3j}^* = d_{3j}^* / \varepsilon_{33}^{*\sigma}. \tag{11}$$

Taking into account Eq. (7), we write the anisotropy factor ${\zeta_k}^*$ as follows:

$${\zeta_k}^* = {\zeta_d}^* \, (s_{11}^{*E} / s_{33}^{*E})^{1/2}. \tag{12}$$

As follows from Eqs. (8) and (11), the anisotropy factor ${\zeta_d}^*$ can be written in the form ${\zeta_d}^* = {g_{33}}^* / {g_{31}}^*$.

3.1 1–3 Composites

Examples of the volume-fraction (m) dependences of the effective parameters of the 1–3 composite are shown in Fig. 2. We remind the reader that the connectivity pattern of the 1–3 composite is shown in inset 2 of Fig. 1; see also Sect. 2.1. In Table 2 we show data on the most important maximum and minimum points of the studied effective parameters related to the 1–3 composites.

The graphs in Fig. 2 a, c and e show the $d_{33}{}^{*}(m)$ and $g_{33}{}^{*}(m)$ dependences that are typical of the piezo-active 1–3 composites with polymer matrices [11, 12, 17, 23]. A max $g_{33}{}^{*}$ is observed at a small volume fraction m_{g33}: as follows from Table 2, the inequality $0.004 \leq m_{g33} \leq 0.033$ holds. It should be noted for comparison that Choy et al. [29] manufactured a 1–3 FC-based composite with small volume fractions of FC rods (approximately 0.033, 0.066 etc.). Thus, the need for a very small m_{g33} value may be a 'stumbling-block' in the technological sense in terms of transducer manufacture. Increasing the absolute value of the difference between elastic compliances of components, i.e., $\mid s_{ab}{}^{(1),E} - s_{ab}{}^{(2),E} \mid$, leads to decreasing the volume fraction m_{g33} (see, for instance, Fig. 2 a and e). The common feature of the studied 1–3 composites consists in the almost equal volume fractions m_{g33} related to max $g_{33}{}^{*}$ and m_{g31} related to min $g_{31}{}^{*}$, see Table 2. The small m_{g33} and m_{g31} values shown in Table 2 are achieved due to the combined effect of the piezoelectric and dielectric properties [12, 17]. Owing to this effect and Eqs. (6 and 11), the aforementioned max $g_{33}{}^{*}$ and min $g_{31}{}^{*}$ are observed in the volume-fraction region, where the dielectric permittivity of the composite $\varepsilon_{33}^{*\sigma} << \varepsilon_{33}{}^{(1),\sigma}$.

In Fig. 2, a and c we see the volume-fraction regions, where $g_{33}{}^{*}(m) \geq 10^3$ mV·m / N. For comparison we mention that the KNNTL-Mn SC is characterised by the piezoelectric coefficient $g_{33}{}^{(1)} = 94.7$ mV·m / N [24], and the $g_{33}{}^{(1)}$ value of the KNNS-BNZH FC equals 21.5 mV·m / N [26]. A high level of the longitudinal

Table 2 Data on maxima and minima of effective parameters of 1–3 composites

Rod material, C1	Matrix material, C2	max $g_{33}{}^{*}$ (in mV·m / N), volume fraction m_{g33} corresponding to max $g_{33}{}^{*}$	min $g_{31}{}^{*}$ (in mV·m / N), volume fraction m_{g31} corresponding to min $g_{31}{}^{*}$	min $\zeta_k{}^{*}$, volume fraction m corresponding to min $\zeta_k{}^{*}$
KNNTL-Mn SC	Araldite	855, 0.041	−267, 0.043	–
	Polyurethane	1290, 0.028	−466, 0.028	−3.00, 0.177
	Polyethylene	3100, 0.014	−1020, 0.012	−5.39, 0.259
KNN-T SC	Araldite	705, 0.033	−244, 0.035	−3.85, 0.249
	Polyurethane	1020, 0.023	−363, 0.023	−4.72, 0.278
	Polyethylene	2300, 0.009	−746, 0.009	−9.84, 0.281
KNNS-BNZH FC	Araldite	326, 0.013	−114, 0.013	−4.05, 0.361
	Polyurethane	541, 0.009	−195, 0.009	−4.95, 0.375
	Polyethylene	1550, 0.004	−511, 0.004	−10.3, 0.354

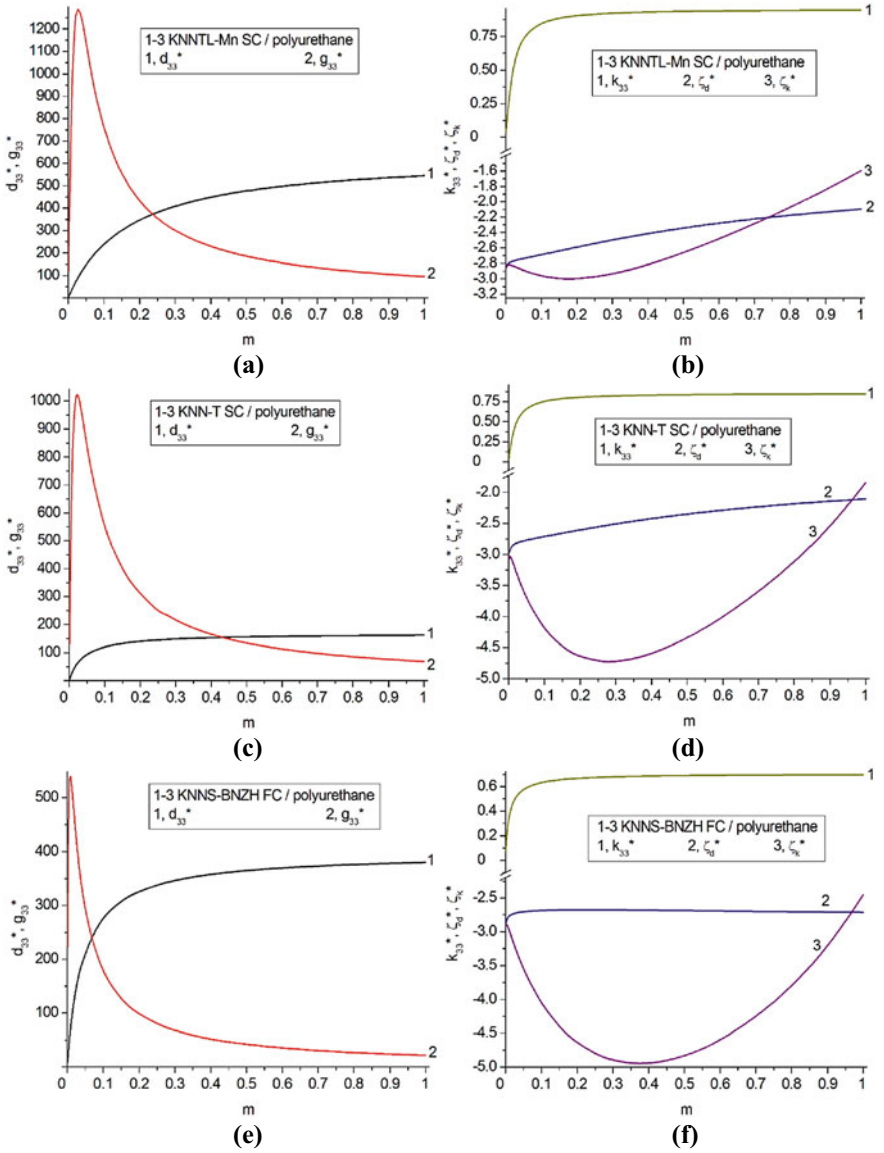

Fig. 2 Piezoelectric coefficients $d_{33}{}^{*}$ (in pC / N) and $g_{33}{}^{*}$ (in mV·m / N), ECF $k_{33}{}^{*}$ and anisotropy factors $\zeta_d{}^{*}$ and $\zeta_k{}^{*}$ of 1–3 KNNTL-Mn SC / polyurethane (a and b), KNN-T SC / polyurethane (c and d), and KNNS-BNZH FC / polyurethane (e and f) composites at the volume fraction $m \geq 0.001$

piezoelectric sensitivity of the composites is achieved in a wide volume-fraction range even despite decreasing $g_{33}{}^{*}(m)$ at $m > m_{g33}$, see Fig. 2, a, c and e.

The monotonic dependence of the ECF $k_{33}{}^{*}(m)$ (curve 1 in Fig. 2 b, d and f) is accounted for by the proportionality $k_{33}{}^{*} \sim d_{33}{}^{*}$ [see Eq. (7)] and by the monotonic $d_{33}{}^{*}(m)$ (see curve 1 in Fig. 2, a, c and e) and $\varepsilon_{33}^{*\sigma}(m) \cdot s_{33}{}^{*E}(m)$ dependences. Curves 2 and 3 in Fig. 2b, d and f suggest the strong difference between the $\zeta_k{}^{*}(m)$ and $\zeta_d{}^{*}(m)$ dependences.

The | min $\zeta_k{}^{*}$ | value increases with increasing the | $s_{ab}{}^{(1),E} - s_{ab}{}^{(2),E}$ | value. A relatively small | $s_{ab}{}^{(1),E} - s_{ab}{}^{(2),E}$ | value related to the 1–3 KNNTL-Mn SC / araldite composite leads to lack of min $\zeta_k{}^{*}$, see the 5th column in Table 2 and constants of components in Table 1. We add that the largest | min $\zeta_k{}^{*}$ | value given in Table 2 is achieved at the largest | $s_{ab}{}^{(1),E} - s_{ab}{}^{(2),E}$ | value, and this is related to the 1–3 KNNS-BNZH FC / polyethylene composite.

In Table 3, we show the effective parameters related to the volume fractions $m = 0.10$ and 0.20. In the overwhelming number of cases shown in the 3rd and 4th columns of Table 3, the conditions $d_{33}{}^{*} > 100$ pC / N and $g_{33}{}^{*} > 100$ mV·m / N

Table 3 Piezoelectric coefficients $d_{33}{}^{*}$ (in pC / N) and $g_{33}{}^{*}$ (in mV·m / N), ECF $k_{33}{}^{*}$ and anisotropy factors $\zeta_d{}^{*}$ and $\zeta_k{}^{*}$ of 1–3 composites at $m = \text{const}$

Rod material, C1	Matrix material, C2	$d_{33}{}^{*}$	$g_{33}{}^{*}$	$k_{33}{}^{*}$	$\zeta_d{}^{*}$	$\zeta_k{}^{*}$
At $m = 0.10$						
KNNTL-Mn SC	Araldite	159	658	0.787	−3.09	−3.20
	Polyurethane	239	761	0.848	−2.69	−2.96
	Polyethylene	407	879	0.911	−2.98	−4.80
KNN-T SC	Araldite	98.4	489	0.715	−2.78	−3.60
	Polyurethane	121	546	0.756	−2.71	−4.19
	Polyethylene	149	618	0.803	−2.99	−8.21
KNNS-BNZH FC	Araldite	224	155	0.591	−2.77	−3.53
	Polyurethane	277	177	0.633	−2.69	−4.05
	Polyethylene	346	202	0.676	−2.98	−7.90
At $m = 0.20$						
KNNTL-Mn SC	Araldite	262	408	0.877	−2.91	−3.05
	Polyurethane	347	433	0.905	−2.59	−3.00
	Polyethylene	474	459	0.931	−2.83	−5.33
KNN-T SC	Araldite	126	296	0.787	−2.65	−3.83
	Polyurethane	141	311	0.806	−2.60	−4.64
	Polyethylene	156	327	0.827	−2.84	−9.60
KNNS-BNZH FC	Araldite	290	91.7	0.644	−2.74	−3.88
	Polyurethane	326	98.2	0.667	−2.68	−4.64
	Polyethylene	364	105	0.688	−2.94	−9.59

hold. The longitudinal ECF k_{33}^* of the KNNTL-Mn- and KNN-T-based composites obeys the inequality $k_{33}^* > 0.7$, see the 5th column in Table 3. Analysing data from the 6th and 7th columns in Table 3, we state that conditions $|\zeta_d^*| \approx 3$ and $|\zeta_d^*| < |\zeta_k^*|$ are valid, irrespective of the components forming the 1–3 composite. The largest $|\zeta_k^*|$ values are achieved in the composites with the polyethylene (i.e., softest) matrix, however even for the KNNTL-Mn- and KNN-T-based composites condition (9) does not hold.

3.2 1–3–0 Composites

Examples of the volume-fraction (m) behaviour of the 1–3–0 KNNTL-Mn-based composite are shown in Fig. 3. Comparing Figs. 3a to 2a, we note that a very sharp max g_{33}^* for the 1–3–0 composite is achieved at the volume fraction of SC $m_{g33} < 0.01$, and the max g_{33}^* value is approximately six times larger than in the case of the 1–3 analog. Comparing Figs. 3b to 2b, we see that for 1–3–0 composites, both the $\zeta_d^*(m)$ and $\zeta_k^*(m)$ dependences are non-monotonic, and the inequality $|\zeta_d^*| > |\zeta_k^*|$ holds at small volume fractions $m << 1$.

The formation of the highly oblate pores ($\rho_p >> 1$) in the polymer medium and increasing the level of porosity m_p leads an increase in the ratio of elastic compliances $s_{11}^{(2),E} / s_{33}^{(2),E}$ and promotes larger anisotropy factors ζ_d^* and ζ_k^* from Eqs. (8), especially at relatively small volume fractions m. The large elastic compliance $s_{33}^{(2),E}$ of the matrix leads to a more rapid increase in the piezoelectric coefficient d_{33}^* of the composite at $m << 1$ in comparison to the increase of $|d_{31}^*|$, and this leads to the pronounced min ζ_d^* (curve 2 in Fig. 3b). The anisotropy factor ζ_k^* is proportional to ζ_d^*, as follows from Eq. (12), and the proportionality factor s_{11}^{*E}/s_{33}^{*E} in Eq. (12)

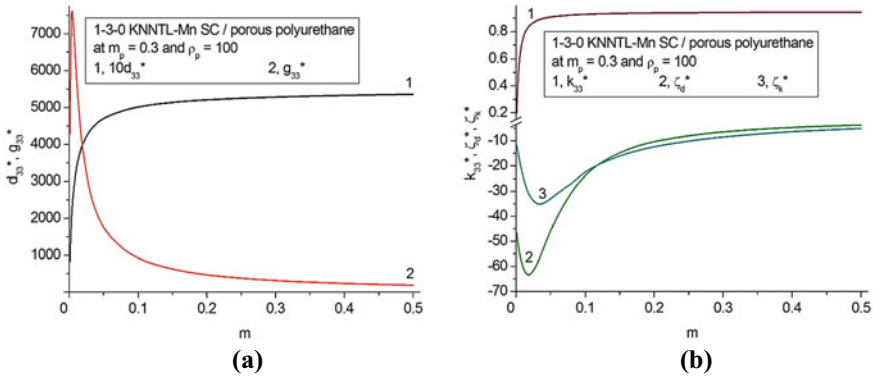

Fig. 3 Piezoelectric coefficients d_{33}^* (in pC / N) and g_{33}^* (in mV·m / N), ECF k_{33}^* and anisotropy factors ζ_d^* and ζ_k^* of the 1–3–0 KNNTL-Mn SC / porous polyurethane composite at the volume fraction of SC $m \geq 0.001$, porosity of the polyurethane matrix $m_p = 0.3$ and aspect ratio of the pore $\rho_p = 100$

Table 4 Data on max $g_{33}{}^*$ (in mV·m / N), min $g_{31}{}^*$ (in mV·m / N) and volume-fraction ranges concerned with validity of conditions (9) and (10) in the 1–3–0 KNNTL-Mn SC / porous polyurethane

ρ_p	m_p	max $g_{33}{}^*$, volume fraction m_{g33} corresponding to max $g_{33}{}^*$	min $g_{31}{}^*$,volume fraction m_{g31} corresponding to min $g_{31}{}^*$	Volume-fraction range $[m_{d1}; m_{d2}]$ of validity of condition (9)	Volume-fraction range $[m_{k1}; m_{k2}]$ of validity of condition (10)
1	0.1	1480, 0.024	−517, 0.025	–	–
	0.2	1730, 0.021	−585, 0.021	–	–
	0.3	2020, 0.018	−669, 0.018	–	–
10	0.1	1920, 0.019	−447, 0.019	–	–
	0.2	2610, 0.014	−467, 0.014	[0.001; 0.117]	[0.073; 0.226]
	0.3	3380, 0.011	−505, 0.011	[0.001; 0.191]	[0.026; 0.354]
100	0.1	3850, 0.009	−192, 0.009	[0.001; 0.338]	[0.001; 0.425]
	0.2	5750, 0.006	−156, 0.005	[0.001; 0.364]	[0.001; 0.472]
	0.3	7660, 0.004	−145, 0.003	[0.001; 0.373]	[0.001; 0.506]

is responsible for the resulting similarity of curves 2 and 3 in Fig. 3b. The main difference between the $\zeta_k{}^*(m)$ and $\zeta_d{}^*(m)$ curves shown in Fig. 3b is observed in the volume-fraction range of $m < 0.1$. In this range the elastic properties of the porous matrix strongly influence the effective properties of the composite, and the approximate equality $s_{11}^{*E}/s_{33}^{*E} \approx s_{11}{}^{(2),E} / s_{33}{}^{(2),E}$ holds.

In Table 4 we show examples of the very high piezoelectric sensitivity ($g_{33}{}^* > 10^3$ mV·m / N) and volume-fraction ranges wherein conditions (9) and (10) for achieving a large anisotropy hold. It should be noted that conditions (9) and (10) are not valid for composites with porous polymer matrices at the aspect ratio $\rho_p < 1$ (prolate pores) [30] or $\rho_p = 1$ (spherical pores). In our opinion, this feature of the $\zeta_k{}^*(m)$ and $\zeta_d{}^*(m)$ dependences of the 1–3–0 composite is accounted for by the active role of an elastic anisotropy of its porous polymer matrix. At the aspect ratio $\rho_p < 1$ or $\rho_p = 1$, the ratio of elastic compliances, $s_{33}{}^{(2),E} / s_{11}{}^{(2),E}$ in the porous matrix is relatively small in comparison to the $s_{33}{}^{(2),E} / s_{11}{}^{(2),E}$ ratio at $\rho_p >> 1$ (see the similar shape and orientation of pores in inset 3 in Fig. 1). We add that the similar influence of the porous polymer matrix on the anisotropy factors $\zeta_d{}^*$ and $\zeta_k{}^*$ from Eqs. (8) is observed in a 1–3–0 composite based on relaxor-ferroelectric single-domain $0.58Pb(Mg_{1/3}Nb_{2/3})O_3 - 0.42PbTiO_3$ SC [23]. Values of $\zeta_d{}^*$ and $\zeta_k{}^*$, which were calculated by means of the matrix method and finite element method in the wide m range at $\rho_p = \text{const}$ and $m_p = \text{const}$, are in good agreement [23].

4 Comparison of Results

The performance of the studied lead-free piezo-active 1–3 and 1–3–0 composites (see Sect. 3) can be compared, in order to consider specific performance parameters of typical 1–3-type composites and related materials. The studied lead-free composites are regarded as advanced materials due to their large piezoelectric coefficient $g_{33}{}^*$ and the relatively large values of parameters such as $d_{33}{}^*$, $k_{33}{}^*$, $|\zeta_d{}^*|$, and $|\zeta_k{}^*|$ [see Eqs. (6)–(8)]. As follows from experimental results [4], a 1–3 lead-free composite based on the $0.965(K_{0.45}Na_{0.55})(Nb_{0.96}Sb_{0.04})O_3 - 0.0375Bi_{0.5}Na_{0.5}Zr_{0.85}Hf_{0.15}O_3$ FC is characterised by the piezoelectric coefficient $d_{33}^* = 350$ pC / N. Our data from Fig. 2, a and e suggest that the d_{33}^* value of the studied 1–3 composites can be larger than the d_{33}^* value from work [23]. The largest $g_{33}{}^*$ value related to a quasi 1–3 dielectrophoretically structured $K_{0.485}Na_{0.485}Li_{0.03}NbO_3$ FC / polydimethylsiloxane composite from work [5] equals 510 mV·m / N. As follows from experimental results [31] on 3–1 and 3–2 $(Na_{0.5}K_{0.5})NbO_3$ / epoxy composites, largest values of their longitudinal piezoelectric coefficients are $d_{33}{}^* = 98$ pC / N and $g_{33}{}^* = 66$ mV·m / N.

A parallel-connected freeze-cast porous material based on the Pb(Zr, Ti)O_3-based FC is characterised by the piezoelectric coefficients $d_{33}^* \sim 10^2$ pC / N and $g_{33}{}^* \approx 40$–100 mV·m / N at $|\zeta_d{}^*| \approx 3$–5 [32]. A highly anisotropic modified $PbTiO_3$ FC [33] is characterised by the piezoelectric coefficient $d_{33} = 56$ pC/N (that is an order-of-magnitude smaller than d_{33}^* of the studied composites; see, for instance, Figs. 2a, c, e and 3a) and by the anisotropy factor ζ_d that is comparable to $\zeta_d{}^*$ of the 1–3–0 composite at $m > 0.2$ (see curve 2 in Fig. 3b). Finally, typical values of parameters of a 1–3-type Pb(Zr, Ti)O_3-based FC / foamed polyurethane composite [34] are $d_{33}^* = 180$ pC / N, $g_{33}{}^* = 495$ mV·m / N and $|\zeta_d{}^*| = 3.36$. The aforementioned values of $d_{33}^* = 180$ pC / N and $g_{33}{}^* = 495$ mV·m / N from work [34] are comparable to the similar parameters of the studied 1–3–0 lead-free composite, see Fig. 3a. However the $|\zeta_d{}^*|$ values of the 1–3–0 lead-free composite (see curve 2 in Fig. 3b) can be approximately 5–10 times larger than $|\zeta_d{}^*|$ of the aforementioned 1–3-type Pb(Zr, Ti)O_3-based composite [34].

5 Conclusion

The piezoelectric performance, electromechanical coupling and anisotropy factors of lead-free 1–3-type composites with components listed in Table 1 have been studied. The main piezoelectric component (see C1 in Fig. 1) is either a domain-engineered ferroelectric SC or FC poled in a specific direction. Large values of the longitudinal piezoelectric coefficient $g_{33}{}^* \sim 10^2$–10^3 mV·m / N and ECF $k_{33}{}^* > 0.7$ are achieved, and conditions (9) and (10) hold in specific volume-fraction ranges, as follows from Figs. 2 and 3, and Tables 2–4. Of independent interest is the relative narrow volume-fraction range at $m << 1$, where the condition $g_{33}{}^* > 10^3$ mV·m / N holds (see Figs. 2a,

b and 3a), i.e., the very high level of piezoelectric sensitivity of the studied lead-free 1–3 and 1–3–0 composites is stated. The large anisotropy of the piezoelectric coefficients $d_{3j}{}^{*}$ and ECFs $k_{3j}{}^{*}$ is achieved in the presence of the heavily oblate pores (at $\rho_p >> 1$) in the polymer matrix of the 1–3–0 composite, and these pores strongly influence the elastic anisotropy of the matrix. The studied lead-free 1–3-type composites can be of interest in piezotechnical applications such as sensors and transducers, where the large piezoelectric coefficients $g_{33}{}^{*}$, ECFs $k_{33}{}^{*}$ and anisotropy factors $\zeta_d{}^{*}$ and $\zeta_k{}^{*}$ from conditions (9) and (10) play the key role.

Acknowledgements The authors would like to thank Prof. Dr. A. E. Panich and Prof. Dr. I. A. Parinov (Southern Federal University, Russia), and Prof. Dr. P. Bisegna (University of Rome Tor Vergata, Italy) for their research interest in the piezoelectric performance of advanced composites. Research was financially supported by Southern Federal University, grant No. VnGr-07/2020-04-IM (Ministry of Science and Higher Education of the Russian Federation).

References

1. D. Zhou, K.H. Lam, Y. Chen, Q. Zhang, Y.C. Chiu, H. Luo, J. Dai, H.L.W. Chan. Sens. a. Actuat. A – Phys. **182**, 95 (2012)
2. V.Yu. Topolov, C.R. Bowen, A.N. Isaeva. IEEE Trans. Ultrason., Ferroelec., a. Freq. Control **65**, 1278 (2018)
3. V.Yu. Topolov, A.N. Isaeva, P. Bisegna, J. Phys. D: Appl. Phys. **53**, 395303 (2020)
4. Q. Ke, W.H. Liew, H. Tao, J. Wu, K. Yao. IEEE Trans. Ultrason., Ferroelec., a. Freq. Control **66**, 1395 (2019)
5. V.L. Stuber, D.B. Deutz, J. Bennett, D. Cannel, D.M. de Leeuw, S. van der Zwaag, P. Groen, Energy Technol. **7**, 177 (2019)
6. C.R. Bowen, V.Yu. Topolov, H.A. Kim. *Modern Piezoelectric Energy-Harvesting Materials* (Springer International Publ., Cham, 2016), 152 p.
7. C.R. Bowen, V.Yu. Topolov, Y. Zhang, A.A. Panich, Energy Technol. **6**, 813 (2018)
8. D. Maurya, M. Peddigari, L.D. Geng, N. Sharpes, V. Annapureddy, H. Palneedi, R. Sriramdas, Y. Yan, H.-C. Song, Y.U. Wang, J. Ryu, S. Priya, J. Mater. Res. **33**, 2235 (2018)
9. L. Jiang, R. Chen, J. Xing, G. Lu, R. Li, Y. Jiang, K. Shung, J. Zhu, Q. Zhou, J. Appl. Phys. **125**, 214501 (2019)
10. R.E. Newnham, D.P. Skinner, L.E. Cross, Mater. Res. Bull. **13**, 525 (1978)
11. V.Yu. Topolov, A.V. Krivoruchko, P. Bisegna, C.R. Bowen, Ferroelectrics **376**, 89 (2008)
12. V.Yu. Topolov, C.R. Bowen, P. Bisegna. *Piezo-Active Composites. Microgeometry—Sensitivity Relations* (Springer International Publ., Cham, 2018), 196 p.
13. V.Yu. Topolov, C.R. Bowen, Mater. Lett. **142**, 265 (2015)
14. C.R. Bowen, V.Yu. Topolov, A.N. Isaeva, P. Bisegna, CrystEngComm **18**, 5986 (2016)
15. V.Yu. Topolov, A.N. Isaeva, P. Bisegna, Sens. a. Actuat. A – Phys. **318**, 112473 (2021)
16. E.K. Akdogan, M. Allahverdi, A. Safari, IEEE Trans. Ultrason. Ferroelec. a. Freq. Control **52**, 746 (2005)
17. V.Yu. Topolov, C.R. Bowen. *Electromechanical Properties in Composites Based on Ferroelectrics* (Springer, London, 2009), 202 p.
18. M.L. Dunn, M. Taya, J. Am. Ceram. Soc. **76**, 1697 (1993)
19. A. El Moumen, M. Tarfaoui, K. Lafdi, Composites B **171**, 166 (2019)
20. M.L. Dunn, M. Taya, Internat. J. Solids Struct. **30**, 161 (1993)
21. J.H. Huang, S. Yu, Compos. Eng. **4**, 1169 (1994)

22. T. Ikeda, *Fundamentals of Piezoelectricity* (Oxford University Press, Oxford, 1990), 263 p.
23. V.Yu. Topolov, A.V. Krivoruchko, P. Bisegna, Composites. Sci. Technol. **71**, 1082 (2011)
24. X. Huo, R. Zhang, L. Zheng, S. Zhang, R. Wang, J. Wang, S. Sang, B. Yang, W. Cao, J. Am. Ceram. Soc. **98**, 1829 (2015)
25. X. Huo, L. Zheng, R. Zhang, R. Wang, J. Wang, S. Sang, Y. Wang, B. Yang, W. Cao, CrystEngComm **16**, 9828 (2014)
26. L. Qiao, G. Li, H. Tao, J. Wu, Z. Xu, F. Li, Ceram. Internat. **46**, 5641 (2020)
27. F. Levassort, M. Lethiecq, C. Millar, L. Pourcelot, IEEE Trans. Ultrason. Ferroelec. a. Freq. Control **45**, 1497 (1998)
28. L.V. Gibiansky, S. Torquato, J. Mech. Phys. Solids **45**, 689 (1997)
29. S.H. Choy, H.L.W. Chan, M.W. Ng, P.C.K. Liu, Integr. Ferroelectr. **63**, 109 (2004)
30. V.Yu. Topolov, A.N. Isaeva, Ferroelectrics **567**, 182 (2020)
31. M. Fukushima, T. Fujiwara, T. Fey, K. Kakimoto, J. Am. Ceram. Soc. **100**, 5400 (2017)
32. Y. Zhang, V. Yu. Topolov, A.N. Isaeva, C.R, Bowen, H. Pearce, H. Khanbareh, Smart Mater. Struct. **28**, 125021 (2019)
33. Y. Xu, *Ferroelectric Materials and Their Applications* (Amsterdam, North-Holland, 1991), 403 p.
34. K.A. Klicker, W.A, Schulze, J.V. Biggers, J. Am. Ceram. Soc. **65**, C208 (1982)

Crystal Structure and Dielectric Properties of Layered Perovskite-Like Solid Solutions $Bi_{3-x}Nd_xTiNbO_9$ ($X = 0$, 0.2, 0.4, 0.6, 0.8, 1.0)

S. V. Zubkov

Abstract The structural and electrophysical characteristics of a number of solid solutions of layered perovskite-like oxides $Bi_{3-x}Nd_xTiNbO_9$ ($x = 0$, 0.2, 0.4, 0.6, 0.8, 1.0) were studied. According to powder X-ray diffraction, it was found that all compounds are single-phase, having the structure of two-layer Aurivillius phases ($m = 2$) with an orthorhombic crystal lattice (group A21am). The temperature dependences of the relative permittivity $\varepsilon/\varepsilon_0(T)$ of compounds were obtained from which it was found that the Curie temperature T_C of perovskite-like oxides $Bi_{3-x}Nd_xTiNbO_9$ ($x = 0$, 0.2, 0.4, 0.6, 0.8, 1.0) decreases with increasing substitution parameter x, reaching $T_C = 430$ °C.

Keywords Layered perovskite-like oxides · Solid solutions · Aurivillius phases (APs) · Dielectric constant · Curie temperature

1 Introduction

Aurivillius phases (APs) [1–3] are a larger family of bismuth-containing layered perovskite-like compounds, the chemical composition of which is described by the general formula $A_{m-1}Bi_2B_mO_{3m+3}$. The crystal structure of the APs is an alternating layer of $[Bi_2O_2]^{2+}$, between which there are m perovskite-like loops $[A_{m-1}B_mO_{3m+1}]^{2-}$, where the A positions are occupied by ions with large radii (Bi^{3+}, Ca^{2+}, Sr^{2+}, Ba^{2+}, Y^{3+}, Pb^{2+}, Na^{+}, K^{+}, Th^{4+}, and Ln^{3+} (lanthanides)), B positions inside the oxygen octahedra are occupied by ions with small radii (Ti^{4+}, Nb^{5+}, Ta^{5+}, W^{6+}, Mo^{6+}, Fe^{3+}, Mn^{4+}, Cr^{3+}, Ga^{3+}).

Layered perovskite-like compounds of bismuth oxides of the APs family are promising lead-free materials for use in piezoelectric devices, especially at high temperatures and high frequencies. In addition to the high Curie temperature, they exhibit correspondingly low temperature coefficients of dielectric and piezoelectric

S. V. Zubkov (✉)
Research Institute of Physics, Southern Federal University, 194, Stachki Ave, Rostov-on Don 344090, Russia
e-mail: svzubkov61@mail.ru

I. A. Parinov et al. (eds.), *Physics and Mechanics of New Materials and Their Applications*, Springer Proceedings in Materials 10,
https://doi.org/10.1007/978-3-030-76481-4_15

losses, low aging rate [4, 5]. In recent years, more attention has been paid to the production and study of new APs. APs such as $SrBi_2Nb_2O_9$ (SBN), $SrBi_4Ti_4O_{15}$ (SBTi), $SrBi_2Ta_2O_9$ (SBTa), $La_{0.75}Bi_{3.25}Ti_3O_{12}$ (BLT), etc., were recognized as excellent materials for non-volatile ferroelectric memory with a short access time [6–10]. Bi_3TiNbO_9 (BTNO) with $m = 2$, which consists of $(Bi_2O_2)^{2+}$ layers between which two layers of $BiTiNbO_7$ are inserted [17], is promising for the manufacture of high-temperature piezoelectric sensors due to their very high Curie temperature T_C (914 °C), despite the fact that the BTNO ceramic piezoelectric module is rather low ($d_{33} < 7$ pC/N) [11].

It was shown in numerous examples [12–20] that substitutions of both *A* and *B* positions of the APs crystal lattice lead to changes in the structure and dielectric properties and significantly affect the polarization processes in these compounds. In this work, we synthesized and studied the crystal lattice, the dielectric and electrophysical characteristics of a number of new solid solutions of layered perovskite-like oxides $Bi_{3-x}Nd_xTiNbO_9$ ($x = 0, 0.2, 0.4, 0.6, 0.8, 1.0$) with corresponding ratio of the number of Bi^{3+} and Nd^{3+} ions in position *A* of the substituted solutions, that affects the dielectric characteristics and the value of the Curie temperature T_C.

2 Experimental Technique

The polycrystalline samples of the solid solutions of layered perovskite-like oxides $Bi_{3-x}Nd_xTiNbO_9$ ($x = 0$, 0.2, 0.4, 0.6, 0.8, 1.0) were synthesized by solid-phase reaction of the corresponding oxides Bi_2O_3, TiO_2, Nb_2O_5 and Nd_2O_3. After weighing and preliminary grinding of the starting compounds, the synthesis was carried out at a temperature of 875 °C (6 h) with following repeated grinding and pressing of tablets with a diameter of 10 mm and a thickness of 1–1.5 mm and final firing at a temperature of 1100 °C (4 hours). X-ray diffraction spectra of the powder were obtained on a DRON-3 M diffractometer with an attachment for powder diffraction GP-13 and an X-ray tube BSV21-Cu. $CuK\alpha_1$, α_2 radiation was extracted from the general spectrum using a Ni-filter. The diffraction patterns were recorded in the range of 2θ-angles from 10° to 65° with a step of 0.04° and an exposure during 4 s. An analysis of the spectrum profile with finding the positions of the lines and their indication (*hkl*) in accordance with the selected unit cell model was carried out using the PCW-2.4 program [21].

For electrical measurements, Ag-Pd electrodes were applied to the flat surfaces of ceramic samples. The measurements were carried out using an E7-20 immitance meter in the frequency range of 100 kHz–1 MHz in the temperature range from room temperature to 960 °C.

3 Experimental

The crystal structure of the APs $Bi_{3-x}Nd_xTiNbO_9$ ($x = 0, 0.2, 0.4, 0.6, 0.8, 1.0$) was determined using X-ray powder diffraction. Diffraction patterns of all compounds correspond to the same phase of APs with $m = 2$ (Fig. 1). It was found that all the obtained APs crystallize in the orthorhombic system with the space group of the unit cell $A2_1am$ (36). Table 1 shows the parameters of the unit cells and their volume, the calculated tolerance (the coefficient t), the maximum values of the relative permittivity $\varepsilon/\varepsilon_0$ at a frequency of 100 kHz and the Curie temperature T °C.

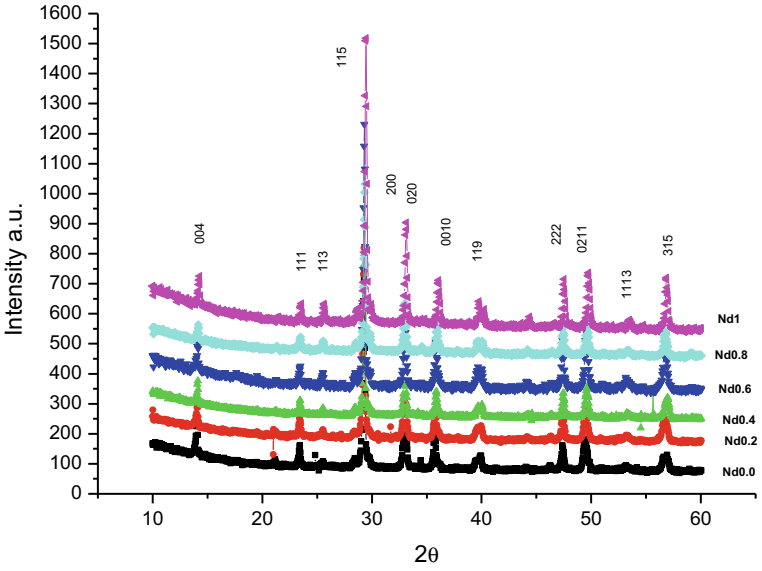

Fig. 1 X-ray diffraction patterns of $Bi_{3-x}Nd_xTiNbO_9$ ($x = 0, 0.2, 0.4, 0.6, 0.8, 1.0$)

Table 1 Unit cell parameters a, b, c and volume V, tolerance-factor t, relative permittivity $\varepsilon/\varepsilon_0$ at frequency of 100 kHz and Curie temperature T_C

	Compound	a, Å	b, Å	c, Å	V, Å^3	t	T_C	$\varepsilon/\varepsilon_0$
1	Bi_3TiNbO_9	5.4004	5.4259	25.1101	738.028	0.9717	920	1300
2	$Bi_{2.8}Nd_{0.2}TiNbO_9$	5.4031	5.4328	25.0519	735.372	0.9691	890	1190
3	$Bi_{2.6}Nd_{0.4}TiNbO_9$	5.3881	5.4151	24.9295	727.37	0.9666	851	550
4	$Bi_{2.4}Nd_{0.6}TiNbO_9$	5.4074	5.4284	24.992	733.603	0.964	760	400
5	$Bi_{2.2}Nd_{0.8}TiNbO_9$	5.4285	5.4452	25.0399	740.16	0.9614	590	175
6	$Bi_2NdTiNbO_9$	5.507	5.5538	25.5388	775.07	0.9589	430	140

As we can see from Table. 1, the volume of the unit cell in the indicated series of solid solutions decreases with increasing x to 0.4 and has an almost linear character. It should be noted that the unit cell parameters increase from $x = 0.4$ to $x = 1$, while the Curie temperature continues to decrease. A decrease in the unit cell parameters in the range from $x = 0.0$ to $x = 0.4$ and the Curie temperature in the entire range from $x = 0.0$ to $x = 1.0$ is associated with the difference in ionic radii in positions A of perovskite-like layers, where Bi^{3+} ions are replaced by ions of a smaller radius Nd^{3+} ($R_{Bi}^{4+} = 1.38$ Å, $R_N^{d3+} = 1.27$ Å). It can be noted that a decrease in the cell volume with increasing x in the range from $x = 0.0$ to $x = 0.4$ is due to a significant decrease in the parameter c along the [001] crystallographic direction, while the parameters a and b decrease insignificantly. Changes in the unit cell parameters of $Bi_{3-x}Nd_xTiNbO_9$ ($x = 0$, 0.2, 0.4, 0.6, 0.8, 1.0) solid solutions in the range from $x =$ 0.0 to $x = 0.4$ with the APs structure are linear in accordance with Vegard's law.

The obtained values of rhombic $\delta b = (b–a)/a$ and tetragonal distortion can serve as one of the parameters characterizing different degrees of distortion of oxygen octahedra of the perovskite layer. Relative elongation of a pseudocubic cell in a perovskite-like layer along the c-axis, $\delta c' = (c' - a_t)/a_t$ is the deviation of the unit cell from the cubic shape, elongation or shortening along the c- axis (where $a_t = (a + b)/2$ is the average value of the tetragonal period, $c' = 3c/(8 + 6m)$ is the average thickness of a single perovskite layer) (Table 2) [4].

As we can see from Table 2, when the value of the parameter x changes from 0 to 0.4 in the APs, a decrease in the rhombic distortion of the pseudoperovskite cell is observed in comparison with undoped Bi_3TiNbO_9. For the entire series of APs, a decrease in the tolerance coefficient t occurs due to a decrease in the number of Bi^{3+} ions with the largest ionic radius, as well as a decrease in the average value of the tetragonal period and the average thickness of one perovskite layer in the range $x =$ 0–0.4. For APs in the range $x = 0$–0.4, the tetragonal distortion changes little; the octahedra are in a compressed state along the c-axis in pseudoperovskite layers.

The relative permittivity $\varepsilon/\varepsilon_0$ and the tangent of the dielectric loss angle tanδ were measured for $Bi_{3-x}Nd_xTiNbO_9$ ($x = 0$, 0.2, 0.4, 0.6, 0.8, 1.0) at frequencies from 100 to 1000 kHz (Fig. 2 a, b, c). The temperature dependences of the dielectric constant

Table 2 V is the unit cell volume, a_t is the parameter of the tetragonal period, c' is the octahedron height along c-axis, δc' is the deviation of the unit cell from the cubic shape, δb is the rhombic distortion and c_0 is the bismuth-oxygen layer and activation energy E_a in various temperature regions

Compound	a_t, Å	c', Å	δc', %	δb, %	c_0, Å	$E_1/E_2/E_3$
Bi_3TiNbO_9	3.833	3.7665	–1.7	0.436	5.02	1.2/0.6/0.02
$Bi_{2.8}Nd_{0.2}TiNbO_9$	3.8311	3.7577	–1.9	0.3928	4.01	0.76/0.24/0.04
$Bi_{2.6}Nd_{0.4}TiNbO_9$	3.8195	3.7394	–2.09	0.3297	4.9859	0.79/0.25/0.031
$Bi_{2.4}Nd_{0.6}TiNbO_9$	3.831	3.748	–1.7	0.436	4.998	0.76/0.23/0.03
$Bi_{2.2}Nd_{0.8}TiNbO_9$	3.844	3.75	–2.5	0.436	5.007	0.8/0.23/0.03
$Bi_2NdTiNbO_9$	3.91	3.83	–1.7	0.436	5.107	0.47/0.09/0.025

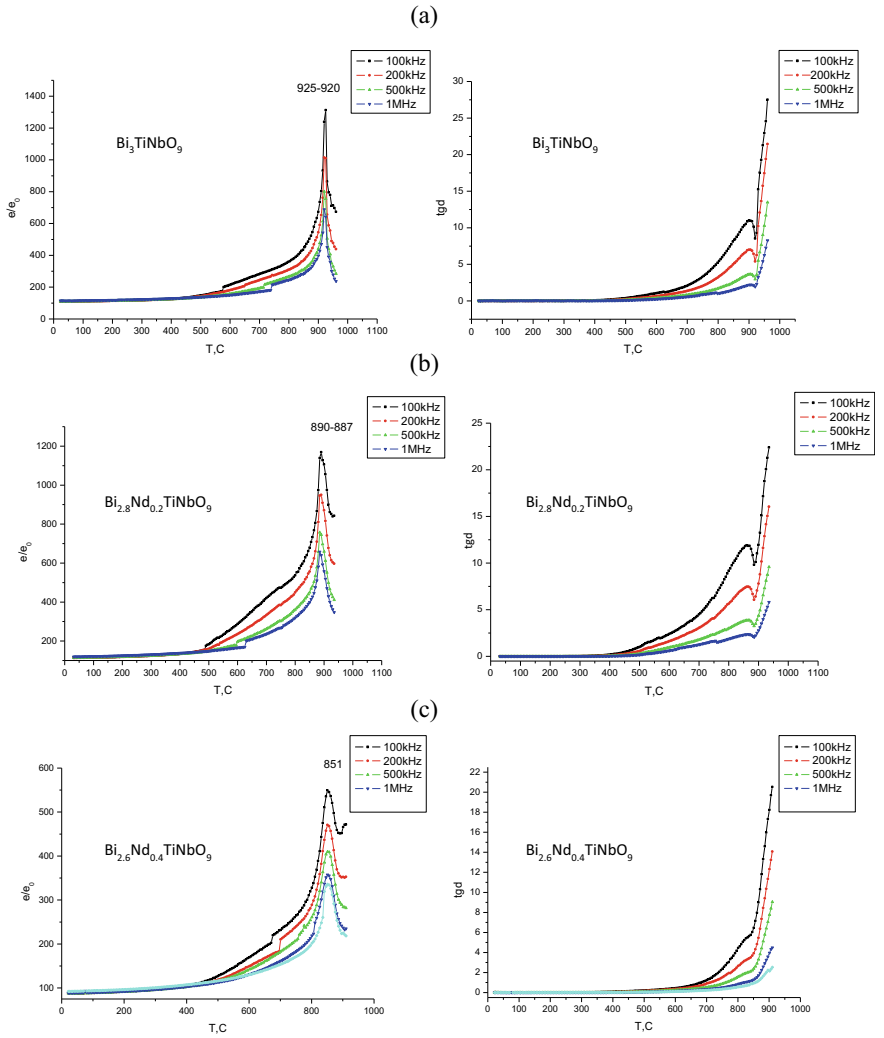

Fig. 2 Temperature dependence of the relative permittivity $\varepsilon/\varepsilon_0$ and the loss tan δ for APs $Bi_{3-x}Nd_xTiNbO_9$ ($x = 0, 0.2, 0.4, 0.6, 0.8, 1.0$) at 0.1–1.0 MHz: **a** Bi_3TiNbO_9, **b** $Bi_{2.8}Nd_{0.2}TiNbO_9$, **c** $Bi_{2.6}Nd_{0.4}TiNbO_9$, **d** $Bi_{2.4}Nd_{0.6}TiNbO_9$, **e** $Bi_{2.2}Nd_{0.8}TiNbO_9$, **f** $Bi_2NdTiNbO_9$

have sharp maxima in the range $x = 0$–0.6, the position of which is related to the Curie temperature for these compounds. Accordingly, at Curie temperatures, clear minima appear on the dielectric loss curves in the range $x = 0$–0.6. The frequency dependence of the position of the maximum dielectric constant is observed for all APs, which indicates the absence of relaxor properties in these compounds. The minimum Curie temperature $T_C \approx 430$ °C was obtained for the composition $Bi_2NdTiNbO_9$. Along with an increase in the parameter x, the Curie temperature T_C in the APs studied

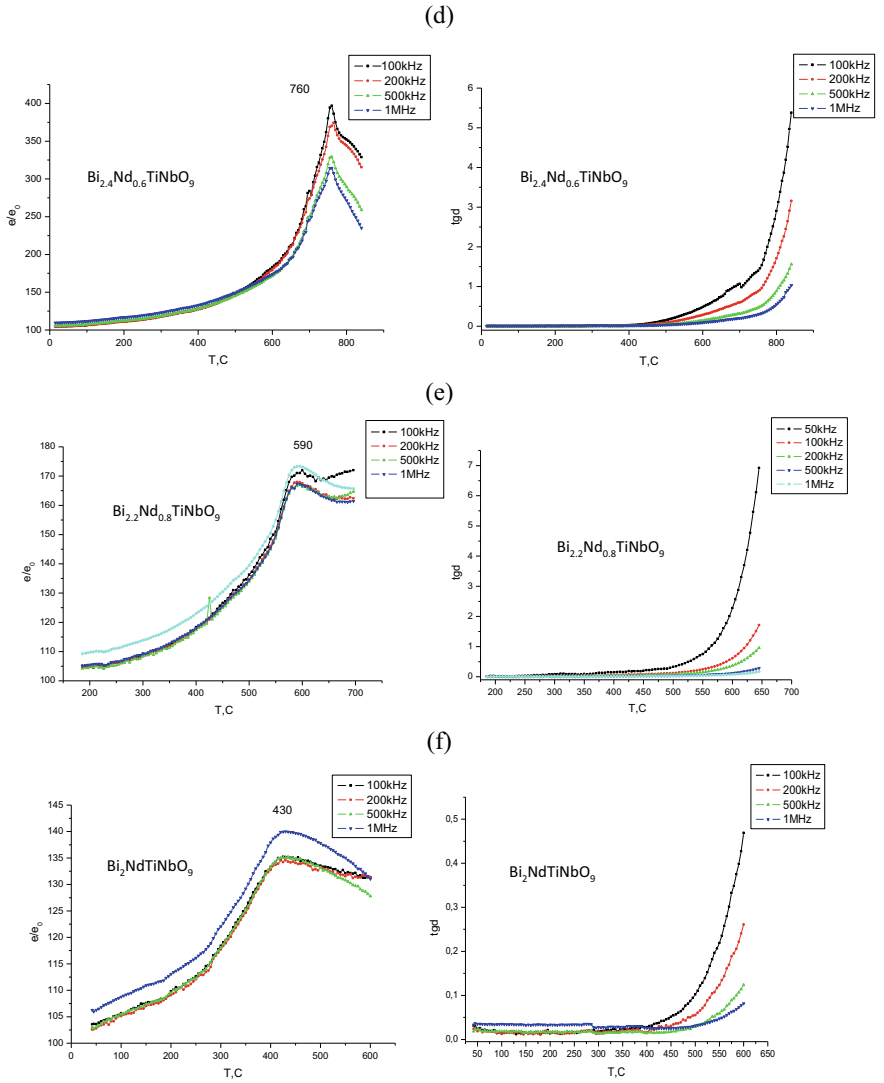

Fig. 2 (continued)

decreases. This dependence is directly related to the correlation between the tolerance coefficient and the temperature T_C, which is characteristic of APs [19, 21]. The tolerance factor t was introduced by Goldschmidt [22] as a parameter that determines the packing of ions in cubic cells:

$$t = (R_A + R_O)/(2^{1/2}(R_B + R_O)), \quad (1)$$

where R_A and R_B are the radii of the cations in positions A and B, respectively, and R_O is the radius of the oxygen ion. Subsequently, this rule was also used to determine the stability of layers of perovskite-like fuel assemblies $[A_{m-1}B_mO_{3m+1}]^{2-}$. When calculating t in this work, we took the Shannon ionic radii [O^{2-} (CN = 6); R_O = 1.40 Å, R_{Bi}^{3+} (CN = 12); R_{Bi}^{3+} = 1.38 Å, R_{Nd}^{3+} (CN = 12); R_{Nd}^{3+} = 1.27 Å, R_{Nb}^{5+} (CN = 6); R_{Nb}^{5+} = 0.64 Å, R_{Ti}^{4+} (CN = 6); R_{Ti}^{4+} = 0.605 Å]. Shannon [22] did not show the ionic radii of R_{Bi}^{3+} for coordination number CN = 12. All ionic radii were determined from the dependence of the ionic radii on the coordination numbers extrapolated to the region of high values. As can be seen from the data in Table 1, for the cases $Bi_{3-x}Nd_xTiNbO_9$ (x = 0, 0.2, 0.4, 0.6, 0.8, 1.0), there is a close to linear dependence on T for the calculated values of the tolerance coefficients t, which makes it possible to predict its value for other values of x in the investigated temperature range.

The temperature dependences of the tangent of the loss angle tanδ (Fig. 2) show a decrease in dielectric losses with decreasing temperature. This is due to the number of charge carriers, the concentration of which decreases with decreasing temperature due to a decrease in oxygen vacancies. However, when considering the tanδ values for different APs at a fixed temperature, for example, T_C, it was found that they differ several times, which indicates a significantly different degree of defectiveness of the APs crystal structure.

The values of the activation energy E_a of charge carriers in $Bi_{3-x}Nd_xTiNbO_9$ (x = 0, 0.2, 0.4, 0.6, 0.8, 1.0) were obtained in low- and high-temperature regions. A typical dependence of ln σ on 1/T, where σ is the specific conductivity, from which the values of E_a were determined, as is shown in Fig. 2 for fuel assemblies $Bi_{2.8}Nd_{0.2}TiNbO_9$.

It can be clearly seen from Fig. 3 that there are three temperature regions in which E_a has significantly differing values. This is due to the fact that in the high-temperature region, the main charge carriers in the APs are intrinsic defects, the

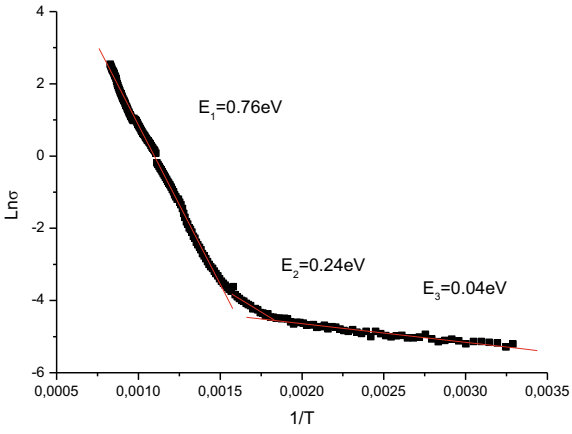

Fig. 3 Dependence of ln σ on 1/T for the $Bi_{2.8}Nd_{0.2}TiNbO_9$ sample at a frequency of 1 MHz

formation of which requires large values of activation energy. At low temperatures, the activation energy E_a is determined mainly by impurity defects, which have significantly lower values.

4 Conclusion

A new series of layered perovskite-like oxides $Bi_{3-x}Nd_xTiNbO_9$ ($x = 0$, 0.2, 0.4, 0.6, 0.8, 1.0) has been synthesized. X-ray diffraction studies have shown that all compounds are single-phase and have a structure similar to the APs with an orthorhombic unit cell (space group $A2_1am$). Nd is the only element in the lantanide series, when doped, the temperature of the base compound decreases. As can be seen, the replacement of Bi^{3+} ions with Nd^{3+} ions leads to a decrease in the parameters of the crystal lattice in the range of $x = 0$, 0.2, 0.4, 0.6. This series $Bi_{3-x}Nd_xTiNbO_9$ ($x = 0$, 0.2, 0.4, 0.6, 0.8, 1.0) was synthesized and studied for the first time.

Acknowledgements The study was financially supported by the Russian Science Foundation (Grant No. 21-19-00423).

References

1. B. Aurivillius, Arkiv. Kemi. **1**, 463 (1949)
2. B. Aurivillius, Arkiv. Kemi. **1**, 499 (1949)
3. B. Aurivillius, Arkiv. Kemi. **37**, 512 (1950)
4. S.V. Zubkov, V.G. Vlasenko, J. Phys. Solid State. **59**(12), 2325 (2017)
5. S.V. Zubkov, V.G. Vlasenko, V.A. Shuvaeva, S.I. Shevtsova, J. Phys. Solid State. **58**(1), 44 (2016)
6. A. Ando, M. Kimura, Y. Sakabe, J. Appl. Phys. **42**, 520 (2003)
7. R.Z. Hou, X.M. Chen, J. Mater. Res. **20**, 2354 (2005)
8. R.Z. Hou, X.M. Chen, Solid State Commun. **130**, 469 (2004)
9. Y. Noguchi, I. Miwa, Y. Goshima, M. Miyayama, Jpn. J. Appl. Phys. **39**, 1259 (2000)
10. Y. Yao, C. Song, P. Bao, D. Su, D.X. Lu, J. Appl. Phys. **95**, 3126 (2004)
11. A. Moure, L. Pardo, C. Alemany, J. Eur. Ceram. **21**, 1399 (2001)
12. V.G. Vlasenko, S.V. Zubkov, V.A. Shuvaeva, Phys. Solid State. **57**, 900 (2015)
13. Z.Y. Zhou, X.L. Dong, H. Chen, H.X. Yan, J. Am. Ceram. Soc. **89**, 1756 (2006)
14. Z.X. Cheng, X.L. Wang, Appl. Phys. Lett. **90**, 222902 (2007)
15. R. Aoyagi, H. Takeda, S. Okamura, T. Shiosaki, Mater. Res. Bull. **38**, 25 (2003)
16. H.X. Yan, C.G. Li, J.G. Zhou, Jpn. J. Appl. Phys. **40**, 6501 (2001)
17. Z.X. Cheng, X.L. Wang, Appl. Phys. Lett. **89**, 032901 (2006)
18. Z.G. Gai, J.F. Wang, Appl. Phys. Lett. **90**, 052911 (2007); J. Phys. D, **43**, 242001 (2010)
19. M. Matsushita, R. Aoyagi, H. Takeda, Jpn. J. Appl. Phys. **43**, 7164 (2004)
20. Z.X. Cheng, X.L. Wang, J. Appl. Phys. **107**, 084105 (2010)
21. W. Kraus, G. Nolze, Powder Cell for Windows, Version2.3. Fed. Inst. Mater. Res. Test., Berlin (1999)
22. R.D. Shannon, Acta Crystallogr. Sect. A: Cryst. Phys. Diffr. Theor. Gen. Crystallogr. **32**, 75 (1976)

Structure and Dielectric Properties of Solid Solutions $Bi_7Ti_{4-x}Sn_xNbO_{21}$ (X = 0.0, 0.1, 0.2, 0.3, 0.4)

S. V. Zubkov and Y. A. Bulygin

Abstract The structural and electrophysical characteristics of a number of solid solutions of layered oxides of the perovskite-type $Bi_7Ti_{4-x}Sn_xNbO_{21}$ ($x = 0.0, 0.1, 0.2, 0.3, 0.4$) are studied. According to X-ray powder diffraction data, all the compounds studied are single-phase and have the structure of Aurivillius phases ($m = 2.5$) with a rhombic crystal lattice (space group I2cm, $Z = 2$). Changes in tetragonal and rhombic distortions of perovskite-like layers in compounds were considered depending on their chemical composition. The temperature dependences of the relative permittivity $\varepsilon(T)$ were measured. It was shown that the Curie temperature T_C of the perovskite-type oxides $Bi_7Ti_{4-x}Sn_xNbO_{21}$ ($x = 0.0, 0.1, 0.2, 0.3, 0.4, 0.5$) linearly decreases with increasing parameter x. The activation energies of charge carriers were obtained in different temperature ranges. It was found that there are three temperature regions with very different activation energies due to the different nature of the charge carriers in the studied compounds. The effect of substitution of Bi^{3+} ions by Sn^{4+} ions are investigated. It was found that for a number of compounds, the substitution of niobium ions by vanadium ions led to an increase in the dielectric constant and a decrease in the dielectric loss.

Keywords Layered perovskite-like oxides · Solid solutions · Aurivillius phases (APs) · Dielectric constant · Curie temperature

1 Introduction

Aurivillius phases (APs) [1–3] form a large family of bismuth-containing layered perovskite type compounds, with the chemical composition described by the general

S. V. Zubkov (✉)
Research Institute of Physics, Southern Federal University, 194, Stachki Ave., Rostov-on-Don 344090, Russia
e-mail: svzubkov61@mail.ru

Y. A. Bulygin
Department "International", Don State Technical University, 1, Gagarina, Rostov-on-Don 344090, Russia

I. A. Parinov et al. (eds.), *Physics and Mechanics of New Materials and Their Applications*, Springer Proceedings in Materials 10,
https://doi.org/10.1007/978-3-030-76481-4_16

formula $A_{m-1}Bi_2B_mO_{3m+3}$. The crystal structure of Aurivillius phases consists of alternating layers $[Bi_2O_2]^{2+}$, which are separated by m perovskite-like layers $[A_{m-1}B_mO_{3m+1}]^{2-}$, where A are the ions with large radii (Bi^{3+}, Ca^{2+}, Nd^{3+}, Sr^{2+}, Ba^{2+}, Pb^{2+}, Na^{+}, $K+$, Y^{3+}, Ln^{3+} (lanthanides)) have the dodecahedral coordination, whereas the B-positions inside oxygen octahedra are occupied by ions with small radii (Ti^{4+}, Nb^{5+}, Ta^{5+}, W^{6+}, Mo^{6+}, $Fe3^{+}$, Mn^{4+}, Cr^{3+}, Ga^{3+}, etc.). At present, considerable interest has been expressed in APs owing to potential practical applications associated with their extraordinary properties. APs are promising materials for use in the design and fabrication of high temperature piezoelectric sensors operating under extreme conditions. Moreover, these materials are considered as elements for nonvolatile ferroelectric random-access memory (FeRAM) devices [4, 5] and as multifunctional materials that exhibit magnetic properties (multiferroics) [6, 7], photoluminescence [8–10], etc. A substantial variability of the composition due to the substitution of A- and B-ions, as well as of the crystal structure due to variations in the number of layers $m = 1$–6, made it possible to obtain a large number of APs [11, 12]. A priority task is to determine correlations between the composition, structure, and dielectric characteristics of new APs. As was shown in our previous study [13], the modification of the composition of well-known APs by means of the addition of small amounts of donor dopants, such as W^{6+}, V^{5+}, Re^{7+}, and others, leads to a decrease in the number of oxygen vacancies, a decrease in the leakage current, and an improvement of the piezoelectric properties of APs ceramics. Moreover, there is an increase of the dielectric permittivity of the doped APs, as well as of their Curie temperature T_C, even though, to a lesser extent. For example, tungsten-doped SBT ceramics of the composition $SrBi_2$ $(W_xTa_{1-x})_2O_9$ ($x = 0$–0.2) demonstrated an increase in the remanent polarization with an increase in the tungsten concentration to $x \leq 0.075$ [14–18].

For APs $Bi_3Ti_{1-x}Sn_xNbO_9$, Zubkov et al. [19] investigated the effect of titanium tin substitution on the structure and dielectric properties. It was shown that the Curie temperature T_C increases and the maximum dielectric constant increases with increasing tin concentration. These changes in the dielectric characteristics of the APs were explained by a decrease in the tolerance factor for doped structures, since the Sn^{4+} ion has a larger ionic radius (0.69 Å for a coordination number (CN = 6) compared to Ti^{4+} ion (0.605 Å, CN = 6). The $Bi_7Ti_4NbO_{21}$ compound belongs to secondary APs with $m = 2.5$, in which layers of the initial APs with $m = 2$ (Bi_3TiNbO_9) and $m = 3$ ($Bi_4Ti_3O_{12}$) alternate regularly. This compound was previously found to have a higher remanent polarization compared to the two parent APs [20, 21].

In this work, we investigated the relationship between the structural characteristics and the electrophysical properties of a number of solid solutions APs $Bi_7Ti_{4-x}Sn_xNbO_{21}$ ($x = 0.0$, 0.1, 0.2, 0.3, 0.4) depending on the chemical composition. X-ray diffraction studies were carried out and the temperature dependences of the dielectric characteristics of new APs from the series: $Bi_7Ti_4NbO_{21}$, $Bi_7Ti_{3.9}Sn_{0.1}NbO_{21}$, $Bi_7Ti_{3.8}Sn_{0.2}NbO_{21}$, $Bi_7Ti_{3.7}Sn_{0.3}NbO_{21}$,

$Bi_7Ti_{3.6}Sn_{0.4}NbO_{21}$ were measured.

2 Experimental

Polycrystalline samples of APs were synthesized by the solid-phase reaction of the corresponding high purity oxides Bi_2O_3, SnO_2, TiO_2, Nb_2O_5. After weighting in accordance with the stoichiometric composition and a thorough grinding of the initial compounds with the addition of ethyl alcohol, the pressed samples were calcined at a temperature of 890 °C for 2 h. Then, the samples were repeatedly ground and pressed into pellets with a diameter of 10 mm and a thickness of 1.0–1.5 mm, followed by the final synthesis of APs at a temperature of 1120 °C (for 4 h). The X-ray diffraction patterns were recorded on a D2BRUKE diffractometer with a Cu X-ray tube. The Cu $K_{\alpha 1,\alpha 2}$ radiation was separated from the total spectrum with the use of a Ni-filter. The X-ray diffraction patterns were measured in the range of 2θ angles from 10° to 65° with a scan step of 0.02° and an exposure of 10 s per point. The analysis of the profiles of the diffraction patterns, the determination of the positions of the lines, their indexing (*hkl*), and refinement of the unit cell parameters were performed by using the PCW 2.4 program [22]. For dielectric permittivity and electrical conductivity measurements, on flat surfaces of APs samples in the form of disks with a diameter of 10 mm and a thickness of approximately 1 mm, electrodes were deposited using an Ag-Pd paste annealed at a temperature of 820 °C (for 1 h). The temperature and frequency dependences of the dielectric characteristics were measured using an E7-20 immittance meter in the frequency range from 100 kHz to 1 MHz and at temperatures in the range from room temperature to 900 °C.

3 Results and Discussion

Powder X-ray diffraction patterns of all investigated solid solutions $Bi_7Ti_{4-x}Sn_xNbO_{21}$ ($x = 0.1, 0.2, 0.3, 0.4$) correspond to single-phase APs with $m = 2.5$ and do not contain additional reflections. Figure 1 shows a powder X-ray diffraction pattern of a $Bi_7Ti_{4-x}Sn_xNbO_{21}$ ($x = 0.0, 0.1, 0.2, 0.3, 0.4$). It was found that all synthesized APs crystallize in an orthorhombic system with a unit cell space group I2cm (46).

(space group I2cm).

For the studied APs samples $Bi_7Ti_{4-x}Sn_xNbO_{21}$ ($x = 0.1, 0.2, 0.3, 0.4, 0.5$), the obtained unit cell parameters are close to those determined earlier: $a = 5.4469$ (4) Å, $b = 5.4121$ (4) Å, $c = 58.0429$ (47) Å [23]; $a = 5.45$ Å, $b = 5.42$ Å, $c = 58.1$ Å [24]; $a = 5.44$ Å, $b = 5.40$ Å, $c = 58.1$ Å [25]; $a = 5.442$ (1) Å, $b = 5.404$ (1) Å, $c = 57.990$ (12) Å (single crystal) [26]. The unit cell structure of APs $Bi_7Ti_4NbO_{21}$ can be described as the alternation of halves of the initial phases with $m = 2$ (Bi_3TiNbO_9) and $m = 3$ ($Bi_4Ti_3O_{12}$). It was previously found that this compound has a higher residual polarization compared to the two initial phases of Aurivillius along the *c*-axis, where the $BiTiNbO_7$ building blocks contain an equal amount of Ti^{4+} and Nb^{5+} ions in the perovskite layer and are separated.

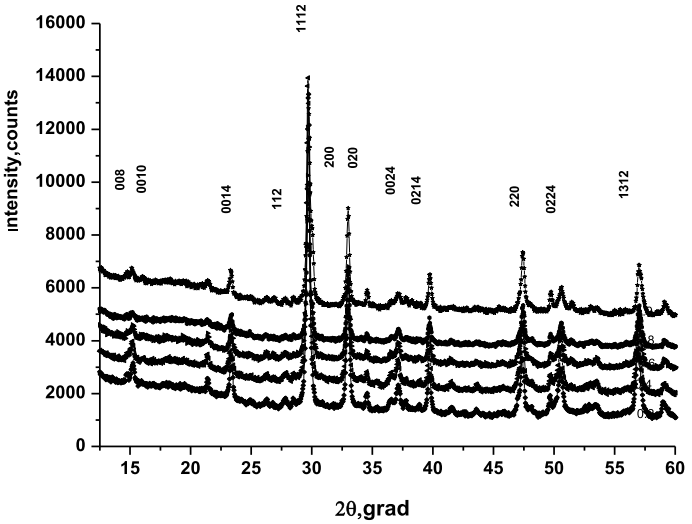

Fig. 1 X-ray powder diffraction patterns of $Bi_7Ti_{4-x}Sn_xNbO_{21}$ ($x = 0.0, 0.1, 0.2, 0.3, 0.4$)

These effects can also be associated with the partial ordering of atoms in the perovskite sublattice due to the significant difference in the radii of atoms located in the same positions in the perovskite layer. To obtain the degree of distortion of the ideal structure of perovskite in Gd^{3+}, we determined the tolerance coefficient t, which is presented in Table 1. The tolerance coefficient was introduced by Goldschmidt [27] as a parameter that determines the packing of ions in cubic unit cells:

$$t = (R_A + R_O)/2^{1/2}(R_B + R_O) \quad (1)$$

where R_A and R_B are the radii of cations in positions A and B, respectively; R_O is the ionic radius of oxygen. In this work, the tolerance coefficient t was calculatedtakinginto accountthe Shannon ionic radii offor the corresponding coordination numbers (CN) (O^{2-} (CN = 6) $R_O = 1.40$ Å, Sn^{4+} (CN = 6) $R_{Sn}{}^{4+} = 0.69$ Å, Nb^{5+} (CN = 6) $R_{Nb} = 0.64$ Å, Ti^{4+} (CN = 6) $R_{Ti} = 0.605$ Å). Shannon [28] did not provide the ionic radius of Bi^{3+} for coordination with CN = 12. Therefore, its

Table 1 Dielectric characteristics of $Bi_7Ti_{4-x}Sn_xNbO_{21}$ ($x = 0.0, 0.1, 0.2, 0.3, 0.4$)

	Compounds	t-factor	$\varepsilon/\varepsilon_0$ (T_1/T_2), 100 kHz	T_1, C	T_2, C	$E_1/E_2/E_3$, eV
1	$Bi_7Ti_4NbO_{21}$	0.973	1800/700	850	665	1.2/0.7/0.02
2	$Bi_7Ti_{3.9}Sn_{0.1}NbO_{21}$	0.972	1300/900	861	691	0.95/0.91/0.1
3	$Bi_7Ti_{3.8}Sn_{0.2}NbO_{21}$	0.9718	1350/1000	851	691	1.5/0.7/0.06
4	$Bi_7Ti_{3.7}Sn_{0.3}NbO_{21}$	0.971	1500/700	855	680	1.07/0.69/0.04
5	$Bi_7Ti_{3.6}Sn_{0.4}NbO_{21}$	0.97	1350/570	860	680	1.05/0.65/0.09

value was determined from the ionic radius with CN = 8 (R_{Bi} = 1.17 Å) multipliedby an approximation factor of 1.136, then for Bi^{3+} (CN = 12) we got R_{Bi} = 1.33 Å.

In addition to the results of structural studies, temperature dependences of the relative permittivity ε were obtained at various frequencies of 100–1000 kHz and various activation energies of charge carriers E_a in a wide temperature range. Figure 2 shows the temperature dependences of the relative permittivity $\varepsilon(T)$ and the loss tan

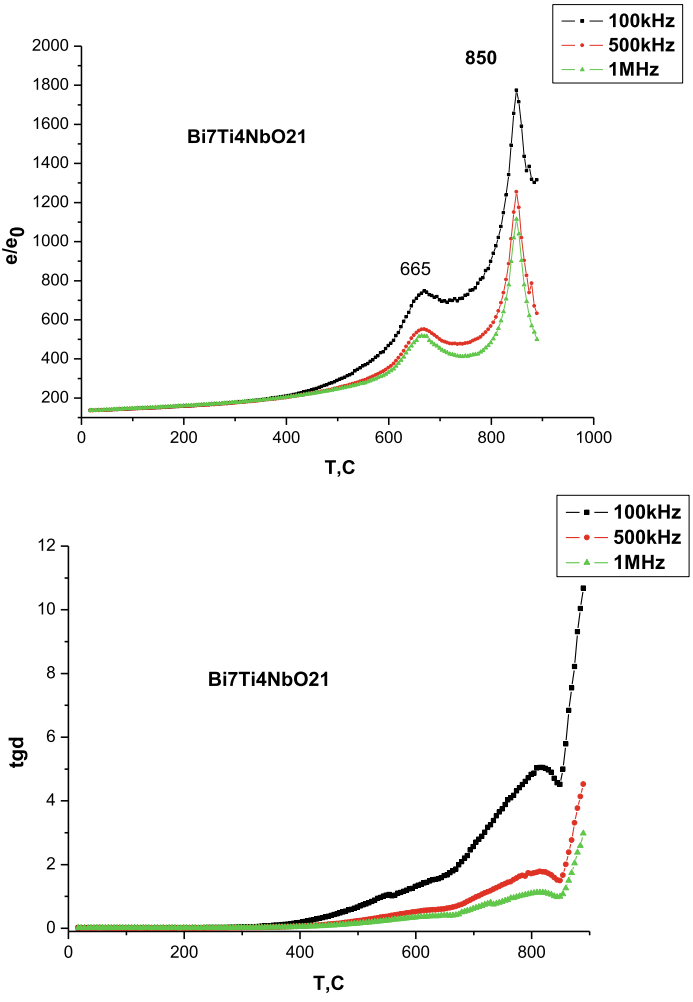

Fig. 2 Temperature dependences of the relative permittivity $\varepsilon/\varepsilon_0$ and the loss tan δ for APs $Bi_7Ti_{4-x}Sn_xNbO_{21}$ (x = 0.0, 0.1, 0.2, 0.3, 0.4) at a frequency of 100 kHz: $Bi_7Ti_4NbO_{21}$, $Bi_7Ti_{3.9}Sn_{0.1}NbO_{21}$, $Bi_7Ti_{3.8}Sn_{0.2}NbO_{21}$, $Bi_7Ti_{3.7}Sn_{0.3}NbO_{21}$, $Bi_7T_{3.6}Sn_{0.4}NbO_{21}$

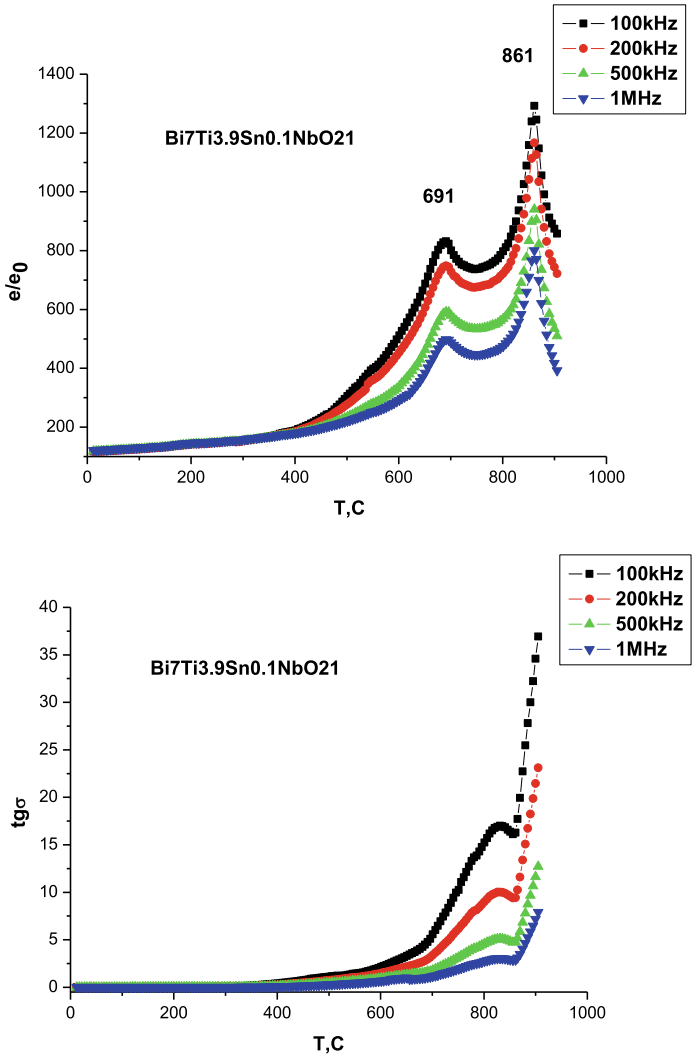

Fig. 2 (continued)

δ for $Bi_7Ti_{4-x}Sn_xNbO_{21}$ ($x = 0.0, 0.1, 0.2, 0.3, 0.4$) at a frequency of 100 kHz – 1 MHz. All $\varepsilon(T)$ dependences have two features at temperatures T_1 and T_2, for which the corresponding values of the permittivity are given in Table 1. The first peak on the $\varepsilon(T)$ dependence at temperature T_2 corresponds to the phase transition from the polar to the polar phase (ferroelectric–ferroelectric), this transition in the temperature range from T_1 to T_2 is accompanied by the removal of distortions for the $Bi_2Ti_3O_{10}$ perovskite block with $m = 3$, while in the $BiTiNbO_7$ perovskite layers with $m = 2$, the distortions of the octahedral layers are retained.

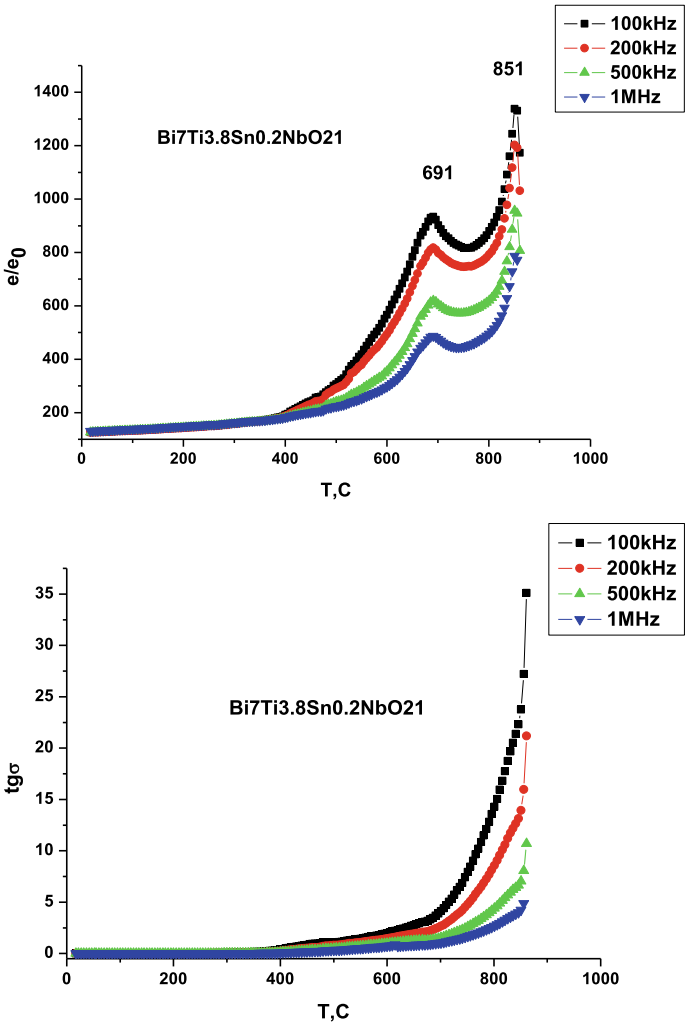

Fig. 2 (continued)

At temperatures above T_1, distortions are removed in both blocks of the perovskite type, and the Sn^{4+} symmetry is close to I4/mmm3. Thus, the temperature T_1 corresponds to the transition from the polar to the nonpolar phase (paraelectric–ferroelectric phase) those are the Curie temperature T_C. Replacement of B ions in Ti^{4+} octahedra by ions with a large ionic radius does not lead to significant changes in the dielectric characteristics of these compounds. Accordingly, one should not expect significant changes in the temperature T_1 from the tolerance coefficient t due to changes in the average radii of the ions B. Figure 2 shows the dependences of the temperatures T_1 and T_2 on the parameters x and t for $Bi_7Ti_{4-x}Sn_xNbO_{21}$,

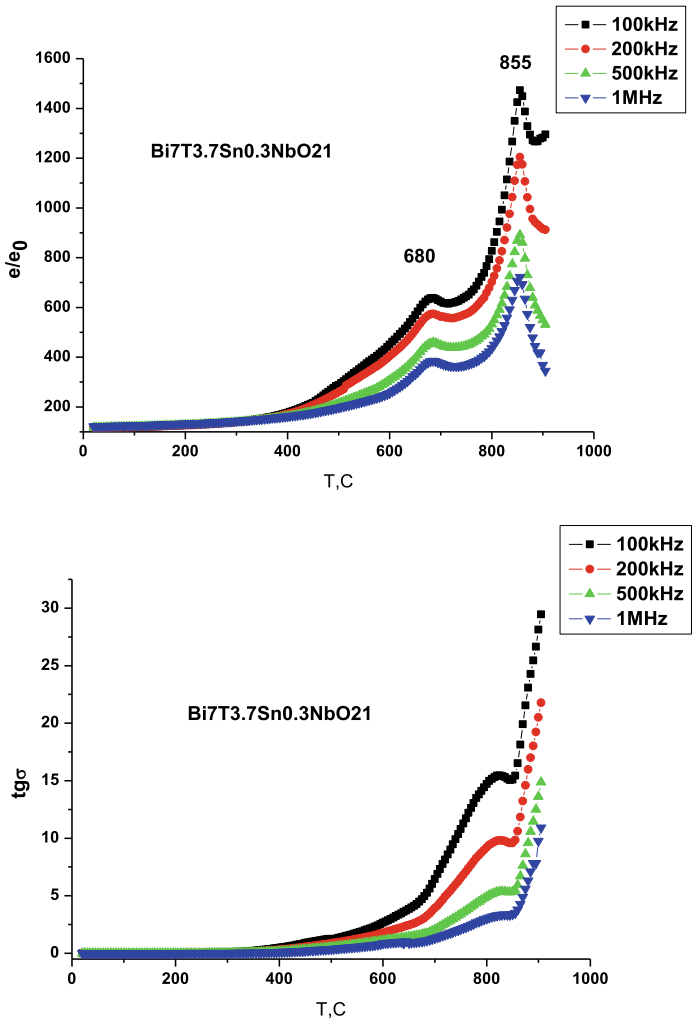

Fig. 2 (continued)

which turned out to be expected for this type of substitution. It should be noted that with an increase in the tin concentration, the increase in the temperature T_2 and T_1 is weakly expressed (it remains practically unchanged for T_1) compared to $T_2(x)$ (which increases by only about 25 °C for $x = 0.1, 0.2$. A possible explanation for the difference in the dependences $T_1(x)$ and $T_2(x)$ can be the assumption that the substitution of Ti^{4+} ions in octahedra for Sn^{4+} ions occur mainly not in the most distorted perovskite layer of $BiTiNbO_7$ with $m = 2$, but to a greater extent in a more symmetric compound $Bi_2Ti_3O_{10}$ with $m = 3$. The maxima on the temperature dependence of the permittivity $\varepsilon(T)$ show the dependence of m on the composition

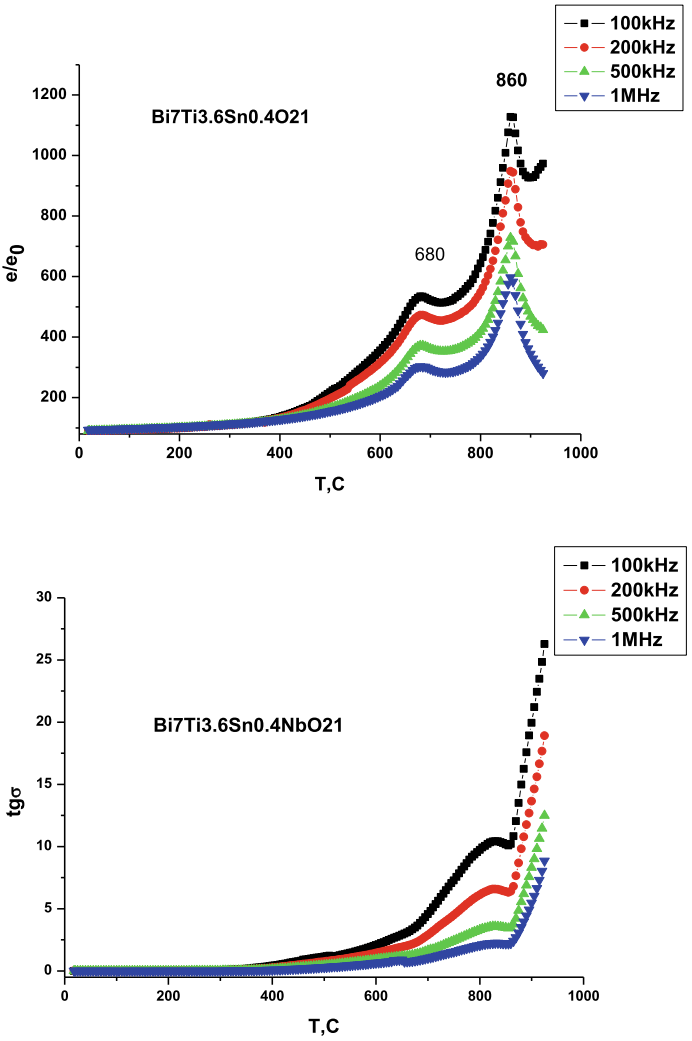

Fig. 2 (continued)

of $Bi_7Ti_{4-x}Sn_xNbO_{21}$ (Table 1). It should be noted that earlier dielectric studies of this system of solid solutions did not reveal any dependence. In our case, we observe a sharp jump in $\varepsilon/\varepsilon_0$ at T_2 for $x = 0.1, 0.2$. Since the dielectric constant $\varepsilon(T)$ depends on many factors (composition, grain size, porosity, concentration of vacancies, etc.), the combination of all these factors usually neutralizes this dependence. A significant increase in the dielectric constant can be explained by the size of the ionic radius, which differs from those previously used for doping. The obtained values of the dielectric loss tangent tan δ for $Bi_7Ti_{4-x}Sn_xNbO_{21}$ ($x = 0.1, 0.2, 0.3, 0.4$) are presented in Fig. 2. For all $Bi_7Ti_{4-x}Sn_xNbO_{21}$ ($x = 0.1, 0.2, 0.3, 0.4$), we observe an

increase in tan δ with increasing x. The obtained values of the activation energy E_a of charge carriers in $Bi_7Ti_{4-x}Sn_xNbO_{21}$ are presented in Table 1.

The activation energy E_a was determined from the Arrhenius equation:

$$\sigma = (A/T)\exp(-E_a/kT) \tag{2}$$

where σ is electrical conductivity, k is Boltzmann constant, and A is constant. A typical dependence of lnσ on $1/kT$ (at a frequency of 100 kHz), which was used to determine the activation energies E_a, is shown in Fig. 3 for the APs $Bi_7Ti_{4-x}Sn_xNbO_{21}$ ($x = 0.1, 0.2, 0.3, 0.4$).

Figure 3 clearly shows that there are three temperature regions, in which the activation energies E_a have significantly different values. For two high-temperature regions, characterized by high activation energies of charge carriers, the values $E_a(1) > E_a(2)$ differ from each other by almost 2 times, and the boundary of the change in the activation energy is close to the phase transition temperature T_1. It should be noted that the values of E_a corresponding to the electrical conductivity in a wide temperature range from 300 °C to T_2 systematically decrease with increasing doping with Nd^{3+} ions for all members of the $Bi_7Ti_{4-x}Sn_xNbO_{21}$ series, while in the high-temperature region above T_1 for E_a such a dependence is not observed. It is known [29] that, in a wide temperature range, the determining factor is ionic conductivity, which occurs by the mechanism of oxygen ions jumping into existing vacancies in the crystal lattice.

This intrinsic conductivity is characterized by relatively high charge carrier activation energies of approximately 1 eV. The doping of Sn^{4+} by different cations can lead to a change in their conductivity, both toward an increase with the formation of additional oxygen vacancies and toward a decrease, when these vacancies are bound with doped metal ions. The systematic decrease in the activation energy in the series of $Bi_7Ti_{4-x}Sn_xNbO_{21}$ with an increase in the concentration of Sn^{4+} ions,

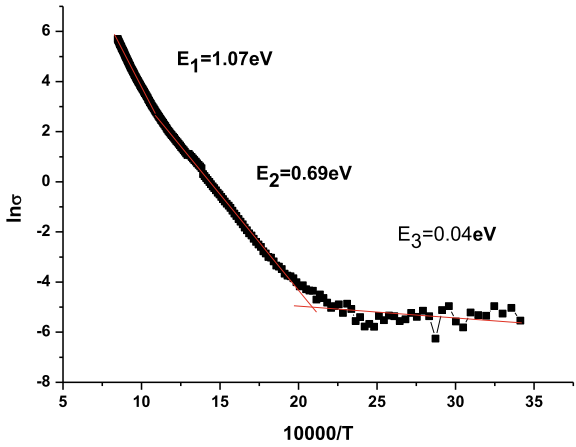

Fig. 3 Dependence of lnσ on 10,000/T for the $Bi_7Ti_{4-x}Sn_xNbO_{21}$ samples

which leads to an increase in the electrical conductivity, indicates the first mechanism of change in the electrical conductivity ofthese Sn^{4+}. The obtained values of for the studied series of $Bi_7Ti_{4-x}Sn_xNbO_2$ are close to the characteristic values of the activation energy (approximately 0.5–1.0 eV) for oxygen vacancies in the Sn^{4+}. The nature of the conductivity in APs at temperatures above T_2 with higher values of E_a (1) > 1.5 eV requires further investigation. In the low-temperature range, the electrical conductivity is predominantly determined by impurity defects with very low activation energies of the order of a few hundredths of an electron-volt.

4 Conclusion

A series of layered bismuth perovskite oxides $Bi_7Ti_{3.9}Sn_{0.1}NbO_{21}$, $Bi_7Ti_{3.8}Sn_{0.2}NbO_{21}$, $Bi_7Ti_{3.7}Sn_{0.7}NbO_{21}$, $Bi_7Ti_{3.6}Sn_{0.4}NbO_{21}$ were synthesized by the solid-state method. The X-ray diffraction studies carried out in our work showed that all the compounds obtained have the PP structure ($m = 2.5$) with an orthorhombic crystal lattice (space group I2cm, $Z = 2$). An analysis of the details of the APs structure showed that an increase in the concentration x of tin x from 0.1 to 0.4 and a partial replacement of bismuth ions with tin ions lead to an increase in the tangent of the dielectric loss angle and a decrease in $\varepsilon/\varepsilon_0$. The temperature dependences $\varepsilon(T)$ in the $Bi_7Ti_{4-x}Sn_xNbO_{21}$ compounds ($x = 0.2$–1.0) exhibit two anomalies: (i) the low-temperature anomaly corresponds to the ferroelectric phase transition, and (ii) the high-temperature anomaly isassociated with the Curie temperature T_C, which corresponds to the ferroelectric phase of the paraelectric transition. Ligation with tin ions (100%) does not lead to a significant shift in low temperature peaks.

Acknowledgements The study was financially supported by the Russian Science Foundation (Grant No. 21-19-00423).

References

1. B. Aurivillius, Arkiv. Kemi. **1**, 463 (1949)
2. B. Aurivillius, Arkiv. Kemi. **58**, 499 (1949)
3. B. Aurivillius, Kemi. **37**, 512 (1950)
4. B.H. Park, B.S. Kang, S.D. Bu, T.W. Noh, J. Lee, W. Jo, Nature (London) **401**, 682 (1999)
5. A.P. de Araujo, J.D. Cuchiaro, L.D. Mcmillan, M.C. Scott, J.F. Scott, Nature (London) **374**, 627 (1995)
6. X. Chen, J. Xiao, Y. Xue, X. Zeng, F. Yang, P. Su, Ceram. Int. **40**, 2635 (2014)
7. V.G. Vlasenko, V.A. Shuvaeva, S.I. Levchenkov, Y.V. Zubavichus, S.V. Zubkov, J. Alloys Compd. **610**, 184 (2014)
8. H. Zou, X. Hui, X. Wang, D. Peng, J. Li, Y. Li, X. Yao, J. Appl. Phys. **114**, 223103 (2013)
9. H. Nakajima, T. Mori, S. Itoh, M. Watanabe, Solid State Commun. **129**, 421 (2004)
10. F. Gao, G.J. Ding, H. Zhou, G.H. Wu, N. Qin, D.H. Bao, J. Electrochem. Soc. **158**(5), G128 (2011)

11. S.V. Zubkov, V.G. Vlasenko, V.A, J. Phys. Solid State, **58**(1), 44 (2016)
12. T. Wang, Hu. Jiacong, H. Yang, Li. Jin, X. Wei, C. Li, F. Yan, Y. Lin, J. Appl. Phys. **121**, 084103 (2017)
13. S.V. Zubkov, V.G. Vlasenko, J. Phys. Solid State. **59**(12), 2325 (2017)
14. I. Coondoo, S.K. Agarwal, A.K. Jha, Mater. Res. Bull. **44**, 1288 (2009)
15. I. Coondoo, N. Panwar, A. K. Jha, Physica B (Amsterdam). **406**, 374 (2011)
16. J.K. Kim, T.K. Song, S.S. Kim, J. Kim, Mater. Lett. **57**(4), 964 (2002)
17. W.T. Lin, T.W. Chiu, H.H. Yu, J.L. Lin, S. Lin, J. Vac. Sci. Technol. A **21**, 787 (2003)
18. Y. Wu, S.J. Limmer, T.P. Chou, C. Nguyen, G.Z. Cao, J. Mater. Sci. Lett. **21**, 947 (2002)
19. S.V. Zubkov**,** J. Advanced Materials, 231 (2020)
20. F. Chu, D. Damjanovic, J. Am. Ceram. Soc. **78**, 3142 (1995)
21. Z.G. Yi, Y. Wang, Y.X. Li, Q.R. Yin, J. Appl. Phys. **99**, 114101 (2006)
22. W. Kraus, G. Nolze, *PowderCell for Windows. Version 2.3* (Federal Institute for Materials Research and Testing, Berlin, 1999)
23. A. Yokoi, H. Ogawa, Mater. Sci. Eng. B **129**, 80 (2006)
24. S. Horiuchi, T. Kikuchi, M. Goto, Acta Crystallogr. Sect. A: Cryst. Phys. Diffr. Theor. Gen. Crystallogr. **33**, 701 (1977)
25. P. Duran, F. Capel, C. Moure, M. Villegas, J.F. Fernandez, J. Tartaj, A.C. Caballero, Eur. Ceram. Soc. **21**, 1 (2001)
26. D. Mercurio, Int. J. Inorg. Mater. **2**(5), 397 (2000)
27. V.M. Goldschmidt, *Geochemische Verteilungsgesetze Der Elemente* (Norske, Oslo, 1927).
28. R.D. Shannon, Acta Crystallogr. Sect. A: Cryst. Phys. Diffr. Theor. Gen. Crystallogr. **32**, 75 (1976)
29. A. Isupov, J. Neorg. Khim. **39**, 731 (1994)

Synthesis, Electronic Structure, Microstructure, and Properties of Vacuum Ion-Plasma Coatings Based on Carbon

Oleg V. Kudryakov, Valery N. Varavka, Igor Yu. Zabiyaka, Andrew V. Sidashov, and Eugeny S. Novikov

Abstract Carbon diamond-like coatings (DLCs) obtained by vacuum ion-plasma technology have been investigated. The study of the microstructure of the coatings was carried out using a high-resolution scanning electron microscope (SEM). The determination of the mechanical properties of the coatings was carried out using the indentation techniques. The study of the electronic structure of the DLC to determine the ratio of electronic configurations sp^3/sp^2 of carbon was carried out by X-ray photoelectron spectroscopy (XPS) using the surface analysis system SPECS by isolating in survey spectra and analyzing the C (KLL) Auger spectra. It is shown that the synthesis of DLC coatings using a gas mixture of acetylene and methylsiloxane forms a gradient distribution of sp^3/sp^2 configurations of carbon, decreasing with depth of the coating. Tests of the tribological properties of coatings were carried out on a TRB friction machine according to the "pin (ball)—plate" scheme. Their results showed that the use of DLC coatings in tribological tests with high loads provides a significant decrease in the coefficient of friction (on average, 2.0–2.5 times). However, this does not guarantee a significant reduction in wear, which is largely determined by the structure of the coating, the wear mechanism and contact phenomena at the "coating-substrate" interface.

Keywords Vacuum ion-plasma technology · Diamond-like coatings (DLCs) · Scanning electron microscopy (SEM) · X-ray photoelectron spectroscopy (XPS) · Indentation · Tribological properties · Wear resistance

O. V. Kudryakov (✉) · V. N. Varavka · I. Yu. Zabiyaka
Department of Physical and Applied Material Science, Don State Technical University, Rostov-on-Don, Russia
e-mail: kudryakov@mail.ru

A. V. Sidashov · E. S. Novikov
Department of Theoretical Mechanics, Rostov State Transport University, Rostov-on-Don, Russia

I. A. Parinov et al. (eds.), *Physics and Mechanics of New Materials and Their Applications*, Springer Proceedings in Materials 10,
https://doi.org/10.1007/978-3-030-76481-4_17

1 Introduction

Among modern methods of surface modification and hardening, vacuum ion-plasma coating is gradually taking the leading position due to the possibility of forming the widest spectrum of functional properties of coatings and their use in a wide variety of industries - from medicine to rocketry. These possibilities are realized due to the practically unlimited combinations of the elemental composition in coatings and the formation of the coating structure at the level of interatomic (or molecular) interactions. Prospects for the development of ion-plasma methods currently lie in the development of new materials and obtaining multifunctional coatings. In this respect, ones of the most attractive research objects in the field of materials science and nanotechnology are carbon materials, in particular, diamond-like coatings (DLCs) . The interest in DLCs is associated with the possibility of relatively simple technological regulation of the ratio of a carbon electronic configurations in the coating: sp^2-bonds, characteristic of graphite, and sp^3-bonds, characteristic of diamond. Due to this variability, the properties of DLCs can also be varied within wide limits: from purely tribotechnical coatings (in the form of solid graphite lubricant) to purely wear-resistant (superhard ones, which are close in hardness to diamond) [1–6]. In this regard, the aim of the work was to study the relationship between the structure of DLCs and their mechanical and tribological characteristics with the prospect of using such coatings in loaded tribocontact pairs.

2 Research Method

The DLCs were applied using a *PLATIT* π^{80} dual-cathode vacuum ion-plasma spraying unit equipped with two arc evaporators with a power of up to 10 kW each. Cleaning of the surface of the samples prior to coating deposition was carried out in a vacuum chamber at a temperature of 300 °C by exposure to a stream of accelerated Ar ions for 5 min. The deposition of the coating was carried out at a temperature of 180–250 °C from a gas mixture of acetylene C_2H_2 and methylsiloxane CH_3-Si–O. This feature of the technology allows the resulting coatings to be classified as CVD coatings. To increase the adhesion of the coating, a number of samples after the surface cleaning operation were subjected to ion implantation (with Nb and Hf ions) in the vacuum chamber of the ion-plasma unit immediately before the deposition of DLCs. The thickness of the coatings varied in the range of 0.4–1.8 μm with optimal values of 1.2–1.4 μm.

The microstructure of coatings, topography of their surface, fractographic features of the friction tracks were studied using a two-beam (electron/ion) scanning electron microscope ZEISS CrossBeam 340 (SEM), which allows using an ion beam (FIB) to etch and perform the sample cross-sections of a given configuration directly in the vacuum chamber of the microscope with high positioning accuracy. The elemental composition of the surfaces under study was monitored using an X-Max 50 N energy

dispersive X-ray detector (EDAX) built into an electron microscope. Dimensional assessment of the thickness of coatings and their layers was performed using the software "AZtec" installed on an electron microscope.

Experimental studies of the electronic structure of the coatings were carried out by X-ray photoelectron spectroscopy (XPS) using the SPECS surface analysis system. An X-ray monochromatic Al-$K\alpha$ line with an energy of 1486.6 eV was used as the exciting radiation. The energy resolution of the analyzer at a constant transmission energy was 0.45 eV on the Ag3d3/2 line. The vacuum during recording of the spectra was maintained at the level of 8×10^{-10} mbar. A survey spectrum was recorded from the coating surface, which was used to determine the qualitative and quantitative composition of the coating surface. In addition, the spectra were used to determine the electronic lines of those chemical elements, by which it is possible to effectively determine the chemical bond in which this or that element participates. It was found experimentally that this relationship changes with depth. To obtain information about these changes, electronic spectra were obtained at different depths from the studied surface of the coatings. In the SPECS surface analysis system, it is possible to carry out layer-by-layer profiling (etching, evaporation) of the coating surface using an ion gun and to take spectra at each depth. Using special built-in software for processing experimental spectra, it is possible to decompose the experimental spectra into components, each of which corresponds to a certain chemical bond [7–10].

The measurement of the mechanical characteristics of the coatings (modulus of elasticity E and hardness H) was carried out using the Nanotest 600 measuring platform using the continuous indentation method [11, 12]. For measurements in the microrange (load—less than 2 N, indentation depth—more than 0.2 μm), a four-sided Vickers indenter was used, for work in the nano-range (an indentation depth—not more than 0.2 μm) was applied a three-sided Berkovich indenter. The measurements were carried out on 3–7 samples of the same type. The average values of the measured characteristics were obtained in the results, taking into account the standard statistical processing of the data. To exclude the influence of unevenness of the surface relief of the coatings on the measurement results of E and H, only those values were taken into account, the deviation of which from the weighted average did not exceed 10%.

The tribological characteristics of DLCs were determined on a TRB machine (Anton Paar Tritec) in sliding friction tests in accordance with the DIN 50,324 and ASTM G99 methods. The main measured values are the coefficient of friction μ, the intensities of the sample volumetric wear J and the counterbody J_K. The tests were carried out according to the "pin-plate" scheme with a normal force on the pin of 10 N and a reciprocating motion of the plate (sample with a coating) with the following parameters: frequency 10 Hz; amplitude 800 μm; test duration 50,000 cycles. The counterbody was a ball of Ø 6.35 mm, made of the WC–Co system and fixed in a pin.

3 Results and Discussion

The structural feature of vacuum ion-plasma DLCs is the uniformity of the structure, which, in turn, is a consequence of the deposition method. This feature distinguishes carbon-based mono-coatings from ion-plasma coatings of other systems (nitride, carbide, oxide, cermet, composite) [13–18] and leads to the fact that the structure of DLCs is not differentiated by microscopy methods (Fig. 1a). For this purpose, more sophisticated research methods are required, therefore, further in this work, the results of studying the structure of DLCs using XPS techniques are presented.

Electron microscopic photographs of the structure of the studied DLCs are shown in Fig. 1: the data of the structural morphology of the coatings, as well as the distribution of the elemental composition in them, shown in Fig. 2, are typical for all samples that participated in the experiments.

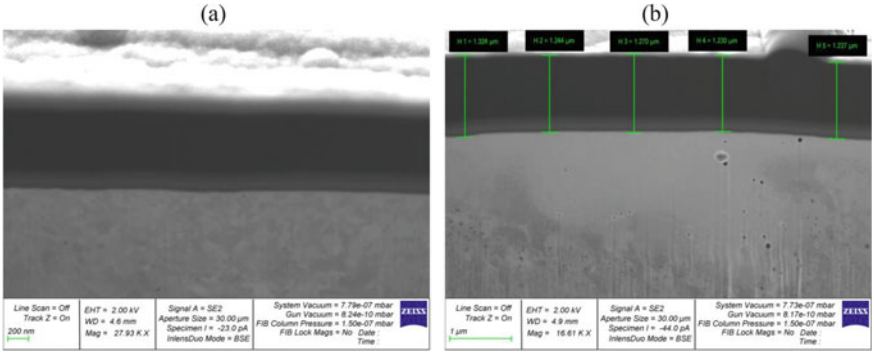

Fig. 1 Cross-section of DLC coatings: **a** on a 12Cr2Ni4 carburized steel substrate, **b** on a 38Cr2MoAl nitrided steel substrate

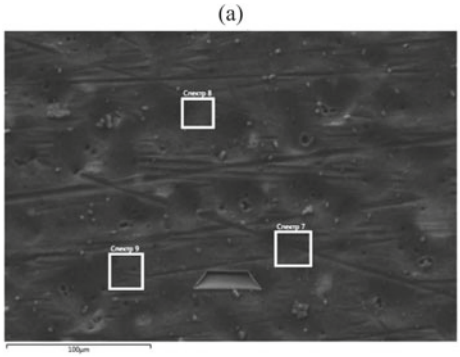

(b)

Element	Spectrum 7	Spectrum 8	Spectrum 9
C	71.74	72.40	72.46
Al	0.10	0.09	0.09
Si	3.21	3.22	3.16
Ti	0.05	–	–
Cr	1.62	1.61	1.47
Mn	0.10	0.09	
Fe	14.78	14.24	14.28
Ni	0.14	–	0.13
Nb	6.45	6.58	6.68
Hf	1.81	1.78	1.72
Sum	100.00	100.00	100.00

Fig. 2 Distribution of elements in the DLC, EDAX-scan over the coating surface: **a** electronic image of the coating surface, **b** chemical composition of the scanned areas (% mass.)

In the result of the application of the deposition technology of DLCs from a gas mixture of acetylene and methylsiloxane, the structure of the coating in the cross-section acquires a two-layer character (Fig. 1): the outer layer of the coating is purely carbon, and the inner layer, making up no more than 30% of the total thickness of the coating, is saturated with silicon. There is no interphase boundary in the form of an interface between the layers, but there is a transition zone in which there is a gradient distribution of Si concentration. The presence of such a zone is characterized positively due to the absence of the problem of adhesion; however, on the other hand, the concentration gradient indicates a nonequilibrium state and metastability of the coating structure. The increased Si content in the coating is shown in Fig. 2b. The presence of Nb and Hf in the same place is due to their ion implantation into the surface layer of the substrate, and the presence of Fe and Cr is a consequence of the "capture" of the substrate elements during EDAX detection.

The task of studying the coating by the XPS method was to determine the types of electronic hybridization of carbon by the depth of the coating. To determine the electronic structure of the coating (that is, the sp^3/sp^2 ratio), C (KLL) Auger spectra were used, extracted from the survey spectra. The test coating had a thickness of about 1.3 μm. Its study was carried out by layer-by-layer profiling (ion etching) of the coating surface over its entire thickness until the appearance of electronic lines of iron in the spectrum. This indicated that the etching process had reached the substrate. Panoramic spectra were taken from the original surface of the DLC and after 10, 20, 30, 70, 90 and 130 min of profiling. Auger electron spectra C (KLL) from the surface of the DLC under study at different profiling times are shown in Fig. 3. Based on these data, the fractions of the carbon states sp^3 and sp^2 were calculated at different depths of the studied diamond-like coating. Without going deep into the methodological subtleties of the calculations, we only note that they are carried out using the parameter δ (eV), which is the distance between the positive and negative extrema of the differential spectra C (KLL) [19–22]. These distances on each spectrum in Fig. 3 are marked with vertical dashed lines, and the value of the parameter δ is given to the left of each spectrum. In the general case, the value of the parameter δ is higher for graphite. Taking as a reference the calibration differential spectra C (KLL) of graphite with 100% sp^2 and diamond (polyethylene) 100% sp^3 and knowing the value of the parameter δ, the fraction of the sp^3 configuration in the DLC coating is determined.

In accordance with the values of the parameter δ in Fig. 3, the sp^3/sp^2 ratio along the depth of the coating changes in a gradient: from 1.96 at the surface to 0.12 at the substrate. This indicates that the fine structure of the DLC is also gradient in depth: as it approaches the substrate, its amorphization occurs and the fraction of the graphite-like component increases. In turn, an increase in the proportion of hybridized sp^3 orbitals near the coating surface indicates a diamond-like coating surface, which should significantly reduce the friction coefficient of such a coating during tribological tests. The experimental data for determining the physical and mechanical properties and testing the tribological characteristics of DLCs and reference samples (uncoated substrates) are present in Table 1, where the average values are given, and the scatter of the measured characteristics for DLCs is shown in parentheses.

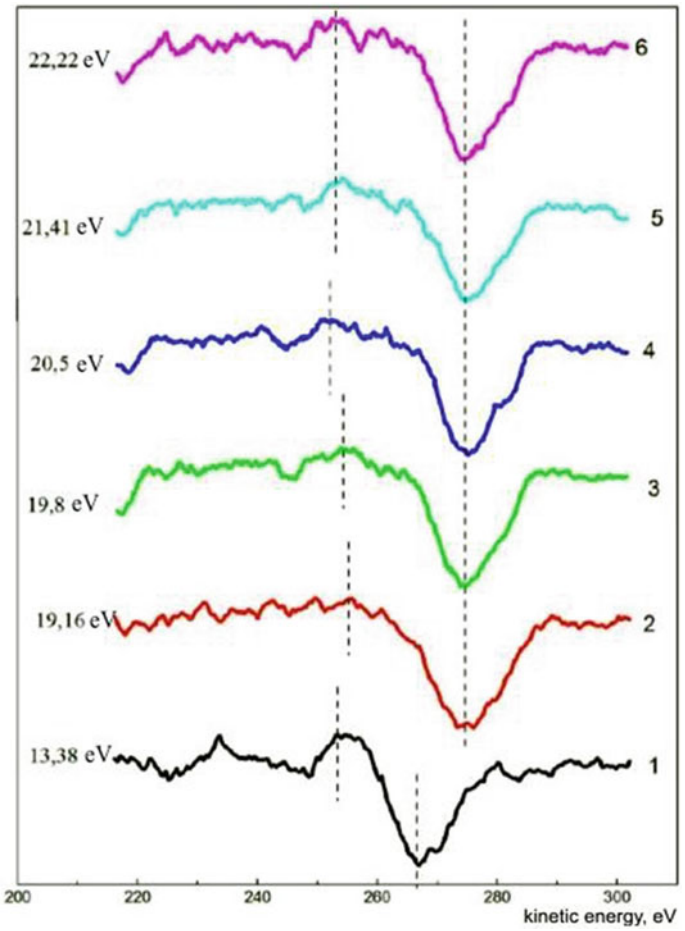

Fig. 3 Differential spectra C (KLL) from the surfaces of the DLC obtained after different times of ion profiling, min: 1 - original surface (without profiling); 2–10; 3–*20*; 3–*30*; 5–*70*; 6–*90*

In addition to the measured values of E and H, the complex of physical and mechanical properties included the ratios H/E and H^3/E^2 obtained by calculation. These values are especially important in studying the behavior of coatings under load, since for coatings they determine the resistance to elastic and plastic deformation, respectively [23, p. 133]. Also the ratio H/E, according to some authors [1, p. 608; 24], correlates directly with friction wear resistance.

Since the investigated carbon coatings contain a fair share of graphite electron hybridization sp^2, one should not expect the highest possible hardness and strength from them. Nevertheless, it follows from Table 1 that, according to the design characteristics, the obtained carbon coatings have a sufficiently high resistance to both elastic H/E and plastic H^3/E^2 deformation and significantly exceed steel after

Table 1 Measurement data of physical, mechanical and tribological properties

Characteristic	Measurement object		
	Steel 38Cr2MoAl (nitrided surface)	Steel 12Cr2Ni4 (carburized surface)	DLC
Physical and mechanical properties			
H, GPa	12	6.32	13.4 (12.4–15.3)
E, GPa	231	201	182.3 (170.6–191.6)
H/E	0.0398	0.0321	0.0739 (0.0689–0.080)
H^3/E^2, GPa	0.02975	0.0066	0.0753 (0.057–0.0976)
Tribological properties			
μ	0.53	0.9	0.36 (0.28–0.50)
J, 10^{-7} mm^3/N/m	4.50	12.30	6.65 (3.88–8.08)
J_K, 10^{-7} mm^3/N/m	3.96	4.46	1.92 (0.91–3.03)

chemical-thermal treatment. According to these indicators, they are quite competitively capable also in comparison with wear-resistant ion-plasma nitride coatings, similar data for which are given in [25]. The experimental data in Table 1 indicate that under the conditions of the tribological tests carried out, the investigated DLCs do not provide significant advantages in wear resistance J in comparison with nitrided steel. At the same time, a decrease in the friction coefficient μ is fixed (by 1.5 times or more) and a decrease in the wear of the counterbody J_K is observed (by about 1.5–2.0 times). In turn, DLCs deposited on a carburized steel surface, significantly inhibit the wear process by reducing all tribotechnical parameters μ, J, J_K. In this case, the coefficient of friction and wear of the counterbody also experience the greatest reduction. Hence, the conclusion suggests itself that the effect of increasing the wear resistance of loaded tribocontact pairs when using DLCs can only be achieved under certain operating conditions. One of these conditions is the optimal combination of substrate and coating. It can be assumed that the contact of homogeneous materials (carburized steel and carbon coating) due to higher adhesion is more preferable than the heterogeneous contact interface "substrate-coating" (nitrided steel and carbon coating). The versatility of DLCs is manifested only in relation to the reduction of the coefficient of friction.

For a clearer understanding of the factors that determine the wear of coatings during friction, a study of the wear zone (friction track) of DLCs was carried out. Its general view and typical morphology are shown in Fig. 4, and the elemental distribution is shown in Fig. 5. The location of the friction track in Figs. 4a and 5 is rotated by 90 degrees in relation to each other.

The friction track after testing consists of two contrasting zones (Fig. 4a): the central light wear zone, in the redistribution of which the coating has not been preserved (in Fig. 4b on the left), and the peripheral dark smooth zone in which

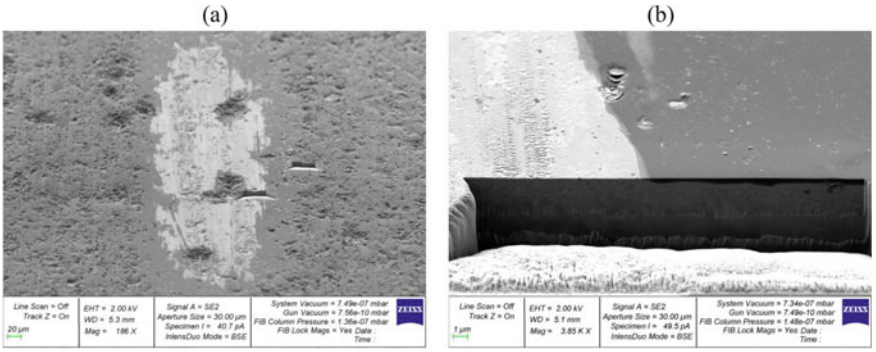

Fig. 4 The structure of the friction track of DLCs: **a** general view of the track at an angle to the surface, **b** cross-section of the wear zone of the track

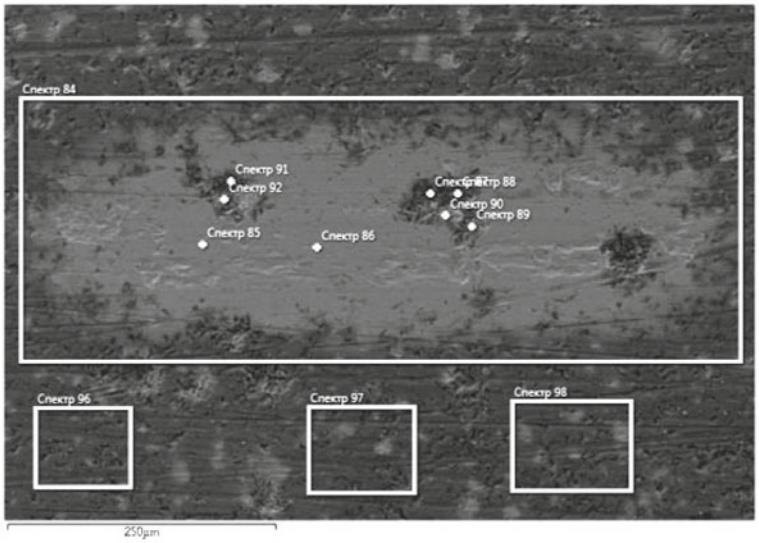

Element	Spectrum No.											
	84	85	86	87	88	89	90	91	92	96	97	98
C	43.51	3.66	3.82	35.19	58.53	64.81	45.11	38.25	36.93	65.01	64.59	63.65
O	4.10	9.45	–	3.45	–	–	7.97	–	3.73	–	–	–
Al	0.81	0.97	0.87	0.60	0.25	0.59	0.38	0.24	0.91	0.49	0.55	0.53
Si	2.66	0.58	0.31	4.79	3.61	3.12	4.57	3.14	1.98	3.43	3.39	3.40
S	–	–	–	–	–	–	–	–	0.08	–	–	–
Ti	–	–	–	–	0.05	–	0.06	–	0.07	–	–	–
Cr	1.72	1.16	1.20	3.92	3.16	2.29	2.98	3.79	2.57	1.87	1.79	1.76
Mn	0.20	0.41	–	–	–	0.27	0.29	0.44	0.37	–	–	–
Fe	45.63	83.29	93.80	51.55	34.24	28.69	38.47	54.13	52.97	28.00	28.26	29.72
Ni	–	–	–	–	–	–	–	–	0.39	–	–	–
Nb	1.37	0.47	–	0.27	–	–	0.17	–	–	1.21	1.42	0.94
Mo	–	–	–	0.24	0.16	0.23	–	–	–	–	–	–
Sum	100.00	100.00	100.00	100.00	100.00	100.00	100.00	100.00	100.00	100.00	100.00	100.00

Fig. 5 Chemical composition (% mass.) of the scanned friction track zones

the coating is partially preserved (in Fig. 4b on right). Both zones are quite typical both in terms of surface morphology and elemental composition. The surface of the central light zone with traces of plastic deformation and microcracks is typical for the nitrided surface of 38Cr2MoAl steel at the beginning of the oxidative wear process [25]. The smooth surface of the peripheral dark zone is typical for DLCs, the wear of which, due to the presence of amorphous graphite, occurs by the abrasion mechanism characteristic of high-strength rubbers [26–28].

The distribution of elements in Fig. 5 also indicates that the wear of the sample under the conditions of the tribological tests carried out occurs due to abrasion of the coating and oxidation of the surface of the steel substrate. Within the entire friction track, the C + Si content in comparison with the Fe + O content changes antibatically. An increase in the amount of Fe in the spectra against the background of a decrease in the amount of C + Si indicates a decrease in the thickness of the DLC coating, up to its complete absence, as, for example, in the zone of localization of Spectrum 85 in Fig. 5. The carbon film does not allow oxygen to penetrate to the steel surface and actively interact with Fe at high temperatures in the friction zone. The distribution of the remaining chemical elements in Fig. 5 is fully consistent with both the logic of the wear process presented here, and with the original distribution of elements in the coating in Fig. 2 (the presence of Nb is a consequence of ion implantation).

Thus, the activation of the wear of the samples occurs during the transition from the abrasion mechanism of the DLC to the oxidative mechanism of wear of the steel surface.

4 Conclusion

The results obtained in this work characterize, on the whole, a higher complex of mechanical properties of the studied DLCs, which is provided by chemical-thermal treatment in the surface layer of steel during nitriding and carburizing. However, this does not guarantee a higher wear resistance of the coatings. Thus, under the conditions of the tribological tests carried out, DLCs showed consistently lower values of the coefficient of friction μ, but not wear, in general. The reason for the decrease in μ can be a large fraction of the graphite component sp^2 in the electronic structure of the coatings, due to which the well-known lubricity of graphite is realized. The mixed (gradient) structure of the investigated coatings, the increased values of the H/E and H^3/E^2 ratios, as well as the specific wear mechanism (abrasion) suggest the possibility of relaxation of fatigue stresses in the coating during unloading at friction. This circumstance opens up prospects for the tribotechnical use of not only superhard DLCs similar in structure to diamond, but also for DLC with mixed electronic structure.

Acknowledgements This research was performed in the framework of financing Russian Science Foundation grant No 21-79-30007.

References

1. I.P. Hayward, I.I. Singer, L.E. Seitzman, Wear **157**, 215 (1992)
2. S.J. Bull, P.R. Chalkar, C. Johnston, V. Moor, Surf. Coat. Technol. **68**, 603 (1994)
3. Nanostructured Coatings. A. Cavaleiro, J.T. de Hosson (Eds.) (Springer Science & Business Media, LLC, New York, 2007), p. 752
4. C.A. Charitidis, E.P. Koumoulos, D.A. Dragatogiannis, Lubricants **1**(2), 22 (2013)
5. Zhencheng Ren, Haifeng Qin, Yalin Dong, G.L. Doll, Chang Ye, Wear, **436–437**, 203031 (2019)
6. B. Huang, Q. Zhou, E.-G. Zhang, Coatings **10**(3), 243 (2020)
7. J.C. Lascovich, R. Giorgi, S. Scaglione, Appl. Surf. Sci. **37**, 17 (1991)
8. P. Mérel, M. Tabbal, M. Chaker, S. Moisa, J. Margot Appl. Surf. Sci. **136**, 105 (1998)
9. A. Mezzi, S. Kaciulis, Surf. Interface Anal. **32**, 1082 (2010)
10. H.J. Steffen, C.D. Roux, D. Marton, J.W. Rabalais, Phys. Rev. **33**(8), 3981 (1991)
11. W.C. Oliver, G.M. Pharr, J. Mater. Res. **7**(6), 1564 (1992)
12. ISO 141577–1:2002 "Metallic materials—Instrumented indentation test for hardness and materials parameters—Part 1: Test method" (2002)
13. O.V. Kudryakov, V.N. Varavka, Inorg. Mater. **51**(15), 1508 (2015)
14. V.N. Varavka, O.V. Kudryakov, A.V. Ryzhenkov, in *Piezoelectrics and Nanomaterials: Fundamentals, Developments and Applications*, ed. by Ivan A. Parinov (Nova Science Publishers: New York, 2015), p. 105
15. O.V. Kudryakov, V.N. Varavka, V.V. Ilyasov, J. Phys: Conf. Ser. **857**, 012025 (2017)
16. V.N. Varavka, O.V. Kudryakov, I.Yu. Zabiyaka, I.S. Morozkin, in *Advanced Materials—Techniques, Physics, Mechanics and Applications*, Springer Proceedings in Physics, ed. by Ivan A. Parinov, Shun-Hsyung Chang, Muaffaq A. Jani (Heidelberg, New York, Dordrecht, London, Springer Cham, 2017) **193**, p. 407
17. V.I. Kolesnikov, V.D. Vereskun, O.V. Kudryakov, D.S. Manturov, O.N. Popov, E.S. Novikov, J. Frict. Wear **41**(2), 169 (2020)
18. O.V. Kudryakov, V.N. Varavka, I.Yu. Zabiyaka, E.A. Yadrets, V.P. Karavaev, Adv. Eng. Res. **20**(3), 269 (2020) (In Russian)
19. M. Dayan, S.V. Pepper, Surf. Sci. **138**, 539 (1983)
20. A.P. Dementjev, M.N. Petukhov, Surf. Interface Anal. **23**, 517 (1996)
21. N. Kumar, A.T. Kozakov, K.J. Sankaran, A.V. Sidashov, Diam. Relat. Mater. **97**, 107337 (2019)
22. N. Kumar, K.J. Sankaran, A.T. Kozakov, A.V. Sidashov, A.V. Nicolskii, K. Haenen, V.I. Kolesnikov, Diam. Relat. Mater. **97**, 107372 (2019)
23. Structure and Properties of Nanocomposite, Hybrid and Polymeric Coatings, A.D. Pogrebnyak, A.A. Lozovan, et al (Eds.), LIBROCOM, Moscow, p. 344 (2011) (In Russian)
24. C. Rebholz, H. Ziegele, A. Leyland, A. Matthews, Surf. Coat. Technol. **115**, 222 (1999)
25. V.I. Kolesnikov, O.V. Kudryakov, IYu. Zabiyaka, E.S. Novikov, D.S. Manturov, Phys. Mesomech. **23**, 570 (2020)
26. V.A. Levchenko, I.A. Buyanovskii, V.D. Samusenko, V.N. Matvienko, Yu.I. Shcherbakov, J Frict Wear **40**(6), 536 (2019)
27. Abrasion of Rubbers. G.I. Brodsky, V.F. Evstratov, et al (Eds.), Chemistry, Moskow, p. 230 (1975) (In Russian)
28. O.V. Kudryakov, V.N. Varavka, I.V. Kolesnikov, E.S. Novikov, I.Yu. Zabiyaka, IOP Conf. Series: Mater. Sci. Eng. **1029**, 012061 (2021)

DFT-Study of Strength of TiAlN Coating on Iron Surface

Yuri F. Migal

Abstract A scheme for estimating the chemical bond strength of the TiAlN coating on the surface of crystalline iron by quantum chemistry methods is proposed. The coating is modeled by a layer with a thickness of several atomic layers and has a two-dimensional periodic structure, the parameters of which are determined by the parameters of the iron lattice. This approach allows us to replace the study of extended bodies with the study of the elementary cell of these bodies. It is shown that the coating on iron, consisting of successive layers of titanium, nitrogen and aluminum atoms, is sufficiently strong and is not inferior in strength to iron itself. When defects appear in the iron structure, the binding energy of the coating with iron becomes less, but it ensures the integrity of the structure of the iron—coating system at low loads on the system.

Keywords Interatomic interactions · Quantum chemistry · DFT · Periodic structure · Elementary cell · Deposited atoms · Reinforcing coatings

1 Introduction

Over the past 15–20 years, there has been a boom in the development of nanometer-thick reinforcing coatings on metal surfaces. Such coatings include the TiAlN, TiAlTa, TiB_2, ZrN, ZrO_2 and many other compounds on the iron surface [1–7]. Similar coatings with a thickness of hundreds and thousands of atomic layers significantly improve strength, tribological, anti-corrosion, and other properties of surfaces. Gradually, this area of knowledge accumulates information about the optimal compositions of such coatings and various fields of their applications. Basically, this information is extracted directly from numerous experiments and therefore it is mainly

Y. F. Migal (✉)
The Southern Scientific Centre of the Russian Academy of Sciences, Rostov-on-Don, Russia
e-mail: ymigal@mail.ru

I. A. Parinov et al. (eds.), *Physics and Mechanics of New Materials and Their Applications*, Springer Proceedings in Materials 10,
https://doi.org/10.1007/978-3-030-76481-4_18

experimental. However, since the studied effects are determined by interatomic interactions, it is obvious that in this case, for a better understanding and adequate description of such processes, we should use general concepts and methods of atomic physics and quantum chemistry.

In this paper, using the methods of quantum chemistry, an attempt is made to consider the strength properties of a simplified model in which a deposited coating with a thickness of several atomic layers has a two-dimensional periodic structure. In this case, it is possible to effectively use approaches in which the study of macroscopic bodies is replaced by the study of one elementary cell of these bodies. In this way, we hope to obtain some general results that are valid at least for some of these coatings.

In real conditions, it is not always possible to create a periodic structure of atoms of some elements on the surface of a metal consisting of atoms of other elements. The parameters of this structure should be determined by the crystal cell of the metal on which the coating is being deposited. The dimensions of deposited atoms should be chosen so that the cell parameters of the created coating are close to the cell parameters of the initial metal to be protected. At the same time, some variation of these values should be allowed. It can be expected that a stable periodic structure of the coating will appear upon condensation of a rarefied low-temperature gas consisting of slowly moving atoms or molecules of elements on the basic metal. In this case, the energy of the deposited particles will be sufficiently low, and the possibility of the appearance of such a structure reduces the probability of the appearance of bulk defects in the system.

The coating will be stronger, if the deposited atoms belong to different elements and, accordingly, have different sizes. The entropy of such an inhomogeneous system will be high, which increase the overall stability of the system. In this paper, we consider Ti, Al, N as elements deposited on the surface of iron. Such a set of dissimilar elements turned out to be quite effective. It is often used in modern research (see, for example, [1–5]).

In this paper, by using a numerical model simulating the TiAlN coating on iron, as well using the DFT approach [8], we consider the following questions:

(i) How does the relative position of atoms of the elements Ti, Al, N in a cell affect the strength of the surface layer, when exposed to a load perpendicular to the coating surface?
(ii) How does the TiAlN coating increase the strength of the surface layer of the basic metal weakened by defects, when exposed to a shear load parallel to the metal surface?

2 System Model and Problem Statement

Figure 1 shows one of the variants of the coating structure of the surface [011] of iron with the FCC-lattice. The model system consists of three layers of Fe-atoms (they are represented by orange balls), above which there are two layers of titanium and aluminum atoms (large gray balls), as well as nitrogen atoms (small blue balls).

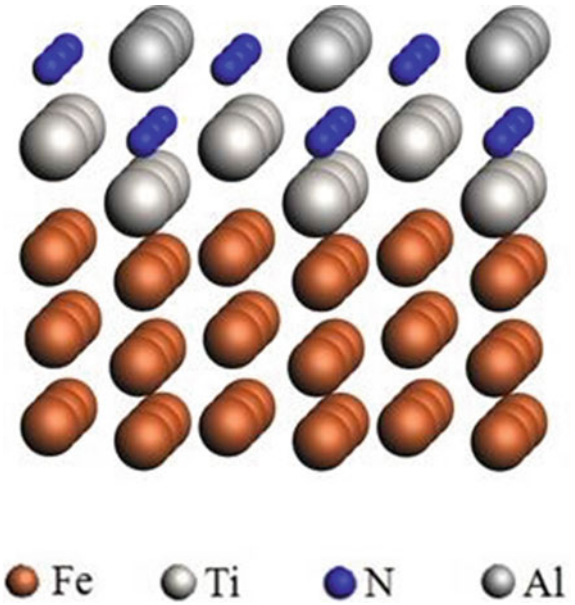

Fig. 1 Polyatomic system simulating a strengthening coating on the surface [011] of iron; here are 9 vertically arranged elementary cells of the surface layer. Each cell consists of 6 Fe-atoms, 2 Ti-atoms, 2 N-atoms, and one Al-atom

Aluminum atoms (dark gray balls), slightly different in shade from titanium atoms, are located in the uppermost layer of the system.

Based on the questions given in the introduction, we reformulate one of the research tasks. It is necessary to consider ways to create a strengthening layer on the defective surface of the metal, which, while not inferior in strength to the base metal, would create "bridges" over the defects. Such bridges should couple together the defect-free parts of the metal surface, increasing the strength and wear resistance of the metal.

3 Choice of Strengthening Elements

Titanium is supposed to be used as one of the coating components. When constructing the atomic model (Fig. 1), the role of this element in the system becomes clear. Since the atomic radius of titanium is greater than the radius of iron atoms (cf.: $R_{Ti} = 0.146$ nm, $R_{Fe} = 0.126$ nm (L. Pauling, 1927)), a surface containing 6 titanium atoms built over a plane of 6 iron atoms cannot be flat. In other words, 6 Ti-atoms do not fit on the same level. Some of these atoms are raised to a higher level. Thus, the monatomic layer of titanium is located on two levels, distorting the flat surface of iron (this fact is shown in Fig. 1).

In the cavities of the surface, formed in this way from titanium atoms, nitrogen atoms are located, the radius of which is relatively small ($R_N = 0.071$ nm). The next (third) layer contains aluminum atoms with $R_{Al} = 0.143$ nm, alternating with nitrogen atoms. (The radii of titanium and aluminum atoms are almost the same!) Thus, a spatial structure with a dense packing is created, which in its periodic properties (lattice parameters) is close to the atomic structure of iron. At the same time, additional stresses do not arise in the system due to the inequality of atomic radii of individual elements.

If it is necessary to create a coating from a large number of layers, in which titanium and aluminum atoms are applied so that they randomly alternate with each other, then in such a more chaotic system entropy increases, which makes the system more stable. Accordingly, the coating in such a system becomes more durable. At the same time, its crack resistance also increases.

4 Strength of the System

To assess the strength of the system shown in Fig. 1, we consider the process of separation (decay) of the system into two parts. There are several possible variants of decay. The first of them is when the coating layer is completely separated from the iron atoms (Fig. 2).

To determine the energy required for such a decay, the energy of the entire system and its individual parts were calculated. The calculations were performed using the ADF software package [8], based on the DFT approach [9], which is successfully used for the calculations of such systems (see, for example, [10]). Let us denote the

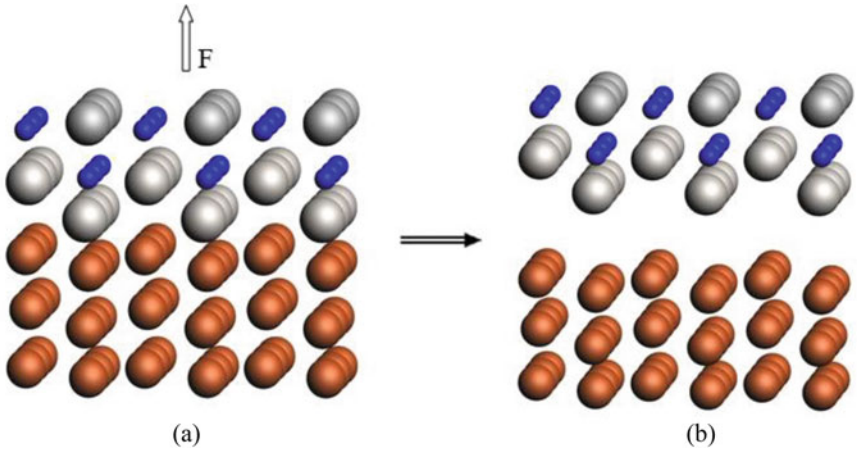

Fig. 2 Decay of a polyatomic system (**a**) into two parts, the coating and the basic metal (**b**)

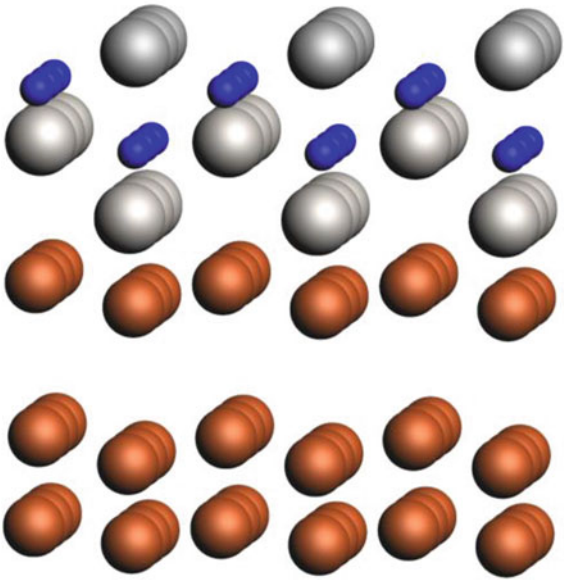

Fig. 3 Decay of a polyatomic system into two parts; the decay surface is located between layers of iron atoms

energy of the whole system as E_0, and the energy of the parts as E_1 (energy of the upper part) and E_2 (energy of the lower part).

The calculations show that $E_0 = -97.29$ eV, $E_1 = -37.70$ eV, $E_2 = -54.91$ eV.

Hence the decay energy is equal to

$$\Delta E = |E_0 - E_1 - E_2| = 4.68eV \tag{1}$$

Another variant of decay is shown in Fig. 3. In this case, the decay occurs on the surface located inside the group of iron atoms.

Calculation of the energy required for this decay is:

$$E_3 = -57.47\ eV,\ E_4 = -35.08\ eV,\ \Delta E = |E_0 - E_3 - E_4| = 4.74\ eV \tag{2}$$

Next, we consider the case when the decay surface is inside the coating (Fig. 4). Calculation in this case gives the following results:

$$E_5 = -29.23\ eV,\ E_6 = -63.60\ eV,\ \Delta E = 4.46\ eV \tag{3}$$

Comparing all three variants of decay, we see that the values of the decay energy in all cases are approximately the same. This indicates that a coating strength is close to that of pure iron.

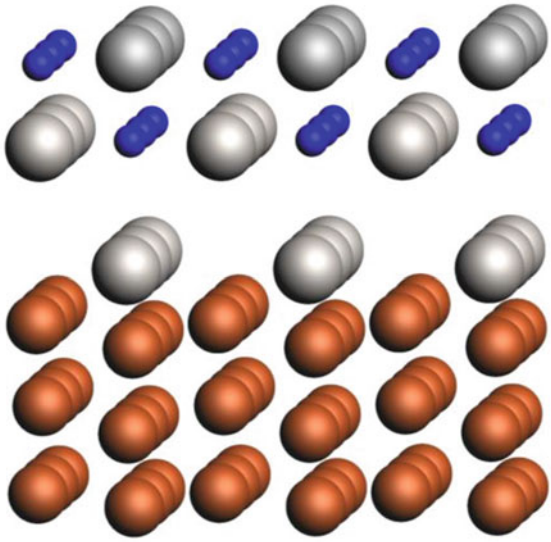

Fig. 4 Decay of a polyatomic system into two parts. The decay surface is located inside the coating

5 Defective Coating on Iron Structure

It was noted above that one of the purposes of coating is to cover with "bridges" areas with defects in the surface layer of iron and reduce the possibility of its destruction. Consider the following model from this viewpoint. Let us there are the following defects in the surface layer of iron: some of Fe atoms are replaced by impurity atoms. We consider silicon as an impurity (Fig. 5).

We calculated the binding energy of the coating with the surface of such a weakened system. The energy of this system (–94.81 eV) is slightly lower on value than the energy of the defect-free system (–97.68 eV).

Next, we consider the breakdown of this system into two parts, the coating and the basic metal (Fig. 6).

Let us calculate the energy required for decay:

$$E_0 = -94.81\,eV,\ E_1 = -53.03\,eV,\ E_2 = -38.14\,eV,\ \Delta E = 3.64\,eV \quad (4)$$

We can see that the decay energy in this case is noticeably lower than in the case of a defect-free structure ($\Delta E = 4.66$ eV). But its value is large enough to provide a certain strength of the system.

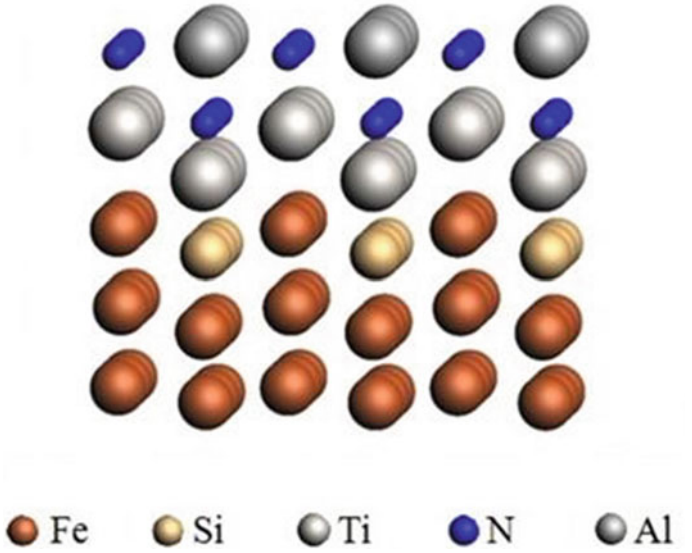

Fig. 5 Polyatomic system simulating an impurity of silicon in the surface [011] layer of iron

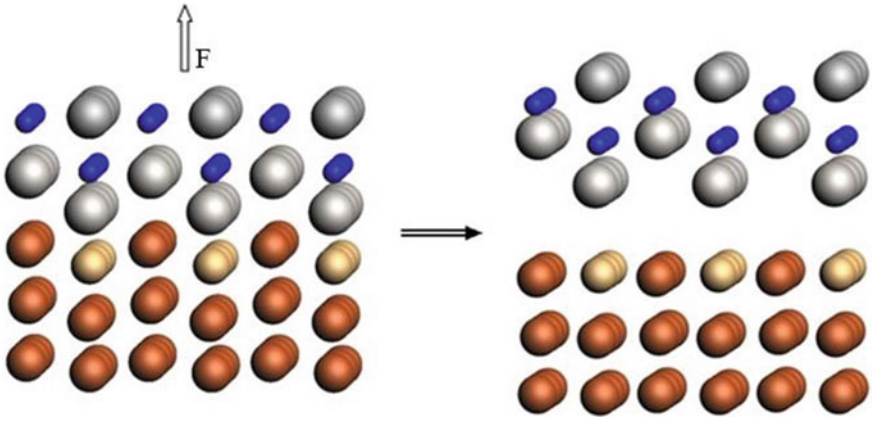

Fig. 6 Decay of a system containing an impurity of silicon atoms

6 Conclusion

Numerical analysis has shown that the coating on iron, consisting of successive layers of titanium, nitrogen and aluminum atoms, is not inferior in strength to pure iron. When defects appear in the structure of iron surface, the binding energy of the coating with iron becomes somewhat less, but it can be expected that the strength of

the coating itself ensures the integrity of the structure of the iron—coating system at low loads on the system.

The results obtained do not contradict the physical meaning and allow us to hope that the methods used in this work can be used for preliminary analysis of the strength properties of metals with coatings having a periodic structure.

Acknowledgements This research was performed within the framework of the state assignment of the Federal Research Centre The Southern Scientific Centre of RAS, number of state registration is AAAA-A16-116012610052-3.

References

1. W.M. Seidl, M. Bartosik, P.H. Mayrhofer, S. Kolozsvári, H. Bolvardi, Surf. Coat. Technol. **347**, 92 (2018)
2. J. Rao, A. Sharma, T. Rose, Coatings **8**(1), 12 (2018)
3. G.A. Almyras, D.G. Sangiovanni, K. Sarakinos, Materials **12**(2), 215 (2019)
4. R.E. Contreras, B.M. Gómez, M.A. Hurtado, N.J. Méndez, C.O. Solís, Surf. Coat. Technol. **378**, 124941 (2019)
5. X. Xu, F. Su, Z. Li, Wear **430–431**, 67 (2019)
6. Z. Lei, Y. Liu, F. Ma, Z. Song, Y. Li, Vacuum **127**, 22 (2016)
7. D. Mao, Y. Xu, L. Dong, J. Wu, M. Zhao, D. Li, Coatings **9**(10), 600 (2019)
8. G. te Velde, F.M. Bickelhaupt, E.J. Baerends, C.F. Guerra, S.J.A. van Gisbergen, J.G. Snijders, T. Ziegler, J. Comp. Chem. **22**(9), 931 (2001)
9. W. Kohn, A.D. Becke, R.G. Parr, J. Phys. Chem. **100**(31), 12974 (1996)
10. Y.F. Migal, V.I. Kolesnikov, I.V. Kolesnikov, Comp. Mater. Science **111**, 503 (2016)

Nanoindentation Derived Mechanical Properties of Au Thin Film Deposited by Pulsed Laser Sputtering on Si Substrate

E. V. Sadyrin, A. L. Nikolaev, A. S. Vasiliev, and I. Yu. Golushko

Abstract Behavior of the mechanical properties of the Au thin film deposited by pulsed laser sputtering technique was studied using nanoindentation at different values of maximum indentation load. The investigation was supplemented by the measurement of the coating thickness and research of the surface relief using scanning electron microscopy. The microgeometrical parameters of the Au film were calculated using 3D optical microscopy. The behavior of the diagrams, demonstrating dependencies of indentation depth on the load applied, was analyzed using the observation of indentation imprints on the optical microscope.

Keywords Nanoindentation · Thin film · Scanning electron microscopy (SEM) · Optical microscopy

1 Introduction

Au films with thickness of a few microns or a fraction of a micron are frequently used as components in MEMS/NEMS [1]. Measurement of the strength properties of such films is a difficult task due to the the small sizes, forces, and displacements involved as well as the need for special sample preparation methods. For the estimation of the mechanical properties of Au thin films nanoindentation experiments are often conducted [2–5], although other techniques can be also used such as microtensile test [6, 7], membrane deflection experiment [8], bulge testing [9] and others. Nanoindentation allows recording the load and depth data with a high resolution thus making it possible to calculate mechanical characteristics with a high accuracy. However, the validity of the results depends on the observance of special measurement conditions and the elimination of undesired influences [10, 11].

This chapter presents a research on behavior of the mechanical properties of the Au thin film deposited by pulsed laser sputtering measured by nanoindentation using

E. V. Sadyrin (✉) · A. L. Nikolaev · A. S. Vasiliev · I. Yu. Golushko
Research and Education Center "Materials", Don State Technical University, Rostov-on-Don 344003, Russia

I. A. Parinov et al. (eds.), *Physics and Mechanics of New Materials and Their Applications*, Springer Proceedings in Materials 10,
https://doi.org/10.1007/978-3-030-76481-4_19

the Berkovich indenter. The investigation was supplemented by the measurement of the coating thickness, microgeometrical parameters and optical observations.

1.1 Research Purpose

Behavior of mechanical properties of the Au film, deposited on the Si substrate depending on the load applied and taking into account the peculiarities of its surface, was studied.

1.2 Research Scope

At this study, we consider the following frameworks of the problem:

(i) deposition of the Au thin film;
(ii) measurement of the thickness of the obtained film;
(iii) understanding of the peculiarities of its surface relief including microgeometrical parameters;
(iv) calculation of the mechanical properties of the film.

2 Research Method

2.1 Deposition of the Au Thin Film

Si (100) substrate was prepared by keeping it in liquids (analytical grade acetone, brought to boil, H_2O_2 with CH_3COOH by volume 1:1, HF 2%, deionized water). Deposition was carried out with an excimer CrF laser at a wavelength of $\lambda = 248$ nm. The laser pulse repetition rate was 10 Hz. The power density of laser radiation was 1.7 J/cm^2. Number of laser pulses $N = 8000$. Spraying was conducted at room temperature. The deposition was conducted by sputtering a pure gold target in a high vacuum at a pressure of 5×10^{-5} mbar.

2.2 SEM Research of the Film

The thickness of the Au film was obtained by the following technique: the sawed notch was applied on the Si substrate prior to preparation. After Au deposition, the sample was chipped by the notch, and the flat end was examined in the place

of the chip using scanning electron microscopy (SEM). The surface subjected to nanoindentation was further examined as well.

2.3 3D Optical Microscopy

The microgeometrical characteristics of the surfaces of the substrate and the Au thin film were collected using the 3D optical microscope (Contour Elite, Bruker, Belgium). The Gaussian regression filter with long cutoff (250 μm) was applied. The microgeometrical parameters were calculated according to ISO 4287.

2.4 Nanoindentation and Optical Microscopy

A nanoindentation device (NanoTest 600 Platform 3, Micro Materials, UK) was used to measure mechanical properties of the film. The experiments were carried out at a constant temperature of 27.0 ± 0.1 °C in a closed chamber, a calibrated diamond Berkovich indenter was used. The thermal drift was recorded and corrected using the device software. The maximum load $P_{\max}$ for all the experiments was 100 mN. Values of the effective Young's modulus E_{eff} and indentation hardness H for each of the areas were obtained using the Oliver—Pharr method [12]. During the test, the indenter displacement h was recorded while the load P was applied. The maximum value of the displacement (attained at $P_{\max}$) was denoted as $h_{\max}$, the output of each experiment was a load–displacement curve. Holding load at its maximum value for a time before unloading made it possible to eliminate the influence of any creep response on the unloading "branch" of the diagram. The optical images of the indentation imprints were collected using the optical microscope integrated into the indentation device.

3 Results and Discussion

The microgeometrical parameters measured on the Si (100) prepared substrate on 3D optical microscope were as follows: $R_a = 1.38$ nm, $R_t = 10.39$ nm. Figure 1 shows the diagram of the surface relief (roughness and waviness) of the film obtained using 3D optical microscopy. The calculated surface microgeometrical parameters measured along 1.3 mm surface site for the film were as follows: $R_a = 4.3$ nm, $R_t = 38.5$ nm.

Figure 2 demonstrates the flat end examined in the place of the chip performed after deposition.

Three probes for thickness were taken in different locations, the averaged result was 369.7 ± 3.1 nm. The surface relief at microscale (Fig. 3) is characterized by

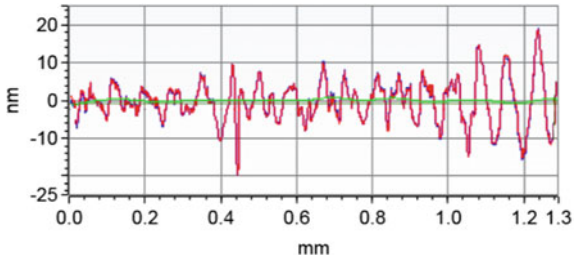

Fig. 1 Surface roughness (red line) and surface waviness (green line) obtained using 3D optical microscope

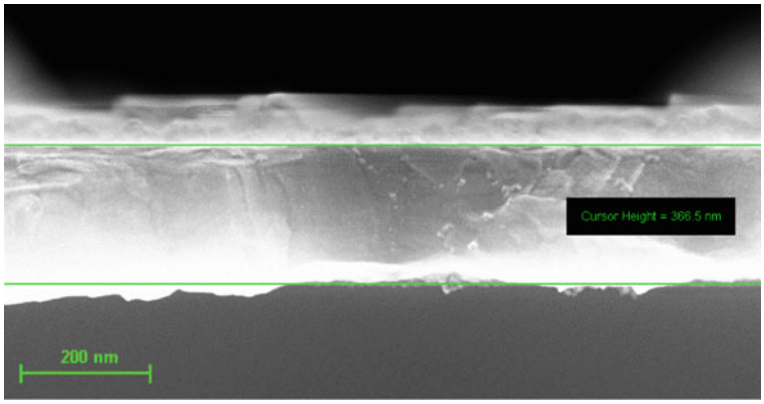

Fig. 2 SEM investigation of the thickness of the film

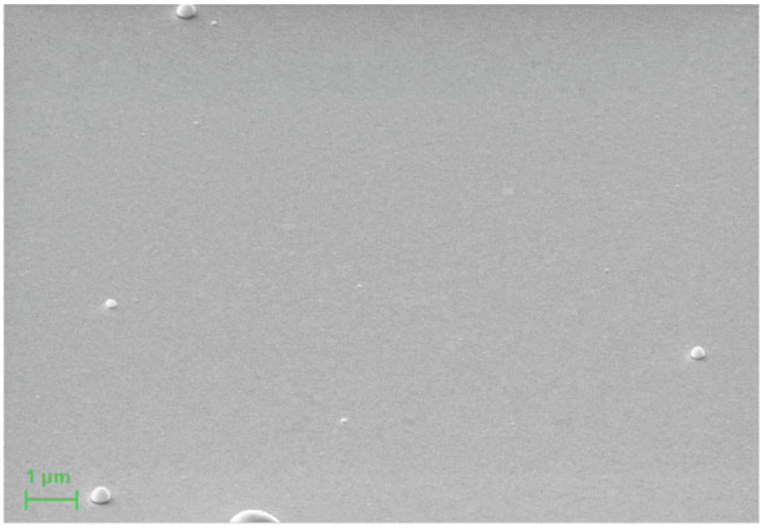

Fig. 3 SEM image of the surface of the Au film at microscale

appearance of a number of spherical artifacts of deposition. However, at nanoscale (Fig. 4), the surface appears to be smooth between the spherical artifacts.

The measurements above justify the overall smoothness of the surface and uniformity of the thickness of the film.

The obtained mechanical properties of the thin film on different values of P_{max} are given in the Table 1. The sites with spherical artifacts were eliminated from the analysis of the mechanical properties after the indentation experiments. Note, that for each indentation series 12 identical indentations were conducted.

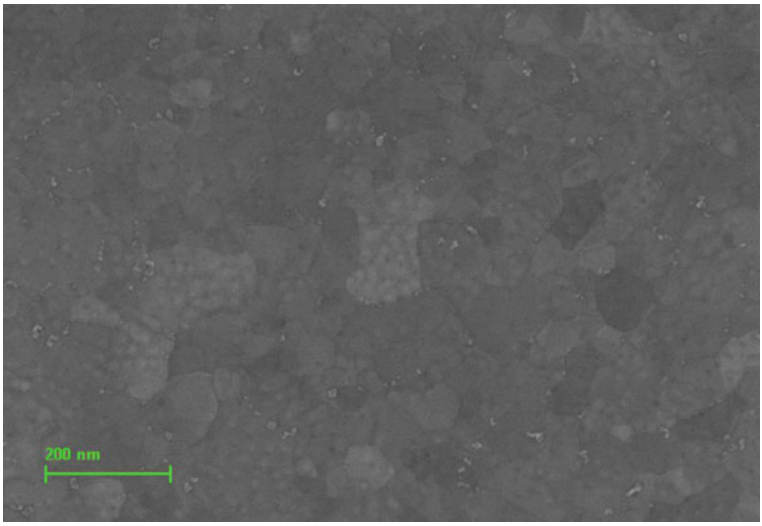

Fig. 4 SEM image of the surface of the Au film at nanoscale

Table 1 Nanoindentation derived mechanical properties of the Au film

$P_{max,}$ mN	h_{max}, nm	E_{eff}, GPa	H, GPa
3	67.09 ± 3.95	420.38 ± 55.05	11.82 ± 0.88
5	101.09 ± 7.11	373.86 ± 32.89	11.11 ± 1.41
10	227.51 ± 13.01	285.81 ± 18.3	5.97 ± 0.61
15	295.17 ± 11.65	279.59 ± 23.03	5.76 ± 0.37
20	336.38 ± 10.86	272.2 ± 9.73	6.22 ± 0.36
25	407.84 ± 9.1	265.84 ± 5.37	5.49 ± 0.24
40	505.98 ± 16.04	258.22 ± 7.72	6.1 ± 0.37
50	567.39 ± 11.39	245.61 ± 6.72	6.26 ± 0.24
65	635.24 ± 15.6	230.45 ± 6.64	6.78 ± 0.33
80	729.01 ± 14.98	208.65 ± 5.33	6.55 ± 0.27
100	821.37 ± 8.84	194.13 ± 2.44	6.78 ± 0.15

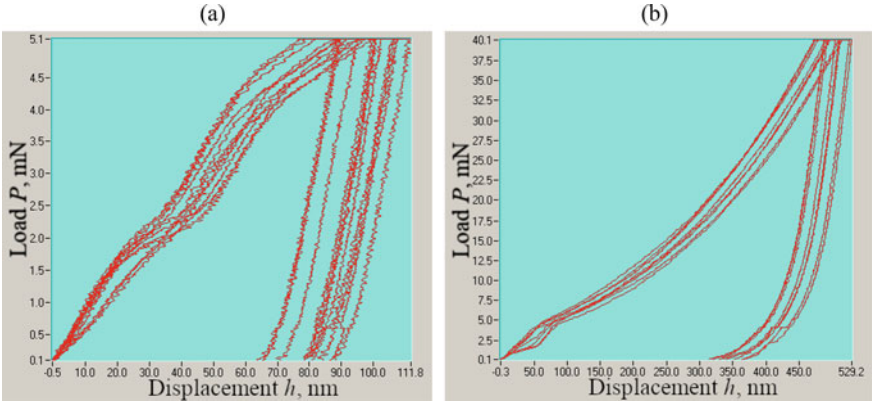

Fig. 5 Load–displacement curves for the selected loads: **a** 5 mN; **b** 40 mN

An overall decrease of the mechanical characteristics was examined. The nanoindentation experiment revealed high values of indentation depth even for small loads (such as 67.09 ± 3.95 nm for 3 mN or 101.09 ± 7.11 nm for 5 nm). Thus, for films with such thickness, the influence of substrate on the obtained mechanical properties is evident even for the most delicate indentation loads. The attempts to perform indentations at smaller P_{max} resulted is serious noises for the load–displacement curves, so they are not presented in the present research. The typical load–displacement curves for different loads observed for the film under study are demonstrated in Fig. 5.

The loading branch behavior (sudden change of its character) was observed for each indentation series on ~ 40 nm indentation depth. Presumably such behavior occurred due to the plastics along the film (despite the fact that the indentation creep was relatively small, see the horizontal segment of the diagram at P_{max}). Another interesting repetitive feature found was the presence of the pop-ups of Au material around indentation imprints after complete unloading (Fig. 6).

The pop-ups of material are clearly visible, they may contribute to the error during the calculation of the contact area. Presumably accurate experimental examination of the mechanical properties of such complex systems as film—substrate (even in the case of a single Au layered film) should be supplemented by the mathematical modelling to obtain the elastic moduli of the coating to avoid influence of the substrate and pop-ups on the results [13–15].

4 Conclusion

The behavior of the mechanical characteristics on the indentation depth was experimentally obtained for the Au thin film deposited on Si substrate by pulsed laser sputtering. The values of the coating thickness and microgeometrical characteristics of the film were derived using SEM and 3D optical microscopy, respectively. The

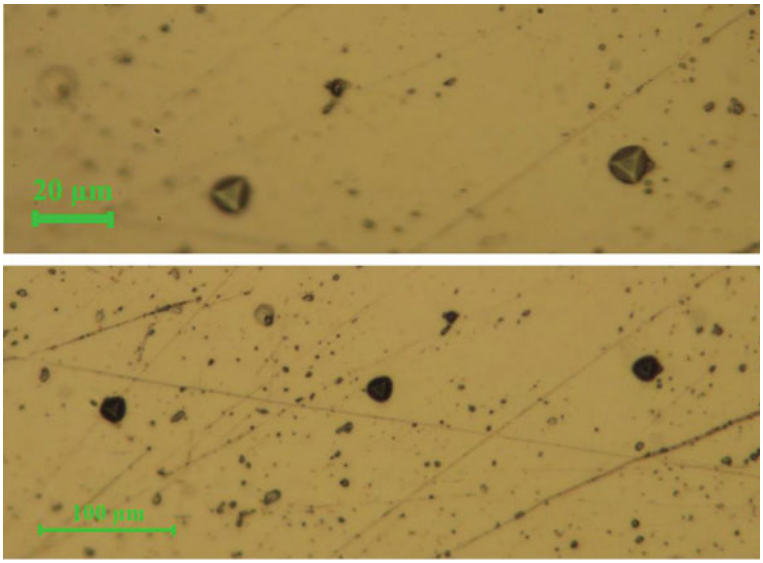

Fig. 6 Optical observation of the indentation imprints

overall decrease of the mechanical characteristics was examined caused by the effect of the substrate on the experiments. For their further clarification the mathematical modelling of the indentation process of the Berkovich indenter into inhomogeneous by depth film-substrate system is required.

Acknowledgements This research was supported by the Russian Science Foundation (RSF) through grant No. 19-19-00444. Characterization of the film was conducted in the Research and Education Center "Materials", Don State Technical University (nano.donstu.ru). The film was deposited in the Educational and Scientific Laboratory of Nanomaterials of the I.I. Vorovich Institute of Mathematics, Mechanics and Computer Science, Southern Federal University, Rostov-on-Don, Russia.

References

1. J.R. Williams, D.R. Clarke, Acta Mater. **56**(8), 1813 (2008)
2. M. Dietiker, R.D. Nyilas, C. Solenthaler, R. Spolenak, Acta Mater. **56**(15), 3887 (2008)
3. N. Moharrami, S.J. Bull, Thin Solid Films **572**, 189 (2014)
4. A.A. Volinsky, N.R. Moody, W.W. Gerberich, J. Mater. Res. **19**(9), 2650 (2004)
5. Y. Cao, D.D. Nankivil, S. Allameh, W.O. Soboyejo, Mater. Manuf. Proc. **22**(2), 187 (2007)
6. S.W. Han, H.W. Lee, H.J. Lee, J.Y. Kim, J.H. Kim, C.S. Oh, S.H. Choa, Curr. Appl. Phys. **6**, e81 (2006)
7. F. Avilés, L. Llanes, A.I. Oliva, J. Mater. Sci. **44**(10), 2590 (2009)
8. H.D. Espinosa, B.C. Prorok, M. Fischer, J. Mech. Phys. Solids **51**(1), 47 (2003)
9. E.I. Preiß, B. Merle, M. Göken, Mater. Sci. Eng. A **691**, 218 (2017)

10. T. Chudoba, F. Richter, Surf. Coat. Technol. **148**(2–3), 191 (2001)
11. M.G. Veprek-Heijman, S. Veprek, Surf. Coat. Technol. **284**, 206 (2015)
12. W.C. Oliver, G.M. Pharr, J. Mater. Res. **7**(6), 1564 (1992)
13. A.S. Vasiliev, E.V. Sadyrin, B.I. Mitrin, S.M. Aizikovich, A.L. Nikolaev, Russ. Eng. Res. **38**(9), 735 (2018)
14. A.S. Vasiliev, S.S. Volkov, E.V. Sadyrin, S.M. Aizikovich, Mathematics **8**(6), 983 (2020)
15. E. Sadyrin, A. Vasiliev, S. Volkov, Acta Polytec. CTU Proc. **27**, 18 (2020)
16. S.S. Volkov, A.S. Vasiliev, E.V. Sadyrin, in *MATEC Web of Conferences*, ed. by H.-G. Gross, H. Khaled, T. Abbasian Najafabadi, D.A. Nguyen, I. Kudish, I.B. Sevostyanov, Y.G. Cen, K. Egiazarian, V. Mladenovic, G. Karapetyan and M. Minkin (EDP Sciences, Les Ulis, 2018), p. 226

Relaxation Processes in Organic Anticorrosive Films

A. S. Bogatin, E. N. Sidorenko, S. P. Shpanko, S. A. Kovrigina, K. G. Abdulvakhidov, and I. O. Nosatschev

Abstract Organic coatings (films), modified with nonorganic anions, are widespread as means of protection of active metals from corrosion in the aggressive industrial environments. It has been established that these films demonstrate high through electrical conductivity and negative electrical capacitance at frequencies of the audio range. The frequency dependence of film samples with negative capacity seems unique. At the decrease of the frequency of the measuring electric field, the capacity module sharply increases and then, after reaching the value of a few tens or even hundreds of microfarads, remains unchanged within a certain low-frequency range. Such a frequency dependence of the capacity confirms that the negative capacity of the films occurs due to the development of relaxation polarization at the inverse intensity of the electric field. For this research on the negative capacity samples with the developed processes of relaxation polarization and the polarization of ionic shift, we have proposed a microscopic model of the development of relaxation polarization and also the impedance description of their electric properties. The tangent of the dielectric loss angle of these films has also a negative value. At the same time, the tangent modulus is defined as the sum of the contribution of the relaxation polarization mechanism itself (due to the absence of a maximum in the frequency dependence of the tangent) and the contribution of the through-conduction mechanism (due to the presence of the frequency maximum of electrical conductivity). The minimum is observed in the frequency dependence of the imaginary part of the complex electrical conductivity (it is negative in the area of frequency dispersion) . The comparison of the electrical parameters of the films, calculated within the framework of the model described here, and those, obtained experimentally, showed their good conformity. Thus the negativity of electric capacity of organic anticorrosive films is actually caused by a mechanism of relaxation nature.

A. S. Bogatin · E. N. Sidorenko (✉) · S. P. Shpanko · S. A. Kovrigina · K. G. Abdulvakhidov · I. O. Nosatschev
Southern Federal University, Rostov-on-Don, Russia
e-mail: si-do-re@mail.ru

I. A. Parinov et al. (eds.), *Physics and Mechanics of New Materials and Their Applications*, Springer Proceedings in Materials 10,
https://doi.org/10.1007/978-3-030-76481-4_20

Keywords Moletronics · Organic anticorrosive films · Negative capacity · Relaxation polarization · Inverse direction of electric field · Impedance spectroscopy

1 Introduction

Micromolecular electronics, alias moletronics, a new direction of microelectronics, has been born and now is growing fast. It is targeted at developing a new element base of electronic devices based on organic molecules and their assemblies. At the molecular level, there have already been created and functioning organic solar panels, switches, inverters, light-emitting diodes, molecular transistors, flexible displays and sensors. Thanks to some special properties of molecular materials, these electronic gadgets are easy to produce, lightweight and commercially accessible. This makes possible to increase the packing density of chip, increase the speed up their operation, reduce power consumption [1, 2].

Before, there have been studied the physico-chemical properties of the films used to protect low alloy steel from corrosion in acidic environment [3–5]. As a compositional inhibitor, we used an organic compound of imidazole class modified with nonorganic anions, thiocyanate ones in particular, introduced as potassium rhodanide (KCNS).

It was found that the film protective properties increase along with the growth in the concentration of nonorganic modifiers and the time of film formation, *t*. Where the modifier KCNS was used, we observed a more complex concentration dependence of the physical and chemical characteristics of the films.

Film conductivity is close to metallic and increases with increasing one-dimensional compression, while the impedance is inductive (negative capacitance). In the frequency band of 10^2 – 10^6 Hz, film spectra show deep dielectric dispersion with its center biased towards the area of lower frequencies when pressure is applied. We observed a two- and even three-fold growth in the module of films capacity taken at 10^2 Hz and pressure increase up to 3.5×10^5 Pa. The surface morphology of the inhibited samples was studied by means of an atomic force microscopy. It was found that each film under study showed an irregular relief with a wide spread of the mean arithmetic and geometric roughness of the film surface. The surface of the films looks like a voluminous conglomerate with a globular structure. The globules are oriented perpendicular to the film surface. The height, diameter, local concentration and appearance of globules depend on the time of film formation (1 – 5 days) and the concentration of KCNS in the mixed inhibitor (10 – 90 mmol/L against the background of a constant concentration of the benzimidazole derivative of 1 mmol/L).

We studied the films produced within three days in the presence of a compositional inhibitor containing 90 mmol/l of KCNS. Such films show a substantial protective property by giving a 25-fold decrease in the corrosion rate of steel in sulphuric acid environment. The photos obtained by means of a scanning electronic microscopy show that the film surface has a cellular structure with the cells of irregular shape

separated by channels. Evidently, the cells are the conglomerates of merged globules that is the case of similar films with haloid modifiers [6].

2 Negative Electric Capacity

Recently, there have been published many studies related to the detection of negative dielectric permettivity (capacity) of the matter [7–9]. The detailed account of the substances with negative dielectric permettivity could be found in [10]. The condensed-matter objects showing negative capacity are plenty. Negative capacity has been observed in crystal and amorphous semiconductors and nanocomposites, electrochemical cells, geological samples, biological membranes, etc. Of course, it makes no sense to talk about a single mechanism for the occurrence of negative capacity for such a variety of objects. However, there are some general peculiar properties of the matter that accompany the appearance of negative capacity. Most of researchers note the inertial conductivity [11, 12], associated with the manifestation of negative dielectric permettivity, although its mechanism is still being discussed. Thus, the paper [13] reports that the appearance of dielectric negative permettivity is associated with filling up the traps and a further release of the charge. The paper [10] explains negative capacity in terms of electric nonlinearity in the local areas of the matter and the associated nonlinear processes of alternating current rectification. Many studies [14] often discuss a plasma-like dispersion described by means of the Drude model. When the capacitive impedance of the object equals zero, the objects under study possess some purely active impedance; the active component of conductivity is the frequency monotonic function [11]. Hence, the observed instance of the appearance of negative capacity may not be attributed to any resonance properties of the *RLC*-type system.

Most of the publications, dedicated to negative capacity, state that the lower is frequency, the higher is the module of the measured capacity of the object. Another nature of the frequency dependence of negative capacity is observed in the organic anticorrosive films we have dealt with. After the capacity module increase due to the decrease in frequency, it reaches the plateau and remains unchanged even though frequency keeps decreasing. Such a frequency-related change of capacity was explained within the framework of the developing process of relaxation polarization at the low frequency region.

3 Negative Electric Capacity Due to the Process of Relaxation Polarity

We offer to make this in the following manner. Let us consider a certain local region of a nonpolar dielectric, where there are own positive and negative ions with the

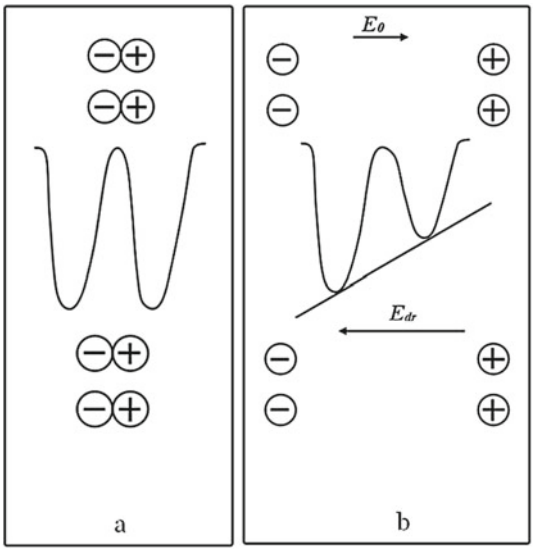

Fig. 1 Model showing the appearance of negative capacity with relaxation polarization developing in the matter; arrangement of the lattice ions: **a** before applying external electric field; **b** after application

centers virtually combined. Moreover, there are some other ions, e.g. impurity ions, whose motion is limited by a certain spatial area. The impurity ion is affected by some electric powers of the surrounding its ions. The energy of the impurity ion has a minimum value in the region of its localization. Let this ion is located in the neighborhood, where the energy has the minimum of the same depth [15]. If the depths of the potential holes for the considered impurity ions are the same, then the probabilities of transitions during the thermal motion of similar ions from left to right and from right to left are the same. In this case, about a half of impurity ions are localized on the left, other half on the right, and, consequently, the dipolar moment of the matter equals zero (Fig. 1a).

The situation changes after the application of an external constant electric field with the strength E_0 to this dielectric sample (Fig. 1b). Its own ions effected by the external electric field shift towards the opposite sides (elastic displacement polarization) and form dipoles. In the spaces between the charges of these dipoles, there appears an electric field, directed against the external one. The places of localization of impurity ions are effected by two electric fields, namely external field with intensity $\boldsymbol{E_0}$ and the one with new dipoles $\boldsymbol{E_{dr}}$. The external field may be regarded homogenous, while intensity of the field produced by the shifted ions depends on the distance from the charges to the places of localization of the doped ions. Since the dipole charges are close to the locations of equilibrium of impurity ions, their field at the distances of 10 – 20 nm may reach 10^5–10^6 V/m and exceed the external field by module.

The resulting field gets directed against the external one in this local area. As a result, in the localization area of impurity ions there appears a new field, inversely directed towards the external one, that is attached to the dielectric sample. Impurity

ions get into this inverse field. The depths of the two potential holes under discussion are now different. Due to the inversion of the resulting field the deeper hole is the one located closer to its own negative ion. Thus, there appears asymmetry in the arrangement of weakly bound impurity ions and correponding thermal ionic polarization. Its contribution to the polarization of the matter is negative towards the one created by the elastic displacement polarization. Should the contribution of the thermal ionic polarization exceed the one from the elastic ion polarization, then the matter, which remains long in the electric field, has negative dielectric permittivity. After applying an alternating low-frequency filed to the substance, the relaxing ions follow changes in the field and contribute to dielectric permittivity. These contributions are negative. However, as the frequency of the alternating electric field increases, the relaxing ions begin to lag behind the field oscillations. Their contribution to the polarization, and hence in the modulus of the dielectric constant of the substance, decreases. With a further increase in the frequency of the field, the permittivity becomes positive, and finally, when all the relaxing ions stop following the field, it reaches a positive value, determined by the ionic shift polarization.

4 Impedance Description of the Relaxation Polarization of Films with Negative Capacity

In terms of impedance spectroscopy, the equivalent circuit of a dielectric in which the described polarizations develop may looks as shown in Fig. 2.

In this circuit diagram, the capacitor C_3 is necessary to explain fast polarization processes (e.g., ion shift polarization). The conductivity of the resistor G_3 describes the through electrical conductivity of the dielectric sample, and the chain $R_4 - C_4$ is introduced to describe the relaxation polarization with the development of the relaxation process in an electric field with an inverted direction of the intensity vector ($-C_4 < 0$). As usual, the time of relaxation, is determined by the product of R_4C_4. The actual C' and the imaginary C'' parts of the complex electric capacity may be described by (1) and (2) expressions.

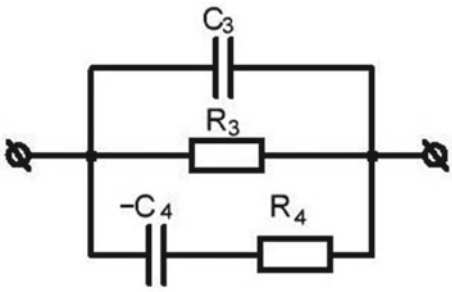

Fig. 2 Equivalent electrical circuit of a dielectric with developing relaxation polarization, when an internal electric field of inverse direction appears

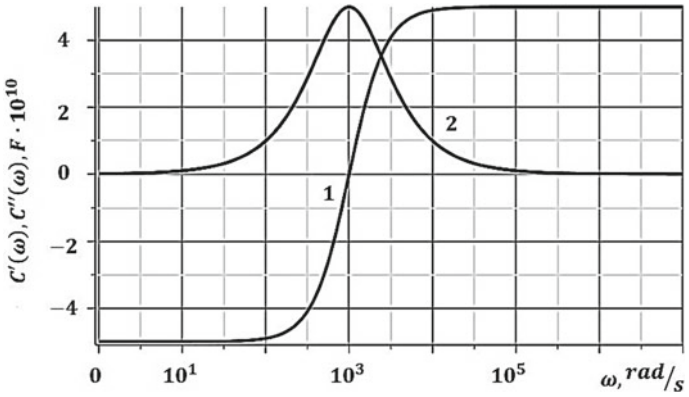

Fig. 3 Frequency dependencies of the real (1) and imaginary (2) parts of capacity for the dielectric with the progressing relaxing polarization at the appearance of an inner electric field with inverse direction. $G_3 = 0$; $C_3 = 5 \times 10^{-10}$F; $R_4 = 10^6$ Ω; $C_4 = 10^{-9}$F

$$C' = \frac{(\omega C_4 R_4)^2 C_3 + C_3 - C_4}{1 + (\omega C_4 R_4)^2} \tag{1}$$

$$C'' = \frac{G_3 + (\omega C_4 R_4)^2 G_3 + (\omega C_4)^2 R_4}{\omega(1 + (\omega C_4 R_4)^2)} \tag{2}$$

Here ω is frequency of changing the electric field; $C_4 > 0$.

Figure 3 shows the frequency dependences of C' and C''. It follows that the frequency dependence of C' is fundamentally different from the similar dependence obtained during the development of the usual relaxation process with a positive capacitance (RPPC) and corresponds to the polarization processes described above. In this case, frequency dependence C'' repeats the similar dependence obtained for the RPPC. Indeed, the derivative taken with respect to frequency from (2) makes possible to obtain expression (3) for finding the frequencies of the extrema in dependence $C(\omega)$

$$C_4^4 R_4^3 (1 + G_3 R_4)\omega^4 - C_4^2 R_4 (1 - 2G_3 R_4)\omega^2 + G_3 = 0 \tag{3}$$

The root of this equation, which suits us in physical terms, has the following form:

$$\omega_1^2 = \frac{1 - 2G_3 R_4 + \sqrt{1 - 8G_3 R_4}}{2(C_4 R_4)^2 (G_3 R_4 + 1)} \tag{4}$$

Thus, the solution of Eq. (2) for $C''(\omega)$ is possible only if

$$G_3 \leq \frac{1}{8R_4} \tag{5}$$

At large through conductivities, no extrema in the $C''(\omega)$ dependencies are observed.

Let us consider the features of the impedance characteristics of samples of a substance during the development of relaxation processes with negative capacitance (RPNC) in them. Let us start with the tangent of the angle of dielectric losses, tan δ. The expression for it look as follows:

$$\begin{aligned} \mathrm{tg}\delta &= \mathrm{tg}\delta_A + \mathrm{tg}\delta_B \\ &= \frac{G_3\left((\omega C_4 R_4)^2 + 1\right)}{\omega\left(C_3\left((\omega C_4 R_4)^2 + 1\right) - C_4\right)} + \frac{\omega R_4 C_4^2}{C_3\left((\omega C_4 R_4)^2 + 1\right) - C_4} \\ &= \frac{(\omega C_4)^2 R_4(G_3 R_4 + 1) + G_3}{\omega\left(C_3\left((\omega C_4 R_4)^2 + 1\right) - C_4\right)} \end{aligned} \tag{6}$$

We see that the expression for the tangent of the dielectric loss angle additively consists of two terms. One of them, *tg* δ_A, describes the contribution to *tg* δ of the through electrical conductivity, and the other one, *tg* δ_B, of the relaxation process itself. The expression for *tg* δ_A has the form:

$$\mathrm{tg}\delta_A = \frac{G_3\left((\omega C_4 R_4)^2 + 1\right)}{\omega\left(C_3\left((\omega C_4 R_4)^2 + 1\right) - C_4\right)} \tag{7}$$

The condition for the existence of the frequency extremum in (7) is obtained from the equation:

$$C_3 G_3 (C_4 R_4)^4 \omega^4 + G_3 (C_4 R_4)^2 (2C_3 + C_4)\omega^2 + G_3(C_3 - C_4) = 0 \tag{8}$$

The analysis (8) shows that the extrema in *tg* $\delta_A(\omega)$ exist only for $C_3 < C_4$, i.e., when the capacitance in the dielectric spectrum actually becomes negative. Here, the value of the extremum is the greater, the greater G_3, while the frequency position of the extremum does not depend on the value of G_3, is determined only by the parameters of the relaxation process.

The equation for *tg* $\delta_B(\omega)$ looks as follows:

$$tg\delta_B = \frac{\omega R_4 C_4^2}{C_3\left((\omega C_4 R_4)^2 + 1\right) - C_4} \tag{9}$$

The expression for the derivative of *tg* δ_B has no real roots at $C_3 < C_4$. Therefore, no extrema in *tg* $\delta_B(\omega)$ can be found in such cases.

For the frequency dependence *tg* δ, the positions of the extrema can be reached from

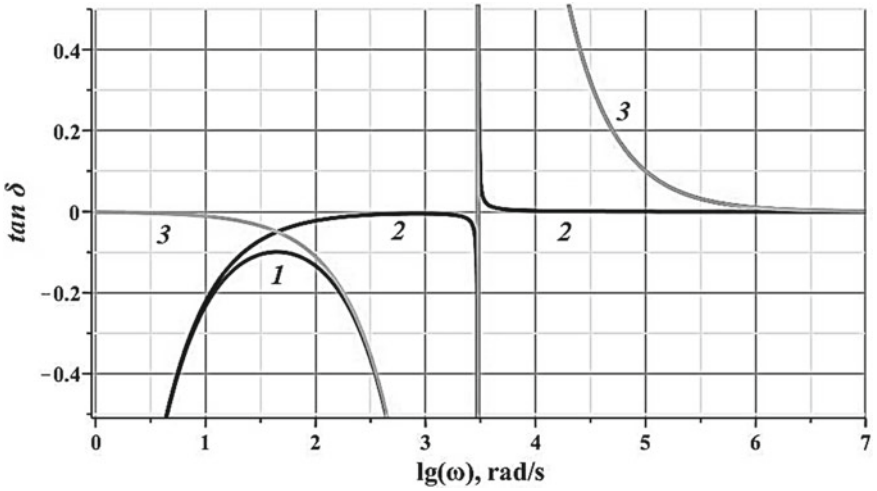

Fig. 4 Frequency dependencies: (1) *tg* δ, (2) *tg* δ_A, (3) *tg* δ_B

$$C_3C_4^4R_4^3(1+G_3R_4)\omega^4 + C_4^2R_4((2G_3R_4-1)C_3-(G_3R_4+1)C_4)\omega^2 + G_3(C_3-C_4)=0 \tag{10}$$

The extrema in the frequency dependences of *tg* δ at negative capacitances will only occur at high through electric conductivities:

$$G_3 > \frac{C_4 - C_3}{R_4(8C_3 + C_4)} \tag{11}$$

The plots in Fig. 4 show the above frequency dependences *tg* δ, *tg* δ_A, *tg* δ_B for a sample of a substance with RPNC.

Another impedance characteristic of relaxation polarization is the complex electrical conductivity G^*. With relaxation polarization with negative capacitance ($C_4 > C_3$) developing, there will always be extrema in the frequency dependences of the imaginary part of the complex conductivity G'' (12).

$$G'' = \frac{\omega^3 C_4^2 R_4^2 C_3 - \omega C_4 + \omega C_3}{1 + (\omega C_4 R_4)^2} \tag{12}$$

Therefore, all the relaxation processes with negative dielectric permettivity are strong. [16, 17]. Indeed, the condition for the presence of extrema in the frequency dependence of G'' can be found by taking the derivative with respect to ω and equating it to zero. The resulting equation looks this way as

$$(C_4R_4)^4\omega^4 + (C_4R_4)^2(2C_3 + C_4)\omega^2 + (C_3 - C_4) = 0 \tag{13}$$

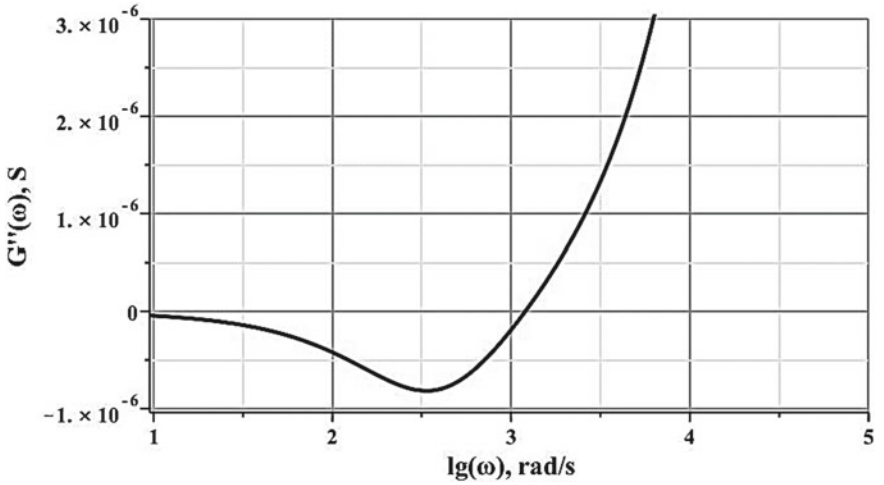

Fig. 5 Frequency dependence of the imaginary part of the complex electrical conductivity for a sample of substance with RPNC: $C_3 = 5 \times 10^{-10}$F; $R_4 = 5 \times 10^5$ Ω; $C_4 = 5 \times 10^{-9}$F:

The equation has real roots at $C_4 > C_3$. Figure 5 shows the frequency dependence of G''.

The formulae obtained after differentiation by frequency (7) and (13) for determining the position of the extrema in the frequency dependences $G"$ and $tg\ \delta_A$ are the same. Therefore, the frequencies of the extrema in these dependences coincide. However, in the dependence $G"(\omega)$, the extremum is the maximum, and in $tg\ \delta_A(\omega)$ is the minimum.

5 Comparison of the Theory and the Experimental Results

The above model for the development of relaxation polarization is Debay. In fact, the distribution of relaxers in the case of negative capacitance may also be different. Figure 6 shows the frequency dependences of the real part of the capacitance and the imaginary part of the conductivity for one of our organic anticorrosive films. The experimental values of the quantities are shown in the plots as dots. The simulation performed shows that the relaxation process developing in these films is lognormal [16] with the distribution width $b = 0.045$. Considering the width of the distribution, the frequency dependences C' and $G"$ were calculated. These curves are shown in the figure as continuous lines.

A very good matching between the calculated curves and experimental data indicates that our assumption about the relaxation nature of the appearance of negative capacitance in organic anticorrosive films is valid.

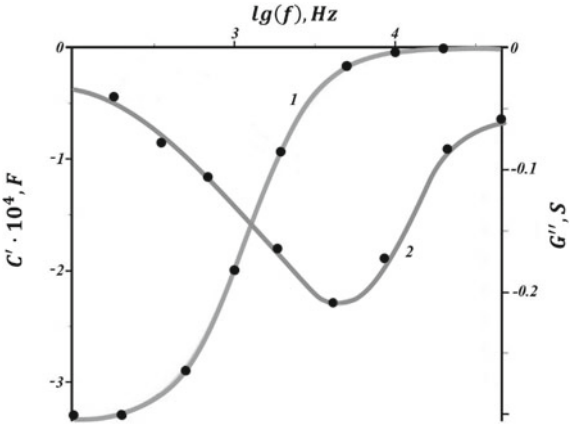

Fig. 6 Frequency dependences of the real parts of the complex capacity (1) and the imaginary parts of the complex electrical conductivity (2) of organic anticorrosive films at room temperature. Experimental values are in points, calculated curves are in continuous lines

References

1. G.S. Plotnikov, V.B. Zaitsev, *Physical Foundations of Molecular Electronics* (Department of Physics, Moscow State University, Moscow, 2000), p. 164
2. N.T. Sudar, V.M. Kapralova, V.V. Loboda, *Materials of Molecular Electronics* (St. Petersburg State Polytechnic University, 2014), p. 107 (In Russian)
3. S.P. Shpanko, E.N. Sidorenko, L.E. Kuznetsova, E.A. Sosin, in *Advanced Materials—Proceedings of the International Conference on "Physics and Mechanics of New Materials and Their Applications", PHENMA 2018*, Springer Proceedings in Physics, ed. by Ivan A. Parinov, Shun-Hsyung Chang, Yun-Hae Kim (Springer Nature, Cham, Switzerland, **224**, 2019), p. 123
4. E.N. Sidorenko, S.P. Shpanko, *Proceedings of the International Conference "Current issues of Electrochemistry, Ecology and Corrosion Protection"*. Tambov, p. 253 (2019) (In Russian)
5. D.A. Grineva, E.N. Sidorenko, S.P. Shpanko, in *Chemistry: Achievements and Prospects* (SFedU Press, Rostov-on-Don-Taganrog, 2020), p. 233 (In Russian)
6. E.N. Sidorenko, S.P. Shpanko, M.A. Bunin, T.I. Debelova, in *Physics and Mechanics of New Materials and Their Applications*, ed. by Ivan A. Parinov, Shun-Hsyung Chang, Banh Tien Long (Nova Science Publishers, New York, 2020), p. 129
7. A.K. Jonscher, J. Chem. Soc. Faraday Trans. **82**(2), 75 (1986)
8. A.P. Boltaev, F.A. Pudonin, Concise Information on Physics. FIAN **7**, 3 (2011). ((In Russian))
9. Yu. V. Kabirov, V.G. Gavrilyachenko, A.S. Bogatin, K.G. Abdulvakhidov, E.V. Chebanova, N.V. Prutsakova, E.B. Rusakova, Eng. Bull. Don. **4** (2017) (In Russian)
10. J. Shulman, Y.Y. Xue, S. Tsui, F. Chen, C.W. Chu, Phys. Rev. B. **80**, 134202 (2009)
11. N.A. Penin, Phys. Technol. Semicond. **3**(4), 626 (1996)
12. N.M. Olekhnovich, Yu.V. Radyush, A.V. Pushkarev, Fizika Tverdogo Tela **54**(11), 2103 (2012)
13. V.G. Gavrilyachenko, Yu.V. Kabirov, E.M. Panchenko, E.I. Sitalo, T.V. Gavrilyachenko, E.V. Milov, N.V. Lyanguzov, Fizika Tverdogo Tela **55**(8), 1540 (2013)
14. V.V. Makarov, A.B. Sherman, Fizika Tverdogo Tela **44**(11), 2101 (2002)
15. G.I. Skanavi, *Physics of Dielectrics*, Moscow-Leningrad. State Publishing House of Technical and Theoretical Literature, (1949), p. 500 (In Russian)
16. A.S. Bogatin, Bull. Russ. Acad. Sci. Phy. **57**(8), 1128 (2011)
17. A.S. Bogatin, A.V. Turik, S.A. Kovrigina, V.N. Bogatina, E.V. Andreev, Bull. Russ. Acad. Sci. Phy. **74**(8), 1066 (2010)
18. A.S. Bogatin, A.L. Bulanova, S.A. Kovrigina, E.V. Andreev, I.O. Nosatschev, Bull. Russ. Acad. Sci. Phy. **84**(11), 1425 (2020)

On Extension of Functional Possibilities of the Optical Interference Meter of the Surface Displacements of Control Objects

Igor P. Miroshnichenko and Ivan A. Parinov

Abstract The chapter describes a new design and operating principle of a new optical interference meter for surface displacements of control objects. This meter implements a new contactles measurement method, namely the method of highlighting the control object surface by laser radiation (or the "luminous point" method). It has advanced functionality in comparison with well-known Russian and foreign analogues by providing the ability to measure the spatial (linear and all angular components) displacements of the surfaces of control objects. The results obtained allow us to improve the quality and informativeness of the measurement results. They can be successfully applied in the process of high-precision measurements of spatial displacements of the surfaces of control objects during experimental studies of promising structures, buildings, structures, etc., when assessing their technical condition and diagnosing the condition of both stationary and mobile diagnostic systems, in mechanical engineering, instrumentation, shipbuilding, aircraft construction, etc.

Keywords Luminous point method · Laser interferometer · Control object · Surface displacements · Interference pattern

1 Introduction

The problem of ensuring safe operation and preventing the occurrence of emergency situations during the operation of man-made objects (structures, buildings, structures, etc.) remains as relevant as ever. Its resolution to date can only be possible by conducting periodic diagnostics of the condition of the marked objects during operation. This allows one to systematically monitor their condition, timely assess the remaining service life and quickly make decisions about the possibility of further

I. P. Miroshnichenko (✉)
Don State Technical University, Rostov-on-Don, Russia
e-mail: ipmir@rambler.ru

I. A. Parinov
Southern Federal University, Rostov-on-Don, Russia

I. A. Parinov et al. (eds.), *Physics and Mechanics of New Materials and Their Applications*, Springer Proceedings in Materials 10,
https://doi.org/10.1007/978-3-030-76481-4_21

operation, or about its completion. Stationary and mobile diagnostic systems are currently being developed and operated to solve the problems of diagnosing the state of the marked objects. For example, in [1, 2], a new optical measuring system is proposed, which provides an increase in the information content and reliability of the results of state diagnostics of structural materials and goods in operation.

In particular, this complex uses new non-contact optical displacement meters based on modern laser technologies and new methods of optical interferometry (see, for example, [3, 4]). The prototype for the design of the meters [3, 4] is a two-way laser interferometer with combined branches, proposed in [5, 6]. The use of displacement meters [3, 4] can significantly increase the information content, reliability and quality of measurement results, and, accordingly, the results of diagnostics of the state of structural materials and goods in operation.

The optical interference displacement meter proposed in [3] is designed for contactless measurements of linear displacements of the control object surfaces. It implements a new measurement method, namely the method of illumination of the control object surface by laser radiation (or the "luminous point" method) , proposed and scientifically justified in [7]. The design of the displacement meter [3] allows for its successful use as part of stationary diagnostic systems. For use in mobile diagnostic systems, a modified design of the meter is proposed in [4], which also implements the method of highlighting the surface of the object of control by laser radiation.

The functional characteristics of displacement meters [3, 4] have been studied in detail during computational, theoretical, and experimental work, the results of which are described in [7, 8], as well as during trial operation when solving practical measurement problems. A significant shortcoming of displacement meters [3, 4] is the inability to simultaneously measure the linear and angular components of the displacement of control object surface, since these meters allow us to measure only the linear displacement (linear component of the displacement) of the control object surface.

In practice, when testing the real control objects, the resulting displacements of their surfaces, as a rule, have both linear and angular components. So, the inability to simultaneously register both linear and angular components significantly reduces the information content and quality of the obtained measurement results. It requires the installation of additional meters for registering the angular components of the resulting movements, complicating the design of the measuring device, etc., that is significantly limit the scope of application of the marked displacement meters [3, 4].

There are known meters of small displacements (see, for example, [9, 10]), also included in the optical measuring setup [1, 2], which allow measuring both the linear and angular components of the displacements of the control object surface using a single meter. The analysis of the experience of their development and operation allows us to identify the main directions for modifying the design of displacement meters [3, 4] to expand their functionality.

The purpose of this work was to develop the design and operating principle of a new optical interference meter for surface displacements of control objects, which has expanded functionality by providing the ability to measure spatial (linear and all

angular components) displacements of the control object surfaces while maintaining the positive qualities of well-known Russian and foreign analogues (reliability, accuracy of measurement results, the ability to adjust the range of measured movements, use as part of stationary and mobile diagnostic setups, etc.).

2 Description of the Design of Proposed Meter

The design of the proposed meter is explained by the diagrams shown in Figs. 1–3. Figure 1 shows a diagram of the proposed meter.

Figure 2 shows a diagram of the proposed meter, illustrating the principle of operation of the meter when forming only the interference pattern A.

Figure 3 shows a diagram of the proposed meter, illustrating the principle of operation of the meter when forming only the interference pattern B. The proposed optical interference displacement meter contains (see Fig. 1) a coherent optical radiation source 1 (laser) , an optical system 2, a beam-splitter 3, a reflector 4, an additional reflector 5, a photodetector 6 and a device 7 for processing measurement results. The

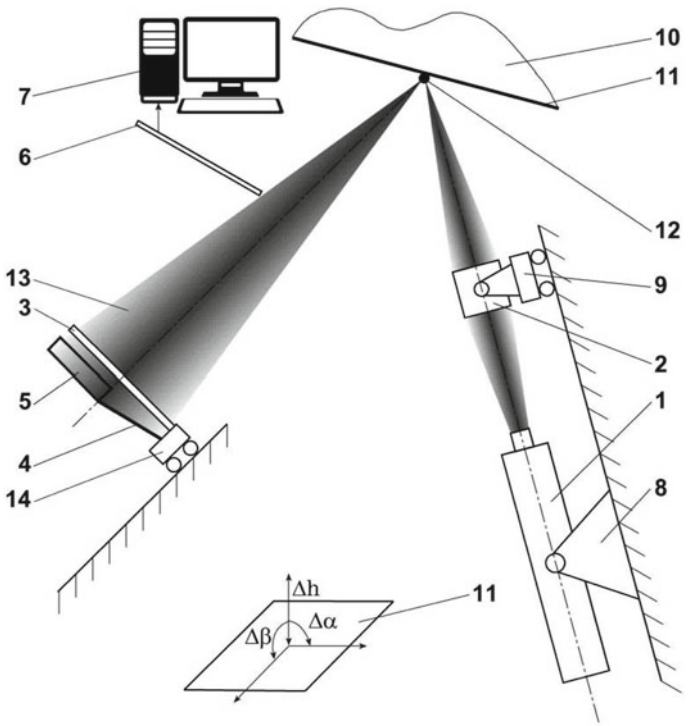

Fig. 1 Diagram of the proposed meter

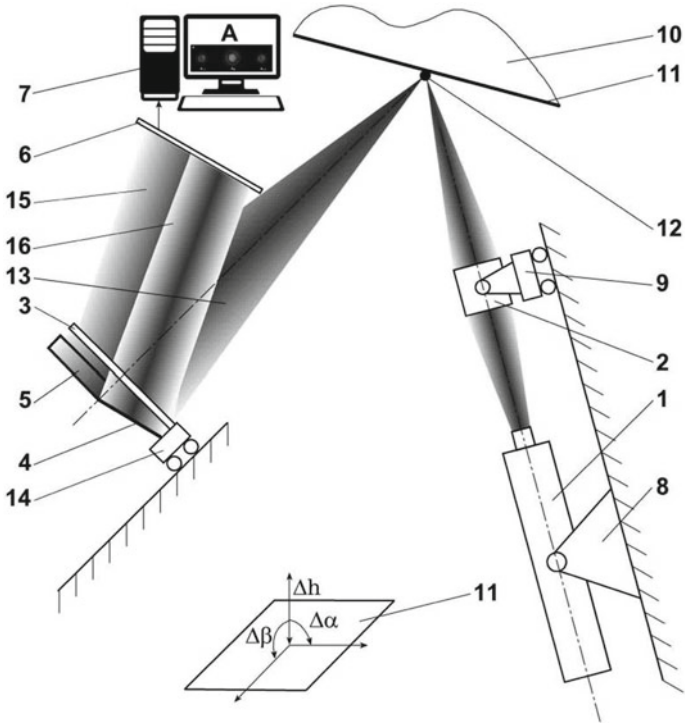

Fig. 2 Diagram of the proposed meter (interference pattern A)

listed components are interconnected and placed on a common base (it is not shown in Figs. 1–3).

The optical radiation source 1 and the optical system 2 are connected individually to separate devices 8 and 9 for adjusting and fixing their positions, respectively, designed to prepare for measurements (meter settings). The control object 10 with the surface 11 is installed on a separate base (it is not shown in Figs. 1–3) in the area of optical contact with the optical system 2. The optical system 2 focuses the radiation of the source 1 on the surface 11 of the control object 10 at the place of measurement 12 in the form of a "luminous point".

The "luminous point" 12 is a point source of radiation 13 with a spherical front reflected from the surface 11 of the control object 10. The beam-splitter 3 is made in the form of a phase lattice, which provides the formation of maxima of –1, 0 and +1 orders of interference patterns. This is investigated, justified and confirmed in [11] in comparison with various other types of beam-splitters. The reflector 4 and the additional reflector 5 are made in the form of optical mirrors with a surface coating facing the inner surface of the beam-splitter 3.

The reflector 4 is removed from the inner surface of the beam-splitter 3 by a distance h and is located under angle α to the beam splitter 3. The additional reflector 5 is removed from the inner surface of the beam-splitter 3 by a distance h and is located

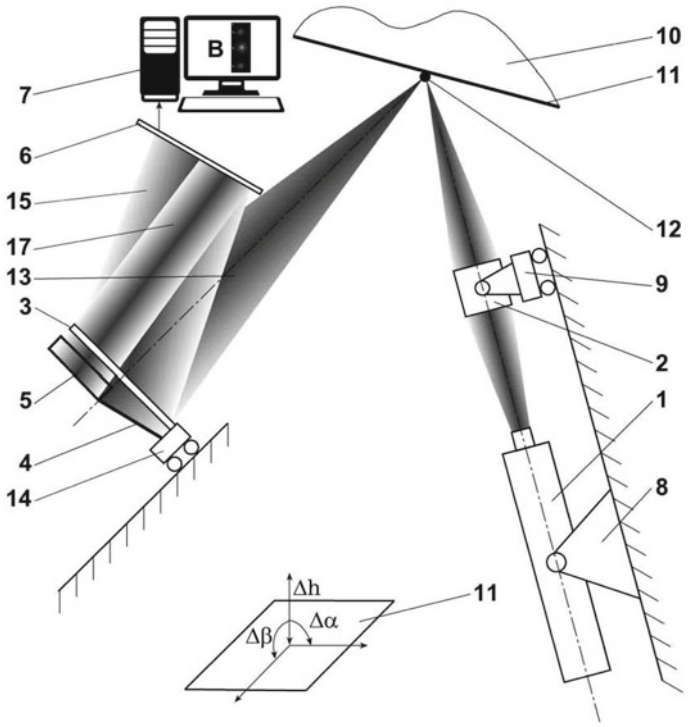

Fig. 3 Diagram of the proposed meter (the interference pattern B)

under angle α to the beam splitter 3. The additional reflector 5 is also rotated relative to the reflector 4 by an angle of 90°. The reflector 4 and the additional reflector 5 are connected individually to separate devices for adjusting and fixing their position (it is not shown in Figs. 1–3), intended for preparing for measurements (meter settings).

In the operating position, the beam splitter 3, the reflector 4 and the additional reflector 5 are rigidly fixed relative to each other, and are also connected to the device 14 for changing their position relative to the surface 11 of the control object 10 (changing the distance between the outer surface of the beam-splitter 3 and the surface 11 of the control object 10).

According to [3, 4], to increase the range of measured displacements, this distance is increased, and when the range of measured displacements is reduced, it is decreased by corresponding changing the position of the device 14. The photodetector 6 is made in the form of a semiconductor matrix and is rigidly fixed in the region at the place, where the interference patterns A and B are formed. It provides registration of the optical field intensities completely over the entire area occupied by the interference patterns A and B.

The device 7 for processing the measurement results based on a PC is electrically connected to the photodetector 6 and is designed to determine the linear Δh and

angular Δa and $\Delta \beta$ components of the surface displacements 11 of the control object 10 based on the results of measuring the optical field intensities in the specified areas of the interference patterns A and B by the photodetector 6, as well as to record and store the obtained measurement results.

3 Description of the Operation Principle of Proposed Meter

The principle of operation of the proposed meter is as follows. When preparing for testing the control object 10, and, accordingly, measuring the displacements of its surface 11, a priori, it is determined (or set) the range of possible values of the displacements of the surface 11 that occur during the tests. With a known range of possible values of the displacements of the surface 11, the device 14 with the beam-splitter 3, the reflector 4 and the additional reflector 5 rigidly fixed to it is placed at a certain distance between the outer surface of the beam-splitter 3 and the surface 11 of the control object 10, corresponding to a known range of changes in displacements. For this purpose, the dependence of the change in the sensitivity of the meter on the distance between the external surface of the beam-splitter 3 and the surface 11 of the control object 10 is used (see, for example, [3, 8, 12]), obtained experimentally during metrological maintenance of the meter. As already noted in [6, 7], to increase the range of measured displacements, this distance is increased, and when the range of measured displacements is reduced, it is decreased by corresponding changing the position of the device 14.

Photodetector 6 is rigidly fixed in the area at the place of formation of interference patterns A and B (see Figs. 2, 3). In the process of measurement, the optical system 2 focuses the radiation source 1 to the surface 11 of the test object 10 according to the place of measurements in the “luminous point” 12. The “luminous point" 12 is a point radiation source 13 with spherical front reflected from the surface 11 of the control object 10.

The radiation 13 falls on the beam-splitter 3, which divides it into two beams. One beam 15 (“reference”) (see Figs. 2, 3) is reflected from the outer surface of the beam-splitter 3 itself, and the other passes to the reflector 4 and the additional reflector 5 (“object”). The second beam is reflected from the reflector 4 and the additional reflector 5 to form a beam 16, respectively (see Fig. 2) formed by the reflector 4, and the beam 17, obtained from the additional reflector 5 (see Fig. 3). Spatial alignment of the beams 15 and 16 with the formation of the interference pattern A occurs in the area of placing the photodetector 6 (see Fig. 2). The image of the interference pattern A with the pointed maxima of –1, 0 and +1 orders is shown in Fig. 4.

The spatial alignment of the beams 15 and 17 with the formation of the interference pattern B also occurs in the area of the placement of the photodetector 6 (see Fig. 3). The image of the interference pattern B with the indicated maxima of –1, 0 and + 1 orders is shown in Fig. 5.

In this case, the interference patterns A and B are formed simultaneously and individually, do not intersect and do not overlap one another, which is due to the

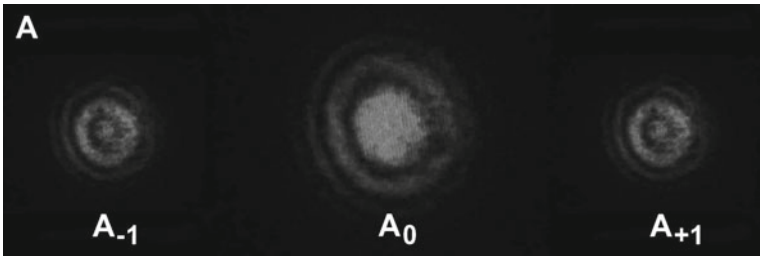

Fig. 4 Image of the interference pattern A obtained by combining the reflected beams 15 and 16, respectively, from the outer surface of the beam-splitter 3 and the reflector 4 (A_{-1}, A_0, A_{+1} are the maxima of –1, 0, and + 1 orders of the interference pattern A, respectively)

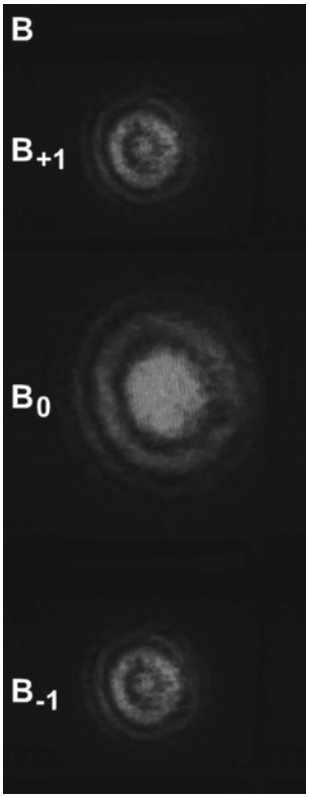

Fig. 5 Image of the interference pattern B obtained by combining the reflected beams 15 and 17, respectively, from the outer surface of the beam splitter 3 and the additional reflector 5 (B_{-1}, B_0, B_{+1} are the maxima of –1, 0 and + 1 orders of the interference pattern B, respectively)

marked placement of the beam splitter 4 and the additional beam splitter 5 relative to each other. The photodetector 6 registers the optical field intensities completely over the entire area occupied by the interference patterns A and B.

In the process of testing at the appearance of a linear Δh and/or angle $\Delta\alpha$ and $\Delta\beta$ displacement components of the surface 11 of the control object 10, there is a change

in the intensity of the optical field in the maxima of –1, 0 and + 1 order of interference patterns A and B, that is recorded by the photodetector device 6. The device 7 for processing the results of measurements associated with the photodetector device 6 determines the linear Δh and angular $\Delta\alpha$ and $\Delta\beta$ components of the displacements of the surface 11 of the control object 10 according to the results of measurements of the intensities of the optical field in the specified areas of the maxima of –1, 0 and + 1 order of interference patterns A and B by the photodetector device 6.

One of the possible processing options (for determining the linear Δh and angular $\Delta\alpha$ and $\Delta\beta$ displacement components of the surface 11 of the control object 10) can be, for example, the solution of a system of transcendental equations of the form:

$$I_i(\Delta h, \Delta\alpha, \Delta\beta) = J_i; i = 1, 2, 3$$

where $I_i(\Delta h, \Delta\alpha, \Delta\beta);\ i = 1, 2, 3$ are the dependences known from [7, 15], respectively, for maxima of the –1, 0, and +1 order, connecting the intensities, respectively, with the linear Δh and angular $\Delta\alpha$ and $\Delta\beta$ components of the surface displacement 11 of the object of control 10; J_i, $i = 1, 2, 3$ are the intensity values measured in the specified regions of maxima –1, 0, and +1 order of interference patterns A and B.

In this case, it is mandatory to use the results of measurements of the intensities simultaneously from the optical fields of both the interference patterns A and B in various combinations on maxima of –1, 0 and + 1 order. Variants of possible areas of interference patterns used to measure the intensity of optical fields are given in [13, 14]. The result is the values of the linear Δh and angular $\Delta\alpha$ and $\Delta\beta$ components of the displacement of the surface 11 of the control object 10, which simultaneously satisfy the values of the intensities J_i, $i = 1, 2, 3$.

Thus, the goal is achieved, namely to expand the functionality of the proposed meter by providing the ability to measure the spatial (linear and all angular components) displacements of the control object surfaces by maintaining the positive qualities of well-known Russian and foreign analogues.

4 Conclusion

In general, it can be noted that a new design and principle of operation of a new optical interference meter for the displacements of control object surfaces have been developed. This meter implements a new contactless measurement method, namely the method of highlighting the surface of the control object by laser radiation (or the "luminous point" method) . It has expanded functionality in comparison with well-known Russian and foreign analogues by providing the ability to measure spatial (linear and all angular components) displacements of control object surfaces.

The proposed meter not only has advanced functionality, but also retains all the positive qualities of well-known Russian and foreign analogues (reliability, accuracy

of measurement results, the ability to adjust the range of measured displacements, use as part of stationary and mobile diagnostic systems, etc.).

The results obtained allow us to improve the quality and informativeness of the measurement results. They can be successfully applied in the process of the high-precision measurements of the spatial displacements of control object surfaces during experimental studies of promising structures, buildings, constructions etc., when assessing their technical condition and diagnosing the condition as part of both stationary and mobile diagnostic setups, in mechanical engineering, instrumentation, shipbuilding, aircraft construction, etc.

Acknowledgements The study was performed under partial support of the Russian Ministry of Education and Science and Russian Foundation for Basic Research (No. 19-08-00365).

References

1. I.P. Miroshnichenko, I.A. Parinov, in *IOP Conference Series: Materials Science and Engineering*, vol. 374 (2018), p. 012052
2. I.P. Miroshnichenko, I.A. Parinov, in *Proceedings of the 2nd Annual International Conference on Material, Machines and Methods for Sustainable Development (MMMS2020).* Lecture Notes in Mechanical Engineering, vol. 324 (Springer Nature Switzerland AG, Switzerland, 2021)
3. V.E. Alekhin, I.P. Miroshnichenko, A.G. Serkin, V.P. Sizov, *Optical Device for Measuring Surface Displacements of Control Objects.* Russian Patent for Invention No. 2343402 (2009) (In Russian)
4. I.P. Miroshnichenko, I.A. Parinov, E.V. Rozhkov, A.G. Serkin, *Optical Interference Device for Measuring Surface Displacements of Control Objects.* Russian Patent for Invention No. 2512697 (2014) (In Russian)
5. A.N. Matveev, *Optics* (Higher School, Moscow, 1985), p. 351 (In Russian)
6. A.S. Batrakov, M.M. Butusov, G.P. Grechka, *Laser Measuring Systems* (Radio and Communications, Moscow, 1981), p. 456 (In Russian)
7. V.E. Alekhin, I.P. Miroshnichenko, V.P. Sizov, Russ. J. Nondestr. Test. **43**(2), 113 (2007)
8. V.E. Alekhin, I.P. Miroshnichenko, V.A. Nesterov, V.P. Sizov, Russ. J. Nondestr. Test. **43**(9), 592 (2007)
9. I.P. Miroshnichenko, A.G. Serkin, V.P. Sizov, *Method of Measuring Linear and Angular Displacements*. Russian Patent for Invention No. 2388994 (2009) (In Russian)
10. I.P. Miroshnichenko, I.A. Parinov, V.P. Sizov, *Method of Measuring Linear and Angular Components of Small Movements of Surfaces of Controlled Objects.* Russian Patent for Invention No. 2606245 (2017) (In Russian)
11. I.P. Miroshnichenko, I.A. Parinov, E.V. Rozhkov, S.-H. Chang, in *Advanced Materials Manufacturing, Physics, Mechanics and Applications*. Springer Proceedings in Physics, vol. 175 (Springer International Publishing, Cham, Heidelberg, New York, Dordrecht, London, Switzerland, 2016), p. 341
12. I.P. Miroshnichenko, I.A. Parinov, in *IOP Conference Series: Materials Science and Engineering*, vol. 572 (2019), p. 012065
13. I.P. Miroshnichenko, I.A. Parinov, E.V. Rozhkov, A.G. Serkin, *Optical Device for Measuring Displacements*. Russian Patent for Invention No. 2373492 (2009) (In Russian)
14. I.P. Miroshnichenko, I.A. Parinov, in *Advances in Structural Integrity. Proceedings of SICE 2016*, vol. 663 (Springer Nature Singapore, Singapore, 2018)

15. I.P. Miroshnichenko, I.A. Parinov, V.P. Sizov, in *Advanced Materials: Proceedings of the International Conference on Physics and Mechanics of New Materials and Their Applications, PHENMA 2019*. Springer Proceedings in Materials, vol. 6 (Springer Nature, Switzerland AG, Switzerland, 2020), p. 203

Mechanics of Advanced Materials

Features of Rayleigh Waves Propagation in Structures with FGPM Coating Made of Various Materials

T. I. Belyankova, E. I. Vorovich, V. V. Kalinchuk, and O. M. Tukodova

Abstract The study of the features of the propagation of surface acoustic waves (SAWs) is based on the solution of boundary value problems of electroelasticity for media with an inhomogeneous coating, the construction of the Green's functions of the medium and the analysis of its dispersion properties. For the cases of electrically open and electrically short-circuited surfaces, the influence of the ratio of the physical parameters of the coating materials, the localization region and the size of the transition zone of one material to another on the features of the propagation of Rayleigh waves is investigated. The results obtained in this work are useful for understanding dynamic processes in piezoelectric structures with an inhomogeneous coating in order to optimize and create new structures and devices based on SAWs with high performance characteristics.

Keywords Inhomogeneous coating · Functionally graded piezoelectric material (FGPM) · Dispersion equation · Surface acoustic waves (SAWs) · Rayleigh waves

1 Introduction

The foundations for the design of various types of acoustoelectronic devices through the use of homogeneous or inhomogeneous ferroelectrics were laid in works [1–3]. The area of application of acoustoelectronic devices is largely determined by the features of propagation and localization of surface acoustic waves on which they operate [4–6]. The development of modern technologies makes it possible to create artificial piezoelectric materials with special properties, oriented for effective use in devices for various purposes, such as high-precision sensors, filters, converters,

T. I. Belyankova (✉) · V. V. Kalinchuk
Southern Scientific Center of Russian Academy of Sciences, Rostov-on-Don, Russian Federation
e-mail: tbelen415@mail.ru

E. I. Vorovich · O. M. Tukodova
Don State Technical University, Rostov-on-Don, Russian Federation

I. A. Parinov et al. (eds.), *Physics and Mechanics of New Materials and Their Applications*, Springer Proceedings in Materials 10,
https://doi.org/10.1007/978-3-030-76481-4_22

generators, power transmission devices, executing devices and microelectromechanical systems (MEMS). This determines the need for a large-scale study of wave propagation processes in inhomogeneous media, in particular, in thin-film structures [6–9], in structures with functionally gradient components [10–17], in layered structures with various kinds of inclusions and coatings of various materials [18–21]. Most of the publications are aimed at studying the features of the behavior of horizontally polarized Love and Bluestein-Gulyaev waves in piezoelectric structures. In addition to high-velocity horizontally-polarized waves, surface Rayleigh waves are widely used in modern acoustoelectronic devices [4–6, 22–26], which are characterized by low propagation losses, a clearly defined velocity and exponential decay with depth. In [25, 26], for structures of an elastic/piezomagnetic substrate covered with a FGPM layer, the influence of the gradient coefficients on the phase velocity of Rayleigh waves was studied.

In this work, to study the effect of coating inhomogeneity on Rayleigh waves, heterostructures in the form of a homogeneous PZT-5H ceramic substrate with an inhomogeneous FGPM coating, which is a composite based on PZT-5H with an interlayer of high- or low-velocity PZT-based ceramics, are considered. The properties of the FGPM material smoothly change in thickness due to a change in the volume fraction of the coating components in this direction. As in [21], the cases of an inhomogeneous layer made of two and three materials were considered, which were considered as combinations of PZT-5H ceramics with high- or low-velocity ceramics based on PZT (PZT DL-61HD—pliable or PZT DL-40—hard) with different area of localization in thickness. The study of the features of the propagation of surface acoustic waves is based on the solution of boundary value problems of electroelasticity for media with an inhomogeneous coating, the construction of the Green's functions of the medium and the analysis of its dispersion properties. The solution is built in Fourier images with subsequent inversion, a combination of analytical representation for homogeneous ones with high-precision numerical reconstruction for inhomogeneous components is used. The influence of the nature, size of the transition zone of materials and localization of the coating inhomogeneity on the features of the frequency distribution of the phase velocities of Rayleigh waves for problems with an electrically open and short case is investigated.

2 Formulation of the Problem

We consider the problem of propagation in the direction of x_1 surface acoustic waves in a piezoelectric medium, which is a homogeneous half-space $x_3 \leq 0$, $|x_1|, |x_2| \leq \infty$. with an inhomogeneous coating $0 \leq x_3 \leq H$ (Fig. 1).

The piezoelectric structure is made on the basis of a 6 mm class piezoelectric, the symmetry axis of which coincides with the axis x_3, the change of coating properties is determined by the expressions:

Fig. 1 Problem geometry

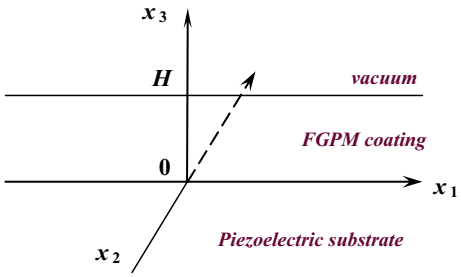

$$\rho^{(1)} = \rho_0 f_\rho^{(1)}(x_3), \quad c_{ij}^{(1)} = c_{ij}^0 f_c^{(1)}(x_3), \quad e_{ij}^{(1)} = e_{ij}^0 f_e^{(1)}(x_3), \quad \varepsilon_{ij}^{(1)} = \varepsilon_{ij}^0 f_\varepsilon^{(1)}(x_3), \tag{1}$$

where ρ_0, c_{ij}^0, e_{ij}^0, ε_{ij}^0 are the density and elastic modules of the substrate material, respectively, the polarization vectors of the substrate and the coating coincide in direction. Harmonic oscillations of the medium are caused by the action of a remote source, the oscillation mode is steady, the dynamic process satisfies the conditions ($k = 1, 3, 4,\ s = 1, 2, 3,\ n = 1, 2$):

$$u_k^{(n)} = u_k^{(n)}(x_1, x_3), \ \partial/\partial x_2 = 0, \ u_2^{(n)} = u_s^{(0)} = 0 \tag{2}$$

The superscript $n = 0$, 1, 2, corresponds to vacuum, cover and half-space, respectively. Further, dimensionless parameters were used [21–23]: $l' = l/h$, $\rho'^{(n)} = \rho^{(n)}/\rho^{(2)}$, $c_{ij}^{'(n)} = c_{ij}^{(n)}/c_{44}^{(2)}$, $e_{ij}^{'(n)} = e_{ij}^{(n)}\xi/c_{44}^{(2)}$, $\varepsilon_{ij}^{'(n)} = \varepsilon_{ij}^{(n)}\varepsilon^{(0)}\xi^2/c_{44}^{(2)}$, $\varepsilon^{(0)}$ is the dielectric constant of vacuum; $\kappa_2 = \omega h/V_S^{(2)}$ and $\kappa_{2e} = \omega h/V_{Se}^{(2)}$ are dimensionless frequencies, $V_S^{(2)} = \sqrt{c_{44}^{(2)}/\rho^{(2)}}$ and $V_{Se}^{(2)} = \sqrt{\left(c_{44}^{(2)} + \left(e_{15}^{(2)}\right)^2/\varepsilon_{11}^{(2)}\right)/\rho^{(2)}}$ are the velocities of bulk shear waves without and taking into account the piezoelectric properties. Further, strokes are omitted.

Oscillations of the piezoactive structure are described by the equations ($n = 1, 2$) [15–17, 21–23]:

$$\nabla \cdot \mathbf{\Theta}^{(n)} = \rho^{(n)} \ddot{\mathbf{u}}^{\mathbf{e}(n)}, \quad \nabla \cdot \mathbf{\Delta}^{(n)} = 0, \tag{3}$$

Equation for vacuum:

$$\Delta\varphi^{(0)} = 0 \tag{4}$$

The surface is assumed to be free from mechanical stress:

$$\mathbf{n} \cdot \mathbf{\Theta}^{(1)}\big|_{x_3 = H} = 0, \tag{5}$$

Two types of electrical conditions are discussed below.

(i) electrically open conditions (open case):

$$\mathbf{n}\cdot\boldsymbol{\Delta}^{(1)}\big|_{x_3=H} = \mathbf{n}\cdot\boldsymbol{\Delta}^{(0)}\big|_{x_3=H}, \quad \varphi^{(1)}\big|_{x_3=H} = \varphi^{(0)}\big|_{x_3=H}, \tag{6}$$

(ii) metalized and grounded surface (short case):

$$\varphi^{(1)}\big|_{x_3=H} = 0. \tag{7}$$

Continuity of displacements and normal components of stresses and induction is assumed at the interface:

$$\begin{aligned} \mathbf{u}^{\mathbf{e}(1)}\big|_{x_3=0} &= \mathbf{u}^{\mathbf{e}(2)}\big|_{x_3=0}, \quad \mathbf{n}\cdot\boldsymbol{\Theta}^{(1)}\big|_{x_3=0} = \mathbf{n}\cdot\boldsymbol{\Theta}^{(2)}\big|_{x_3=0}, \\ \mathbf{n}\cdot\boldsymbol{\Delta}^{(1)}\big|_{x_3=0} &= \mathbf{n}\cdot\boldsymbol{\Delta}^{(2)}\big|_{x_3=0}. \end{aligned} \tag{8}$$

At infinity, the damping condition is satisfied:

$$\mathbf{u}^{\mathbf{e}(2)}\big|_{x_3\to-\infty} \to 0, \varphi^{(0)}\big|_{x_3\to\infty} \to 0 \tag{9}$$

In relations (3)–(9) the following designations are used: $\mathbf{u}^{\mathbf{e}(n)} = \left\{u_1^{(n)}, u_3^{(n)}, u_4^{(n)} = \varphi^{(n)}\right\}$ is the extended vector of displacements, $\varphi^{(n)}$ is the function of electric potential, $\rho^{(n)}$ is the material density of n-th component. The components of the stress tensor $\boldsymbol{\Theta}^{(n)}$ and the induction vector of the medium $\boldsymbol{\Delta}^{(n)}$ are represented in the form [15–17, 21–23]:

$$\Theta_{lk}^{(n)} = \theta_{lksp}^{(n)} u_{s,p}^{(n)} + \theta_{lk4p}^{(n)} \varphi_{,p}^{(n)}, \quad D_l^{(n)} = \theta_{l4sp}^{(n)} u_{s,p}^{(n)} + \theta_{l44p}^{(n)} \varphi_{,p}^{(n)}, \quad k,l,s,p = 1,2,3, \tag{10}$$

where $\theta_{lksp}^{(n)} = c_{lksp}^{(n)}$, $\theta_{lk4p}^{(n)} = e_{plk}^{(n)}$, $\theta_{l4sp}^{(n)} = e_{lsp}^{(n)}$, $\theta_{l44p}^{(n)} = -\varepsilon_{lp}^{(n)}$; $c_{lksp}^{(n)}$, $e_{lsp}^{(n)}$, $\varepsilon_{ij}^{(n)}$ are the components of elastic constants tensors, piezoelectric modules and dielectric permittivity tensor, respectively.

Taking into account (1)–(2), representations (10) and material properties, the boundary value problem (3)–(9) is described by the equations [22, 23] for inhomogeneous coating $0 \le x_3 \le H$:

$$\begin{aligned} &\mathbf{L}_1^{(1)}\left[u_1^{(1)}\right] + \theta^{(1)} u_{3,13}^{(1)} + \psi^{(1)} u_{4,13}^{(1)} + c_{44,3}^{(1)} u_{1,3}^{(1)} + c_{44,3}^{(1)} u_{3,1}^{(1)} + e_{15,3}^{(1)} u_{4,1}^{(1)} = 0 \\ &\theta^{(1)} u_{1,13}^{(1)} + \mathbf{L}_2^{(1)}\left[u_3^{(1)}\right] + \mathbf{L}_3^{(1)}\left[u_4^{(1)}\right] + c_{13,3}^{(1)} u_{1,1}^{(1)} + c_{33,3}^{(1)} u_{3,3}^{(1)} + e_{33,3}^{(1)} u_{4,3}^{(1)} = 0, \\ &\psi^{(1)} u_{1,13}^{(1)} + \mathbf{L}_3^{(1)}\left[u_3^{(1)}\right] + \mathbf{L}_4^{(1)}\left[u_4^{(1)}\right] + e_{31,3}^{(1)} u_{1,1}^{(1)} + e_{33,3}^{(1)} u_{3,3}^{(1)} - \varepsilon_{33,3}^{(1)} u_{4,3}^{(1)} = 0 \end{aligned} \tag{11}$$

for substrate $x_3 \le 0$:

$$\begin{aligned}
\mathbf{L}_1^{(2)}\left[u_1^{(2)}\right] + \theta^{(2)} u_{3,13}^{(2)} + \psi^{(2)} u_{4,13}^{(2)} &= 0 \\
\theta^{(2)} u_{1,13}^{(2)} + \mathbf{L}_2^{(2)}\left[u_3^{(2)}\right] + \mathbf{L}_3^{(2)}\left[u_4^{(2)}\right] &= 0, \\
\psi^{(2)} u_{1,13}^{(2)} + \mathbf{L}_3^{(2)}\left[u_3^{(2)}\right] + \mathbf{L}_4^{(2)}\left[u_4^{(2)}\right] &= 0
\end{aligned} \tag{12}$$

for vacuum $x_3 > H$:

$$\sum_{k=1,3} u_{4,kk}^{(0)} = 0. \tag{13}$$

Boundary conditions:

$$\begin{aligned}
\Theta_{31}^{(1)}\Big|_{x_3=H} &= \left[c_{44}^{(1)}\left(u_{1,3}^{(1)} + u_{3,1}^{(1)}\right) + e_{15}^{(1)} u_{4,1}^{(1)}\right]\Big|_{x_3=H} = 0 \\
\Theta_{33}^{(1)}\Big|_{x_3=H} &= \left[c_{13}^{(1)} u_{1,1}^{(1)} + c_{33}^{(1)} u_{3,3}^{(1)} + e_{33}^{(1)} u_{4,3}^{(1)}\right]\Big|_{x_3=H} = 0
\end{aligned} \tag{14}$$

$$\begin{aligned}
D_3^{(1)}\Big|_{x_3=H} &= \left[e_{31}^{(1)} u_{1,1}^{(1)} + e_{33}^{(1)} u_{3,3}^{(1)} - \varepsilon_{33}^{(1)} u_{4,3}^{(1)}\right]\Big|_{x_3=H} = D_3^{(0)}\Big|_{x_3=H}, \\
u_4^{(1)}\Big|_{x_3=H} &= u_4^{(0)}\Big|_{x_3=H}
\end{aligned} \tag{15}$$

$$u_4^{(1)}\Big|_{x_3=H} = 0 \tag{16}$$

$$\begin{aligned}
&u_1^{(1)}\Big|_{x_3=0} = u_1^{(2)}\Big|_{x_3=0}, \quad u_3^{(1)}\Big|_{x_3=0} = u_3^{(2)}\Big|_{x_3=0}, \quad u_4^{(1)}\Big|_{x_3=0} = u_4^{(2)}\Big|_{x_3=0} \\
&\Theta_{31}^{(1)}\Big|_{x_3=0} = \Theta_{31}^{(2)}\Big|_{x_3=0}, \quad \Theta_{33}^{(1)}\Big|_{x_3=0} = \Theta_{33}^{(2)}\Big|_{x_3=0}, \quad D_3^{(1)}\Big|_{x_3=0} = D_3^{(2)}\Big|_{x_3=0}
\end{aligned} \tag{17}$$

$$u_1^{(2)}, u_3^{(2)}, u_4^{(2)}\big|_{x_3\to-\infty} \to 0, \quad u_4^{(0)}\big|_{x_3\to\infty} \to 0 \tag{18}$$

In formulae (11) and (12) the notations are used:

$$\begin{aligned}
&\mathbf{L}_1^{(n)} = c_{11}^{(n)}\frac{\partial^2}{\partial x_1^2} + c_{44}^{(n)}\frac{\partial^2}{\partial x_3^2} + \rho^{(n)}\kappa_2^2, \quad \mathbf{L}_2^{(n)} = c_{44}^{(n)}\frac{\partial^2}{\partial x_1^2} + c_{33}^{(n)}\frac{\partial^2}{\partial x_3^2} + \rho^{(n)}\kappa_2^2 \\
&\mathbf{L}_3^{(n)} = e_{15}^{(n)}\frac{\partial^2}{\partial x_1^2} + e_{33}^{(n)}\frac{\partial^2}{\partial x_3^2}, \quad \mathbf{L}_4^{(n)} = -\varepsilon_{11}^{(n)}\frac{\partial^2}{\partial x_1^2} - \varepsilon_{33}^{(n)}\frac{\partial^2}{\partial x_3^2} \\
&\theta^{(n)} = c_{13}^{(n)} + c_{44}^{(n)}, \quad \psi^{(n)} = e_{15}^{(n)} + e_{31}^{(n)}
\end{aligned}$$

Next, consider two problems:

Problem I—"open case", is described by equations of motion (11)–(13) with boundary conditions (14), (15) and (17), (18);

Problem II—"short case", is described by equations of motion (11), (12) with boundary conditions (14), (16)–(18).

3 The Solution of the Problem

The solution of problems I and II is built in the Fourier images, α is the parameter of the coordinate x_1 transformation [22, 23]:

$$U_p^{(1)}(\alpha, x_3) = \sum_{k=1}^{6} c_k^{(1)} y_{sk}^{(1)}(\alpha, x_3), \quad p = 1, 3, 4, \quad s = 4, 5, 6, \tag{19}$$

$$U_p^{(2)}(\alpha, x_3) = \sum_{k=1}^{3} f_{pk}^{(2)} c_k^{(2)} e^{\sigma_k^{(2)} x_3}, \quad U_4^{(0)}(\alpha, x_3) = c_1^{(0)} e^{-\alpha x_3} \tag{20}$$

The functions ${y_{sk}}^{(1)}(\alpha, x_3)$ in (19) are linearly independent solutions to the Cauchy problem with initial conditions ${y_{sk}}^{(1)}(\alpha, 0) = \delta_{sk}$ for the equation:

$$\mathbf{Y}^{(1)\prime} = \mathbf{M}^{(1)}(\alpha, x_3)\mathbf{Y}^{(1)}, \mathbf{Y}^{(1)} = \begin{pmatrix} \mathbf{Y}_\Sigma^1 \\ \mathbf{Y}_u^1 \end{pmatrix}$$
$$\mathbf{Y}_\Sigma^1 = \begin{Vmatrix} \Theta_{31}^{F(1)} \\ \Theta_{33}^{F(1)} \\ D_3 \end{Vmatrix}, \mathbf{Y}_u^1 = \begin{Vmatrix} U_1^{(1)} \\ U_3^{(1)} \\ U_4^{(1)} \end{Vmatrix} . \tag{21}$$

Here $\Theta_{31}^{F(n)}$, $\Theta_{33}^{F(n)}$, $D_3^{F(n)}$, $U_k^{(n)}$ are the Fourier transforms of the stress tensor components, induction vector (10), extended displacement vector; δ_{kp} is the Kronecker symbol. The matrix $\mathbf{M}^{(1)}(\alpha, x_3)$ has the form:

$$\mathbf{M}^{(1)}(\alpha, x_3) = \begin{pmatrix} 0 & m_{12} & m_{13} & m_{14} & 0 & 0 \\ m_{21} & 0 & 0 & 0 & m_{25} & 0 \\ m_{31} & 0 & 0 & 0 & 0 & m_{36} \\ m_{41} & 0 & 0 & 0 & m_{45} & m_{46} \\ 0 & m_{52} & m_{53} & m_{54} & 0 & 0 \\ 0 & m_{62} & m_{63} & m_{64} & 0 & 0 \end{pmatrix} \tag{22}$$

where.

$m_{12} = i\alpha g_1/g_0$, $m_{13} = i\alpha g_2/g_0$, $m_{14} = P_1 - \alpha^2\left(c_{13}^{(1)} g_1 + e_{31}^{(1)} g_2\right)/g_0$,

$m_{21} = i\alpha$, $m_{25} = -\rho^{(1)}\kappa_2^2$, $m_{31} = i\alpha e_{15}^{(1)}/c_{44}^{(1)}$, $m_{36} = -\alpha^2\left(c_{44}^{(1)}\varepsilon_{11}^{(1)} + \left(e_{15}^{(1)}\right)^2\right)/c_{44}^{(1)}$,

$m_{41} = \left(c_{44}^{(1)}\right)^{-1}$, $m_{45} = m_{21}$, $m_{46} = m_{31}$, $m_{52} = \varepsilon_{33}^{(1)}/g_0$, $m_{53} = e_{33}^{(1)}/g_0$,

$m_{54} = m_{12}$, $m_{62} = m_{53}$, $m_{63} = c_{33}^{(1)}/g_0$, $m_{64} = m_{13}$,

$$g_0 = \varepsilon_{33}^{(1)} c_{33}^{(1)} + \left(e_{33}^{(1)}\right)^2, \quad g_1 = c_{13}^{(1)}\varepsilon_{33}^{(1)} + e_{33}^{(1)} e_{31}^{(1)}, \quad g_2 = c_{13}^{(1)} e_{33}^{(1)} - c_{33}^{(1)} e_{31}^{(1)},$$

$$P_1 = c_{11}^{(1)}\alpha^2 - \rho^{(1)}\kappa_2{}^2$$

The parameters participating in representation (20) satisfy the characteristic equation:

$$\det \mathbf{M}_\sigma^{(2)}(\sigma) = 0, \quad \mathbf{M}_\sigma^{(2)}(r) = \begin{pmatrix} c_{44}^{(2)}r^2 - P_1 & -i\alpha\theta^{(2)}r & -i\alpha\psi^{(2)}r \\ -i\alpha\theta^{(2)}r & c_{33}^{(2)}r^2 - P_2 & e_{33}^{(2)}r^2 - e_{15}^{(2)}\alpha^2 \\ -i\alpha\psi^{(2)}r & e_{33}^{(2)}r^2 - e_{15}^{(2)}\alpha^2 & -\varepsilon_{33}^{(2)}r^2 + \varepsilon_{11}^{(2)}\alpha^2 \end{pmatrix},$$

$$P_1 = c_{11}^{(2)}\alpha^2 - \kappa_2^2, \quad P_2 = c_{44}^{(2)}\alpha^2 - \kappa_2^2,$$

the coefficients $f_{pk}^{(2)}$ are determined by solving a homogeneous system of linear equations with a matrix $\mathbf{M}_\sigma^{(2)}\left(\sigma_k^{(2)}\right)$. Unknown coefficients in representations (19), (20) are determined when the boundary conditions are satisfied. The solution of equation system (21), (22) is constructed numerically; a modification of the Runge–Kutta method is used in this work.

4 Dispersion Equations

The structure of the dispersion equations for problems I and II can be represented in the form [15–17, 22]:

$$det\mathbf{A} = 0, \quad \mathbf{A} = \begin{pmatrix} \mathbf{B}^{(1)}(H) & \mathbf{G}^{(1)} \\ \mathbf{A}^{(1)}(0) & \mathbf{B}^{(2)}(0) \end{pmatrix}. \tag{23}$$

The sizes of the matrix and matrices of its components are determined by the geometry of the problem and the boundary conditions. By virtue of the accepted initial conditions of the Cauchy problem, both for problem I and for problem II, the matrix $\mathbf{A}^{(1)}(0)$ is unit and has dimension 6×6. For problem I, the matrix $\mathbf{A}$ has a dimension 10×10, its components in accordance with the boundary conditions (14), (15), (17), (18) are represented as

$$B^{(1)}(H) = \begin{pmatrix} y_{11}^{(1)} & y_{12}^{(1)} & y_{13}^{(1)} & y_{14}^{(1)} & y_{15}^{(1)} & y_{16}^{(1)} \\ y_{21}^{(1)} & y_{22}^{(1)} & y_{23}^{(1)} & y_{24}^{(1)} & y_{25}^{(1)} & y_{26}^{(1)} \\ \gamma y_{31}^{(1)} & \gamma y_{32}^{(1)} & \gamma y_{33}^{(1)} & \gamma y_{34}^{(1)} & \gamma y_{35}^{(1)} & \gamma y_{36}^{(1)} \\ \gamma y_{41}^{(1)} & \gamma y_{42}^{(1)} & \gamma y_{43}^{(1)} & \gamma y_{44}^{(1)} & \gamma y_{45}^{(1)} & \gamma y_{46}^{(1)} \end{pmatrix}, \quad G^{(1)} = \begin{pmatrix} 0\,0\,0 & 0 \\ 0\,0\,0 & 0 \\ 0\,0\,0 & -\varepsilon^{(0)}\alpha \\ 0\,0\,0 & -1 \end{pmatrix}, \tag{24}$$

$$\mathbf{B}^{(2)}(0) = \begin{pmatrix} -l_{11}^{(2)} & -l_{12}^{(2)} & -l_{13}^{(2)} & 0 \\ -l_{21}^{(2)} & -l_{22}^{(2)} & -l_{23}^{(2)} & 0 \\ -l_{31}^{(2)} & -l_{32}^{(2)} & -l_{33}^{(2)} & 0 \\ -f_{11}^{(2)} & -f_{12}^{(2)} & -f_{13}^{(2)} & 0 \\ -f_{31}^{(2)} & -f_{32}^{(2)} & -f_{33}^{(2)} & 0 \\ -f_{41}^{(2)} & -f_{42}^{(2)} & -f_{43}^{(2)} & 0 \end{pmatrix},$$

here

$$\gamma = e^{\alpha H},\ l_{1k}^{(2)} = c_{44}^{(2)}\sigma_k^{(2)} f_{1k}^{(2)} - i\alpha c_{44}^{(2)} f_{3k}^{(2)} - i\alpha e_{15}^{(2)} f_{4k}^{(2)},$$

$$l_{2k}^{(2)} = -i\alpha c_{13}^{(2)} f_{1k}^{(2)} + c_{33}^{(2)}\sigma_k^{(2)} f_{3k}^{(2)} + e_{33}^{(2)}\sigma_k^{(2)} f_{4k}^{(2)},$$
$$l_{3k}^{(2)} = -i\alpha e_{31}^{(2)} f_{1k}^{(2)} + e_{33}^{(2)}\sigma_k^{(2)} f_{3k}^{(2)} - \varepsilon_{33}^{(2)}\sigma_k^{(2)} f_{4k}^{(2)}.$$

For Problem II, the matrix $\mathbf{A}$ has the dimension 9×9, $\mathbf{G}^{(1)}$ is the zero matrix of the dimension 3×3, the matrices $\mathbf{B}^{(1)}(H)$ and $\mathbf{B}^{(2)}(0)$ are obtained by deleting the 3rd row and 4th zero column from representations (24) of the corresponding matrices of Problem I. For Problem II, the matrix $\mathbf{B}^{(1)}(H)$ contains the coefficient $\gamma = 1$.

5 Numerical Analysis

The study of the propagation of surface acoustic waves in piezoelectric structures with an inhomogeneous coating was carried out on models in which the properties of the coating material continuously change from the parameters of the substrate material to the parameters of the material of one inclusion (two-component model), or to the parameters of materials of two different inclusions (three-component model). Piezoelectric structures made of various types of piezoceramics based on PZT are considered (Table 1) [21]. Materials m_1 and m_2, m_3, represent the substrate material, namely ceramics PZT-5 and materials of inclusions, namely PZT DL-61HD and PZT DL-40, respectively.

Under the assumptions of item 2, we represent the functions $f_s^{(1)}(x_3)$ ($s = \rho,\ c,\ e,\ \varepsilon$) in the form:

$$f_s^{(1)}(x_3) = g_s^1 + g_s^2 f(x_3). \tag{25}$$

Parameters $g_s^1,\ g_s^2$ are determined by the values of the moduli of the substrate material and materials of inclusions, $f(x_3)$ determines the nature of the change in the parameters over the thickness of the coating, the localization of changes and the size of the transition zone from one material to another. Figures 2a–c show the functional dependences of changes in the properties of the coating material over thickness for two-component (Fig. 2a, b) and three-component (Fig. 2c, curves 4, 5) models. As

Table 1 Material parameters

	$\rho \cdot 10^3$ kg·m^{-3}	$c_{ij} \cdot 10^{11}$ N·m^{-2}					e_{ij} C·m^{-2}			$\varepsilon_{ij}/\varepsilon^{(0)}$	
		c_{11}	c_{12}	c_{13}	c_{33}	c_{44}	e_{15}	e_{31}	e_{33}	ε_{11}	ε_{33}
m_1	7.75	1.21	0.754	0.752	1.11	0.211	12.3	– 5.40	15.8	916	830
m_2	8.20	1.46	0.960	1.00	1.30	0.390	33.1	– 15.8	25.3	2810	2520
m_3	7.70	1.78	1.01	0.920	1.24	0.230	6.20	– 0.10	9.00	290	210

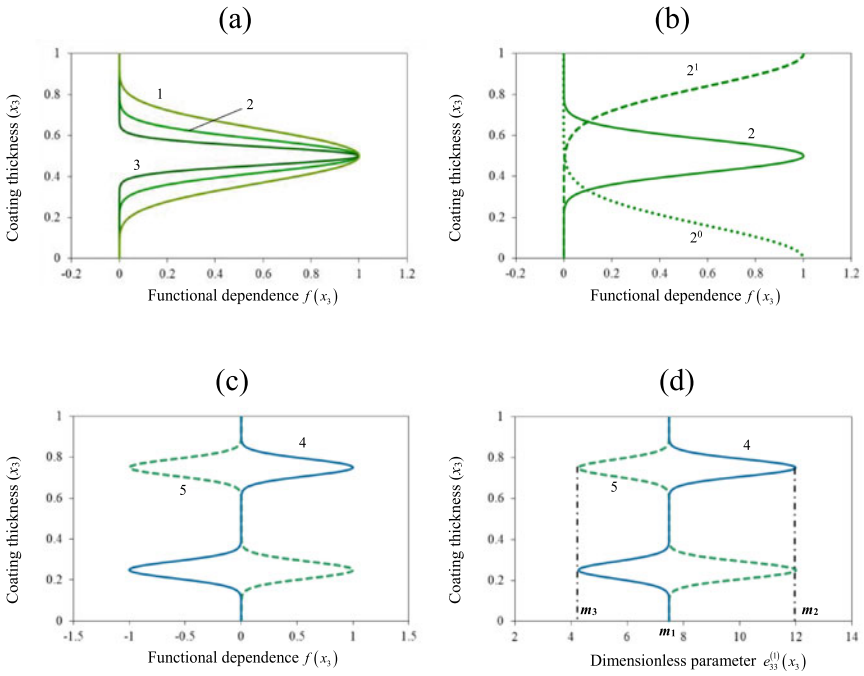

Fig. 2 Laws of coating properties changes

an example, Fig. 2d shows the change in the dimensionless parameter $e_{33}^{(1)}(x_3)$ for the three-component models $m_1/m_2/m_3$ (solid line, curve 4) and $m_1/m_3/m_2$ (dashed line, curve 5). In Fig. 2a, numbers 1, 2, 3 mark curves with different values of the transition zone of materials with a median localization of inhomogeneity, superscripts in Fig. 2b shows the curves with the localization of the inhomogeneity at the surface (index 1, dashed line) and at the boundary with the substrate (index 0, dotted line).

Figures 3 and 4 show the effect of the coating structure on the phase velocities of SAWs for piezoelectric structures with a two-component coating under the conditions of problem II (Figs. 3) and problem I (Figs. 4). Figure 5 shows graphs of SAWs velocities in structures of three materials for problem I and II. The figures show the behavior of the relative phase velocities $V_F^I / V_{Se}^{(2)}$ and $V_F^{II} / V_{Se}^{(2)}$, calculated for problem I and problem II. The numbers and superscripts in the figures mark the SAWs velocity curves for the coatings shown in Fig. 2a–c.

Figures 3a–c show the effect of inclusion localization at different thicknesses in a coating of m_1/m_2. For comparison, Fig. 3d shows the effect of inclusion localization for a coating of m_1/m_3. The numbers 1, 2, and 3 mark the curves corresponding to the maximum, average, and minimum thickness of the inclusion, the superscripts 0 and 1 mark the curves corresponding to the location of the inclusion in the lower or upper coating area, the curves without the index correspond to the case where the inclusion is located in the middle of the coating.

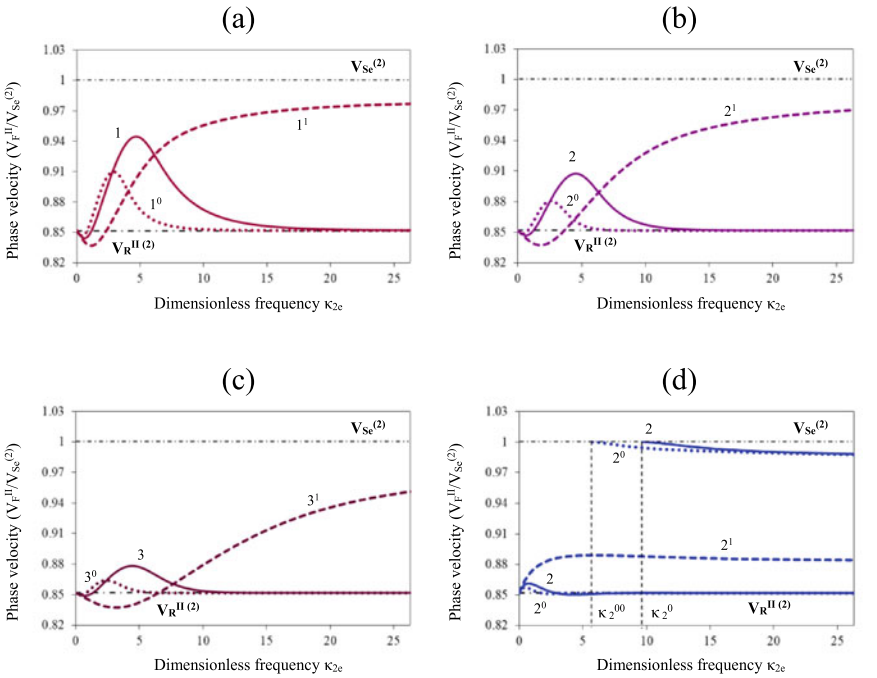

Fig. 3 Influence of localization of heterogeneity on SAWs velocity. Problem II: (a)–(c) coating m_1/m_2, (d) coating m_1/m_3

It can be seen from the figures that when an inclusion from m_2 is localized near the coating surface, the velocity first decreases, then sharply increases to the maximum values for this coating. A decrease of the inclusion thickness does not qualitatively change the behavior of the velocity, but leads to an increase of the range frequency in which the velocity changes. The localization of the inclusion in the middle or lower part of the coating leads to qualitative changes: the velocity first increases and then sharply decreases, asymptotically reaching the value $V_R^{II\,(2)}$. A decrease of the inclusion thickness does not qualitatively change the behavior of the velocity, but leads to a decrease of the maximum value in the low-frequency range.

In the case of a low-velocity inclusion from m_3, the structure of the surface wave field changes significantly. The localization of the inclusion at the surface leads to a sharp increase of the SAWs velocity in the low-frequency range. Further, the velocity value remains almost unchanged. Localization of the inclusion in the middle or lower part of the coating leads to a qualitative change in the first mode and to the appearance of a second high-velocity SAWs mode.

Figures 4a, b show the difference of SAWs velocity of piezoelectric structures with an inhomogeneous coating of m_1/m_2 (Fig. 4a) and m_1/m_3 (Fig. 4b) for problems I and II, respectively. The numbers 1, 2, and 3 mark the curves for different values of the inclusion thickness. The superscripts correspond to different levels of its location

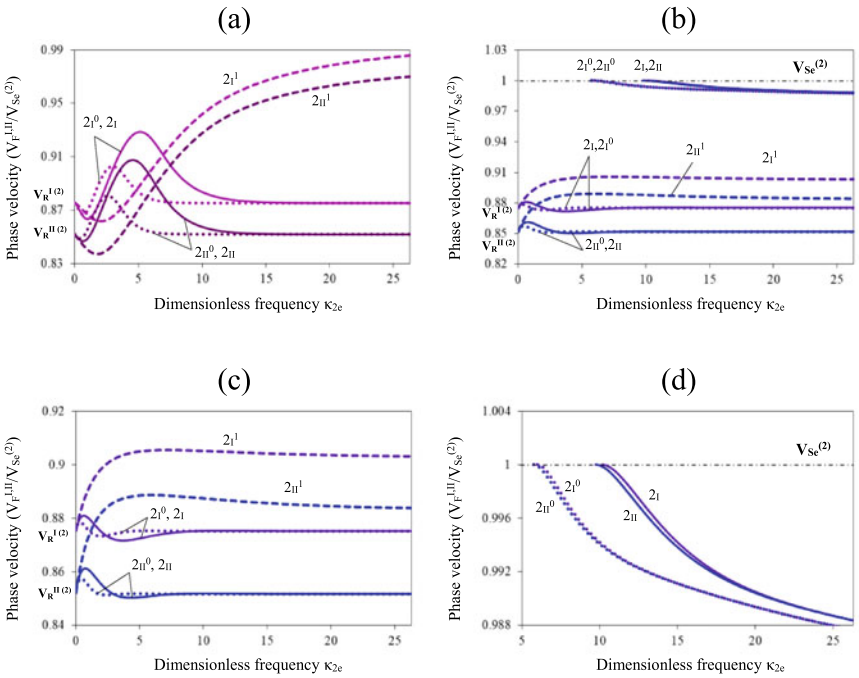

Fig. 4 Influence of the thickness and localization of the inclusion on the SAWs velocity for problems I and II: **a** coating from m_1/m_2; **b** cover from m_1/m_3; **c**, **d** fragments of (**b**)

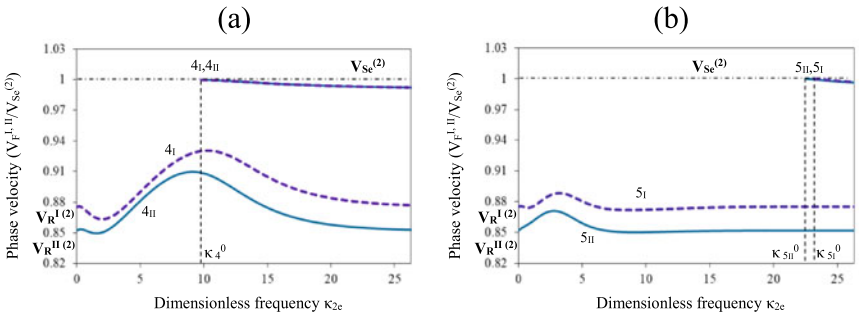

Fig. 5 Influence of the coating structure of three materials on the SAWs velocity:**a** coating from $m_1/m_2/m_3$, **b** coating from $m_1/m_3/m_2$

in the coating. The subscripts I and II designate the SAWs velocity curves for open and short case, respectively. Figures 4c and d show fragments of Fig. 4b.

It can be seen from the figures that, in contrast to [21], the SAWs structure for short case (II) and open case (I) does not qualitatively differ. The characteristic features of the SAWs behavior are retained depending on the type and localization

of the inclusion. The SAWs velocities in Problem I slightly exceed the velocities in Problem II.

Figures 5a, b show graphs of SAWs velocities in piezoelectric structures with a coating of three materials $m_1/m_2/m_3$ (Fig. 5a) and $m_1/m_3/m_2$ (Fig. 5b) for problems I and II. Numbers 4 and 5 mark the velocity curves for coatings shown in Figs. 2c and (d), respectively, the subscripts denote the SAWs velocities of problems I and II.

Figures 5a and b shown that the SAWs for coatings of three materials is determined by the location of inclusions from m_2 and m_3. When the m_2 inclusions are located in the upper part of the coating at a frequency $k_2 = 10$, the maximum of the velocity of the first SAW mode is pronounced. The second mode appears at the same frequency. The difference between open and short case is only in the magnitude of the SAWs velocity. When inclusion from m_3 is located in the upper part of the coating, the maximum velocity is lower in value and is shifted downward in frequency. The frequency of the appearance of the second mode has increased significantly, its values for the short and open cases differ, which can significantly affect the coefficient of electromechanical coupling (CEMC) .

Figures 6a, b illustrate the effect of localization of inhomogeneity in a two-component coating of m_1/m_2 (Fig. 6a) and m_1/m_3 (Fig. 6b) on the value of the effective CEMC [27] K_S^2, calculated for the first modes of SAWs ($K_S^2 = \left(\left(V_F^I\right)^2 - \left(V_F^{II}\right)^2\right)/\left(V_F^I\right)^2, V_F^{I,II}$ are the phase velocities of the SAWs for open and short case). The figures show the curves for the average thickness of the inclusion, the superscripts correspond to different levels of its location in the coating.

It can be seen from the figures that the nature of the CEMS change is determined by the type of inclusion and the place of its localization. Of greatest interest for applications may be a coating with an inclusion from m_2 in the middle. The maximum CEMS in this case is 25% higher than the CEMS for the half-space. It is respectively 15.5% or 10.1% higher than the CEMS maxima for similar coatings with inclusions localized in the lower or upper zone, respectively. The CEMS of a coating with an inclusion of m_3 at any position does not exceed the CEMS for the half-space. The lowest CEMS value is possessed by a coating with an inclusion localized near the

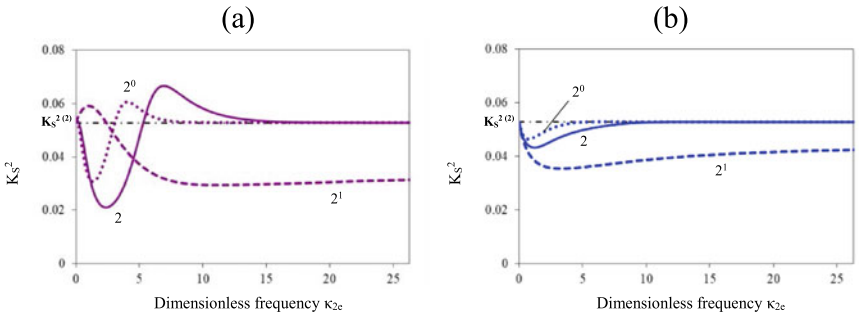

Fig. 6 Influence of localization of coating heterogeneity on the coefficient of electromechanical coupling $K_S{}^2$: **a** coating from m_1/m_2, **b** coating from m_1/m_3

surface. The type of inclusion (from m_2 or from m_3) does not matter in this case. CEMS at high frequencies with this localization is 43% less than CEMS for coatings with a different localization of inclusions.

6 Conclusion

The paper investigates the features of the behavior of Rayleigh waves in piezoelectric structures with a functionally graded coating. The piezoelectric structure is a homogeneous substrate made of PZT-5H ferroelectric ceramics with a FGPM coating, the properties of which are continuously changing over the thickness. The influence of the ratio of the physical parameters of the coating materials, the thickness of the inclusion, and the region of its localization on the features of the propagation of SAWs is investigated. For a two-component coating, it was found that the presence of a high-velocity inclusion in the upper part significantly increases the SAWs velocity. Output frequency at the maximum value depends on the thickness of inclusions. The presence of a low-speed inclusion inside the coating leads to the appearance of a second high-velocity SAWs mode, the output frequency of which depends on the location of the inhomogeneity in the coating: the lower the inhomogeneity is localized, the lower the output frequency. Within the framework of a three-material coating model, the frequency dependence of the influence of the nature and localization of inhomogeneities on the structural features of the surface wave field is shown. It was found that the nature of the change in CEMS is determined by the type of inclusion and the place of its localization. Of greatest interest for applications may be a covering with an inclusion from m_2 in the middle. The maximum CEMS in this case is 25% higher than the CEMS for the half-space. The results obtained in this work are useful in the optimization and design of new structures and devices on SAWs with high performance.

Acknowledgements This work was carried out within the framework of the implementation of the state assignment of the Southern Scientific Center of the Russian Academy of Sciences, state registration number 01201354242 with partial financial support from the Russian Foundation for Basic Research, projects 19-08-01051, 19-01-00719.

References

1. W.P. Mason, *Physical Acoustics and the Properties of Solids* (Van Nostrand, Princeton N.J., 1958)
2. E. Dieulesaint, D. Royer. *Ondes Elastiques Dans Les Solides. Application au Traitement du Signal* (Masson, Paris, 1974) (In French)
3. H. Matthews, *Surface Wave Filters: Design, Construction and Use* (Wiley, New York, 1977)
4. I.A. Viktorov, *Rayleigh and Lamb Waves: Physical Theory and Applications* (Plenum Press, New York, 1967)

5. S.V. Biryukov, Y.V. Gulyaev, V.V. Krylov, V.P. Plessky, *Surface Acoustic Waves in Inhomogeneous Media* (Springer, New York, 1995)
6. K. Hashimoto, *Surface Acoustic Wave Devices in Telecommunications: Modelling and Simulation* (Springer, Berlin and Heidelberg, 2000)
7. N. Emanetoglu, C. Gorla, Y. Liu, S. Liang, Y. Lu, Mater. Sci. Semicond. Process. **2**(3), 247 (1999)
8. T. Omori, K. Hashimoto, M. Yamaguchi, Proc. Int. Symp. Acoust. Wave Dev. Fut. Mobile Comm. Syst. **245** (2001)
9. P. Kirby, Q.-X. Su, E. Komuro, M. Imura, Q. Zhang, R. Whatmore, Integr. Ferroelectr.: Int. J. **41**(1–4), 91 (2001)
10. F. Jin, Z. Wang, T. Wang, Int. J. Eng. Sci **39**, 1271 (2001)
11. X.Y. Li, Z.K. Wang, S.H. Huang, Int. J. Solids Struct. **41**, 7309 (2004)
12. B. Collet, M. Destrade, G.A. Maugin, Eur. J. Mech. A Solids **25**, 695 (2006)
13. X. Cao, F. Jin, I. Jeon, T.J. Lu, Int. J. Solids Struct. **46**, 4123 (2009)
14. X. Cao, F. Jin, I. Jeon, NDT&E Int. **44**, 84 (2011)
15. T.I. Belyankova, E.I. Vorovich, V.V. Kalinchuk, O.M. Tukodova, IEEE Dyn. Syst. Mech. Mach. (Dyn.), **1** (2017). https://doi.org/10.1109/Dynamics.2017.8239435.
16. T.I. Belyankova, V.V. Kalinchuk, Mech. Adv. Mater. Struct. **28**(5), 486 (2021)
17. I.E. Andzhikovich, T.I. Belyankova, V.V. Kalinchuk, GYu. Levi, M.O. Levi, V.A. Lyzhov, Mater. Phys. Mech. **42**, 749 (2019)
18. Z.-H. Qian, F. Jin, S. Hirose, Ultrasonics **51**, 853 (2011)
19. P. Li, F. Jin, T.-J. Lu, Acta Mech. Sin. **28**(4), 1087 (2012)
20. Z.N. Danoyan, G.T. Piliposian, Int. J. Solids Struct. **45**, 431 (2008)
21. T.I. Belyankova, E.I. Vorovich, V.V. Kalinchuk, O.M. Tukodova, J. Adv. Dielectr. **10**(1, 2), 2060017 (2020)
22. T.I. Belyankova, V.V. Kalinchuk, *Dynamics of a Surface of Inhomogeneous Media* (Fizmatlit, Moscow, 2009). ((In Russian))
23. V.V. Kalinchuk, T.I. Belyankova, *Dynamic Contact Problems for Prestressed Electroelastic Solids* (Fizmatlit, Moscow, 2006). ((In Russian))
24. I. Ben Salah, M.H. Ben Ghozlen, Phys. Procedia **2**(3), 1377 (2009)
25. I. Ben Salah, A. Njeh, M.H. Ben Ghozlen, A theoretical study of the propagation of Rayleigh waves in a functionally graded piezoelectric material (FGPM). Ultrasonics, **52**(2), 306–314 (2012)
26. H. Ezzin, M. Mkaoir, M. B. Amor, Rayleigh wave behavior in functionally graded magneto-electro-elastic material. Superlattices Microstruct. **112**, 455–469 (2017)
27. D. Royer, E. Dieulesaint, Elastic waves in solids I: Free and guided propagation (Springer, Berlin, 2000)

Numerical Methods for Simulation of Elastic Wave Propagation in Layered Periodic Elastomer Composites

Sergey I. Fomenko, Mikhail V. Golub, Artur D. Khanazaryan, and Alisa N. Shpak

Abstract Two numerical methods are proposed to investigate wave propagation in layered phononic crystals composed of elastomers. The semi-analytical method is suggested to simulate and analyse the wave-fields in a layered phononic crystal of finite thickness in the case of oblique incidence. It is shown that semi-analytical method, where the wave-fields are calculated in terms of transfer matrix eigenvalues of a unit-cell, provides numerical stability. Dispersion equation for the infinite periodic layered composite made of elastomers is also formulated and solved via the spectral element method employing Lagrange interpolation polynomials at Gauss–Lobatto–Legendre nodal points and periodic boundary conditions. A comparison between the two methods and with known results is provided.

Keywords Elastic wave · Simulation · Phononic crystal · Elastomer · Spectral element method · Transfer matrix · Dispersion

1 Introduction

Nowadays composite materials and smart structures are used extensively in aerospace, mechanical and civil engineering, and many high-performance products due to their enhanced properties. Moreover, a novel class of composites providing unique properties and called metamaterials is now being intensively introduced into practice [1–3]. Metamaterials are composites periodically designed in order to produce special properties such as negative refraction [1], band-gaps [2, 3], tunable properties [4] arising from the consolidation of several material components. Wave propagation in acoustic/elastic metamaterials or phononic crystals is intensively studied to manipulate mechanical waves. Thus, acoustic metamaterials can provide required acoustic properties, e.g. wider band-gap, specific resonances or negative refractive index. Accordingly, the dynamic behaviour of complex structures made

S. I. Fomenko (✉) · M. V. Golub · A. D. Khanazaryan · A. N. Shpak
Institute for Mathematics, Mechanics and Informatics, Kuban State University, Krasnodar, Russian Federation
e-mail: sfom@yandex.ru

I. A. Parinov et al. (eds.), *Physics and Mechanics of New Materials and Their Applications*, Springer Proceedings in Materials 10,
https://doi.org/10.1007/978-3-030-76481-4_23

of acoustic metamaterials should be efficiently simulated and understood. Introduction of elastomers, as components of phononic crystals and acoustic metamaterials, allows more efficient manipulating of the wave energy flow. However, wave propagation and diffraction in acoustic metamaterials with elastomers have been studied for a relatively low number of problems [5–8]. Moreover, the standard finite element software, e.g. COMSOL Multiphysics, often does not provide user with enough tools for the simulation of arbitrary stiffness, piezoelectric and dielectric constants tensors. The main objective of this study is to propose efficient numerical tools for the simulation of periodic elastomer layered composites.

In this study, numerical methods to investigate wave motion in layered phononic crystals (LPnCs) composed of elastic and dielectric elastomers are presented. Infinite periodic structures and structures composed of a finite number of unit-cells, surrounded by two elastic half-spaces are considered. A semi-analytical method is developed to simulate and analyse the wave-fields in a layered phononic crystal of finite thickness in the case of oblique incidence when the wave-fields are calculated in terms of transfer matrix eigenvalues of a unit-cell which provides numerical stability [3, 9]. Dispersion equation for the periodic layered composite made of elastomers is formulated and solved via the spectral element method employing Lagrange interpolation polynomials at Gauss–Lobatto–Legendre points and periodic boundary conditions [10]. The influence of material and geometrical properties of layers on wave transmission through layered phononic crystals made of elastomers is investigated.

2 Mathematical Modelling of Periodic Composite

2.1 Formulation of the Problem

Let us consider periodic infinite LPnC consisting of elastomer unit-cells of thickness H, where each unit-cell is made of $L = 2$ sub-layers (see Fig. 1). The Cartesian coordinates $\boldsymbol{x} = (x_1, x_2)$ are introduced so that the interfaces of the LPnC are parallel to the x_1-axis. To denote layers $V^{(n)} = \{|x_1| \le \infty, z_{n-1} \le x_2 \le z_n\}$ of thickness $h_n = z_n - z_{n-1}$ the superscript n is employed. Material properties of n-th sub-layer are defined by the stiffness tensor $C^{(n)}_{ijkl}$, which has no symmetry in the general case of elastomer material [6], and mass density $\rho^{(n)}$.

The governing equations for harmonic steady-state in-plane motion with the angular frequency ω can be written for each sub-layer $V^{(n)}$ in terms of stress tensor σ_{ij} and displacement vector $\boldsymbol{u} = \{u_1, u_2\}$ as follows:

$$\sum_{j=1}^{2} \frac{\partial \sigma^{(n)}_{ij}(\boldsymbol{x})}{\partial x_j} + \rho^{(n)} \omega^2 u^{(n)}_i(\boldsymbol{x}) = 0. \tag{1}$$

Constitutive relations:

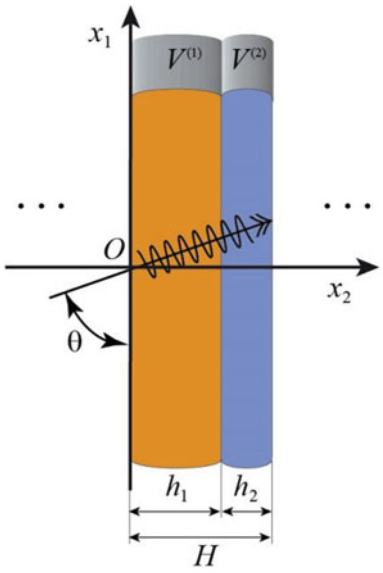

Fig. 1 Geometry of the problem for infinite LPnC

$$\sigma_{ij}^{(n)} = C_{ijkl}^{(n)} \frac{\partial u_k^{(n)}}{\partial x_l} \tag{2}$$

allow us to relate the components of stress tensor σ_{ij} and the components of displacement vector u_k. Substitution of constitutive relations (2) into governing equations (1) leads to the following equations:

$$\sum_{j=1}^{2} \sum_{k=1}^{2} \sum_{l=1}^{2} C_{ijkl}^{(n)} \frac{\partial^2 u_k^{(n)}(\boldsymbol{x})}{\partial x_l \partial x_j} + \rho^{(n)} \omega^2 u_i^{(n)}(\boldsymbol{x}) = 0 \tag{3}$$

where governing equations in n-th sub-layer are expressed in terms of displacement vector. Hereinafter the superscript n is omitted.

The wave-field **u** in the structure excited by the plane wave incident at an angle θ (Fig. 1) with respect to x_2-axis with wavenumber ζ is given by

$$\mathbf{u}(\mathbf{x}, \omega) = \mathbf{U}(x_2, k, \theta, \omega) \exp(\mathrm{i}\, \zeta_1\, x_1). \tag{4}$$

Here **U** is the vector of the complex amplitudes of the displacements, $\overline{\boldsymbol{\zeta}} = \{\zeta_1, \zeta_2\} = \{\zeta \sin(\theta), \zeta \cos(\theta)\}$ is the wave propagation vector of the incident wave; $\mathrm{i} = \sqrt{-1}$ is the imaginary unit. Therefore the problem is reduced to one-dimensional statement in terms of complex amplitudes.

Due to the periodicity, the Floquet boundary conditions are stated at the outer interface of the unit-cell of LPnC:

$$u_k(x_1, H)=u_k(x_1, 0)\mathrm{e}^{-\mathrm{i}\zeta_2 H}, \tag{5}$$

$$\sigma_{i2}(x_1, H)=\sigma_{i2}(x_1, 0)\mathrm{e}^{-\mathrm{i}\zeta_2 H}. \tag{6}$$

2.2 The Transfer Matrix Method

Governing equations (3) for an anisotropic elastic medium (including the case of anisotropic elastomers, where elastic constants C_{ijkl} are not symmetric) can be rewritten in terms of the complex amplitude vector as follows:

$$\mathbf{B_2}\frac{\partial^2}{\partial x_2^2}\boldsymbol{U} = \mathbf{B_1}\frac{\partial}{\partial x_2}\boldsymbol{U} + \mathbf{B_0}\boldsymbol{U}, \tag{7}$$

$$\begin{aligned}
&\mathbf{B}_0 = (B_{0;im}), \quad B_{0;im} = C_{i1m1}\zeta_1^2 - \rho\omega^2\delta_{im};\\
&\mathbf{B}_1 = (B_{1;im}), \quad B_{1;im} = -\mathrm{i}\,\zeta_1(C_{i2m1} + C_{i1m2});\\
&\mathbf{B_2} = (B_{2;im}), \quad B_{2;im} = C_{i2m2}; \quad i, m = 1, 2,
\end{aligned}$$

where δ_{im} is the Kronecker delta.

The continuity conditions of the elastic displacements, normal (σ_{22}) and tangential (σ_{21}) stresses at the internal interfaces $z = a_k$ can be written in terms of the generalized state vector $\mathbf{y}(x_1, x_2) = \{u_1, u_2, \sigma_{21}, \sigma_{22}\}$ as

$$\mathbf{y}(x_1, a_k - 0) = \mathbf{y}(x_1, a_k + 0). \tag{8}$$

Therefore, it is useful to rewrite the system of differential equations (7) in terms of the complex amplitude $\mathbf{Y}(x_2, k, \theta, \omega)$ of the generalized state vector

$$\frac{\partial \mathbf{Y}}{\partial x_2} = \mathbf{K}\mathbf{Y}. \tag{9}$$

where

$$\mathbf{K} = \mathbf{L}\,\mathbf{P}\,\mathbf{L}^{-1}; \quad \mathbf{P} = \begin{pmatrix} \mathbf{0}_2 & \mathbf{I}_2 \\ \mathbf{B}_2^{-1}\mathbf{B}_0 & \mathbf{B}_2^{-1}\mathbf{B}_1 \end{pmatrix}; \ \mathbf{L} = \begin{pmatrix} \mathbf{I}_2 & \mathbf{0}_2 \\ \mathbf{B}_3 & \mathbf{B}_2 \end{pmatrix}.$$

Here $\mathbf{I}_n$ and $\mathbf{0}_n$ are the unit and zero matrices of n-th size.

The fundamental solution of (8) has the following matrix form:

$$\mathbf{Y} = \mathbf{M}\,\mathbf{E}(x_2)\,\mathbf{c}. \tag{10}$$

where $\mathbf{c}$ is a vector of arbitrary constants. The matrices $\mathbf{E}$ and $\mathbf{M}$ are composed of the eigenvalues and the eigenvectors of the matrix $\mathbf{K}$ in (9), and they have the following forms:

$$\mathbf{E} = \text{diag}\{e^{q_1 z}, e^{q_2 z}, e^{q_3 z}, e^{q_4 z}\}, \quad \mathbf{M} = (\mathbf{m}_1, \mathbf{m}_2, \mathbf{m}_3, \mathbf{m}_4),$$
$$(\mathbf{K} - q_i \mathbf{I}_4)\mathbf{m}_i = 0, \quad i = 1, 2, 3, 4.$$

The solution (10) in a matrix form provides the transfer matrix (T-matrix) relation as

$$\mathbf{Y}_R = \mathbf{T}_{layer}\, \mathbf{Y}_L,$$

$$\mathbf{T}_{layer}(k, \theta, \omega) = \mathbf{M} \cdot \mathbf{E}(h) \cdot \mathbf{M}^{-1}, \tag{11}$$

where h is the width of the layer, $\mathbf{Y}_L$ and $\mathbf{Y}_R$ are the values of $\mathbf{Y}$ at the left and right interfaces of the layer.

The transfer matrix of the unit-cell, consisted of L sub-layers, is a composition of the T-matrices for each sub-layer as follows:

$$\mathbf{T}_{cell} = \mathbf{T}_L \cdot \mathbf{T}_{L-1} \cdots \mathbf{T}_1.$$

The most interesting phenomenon of phononic crystals is the existence of band-gaps or stop-bands. Band-gaps are frequency ranges, where the transmission of elastic waves in the phononic crystal is almost impossible due to exponentially decreasing of transmitted wave amplutudes from the unit cell to the unit cell. All the frequency ranges, where a non-zero wave transmission is observed, are called pass-bands.

The special type of pass-bands with low transmission (corresponding to band-gaps in practice) was identified and observed in the papers [3, 9] for the case of a finite number of unit cells between elastic half-spaces. In order to simulate the plane wave scattering by a layered phononic crystal between two half-spaces, the transfer matrix method can be used as well. In this case, the total T-matrix for the whole layered periodic structure is composed of N T-matrices of the unit cells, i.e., $\mathbf{T} = \mathbf{T}_{cell}^N$. Therefore, the solution is constructed in terms of eigenvalues of the transfer matrix of the whole unit cell [3].

Floquet-Bloch waves are known as special type of waves propagated through the periodic structure with an infinite number of unit cells. The dispersion equation for these waves has the following form:

$$|\mathbf{T}_{cell}(\zeta, \theta, \omega) - \exp(\mathrm{i}\, \zeta\, \cos\theta H)\, \mathbf{I}| = 0, \tag{12}$$

where ζ is a wavenumber of a Floquet-Bloch wave propagating in the periodic structure composed of layered unit cells.

The analysis of band-gaps and pass-bands is based on dispersion equation (12). The localization factor γ as the minimal attenuation factor of all excited waves can be applied. At the frequencies lying within a pass-band, at least one Floquet-Bloch wave can propagate without attenuation ($\gamma = 0$). The frequency range in which all Floquet-Bloch waves are attenuating corresponds to a band-gap ($\gamma > 0$).

2.3 The Spectral Element Method

For the considered statement of the problem (see Fig. 1) given by governing equations (1) and boundary conditions (5) and (6), the dispersion problem can be also solved by the spectral element method [11]. Unlike the transfer matrix method, where the complex amplitudes (4) are exploited, in this case, it is useful to represent the components of the displacement vector and stresses as follows:

$$\begin{aligned} u_k(x_1, x_2) &= \tilde{u}_k(x_2) \mathrm{e}^{\mathrm{i}(\zeta_1 x_1 + \zeta_2 x_2)}, \quad k = 1, 2; \\ \sigma_{ij}(x_1, x_2) &= \tilde{\sigma}_{ij}(x_2) \mathrm{e}^{\mathrm{i}(\zeta_1 x_1 + \zeta_2 x_2)}, \quad i, j = 1, 2. \end{aligned} \tag{13}$$

In terms of amplitudes $\tilde{u}_k$ and $\tilde{\sigma}_{ij}$, governing equations (1) and Floquet boundary conditions (5) and (6) can be written as follows:

$$\frac{d\tilde{\sigma}_{i2}(x_2)}{dx_2} + \mathrm{i}\zeta_1 \tilde{\sigma}_{i1}(x_2) + \mathrm{i}\zeta_2 \tilde{\sigma}_{i2}(x_2) + \rho\omega^2 \tilde{u}_i(x_2) = 0, \tag{14}$$

$$\tilde{u}_k(H) = \tilde{u}_k(0), \tag{15}$$

$$\tilde{\sigma}_{i2}(H) = \tilde{\sigma}_{i2}(0). \tag{16}$$

The interpolation polynomials, based on Gauss–Legendre–Lobatto grid $C^{i_1}\left(\xi^{l_1}\right)$, are employed as basis functions to expand the complex-valued displacement amplitudes:

$$\tilde{u}_k(x_2) = \sum_{l_1=1}^{M} \sum_{i_1=1}^{N} u_k^{l_1 i_1} C^{i_1}\left(\xi^{l_1}\right) = \sum_{I} u_k^I C^{i_1}\left(\xi^{l_1}\right). \tag{17}$$

The Gauss–Legendre–Lobatto polynomials $C^i\left(\chi_j\right)$ are non-zero only, if $i = j$: $C^i\left(\chi_j\right) = \delta_{ij}$. The values of derivative at the nodal points χ_k are designated as

$$\frac{dC^i(\chi_k)}{d\xi} = D_k^i.$$

The global coordinate x_2 are transformed into local coordinates ξ^l at each element l:

$$\xi^l = \frac{2x_2 - x_2^{l+1} - x_2^l}{x_2^{l+1} - x_2^l}, \quad x_2 = \frac{x_2^{l+1} - x_2^l}{2}\xi^l + \frac{x_2^{l+1} + x_2^l}{2},$$

$$\frac{d}{dx_2} = r^l \frac{d}{d\xi^l}, \quad r^l = \frac{2}{x_2^{l+1} - x_2^l}.$$

Here index $I(l_1, i_1)$ is introduced for simplicity, and I is in the range $1, \ldots, MN$, more details can be found in [11].

The relations for stresses can be written via (13) and (17):

$$\tilde{\sigma}_{ij}(x_2) = \sum_{k=1}^{2} \sum_{I} u_k^I \left[\mathrm{i}\zeta_1 C^{i_1}\left(\xi^{l_1}\right) C_{ijk1} + C_{ijk2} \left(\frac{dC^{i_1}\left(\xi^{l_1}\right)}{dx_2} + \mathrm{i}\zeta_2 C^{i_1}\left(\xi^{l_1}\right) \right) \right]. \quad (18)$$

According to the Bubnov–Galerkin method, projection functions are chosen so that they coincide with basis functions, i.e.

$$v_i^{k'}(x_2) = \delta_{k'i} C^{i_2}\left(\xi^{l_2}\right). \quad (19)$$

Due to periodic boundary conditions (15), the conditions:

$$v_i^{k'}(H) = v_i^{k'}(0) \quad (20)$$

are chosen for projection functions. The latter allows obtaining the variational formulation without additional terms (see [12] for more details):

$$\mathrm{i}\zeta_1 \sum_{i=1}^{2} \int_0^H \tilde{\sigma}_{i1}(x_2) v_i^{k'}(x_2)\, dx_2 + \mathrm{i}\zeta_2 \sum_{i=1}^{2} \int_0^H \tilde{\sigma}_{i2}(x_2) v_i^{k'}(x_2)\, dx_2$$
$$+ \sum_{i=1}^{2} \int_0^H \frac{d\tilde{\sigma}_{i2}(x_2)}{dx_2} v_i^{k'}(x_2)\, dx_2 + \rho\omega^2 \sum_{i=1}^{2} \int_0^H \tilde{u}_i(x_2) v_i^{k'}(x_2)\, dx_2 = 0. \quad (21)$$

Therefore, the system:

$$\sum_{I} \sum_{k=1}^{2} \left(A_{I'I}^{k'k}(\zeta) - \omega^2 \breve{A}_{I'I}^{k'k} \right) u_k^I = f_{I'}, \quad (22)$$

$$A_{I'I}^{k'k}(\zeta) = \sum_{i=1}^{2} \delta_{k'i}\delta_{l_1 l_2} \left[\begin{array}{l} -\delta_{i_1 i_2} \dfrac{1}{r^{l_1}} \mathrm{w}_{i_1} \displaystyle\sum_{j=1}^{2}\sum_{m=1}^{2} C_{ijkm}\zeta_j\zeta_m - C_{i2k2} r^{l_1} \sum_{p=1}^{N} \mathrm{w}_p D_p^{i_2} D_p^{i_1} + \\ +\mathrm{i}\, \mathrm{w}_{i_2} D_{i_2}^{i_1} \displaystyle\sum_{j=1}^{2} \zeta_j C_{ijk2} - \mathrm{i}\, \mathrm{w}_{i_1} D_{i_1}^{i_2} \sum_{m=1}^{2} \zeta_m C_{i2km} \end{array} \right],$$

$$\breve{A}_{I'I}^{k'k} = -\frac{\rho}{r^{l_1}} \delta_{k'k}\delta_{l_1 l_2} \mathrm{w}_{i_1} \delta_{i_1 i_2}.$$

can be composed with the components $f_{I'}$ in the right-hand side describing a given surface load. Here index $I'(l_2, i_2)$ is used to address projection functions in the same manner as index $I(l_1, i_1)$ numerating basis functions.

For the purposes of the present study, the dispersion equation:

$$\det\left(\mathbf{A}(\zeta) - \omega^2 \breve{\mathbf{A}}\right) = 0, \tag{23}$$

can be written in terms of the wavenumber ζ and matrices $\mathbf{A} = (A_{I'I}^{k'k})$, $\breve{\mathbf{A}} = (\breve{A}_{I'I}^{k'k})$. The latter can be reduced to the eigenvalue problem:

$$\det(\mathbf{B} - \lambda_n \mathbf{I}) = 0, \quad \mathbf{B} = \breve{\mathbf{A}}^{-1} \mathbf{A}(\zeta), \quad \omega_n = \sqrt{\lambda_n},$$

where $\mathbf{I}$ is the identity matrix of MN-size.

3 Numerical Analysis

Shear waves propagation in finitely deformed layered phononic crystal was investigated for oblique incidence in [6], where the constitutive behaviour of each phase was defined by neo-Hookean strain energy function. To have nearly incompressible phases, Li et al. (2018) set a high ratio between the two Lamé constants and shear modulus. To validate two presented numerical approaches, comparison with results presented in [6] has been provided.

In [6], plane strain condition with applied macroscopic tensile deformation (stretch ratio is denoted by s) along the layers was assumed and, correspondingly, only eight components of stiffness tensor are non-zero:

$$C_{1111} = \Lambda + \left(1 + \frac{1}{s}\right)\mu; \quad C_{1212} = s^2\mu; \quad C_{2121} = \frac{\mu}{s};$$

$$C_{1221} = C_{2112} = \mu; \quad C_{1122} = C_{2211} = \Lambda; \quad C_{2222} = \Lambda + \left(1 + s^2\right)\mu.$$

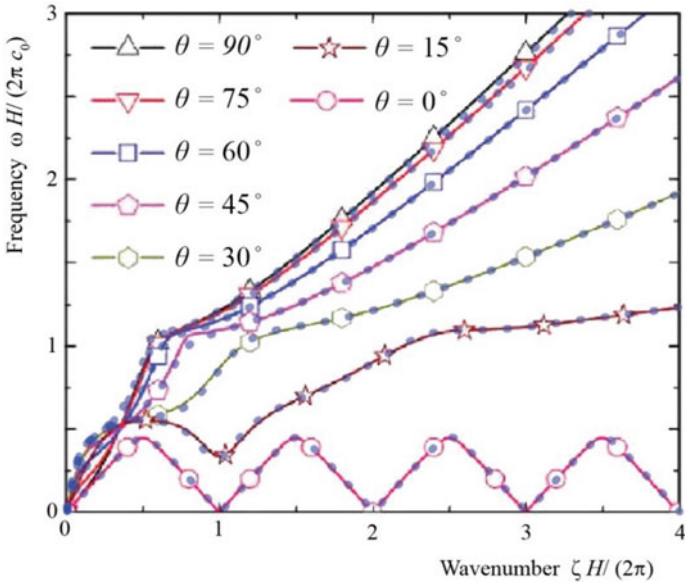

Fig. 2 Dispersion diagrams computed by finite element method and presented in [6] (Fig. 4a) and the both presented methods (blue dotted line) for validation

The comparison of the both numerical methods with results, obtained in [6], are shown in Fig. 2, where periodic elastomer with two-layered unit-cell was considered for undeformed state ($s = 1$). It should be noted that the semi-analytical method and the spectral element method provide the same results with the relative error smaller than 0.0001.

The thicknesses of sub-layers, composing unit-cell, are set $h_2/h_1 = 4$, whereas materials constants: $\Lambda^{(1)} = 500$ GPa; $\mu^{(1)} = 500$ MPa; $\Lambda^{(2)} = 5$ GPa; $\mu^{(2)} = 5$ MPa. In the case of the other values of stretch ratio s, the comparison with [6], where only shear band-gaps were studied, exhibit worse agreement.

To demonstrate the influence of the stretching ratio and the thicknesses of sub-layers on band-gaps and pass-bands, the localization factor γ is exhibited in Fig. 3 for two different thicknesses ratios ($h_1/H = 0.2$ and $h_1/H = 0.8$) and normal incidence ($\theta = 0$). The dark zones, where $\gamma > 0$, correspond to band gaps, while white domains are related to pass-bands. One can see that increase of the stretching ratio leads to the shift of the band gaps to lower frequencies and increase of the thickness of softer layer (sub-layer 2) leads to the decrease of the widths of band-gaps.

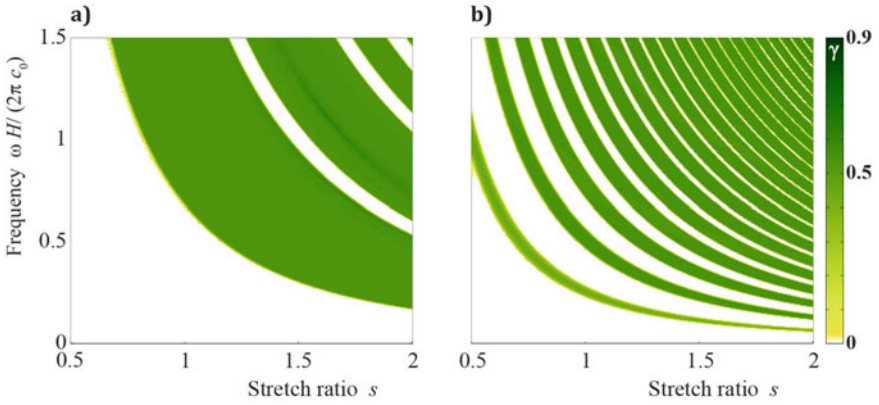

Fig. 3 Localization factor γ for two different thickness ratios: **a** $h_1/H = 0.2$; **b** $h_1/H = 0.8$

4 Conclusion

In this study, two numerical methods (the semi-analytical method based on T-matrices and the spectral element method) are present to solve dispersion relation for the layered periodic elastomer composite. The semi-analytical method demands slightly less computational resources than modified spectral element method since it does not need extra discretization of the domain. Anyways, the both presented methods are suggested to be applied for the investigation of the properties of the waves propagating in phononic crystals and acoustic metamaterials including elastomers. The method can be naturally extended to dielectric elastomers and to the three-dimensional case. A comparison with known results is provided.

Acknowledgements The authors express their deep gratitude to Prof. Stephan Rudykh (Department of Mechanical Engineering, University of Wisconsin—Madison) and Dr. Pavel Galich (Faculty of Aerospace Engineering, Technion—Israel Institute of Technology) for fruitful discussion and provided data.

The authors are grateful to the support of the Russian Foundation for Basic Research and the Krasnodar Regional Administration (Project 19-41-230012).

References

1. M.-H. Lu, L. Feng, Y.-F. Chen, Mater. Today **12**, 34 (2009)
2. J.O. Vasseur, P.A. Deymier, G. Frantziskonis, G. Hong, B. Djafari-Rouhani, L. Dobrzynski, J. Phys.: Condens. Matter **10**, 6051 (1998)
3. S.I. Fomenko, M.V. Golub, A. Chen, Y. Wang, C. Zhang, J. Sound Vib. **439**, 219–240 (2019)
4. O. Bilal, A. Foehr, C. Daraio, Adv. Mater. **29**, 1700628 (2017)
5. P.I. Galich, S. Rudykh, J. Appl. Mech. **84**(9), 091002 (2017)
6. J. Li, V. Slesarenko, P.I. Galich, S. Rudykh, Mech. Res. Commun. **87**, 21 (2018)

7. M. Mohajer, J. Zhou, L. Jiang, Int. J. Solids Struct. **208–209**, 93 (2021)
8. L. Yuan, P. Zhao, Y. Ding, B. Ding, J. Du, T. Ma, J. Wang. Crystals. **10**, 799 (2020)
9. S.I. Fomenko, M.V. Golub, T.Q. Bui, Y. Wang, C. Zhang, Int. J. Solids Struct. **51**(13), 2491 (2014)
10. D. Komatitsch, J.P. Vilotte, R. Vai, J.M. Castillo-Covarrubias, F.J. Sanchez-Sesma, Int. J. Numer. Methods Eng. **45**, 1139 (1999)
11. M.V. Golub, A.N. Shpak, Appl. Math. Model. **65**, 234 (2019)
12. E.B. China, A.A. Mokhtari, A. Srivastava, N. Sukumar, J. Comput. Phys. **427**, 110066 (2021)

Asymptotics of Displacements in Back-Reflected Ultrasonic Waves from a 3D Defect Located in an Elastic Material

Nikolay V. Boyev

Abstract In this work, the main term of the asymptotics of the displacement amplitude is obtained in the case of backscattering of longitudinal and transverse waves in the far-field approximation. The practical importance of this study lies in the fact that when detecting obstacles in acoustic media and defects in elastic media, ultrasonic non-destructive testing uses sounding by high-frequency acoustic and elastic waves in the echo mode. This type of scanning allows one to get the transit time of the reflected echo signal in any direction and its amplitude. Such data form the basis of the method for reconstruction of complex obstacles.

Keywords Wave · Asymptotics · Reflection · Transformation

1 Introduction

In many problems of ultrasonic non-destructive testing (UNDT), the measurement of the characteristics of the wave field occurs in the echo mode [1]. This means that by sending a signal from any point of the medium to the surface of the scatterer, in the future we fix the characteristics of the reflected signal at the same point. This model is implemented on scatterers located in both acoustic and elastic media [2–5]. For example, in ultrasonic testing, when a defect is detected in metal samples, separately-aligned sensors are used that operate on longitudinal waves both in the contact mode with the defect surface and in installations that implement the immersion method of control. However, the existence of two types of waves in an elastic medium and their possible transformation on the boundary surface of an obstacle [6, 7], located in an elastic medium, require substantiation of the applied models in UNDT. This is of particular relevance in the inverse problems of ultrasonic testing. In this work, geometric inverse problems are formulated that can be used to create algorithms for real applied ultrasonic testing problems for reconstructing the shapes of spatial

N. V. Boyev (✉)
Southern Federal University, 105/42 Bolshaya Sadovaya Str., Rostov-on-Don 344006, Russian Federation
e-mail: nvboev@sfedu.ru

I. A. Parinov et al. (eds.), *Physics and Mechanics of New Materials and Their Applications*, Springer Proceedings in Materials 10,
https://doi.org/10.1007/978-3-030-76481-4_24

defects in linear elastic media. First, let us outline a scheme for studying single scattering of short elastic waves by cavities in elastic media.

2 Single Reflection of a Spherical Wave from the Surface of the Cavity

2.1 Problem Statement

The scattering problem in a local setting is considered. Let a spherical monochromatic high-frequency wave fall from a point $\overline{x}_0$ of an infinite elastic medium onto the boundary surface of a cavity in it (see Figs. 1, 2). The wave is generated by the force $\widetilde{\mathbf{Q}}\, e^{-i\omega t}$ concentrated at the point $\overline{x}_0$, where ω is the oscillation frequency. In this case, displacements at a point y in elastic space are determined by the Kupradze matrix [8]:

$$U_j^{(k)}(y, \overline{x}_0) = U_{jp}^{(k)}(y, \overline{x}_0) + U_{js}^{(k)}(y, \overline{x}_0), \quad k, j = 1, 2, 3,$$

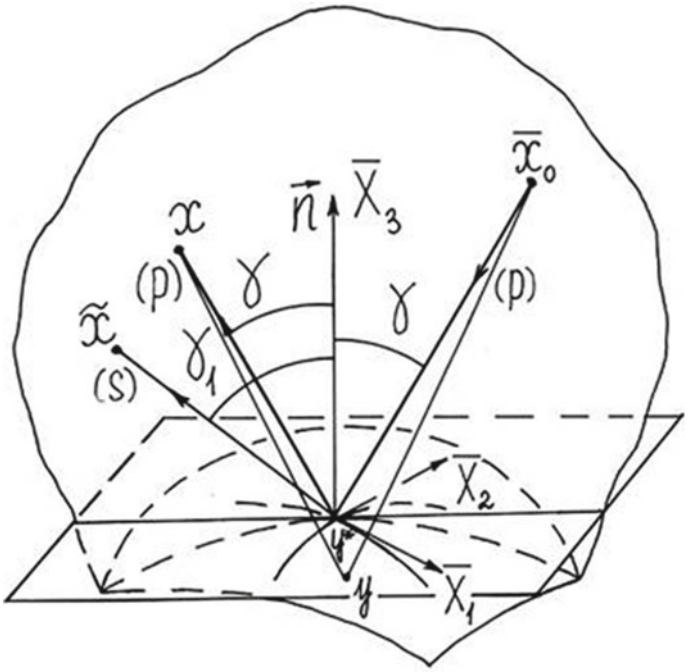

Fig. 1 Single scattering of the high-frequency longitudinal wave in the longitudinal reflection (p –p reflection) and transformation of the longitudinal wave to the transverse one (p –s transformation) on the free boundary of the cavity, located inside the elastic medium

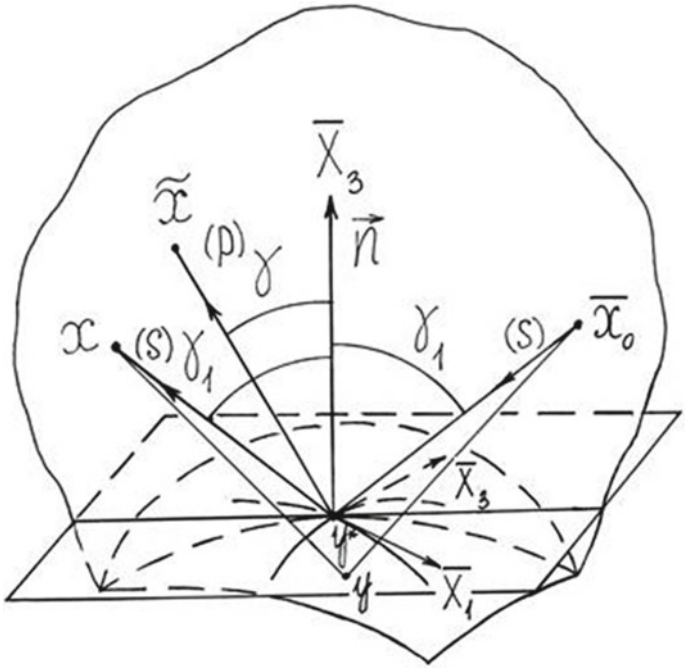

Fig. 2 Single reflection of a high-frequency transverse wave into a transverse one ($s - s$ reflection) and transformation of a transverse wave into a longitudinal one ($s - p$ transformation) on the free surface of a cavity in an elastic medium

$$U_{jp}^{(k)}(y,\overline{x}_0) = -\frac{1}{4\pi\rho\omega^2}\frac{\partial^2}{\partial y_k \partial y_j}\left(\frac{e^{ik_pR_0}}{R_0}\right), \quad R_0 = |\overline{x}_0 - y|,$$
$$U_{js}^{(k)}(y,\overline{x}_0) = \frac{1}{4\pi\rho\omega^2}\left[k_s^2\delta_{kj}\left(\frac{e^{ik_sR_0}}{R_0}\right) + \frac{\partial^2}{\partial y_k \partial y_j}\left(\frac{e^{ik_sR_0}}{R_0}\right)\right]. \tag{1}$$

Here λ, μ are the Lamé parameters, $k_p = \omega/c_p$, $k_s = \omega/c_s$, c_p, c_S are the wave numbers and velocities of longitudinal and transverse waves, ρ is the density of the elastic material, δ_{kj} are the Kronecker symbols.

The purpose of this section is to briefly describe the study of the amplitude and phase characteristics of a single scattered field on the surface of a stress-free cavity.

2.2 Solution Method

The problem is investigated in the mode of harmonic oscillations. For displacements in an elastic medium, the time dependence is taken in the form:

$$\mathbf{u}(x_1, x_2, x_3, t) = \mathrm{Re}\big[\mathbf{u}(x_1, x_2, x_3)\exp(-i\omega t)\big].$$

The elements of the Kupradze matrix determine at the point y in the radial direction $\mathbf{q} = \overline{\mathbf{x}}_0\mathbf{y}/|\overline{\mathbf{x}}_0\mathbf{y}|$ nonzero displacements in the longitudinal (p-wave) and transverse (s-wave) components of the propagating wave, which in the high-frequency oscillation mode at $k_p \to \infty$ and $k_s \to \infty$ in the $\mathbf{q}$ and $\mathbf{q}_1$ directions have the following asymptotic representations:

$$\mathbf{u}_{\mathbf{q}}^{(p)}(y) = \widetilde{Q}_{\mathbf{q}}\mathbf{q}\frac{k_p^2}{4\pi\rho\omega^2}\frac{e^{ik_pR_0}}{R_0}\left[1 + \mathrm{O}\left(\frac{1}{k_pR_0}\right)\right], \tag{2}$$

$$\mathbf{u}_{\mathbf{q}_1}^{(s)}(y) = \widetilde{Q}_{\mathbf{q}_1}\mathbf{q}_1\frac{k_s^2}{4\pi\rho\omega^2}\frac{e^{ik_sR_0}}{R_0}\left[1 + \mathrm{O}\left(\frac{1}{k_sR_0}\right)\right]. \tag{3}$$

Here $\widetilde{Q}_{\mathbf{q}}$ and $\widetilde{Q}_{\mathbf{q}_1}$ are the projections of the force $\widetilde{\mathbf{Q}}$ on the directions $\mathbf{q}$ and $\mathbf{q}_1$. The tangential direction $\mathbf{q}_1$ is perpendicular to $\mathbf{q}$.

The Cartesian components of the displacement vector in the wave, reflected from the free boundary surface at the point x of the elastic medium, are determined by the Somiliana integral [9]:

$$u_k(x) = \iint\limits_S \mathbf{T}_y[\mathbf{U}^{(k)}(y, x)] \cdot \mathbf{u}(y)\, dS_y, \tag{4}$$

$$\mathbf{T}_y\big[\mathbf{U}^{(k)}(y, x)\big] = 2\mu\frac{\partial\mathbf{U}^{(k)}}{\partial n} + \lambda\,\mathbf{n}\,\mathrm{div}\big(\mathbf{U}^{(k)}\big) + \\ + \mu\big(\mathbf{n}\times\mathrm{rot}\big(\mathbf{U}^{(k)}\big)\big). \tag{5}$$

In representations (4) and (5), the elements of the Kupradze matrix $\mathbf{U}^{(k)}(y, x)$ are obtained from the elements of the matrix $\mathbf{U}^{(k)}(y, \overline{x}_0)$ (1) by replacing $\overline{x}_0$ by x and R_0 s by $R = |y - x|$, $\mathbf{T}_y$ is the force vector at the point y, $\mathbf{u}(y)$ is the vector of the total displacement field on the boundary surface of the cavity, $\mathbf{n}$ is the normal to the surface S directed towards elastic media.

Let us select in the vectors of the total displacement field on the boundary surface and in the vector of the force $\mathbf{T}_y$ at the point y, the terms, determined by the longitudinal (p) and transverse (s) waves:

$$u_k(x) = \iint\limits_S \big\{\mathbf{T}_y[\mathbf{U}_p^{(k)}(y, x)] + \mathbf{T}_y[\mathbf{U}_s^{(k)}(y, x)]\big\} \cdot [\mathbf{u}(p; y) + \mathbf{u}(s; y)]dS_y, \tag{6}$$

$$u_k(x) = \iint\limits_S \mathbf{T}_y[\mathbf{U}_p^{(k)}(y, x)] \cdot \mathbf{u}(p; y)dS_y + \\ + \iint\limits_S \mathbf{T}_y[\mathbf{U}_s^{(k)}(y, x)] \cdot \mathbf{u}(p; y)\, dS_y +$$

$$+ \iint_S \mathbf{T}_y[\mathbf{U}_p^{(k)}(y,x)] \cdot \mathbf{u}(s;y) dS_y +$$

$$+ \iint_S \mathbf{T}_y[\mathbf{U}_s^{(k)}(y,x)] \cdot \mathbf{u}(s;y)\, dS_y, \tag{7}$$

Here $\mathbf{u}(p;y)$ ($\mathbf{u}(s;y)$) is the vector of total displacement at the boundary S, formed when a longitudinal (transverse) wave falls on the boundary S. The first and last terms in (7) describe $p-p$ and $s-s$reflections, and the second and third $p-s$ and $s-p$transformations.

The asymptotic solution written out below has a local character and gives the main asymptotic term of the amplitude of displacements of the scattered field in a small neighborhood of any ray emerging from the point $\overline{x}_0$, reflected from the surface of the cavity at point y^* and arriving at the point x of the elastic medium.

3 Single Reflection of a Longitudinal Wave from the Surface of the Cavity

Let us consider in detail the propagation in an elastic medium of the longitudinal (p) component (2) of a spherical wave (1) in a fixed direction $\mathbf{q}$, at which the p-wave interacts with the free surface of the cavity and is reflected from it (Fig. 1). In this case, the longitudinal p-wave will be reflected into a wave ($p-p$reflection) and transformed into a transverse s-wave ($p-s$transformation) .

The points of reception x at reflection $p-p$ and $\tilde{x}$ at $p-s$transformation will be different and will be located on the rays along which the reflected longitudinal and transverse waves propagate. In this case, the point y^* of intersection of the smooth surface of the cavity with the direction $\mathbf{q} = \overline{\mathbf{x}}_0\mathbf{y}^*/|\overline{\mathbf{x}}_0\mathbf{y}^*|$ will be the point of specular reflection of the incident p-wave (2) . Below, there is a diagram of a method for obtaining explicit expressions for the amplitudes of the reflected and transformed waves at the receiving points x and $\tilde{x}$.

3.1 The Case of p − p Reflection

The direction of incidence of the wave $\mathbf{q} = \{-\cos\ \alpha, -\cos\ \beta, -\cos\ \gamma\}$ will be referred to the right-hand Cartesian coordinate system $O\overline{X}_1\overline{X}_2\overline{X}_3$ at the point y^*, the $O\overline{X}_3$ axis of which coincides with the outer normal $\mathbf{n}$ (directed towards the elastic medium) to the cavity surface, and the $O\overline{X}_1$ and $O\overline{X}_2$ axes coincide with the tangents to the surface curvature lines at the point y^* (see Fig. 1). In this coordinate system, the vector $\mathbf{q}_1$ has coordinates $\{-ctg\gamma\cos\alpha, -ctg\gamma\cos\beta, -\sin\gamma\}$, and the normal is $\mathbf{n} = \{0, 0, 1\}$.

The first term in the integral representation (7) allows one to obtain the following basic representation of radial displacement $u_r^{(p)}(x)$ (after taking slowly varying functions outside the integral sign in the high-frequency approximation):

$$u_r^{(p)}(x) = \frac{\overline{Q}_{\mathbf{q}}}{4\pi\mu} i \frac{k_p^2}{k_s^2} \cdot \frac{k_p}{2\pi} \frac{\cos\gamma}{L_0 L} V_{pp}(y^*) \iint\limits_S e^{ik_p\phi_{pp}} dS,$$
$$\phi_{pp} = |\overline{x}_0 - y| + |y - x|, \quad L_0 = |\overline{x}_0 - y^*|, \quad L = |y^* - x|. \tag{8}$$

Here V_{pp} is the reflection coefficient $p - p$ [6, 7].

An asymptotic estimate of the integral in representation (8) by the method of the two-dimensional stationary phase [10] is given in [11–13]. Using this estimate, we write out the main term of the amplitude of the radial displacement in the reflected p-wave.

$$u_r^{(p)}(x) = \frac{\widetilde{Q}_{\mathbf{q}}}{4\,\pi\,\mu} \frac{k_p^2}{k_s^2} V_{pp}(y^*) \cos\gamma \times$$
$$\times \frac{\exp\left\{i\left[k_p(L_0 + L) + \frac{\pi}{4}\left(\delta_2^{(pp)} - 2\right)\right]\right\}}{L_0 L \sqrt{\left|\det\left(D_2^{(pp)}\right)\right|}}, \tag{9}$$

where $D_2^{(pp)}$ is the Hessian matrix of the symmetric structure $\left(d_{ij} = d_{ji};\quad i,\ j = 1, 2\right)$, and $\delta_2^{(pp)} = \operatorname{sign} D_2^{(pp)}$ is the difference between the number of positive and negative eigenvalues of the matrix $D_2^{(pp)}$. The explicit form of expression (9) is given below in formula (17).

3.2 The Case of $p - s$ Transformation

In this case, the Cartesian coordinates of the displacement vector $u_k^{(s)}(\tilde{x}),\quad k = 1, 2, 3$ are determined by the second term of the integral representation (7). The main terms of the short-wavelength asymptotics of the elements of the Kupradze matrix make it possible to write down the integral representation of the only nonzero tangential component of the displacements in the local spherical coordinate system at the receiving point (after moving slowly varying functions outside the integral sign in the high-frequency approximation):

$$u_\theta^{(s)}(\tilde{x}) = \frac{\widetilde{Q}_{\mathbf{q}}}{4\,\pi\,\mu} i \left(\frac{k_p}{2\pi}\right) \frac{\cos\gamma_1}{L_0 L_1} V_{ps}(y^*) \iint\limits_S e^{ik_p\phi_{ps}} dS, \tag{10}$$

$$\phi_{ps} = |\overline{x}_0 - y| + \frac{k_s}{k_p}|y - \tilde{x}|, \quad L_0 = \left|\overline{x}_0 - y^*\right|, \quad L_1 = \left|y^* - \tilde{x}\right|. \tag{11}$$

Here $V_{ps}(y^*)$ is the $p - s$transformation coefficient [6, 7].

An asymptotic estimate of the integral in representation (10) by the method of two-dimensional stationary phase [10] is given in [12], when considering the reflection of a longitudinal wave from the scatterer surface. Using this estimate, the main term of the amplitude of tangential displacement in the reflected s-wave is written out in formula (18) below.

4 Single Reflection of a Shear Wave from the Surface of the Cavity

Let us consider the propagation in an elastic medium of the transverse (s) component (3) of a spherical wave (1) in a fixed direction $\mathbf{q}$, at which the s-wave interacts with the free surface of the cavity and is reflected from it (Fig. 2). In this case, the transverse wave will be reflected in the s-wave ($s - s$reflection) and transformed into a longitudinal p-wave ($s - p$transformation) .

4.1 The Case of s − s Reflection

This reflection is determined by the fourth term in the integral representation (7). In the high-frequency approximation, the leading term of the asymptotics of the tangential displacement $u_\theta^{(s)}(x)$ is found from the integral representation:

$$u_\theta^{(s)}(x) = \frac{\widetilde{Q}_{\mathbf{q}_1}}{4\pi\mu} i \frac{k_s}{2\pi} \frac{\cos\gamma_1}{L_0 L_1} V_{ss}\left(y^*\right) \iint\limits_S e^{ik_s\phi_{ss}} dS_y, \tag{12}$$

$$\phi_{ss} = |\overline{x}_0 - y| + |y - x|.$$

The ray representation of the displacement $u_\theta^{(s)}$ was obtained on the basis of the stationary phase method [10], the application of which to the integral representation (12) is described in [12] and has the form:

$$u_\theta^{(s)}(x) = \frac{\overline{Q}_{\mathbf{q}_1}}{4\pi\mu} V_{ss}\left(y^*\right) \frac{\exp\left\{i\left[k_s(L_0 + L_1) + \frac{\pi}{4}\left(\delta_2^{(ss)} - 2\right)\right]\right\}}{L_0 L_1 \sqrt{\left|\det\left(D_2^{(ss)}\right)\right|}}, \tag{13}$$

where V_{ss} is the $s-s$reflection coefficient [6, 7], $D_2^{(ss)}$ is the Hessian matrix of the symmetric structure $\left(d_{ij}=d_{ji};\quad i,j=1,2\right)$, and $\delta_2^{(ss)}=\operatorname{sign}D_2^{(ss)}$ is the difference between the number of positive and negative eigenvalues of the matrix $D_2^{(ss)}$. The explicit form of expression (13) is given below by formula (27).

4.2 The Case of s − p Transformation

This transformation is determined by the third term of the integral representation (7). The main term of the asymptotics of the integral representation of the radial displacement component at the receiving point $u_r^{(p)}(\tilde{x})$ is transformed to the form:

$$u_r^{(p)}(x)=\frac{\widetilde{Q}_{\mathbf{q}_1}}{4\pi\mu}i\frac{k_p}{2\pi}\frac{\cos\gamma}{L_0L}V_{sp}\left(y^*\right)\iint\limits_S e^{ik_p\phi_{sp}}dS_y, \tag{14}$$

$$\phi_{sp}=\frac{k_s}{k_p}|\overline{x}_0-y|+|y-\tilde{x}|,\quad L_0=\left|\overline{x}_0-y^*\right|,\quad L=\left|y^*-\tilde{x}\right|.$$

where V_{sp} is the $s-p$transformation coefficient [6, 7].

The application of the two-dimensional stationary phase method to the integral representation (14) makes it possible, within the geometric theory of diffraction (GTD), to obtain an explicit expression for the displacement $u_r^{(p)}(\tilde{x})$. It is written out in this paper below (28).

5 Back Reflection of a Longitudinal Elastic Wave in 2D and 3D Elastic Media

We will assume that the cavity defect is located at a sufficient distance from the oscillation source, which makes it possible to use the far-field approximation at high oscillation frequencies in calculating the waves incident and reflected from the defect surface. Frequently in UNDT for detection of defects in structural elements, separate-aligned sensors operating on longitudinal waves are used. Such sensors usually work in echo mode. In this case, the emitted longitudinal wave interacts with the surface of an obstacle, located in an elastic medium, scatters at the boundary of the obstacle, and the sensor detects the wave that came from the defect. If the surface of the scatterer is smooth, then the first arriving pulse will be reflected from the vicinity of a point on the surface, the normal in which is parallel to the direction of propagation of the high frequency radiated longitudinal wave. Analyzing the formulae for reflected longitudinal and transverse waves from obstacle surfaces in two-dimensional [14]

and spatial [12, 13] cases, we will show that the main term of the reflected incoming wave will be determined by the longitudinal wave.

Let us write down the explicit expressions for the principal terms of the displacement amplitudes in reflected waves with s-reflection and x-transformation obtained in [14] in the two-dimensional case and in [12] in the three-dimensional case.

In the case of a two-dimensional problem:

(i) $p - p$reflection:

$$u_r^{(p)}(x) = \widetilde{Q}_{\mathbf{q}} V_{pp}(y^*) \frac{\exp\left\{i\left[k_p(L_0+L) + \frac{\pi}{4}(\delta-1)\right]\right\}}{\sqrt{\left|L_0 + L - \frac{2\,L_0 L}{\rho\,\cos\,\gamma}\right|}},$$

$$u_\theta^{(p)}(x) = 0 \tag{15}$$

$$\delta = \operatorname{sign}\left(L_0 + L - \frac{2\,L_0 L}{\rho\cos\gamma}\right)$$

(ii) $p - s$reflection:

$$u_\theta^{(s)}(\tilde{x}) = \widetilde{Q}_{\mathbf{q}} \left(\frac{k_s}{k_p}\right)^{3/2} \frac{\cos\,\gamma_1\; V_{ps}(y^*)}{\sqrt{L_0 L_1}} \frac{\exp\left\{i\left[k_p L_0 + k_s L_1 + \frac{\pi}{4}\left(\delta_{ps}-1\right)\right]\right\}}{\sqrt{\left|\frac{\cos^2\gamma}{L_0} + \frac{k_s\cos^2\gamma_1}{k_p L_1} + \frac{\cos\gamma}{\rho} + \frac{k_s\cos\gamma_1}{k_p\rho}\right|}}$$

$$u_r^{(s)}(\tilde{x}) = 0, \tag{16}$$

$$\delta_{ps} = sign\left(\frac{\cos^{2\cdot}\gamma}{L_0} + \frac{k_s\cos^{2\cdot}\gamma_1}{k_p L_1} + \frac{\cos\gamma}{\rho} + \frac{k_s\cos\gamma_1}{k_p\rho}\right).$$

In the case of a 3D problem:

(i) $p - p$reflection:

$$u_r^{(p)}(x) =$$

$$= \frac{B \times V_{pp}(y^*)\exp\left[ik_p(L_0+L) + \frac{\pi}{4}\left(\delta_2^{(pp)} - 2\right)\right]}{\sqrt{(L_0+L)^2 + 2L_0L(L_0+L)\left(2H\;\cos^2\gamma + \tilde{k}\sin^2\gamma\right)\cos^{-1}\gamma + 4L_0^2L^2K}},$$

$$u_\theta^{(p)}(x) = 0,$$

$$u_\psi^{(p)}(x) = 0. \tag{17}$$

$$\delta_2^{(pp)} = \operatorname{sign} D_2^{(pp)},\ B = \frac{\widetilde{Q}_q}{4\,\pi\,\mu}\frac{k_p^2}{k_s^2}.$$

(ii) (ii)$p-s$reflection:

$$u_\theta^{(s)}(\tilde{x}) = \frac{\widetilde{Q}_{\mathbf{q}}}{4\pi}\frac{k_s^2}{k_p}V_{ps}(y^*)\cos\ \gamma_1\frac{\exp\left\{i\left[k_pL_0+k_sL_1+\frac{\pi}{4}\left(\delta_2^{(ps)}-2\right)\right]\right\}}{L_0L_1\sqrt{\left|\det\left(D_2^{(ps)}\right)\right|}},$$

$$u_r^{(s)}(\tilde{x}) = 0,$$

$$u_\psi^{(s)}(x) = 0, \tag{18}$$

$$\delta_2^{(ps)} = \operatorname{sign} D_2^{(ps)},$$

where the elements of the symmetric ($d_{12} = d_{21}$) Hesse matrix $D_2^{(ps)} = d_{ij},\quad i, j = 1, 2$ have the form:

$$d_{11} = L_0^{-1}\sin^2\alpha + \frac{k_s}{k_p}L_1^{-1}\sin^2\alpha_1 - k_1\left(\cos\ \gamma - \frac{k_s}{k_p}\cos\gamma_1\right)$$

$$d_{12} = -\left(L_0^{-1}\cos\alpha\cos\beta + \frac{k_s}{k_p}L_1^{-1}\cos\alpha_1\cos\beta_1\right)$$

$$d_{22} = L_0^{-1}\sin^2\beta + \frac{k_s}{k_p}L_1^{-1}\sin^2\beta_1 + k_2\left(\cos\ \gamma - \frac{k_s}{k_p}\cos\gamma_1\right)$$

In the case of backward reflection, we are interested in the displacements in the reflected waves at the radiation point $\overline{x}_0$. Let us investigate the limiting values of $u_r^{(p)}(x)$ and $u_\theta^{(s)}(\tilde{x})$ for $x \to \overline{x}_0$ and $\tilde{x} \to \overline{x}_0$.

Let us take into account that $\lim\limits_{\substack{x\to\overline{x}_0\\(\gamma\to 0)}} V_{pp}(y^*) = -1$, and $\lim\limits_{\substack{x\to\overline{x}_0\\(\gamma\to 0)}} V_{ps}(y^*) = 0$.

We find that the main term of the asymptotics of the displacements of the wave arriving at point $\overline{x}_0$ is determined by the main term of the displacements in the reflected longitudinal wave:

in the two-dimensional case:

$$u_r^{(p)}(\overline{x}_0) = \frac{\widetilde{Q}_{\mathbf{q}}\exp\left\{i\left[2k_pL_0+\frac{\pi}{4}(\delta-1)\right]\right\}}{\sqrt{2L_0\left(1+\frac{L_0}{\rho}\right)}}, \tag{19}$$

in the three-dimensional case:

$$u_r^{(p)}(\overline{x}_0) = \frac{\widetilde{Q}_{\mathbf{q}} \exp\left\{i\left[2k_p L_0 + \frac{\pi}{4}\left(\delta_2^{(pp)} - 2\right)\right]\right\}}{2L_0\sqrt{1 + 2L_0 H + L_0^2 K}}, \tag{20}$$

$$\left(\alpha = \frac{\pi}{2} \to \sin\frac{\pi}{2} = 1, \quad \beta = \frac{\pi}{2} \to \sin\beta = 1, \quad \gamma = 0 \to \cos\gamma = 1\right)$$

where H is the average curvature of the surface.

In the far-field approximation (L_0 is sufficiently large), we obtain the known results from formulae (19) and (20).

In the two-dimensional case [1]:

$$u_r^{(p)}(\overline{x}_0) = \frac{\widetilde{Q}_{\mathbf{q}} \exp\left[i\frac{\pi}{4}(\delta - 1)\right]}{\sqrt{2}L_0} \cdot \sqrt{\rho}\exp\left(i\ 2\ k_p L_0\right). \tag{21}$$

Up to a factor

$$u_r^{(p)}(\overline{x}_0) \sim \sqrt{\rho}\exp\left(i\ 2\ k_p L_0\right). \tag{22}$$

In the three-dimensional case [15]:

$$u_r^{(p)}(\overline{x}_0) = \frac{\widetilde{Q}_{\mathbf{q}} \exp\left[i\frac{\pi}{4}\left(\delta_2^{(pp)} - 2\right)\right]}{2L_0^2} \cdot K^{-\frac{1}{2}} \exp\left(i\ 2\ k_p L_0\right). \tag{23}$$

Up to a factor

$$u_r^{(p)}(\overline{x}_0) \sim \sqrt{R_1 R_2}\exp\left(i\ 2\ k_p L_0\right). \tag{24}$$

6 Back Reflection of a Transverse Elastic Wave in 2D and 3D Elastic Media

If the separately aligned sensor operates on transverse waves, then the emitted transverse wave in the $\mathbf{q}$ direction interacts with the surface of an obstacle located in an elastic medium, scatters at the boundary surface, and the sensor detects a wave coming from the defect.

Let us write down explicit expressions for the principal terms of the displacement amplitudes in reflected waves at $s - s$reflection and $s - p$transformation, obtained in [14, 12].

In the case of a two-dimensional problem [14]:

(i) $s-s$reflection:

$$u_{\theta}^{(s)}(x)=\widetilde{Q}_{\mathbf{q}_1}V_{ss}(y^*)\frac{\exp\{i[k_s(L_0+L_1)+\frac{\pi}{4}(\delta-1)]\}}{L_0L_1\sqrt{\left|\left(L_0+L_1+\frac{2L_0L_1}{\rho\cos\gamma_1}\right)\right|}},$$
$$u_{r}^{(s)}(x)=0, \tag{25}$$
$$\delta=\operatorname{sign}\left(L_0+L_1+\frac{2L_0L_1}{\rho\cos\gamma_1}\right);$$

(ii) $s-p$reflection:

$$u_{r}^{(p)}(\tilde{x})=\widetilde{Q}_{\mathbf{q}_1}\frac{k_p^2}{2\,k_s^2}\frac{\cos\gamma}{\sqrt{L_0L}}V_{pp}(y^*)\frac{\exp\{i[k_sL_0+k_pL+\frac{\pi}{4}(\delta_{sp}-1)]\}}{\sqrt{\left|\frac{k_s\cos^{2\cdot}\gamma_1}{k_pL_0}+\frac{\cos^{2\cdot}\gamma}{L}+\frac{k_s\cos\gamma_1}{k_p\rho}+\frac{\cos\gamma}{\rho}\right|}}$$
$$u_{\theta}^{(p)}(\tilde{x})=0, \tag{26}$$
$$\delta_{sp}=\operatorname{sign}\left(\frac{k_s\cos^{2\cdot}\gamma_1}{k_pL_0}+\frac{\cos^{2\cdot}\gamma}{L}+\frac{k_s\cos\gamma_1}{k_p\rho}+\frac{\cos\gamma}{\rho}\right).$$

In the case of a three-dimensional problem [12]:

(i) $s-s$reflection:

$$u_{r}^{(s)}(x)=0,$$
$$u_{\psi}^{(s)}(x)=0,$$
$$u_{\theta}^{(s)}(x)=\frac{B_1\times V_{ss}(y^*)\exp\left[ik_s(L_0+L_1)+\frac{\pi}{4}\left(\delta_2^{(ss)}-2\right)\right]}{\sqrt{(L_0+L_1)^2+2L_0L_1(L_0+L_1)\left(2H\cos^2\gamma_1+\tilde{k}\sin^2\gamma_1\right)\cos^{-1}\gamma_1+4L_0^2L_1^2K}} \tag{27}$$
$$\delta_2^{(ss)}=sign\,D_2^{(ss)},\ B_1=\frac{\widetilde{Q}_{\mathbf{q}_1}}{4\,\pi\,\mu},$$

where $K=k_1k_2$ is the Gaussian curvature, and $H=(k_1+k_2)/2$ is the average curvature of the surface at the point of specular reflection y^*, and $\tilde{k}$ is the curvature of the normal section of the reflector surface by the beam plane x_0-y^*-x. The curvature

$\tilde{k}$ is determined by the Euler formula: $\tilde{k} = k_1 \cos^2\tilde{\phi} + k_2 \sin^2\tilde{\phi}$ ($\cos\tilde{\phi} = \cos\alpha/\sin\gamma$, $\sin\tilde{\phi} = \cos\beta/\sin\gamma$), which expresses the curvature of an arbitrary normal section in terms of the principal curvatures k_1, k_2 of the surface and the angle $\tilde{\phi}$ formed by the tangent of this normal section with the first principal direction.

(ii) $s - p$reflection:

$$u_r^{(p)}(x) = \widetilde{Q}_{\mathbf{q}_1} V_{sp}(y^*) \cos\gamma k_p k_s \frac{\exp\left\{i\left[k_s L_0 + k_p L + \frac{\pi}{4}\left(\delta_2^{(sp)} - 2\right)\right]\right\}}{L_0 L\sqrt{\left|\det\left(D_2^{(sp)}\right)\right|}},$$

$$u_r^{(s)}(x) = 0,$$

$$u_\psi^{(s)}(x) = 0, \tag{28}$$

$$d_{11} = \frac{k_s}{k_p} L_0^{-1} \sin^2\alpha_1 + L^{-1}\sin^2\alpha + k_1\left(\frac{k_s}{k_p}\cos\gamma_1 - \cos\gamma\right),$$

$$d_{12} = -\left(\frac{k_s}{k_p} L_0^{-1}\cos\alpha_1\cos\beta_1 + L^{-1}\cos\alpha\cos\beta\right),$$

$$d_{22} = \frac{k_s}{k_p} L_0^{-1}\sin^2\beta_1 + L^{-1}\sin^2\beta + k_2\left(\frac{k_s}{k_p}\cos\gamma_1 - \cos\gamma\right),$$

where the elements of the symmetric matrix of the Hessian $D_2^{(sp)} = d_{ij}$, $i, j = 1, 2$ are determined by formulae (28), $\delta_2^{(sp)} = \operatorname{sign} D_2^{(sp)}$ is the difference between the number of positive and negative eigenvalues of the matrix $D_2^{(sp)}$.

In the case of backward reflection, we are interested in the displacements in the reflected waves at the radiation point $\overline{x}_0$. Let us examine the limiting values of $u_\theta^{(s)}(x)$ and $u_r^{(p)}(\tilde{x})$ for $x \to \overline{x}_0$ and $\tilde{x} \to \overline{x}_0$.

Let us take into account that $\lim\limits_{\substack{x \to \overline{x}_0 \\ (\gamma \to 0)}} V_{ss}(y^*) = -1$, and $\lim\limits_{\substack{x \to \overline{x}_0 \\ (\gamma \to 0)}} V_{sp}(y^*) = 0$.

We get that the main term of the asymptotics of the displacements of the wave arriving at the point x_0 in the backward reflected transverse wave:

in the two-dimensional case:

$$u_\theta^{(s)}(\overline{x}_0) = \frac{\widetilde{Q}_{\mathbf{q}_1}\exp\left\{i\left[2k_s L_0 + \frac{\pi}{4}(\delta - 1)\right]\right\}}{\sqrt{2L_0\left(1 + \frac{L_0}{\rho}\right)}}. \tag{29}$$

in the three-dimensional case:

$$u_{\theta}^{(s)}(\overline{x}_0) = \frac{\widetilde{Q}_{\mathbf{q}_1} \exp\left\{i\left[2k_s L_0 + \frac{\pi}{4}\left(\delta_2^{(ss)} + 2\right)\right]\right\}}{2L_0\sqrt{1 + L_0(k_2 + k_1) + L_0^2 K}}. \tag{30}$$

In the far-field approximation (L_0 is large enough), from formulae (29) and (30), we obtain the following results.

In the two-dimensional case:

$$u_{\theta}^{(s)}(\overline{x}_0) = \frac{\widetilde{Q}_{\mathbf{q}_1} \exp\left[i\frac{\pi}{4}(\delta - 1)\right]}{\sqrt{2}L_0} \cdot \sqrt{\rho}\exp(i\ 2\ k_s L_0). \tag{31}$$

Up to a factor

$$u_{\theta}^{(s)}(\overline{x}_0) \sim \sqrt{\rho}\exp(i\ 2\ k_s L_0). \tag{32}$$

In the three-dimensional case:

$$u_{\theta}^{(s)}(\overline{x}_0) = \frac{\widetilde{Q}_{\mathbf{q}_1} \exp\left[i\frac{\pi}{4}\left(\delta_2^{(ss)} - 2\right)\right]}{2L_0^2} \cdot K^{-\frac{1}{2}} \exp(i\ 2\ k_s L_0). \tag{33}$$

Up to a factor

$$u_{\theta}^{(s)}(\overline{x}_0) \sim \sqrt{R_1 R_2}\exp(i\ 2\ k_s L_0). \tag{34}$$

Let us consider the same model of echo-mode of sound detection of obstacles in an acoustic environment. We will proceed from the expression for the main asymptotic term of the pressure amplitude at point x in the wave reflected from the scatterer surface [11].

$$p(x) = \\ = \frac{\widetilde{Q}_{\mathbf{q}} \exp\left[ik(L_0 + L) + \frac{\pi}{4}(\delta_2 - 2)\right]}{\sqrt{(L_0 + L)^2 + 2L_0 L(L_0 + L)\left(2H\cos^2\gamma + \tilde{k}\sin^2\gamma\right)\cos^{-1}\gamma + 4L_0^2 L^2 K}}. \tag{35}$$

For backscattering at point x_0, we obtain the pressure:

$$p(\overline{x}_0) = -\frac{\widetilde{Q}_{\mathbf{q}} \exp\left\{i\left[2kL_0 + \frac{\pi}{4}(\delta_2 - 2)\right]\right\}}{2L_0\sqrt{1 + 2L_0 H + L_0^2 K}}. \tag{36}$$

In the far-field approximation (L_0 is large enough):

$$p(\overline{x}_0) = -\frac{\widetilde{Q}_{\mathbf{q}} \exp\left[i\frac{\pi}{4}(\delta_2 - 2)\right]}{2L_0^2} \cdot K^{-\frac{1}{2}} \exp(i\ 2\ k_s L_0). \tag{37}$$

Up to a factor

$$p(\overline{x}_0) \sim \sqrt{R_1 R_2} \exp(i\ 2\ kL_0). \tag{38}$$

If sounding in the echo-mode of an obstacle, located in the acoustic environment, is carried out by a sensor moving along a circle of radius R with a center, located inside the diffuser, then $R = L_0 + p(\mathbf{q})$, where $p(\mathbf{q})$ is a distance to the tangent to the surface perpendicular to R. Distance $L_0 = R - p(\mathbf{q})$. Therefore, up to a factor:

$$p(\overline{x}_0) \sim \sqrt{R_1 R_2} \exp(-i\ 2\ k\ p(\mathbf{q})). \tag{39}$$

Let us compare the expressions for the main asymptotic terms of the amplitudes in the far field of reflected waves in acoustic (37) and elastic (23) and (33) media. They differ in insignificant factors and are determined by the same dependences on the product of the principal radii of curvature of the surface and the distance to the tangent to the surface of the obstacle. This circumstance is essentially used in the development of methods for the reconstruction of obstacles of complex non-convex shape, located in acoustic and elastic media [2–5].

7 Conclusion

The main conclusion based on the results of the studies presented in this work is that the form of the dependences of the main terms of the asymptotic expansions of the amplitudes of the waves reflected in the echo-mode in the far field on the geometric parameters of the problem coincide in acoustic [13–16] and elastic media [12, 14, 17] up to insignificant factors. Expressions of the main term of the wave reflected in the echo-mode are determined by the shape of the surface (Gaussian curvature), the wavenumber and the function of the distance from some center inside the obstacle to the tangent to the surface of the scatterer.

References

1. I.N. Ermolov, *Theory and Practice of Ultrasonic Testing* (Mechanical Engineering, Moscow, 1981). ((In Russian))
2. N.V. Boev, A.O. Vatul'yan, M.A. Sumbatyan, Akusticheskiy Zhurnal **43**(4), 458 (1997) (In Russian)
3. N.V. Boev, I.I. Vorovich, M.A. Sumbatyan, Izvestiya RAN: Mech. Tverdogo Tela **5**, 38 (1992). ((In Russian))
4. N.V. Boev, V.M. Zotov, E.A. Troyan, Akusticheskiy Zhurnal **49**(5), 585 (2003) (In Russian)

5. N.V. Boev, M.A. Sumbatyan, Akusticheskiy Zhurnal **45**(2), 164 (1999) (In Russian)
6. L. Brekhovskikh, *Waves in Layered Media* (Academic Press, New York, 2012)
7. V.T. Grinchenko, V.V. Myaleshka, *Harmonic Oscillations and Waves in Elastic Bodies, 8* (Naukova Dumka, Kiev, 1981). ((In Russian))
8. V.D. Kupradze, *Potential Methods in the Theory of Elasticity* (Israel Program for Scientific Translations, Jerusalem, 1965)
9. V. Novatsky, *Theory of Elasticity* (Mir, Moscow, 1975). ((In Russian))
10. M.V. Fedorjuk, *Saddle Point Method* (Nauka, Moscow, 1977). ((In Russian))
11. N.V. Boyev, M.A. Sumbatyan, Doklady AN **392**(5), 614 (2003)
12. A. Pompei, M.A. Sumbatyan, N.V. J. Sound Vib. **302**(4–5), 925 (2007)
13. D.A. McNamara, C.W.I. Pistorius, I.A.G. Malherbe, *Introduction to the Uniform Geometrical Theory of Diffraction* (Artech House, Norwood 1990)
14. M.A. Sumbatyan, N.V. Boyev, J. Acoust. Soc. Am. **95**(5), 2347 (1994)
15. E.L. Shenderov, *Wave Tasks of Hydroacoustics* (Sudostroenie, Leningrad, 1972). ((In Russian))
16. V.M. Babich, V.S. Buldyrev, *Asymptotic Methods in Short-Wavelength Diffraction Theory* (Alpha Science, New York, 2008)
17. N.V. Boyev, in *Advanced Materials. Springer Proceedings in Materials,* vol. 6, ed. by I.A. Parinov, S.-H. Chang, B.T. Long (Springer Cham, Switzerland, 2020), p.369

Vibrations of the Auxetic Shell in the Liquid

A. S. Yudin

Abstract Vibrations analysis of shell structures in a liquid is relevant in cases, when a high noise level is an undesirable characteristic of the object. The vibration amplitudes of the shell surface in contact with the liquid and the noise levels in the environment are correlated. Therefore, to reduce vibration and noise levels, a set of methods is used, which include means of vibration isolation, vibration and noise absorption. Due to the development of new technologies, the analysis of effects from the use of non-traditional materials is also relevant in this area. As shown by mathematical modeling, they have the effect of reducing vibration levels. Testing was performed on the example of a thin light reinforced aircraft-type shell [A.S. Yudin, S.A. Yudin, in Proceedings of the 2015 International Conference on Physics and Mechanics of New Materials and Their Applications, devoted to 100-year Anniversary of the Southern Federal University, ed. by I.A. Parinov, S.H. Chang, V.Yu. Topolov (Nova Science Publishers, New York, 2016), p. 447]. In this paper, the analysis of vibrations in the liquid of a heavier and stronger shell that can withstand high levels of external pressure is performed. The comparison of materials with properties of auxetics and traditional ones is given.

Keywords Shell of revolution · Reinforced shell · Auxetic · Acoustic medium · Amplitude-frequency characteristic (AFC) · Resonance frequencies

1 Influence of Liquid Modeling

In the vibroacoustic calculation of vibrations of shells and linear media, the stage of determining the reaction of dynamic pressure on the contact surface is of considerable complexity. To do this, it is necessary to solve the Fredholm-type integro-differential problem on the shell surface, using the Helmholtz integral in the correct formulation. Such approaches based on the method of proper forms and iterative methods

A. S. Yudin (✉)
I. I. Vorovich Institute of Mathematics, Mechanics and Computer Sciences, Southern Federal University, Rostov-on-Don, Russia
e-mail: ayudin@sfedu.ru

I. A. Parinov et al. (eds.), *Physics and Mechanics of New Materials and Their Applications*, Springer Proceedings in Materials 10,
https://doi.org/10.1007/978-3-030-76481-4_25

are developed in [2] for shells of rotation. However, they are resource-intensive methods that have little flexibility to change the design parameters for multivariate calculations. Their development into non-axisymmetric shells is difficult.

In this sense, the method of modeling local impedance is more convenient and effective, when a priori the relationship between the amplitudes of dynamic pressure and velocity (or displacement) on the shell surface is set. The acceptability of this approach was checked by comparison with more accurate methods on shells of revolution, especially for far-field calculations.

The idea of a method for modeling local impedance seems to have been first explicitly proposed in [3], where the simplest formulae for medium impedances at high and low frequencies are considered. Here, more general formulae are used that are suitable for a wide range of frequencies.

From the solution of acoustic equations in a cylindrical coordinate system by the method of separation of variables, it is possible to obtain an impedance for the 1st circumferential mode that relates the amplitudes of dynamic pressure and particle velocities of an ideal unbounded medium on the surface of an infinitely long cylindrical shell of radius R [4]:

$$p_{nk} = Z_{cnk} c_{nk}, \quad Z_{cnk} = \frac{s_o i \rho_c c_c \gamma_o H_n^{(s_o)}(\gamma)}{\gamma H_n^{(s_o)'}(\gamma)}, \tag{1}$$

where ρ_c, c_c are density and speed of sound propagation in the medium, $s_o = \pm 1$; n is a number of waves in the circumferential direction; $\gamma_o = k_\omega R$, $\gamma = k_r R$, $k_r = \sqrt{k_\omega^2 - k_z^2}$, $k_\omega = \omega / c_c$, $k_z = k\pi / L$; k_r, k_z are wave numbers; for a plane problem, when the solution does not depend on z, $k_z = 0$, $k_r = k$, $\gamma = \gamma_o$; L is the some characteristic size, which in the case of applying the impedance to the final shell corresponds to its length; $H_n^{(s_0)}$, $H_n^{(s_0)'}$ are the Hankel functions and their derivatives on the argument. The value $s_0 = 1$ corresponds to the Hankel function of the first kind, and the value $s_0 = -1$ corresponds to the Hankel function of the second kind:

$$H_n^{(s_o)}(\gamma) = J_n(\gamma) + s_o i \Upsilon_n(\gamma), \quad H_n^{(s_o)\prime}(\gamma) = n H_n^{(s_o)}(\gamma)/\gamma - H_{n+1}^{(s_o)}(\gamma), \tag{2}$$

where J_n, Υ_n are the Bessel functions of the first and second kind.

Let us go to (1) from velocities c_{nk} to displacements w_{nk}, using that $c_{nk} = -s_o i \omega w_{nk}$, we get:

$$p_{nk} = Z_{wnk} w_{nk}, \quad Z_{wnk} = \frac{\omega \rho_c c_c \gamma_o H_n^{(S_o)}(\gamma)}{\gamma H_n^{(S_o)\prime}(\gamma)}, \tag{3}$$

where Z_{wnk} is the dynamic stiffness coefficient of the medium, which makes sense.

For numerical implementation, equations and formulae are converted to dimensionless form by the formulae:

$$\begin{aligned}
&\tilde{p}_{nk} = p_{nk}\nu_*/(E_*\varepsilon_1^2), \quad \tilde{\rho}_c = \rho_c/\rho_*, \quad \tilde{w}_{nk} = w_{nk}/h_*,\\
&\tilde{c}_c = c_c/c_*, \quad \Omega = \omega R_*/c_*, \quad \Omega_1 = \Omega/(\tilde{k}_2\tilde{c}_c) = \gamma_o,\\
&\tilde{R} = R/R_*, \quad \tilde{L} = L/R_*, \quad \tilde{k}_2 = 1/\tilde{R},\\
&\varepsilon_* = h_*/R_*, \quad \overline{\nu}_* = 1-\nu_*^2, \quad c_* = \sqrt{E_*/(\rho_*\overline{\nu}_*)},\\
&\gamma = \Omega_1\kappa, \quad \kappa = \sqrt{1-\kappa_1^2},\ \kappa_1 = m\pi c_c/(\omega L) = m\pi\tilde{c}_c/(\Omega\tilde{L}).
\end{aligned} \tag{4}$$

The dimensionless analog of formula (3) has the form:

$$\tilde{\rho}_{nk} = \tilde{Z}_{wnk}\tilde{w}_{nk}, \quad \tilde{Z}_{wnk} = \frac{\Omega\tilde{\rho}_c\tilde{c}_c H_n^{(S_o)}(\Omega_1\kappa)}{\varepsilon_*\kappa H_n^{(S_o)\prime}(\Omega_1\kappa)}. \tag{5}$$

For $\kappa_1 > 1$, the argument of Hankel functions becomes purely imaginary, and they can be represented via Macdonald functions, or modified Bessel functions of the first ($s_0 = 1$) and second ($s_0 = -1$) kind. In this case $\tilde{Z}_{wn}$ is represented as

$$\tilde{Z}_{wn} = \frac{\Omega\tilde{\rho}_c\tilde{c}_c K_n^{(s_o)}(\Omega_1|\kappa|)}{\varepsilon_*|\kappa|K_n^{(s_o)\prime}(\Omega_1|\kappa|)} \equiv \tilde{Z}_n^-, \tag{6}$$

where $K_n^{(s_o)}$ are the MacDonald functions, valid and positive with a valid and positive argument $K_n^{(s_o)\prime} = nK_n^{(s_o)}(x)/x - K_{n+1}^{(s_o)}(x)$.

When $n \neq 0$ and a small argument $x = \Omega_1|\kappa| \to 0$

$$K_n^{(s_o)}(x) \to \frac{(n-1)!}{2}\left(\frac{2}{x}\right)^n, \quad K_n^{(s_o)\prime}(x) \to \frac{n!}{4}\left(\frac{2}{x}\right)^{n+1}, \quad \tilde{Z}_n^- \to -\frac{\tilde{\rho}_c\Omega^2}{\varepsilon_* n\tilde{k}_2}. \tag{7}$$

When $n = 0$ and $x \to 0$, then $K_0^{(s_o)}(x) \to 0.11593 - \ln x$, $K_0^{(s_o)\prime}(x) \to -K_1^{(s_o)}(x) \to 1/x$,

$$\tilde{Z}_0^- \to -\frac{\tilde{\rho}_c\Omega^2}{\varepsilon_*\tilde{k}_2}(\ln x - 0.11593). \tag{8}$$

The presented formulae are derived for the cylinder. When they are used on rotation shells, alternative options arise. In one of them, we can replace R with the polar radius of the shell (r) at a given point on the generator, and then $k = 1/R$. In another variant, k can be interpreted as the curvature of the normal section in the circumferential direction, and then $k = k_2 = (\sin\beta)/r$, where β is the angle of inclination of the normal of the generator to the axis of rotation.

2 Equations of Oscillations

Let us consider a shell of revolution in a system of curved orthogonal coordinates, which lines coincide with the lines of the main curvatures. According to the hypothesis of a direct nonorthogonal material normal, the displacement of shell points is defined as follows:

$$U(\alpha_1,\ \alpha_2,\ z) = u(\alpha_1,\ \alpha_2) + z\varphi_1(\alpha_1,\ \alpha_2),$$

$$V(\alpha_1,\ \alpha_2,\ z) = v(\alpha_1,\ \alpha_2) + z\varphi_2(\alpha_1,\ \alpha_2),$$

$$W(\alpha_1,\ \alpha_2,\ z) = w(\alpha_1,\ \alpha_2), \tag{9}$$

where *u, v, w* are the components of moving points of the median surface of the shell; φ_1, φ_2 are the angles of rotation of the normal to the median surface. The number of degrees of freedom of the material normal here is equal to five.

In this case, the linear strain relations have the form:

$$\begin{array}{l}\varepsilon_{11}(a_1,\ a_2,\ z) = E_{11}(a_1,\ a_2) + zK_{11}(a_1,\ a_2),\ \varepsilon_{13}(\alpha_1,\ \alpha_2,\ z) = E_{13}(\alpha_1,\ \alpha_2),\ (1 \leftrightarrow 2),\\ \varepsilon_{12}(\alpha_1,\ \alpha_2,\ z) = E_{12}(\alpha_1,\ \alpha_2) + zK_{12}(\alpha_1,\ \alpha_2),\ \varepsilon_{33}(\alpha_1,\ \alpha_2,\ z) = 0.\end{array} \tag{10}$$

Here E_{jj}, E_{12}, E_{j3}, K_{jj}, K_{12}, $j = 1, 2$, are the strains of tension-compression, tangential and transverse shear, changes in curvature, torsion of the median surface of the shell, respectively. They are related to the displacement components and rotation angles of the normal by the formulae:

$$\begin{array}{l}E_{11} = \frac{1}{A_1}\frac{\partial u}{\partial \alpha_1} + \frac{1}{A_1A_2}\frac{\partial A_1}{\partial \alpha_2}v + k_1 w,\ E_{13} = \varphi_1 - \vartheta_1,\ (1 \leftrightarrow 2),\\ E_{12} = \frac{1}{A_1}\frac{\partial v}{\partial \alpha_1} - \frac{1}{A_1A_2}\frac{\partial A_1}{\partial \alpha_2}u + \frac{1}{A_2}\frac{\partial u}{\partial \alpha_2} - \frac{1}{A_1A_2}\frac{\partial A_2}{\partial \alpha_1}v,\\ K_{11} = \frac{1}{A_1}\frac{\partial \varphi_1}{\partial \alpha_1} + \frac{1}{A_1A_2}\frac{\partial A_1}{\partial \alpha_2}\varphi_2,\quad (1 \leftrightarrow 2)\\ K_{12} = \left(\frac{1}{A_1}\frac{\partial \varphi_2}{\partial \alpha_1} - \frac{1}{A_1A_2}\frac{\partial A_1}{\partial \alpha_2}\varphi_1\right) + \left(\frac{1}{A_2}\frac{\partial \varphi_1}{\partial \alpha_2} - \frac{1}{A_1A_2}\frac{\partial A_2}{\partial \alpha_1}\varphi_2\right),\\ \vartheta_1 = k_1 u - \frac{1}{A_1}\frac{\partial w}{\partial \alpha_1},\ \ \vartheta_2 = k_2 v - \frac{1}{A_2}\frac{\partial w}{\partial \alpha_2},\end{array} \tag{11}$$

where A_1, A_2 are the Lamé coefficients; k_1, k_2 are the main curvatures of the middle surface of the shell.

For shells of revolution, the kinematic relations (11) can be written as follows:

$$E_{11} = u' + k_1 w,\ \ E_{22} = v^{\bullet} + \psi u + k_2 w,\ \ E_{12} = v' + u^{\bullet} - \psi v,$$

$$K_{11} = \varphi_1',\ \ K_{22} = \varphi_2^{\bullet} + \psi\varphi_1,\ \ K_{12} = \varphi_2' + \varphi_1^{\bullet} - \psi\varphi_2,$$

$$E_{13} = \varphi_1 - \vartheta_1, \;\; E_{23} = \varphi_2 - \vartheta_2, \; \vartheta_1 = k_1 u - w', \;\; \vartheta_2 = k_2 v - w^{\bullet},$$

$$(\cdot)' = \frac{1}{A_1}\frac{\partial()}{\partial\alpha_1}, \;\; (\cdot)^{\bullet} = \frac{1}{A_2}\frac{\partial()}{\partial\alpha_2}, \;\; \psi = \frac{1}{A_1 A_2}\frac{\partial A_2}{\partial\alpha_1}. \tag{12}$$

In the cylindrical shell version:

$$\begin{array}{l} k_1 = 0, k_2 = 1/R_c, \psi = 0, A_2 = R_c, \\ E_{11} = u', \;\; E_{22} = v^{\bullet} + k_2 w, \;\; E_{12} = v' + u^{\bullet}, K_{11} = \varphi_1', \;\; K_{22} = \varphi_2^{\bullet}, \;\; K_{12} = \varphi_2' + \varphi_1^{\bullet}, \\ E_{13} = \varphi_1 - \vartheta_1, \;\; E_{23} = \varphi_2 - \vartheta_2, \vartheta_1 = -w', \;\; \vartheta_2 = k_2 v - w^{\bullet}. \vartheta_1 = -w', \;\; \vartheta_2 = k_2 v - w^{\bullet}. \end{array} \tag{13}$$

Further consider the steady-state forced harmonic vibrations of a shell with the dependence of quantities on time t in the form: $F(\alpha_1, \alpha_2, t) = F_a(\alpha_1, \alpha_2)e^{-i\omega}$, where F_a is the complex amplitude included in the equation of harmonic magnitudes ω is the circular frequency of the driving load.

We will write the shell oscillation equations with respect to complex amplitudes, for which we will keep the notation of the initial values. In the variant of the shells of revolution taking into account the reaction of the external environment they have the form:

$$\begin{array}{l} T_{11}' + \psi(T_{11} - T_{22}) + S^{\bullet} + k_1 Q_{11} + \omega^2(bu + c\varphi_1) + q_1 = 0, \\ S' + 2\psi S + T_{22}^{\bullet} + k_2 Q_{22} + \omega^2(bv + c\varphi_2) + q_2 = 0, \\ Q_{11}' + \psi Q_{11} + Q_{22}^{\bullet} - k_1 T_{11} - k_2 T_{22} + \omega^2 bw + q_3 - K_L p = 0, \\ M_{11}' + \psi(M_{11} - M_{22}) + H^{\bullet} - Q_{11} + \omega^2(cu + d\varphi_1) = 0, \\ H' + 2\psi H + M_{22}^{\bullet} - Q_{22} + \omega^2(cv + d\varphi_2) = 0, \end{array} \tag{14}$$

where T_{jj}, Q_{jj}, H, S, M_{jj} are internal forces and moments brought to the main surface; p is a dynamic pressure of the external environment; K_L is a switch that takes the value 1 in the presence of liquid and 0 in the absence of it;

$$b = \int\limits_h \rho \, dz, \;\; c = \int\limits_h \rho z \, dz, \;\; d = \int\limits_h \rho z^2 dz, \tag{15}$$

where ρ is the density of the shell material and ribs.

For cylindrical shell, we have:

$$\begin{array}{l} T_{11}' + S^{\bullet} + \omega^2(bu + c\varphi_1) + q_1 = 0, \\ S' + T_{22}^{\bullet} + k_2 Q_{22} + \omega^2(bv + c\varphi_2) + q_2 = 0, \\ Q_{11}' + Q_{22}^{\bullet} - k_2 T_{22} + \omega^2 bw + q_3 - K_L p = 0, \\ M_{11}' + H^{\bullet} - Q_{11} + \omega^2(cu + d\varphi_1) = 0, \\ H' + M_{22}^{\bullet} - Q_{22} + \omega^2(cv + d\varphi_2) = 0, \end{array} \tag{16}$$

In the case of constructive orthotropy, the elasticity relations have the form:

$$T_{11} = B_{11}E_{11} + B_{12}E_{22} + A_{11}K_{11} + A_{12}K_{22}, T_{22} = B_{12}E_{11} + B_{22}E_{22} + A_{12}K_{11} + A_{22}K_{22},$$
$$M_{11} = A_{11}E_{11} + A_{12}E_{22} + D_{11}K_{11} + D_{12}K_{22}, M_{22} = A_{12}E_{11} + A_{22}E_{22} + D_{12}K_{11} + D_{22}K_{22}, \quad (17)$$
$$S = B_{33}E_{12} + A_{33} \cdot 2K_{12}, \; H = A_{33}E_{12} + D_{33} \cdot 2K_{12}, Q_{11} = G_{13}E_{13}, \;\; Q_{22} = G_{23}E_{23},$$

where B_{ij}, A_{ij}, D_{ij}, G_{ij} are the specified stiffness of the reinforced shell, taking into account the edges of the "smearing" scheme. The inertia characteristics of the shell are determined by integrating the specific mass of the shell and the edges along the cross-section of the wall.

3 The Solution Procedure

Since we consider axisymmetric constructions, we can separate the circumferential coordinate α_2 in the equations presented above. Let us restrict ourselves to the normal load q_3, which is symmetrically located relative to the reference point of the circumferential coordinate. Then the Fourier series expansions can be performed either by cosines or by sinuses. For example:

$$w = \sum_{n=0}^{\infty} w_n \cos n\alpha_2, \quad v = \sum_{n=0}^{\infty} v_n \sin n\alpha_2,$$
$$T_{11} = \sum_{n=0}^{\infty} {}_{11n} \cos n\alpha_2, \quad q_3 = \sum_{n=0}^{\infty} q_{3n} \cos n\alpha_2, \quad (18)$$

etc. The components of the stress-strain state are decomposed: by cosines u, w, φ_1,ϑ_1, E_{11}, E_{22}, $E12$, $E12$, $E23$, $K11$, $K22$, $K12$, $T11$, $T22$, $M11$, $M22$, $Q11$; by sine v,φ_2, ϑ_2, $E12$, $K12$, S, H, $Q22$.

In the main relations and equations, we pass on to dimensionless quantities using the main normalizing parameters. E_*, ν_*, R_*, h_*, ρ_*. They have the meaning and dimension of the characteristic: Young's modulus, Poisson's ratio, radius of curvature or linear size (large), thickness (small size), density of the material, respectively. From the main normalizing parameters, combinations of divisors with the dimension of the normalized values are formed.

Designations are introduced:

$\varepsilon_* = h_*/R_*$ is a thinwalled parameter;

$\overline{\nu}_* = 1-\nu_*^2$; $B_* = E_*h_*/\overline{\nu}_*$, $A_* = E_*h_*^2/\overline{\nu}_*$, $D_* = E_*h_*^3/\overline{\nu}_*$ are the normalizing values for the coefficients of reduced stiffness in elasticity ratios;

$c_* = \sqrt{E_*/(\rho_*\overline{\nu}_*)}$ is a characteristic speed of sound in the shell material;

$F_* = R_*h_*/\overline{\nu}_*$, $S_* = R_*h_*^2/\overline{\nu}_*$ $J_* = R_*h_*^3/\overline{\nu}_*$ are the values for normalizing the parameters of the cross-section of the edges (areas and moments of inertia).

We also introduce a dimensionless frequency parameter, associated with the circular frequency, $\omega = 2\pi f$, where f is a frequency in Hertz, by the formula $\Omega = \omega R_*/c_*$.

Formulae for the transition to dimensionless quantities have the form:

$$
\begin{aligned}
&\{U,\ V,\ W,\ u,\ v,\ w\}_U = \{\ldots\}_D/h_*,\ \{A_1,\ A_2\}_U = \{\ldots\}_D/R_*,\\
&\{k_1,\ k_2,\ \psi;\ \tau_1,\ \tau_2;\ K_{11},\ K_{22},\ K_{12}\}_U = \{\ldots\}_D \cdot R_*,\\
&\{\vartheta_1,\ \vartheta_2,\ \varphi_1,\ \varphi_2;\ \varepsilon_{11},\ \varepsilon_{22},\ \varepsilon_{12};\ \Omega_1,\ \Omega_2;\ E_{11},\ E_{22},\ E_{12}\}_U = \{\ldots\}_D/\varepsilon_*,\\
&\{M_{11},\ M_{22},\ H\}_U = \{\ldots\}_D R_*/D_*,\ \{T_{11},\ T_{22},\ S;\ Q_{11},\ Q_{22}\}_U = \{\ldots\}_D R_*/A_*,\\
&\{q_1,\ q_2,\ q_3\}_U = \{\ldots\}_D R_*^2/A_*,\ \{\rho_1,\ \rho_{1j},\ \Delta_j\}_U = \{\ldots\}_D/(\rho_* h_*),\\
&\{\rho_{(\lambda)},\ \rho_{pj}\}_U = \{\ldots\}_D/\rho_*,\ \{B_{jk},\ B_{j(\lambda)},\ B_{pj},\ \overline{G}_{(\lambda)},\ G_{13},\ G_{23}\}_U = \{\ldots\}_D/B_*,\\
&\{A_{jk}\}_L = \{\ldots\}_D/A_*,\ \{D_{jk}\}_L = \{\ldots\}_D/D_*, \{E_{(\lambda)},\ G_{(\lambda)},\ E_{pj},\ G_{pj}\}_U\{\ldots\}_D/E_*,\\
&\{J_{pj},\ I_{pj},\ I^o_{pj}\}_U = \{\ldots\}_D/J_*,\ \{F_{pj}\}_U = \{\ldots\}_D/F_*,\ j,\ k = 1,\ 2,\ 3.
\end{aligned}
\tag{19}
$$

In formulae (19), the dimensionless quantities are grouped by curly brackets with the index "U" in the left parts of the equalities. Their dimensional (normalized) analogs are implied in brackets with the index "D" in the right parts of the formulae.

For vibroacoustic analysis of complex structures, calculations of amplitude-frequency characteristics (AFCs) are performed pointwise for discrete values of the driving frequency parameter. This is quite a long and painstaking work. Examples of such AFCs are given in [2]. However, in the case of comparative analysis of the influence of the properties of different materials on the vibrational characteristics, a very convenient model is a reinforced cylindrical shell with a free support of the ends. This model allows representation of the solution in series and construction of the frequency response as a function of the frequency parameter. In addition, this model is also informative for more complex structures, since it is a typical section of composite shells. As the frequency increases, the vibrations are localized on a separate excited section, and the effect of shortening the long structure to a single section works, which determines the main contribution to the acoustic field.

We apply the method of complex amplitudes to the equations for a cylindrical shell and separate the n-th circumferential mode. After the transition to dimensionless quantities kinematic relations are reduced to the form:

$$
\begin{aligned}
&E_{11n} = u_n',\ \ E_{22n} = nv_n + w_n,\ \ E_{12n} = v_n' - nu_n,\\
&K_{11n} = \varepsilon_* \varphi_{1n}',\ \ K_{22n} = \varepsilon_* n\varphi_{2n},\ \ K_{12n} = \varepsilon_*(\varphi_{2n}' - n\varphi_{1n}),\\
&E_{13n} = \varphi_{1n} - \vartheta_{1n},\ \ E_{23n} = \varphi_{2n} - \vartheta_{2n},\ \vartheta_{1n} = -w_n',\ \ \vartheta_{2n} = v_n + nw_n;
\end{aligned}
\tag{20}
$$

The simplest analytical solution is constructed for free support: $v = 0$, $M_{11} = 0$, $T_{11} = 0$, $w = 0$, $Q_{11} = 0$, $\varphi_2 = 0$. These conditions and homogeneous ($q_{3n} = 0$) (11)–(13) are satisfied by the following forms of natural oscillations:

$$
u_n(x) = u_{nk}\cos(mx),\ \ v_n(x) = v_{nk}\sin(mx),\ \ w_n(x) = w_{nk}\sin(mx),
$$

$$
\varphi_{1n}(x) = \varphi_{1nk}\cos(mx),\ \ \varphi_{2n}(x) = \varphi_{2nk}\sin(mx),
\tag{21}
$$

where $m = k\pi\ /L$, k is the number of longitudinal half-waves, and $x = \alpha_1$ is the longitudinal coordinate. We will also denote the circumferential coordinate $\theta = \alpha_2$.

The problems of forced vibrations can be solved by decomposing the amplitudes of displacements according to the proper forms of vibrations (21), i.e. in Fourier series and along the longitudinal coordinate. This provides separation of equations for determining coefficients by model numbers.

By the circumferential coordinate θ, cosine and sine series expansions are performed on the range $(0, 2\pi)$ due to the symmetry of the load in the Diametric plane, which we assume. In the longitudinal direction, solutions on the range $(0, L)$ are also represented by rows of sine and cosine. There are no restrictions on load coordinates along the length of the shell. Here we decompose even and odd functions on the range $(-L, L)$, which are formally considered as a continuation of the solution on the range $(-L, 0)$ in an even or odd way. We are only interested in the part on the range $(0, L)$ of the shell. Therefore, the number n is the number of waves in the circumferential direction, and k is the number of half-waves on the generating shell.

The solution in rows for displacements and rotation angles as functions of coordinates and frequency has the form:

$$
\begin{aligned}
u(x,\,\theta,\,\Omega) &= \sum_{k=1}^{M} u_{0k}(\Omega)\cos[(k\pi/L)x] + \sum_{k=1}^{M}\sum_{n=1}^{N} u_{nk}(\Omega)\cos[(k\pi/L)x]\cos(n\theta),\\
v(x,\,\theta,\,\Omega) &= \sum_{k=1}^{M}\sum_{n=1}^{N} v_{nk}(\Omega)\sin[(k\pi/L)x]\sin(n\theta),\\
w(x,\,\theta,\,\Omega) &= \sum_{k=1}^{M} w_{0k}(\Omega)\sin[(k\pi/L)x] + \sum_{k=1}^{M}\sum_{n=1}^{N} w_{nk}(\Omega)\sin[(k\pi/L)x]\cos(n\theta),\\
\varphi_1(x,\,\theta,\,\Omega) &= \sum_{k=1}^{M} \varphi_{10k}(\Omega)\cos[(k\pi/L)x] + \sum_{k=1}^{M}\sum_{n=1}^{N} \varphi_{1nk}(\Omega)\cos[(k\pi/L)x]\cos(n\theta),\\
\varphi_2(x,\,\theta,\,\Omega) &= \sum_{k=1}^{M}\sum_{n=1}^{N} \varphi_{2nk}(\Omega)\sin[(k\pi/L)x]\sin(n\theta).
\end{aligned}
\tag{22}
$$

Using decompositions of this type in all relations and equations, we obtain for coefficients of trigonometric series:

$$
\begin{aligned}
&E_{11nk} = -mu_{nk},\quad E_{22nk} = nv_{nk} + w_{nk},\ E_{12nk} = mv_{nk} - nu_{nk},\\
&K_{11nk} = -\varepsilon_* m\varphi_{1nk},\quad K_{12nk} = \varepsilon_* n\varphi_{2nk},\ K_{12n} = \varepsilon_*(m\varphi_{2nk} - n\varphi_{1nk}),\\
&E_{13nk} = \varphi_{1nk} + \vartheta_{1nk},\quad E_{23nk} = \varphi_{2nk} + \vartheta_{2nk},\\
&\vartheta_{1nk} = -mw_{nk},\quad \vartheta_{2nk} = v_{nk} + nw_{nk},\ \vartheta_{2n} = v_n + nw_n;
\end{aligned}
\tag{23}
$$

$$\begin{aligned}
&T_{11nk} = B_{11}E_{11nk} + B_{12}E_{22nk} + A_{11}K_{11nk} + A_{12}K_{22nk},\\
&T_{22nk} = B_{12}E_{11nk} + B_{22}E_{22nk} + A_{12}K_{11nk} + A_{22}K_{22nk},\\
&M_{11nk} = A_{11}E_{11nk} + A_{12}E_{22nk} + D_{11}K_{11nk} + D_{12}K_{22nk},\\
&M_{22nk} = A_{12}E_{11nk} + A_{22}E_{22nk} + D_{12}K_{11nk} + D_{22}K_{22nk},\\
&S_{nk} = B_{33}E_{12nk} + 2A_{33}K_{12nk},\ H_{nk} = A_{33}E_{12nk} + 2D_{33}K_{12nk},\\
&Q_{11nk} = G_{13}E_{13nk},\ \ Q_{22nk} = G_{23}E_{23nk};
\end{aligned} \tag{24}$$

$$\begin{aligned}
&mT_{11nk} + nS_{nk} + \Omega^2(bu_{nk} + \varepsilon_* c\varphi_{1nk}) = 0,\\
&-mS_{nk} - nT_{22nk} + Q_{22nk} + \Omega^2(bv_{nk} + \varepsilon_* c\varphi_{2nk}) = 0,\\
&-mQ_{11nk} + nQ_{22nk} - T_{22nk} + \Omega^2(b - K_L Z_{nk})w_{nk} + q_{3nk} = 0,\\
&mM_{11nk} + nH_{nk} - Q_{11nk}/\varepsilon_* + \Omega^2(cu_{nk} + \varepsilon_* d\varphi_{1nk}) = 0,\\
&-mH_{nk} - nM_{22nk} - Q_{22nk}/\varepsilon_* + \Omega^2(cv_{nk} + \varepsilon_* d\varphi_{2nk}) = 0.
\end{aligned} \tag{25}$$

We will consider the load acting on the normal to the shell, and equivalent to the concentrated force Q_3. Let l is the length of the platform at the longitudinal coordinate, δ_1 is the length of its midline segment (as in a trapezoid); 2δ is the coverage angle at the circumferential coordinate; x_1, θ_1 are the longitudinal and angular coordinates of the center of the platform, $S = l\delta_1$ is the area of the load application zone.

Let us move on to dimensionless quantities using the formulae:

$$\begin{aligned}
&\{l,\ \delta_1\}_U = \{l,\ \delta_1\}_D/R_*,\ \ \{Q_3\}_U = \{Q_3\}_D(1-\nu_*^2)/E_*h_*^2,\\
&\{q_3\}_U = \{q_3\}_D(1-\nu_*^2)R_*^2/E_*h_*^2.
\end{aligned} \tag{26}$$

Then (in dimensionless form) the concentrated force is "smeared" on the site into a normal load of intensity $q_{3a} = Q_3/(l\delta_1)$ distributed over the surface within the site. In the area of determining curved coordinates $\{x \in (0, L); \theta \in (0, 2\pi)\}$ corresponding to the shell under consideration, the distributed load can be set using the Heaviside step function $H(x)$, which is equal to 0, for $x < 0$ and 1, for $x \geq 0$.

Then in the definition area $q_3(x, \theta) = q_{3a}\Phi_1(x)\Phi_2(\theta)$, where

$$\begin{aligned}
&\Phi_1(x) = [H(x - (x_1 - l/2)) - H(x - (x_1 + l/2))],\\
&\Phi_2(\theta) = [H(\theta - (\theta_1 - \delta)) - H(\theta - (\theta_1 + \delta))].
\end{aligned} \tag{27}$$

The cosine expansion of an even function $\Phi_2(\theta)$ has the form:

$$\Phi_2(\theta) = \delta/\pi + \sum_{n=1}^{N} [2/(n\pi)]\sin(n\delta)\cos(n\theta_1)\cos(n\theta). \tag{28}$$

Continue $\Phi_1(x)$ on the range $(-L, 0)$ in an odd way. The corresponding expansion in the range $(-L, L)$ by sine has the form:

$$\Phi_1(x) = \sum_{k=1}^{M} [4/(k\pi)]\ \ \sin[(k\pi/L)l/2)]\ \ \sin[(k\pi/L)x_1]\ \ \sin[(k\pi/L)x)]. \tag{29}$$

Thus, the normal load $q_3(x, \theta)$ is approximated by a double trigonometric series:

$$q(x,\theta) = \frac{a_{\theta 0}}{2}\sum_{k=1}^{M} a_{xk}\sin[(k\pi/L)x] + \sum_{n=1}^{N}\sum_{k=1}^{M} a_{\theta n}a_{xk}\sin[(k\pi/L)x]\cos(n\theta), \quad (30)$$

where

$$\begin{aligned} a_{\theta 0} &= q_{3a}2l/L, \quad a_{\theta n} = q_{3a}[2/(n\pi)]\ \sin(n\delta)\ \cos(n\theta_1), \\ a_{xk} &= q_{3a}[4/(k\pi)]\ \sin[(k\pi/L)l/2]\ \sin(mx_1)\,. \end{aligned} \quad (31)$$

or

$$q(x,\theta) = \sum_{n=0}^{N}\sum_{k=1}^{M} q_{nk}\sin[(k\pi/L)x]\cos(n\theta),\ q_{0k} = a_{\theta 0}a_{xk}/2,\ \ q_{nk} = a_{\theta n}a_{xk}. \quad (32)$$

We substitute (23) into (24) and then into (25). By collecting the coefficients for u_{nk}, v_{nk}, w_{nk}, φ_{1nk}, φ_{2nk}, we obtain an algebraic system of equations of the fifth order for determining the coefficients of series (27) for $n > 0$: $KX = B$.

Here $K = \left[K_{\lambda\mu}\right]$, $\lambda, \mu = 1, \ldots, 5$ is the matrix of the system; X is a column of unknowns with elements $X_1 = u_{nk}$, $X_2 = v_{nk}$, $X_3 = w_{nk}$, $X_4 = \varphi_{1nk}$, $X_5 = \varphi_{2nk}$; B is the right part that depends on the normal load coefficients: $B = [0, 0, q_{nk}, 0, 0]^{\mathrm{T}}$.

The elements of the matrix K are defined by the formulae:

$$\begin{aligned}
&K_{11} = b\Omega^2 - B_{11}m^2 - B_{33}n^2,\ \ K_{12} = mn(B_{12} + B_{33}),\ \ K_{13} = B_{12}m,\\
&K_{14} = \varepsilon_*(c\Omega^2 - A_{11}m^2 - 2A_{33}n^2),\ \ K_{15} = \varepsilon_* m(A_{12}m + 2A_{33}n);\\
&K_{21} = mn(B_{12} + B_{33}),\ \ K_{22} = b\Omega^2 - B_{33}m^2 - B_{22}n^2 - G_{23},\ K_{23} = -n(B_{22} + G_{23});\\
&K_{24} = \varepsilon_* mn(A_{12} + 2A_{33}),\ \ K_{25} = \varepsilon_*(c\Omega^2 - 2A_{33}m^2 - A_{22}n^2) + G_{23};\\
&K_{31} = B_{12}m,\ \ K_{32} = -n(B_{22} + G_{23}),\ K_{33} = (b\Omega^2 - K_L Z_{nk}) - G_{13}m^2 - G_{23}n^2 - B_{22},\\
&K_{34} = \varepsilon_*(A_{12}m + A_{22}n) - G_{13}m,\ \ K_{35} = n(G_{23} - \varepsilon_* A_{22}\,);\\
&K_{41} = -(A_{11}m^2 + A_{33}n^2),\ \ K_{42} = mn(A_{12} + A_{33}),\ K_{43} = m(A_{12} - G_{13}/\varepsilon_*),\\
&K_{44} = \varepsilon_*(d\Omega^2 - D_{11}m^2 - 2D_{33}n^2) - G_{13}/\varepsilon_*,\ K_{45} = \varepsilon_* mn(D_{12} + 2D_{33});\\
&K_{51} = mn(A_{12} + A_{33}),\ K_{52} = c\Omega^2 - A_{22}n^2 - A_{33}m^2 + G_{23}/\varepsilon_*,\ K_{53} = n(G_{23}/\varepsilon_* - A_{22}),\\
&K_{54} = \varepsilon_* mn(D_{12} + 2D_{33}),\ K_{55} = \varepsilon_*(d\Omega^2 - 2D_{33}m^2 - D_{22}n^2) - G_{23}/\varepsilon_*.
\end{aligned} \quad (33)$$

The equations for determining the coefficients of the zero circumferential mode are processed separately. The problem is reduced to a system of three algebraic equations: $PY = C$, regarding $Y_1 = u_{0k}$, $Y_2 = w_{0k}$, $Y_3 = \varphi_{10k}$, where $P = [P_{ij}]$, $i, j = 1, 2, 3$, $Y = [Y_i]$, $C = [0, q_{0k}, 0]^{\mathrm{T}}$,

$$P = \begin{bmatrix} P_{11} & P_{12} & P_{13} \\ P_{21} & P_{22} & P_{23} \\ P_{31} & P_{32} & P_{33} \end{bmatrix},\ Y = \begin{bmatrix} Y_1 \\ Y_2 \\ Y_3 \end{bmatrix},\quad C = \begin{bmatrix} 0 \\ q_{0k} \\ 0 \end{bmatrix}, \quad (34)$$

$$\begin{array}{l} P_{11} = b\Omega^2 - B_{11}m^2,\ \ P_{12} = B_{12}m,\ \ P_{13} = \varepsilon_*(c\Omega^2 - A_{11}m^2); \\ P_{21} = B_{12}m,\ \ P_{22} = (b\Omega^2 - K_L Z_{0k}) - G_{13}m^2 - B_{22},\ P_{23} = \varepsilon_* m A_{12} - G_{13}m; \\ P_{31} = c\Omega^2 - A_{11}m^2,\ \ P_{32} = m(A_{12} - G_{13}/\varepsilon_*),\ P_{33} = \varepsilon_*(d\Omega^2 - D_{11}m^2) - G_{23}/\varepsilon_*. \end{array} \quad (35)$$

Here the coefficient of influence of the liquid is present in the elements K_{33} and P_{22}.

4 Amplitude-Frequency Characteristics and Resonances

Let us consider the vibrations of a reinforced cylindrical shell made of a material with Young's modulus E, with Poisson coefficients $\nu = 0.3$ and $\nu = -0.3$, and density ρ. The scattering of vibrational energy in the shell is taken into account through a complex module $E = E_o(1 - i\eta)$. Loss coefficient $\eta = 0.03$. The driving harmonic force is applied in the middle of the shell length.

Let us denote the length of the shell L, and the radius of the median surface R. The ratio L/R is set to 3.14. The relative thin-walled parameter of the shell $\varepsilon_* = h/R = 0.01$, where h is the thickness of the shell.

The shell is supported by regularly annular ribs with a pitch of $l_r/R = 0.2$. The cross-section of the ribs is rectangular $\delta_r \times h_r$, where δ_r is a section width, h_r is a height. Relationships $\delta_r/h = 1$, $h_r/h = 8$. Cross-section area of the rib is $\delta_r h_r$, proper moments of inertia relative to the symmetry axes are $I_r = \delta_r h_r^3/12$, $I_{1r} = \delta_r^3 h_r/12$. Torsion moment of inertia is $J_r = 4I_r I_{1r}/(I_r + I_{1r})$. Normal eccentricity to the shell of the center of gravity of the edge relative to the median surface $z_{or} = (h + h_r)/2$. The main moment of inertia of the cross-section of the edge relative to the forming median surface $I_{or} = I_r + z_{or}^2 F$. The tension-compression stiffness of the rib and the main bending stiffness relative to the forming shell will be as follows: $B_r = EF_r/l_r$, $D_r = EI_{or}/l_r$. The rigidity of the shell, tensile-compression and cylindrical bending stiffness are $B = Eh/(1 - \nu^2)$, $D = Eh^3/[12(1 - \nu^2)]$.

Other shear and torsional stiffnesses are: $G_c = Eh/[2(1 + \nu)]$, $G_v = G_c h^2/12$, $G_{vr} = EJ_r/[2(1 + \nu)l_r]$.

Inertia parameters b, c, d are:

$$b = \rho\{h + F_r/[l_r(1 - \nu^2)]\},\ \ c = \rho F_r h_r(h + h_r)/(2l_r),$$
$$d = \rho h^3/12 + \rho F_r h_r(3h^2 + 6hh_r + 4h_r^2)/(12l_r),$$

The reduced stiffness of the structural anisotropy is determined by the formulae:

$$B_{11} = B,\ \ B_{22} = B + B_r,\ \ B_{12} = \nu B,\ D_{11} = D,\ \ D_{22} = D + D_r,\ \ D_{12} = \nu D,$$

$$A_{11} = 0,\ \ A_{22} = B_r z_{or},\ \ A_{12} = 0,\ B_{33} = G_c,\ \ A_{33} = 0,\ \ D_{33} = G_v + G_{vr},$$

The stiffness of the transverse shift will be set using the coefficient from B_{33} : $G_{13} = G_{23} = K_G B_{33}$.

When moving to dimensionless quantities, we will take the following as characteristic quantities: $E_* = E_o$, $\nu_* = \nu$, $R_* = R$, $h_* = h$, $\rho_* = \rho$. We will normalize the stiffness in the elasticity ratios using the following values: $B_* = E_o h/(1-\nu^2)$, $A_* = B_n h$, $D_* = B_* h^2$

$$\{\tilde{A}_{jk},\ \tilde{A}_{33}\} = \{A_{jk},\ A_{33}\}/A_*,\ \{\tilde{B}_{jk},\ \tilde{B}_{33}\} = \{B_{jk},\ B_{33}\}/B_*,$$
$$\{\tilde{D}_{jk},\ \tilde{D}_{33}\} = \{D_{jk},\ D_{33}\}/D_*,\ j,k = 1,2.$$

The real parts of dimensionless stiffness coefficients get the following values:

$$\tilde{A}_{11} = 0,\ \tilde{A}_{12} = 0,\ \tilde{A}_{22} = 1.638,\ \tilde{A}_{33} = 0,$$

$$\tilde{B}_{11} = 1,\ \tilde{B}_{12} = 0.3,\ \tilde{B}_{22} = 1.364,\ \tilde{B}_{33} = 0.35,\ \tilde{G}_{13} = \tilde{G}_{23} = 0.1\tilde{B}_{33} = 0.035;$$

$$\tilde{D}_{11} = 0.083,\ \tilde{D}_{12} = 0.025,\ \tilde{D}_{22} = 9.396,\ \tilde{D}_{33} = 0.075.$$

The transition to dimensionless inertial parameters is performed, using the formulae:

$$\tilde{b} = b/(\rho h),\ \tilde{c} = c/(\rho h^2),\ \tilde{d} = d/(\rho h^3).$$

Dimensionless inertial parameters have the following values:

$$\tilde{b} = 1.44,\ \tilde{c} = 72,\ \tilde{d} = 409.417.$$

The speed of sound in the shell material $c_o = \sqrt{E/[\rho(1-\nu^2)]}$ is taken as a characteristic value for normalization. Then the dimensionless speed of sound in the shell: $\tilde{c}_o = 1$. The density of the medium and the speed of sound in the external environment, in which the shell is immersed are normalized by similar values for the shell. We focus on the steel-water ratio. Then the dimensionless density of the medium: $\tilde{\rho}_c = \rho_c/\rho \approx 0.128$, $\tilde{c}_c = c_c/c_o \approx 0.3$. Dimensionless frequency parameter is entered by the formula: $\Omega = \omega R/c_o$, where ω is the circular frequency.

The transition to dimensionless loading is given by the formulae (31). The principle of superposition works in a linear problem. Usually in dimensionless form we set a single concentrated force $\tilde{Q}_3 = 1$. This is a computational technique. When returning to real structures and loads, the vibration levels are determined by proportional recalculation. However, we can also remember that in a real dimensional situation, the applicability of linear theory is limited by the smallness of deflections no more than the thickness of the shell. So for a change, let us put a load here $\tilde{Q}_3 = 0.0075$, that gives dimensionless oscillation amplitudes less than one.

So, the shell is placed in an unlimited ideal heavy acoustic medium (water), the stationary vibrations of which are modeled in a linear approximation by the Helmholtz equations. We study the influence of the medium on vibration levels and the reduction of resonance frequencies on the amplitude-frequency characteristics (AFC) of input pliability. The frequency range is considered, including the first three or four noticeably manifested resonance frequencies. For this construction, they go for n values in the order 2, 3, 4, 5.

Since we took a heavier shell that differs from the previously tested one, we will first look at the options without liquid. In Fig. 1, the normal ($\nu = 0.3$) and auxetic ($\nu = -0.3$) shells are represented. As you can see, the effect of shifting up the resonance frequencies and reducing the vibration levels for this shell is preserved.

Let us compare the AFC for an auxetic shell ($\nu = -0.3$) in liquid ("wet") and without liquid ("dry"), (see Fig. 2). A significant decrease of the resonance frequency is obvious due to added mass effect of fluid. So, the first frequency decreases by about 50%.

Let us compare the vibrations of normal and auxetic shells placed in a liquid. Figure 3 shows the frequency response, where the solid curve corresponds to $\nu = 0.3$, and the dotted curve corresponds to $\nu = -0.3$. The effect of shifting the resonance frequencies up and a certain decrease in the resonance amplitudes of the auxetic shell also observed here, as in the dry shell, in relation to the normal shell. The liquid has an effect on reducing peak levels.

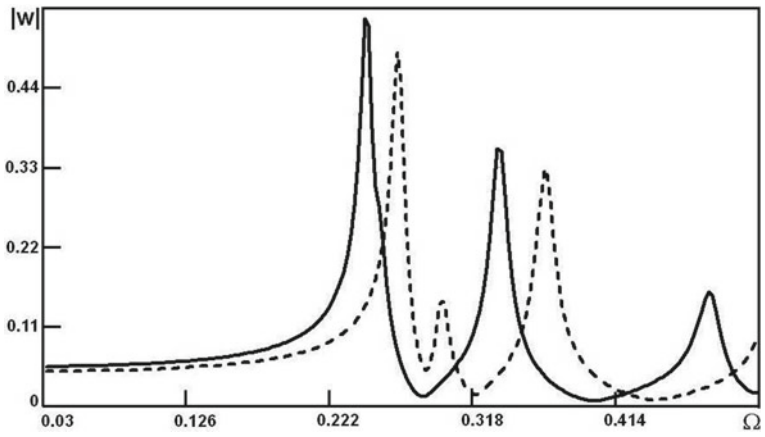

Fig. 1 Comparison of normal (solid) and auxetic (dotted) shells outside the liquid

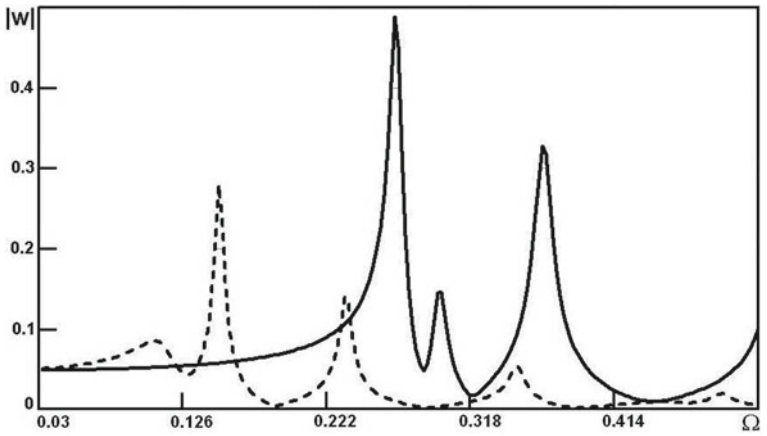

Fig. 2 AFC of the auxetic shell outside the liquid (solid) and in the liquid (dotted line)

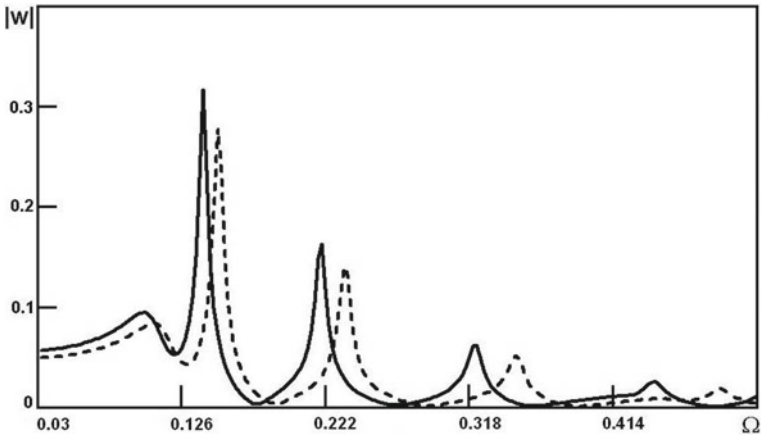

Fig. 3 AFC comparison of a normal ($\nu = 0.3$, solid) and an auxetic shell ($\nu = -0.3$, dotted) in a liquid

Acknowledgements Research was financially supported by Southern Federal University, grant No. VnGr-07/2020-04-IM (Ministry of Science and Higher Education of the Russian Federation).

References

1. A.S. Yudin, S.A. Yudin, in *Proceedings of the 2015 International Conference on Physics and Mechanics of New Materials and Their Applications, devoted to 100-year Anniversary of the*

Southern Federal University, ed. by I.A. Parinov, S.H. Chang, V.Yu. Topolov (Nova Science Publishers, New York, 2016), p. 447
2. A.S.Yudin, in *Advanced Materials. Physics, Mechanics and Applications. Springer Proceedings in Physics*, vol. 152, ed. by I.A. Parinov, S.H. Chang, V.Yu. Topolov (2014), p. 181
3. G. Chertock, J. Acoust. Soc. Amer. **36**(7), 1305 (1964)
4. E. Skouchik, *Fundamentals of Acoustics*, vol. 2. (Mir, Moscow, 1976) (In Russian)

Oscillation Equations for Non-axisymmetric Shells

A. S. Yudin

Abstract The basic equations intended for solving the problems of vibrations of composite shells of complex geometry are presented. The equations of motion are derived on the basis of the Hamilton—Ostrogradsky principle and kinematic relations that take into account transverse shear deformations. The elasticity relations for transversally isotropic shells are given.

Keywords Skew-angle basis · Shells of complex geometry · Hamilton—Ostrogradsky principle · Equations of motion · Deformation components · Transverse shear deformation · Elasticity relations

1 Some Information for Space with Skew-Angle Basis

1.1 Parametrization and Metric Tensors

The theory of shells of complex geometry is constructed in a system of curved coordinates with an oblique basis. We give some basic relations for such a system.

In the three-dimensional Euclidean space x^k, a system of generalized curvilinear coordinates $\alpha^i \equiv \alpha_i$ is introduced, so that the radius-vector $\boldsymbol{r}(x^k)$ of an arbitrary point P can be considered as function of α_i. The main basis of the system is defined by a trihedron of non-planar vectors $\boldsymbol{\gamma}_p = \boldsymbol{r}_{,p}$, $p = 1, 2, 3$, where $(\ldots)_{,p} = \partial(\ldots)/\partial\alpha_p$ are the partial derivatives of the coordinate with the number p.

The square of the arc element (the differential of the length function) of the spatial curve in the generalized system is given by the quadratic form:

$$(ds)^2 = H_{ij} d\alpha^i d\alpha^j, \; i, j = 1, 2, 3, \tag{1.1}$$

A. S. Yudin (✉)
I. I. Vorovich Mathematics, Mechanics and Computer Sciences Institute, Southern Federal University, Rostov-on-Don, Russia
e-mail: ayudin@sfedu.ru

I. A. Parinov et al. (eds.), *Physics and Mechanics of New Materials and Their Applications*, Springer Proceedings in Materials 10,
https://doi.org/10.1007/978-3-030-76481-4_26

where H_{ij} are the elements of the matrix of the main metric tensor of the system α^i:

$$H_{ij} = \boldsymbol{\gamma}_i \cdot \boldsymbol{\gamma}_j, \quad \boldsymbol{\gamma}_p = \boldsymbol{r}_{,p}, \quad H_{ii} = |\boldsymbol{\gamma}_i|^2, \quad H_{ij} = \sqrt{H_{ii} H_{jj}} \cos \psi_{ij}. \tag{1.2}$$

Here ψ_{ij} are the angles between the vectors $\boldsymbol{\gamma}_i, \boldsymbol{\gamma}_j$. In (1.1) and further on, the rule of summation by the repeated top and bottom indices is adopted.

The volume of a parallelepiped constructed on vectors $\boldsymbol{\gamma}_p$ is given by their mixed product

$$\boldsymbol{\gamma}_1 \cdot (\boldsymbol{\gamma}_2 \times \boldsymbol{\gamma}_3) = \det ||\partial x^k / \partial \alpha_i|| = (H)^2. \tag{1.3}$$

In general, the trihedron is oblique. Therefore, we can enter a mutual basis $\boldsymbol{\gamma}^p$, $p = 1, 2, 3$:

$$\boldsymbol{\gamma}^1 = (\boldsymbol{\gamma}_2 \times \boldsymbol{\gamma}_3)/(H)^2, \quad \boldsymbol{\gamma}^2 = (\boldsymbol{\gamma}_3 \times \boldsymbol{\gamma}_1)/(H)^2, \quad \boldsymbol{\gamma}^3 = (\boldsymbol{\gamma}_1 \times \boldsymbol{\gamma}_2)/(H)^2. \tag{1.4}$$

The scalar product $\boldsymbol{\gamma}^i \cdot \boldsymbol{\gamma}_k = \delta^i_k$, where δ^i_k is the Kronecker symbol;$\boldsymbol{\gamma}_k = H_{ki} \boldsymbol{\gamma}^i$.

The components of the mutual metric tensor are given by the relations $H^{ik} = \boldsymbol{\gamma}^i \cdot \boldsymbol{\gamma}^k$:

$$H^{11} = [H_{22} H_{33} - (H_{23})^2]/(H)^2, \quad H^{12} = H^{21} = (H_{23} H_{13} - H_{12} H_{33})/(H)^2 \tag{1.5}$$

etc. Other components can be obtained by a circular permutation of the indexes.

There are formulae:

$$\boldsymbol{\gamma}^i = H^{ij} \boldsymbol{\gamma}_j, |H^{ii}| = |\boldsymbol{\gamma}^i|^2, \quad H^{ij} = \sqrt{H^{ii} H^{jj}} \cos \psi^{ij}, \tag{1.6}$$

where ψ^{ij} are the angles between the vectors of the mutual basis. The components H_{ki}, H^{im} are related by the ratio: $H_{ki} H^{im} = \delta^m_k$.

An arbitrary vector $\boldsymbol{a}$ can be decomposed in the main and mutual bases:$\boldsymbol{a} = \boldsymbol{a}^k \boldsymbol{\gamma}_k = a_k \boldsymbol{\gamma}^k$. The quantities a^k are called contravariant, and a_k are the covariant components of the vector $\boldsymbol{a}$. They are connected by relations:$a_k = H_{ki} a^i$, $a^i = H^{ik} a_k$.

1.2 Differentiation of Vectors

The differentiation of the vectors $\boldsymbol{\gamma}_j$ is performed by the formulae:

$$\boldsymbol{\gamma}_{j,j} = \boldsymbol{\gamma}_{j,i} = r_{,ij} = \Gamma^s_{ij} \boldsymbol{\gamma}_s. \tag{1.7}$$

Here $\Gamma^s_{ij} = \Gamma^s_{ji}$ are the Christoffel symbols of the second kind. To define them, we introduce Γ^s_{ijk}, namely Christoffel symbols of the first kind:

$$\Gamma^s_{ijk} = \Gamma_{jik} = 0.5\,(H_{ik,j} + H_{jk,i} - H_{ij,k}). \tag{1.8}$$

Then

$$\Gamma^s_{ij} = \Gamma_{ijt} H^{ts}. \tag{1.9}$$

The derivatives of γ_i can be expressed in terms of the vectors of the mutual basis:

$$\boldsymbol{\gamma}_{i,j} = \boldsymbol{\gamma}_{j,i} = r_{i,j} = \Gamma_{ijt}\boldsymbol{\gamma}^t. \tag{1.10}$$

The differentiation of the vectors of the mutual basis is performed by the formulae:

$$\gamma_{,j}^{\ i} = -\Gamma^i_{jt}\gamma^t. \tag{1.11}$$

Based on (1.7)–(1.11), we obtain formulae for differentiating an arbitrary vector $\boldsymbol{u}(u^p)$:

$$\boldsymbol{u}_{,k} = \nabla_k u^p \boldsymbol{\gamma}_p = \nabla_k u_p \boldsymbol{\gamma}^p, \tag{1.12}$$

where

$$\nabla_k u_p = u_{p,k} - \Gamma^t_{pk} u_t;\ \nabla_k u^p = u^p_{,k} + \Gamma^p_{kt} u^t. \tag{1.13}$$

In the case of an orthogonal coordinate system, $H_{ij} = H^{ij} = 0$ for $i \neq j$, and then

$$ds^2 = H_{ii} d\alpha^i d\alpha^i; \tag{1.14}$$

$$\boldsymbol{\gamma}_k = H_{kk}\boldsymbol{\gamma}^k;\ \boldsymbol{\gamma}^k = H^{kk}\boldsymbol{\gamma}_k;\ \ H^{kk} = 1/H_{kk}. \tag{1.15}$$

1.3 Relations for Surfaces

1.3.1 Metric Tensors of the First and Second Kind.

Let S is a sufficiently smooth surface defined by the parametrization:

$$\boldsymbol{\rho} = \boldsymbol{\rho}(\alpha^1, \alpha^2). \tag{1.16}$$

Let, further, $\boldsymbol{e}_k = \boldsymbol{\rho}_{,k}$, $k = 1, 2$, $\boldsymbol{e}_3 = \boldsymbol{n}$ is the main trihedron on S, and let $\boldsymbol{e}_k = \boldsymbol{\rho}_{,k}$, $k = 1, 2$, $\boldsymbol{e}_3 = \boldsymbol{n}$ is the coefficients of the first and second quadratic forms, which are known to be components of second-order tensors $\hat{g}$ and $\hat{\kappa}$. The components are calculated using the following formulae:

$$g_{ij} = \boldsymbol{e}_{,i} \times \boldsymbol{e}_{,j} = \boldsymbol{\rho}_{,i} \times \boldsymbol{\rho}_{,j}, i, j = 1, 2, \kappa_{ij} = [(\boldsymbol{\rho}_{,ij} \times \boldsymbol{\rho}_{,1}) \cdot \boldsymbol{\rho}_{,2}](D)^{-1}, \quad (D)^2 = \det \hat{g} = g_{11}g_{22} - (g_{12})^2. \tag{1.17}$$

In square brackets there is a mixed product. The contravariant and mixed components g_{ij}, κ_{ij} are given by the relations:

$$g^{11} = g_{22}/(D)^2, \quad g^{12} = g^{21} = -g_{12}/(D)^2 = -g_{21}/(D)^2, \quad g^{22} = g_{11}/(D)^2, \quad g_i^j = \delta_i^j, \kappa_i^j = g^{js}\kappa_{si}, \kappa^{ij} = g^{it}g^{js}\kappa_{ts}. \tag{1.18}$$

The unit ort of the normal $\boldsymbol{n}$ is defined by the formula:

$$\boldsymbol{n} = \boldsymbol{e}_3 = (\boldsymbol{e}_1 \times \boldsymbol{e}_2)/D. \tag{1.19}$$

For the mutual basis $\boldsymbol{e}^i$ on the surface S, we have:

$$\boldsymbol{e}^i = g^{is}\boldsymbol{e}_s, \quad i, s = 1, 2, \quad \boldsymbol{e}^3 = \boldsymbol{e}_3 = \boldsymbol{n}. \tag{1.20}$$

The angle between the vectors of the main basis is given by the formula:

$$sin\,\psi = \frac{D}{\sqrt{g_{11}g_{22}}}. \tag{1.21}$$

1.3.2 *Differentiation of Vectors.*

The formulae for differentiating the vectors $\boldsymbol{e}_k$ and $\boldsymbol{e}^k$ on the surface S have the form:

$$\boldsymbol{e}_k, p = \Gamma_{kp}^s \boldsymbol{e}_s + \kappa_{kp}\boldsymbol{n}, \boldsymbol{e}^k, p = -\Gamma_{ps}^k \boldsymbol{e}^s + \kappa_p^k \boldsymbol{n}, \quad \boldsymbol{n}, p = -\kappa_p^s \boldsymbol{e}_s = -k_{ps}\boldsymbol{e}^s, k, \; p, \; s = 1, 2. \tag{1.22}$$

The Kristoffel symbols of the second kind Γ_{kp}^s included in (1.22) for the surface S are defined in terms of the Kristoffel symbols of the first kind of the surface by means of the relations:

$$\Gamma_{ki}^m = g^{mi}\Gamma_{kij}. \tag{1.23}$$

The Christoffel symbols Γ_{kpt} and Γ^s_{kp} are related to the coefficients of the first quadratic form:

$$\begin{gathered}\Gamma_{111} = 0.5g_{11,1}\,,\ \ \Gamma_{121} = \Gamma_{211} = 0.5g_{11,2}\,,\ \ \Gamma_{221} = g_{12,2} - 0.5g_{22,1}\,,\\ \Gamma^1_{11} = 0.5(g_{22}g_{11,1} + g_{12}g_{11,2} - 2g_{12}g_{12,1})/(D)^2,\\ \Gamma^1_{12} = \Gamma^1_{21} = 0.5\,(g_{22}g_{11,2} - g_{12}g_{22,1})/(D)^2,\\ \Gamma^1_{22} = 0.5\,[g_{11}(2g_{12,2} - g_{22,1}) - g_{12}g_{22,2}]/(D)^2,\ \ 1 \leftrightarrow 2.\end{gathered} \tag{1.24}$$

Let $\boldsymbol{u}(u^s)$ is an arbitrary vector given on the surface of S. The formulae for differentiating $\boldsymbol{u}$ by α_s have the form:

$$\begin{aligned}&\boldsymbol{u}_{,k} = \nabla_k \boldsymbol{u}^p e_p = \nabla_k u_p \boldsymbol{e}^p,\\ &\nabla_k u^p = u^p_{,k} + \Gamma^p_{ks} u^s - \kappa^p_k u^3,\\ &\nabla_k u_p = u_{p,k} + \Gamma^s_{kp} u_s - \kappa_{kp} u_3,\ \nabla_k u_3 = u_{3,k} + \kappa^s_k u_s.\end{aligned} \tag{1.25}$$

1.3.3 *The Metric of the Orthogonal Coordinate System.*

Let α_1, α_2 is an orthogonal parametrization on S, which means:

$$g_{12} = g_{21} = g^{12} = g^{21} = 0. \tag{1.26}$$

Further

$$\begin{aligned}&g^{kk} = (g_{kk})^{-1},\ \ k = 1,\ 2,\ \ (D)^2 = g_{11}g_{22},\\ &\kappa^j_i = g^{jt}\kappa_{ti},\ \boldsymbol{e}^i = \boldsymbol{e}_i/g_{ii},\ \boldsymbol{e}^3 = \boldsymbol{e}_3 = \boldsymbol{n}.\end{aligned} \tag{1.27}$$

The Christoffel symbols in this case are given by the relations:

$$\begin{gathered}\Gamma_{111} = 0.5g_{11,1}\,,\ \Gamma_{121} = \Gamma_{211} = 0.5g_{11,2}\,,\ \ \Gamma_{221} = -0.5g_{22,1}\,,\\ \Gamma^1_{11} = 0.5g_{11,1}/g_{11},\ \Gamma^1_{12} = \Gamma^1_{21} = 0.5g_{11,2}/g_{11},\\ \Gamma^1_{22} = -0.5g_{22,1}/g_{11},\ \ 1 \leftrightarrow 2.\end{gathered} \tag{1.28}$$

If, in addition, the parametrization refers to the lines of principal curvatures, then

$$\kappa^2_1 = \kappa^1_2 = \kappa_{12} = \kappa_{21} = \kappa = \kappa^{21} = 0. \tag{1.29}$$

More complete information from tensor algebra and tensor analysis can be found in [1].

1.4 A Special Curved Coordinate System in Space

Let the normal $\boldsymbol{n} = \boldsymbol{e}_3$ is constructed on the surface S at some point $P(\alpha_1,\alpha_2)$. We will characterize the position of the point Q on this normal by the coordinate α_3, corresponding to the distance from Q to the surface S. Thus, at least in some neighborhood of the surface S, a parametrization of the space α_1, α_2, α_3 is formed, which is called S-parametrization, and α_k are S-coordinates. The position of an arbitrary point Q in space will be determined by the vector relation:

$$\boldsymbol{r}(\alpha^1, \alpha^2, \alpha^3) = \boldsymbol{\rho}(\alpha^1, \alpha^2) + \alpha^3 \boldsymbol{n}(\alpha^1, \alpha^2). \tag{1.30}$$

The S-parametrization generates a trihedron $\boldsymbol{\gamma}_k = \mathbf{r}_{,k}$ at each point in the space. However, in the theory of shells, it is advisable to use a different trihedron at each point of the trihedral space, obtained by transferring the vectors $\boldsymbol{e}_1$, $\boldsymbol{e}_2$ from the surface along the normal to the point Q. The vector $\boldsymbol{e}_3 = \boldsymbol{n}$ will be used as the third vector of the trihedron. This trihedron will be called the $\boldsymbol{e}$-trihedron.

The components of the metric tensor of the trihedron $\boldsymbol{e}$ will be as follows:

$$\begin{gathered} H_{ij} = g_{ij}, \quad H^{ij} = g^{ij}, \quad i, j = 1, 2, \\ H_{13} = H_{23} = H^{13} = H^{23} = 0, \quad H_{33} = H^{33} = 1. \end{gathered} \tag{1.31}$$

The formulae for differentiating the vectors $\boldsymbol{e}$ of a trihedron are completely defined if we add the relations to (1.22):

$$\boldsymbol{e}_{k,3} = \boldsymbol{e}^k_{,3} = 0. \tag{1.32}$$

The formulae for differentiating an arbitrary vector $\boldsymbol{u}$ in $\boldsymbol{e}$-coordinates get the form:

$$\boldsymbol{u}_{,k} = \nabla_k u^p \boldsymbol{e}_p = \nabla_k u_p \boldsymbol{e}^p; \tag{1.33}$$

$$\begin{gathered} \nabla_k u^p = u^p{}_{,k} + \Gamma^p_{ks} u^s - \kappa^p_k u^3, \ \nabla_k u^3 = u^3{}_{,k} + \kappa_{ks} u^s, \quad p, k, s = 1, 2, \\ \nabla_3 u^t = u^t{}_{,3}, \quad t = 1, 2, 3, \\ \nabla_k u_p = u_p{}_{,k} - \Gamma^s_{kp} u_s - k_{kp} u_3, \ \nabla_k u_3 = u_3{}_{,k} + u_s, \ \nabla_3 u_t = u_t{}_{,3}. \end{gathered} \tag{1.34}$$

2 Deformation Components in S-coordinates

Many scientists were engaged in the derivation of the equations of the theory of shells. I. G. Bubnov, L. Donell, T. Karman, K. Marguerre, H. M. Mushtari, V. Z. Vlasov, I. I. Vorovich and others were engaged in the construction of a quadratic version of the geometrically nonlinear theory of mean bending on the basis of simplifications

accepted in the theory of shells. Basically, this applies to orthogonal coordinate systems.

We are interested in a linear variant for a skew-angle coordinate system. Since the derivation of the strain components in this generalized case takes up a voluminous space, we will give only the final formulae in an expanded form, without going into the construction technique. The output technique can be found, for example, in [2].

It is assumed that the relative elongation of the shell fibers during deformation is small. The shifts (the angles of rotation of the fibers) are also small. Based on the direct normal hypothesis, the displacement and strain tensor components of the shell depend linearly on the normal coordinate:

$$\begin{gathered}\boldsymbol{u}(\alpha_1, \alpha_2, \alpha_3) = \boldsymbol{u}_0(\alpha_1, \alpha_2) + \alpha_3 u_1(\alpha_1, \alpha_2), \alpha_3 = z, \\ \boldsymbol{u} = \boldsymbol{u}_0 + z\boldsymbol{u}_1, \;\; \boldsymbol{u}_0 = \boldsymbol{u}^j \boldsymbol{e}_j, \;\; \boldsymbol{u}_1 = v^j \boldsymbol{e}_j;\end{gathered} \tag{2.1}$$

$$e_{ij} = \overset{o}{e}_{ij} + z \overset{1}{e}_{ij}, \;\; i, \; j = 1, 2, 3. \tag{2.2}$$

Here $\boldsymbol{u}_0$ is the displacement vector of the main surface, and $\boldsymbol{u}_1$ is the rotation vector of the normal. The rotation of the normal in its axis is usually neglected. The vectors define the main basis. Components with upper indices are called contravariant, and components with lower indices are called covariant.

The formulas for the deformation components in the expanded form have the form:

$$\begin{aligned}
&\overset{o}{\gamma}_{11} = \overset{o}{e}_{11} = g_{11}(u^1)_{,1} + g_{12}(u^2)_{,1} + 0.5[(g_{11})_{,1}\, u^1 + (g_{11})_{,2}\, u^2] - k_{11}u^3, \\
&\overset{o}{\gamma}_{22} = \overset{o}{e}_{22} = g_{22}(u^2)_{,2} + g_{12}(u^1)_{,2} + 0.5[(g_{22})_{,2}\, u^2 + (g_{22})_{,1}\, u^1] - k_{22}u^3, \\
&\overset{o}{\gamma}_{12} = 2\overset{o}{e}_{12} = g_{12}(u^1)_{,1} + g_{22}(u^2)_{,1} + g_{11}(u^1)_{,2} + g_{12}(u^2)_{,2} + (g_{12})_{,1}\, u^1 \\
&\quad + (g_{12})_{,2}\, u^2 - 2k_{12}u^3, \\
&\overset{o}{\gamma}_{13} = 2\overset{o}{e}_{13} = g_{11}v^1 + g_{12}v^2 + (u^3)_{,1} + k_{11}u^1 + k_{12}u^2, \\
&\overset{o}{\gamma}_{23} = 2\overset{o}{e}_{23} = g_{12}v^1 + g_{22}v^2 + (u^3)_{,2} + k_{12}u^1 + k_{22}u^2, \\
&\overset{1}{\gamma}_{11} = \overset{1}{e}_{11} = g_{11}(v^1)_{,1} + g_{12}(v^2)_{,1} + 0.5[(g_{11})_{,1}\, v^1 + (g_{11})_{,2}\, v^2], \\
&\overset{1}{\gamma}_{22} = \overset{1}{e}_{22} = g_{22}(v^2)_{,2} + g_{12}(v^1)_{,2} + 0.5[(g_{22})_{,2}\, v^2 + (g_{22})_{,1}\, v^1], \\
&\overset{1}{\gamma}_{12} = 2\overset{1}{e}_{12} = g_{12}(v^1)_{,1} + (v^2)_{,1} + g_{22}(v^1)_{,2}\, g_{11} + g_{12}(v^2)_{,2} + (g_{12})_{,1}\, v^1 + (g_{12})_{,2}\, v^2.
\end{aligned} \tag{2.3}$$

Here g_{ij}, κ_{ij} are the components of the metric tensors. The values $\overset{o}{\underset{13}{\gamma}}$ and $\overset{o}{\underset{23}{\gamma}}$ determine the transverse shear deformation.

Next, we will need variations of the strain components for generalized displacements:

$$
\begin{aligned}
&\delta\overset{o}{\underset{11}{\gamma}} = g_{11}(\delta u^1)_{,1} + g_{12}(\delta u^2)_{,1} + 0.5[(g_{11})_{,1}\,\delta u^1 + (g_{11})_{,2}\,\delta u^2] - k_{11}\delta u^3,\\
&\delta\overset{o}{\underset{22}{\gamma}} = g_{22}(\delta u^2)_{,2} + g_{12}(\delta u^1)_{,2} + 0.5[(g_{22})_{,2}\,\delta u^2 + (g_{22})_{,1}\,\delta u^1] - k_{22}\delta u^3,\\
&\delta\overset{o}{\underset{12}{\gamma}} = g_{12}(\delta u^1)_{,1} + g_{22}(\delta u^2)_{,1} + g_{11}(\delta u^1)_{,2} + g_{12}(\delta u^2)_{,2} + g_{12,1}\delta u^1\\
&\quad + g_{12,2}\delta u^2 - 2k_{12}\delta u^3,\\
&\delta\overset{o}{\underset{13}{\gamma}} = g_{11}\delta u^1 + g_{12}\delta v^2 + (\delta u^3)_{,1} + k_{11}\delta u^1 + k_{12}\delta u^2,\\
&\delta\overset{o}{\underset{23}{\gamma}} = g_{12}\delta v^1 + g_{22}\delta v^2 + (\delta u^3)_{,2} + k_{12}\delta u^1 + k_{22}\delta u^2,\\
&\delta\overset{1}{\underset{11}{\gamma}} = g_{11}(\delta v^1)_{,1} + g_{12}(\delta v^2)_{,1} + 0.5[(g_{11})_{,1}\,\delta v^1 + (g_{11})_{,2}\,\delta v^2],\\
&\delta\overset{1}{\underset{22}{\gamma}} = g_{22}(\delta v^2)_{,2} + g_{12}(\delta v^1)_{,2} + 0.5[(g_{22})_{,2}\,\delta v^2 + (g_{22})_{,1}\,\delta v^1],\\
&\delta\overset{1}{\underset{12}{\gamma}} = g_{12}(\delta v^1)_{,1} + g_{22}(\delta v^2)_{,1} + g_{11}(\delta v^1)_{,2} + g_{12}(\delta v^2)_{,2} + (g_{12})_{,1}\,\delta v^1 + (g_{12})_{,2}\,\delta v^2.
\end{aligned}
\tag{2.4}
$$

3 Equations of Motion in Forces and Moments

To derive the equations of motion, we use the Hamilton-Ostrogradsky principle. Since the transverse shift is taken into account, the material normal has five degrees of freedom. This leads to equations with simpler operators than in the case of the Kirchhoff hypotheses.

Let the shell together with the reinforcements occupy the volume V, which is formed by the integral over the area of the main surface S of the function of the distance between the front surfaces (h_o).

Consider the bilinear representation of the potential energy of the structure as a three-dimensional body. In this case, we do not take into account the normal compression energy in accordance with the Kirchhoff hypothesis $t^{33} \approx 0$:

$$\Pi = 0.5 \iiint\limits_V (\hat{t} \bullet \bullet \hat{e}) dV$$

$$= 0.5 \iiint\limits_V [t^{11}e_{11} + t^{22}e_{22} + 2t^{12}e_{12} + 2t^{13}e_{13} + 2t^{23}e_{23}]dV \tag{3.1}$$

Here the volume element $dV = dSdz$, the area element $dS = Dd\alpha_1 d\alpha_2$,

$$D = (\det \hat{g})^{1/2} = [g_{11}g_{22} - (g_{12})^2]^{1/2}. \tag{3.2}$$

Substituting (2.2) into (3.1), we get:

$$\Pi = \overset{0}{\Pi} + \overset{1}{\Pi}, \tag{3.3}$$

where

$$\overset{0}{\Pi} = 0.5 \iint\limits_S [T^{11} \underset{11}{\overset{o}{\gamma}} + T^{12} \underset{12}{\overset{o}{\gamma}} + T^{22} \underset{22}{\overset{o}{\gamma\gamma}} + T^{13} \underset{13}{\overset{o}{\gamma}} + T^{23} \underset{23}{\overset{o}{\gamma}}]dS, \tag{3.4}$$

$$\overset{1}{\Pi} = 0.5 \iint\limits_S [M^{11} \underset{11}{\overset{o}{\gamma}} + M^{12} \underset{12}{\overset{o}{\gamma}} + M^{22} \underset{22}{\overset{o}{\gamma}}]dS. \tag{3.5}$$

Here we introduce the integral characteristics of the stress state of the structure, that is the contravariant components of the tensors of internal forces and moments:

$$T^{ij} = \int\limits_{(h_o)} t^{ij}dz, \quad M^{ij} = \int\limits_{(h_o)} zt^{ij}dz. \tag{3.6}$$

In the kinetic energy of the structure, taking into account (2.1),

$$K = \iiint\limits_V \rho(\boldsymbol{u}_{,t})^2 dV = \iint\limits_S [\int\limits_{(h_o)} \rho(\boldsymbol{u}_{0,t} + z\boldsymbol{u}_{1,t})^2 dz]dS \tag{3.7}$$

also the integration through the thickness is performed. After deploying the integrand and integrating over z, we get:

$$\begin{aligned}(\boldsymbol{u}_{,t})^2 &= \boldsymbol{u}_{,t} \cdot \boldsymbol{u}_{,t} = (u^k{}_{,t}\, \boldsymbol{e}_k + zv^k{}_{,t}\, \boldsymbol{e}_k) \cdot (u^l{}_{,t}\, \boldsymbol{e}_l + zv^l{}_{,t}\, \boldsymbol{e}_l) \\ &= u^k{}_{,t}\, u^l{}_{,t}\, g_{kl} + z(v^k{}_{,t}\, u^l{}_{,t} + u^k{}_{,t}\, v^l{}_{,t})g_{kl} + z^2 v^k{}_{,t}\, v^l{}_{,t}\, g_{kl}; \end{aligned} \tag{3.8}$$

$$K = 0.5 \iint\limits_S [\rho_1 u^k{}_{,t}\, u^l{}_{,t}\, g_{kl} + \rho_2(v^k{}_{,t}\, u^l{}_{,t} + u^k{}_{,t}\, v^l{}_{,t})g_{kl} + \rho_3 v^k{}_{,t}\, v^l{}_{,t}\, g_{kl}]dS, \tag{3.9}$$

where

$$\rho_1 = \int\limits_{(h_o)} \rho dz, \rho_2 = \int\limits_{(h_o)} \rho z dz, \; \rho_3 = \int\limits_{(h_o)} \rho z^2 dz. \tag{3.10}$$

The coefficients (3.10) characterize the inertial properties of the shell and depend on the mass distribution over the thickness. The coefficient ρ_1 determines the inertia of linear displacements and corresponds to the specific (per unit area of the main surface) mass of the structure, ρ_3 characterizes the inertia of turns; ρ_2 defines the asymmetry of the mass distribution relative to the main surface. It vanishes with a symmetric mass distribution.

In accordance with the Hamilton-Ostrogradsky principle, for the true state of dynamic equilibrium in the absence of loads on the boundary contours, the following variational functional must vanish:

$$\int\limits_{t_0}^{t_1} (-d\Pi + dK + dA)dt = 0. \tag{3.11}$$

Here variation of the potential energy of deformation has the form:

$$\begin{aligned}\delta\Pi = \iint\limits_S (&T^{11}\delta\gamma^o_{11} + T^{22}\delta\gamma^o_{22} + T^{12}\delta\gamma^o_{12} + T^{13}\delta\gamma^o_{13} + T^{23}\delta\gamma^o_{23} \\ &+ M^{11}\delta\gamma^1_{11} + M^{22}\delta\gamma^1_{22} + M^{12}\delta\gamma^1_{12})Dd\alpha_1 d\alpha_2\end{aligned} \tag{3.12}$$

variation of the kinetic energy has the form:

$$\begin{aligned}\delta K = \iint\limits_S &\{\rho_1[u^k_{,t}(du^l)_{,t} + u^l_{,t}(du^k)_{,t}]g_{kl} + \rho_2[v^k_{,t}(du^l)_{,t} + u^l_{,t}(dv^k)_{,t} + u^k_{,t}(dv^l)_{,t} \\ &+ v^l_{,t}(du^k)_{,t}]g_{kl} + +\rho_3[v^k_{,t}(\delta v^l)_{,t} + v^l_{,t}(\delta v^k)_{,t}]g_{kl}\}Dd\alpha_1 d\alpha_2\end{aligned} \tag{3.13}$$

and the elementary work of external forces brought to the main surface of the shell has the form:

$$\delta A = \iint\limits_S \boldsymbol{p}\cdot\delta\boldsymbol{u}_o Dd\alpha_1 d\alpha_2 \tag{3.14}$$

In (3.14), $\boldsymbol{p} = p^k\boldsymbol{e}_k$ is the distributed load vector, $\delta\boldsymbol{u}_o = \delta u^l\boldsymbol{e}_l$, so that $\boldsymbol{p}\cdot\delta\boldsymbol{u}_o = p^k\delta u^l g_{kl}$. After expanding over all indexes, expressions (3.13), (3.14) get the form:

$$\delta K = \iint\limits_S \{\, \rho_1[u^1_{,t}(\delta u^1)_{,t} g_{11} + (u^1_{,t}(\delta u^2)_{,t} + u^2_{,t}(\delta u^1)_{,t}) g_{12}$$
$$+ u^2_{,t}(\delta u^2)_{,t} g_{22} + u^3_{,t}(\delta u^3)_{,t}$$
$$+ \rho_1[u^1_{,t}(\delta u^1)_{,t} g_{11} + (u^1_{,t}(\delta u^2)_{,t} + u^2_{,t}(\delta u^1)_{,t}) g_{12} + u^2_{,t}(\delta u^2)_{,t} g_{22} + u^3_{,t}(\delta u^3)_{,t}$$
$$+ \rho_2[(v^1_{,t}(\delta u^1)_{,t} + u^1_{,t}(\delta v^1)_{,t}) g_{11} + (v^1_{,t}(\delta u^2)_{,t} + u^2_{,t}(\delta v^1)_{,t} + u^1_{,t}(\delta v^2)_{,t}$$
$$+ v^2_{,t}(\delta u^1)_{,t}] g_{12} + +(v^2_{,t}(\delta u^2)_{,t} + u^2_{,t}(\delta v^2)_{,t}) g_{22}] + \rho_3[v^1_{,t}(\delta v^1)_{,t} g_{11} + (v^1_{,t}(\delta v^2)_{,t}$$
$$+ v^2_{,t}(\delta v^1)_{,t}) g_{12} + v^2_{,t}(\delta v^2)_{,t}) g_{22}]\} D d\alpha_1 d\alpha_2; \tag{3.15}$$

$$\delta A = \iint\limits_S [p^1 \delta u^1 g_{11} + (p^1 \delta u^2 + p^2 \delta u^1) g_{12} + p^2 \delta u^2 g_{22} + p^3 \delta u^3] D d\alpha_1 d\alpha_2. \tag{3.16}$$

The relations (2.4) are substituted in (3.12) and, further, together with (3.15), (3.16) are introduced into (3.11). After deployment (3.11), integration operations are performed in parts (transfer of derivatives). In this case, contour integrals related to the boundary conditions appear. Since the variations of the displacement components are independent, the integral (3.11) will vanish, if the coefficients for variations are collected in the integrand and equated to zero. Having done this, we get five equations of motion in forces and moments:

$$(T^{11} g_{11} D)_{,1} - 0.5\, T^{11} (g_{11})_{,1}\, D + (T^{12} g_{12} D)_{,1} + (T^{12} g_{11} D)_{,2} - T^{12} (g_{12})_{,1}\, D$$
$$+ (T^{22} g_{12} D)_{,2} - 0.5 T^{22} (g_{22})_{,1}\, D - T^{13} k_{11} D - T^{23} k_{12} D$$
$$- \rho_1 D[(u^1)_{,tt}\, g_{11} + (u^2)_{,tt}\, g_{12}]$$
$$- \rho_2 D[(v^1)_{,tt}\, g_{11} + (v^2)_{,tt}\, g_{12}] + D(p^1 g_{11} + p^2 g_{12}) = 0,$$
$$(T^{11} g_{12} D)_{,1} - 0.5\, T^{11} (g_{11})_{,2}\, D + (T^{12} g_{22} D)_{,1} + (T^{12} g_{12} D)_{,2} - T^{12} (g_{12})_{,2}\, D$$
$$+ (T^{22} g_{22} D)_{,2} - 0.5 T^{22} (g_{22})_{,2}\, D - T^{13} k_{12} D - T^{23} k_{22} D$$
$$- \rho_1 D[(u^1)_{,tt}\, g_{12} + (u^2)_{,tt}\, g_{22}]$$
$$- \rho_2 D[(u^1)_{,tt}\, g_{12} + (u^2)_{,tt}\, g_{22}] + D(p^1 g_{12} + p^2 g_{22}) = 0; \tag{3.17}$$

$$T^{11} k_{11} D + 2T^{12} k_{12} D + T^{22} k_{22} D + (T^{13} D)_{,1} + (T^{23} D)_{,2} - \rho_1 D (u^3)_{,tt} + p^3 D = 0; \tag{3.18}$$

$$- T^{13} g_{11} D - T^{23} g_{12} D + (M^{11} g_{11} D)_{,1} - 0.5 (g_{11})_{,1}\, M^{11} D + (M^{12} g_{12} D)_{,1}$$
$$+ (M^{12} g_{11} D)_{,2} - M^{12} (g_{12})_{,1}\, D + (M^{22} g_{12} D)_{,2} - 0.5 M^{22} (g_{22})_{,1}\, D$$
$$- \rho_2 D[(u^1)_{,tt}\, g_{11} + (u^2)_{,tt}\, g_{12}] - \rho_3 D[(v^1)_{,tt}\, g_{11} + (v^2)_{,tt}\, g_{12}] = 0; \tag{3.19}$$

$$- T^{13} g_{12} D - T^{23} g_{22} D + (M^{11} g_{12} D)_{,2} - 0.5 M^{11} (g_{12})_{,2}\, D + (M^{12} g_{22} D)_{,1}$$

$$+ (M^{12} g_{12} D)_{,2} - M^{12} (g_{12})_{,2}\, D + (M^{22} g_{22} D)_{,2} - 0.5 M^{22} (g_{22})_{,2}\, D$$
$$- \rho_2 D[(u^1)_{,tt}\, g_{12} + (u^2)_{,tt}\, g_{22}] - \rho_3 D[(v^1)_{,tt}\, g_{12} + (v^2)_{,tt}\, g_{22}] = 0. \quad (3.20)$$

The transition to harmonic oscillations is equivalent to replacing the operator $(\ldots)_{,tt}$ with $-\omega^2(\ldots)$. We will keep the designations of the initial values for the amplitudes. After performing the differentiation and reducing the similar ones, we obtain the corresponding oscillation equations for the amplitudes:

$$g_{11}(T^{11})_{,1} + g_{12}(T^{12})_{,1} + g_{11}(T^{12})_{,2} + g_{12}(T^{22})_{,2} + a_{11}T^{11} + a_{12}T^{12} + a_{22}T^{22}$$
$$- k_{11}T^{13} - k_{12}T^{23} + \omega^2[\rho_1(g_{11}u^1 + g_{12}u^2) + \rho_2(g_{11}v^1 + g_{12}v^2)]$$
$$+ g_{11}p^1 + g_{12}p^2 = 0, \quad (3.21)$$

$$g_{12}(T^{11})_{,1} + g_{22}(T^{12})_{,1} + g_{12}(T^{12})_{,2} + g_{22}(T^{22})_{,2} + b_{11}T^{11} + b_{12}T^{12} + b_{22}T^{22}$$
$$- k_{12}T^{13} - k_{22}T^{23} + \omega^2[\rho_1(g_{12}u^1 + g_{22}u^2) + \rho_2(g_{12}v^1 + g_{22}v^2)]$$
$$+ g_{12}p^1 + g_{22}p^2 = 0, \quad (3.22)$$

$$(T^{13})_{,1} + (T^{23})_{,2} + d_1 T^{13} + d_2 T^{23} + k_{11}T^{11} + 2k_{12}T^{12} + k_{22}T^{22} + \rho_1\omega^2 u^3 + p^3 = 0, \quad (3.23)$$

$$g_{11}(M^{11})_{,1} + g_{12}(M^{12})_{,1} + g_{11}(M^{12})_{,2} + g_{12}(M^{22})_{,2} + a_{11}M^{11} + a_{12}M^{12} + a_{22}M^{22}$$
$$- g_{11}T^{13} - g_{12}T^{23} + \omega^2[\rho_2(g_{11}u^1 + g_{12}u^2) + \rho_3(g_{11}v^1 + g_{12}v^2)] = 0, \quad (3.24)$$

$$g_{12}(M^{11})_{,1} + g_{22}(M^{12})_{,1} + g_{12}(M^{12})_{,2} + g_{22}(M^{22})_{,2} + b_{11}M^{11} + b_{12}M^{12} + b_{22}M^{22}$$
$$- g_{12}T^{13} - g_{22}T^{23} + \omega^2[\rho_2(g_{12}u^1 + g_{22}u^2) + \rho_3(g_{12}v^1 + g_{22}v^2)] = 0, \quad (3.25)$$

where

$$a_{11} = 0.5(g_{11})_{,1} + g_{11}d_1, \quad a_{12} = (g_{11})_{,2} + g_{12}d_1 + g_{11}d_2,$$
$$a_{22} = (g_{12})_{,2} + g_{12}d_2 - 0.5(g_{22})_{,1}; \quad (3.26)$$

$$b_{11} = (g_{12})_{,1} + g_{12}d_1 - 0.5(g_{11})_{,2}, \quad b_{12} = (g_{22})_{,1} + g_{22}d_1 + g_{12}d_2,$$
$$b_{22} = 0.5(g_{22})_{,2} + g_{22}d_2; \quad (3.27)$$

$$d_1 = (D)_{,1}/D; \quad d_2 = (D)_{,2}/D. \quad (3.28)$$

If the shell has boundaries, then after the transfer of derivatives and integration in parts in (3.11), contour integrals are formed. The requirement of their vanishing allows us to formulate boundary conditions. Thus, on the contours corresponding to the fixed α_1, the contour integrals with respect to α_2 must vanish. The edges of the

shell are considered free from active edge loads. Collecting the coefficients for the variations of the displacements, we get:

$$\int_{\alpha_2} \{[-(T^{11}g_{11} + T^{12}g_{12})\delta u^1 + (T^{11}g_{12} + T^{12}g_{22})\delta u^2 + T^{13}\delta u^3 + (M^{11}g_{11} + M^{12}g_{12})\delta v^1 + (M^{11}g_{12} + M^{12}g_{22})\delta v^2]D\}d\alpha_2 = 0. \quad (3.29)$$

If the transverse shifts are neglected ($\varepsilon_{13} \sim \varepsilon_{23} \sim 0$), then the normal remains orthogonal after the deformation. This means that the rotation angles v^1 and v^2 are connected, and they can be expressed in terms of the components of the displacement vector of the main surface $\boldsymbol{u}_0$. In this case, the normal has three degrees of freedom. The corresponding formulae for v^1 and v^2 have the form.

$$v^1 = -g^{11}[(u^3)_{,1} + \kappa_{11}u^1 + \kappa_{12}u^2] - g^{12}[(u^3)_{,2} + \kappa_{12}u^1 + \kappa_{22}u^2]; \quad (3.30)$$

$$v^2 = -g^{12}[(u^3)_{,1} + \kappa_{11}u^1 + \kappa_{12}u^2] - g^{22}[(u^3)_{,2} + \kappa_{12}u^1 + \kappa_{22}u^2]. \quad (3.31)$$

The contravariant and covariant components of the metric tensor are related by the formulae:

$$g^{11} = g_{22}/(D)^2, \quad g^{12} = -g_{12}/(D)^2, \quad g^{22} = g^{11}/(D)^2. \quad (3.32)$$

The relations (3.30), (3.31) correspond to the theory of the Kirchhoff–Love type. They can be used to derive both the equations of motion and the boundary conditions.

In the case of homogeneous conditions on the contour, either the variations of the displacement components or the coefficients for them vanish. More complex cases require special consideration.

To close the system, the kinematic relations and the oscillation equations are supplemented by the elasticity relations. For now, we will limit ourselves to the option for isotropic shells.

4 Elasticity Relations for Isotropic Shells

For the time being, we will limit ourselves to the case of transversally isotropic shells. The generalized Hooke's law in non-orthogonal curvilinear coordinates in the three-dimensional version is written using the metric tensor. When written in component form, the linear relations link the contravariant components of the Cauchy tensor and the covariant components of the strain tensor. For an isotropic shell [1]:

$$t^{sk} = 2\mu\left(\frac{\nu}{1-\nu}H^{sk}H^{mn} + H^{sm}H^{kn}\right)\varepsilon_{mn}. \quad (4.1)$$

By the rule of omitting indexes $t_{sk} = H_{sr} H_{km} t^{rm}$ in the e-trihedron of a special coordinate system, by virtue of (1.31) $t^{33} = t_{33} = t^{(33)} = t_{(33)}$, i.e., the contravariant, covariant, and physical components of the normal stresses coincide. The physical components of the second-rank tensor are introduced by analogy with the physical components of the vector:

$$t_{(sk)} = t_{sk}/\sqrt{H_{ss} H_{kk}}, \quad t^{(sk)} = t^{sk}/\sqrt{H^{ss} H^{kk}}. \tag{4.2}$$

We pass in (4.1) to the metric of a special coordinate system for shells in accordance with (1.31). In the theory of shells, stresses $t_{(33)}$ neglected, considering them equal to zero. Then, in (4.1), the transverse strain component can be expressed from the equation $t^{33} = 0$ as

$$\varepsilon_{33} = \frac{-\nu}{1-\nu}(\varepsilon_{11} g_{12} + 2\varepsilon_{12} g_{12} + \varepsilon_{22} g_{22}). \tag{4.3}$$

We substitute its expression in the other relations for the stresses. Then in the expanded form they get the form:

$$\begin{aligned}
t^{11} &= \frac{E}{1-\nu^2}\{(g^{11})^2 \varepsilon_{11} + [\nu g^{11} g^{22} + (1-\nu)(g^{12})^2]\varepsilon_{22} + 2 g^{11} g^{12} \varepsilon_{12}\},\\
t^{22} &= \frac{E}{1-\nu^2}\{[\nu g^{11} g^{22} + (1-\nu)(g^{12})^2]\varepsilon_{11} + (g^{11})^2 \varepsilon_{11} + 2 g^{11} g^{12} \varepsilon_{12}\},\\
t^{12} &= \frac{E}{1-\nu^2}\{g^{11} g^{12} \varepsilon_{11} + [(1-\nu) g^{11} g^{22} + (1+\nu)(g^{12})^2]\varepsilon_{12} + g^{12} g^{22} \varepsilon_{22}\},\\
t^{13} &= \frac{E}{1+\nu^2}(g^{11}\varepsilon_{13} + g^{12}\varepsilon_{23}), \quad t^{23} = \frac{E}{1+\nu^2}(g^{12}\varepsilon_{13} + g^{22}\varepsilon_{23}).
\end{aligned} \tag{4.4}$$

For transversally isotropic shells, the transverse shear stiffness is set independently. Therefore, the last two relations from (4.4) are modified as

$$t^{13} = \mu_{13}(g^{11}\gamma_{13} + g^{12}\gamma_{23}), \; t^{23} = \mu_{23}(g^{12}\gamma_{13} + g^{22}\gamma_{23}), \tag{4.5}$$

where μ_{13}, μ_{23} are the transverse shear moduli. In the case of complete isotropy, $\mu_{13} = \mu_{23} = E/[2(1+\nu)]$.

In accordance with the hypothesis of direct normal components of strain are linearly dependent on the transverse coordinates $\alpha_3 = z$:

$$\begin{aligned}
\varepsilon_{11} = \overset{0}{\underset{11}{\gamma}} + z \overset{1}{\underset{11}{\gamma}}, \quad 2\varepsilon_{12} = \gamma_{12} = \overset{0}{\underset{12}{\gamma}} + z \overset{1}{\underset{12}{\gamma}}, \quad \varepsilon_{22} = \overset{0}{\underset{22}{\gamma}} + z \overset{1}{\underset{22}{\gamma}},\\
2\varepsilon_{13} = \gamma_{13} = \overset{0}{\underset{13}{\gamma}}, \quad 2\varepsilon_{23} = \gamma_{23} = \overset{0}{\underset{23}{\gamma}}.
\end{aligned} \tag{4.6}$$

The specific (per unit area of the S–surface) potential energy of deformation of the shell is written as

$$\Pi_o = 0.5 \int_{-h/2}^{h/2} (t^{11}\gamma_{11} + t^{12}\gamma_{12} + t^{22}\gamma_{22} + t^{13}\gamma_{13} + t^{23}\gamma_{23})dz. \tag{4.7}$$

After substituting (4.4)–(4.6) into (4.7) and integrating over the thickness of the shell, Π_0 gets the form of a square shape from the deformation components of the median surface. The derivatives of Π_0 with respect to the strain components give the relations of elasticity in forces and moments:

$$\begin{gathered}
T^{11} = B^{11}_{(0)} \overset{0}{\underset{11}{\gamma}} + B^{12}_{(0)} \overset{0}{\underset{12}{\gamma}} + B^{13}_{(0)} \overset{0}{\underset{22}{\gamma}}, \quad T^{12} = B^{12}_{(0)} \overset{0}{\underset{11}{\gamma}} + B^{22}_{(0)} \overset{0}{\underset{12}{\gamma}} + B^{23}_{(0)} \overset{0}{\underset{22}{\gamma}}, \\
T^{22} = B^{13}_{(0)} \overset{0}{\underset{11}{\gamma}} + B^{23}_{(0)} \overset{0}{\underset{12}{\gamma}} + B^{33}_{(0)} \overset{0}{\underset{22}{\gamma}}, \\
T^{13} = G^{11}_{(0)} \overset{0}{\underset{13}{\gamma}} + G^{12}_{(0)} \overset{0}{\underset{23}{\gamma}}, \quad T^{23} = G^{12}_{(0)} \overset{0}{\underset{13}{\gamma}} + G^{23}_{(0)} \overset{0}{\underset{23}{\gamma}}, \\
M^{11} = D^{11}_{(0)} \overset{1}{\underset{11}{\gamma}} + D^{12}_{(0)} \overset{1}{\underset{12}{\gamma}} + D^{13}_{(0)} \overset{1}{\underset{22}{\gamma}}, \\
M^{13} = D^{13}_{(0)} \overset{1}{\underset{11}{\gamma}} + D^{23}_{(0)} \overset{1}{\underset{12}{\gamma}} + D^{33}_{(0)} \overset{1}{\underset{22}{\gamma}}.
\end{gathered} \tag{4.8}$$

The zero in parentheses at the bottom means that the stiffness in (4.8) corresponds to a smooth shell. In the future, the relations will be generalized to the constructively anisotropic version. The stiffness coefficients of the isotropic shell are determined by the formulae:

$$\begin{gathered}
B^{ij}_{(0)} = Bc^{ij}_{(0)}, \quad D^{ij}_{(0)} = Dc^{ij}_{(0)}, \quad i, j = 1, 2, 3, \\
B = Eh/(1-\nu^2), \quad D = Eh^3/[12(1-\nu^2)], \\
c^{11}_{(0)} = (g^{11})^2, \quad c^{12}_{(0)} = g^{11}g^{12}, \quad c^{13}_{(0)} = \nu g^{11}g^{22} + (1-\nu)(g^{12})^2, \\
c^{22}_{(0)} = [(1-\nu)g^{11}g^{22} + (1+\nu)(g^{12})^2]/2, \quad c^{23}_{(0)} = g^{12}g^{22}, \quad c^{33}_{(0)} = (g^{22})^2, \\
G^{11}_{(0)} = \mu_{13}hg^{11}, \quad G^{12}_{(0)} = (\mu_{13} + \mu_{23})hg^{12}/2, \quad G^{22}_{(0)} = \mu_{23}hg^{22}.
\end{gathered} \tag{4.9}$$

The detailed (component) form of the presented equations is necessary for further application of numerical methods.

Acknowledgements The research was financially supported by Southern Federal University, grant No. VnGr-07/2020-04-IM (Ministry of Science and Higher Education of the Russian Federation).

References

1. A.I. Lurie, *Theory of Elasticity* (Moscow, Nauka, 1970) p. 94 (In Russian)
2. V.V. Novozhilov, K.F. Chernykh, E.I. Mikhailovsky, *Linear Theory of Shells.* Leningrad Politechnika (1991) p. 656 (In Russian)

Contact Interaction Between Parabolic Punch and Elastic Strip Bonded to Poroelastic Half-Plane

M. I. Chebakov and E. M. Kolosova

Abstract Plane contact problem of interaction between rigid punch and elastic strip bonded to poroelastic half-plane is considered. Half-plane deformation is modeled on the base of Cowin-Nunziato poroelastic bodies equations. It is assumed that punch's base is in the form of parabola, friction in the contact area is neglected. Using integral Fourier's transformation, the problem is reduced to singular integral equation on unknown contact stress. The collocation method is utilized to solve equation. The values of contact stresses, the values of the contact area, and the relative deformation of the surface outside the punch were obtained. A comparative analysis of the investigated quantities for various values of the parameters of the elastic layer and the poroelastic foundation is carried out. Numerical results are present in the form of plots.

Keywords Contact problem · Poroelastic materials · Cowin-Nunziato model · Flat problem · Parabolic punch · Strip · Collocation · Indentation problem

1 Introduction

Poroelastic materials have unique physical, mechanical, acoustic, electrical and thermal properties. This type of materials has found wide application in various fields of human activity. Due to the optimal balance of weight and strength, it is widely used in the space industry. Aluminum foam is of particular interest among poroelastic materials.

Control and assessment of mechanical properties in the process of designing such materials are great interest. There are some approaches.

One of the approaches to model porous materials was developed by Cowin and Nunziato [1]. This theory, called microdilation theory, was utilized to study porous bodies with empty pores. It uses linear elasticity theory with an additional kinematic

M. I. Chebakov (✉) · E. M. Kolosova
I. I. Vorovich Mathematics, Mechanics and Computer Sciences Institute, Southern Federal University, Rostov-on-Don, Russia
e-mail: michebakov@yandex.ru

I. A. Parinov et al. (eds.), *Physics and Mechanics of New Materials and Their Applications*, Springer Proceedings in Materials 10,
https://doi.org/10.1007/978-3-030-76481-4_27

variable that describes the properties of porosity change. Therefore, deformation and porosity are related fields that have a common response to external loads applied to the body.

The linear theory was described in [2]. A number of studies have been carried out in recent years. In [3, 4], contact problems were solved within the framework of a flat formulation for a half-plane and a strip, respectively. In [5–8], axisymmetric contact problems for a poroelastic half-space, a poroelastic layer, and an elastic layer fixed on a poroelastic half-space are regarded. In [9], an axisymmetric problem for an arbitrary system of loads is presented. An analytical solution is obtained using an integral transformation.

Despite many researches carried out within the framework of the microdilation theory, it is still considered that this theory was not studied enough from a physical point of view. Thus, in [10], an attempt was made to analyze the ranges of material parameters, which the considered theory operates with.

Article [11] is devoted to the question of eigenvalues of piezoelectric bodies with empty pores, covered with a system of electrodes, in contact with massive rigid flat punches. A significant contribution to the development of the Cowin-Nunziato theory was made in [12, 13], where static and dynamic problems for two-dimensional and three-dimensional domains were considered using the finite element method. Within this study custom finite element types have been developed for the Cowin-Nunziato theory.

2 Problem Formulation

Let us consider plane problem of interaction between rigid punch and elastic strip $0 \le y \le h$, bonded to poroelastic half-plane $y < 0$ in Cartesian $(x,\ y)$. Deformation is described by Cowin–Nunziato equations [2–4]. The base of the punch is assumed to be parabolic. It is worth mentioning that in [3, 4] contact problems were reviewed for a poroelastic half-plane and a poroelastic strip.

The deformation of a half-plane consisting of a homogeneous isotropic material with empty pores, according to the Cowin-Nunziato theory, is described for $k = 2$ by the following system of partial differential equations [2–4]:

$$\begin{gathered}
\mu_k \Delta u_k + (\lambda_k + \mu_k)\left(\frac{\partial^2 u_k}{\partial x^2} + \frac{\partial^2 w_k}{\partial x \partial y}\right) + \beta \frac{\partial \Phi}{\partial x} = 0 \\
\mu_k \Delta w + (\lambda_k + \mu_k)\left(\frac{\partial^2 u_k}{\partial x \partial y} + \frac{\partial^2 w_k}{\partial y^2}\right) + \beta \frac{\partial \Phi}{\partial y} = 0 \\
\alpha \Delta \Phi - \xi \Phi - \beta\left(\frac{\partial u_k}{\partial x} + \frac{\partial w_k}{\partial y}\right) = 0
\end{gathered} \tag{1}$$

where, μ_k and λ_k are Lame's parameters, α is the voids diffusion parameter, β is the parameter of the relationship between microdilation and macrodilation properties, ξ is the "void stiffness" modulus. The function $\Phi(x, y)$ describes pore volume changing, u_k and w_k are the displacements along x- and y-axis, respectively. In the case, when $k=2$ and $\beta = 0$, first two equations from (1) describe pure elastic deformation of half-plane $y < 0$.

The deformation of the elastic strip $0 \le y \le h$ is described by the first two equations of (1) for $k=1$ and $\beta = 0$.

The stress tensor components in the poroelastic half-plane are determined from the following relations for $k=2$:

$$\sigma_x^k = \frac{\mu_k}{c_k^2}\left[\frac{\partial u_k}{\partial x} + \left(1 - 2c_k^2\right)\frac{\partial w_k}{\partial y} + H\Phi\right]$$

$$\sigma_y^k = \frac{\mu_k}{c_k^2}\left[\left(1 - 2c_k^2\right)\frac{\partial u_k}{\partial x} + \frac{\partial w_k}{\partial y} + H\Phi\right], \tau_{xy}^k = \mu_k\left(\frac{\partial u_k}{\partial y} + \frac{\partial w_k}{\partial x}\right) \quad (2)$$

Here the following notation is used [3, 4]:

$$c_k^2 = \frac{\mu_k}{\lambda_k + 2\mu_k} = \frac{1 - 2\nu_k}{2(1 - \nu_k)}; H = \frac{\beta}{\lambda_2 + 2\mu_2}$$

where ν_k $(k = 1, 2)$ is the Poisson's ratio for the strip $0 \le y \le h$ and half-plane $y < 0$, respectively.

Relations (2) determine stresses in the elastic strip $0 \le y \le h$ if $k=1$ and $H = 0$ $(\beta = 0)$.

Boundary conditions can be written in the following form

$$\tau_{xy}^1 = 0,\ \frac{\partial \Phi}{\partial y} = 0\ (y = h),\ \sigma_y^1 = q(x)(y = h,\ |x| \le a)\ \sigma_y^1 = 0\ (y = h,\ |x| > a)$$

$$\tau_{xy}^1 = \tau_{xy}^2,\ \sigma_y^1 = \sigma_y^2,\ w_1 = w_2,\ u_1 = u_2,\ \frac{\partial \Phi}{\partial y} = 0\ (y = 0) \quad (3)$$

where $q(x)$ are the unknown contact stresses, to define which integral equations (9), (10) will be constructed, $|x| \le a$ are the unknown contact area, that can be set up from the condition: $q(a) = 0$,

$$\int_{-a}^{a} q(x)dx = P \quad (4)$$

where P is the force, applied to the punch. So, punch moves progressively in negative direction of the y-axis.

In the direction $y \to -\infty$, stresses and displacements in the half-plane fade.

3 Integral Equation Construction

Using Fourier's transform representation of the unknown functions in the system (1), respectively, for the elastic strip ($k = 1, \Phi = 0$) and poroelastic half-plane ($k = 2$), we can obtain displacements of the boundary $y = h$ according to the relation:

$$w(t) = l_2^{-1} w_1(t l_2) = \frac{1}{\pi} \int_{-b}^{b} p(\tau)\, k(t-\tau)\, d\tau, \;\; k(y) = \int_0^{\infty} L(u) \cos uy du \qquad (5)$$

where $w(t)$ is the dimensionless displacement of the boundary $y = h$ under the action of a given force. $b = a/l_2$ is the dimensionless value, $p(\tau) = \frac{1-\nu_1}{\mu_1} q(\tau\, l_2)$ is the dimensionless reduced contact stress at the boundary $y = h$;

$$L(u) = \frac{L_{10} + L_{11}\mu + L_{12}\mu^2}{L_{20} + L_{21}\mu + L_{22}\mu^2} \qquad (6)$$

$$L_{10} = 2\left(1 - c_1^2\right)\,(sh(2ud) + 2ud)\left(c_2^2 m_2 - m_1\right),$$
$$L_{11} = -4m_1 ch(2ud) + c_1^2 c_2^2 m_2 sh(2ud)$$

$$L_{12} = -\left[\left(1 + c_1^2\right)sh(2ud) + 2du\left(c_1^2 - 1\right)\right]\left(c_2^2 m_2 + m_1\right)$$

$$L_{20} = 4u\left(1 - c_1^2\right)^2\left(ch(2ud) - 2u^2 d^2 - 1\right)\left(c_2^2 m_2 - m_1\right)$$

$$L_{21} = 8u\left(1 - c_1^2\right)\left[c_1^2 c_2^2 m_2 ch(2ud) - m_1 sh(2ud) - c_2^2 m_2\left(2u^2 d^2\left(c_1^2 - 1\right) + c_1^2\right)\right]$$

$$L_{22} = 4u\left(c_2^2 m_2 + m_1\right)\left[\left(c_1^4 - 1\right)ch(2ud) - 2u^2 d^2\left(1 - c_1^2\right)^2 - c_1^4 - 1\right]$$

$$h = d\, l_2, \;\; \tau = \frac{u}{l_2}, \;\; T = \sqrt{u^2 - N + 1},$$
$$m_1 = T(T + u)(1 - N), \;\; m_2 = 2Nu^2 - T - T^2$$

We used the following notation [3, 4]: $N = \frac{l_2^2}{l_1^2} H = \frac{\beta^2}{\xi(\lambda_2 + 2\mu_2)}$ is the dimensionless value, that characterizes porosity of the half-plane, $l_1^2 = \frac{\alpha}{\beta}$, $l_1^2 = \frac{\alpha}{\beta}$, ($l_1$, l_2 are measured in meters). In [3], it was shown, that $0 \le N < 1 - c_2^2$. Note that, with increasing N, half-plane material porosity grows.

Furthermore, it can be shown that $\lim uL(u) = 1$ $(u \to \infty)$.

Subsequently $p(t)$, $|t| \le b$, $w(t)$ will be named respectively contact stresses, contact area and displacement.

Let us consider parabolic rigid punch's impact frictionless into the strip $y = h$, then displacement of the surface ($y = h$) in the unknown contact area $|x| \le a$ will be $w_1(x) = -(\delta - x^2/(2R))$ (where R is the parabola curvature radius at the top).

By assuming that under the punch contact stresses are unknown, utilizing relations (5) we obtain integral equation with a logarithmic kernel:

$$\int_{-b}^{b} p(\tau)\, k(t-\tau)\, d\tau = -\pi(\delta^* - t^2/(2R^*)) \quad (|t| \le b) \tag{7}$$

where $\delta^* = \delta/l_2,\ R^* = R/l_2$.

Let

$$M(u) = L(u) - 1/u \tag{8}$$

In this case to solve integral equation a numerical scheme, proposed in [3], will be used. For this purpose in the result of differentiating, we obtain integral equation with singular kernel:

$$\int_{-b}^{b} p(\tau) K(t-\tau) d\tau = \pi\ t/R^* \quad (|t| \le b) \tag{9}$$

$$K(y) = \frac{1}{y} + \int_0^{\infty} uM(u) \sin uy du \tag{10}$$

Integral in (10) converges, taking into account that $\lim uM(u) = 0\ (u \to \infty)$, $\lim uM(u) = const\ (u \to 0)$.

It is known [14] that any unbalanced load, applied to boundary level $y = h$ leads to infinite logarithmic increase in displacements. However, we can calculate the relative displacement of the surface $y = h$, to realize this, we study the following value:

$$w^*(t) = \pi[w(t) - w(0)] = \int_{-b}^{b} p(\tau)\, k^*(t,\tau)\, d\tau \tag{11}$$

$$k^*(t,\tau) = 2\int_0^{\infty} L(u) \sin\frac{u\,(t-2\tau)}{2} \sin\frac{ut}{2} du \tag{12}$$

Integral (12) converges taking into account the behavior of the function $L(u)$ at zero and at infinity.

4 Solution of Integral Equation

To solve integral equation (9), we utilize collocation method [3, 4, 15]. Let us divide segment [–b, b] into n segments $l_j = [-b + \varepsilon(j-1),\ -b + \varepsilon\, j]$, $(j = 1, .., n)$, $\varepsilon = 2b/n$ and designate a set of points $\tau_j = -b + \varepsilon(j - 1/2)$ $(j = 1, 2, ..., n)$, $t_i = -b + \varepsilon\, i$ $(i = 1, 2, ..., n-1)$.

Then integral equation can be reduced to the solution of equation set [3, 4, 15]:

$$\varepsilon \sum_{j=1}^{n} a_{ij} p_j = t_i / R^* \ (i = 1..n-1) \quad (a_{ij} = K(t_i - \tau_j)) \tag{13}$$

$$\varepsilon \sum_{j=1}^{n} p_j = \tilde{P} \left(\tilde{P} = \int_{-b}^{b} p(\tau) d\tau \right), \tag{14}$$

where $p_j = p(\tau_j)$, $\tilde{P}$ is the reduced force, applied to the punch (in what follows we omit the word «reduced»).

Another scheme of reducing the integral equation to the system is possible:

$$\sum_{j=1}^{n} a_{ij} p_j = t_i / R^* \ (i = 1..n) \tag{15}$$

Then the value of the force $\tilde{P}$ applied to the punch will give the first relation from (14). The proposed schemes for solving the integral equation differ in that in the first case, the force $\tilde{P}$ is set, the system is solved with respect to the contact stresses p_j at the collocation points, and the contact area b is defined from the condition that the stress on the boundary of the contact area is zero. In the second case, the contact area b is specified, and after solving the system with respect to the contact stresses p_j, the force $\tilde{P}$ is defined at the collocation points.

Further calculations showed that both schemes give the same result. Namely, if the value $\tilde{P}$, found in the second scheme, is taken as an initial parameter in the first scheme, then we will get the same values of the contact area b and contact stresses p_j as in the second scheme.

It is easy to show that

$$\begin{aligned} a_{ij} &= a_{1,j-i+1} \ (2 \le i \le n-1,\ i \le j \le n), \\ a_{ij} &= a_{1,i-j+2} \ (2 \le i \le n-1,\ 1 \le j \le i-1) \end{aligned} \tag{16}$$

Relations (16) can significantly reduce the calculations. It is enough to calculate the elements of the first row of the matrices of systems (13) and (15) only, and the remaining elements are expressed in terms of them.

The found values of the contact stresses p_j can be used to calculate the relative deformation of the line at level $y = h$. Utilizing (11), we find

$$w^*(t) = \varepsilon \sum_{i=1}^{n} p_i \, k^*(t, \tau_i) \tag{17}$$

5 Numerical Calculations

On the basis of the scheme for solving the integral equation suggested above, we calculated the contact stresses under the punch and the relative deformation of the surface $y = h$. In the calculations, the main attention was paid to the influence of the parameters N, μ and the thickness of the elastic layer $d = h/l_2$ on the investigated values.

To control the accuracy of the proposed scheme for solving the problem, consider a particular case, when $N = 0$, $b = 1$, $R^* = 2$, $\mu = 1$. In this case, we have the problem of the interaction between punch and elastic half-plane $y \le h$, which has an exact solution [16]. Thereby, the exact formula from [16] for the contact stresses $p(t)$ and the force $\tilde{P}$ take the form:

$$p(t) = \frac{1}{R^*}\sqrt{b^2 - t^2}, \quad \tilde{P} = \frac{\pi b^2}{2R^*}, \tag{18}$$

For such a problem, the contact stresses were calculated using the scheme (15) and formulas (18). The results are shown in Table 1, which shows the calculations according to the scheme (15) for $n = 100$ (second row), $n = 100$ (third row) and by formulas (18) (fourth row). The first line of the table contains the coordinates of the points under the punch. The last column of the table gives the values of the force $\tilde{P}$.

As can be seen from Table 1, for $n = 500$, the results practically coincide with the exact solution in the inner region of the contact; the largest error is observed in the vicinity of the edge of the punch.

For the problem, formulated above, plots show the calculation results of contact stresses and relative deformation at the surface $y = h$ for some values of the parameters N, μ, d.

Table 1 Calculation results

t	0.01	0.21	0.41	0.61	0.81	0.95	0.99	$\tilde{P}$
$n = 100$	0.502	0.491	0.459	0.399	0.299	0.164	0.0885	0.793
$n = 500$	0.500	0.489	0.457	0.397	0.294	0.158	0.0741	0.787
(18)	0.500	0.489	0.456	0.396	0.293	0.156	0.0705	0.785

Figures 1a, 2a, 3a, 4a present contact stresses $p(t)$ for some values of the parameters N, μ, d. Figs 1b, 2b, 3b, 4b show plots of the relative deformation shape $w^*(t)$ at $y = h$, respectively, for the same values of the parameters N, μ, d. In the calculations, it was assumed: $\tilde{P} = 1$, $R^* = 2$, $\nu_1 = \nu_2 = 0.3$.

In Fig. 1, the plots are presented for values $d = 0.1$, $N = 0.5$ and three values of μ. Note that if μ equals 2, 1 and 0.5, then the contact area b equals 0.871, 1.173 and 1.645, respectively. In Fig. 2, the plots are presented for $\mu = 0.5$, $N = 0.5$ and three values of d. Note that if d equals 0.1, 0.25 and 0.5, then the contact area equals

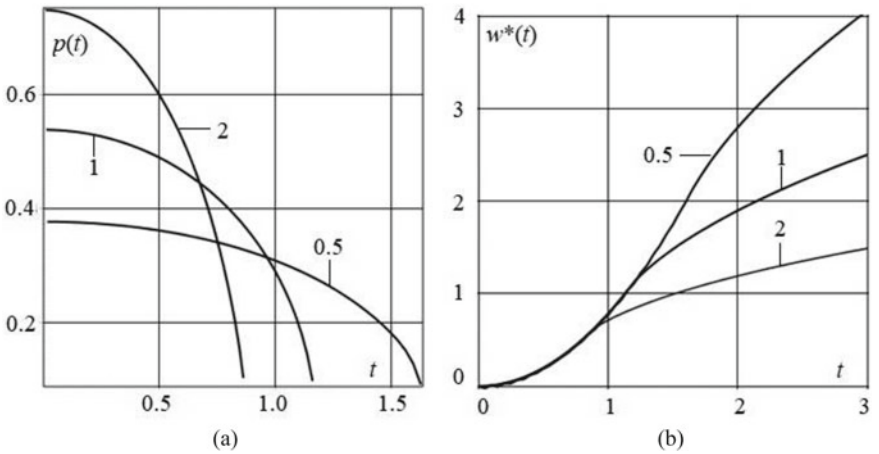

Fig. 1 **a** Contact stresses; **b** relative deformation at surface $y = h$ for $d = 0.1$, $N = 0.5$ and $\mu = 2$, 1 and 0.5 ($b = 0.871$, 1.173 and 1.645, respectively)

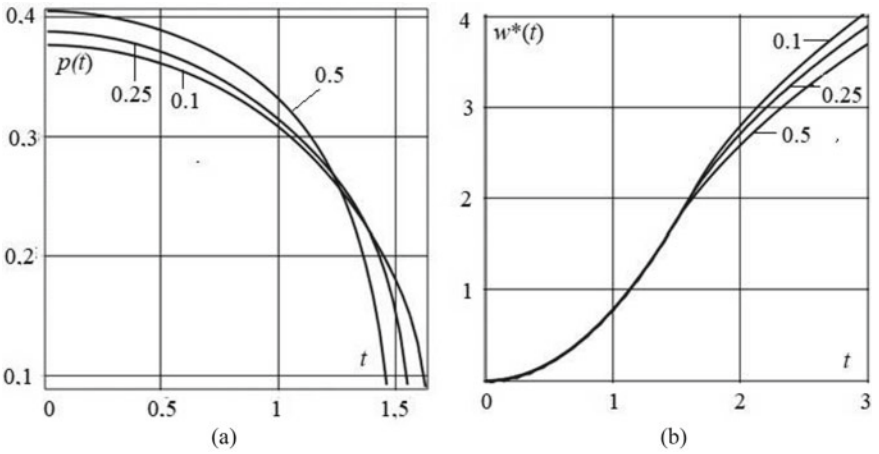

Fig. 2 **a** Contact stresses; **b** relative deformation at surface $y = h$ for $\mu = 0.5$, $N = 0.5$ and $d = 0.1$, 0.25 and 0.5 ($b = 1.645$, 1.568 and 1.478, respectively)

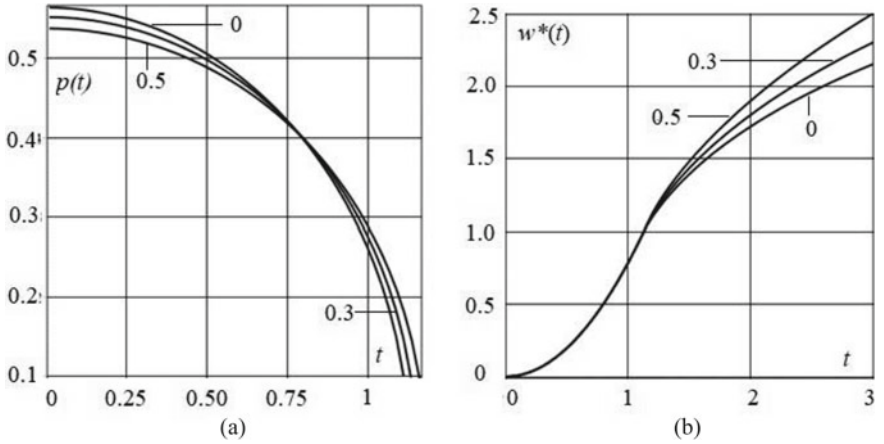

Fig. 3 **a** Contact stresses; **b** relative deformation at surface $y = h$ for $\mu = 1$, $d = 0.1$ and $N = 0$, 0.3 and 0.5 ($b = 1.123$, 1.146 and 1.173, respectively)

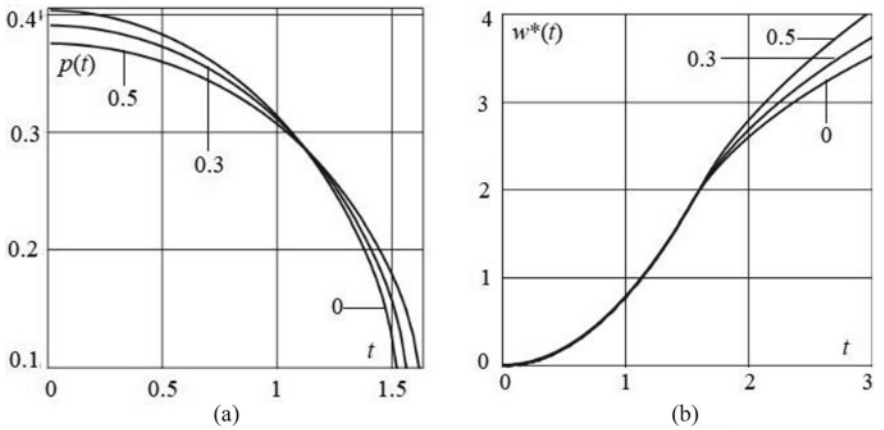

Fig. 4 **a** Contact stresses; **b** relative deformation at surface $y = h$ for $\mu = 0.5$, $d = 0.1$ and $N = 0$, 0.3 and 0.5 ($b = 1.539$, 1.583 and 1.641, respectively)

1.645, 1.568 and 1.478, respectively. In Fig. 3, the plots are presented for $\mu = 0.5$, $d = 0.1$ and three values of N. Note that if N equals 0, 0.3 and 0.5, then the contact area b equals 1.123, 1.146 and 1.173, respectively. In Fig. 4, the plots are presented for $\mu = 1$, $d = 0.1$ and three values of N. Note that if N equals 0, 0.3 и 0.5, the contact area b equals 1.539, 1.583 and 1.641. The parameters μ, d, N are also presented in Figs. 1, 2, 3, 4.

6 Conclusions

The calculation results, including those given in Table 1, show that with a constant value of the force $\tilde{P}$, acting on the punch and constant values of other parameters, the contact stresses $p(t)$ under the punch decrease with decreasing μ, the contact area b increases, and the surface deformation $w^*(t)$ at line $y = h$ also increases. The same picture is observed with a decrease in the parameter N and fixed values of other parameters.

With an increase in the relative thickness d of the elastic layer and fixed values of other parameters, contact stresses increase, the contact zone and surface deformation decrease.

Acknowledgements Research was financially supported by Southern Federal University, grant No. VnGr-07/2020-07-IM (Ministry of Science and Higher Education of the Russian Federation).

References

1. G.W. Nunziato, S.C. Cowin, Arch. Ration. Mech. Anal. **72**, 175 (1979)
2. S.C. Cowin, G.W. Nunziato, J. Elast. **13**, 125 (1983)
3. A. Scalia, M.A. Sumbatyan, J. Elast. **60**, 91 (2000)
4. A. Scalia, Int. J. Eng. Sci. **40**, 401 (2002)
5. M.I. Chebakov, A.A. Poddubny, E.M. Kolosova, A.R. Alexiev, R.Z. Iankov, Comptes rendus de l'Acad emie bulgare des Sciences (Доклади на Болгарската академия науките). **73**(6), 846 (2020)
6. E.M. Kolosova, M.I. Chebakov, Mech. Solids **55**(6), 857 (2020)
7. M.I. Chebakov, E.M. Kolosova, Mech. Compos. Mater. **56**(6), 769 (2020)
8. M.I. Chebakov, A.A. Poddubny, E.M. Kolosova, A. Alexiev, M. Datcheva, Mater. Phys. Mech. **44**(3), 423 (2020)
9. D. Iesan, L. Nappa, Int. J. Solids Struct. **40**, 5271 (2003)
10. H. Ramézani, H. Steeb, J. Jeong, European J Mech. A/Solids. **34**, 130 (2012)
11. G. Iovane, A.V. Nasedkin, Appl. Math. Model. **34**, 60 (2010)
12. G. Iovane, A.V. Nasedkin, Comput. Struct. **87**, 981 (2009)
13. G. Iovane, A.V. Nasedkin, Comput. Struct. **84**, 19 (2005)
14. N.I. Muskhelishvili, *Some Basic Problems of the Mathematical Theory of Elasticity* (Noordhoff, Groningen, Holland, 1953) p. 704
15. S.M. Belotserkovsky, I.K. Lifanov, *Numerical Methods in Singular Integral Equations and Their Applications to Aerodynamics, Theory of Elasticity and Electrodynamics* (Nauka, Moscow, 1985) (In Russian)
16. V.M. Alexandrov, M.I. Chebakov, *Introduction in Mechanics of Contact Interactions* (OOO "TsVVR", Rostov-on-Don, 2007) p. 114 (In Russian)

Application of Generative Neural Networks and Nondestructive Testing in Defect Detection Problem

Pavel Vasiliev and Alexander Senichev

Abstract The development of machine learning methods has given a new impetus in the field of solving inverse mechanics problems. Many papers show the successful application of well-proven techniques of ultrasonic, magnetic, thermal non-destructive testing with the latest methods based on machine learning and neural networks, in particular. This paper demonstrates the potential of applying the machine learning methods to the task of two-dimensional ultrasonic imaging. We have built a model of acoustic ultrasonic non-destructive testing that simulates the sounding of the inspecting object and the propagation of an ultrasonic wave in it. In the course of the set of numerical experiments we have created a data set for training of convolutional neural networks. The presented results show a high degree of informativeness of the ultrasonic response and its agreements to the real form of the internal defect inside the inspection object.

Keywords Convolutional neural networks · Ultrasonic · Nondestructive testing · FDTD · Defect

1 Introduction

In this paper the authors investigate the possibilities of applying neural network technologies in solving inverse problems of mechanics, in particular in the problem of two-dimensional visualization of internal defects. These methods are widely used in medicine, civil engineering, nondestructive testing, and other fields.

In the work [1] the authors developed a system to detect cracks in steel structures and estimate their depth based on 2D images. The goal of the work is to develop an affordable and user-friendly inspection system to replace expensive measuring devices. The authors proposed a learning strategy, and several neural network structures. During neural network training, the average intensity profiles of two-dimensional steel cracks were input into the neural network along with the

P. Vasiliev (✉) · A. Senichev
Department of Information Technologies, Don State Technical University, Rostov-on-Don, Russia
e-mail: lyftzeigen@mail.ru

I. A. Parinov et al. (eds.), *Physics and Mechanics of New Materials and Their Applications*, Springer Proceedings in Materials 10,
https://doi.org/10.1007/978-3-030-76481-4_28

maximum depth of steel cracks measured with a laser microscope. The average error of the neural network is 18% on the test sample, which is better compared to the previous works of the authors. The quality of defect depth detection is improved by applying a new training strategy and crack depth estimation tool.

The authors proposed the deep learning methods for detecting defects in nondestructive inspection images; it was illustrated in their work [2]. Such approaches require marked-up image data with defects. The authors propose a deep transfer learning model for extracting signs of internal defects in X-ray images of aviation composites. The authors investigated a method for automatically detecting inclusion defects in X-ray images using the proposed model. Experimental results show that the model can achieve a classification accuracy of 96% (by F1 metric) with satisfactory detection results.

A method to reconstruct and visualize internal defects as 3D images using economical and fast pulse thermography technology is proposed in the work [3]. A new method for rapid assessment of defect depth and thickness simultaneously based on a single one-sided inspection is presented. The feasibility and effectiveness of the proposed solution is demonstrated by inspecting a composite specimen and a steel specimen with semi-closed air gaps. For the composite sample, this method can provide a relatively low, in the range of 10%, average relative error of the estimated total 3D defect volume.

The main causes of solid rocket motor failures are discussed in the work [4]. Flaking at the propellant/shell/insulation interface is critical to engine integrity. Current solutions are usually limited to methods for assessing the structural integrity of rocket engines and visual inspection of their components. This paper presents an improved algorithm for detecting sleeve surface defects that can disrupt the solid rocket fuel/insulation bond. The use of local binary patterns (LBPs) provides a structural and statistical approach to analyzing the texture of engine image samples. The neural network analyzes the engine image samples and classifies each pixel into one of three classes: serviceable, foreign object, and defect. Several tests with varying different parameters were performed to find the optimal neural network configuration, and the result was the best classification accuracy of 99.08%, 90.66% and 99.48% for the respective classes.

In the work [5], the authors provide a brief overview of artificial intelligence algorithms applicable to nondestructive testing. It is focused on two methods: artificial neural networks and fuzzy logic. Selected examples of application of these methods in digital radiography and vortex-current method are given.

The authors in their work [6] explores the potential of deep learning methods for electromagnetic inversion This approach does not require a gradient calculation and produces results immediately after training the network. Deep neural networks based on a fully convolutional architecture are trained on large sets of synthetic data obtained with full three-dimensional simulations. The effectiveness of the method is demonstrated on models of great practical importance, representing the scenario of monitoring the electromagnetic field of carbon dioxide accumulation underground with a controlled source at the surface.

Previously, the authors have investigated some problems that combine modern methods of deep machine learning and well-proven classical approaches to defect identification [7–9].

1.1 Research Purpose

In this paper, a neural network model is considered as a pilot study, based on which two-dimensional acoustic imaging of internal defects is carried out. We have built a trial model of nondestructive ultrasonic inspection, on the basis of which a set of numerical experiments is carried out. The results of these experiments serve as a basis for training the neural network and its validation.

2 Research Method

We propose a method of identification and visualization of internal defects based on ultrasonic nondestructive testing and generative neural network model. The input of the convolutional neural network is an ultrasonic signal obtained at the internal points of the control object. The output generates an image that visualizes the internal defect. To demonstrate the possibilities and prospects of development of this method, the inner part of a steel plate is chosen as an object of study. Inside the plate there may be a defect marked by a lack of material. The shape, size and orientation of the defect may vary. The approach is to conduct a series of numerical experiments from which it is possible to train a deep neural network model. By varying the geometric parameters of the defect and modeling the acoustic ultrasonic wave propagation, a training set is created for each case. Based on the collected data, it is possible to build the optimal structure of the neural network model and to train it.

2.1 Finite Difference Method in the Time Domain

This method was proposed by Kane Yee [10], and it belongs to the class of mesh methods for solution of differential equations. At present, this method has found wide application in a number of problems of modeling environments with both dispersive and nonlinear properties, from geophysics to optical range problems. The finite-difference time-domain method in the acoustic formulation is used to perform simulations of sound propagation in fluid media, such as air or liquids. However, in some cases this method can also be applied to elastic media to simplify the solution of problems. In this method, the velocity and acoustic pressure of the particles of the simulated object are placed one after the other in the mesh nodes. Their values are

then calculated sequentially, allowing the sound field propagation to be calculated over time.

The mathematical model of flexural steady vibrations of a bimorph circular plate can be reduced to the boundary problem of electro-elasticity, which consists of a system of differential equations [11, 12].

The basic equations of this acoustic model in the flat formulation are:

$$\begin{cases} \frac{\partial p}{\partial t} = -k\left(\frac{\partial v_x}{\partial x} + \frac{\partial v_y}{\partial y}\right) \\ \frac{\partial v_x}{\partial t} = -\frac{1}{\rho}\frac{\partial p}{\partial x}, \frac{\partial v_y}{\partial t} = -\frac{1}{\rho}\frac{\partial p}{\partial y} \end{cases} \tag{1}$$

where p is the pressure, v is the velocity, k is the bulk modulus of elasticity, ρ is the density of the medium.

The values of spatial Δx and temporal Δy resolutions affect how accurately and steadily the acoustic field will be calculated. These values cannot be set independently and must be chosen taking into account each other.

First of all, Δx should be set based on accuracy considerations. In this case, accuracy and stability are independent of each other. The simulation can proceed steadily but with low accuracy in the case of a coarse mesh. The accuracy of the solution with this method depends on many factors. In this case, Δx and Δy can be set as

$$\Delta x = \frac{\lambda_{min}}{10} \sim \frac{\lambda_{min}}{20}, \Delta t \leq \frac{1}{\sqrt{d}}\frac{\Delta x}{c_{max}} \tag{2}$$

where λ_{min} is the wavelength that propagates in the simulated space, c_{max} is the highest value of sound velocity in the simulated medium, d is the value of dimensionality, for the plane problem is the value of dimensionality, $d = 2$.

A reference model of acoustic ultrasonic wave propagation in COMSOL package is constructed. Accordingly, the solution is carried out by the finite element method and the finite difference method. Below (Fig. 1) shows the normalized values of acoustic pressure read at the model point. The model is a square area made of steel with a hole inside. Slight differences in the shape of the signal are due to the way of setting the source of ultrasonic vibrations. In the case of FEM, these points are on the circle, in the case of FDTD, the point is at the grid node.

Since the mesh has a limited size and there is no possibility to simulate acoustic wave propagation outside this area, special boundary conditions are applied, in particular, Moore's absorption layers or Perfect Matched Layers (PML [11]). These conditions significantly reduce the reflectivity of the boundaries of the region, in which the simulation takes place, and create the effect of the passage of waves beyond the boundaries of this region.

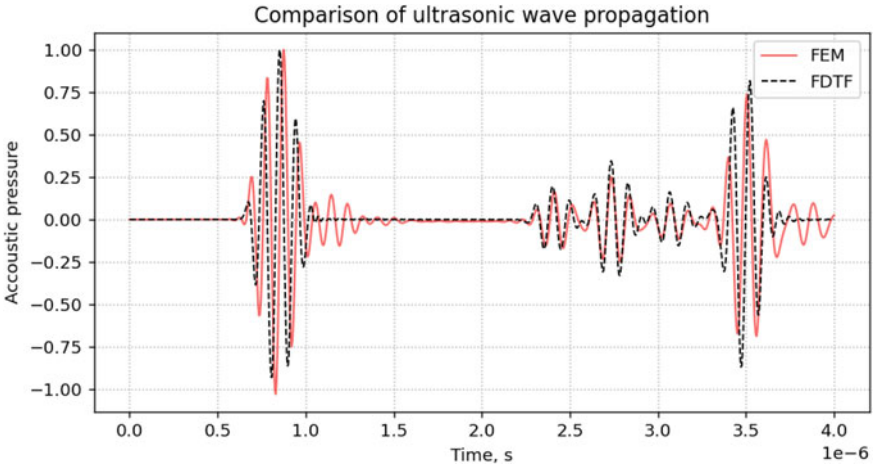

Fig. 1 Form of direct and reflected ultrasonic signal

2.2 Non-Destructive Testing Model

The inner part of the steel plate containing the defect is chosen as the nondestructive test pattern. The size of the investigated area is 20×20 mm^2. Defects are represented as geometrical figures of ellipse, triangle, square, and rectangle. The physical parameters of the defects vary with respect to the simulated area within the following limits. The defect position is from 0.3 to 0.7, the defect size is from 0.1 to 0.35, the defect angle is from 0° to 360°. The input signal consists of a fixed number of discrete values specified by the experiment time. The experiment time is chosen in such a way that the probing pulse, reflected from the defect, is able to overcome the distance and return to the point of initiation signal. The frequency of the probing pulse is 10 MHz.

The model makes it possible to assess the feasibility of the proposed method and the future prospects for its use. The ultrasonic signal is set at an internal point of the test object. The points imitating transducers that read the transmitted and reflected signals are located on the different sides of the supposed location of the defect. Such a virtual model allows one to estimate the influence of some experimental parameters on the neural network performance. Based on the implemented approach, it is possible to build models reflecting real technical problems. Below (see Fig. 2), we show propagation and reflection of ultrasonic waves from the defect inside the investigated area.

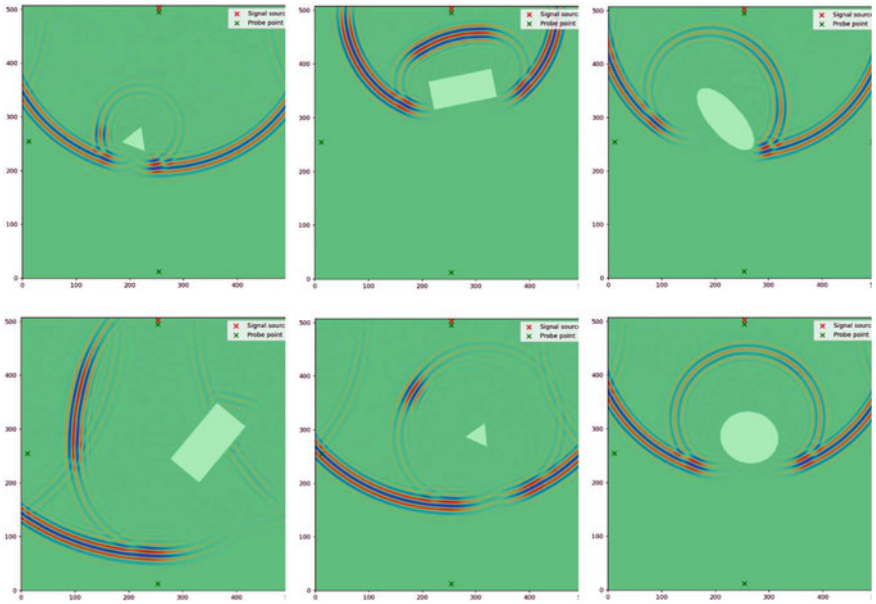

Fig. 2 Propagation of the ultrasonic wave and its reflection from various defects

2.3 Neural Network Model

Convolutional Neural Networks (CNN) is a special neural network tool for processing data having a grid structure (two-dimensional images, one-dimensional signals) [12]. It is currently one of the fastest growing and most promising deep learning tools [13–15].

They have also proven extremely successful in other practical applications, including video analysis and time series data processing (the latter can be thought of as a one-dimensional grid that processes samples at fixed ranges). SNN is a key example of the successful application of ideas derived from brain research (inspired to some extent by the structure of the mammalian visual system). As the name implies, the convolutional network uses a convolution operation, i.e. filtering with a feature map or kernel, instead of a general matrix multiplication in fully connected networks (in fact, convolution corresponds to a product on a sparse matrix).

2.4 Model Training and Validation

In a set of numerical experiments, 17,000 problems with different defect geometries were solved. 14,000 instances were used for training, 2,000 for testing and 1,000 for validation.

In training, the measure of success is the learning error. When testing a neural network model on test data that was previously unavailable to the network, its ability to generalize is determined. In the process of testing, the testing error is calculated. Thus, the performance of the model can be judged by two key factors. The first is to achieve the smallest learning error. The second is to reduce the difference between the training and testing error.

Common regularization approaches are used in the training of a neural network model. The simplest of these are early stopping and the use of dropout techniques. The batch normalization technique is also applied [16] for convolution layers. These methods provide more robust model training. Due to the sufficient size of the training sample and the complexity of data augmentation, the latter is not performed.

Training a neural network is the equivalent of solving an optimization problem in which a minimum loss function is found. This function shows how well the model performs its task. The correct choice of the loss function has a great impact on the training result. In this problem, the best choice would be to use Jaccard's similarity coefficient (Intersection over Union). This coefficient is often used in computer vision problems and is defined as

$$IoU = \frac{|A \cap B|}{|A \cup B|} = \frac{|A \cap B|}{|A| + |B| - |A \cap B|}. \tag{3}$$

Accordingly, the loss function is defined as $1 - IoU$ and reflects the difference between these two instances. It is also known as the Jaccard distance. Also, the metric $F1 = \frac{2 \times IoU}{IoU+1}$, which reflects the harmonic mean between completeness and accuracy, is used to evaluate the quality of the neural network model.

One of the most popular algorithms Adam is used for training, the use of which is described in [17]. We apply the open-source library TensorFlow and the Keras framework. These software solutions contain most of the state-of-the-art algorithms and models. It took 200 epochs of training to achieve an acceptable level of model performance.

3 Results and Discussion

Application of neural network approach to solving inverse problems has long been proven [6, 8, 18]. With the development of machine learning and new techniques, new data interpretation methods are becoming available and new opportunities for solving classical mechanics and flaw detection problems are emerging.

The authors have presented a convolutional neural network model developed to solve the problem of internal defect imaging based on ultrasonic nondestructive testing methods. The model is small in size, with 3.8 million parameters. Its simplicity and versatility provide a high learning curve and a wide range of applications in a class of related problems. The authors use the FDTD method to simulate the propagation of ultrasonic waves and present a comparison of its results with the results of the finite element method. The choice of this method allowed us to increase the speed of calculation of models compared to the problems solved earlier [19].

After training the neural network, the model is validated on the corresponding dataset. For general estimation of the model performance, the metric F1 described above is applied. In general, the accuracy of the proposed method is at a high level. The average F1 metric for the entire validation sample is 91%, as demonstrated below (Fig. 3).

4 Conclusion

This paper demonstrates the potential of applying machine learning techniques to the task of ultrasound imaging. We have built a test model of a nondestructive inspection. Based on this model, a data set is prepared for training the neural network. We propose a convolutional neural network model which allows us to predict the shape, position and orientation of defects inside a solid body. The results show high informative value of the ultrasound response and its correspondence with the real shape of the internal defect. We believe that the combination of proposed methods in this approach can serve as a good starting point for future research in the field of defectoscopy and inverse problems, in general.

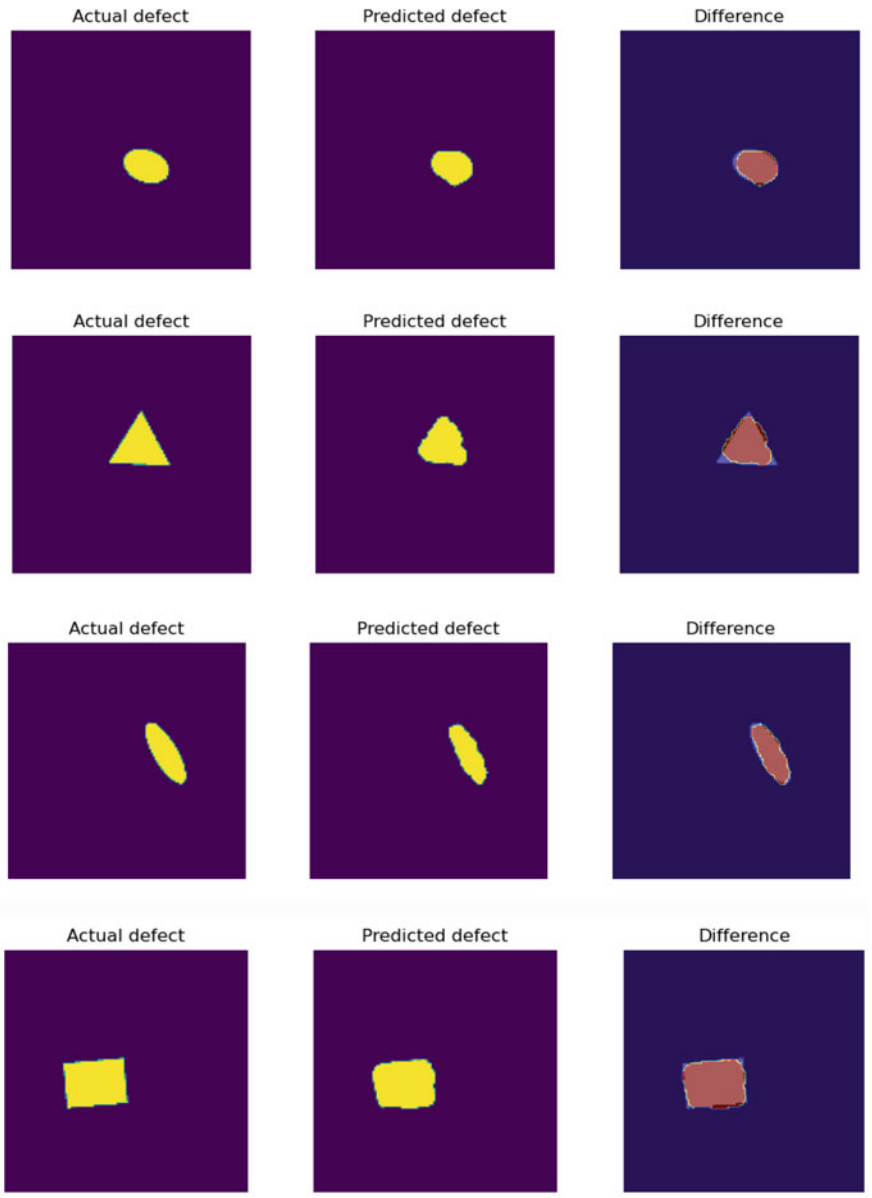

Fig. 3 Results of visualization of the defect by a neural network: on the left is the original defect; visualization of the defect, based on the ultrasound response, is reflected on the middle; on the right is the difference between the original and recovered samples

Acknowledgements The reported study was funded by RFBR, project numbers 20-31-90026 and 19-08-00074A.

References

1. Y.S. Mohamed, H.M. Shehata, M. Abdellatif, T.H. Awad, Alex. Eng. J. **58**(4), 1167 (2019)
2. Y. Gong, H. Shao, J. Luo, Z. Li, Compos. Struct. **252**, 112681 (2020)
3. A. Sirikham, Y. Zhao, H. Liu, Y. Xu, S. Williams, J. Mehnen, Infrared Phys. Technol. **104**, 103151 (2020)
4. L.F.S. Hoffmann, F.C.P. Bizarria, J.W.P. Bizarria, Polym. Test. **88**, 106559 (2020)
5. R. Sikora, P. Baniukiewicz, T. Chady, P. Lopato, G. Psuj, in *18th World Conference on Nondestructive Testing*, (Durban, South Africa 2012) (2014), pp. 16–20
6. V. Puzyrev, Geophys. J. Int. **218**(2), 817 (2019)
7. A.N. Soloviev, B.V. Sobol, P.V. Vasiliev, Advanced Materials, in *Springer Proceedings in Physics*, vol. 193, ed by I.A. Parinov, S.H. Chang, M.A. Jani (Springer, Cham, 2017), p. 381
8. A. Soloviev, B. Sobol, P. Vasiliev, A.Senichev, Advanced Materials, in*Proceedings in Materials*, vol. 6, ed. by. I.A. Parinov, S.H. Chang, B.T. Long (Springer, Cham, 2020), p. 587
9. B.V. Sobol, A.N. Soloviev, E.V. Rashidova, P.V. Vasiliev, PNRPU Mech. Bull. **4**, 165 (2019)
10. K. Yee, IEEE Trans. Antennas Propag. **14**, 302 (1966)
11. J. Berenger, J. Comput. Phys. **114**(2), 185 (1994)
12. Y. LeCun, B. Boser, J.S. Denker, D. Henderson, R.E. Howard, W. Hubbard, L.D. Jackel, Neural Comput. **1**(4), 541 (1989)
13. I. Goodfellow, Y. Bengio, A. Courville, Y. Bengio, *Deep Learning*, vol. 1 (MIT Press, Cambridge, 2016)
14. A. Krizhevsky, I. Sutskever, G.E. Hinton, in *Advances in Neural Information Processing Systems* (2012), p. 1097
15. K. He, X. Zhang, S. Ren, J. Sun, in *Proceedings of the IEEE Conference on Computer Vision and Pattern Recognition*, (2016) p. 770
16. S. Ioffe, C. Szegedy, in *Proceedings of the 32nd International Conference on Machine Learning, Lille, 6–11 July*, vol. 37 (2015), p. 448
17. D. P. Kingma, J. Ba, Adam: A method for stochastic optimization (2014). arXiv:1412.6980
18. Y. Nagatani, S. Okumura, S. Wu, T. Matsuda, Two-dimensional Ultrasound Imaging Technique based on Neural Network using Acoustic Simulation (2020). arXiv:2004.08775
19. A.N. Solov'ev, B.V. Sobol', P.V. Vasil'ev, Russ. J. Nondestr. Test. **52**(3), 119 (2016)

A Comparison Study by Simulation/Experiment to Verify the Effect of Predicted Forming Limit Diagram Based on Graphical Method at Elevated Temperature for SPCC Sheet Material

Luyen The-Thanh, Mac Thi-Bich, Banh Tien-Long, and Nguyen Duc-Toan

Abstract Sheet metal forming processing based on the deformation of materials has taken an important position with an increasing proportion in mechanical manufacturing and metallurgy. In this study, in order to predict more accuracy forming limit curve (FLC) at elevated temperature, the uniaxial tensile test of SPCC sheet material at 150 °C was first performed to obtain the stress-strain curve at 150 °C. The graphical method based on the Modified Maximum Force Criterion (MMFC) was then applied to estimate the FLCs according to the hardening law of Swift at 150 °C elevated temperature. After that, the obtained FLCs data were used for numerical simulation using the finite element method (FEM) to predict the fracture heights of the SPCC sheet material cup by deep-drawing process and compare with corresponding experimental results. Comparison results between simulation and experiments show that Swift's hardening model presents good predictions for fracture height compared to experimental data.

Keywords Forming limit curve (FLC) · SPCC sheet material · Graphical method · Modified maximum force criterion (MMFC) · Elevated temperature · Finite element method (FEM)

1 Introduction

There are many factors that can affect the results of simulating the formability of the sheet forming product, but in order to quickly predict the fracture and crack

L. The-Thanh · M. Thi-Bich · B. Tien-Long
Faculty of Mechanical Engineering, Hung Yen University of Technology and Education, Hung Yen 100000, Vietnam

B. Tien-Long · N. Duc-Toan (✉)
School of Mechanical Engineering, Hanoi University of Science and Technology, 1A-Dai Co Viet Street, Hai Ba Trung District, Hanoi City 100000, Vietnam
e-mail: toan.nguyenduc@hust.edu.vn

I. A. Parinov et al. (eds.), *Physics and Mechanics of New Materials and Their Applications*, Springer Proceedings in Materials 10,
https://doi.org/10.1007/978-3-030-76481-4_29

phenomenon of the sheet material after forming, the forming limit curve (FLC) of the material is the most important input. Many studies have been done to evaluate the forming limit curve (FLC) of the materials tested experimentally and theoretically.

Following the experimental approach, the Nakazima test [1] and the Marciniak Kuczynski test [2] are the common methods that have been widely used to clarify the FLCs for forming sheet metals. However, this experimental method is time-consuming and computationally expensive. Therefore, basic theoretical researches have been made to clarify the FLC prediction. The theoretical works can be listed as: Swift [3] pioneered the spread and progression of holes and crack in the material. Inheriting that study, Hill [4] proposed a model by varying the sheet thickness at the location where the crack appears. Hora et al. [5] developed Swift's research and proposed a modified maximum force criterion (MMFC) by considering the instantaneous strain state on the specimen until achieved maximum force.

Currently, finite element (FE) simulation is an indispensable tool to study, evaluate and differentiate physical phenomena that are modeled by different theoretical and experimental equations, and meanwhile, some studies focus on thermomechanical simulation combined with high-temperature deformation [6–13].

This study constructs the FLC forming limit curve of SPCC material at room temperature by a graphical method based on (MMFC) . FLC prediction data have been compared with corresponding empirical data through Hecker's samples, which results in a high consensus between experimental and predictive results. The study has then made a prediction of the forming limit curve (FLC) at high temperature based on the FLC at room temperature and the ratio of equivalent fracture strain between high/room temperature. The comparison results of the deep-drawing process show a good agreement between the fracture prediction at high temperature through FE simulation and experiment.

2 Material Properties

2.1 Chemical Composition of SPCC Material

In this study, the tests were performed on the SPCC metal sheet in order to obtain the data needed to develop a model that predicts the formability for the deep-drawing process of the cylinder cup. The chemical composition of the material is shown in Table 1.

Table 1 Chemical composition of SPCC materials

Material	C	Mn	P	S
SPCC	<0.1	<0.45	<0.035	<0.04

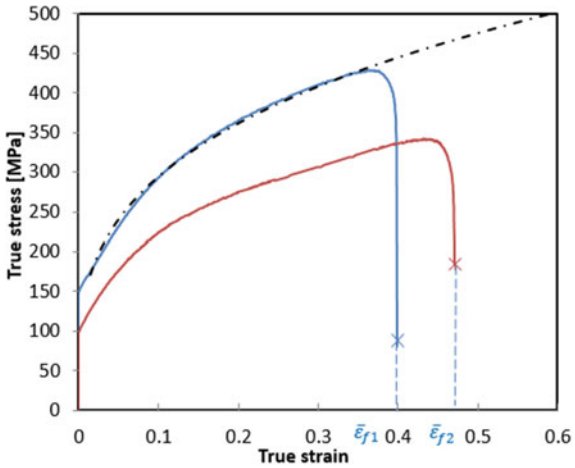

Fig. 1 Flow stress curves of SPCC sheet material at different temperatures

Table 2 Properties of SPCC materials at different temperatures

Materials	SPCC	
Property	Room temperature	150°C
Yield stress (MPa)	152.1	112.6
Tensile strength (MPa)	428.8	341.8
Density (ρ, kg/mm^3)	7.8×10^{-6}	
Elastic modulus (E, kN/mm^2)	210	
Poisson ratio (μ)	0.3	

2.2 Determining the Mechanical Properties of Experimental Materials

Mechanical properties of SPCC materials are determined through uniaxial tensile tests. In the tensile test at room and high temperature of 150 °C. Measurement results are expressed in Fig. 1 and material properties are presented in Table 2.

3 Modified Maximum Force Criterion and Graphical Method

3.1 Graphical Method Applied to SPCC Materials Used in the Study

This study uses the equivalent stress, determined by the Hill stress function by 1948 with Swift model [3]. The following equation is applied to describe SPCC sheet

material properties:

$$\bar{\sigma} = C(\varepsilon_0 + \bar{\varepsilon})^n \tag{1}$$

where $C = 584.4$ MPa; $\varepsilon_0 = 0.002$; $n = 0.3$.

The equivalent stress, determined by the Hill stress function in 1948, is calculated as follows:

$$\bar{\sigma} = \sqrt{G\sigma_1^2 + F\sigma_2^2 + H(\sigma_1 - \sigma_2)^2}. \tag{2}$$

where G, F and H are constants calculated from R-values as follows:

$$\begin{cases} F = \frac{1}{2R_{22}^2} + \frac{1}{2R_{33}^2} - \frac{1}{2R_{11}^2} \\ G = \frac{1}{2R_{11}^2} + \frac{1}{2R_{33}^2} - \frac{1}{2R_{22}^2} \\ H = \frac{1}{2R_{11}^2} + \frac{1}{2R_{22}^2} - \frac{1}{2R_{33}^2} \end{cases} \tag{3}$$

where R_{11}, R_{22}, R_{33}, R_{12}, R_{13} and R_{23} anisotropic ratios. For the plane stress case, only four stress ratios are required. It is assumed here that the rolling direction (RD) is the user-defined reference stress, then $R_{11} = 1$ and $R_{22} = 1.0143$, $R_{33} = 1.2026$ is calculated using the following system of equations:

$$\begin{cases} R_{22} = \sqrt{\frac{r_{90}(r_0+1)}{r_0(r_{90}+1)}} \\ R_{33} = \sqrt{\frac{r_{90}(r_0+1)}{(r_0+r_{90})}} \end{cases} \tag{4}$$

In order to simply obtain FLC for SPCC steel sheet material, a graphical method was used in this study. The plane strain phase is first selected and replaced into the the following inequality:

$$\frac{H'}{H} \geq \frac{1}{\boldsymbol{g}(\alpha)}\left[1 - \frac{f'(\alpha)}{f(\alpha)}\frac{\beta}{\beta'(\alpha)}\frac{1}{\varepsilon_1}\right]$$
$$\frac{H'}{H} \geq \frac{1}{\boldsymbol{g}(\alpha)} khi(\beta = 0) \tag{5}$$

This inequality is built based on the formula of (MMFC) [5, 14–16].

Under any deformation stage, Inequality (5) can be rewritten as

$$\frac{H'}{H} \geq A - \frac{B}{\varepsilon} \tag{6}$$

where

$$A = 1/\boldsymbol{g}(\alpha) \tag{7}$$

$$B = \left(f'/f\right)\left(\beta/\beta'\right) \tag{8}$$

$A(\alpha)$ and $B(\alpha)$ can be determined from the Hill stress function by applying Eqs. (4) to (6)–(8). The results are also presented in Eqs. (9)–(15), Table 4 and Fig. 5.

$$f(\alpha) = \sqrt{(G+H) - 2H\alpha + (F+H)\alpha^2} \tag{9}$$

$$f'(\alpha) = \frac{[-H + (F+H)\alpha]}{\sqrt{(G+H) - 2H\alpha + (F+H)\alpha^2}} \tag{10}$$

$$\beta(\alpha) = \frac{(F+H)\alpha - H}{-H\alpha + (G+H)} \tag{11}$$

$$\beta'(\alpha)\frac{(F+H)(G+H) - H^2}{[-H\alpha + (G+H)]^2} \tag{12}$$

$$\boldsymbol{g}(\alpha) = \frac{\sqrt{(G+H) - 2H\alpha + (F+H)\alpha^2}}{-H\alpha + (G+H)} \tag{13}$$

where

$$A(\alpha) = \frac{-H\alpha + (G+H)}{\sqrt{(G+H) - 2H\alpha + (F+H)\alpha^2}} \tag{14}$$

$$B(\alpha) = \frac{-H + (F+H)\alpha}{(G+H) - 2H\alpha + (F+H)\alpha^2} \frac{[(F+H)\alpha - H][-H\alpha + (G+H)]}{(F+H)(G+H) - H^2} \tag{15}$$

The calculated for special strain modes such as plane strain (PS) ($\beta = 0$), uniaxial tensile strain (UTS) ($\beta = -1/2$) and biaxial strain (BS) ($\beta = 1$), the results could be taken as listed in Table 3 for A and B in Eqs. (14, 15). Based on the calculated values and the above-mentioned equations, Eq. (5) can be plotted as shown in Fig. 2 by applying Swift models.

According to the graphical method, equivalent strains can be determined. To calculate minor and major strains through Eqs. (16)–(18), FLC is obtained by drawing

Table 3 Variable constants are identified in special strain modes based on Hill stress function

Forming mode		(UTS)	(PS)	(BS)
Hill (1948)	α	0	0.5	1
	β	−0.5	0	1
	$A(\alpha)$	1	0.882	0.439
	$B(\alpha)$	0.791	0	0.091

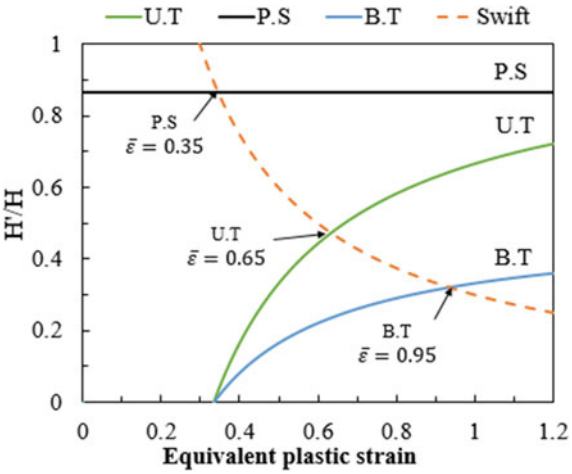

Fig. 2 Graphical method to predict forming limit curve of SPCC sheet metal

from three special strain points as shown in Fig. 3:

$$\varepsilon_1 = \bar{\varepsilon} / \frac{R_m + 1}{\sqrt{2R_m + 1}} \sqrt{1 + \frac{2R_m}{R_m + 1}\beta + \beta^2} \tag{16}$$

$$\varepsilon_2 = \beta \cdot \varepsilon_1 \tag{17}$$

$$R_m = \frac{1}{4}(r_0 + 2r_{45} + r_{90}) \tag{18}$$

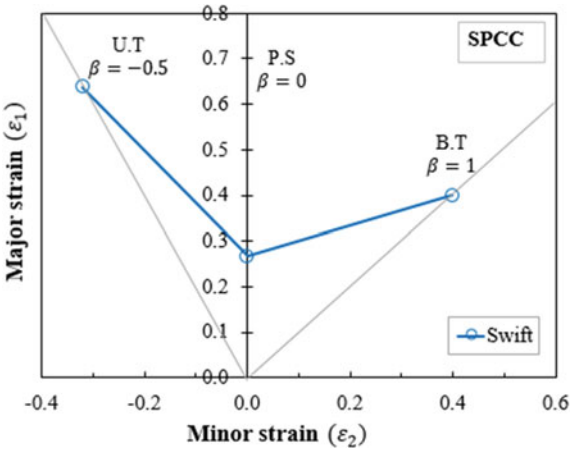

Fig. 3 FLC is calculated based on a graphical method for SPCC sheet material

where ε_1, ε_2 are the major and minor strains, $\bar{\varepsilon}$ is the equivalent strain, β is the strain ratio, R_m is Lankford value.

3.2 FLC Prediction At High Temperature

To estimate the FLC for SPCC steel at high temperatures, the fracture strain of the tensile test at room and high temperature from Table 1 and Fig. 1 could be used. From the fracture data, it could be determined the ratio of high temperature compared to the room temperature shown in Table 4.

where ratio (i) of failure points at high ($\bar{\varepsilon}_f^{Temp}$) and room ($\bar{\varepsilon}_f^{Room}$) temperatures:

$$i = \bar{\varepsilon}_f^{Temp} / \bar{\varepsilon}_f^{Room} \tag{19}$$

According to the data on the FLCs based on the graphic method of SPCC material at room temperature and the ratio of the failure points at 150 °C, it could be built the FLC at an elevated temperature of 150 °C. From Eqs. (17, 18) and parameters in Table 4, it could be determined the major and minor strains at elevated temperature as shown in Table 5 and Fig. 4.

Table 4 Fracture strain values at different temperatures

T	Temperatures (25 °C)	150 °C
ε_f	0.399	0.471
i	1	1.180

Table 5 Calculated constants at plane strain, uniaxial tension,and equibiaxial tension stages at different temperatures

Forming mode		(UTS)	(PS)	(BS)
Temperatures (25°C)	ε_1	0.638	0.267	0.399
	ε_2	−0.319	0.000	0.399
150°C	ε_1	0.753	0.315	0.471
	ε_2	−0.376	0.000	0.471

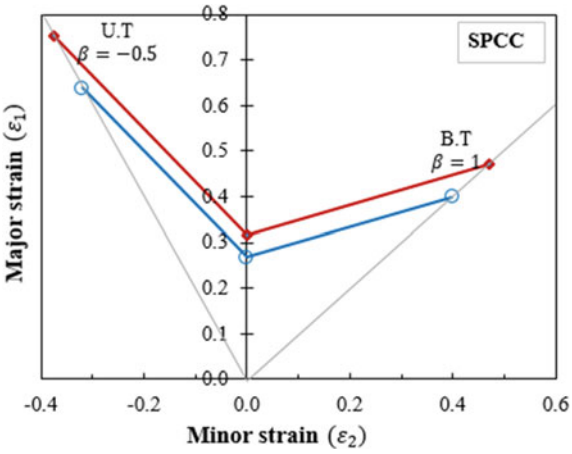

Fig. 4 FLC at different temperature of SPCC material

4 Experimental and FE Simulation Results of Deep Drawing Process

4.1 Experimental Setup

The experimental product is a cylindrical cup made of SPCC sheet material with a thickness of 0.6 mm shown in Fig. 5 and Table 5. This study determines the maximum depth that can be achieved, when the fracture occurs of the experimental deep drawing process, the results will be used as data to compare with the fracture height of the finite element simulation (FEM) according to the FLC data using the built-in graphical method based on the Swift hardening model.

The deep-drawing process of the cylindrical cup is machined on a hydraulic press with a maximum load capacity of 150 tons. Lubricants used in the deep-drawing process are commercially available oils. In this study, the friction between the punch,

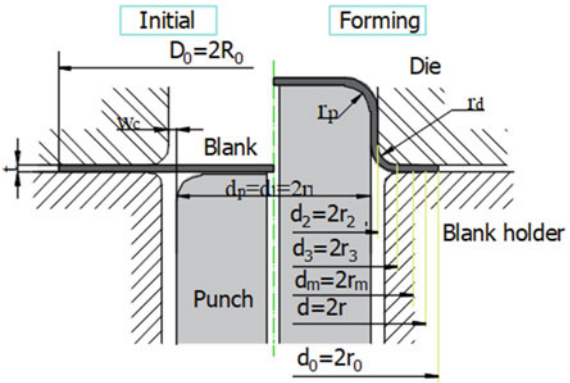

Fig. 5 Geometry of drawing dies assembly

Table 6 Fixed geometry, technology, and physical parameters of the cylindrical cup of deep drawing process

Parameters	
Diameter of workpiece (D_0)	150 mm
Workpiece thickness (t)	0.6 mm
Diameter of punch (d_p)	67 mm
Corner radius of die (r_d)	6 mm
Corner radius of punch (r_p)	4 mm
The gap between punch and die (w_c)	1 mm
Coefficient of friction between punch and blank (μ_p)	0.25
Coefficient of friction between blank holder and blank (μ_h)	0.125
Coefficient of friction between die and blank (μ_d)	0.125

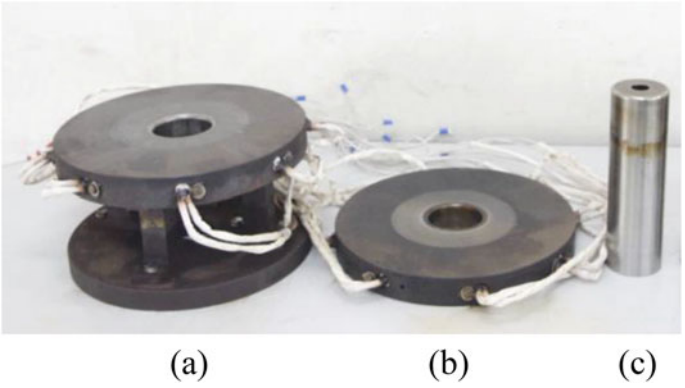

Fig. 6 Test setup for the deep drawing process: **a** die; **b** force blank holder; **c** punch

die, blank holder during the deep-drawing process is referenced [13] and is assumed as shown in Table 6. The experimental die and punch are shown in Fig. 6. Table 5 depicts the geometrical, technological and physical parameters of punch and die for the deep drawing process of the cylindrical cup.

4.2 FE Simulation

In this study, ABAQUS (6.13) software [17] is used to simulate the deep drawing of the cylindrical cup with a 3D CAD model as shown in Fig. 7. In which the punch is kept fixed, the blank holder and the die moving vertically to reach the size of the forming part. The rigid body model is used for the punch, blank holder, and die, whose motion is represented by the motion of a button, defined as the fixed

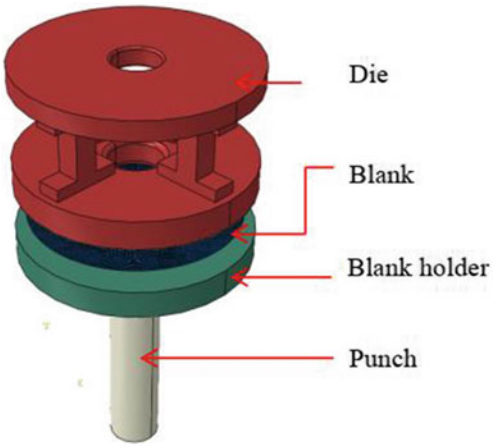

Fig. 7 FE model in Abaqus

reference button. The blank is modeled as a shell model and the mesh is divided into an integrated reduced S4R element type.

5 Results and Discussion

To verify the effect of temperature on FLC prediction on the fracture cup height of the deep drawing process for SPCC sheet material, the input data based on the FLC predicted at room and elevated temperatures were adopted. The simulation results were presented in Fig. 8. In the FE simulation of the deep drawing process, the fracture cup heights occur, when the FLC fracture criterion value reaches 1.0. Here, the fracture cup heights at room and high temperature could be measured as shown in Fig. 8a, b, respectively. Table 7 expresses predicted errors of simulation results, when comparing with the corresponding test. The percentage deviation between the fracture cup height of FEM simulation prediction and the corresponding measurement experiment was estimated as

$$\Delta h(\%) = (|h_{\text{Sim}} - h_{\text{Exp}}|)/h_{\text{Exp}} \tag{20}$$

6 Conclusion

This study has applied the graphical method to estimate and predict the forming limit curve (FLC) of the SPCC steel sheet at room and elevated temperatures. The fracture criteria based on FLC prediction were adopted in the FEM simulation model and

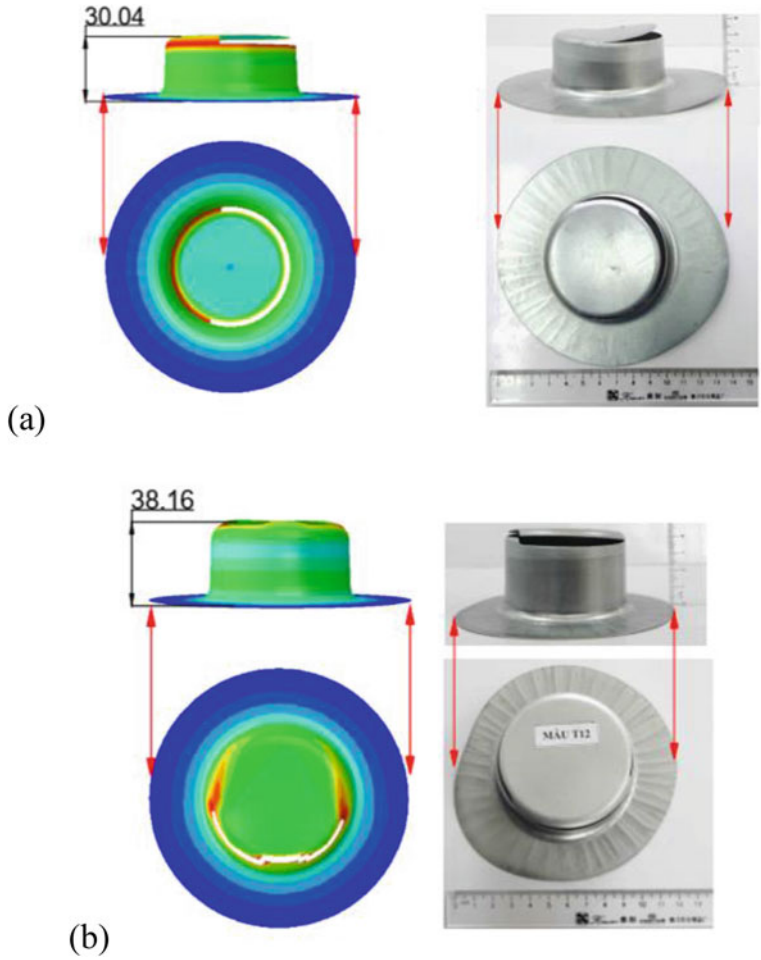

Fig. 8 Comparison between prediction and simulation of fracture height at: **a** room and **b** high temperatures

Table 7 Percentage deviation of fracture cup height between experiment and FEM simulations

Fracture height at	Experiment h_{Exp} (mm)	Simulation h_{Sim} (mm)	Error Δh (%)
Room temperature	33.2	30.04	9.52
150 °C	41.8	38.16	8.71

compared with corresponding experiments of the deep drawing process for the cylindrical cup. Predictions of deformed cup height using FLC predictions according to

Swift hardening law were compared with corresponding experiments. The comparison results show that the Swift hardening law presents a good prediction for fracture cup height of 9.52 and 8.71% deviation at room and 150 °C, respectively.

Acknowledgments This research is funded by Vietnam National Foundation for Science and Technology Development (NAFOSTED) under grant number 107.02-2019.300.

References

1. E. Fictorie, A.H. van den Boogaard, E.H. Atzema, Int. J. Mater. Form. **3**, 1179 (2010)
2. Z. Marciniak, K. Kuczyński, Int. J. Mech. Sci. **9**, 609 (1967)
3. H.W. Swift, J. Mech. Phys. Solids **1**, 1 (1952)
4. R.A. Hill, Proc. R. Soc. A Math. Phys. Eng. Sci. **193**, 281 (1948)
5. P. Hora, L. Tong, B. Berisha, Int. J. Mater. Form. **6**, 267 (2013)
6. N. Duc-Toan, B. Tien-Long, J. Dong-Won, Y. Seung-Han, K. Young-Suk, High Temp. Mater. Process. **31**, 37 (2015)
7. N. Duc-Toan, K. Young-Suk, J. Dong-Won, Met. Mater. Int. **18**, 583 (2012)
8. N. Duc-Toan, Y. Seung-Han, J. Dong-Won, B. Tien-Long, K. Young-Suk, Int. J. Adv. Manuf. Technol. **62**, 551 (2012)
9. Y.C. Lin et al., Mater. Des. **74**, 108 (2015)
10. Y.C. Lin et al., Mater. Sci. Eng., A **711**, 293 (2018)
11. D.T. Nguyen, J.G. Park, Y.S. Kim, Trans. Indian Inst. Met. **69**, 1343 (2016)
12. T.-T. Luyen, Q.-T. Pham, Y.-S. Kim, D.-T. Nguyen, J. Korean Soc. Precis. Eng. **36**, 883 (2019)
13. L. The-Thanh, B. Tien-Long, T. The-Van, N. Duc-Toan, Adv. Mech. Eng. **11**, 1 (2019)
14. Q.T. Pham, D.T. Nguyen, J.J. Kim, Y.S. Kim, Key Eng. Mater. **794**, 55 (2019)
15. Q.T. Pham, D.T. Nguyen, J.J. Kim, Y.S. Kim. Key Eng. Mater. **794 KEM**, 55 (2019)
16. Q.T. Pham, B.H. Lee, K.C. Park, Y.S. Kim, Int. J. Mech. Sci. **140**, 521 (2018)
17. D. Hibbit, B.K. and P. S. ABAQUS/CAE User's Manual. Ver. 6.10.1. ABAQUS Inc. 847p (2001)

Fatigue Crack Growth Rate and Intrinsic Threshold Stress Intensity

R. Sunder

Abstract In atmospheric fatigue, intrinsic threshold stress intensity, $\Delta K_{th,i}$, far from being a material constant, varies significantly. It is controlled by a certain computable, load-history sensitive, near-tip residual stress, σ*, that appears to moderate crack-tip diffusion kinetics and thereby determines $\Delta K_{th,i}$, the incremental K required for an open crack to extend by fatigue. This demands reconsideration of the relationship between near-threshold crack growth rates and applied effective stress intensity range, ΔK_{eff}. Its practical implementation requires considerations of Linear Hysteretic Fracture Mechanics (LHFM). LHFM is applied to translate applied K, to near-tip cyclic inelastic stress–strain response. The new relationships permit extension of fracture mechanics considerations to short cracks including defects in additive manufactured materials and naturally forming cracks in components over high-cycle and very high-cycle (HCF/VHCF) regimes. Most importantly, the new approach permits handling near-threshold fatigue response both under constant amplitude as well as under variable-amplitude loading, representative of actual service conditions. It also permits re-interpretation of test data obtained by the so-called cyclic *R*-curve and compression-compression pre-cracking techniques.

Keywords Intrinsic threshold stress intensity · Near-tip residual stress · Near-threshold crack growth rate

1 Introduction

d*a*/d*N versus* ΔK curves obtained using standard practices such as ASTM E647 [1] serve as vital inputs to comparative evaluation of materials in design trade-off studies, residual fatigue life analyses required to assess structural integrity, safe life and life between inspections as well as in fundamental research. The discovery of fatigue crack closure [2] and incorporation of algorithms for its estimation into standard test practice permitted correction for the stress ratio effect. A vital point on this

R. Sunder (✉)
BISS Division, ITW-India (P) Ltd, Bangalore, India
e-mail: rs@biss.in

I. A. Parinov et al. (eds.), *Physics and Mechanics of New Materials and Their Applications*, Springer Proceedings in Materials 10,
https://doi.org/10.1007/978-3-030-76481-4_30

curve is ΔK_{th}, the threshold stress intensity range. Its estimation and interpretation remain controversial. This parameter is extremely crucial, particularly to applications involving extended endurance and long periods between inspections, i.e., to residual life estimates in HCF and VHCF regimes. Note also, that ΔK_{th} may influence crack growth rates right up to 10^{-4} mm/cycle.

Engineering applications involve naturally forming cracks that grow under increasing stress intensity. Laboratory testing for ΔK_{th} involves long cracks seeing load shedding. It obviously does not replicate conditions of practical interest. Long crack ΔK_{th} may not apply to naturally forming short cracks that are too short to see the consequences of certain 'extrinsic' factors [3]. Observed variations in laboratory estimates of ΔK_{th} as a function K_{max} or stress ratio, R, are typically attributed to these 'extrinsic' factors including fatigue crack closure due to plasticity, crack wake roughness and debris formation [3–5]. Implicit in such understanding is the assumption that 'intrinsic' threshold stress intensity is a material constant equal to a certain $\Delta K_{th,eff}$ (that is devoid of the main extrinsic component, namely, crack closure). The actual break-up of ΔK_{th} into its two supposed constituents has remained an enigma, given the lack of credible means to define, let alone, determine *either* of the two. On the premise that the lowest possible ΔK_{th} would represent a certain intrinsic property, different methods have been exercised in attempts to bridge the gap between laboratory test data and engineering application involving naturally forming cracks. The compression pre-cracking method is one of them [6, 7] and it is backed by numerical computations of crack closure as influenced by the process [8]. The so-called 'Cyclic *R*-Curve' is another method [9, 10]. Both these methods follow from the consideration, that by inducing reversed yield at the crack initiator, the effective notch root stress ratio even under applied compression-compression loading will turn tensile, leading to closure-free conditions under subsequent tensile stress ratio. A much simpler method to resolve the issue has been suggested that assumes that ΔK_{th} values obtained under high applied stress ratio will be associated with closure free conditions and therefore represent intrinsic component of ΔK_{th} [3]. Indeed, ΔK_{th} has been shown to progressively decrease with increasing applied stress ratio and K_{max} [11–13]. However, it remains unclear, whether it eventually does plateau in support of the crucial assumption behind the method. After all, common to all these approaches is the presumption of intrinsic threshold stress intensity as a material constant.

The so called 'two parameter approach' may appear to be by far the simplest LEFM interpretation of crack growth rate all the way down to threshold [14–17]. According to this approach, crack growth rate uniquely relates to a given combination of K_{max} and ΔK. As K_{max} approaches K_c, crack growth rate will obviously accelerate due to the increase of the quasi-static component. In the Paris Regime, the K_{max} effect can be traced to crack closure. And for reasons that are forthcoming, near-threshold crack growth rates are in addition, sensitive to K_{max} due to environmental action. In each of these stages, the very nature of the relationship between da/dN and the combination of K_{max} and ΔK will be different, being associated with vastly different mechanisms. Clearly, the two-parameter approach presents a rather simplistic picture

of an extremely interesting, but complex phenomenon. A picture, that is rendered even more complex under random load history associated with engineering application.

Finally, engineering applications involve service load history that is seldom similar to constant amplitude conditions prescribed by standard testing practices such as ASTM E647. It is generally assumed that one or more of the load interaction models will handle the difference between the two. However, available computer software in industrial use ignores the effect of variable amplitude loading on fatigue thresholds. This restricts their potential usefulness to residual fatigue lives of the order of tens, or at best, a few hundred thousand load cycles. The current study describes the framework to render laboratory crack growth rate data over their entire range, right from threshold to fracture in a manner, that suits engineering application as well as serves the purpose of future research. Its focus is on intrinsic threshold stress intensity, $\Delta K_{th,i}$ and near-threshold fatigue crack growth rates.

The next section explains why atmospheric $\Delta K_{th,i}$, cannot be a material constant and identifies a computable parameter, in the form of near-tip residual stress, σ^*, to which $\Delta K_{th,i}$ has been found to be uniquely related [18, 19].[1] The envelope of σ^* variation under both constant amplitude as well as variable amplitude loading, including the partial cases that represent cyclic *R*-curve and compression—compression loading conditions are described. This is followed by listing of $\Delta K_{th,i}$ *versus* σ^* relationships for a variety of materials obtained in previous work. New crack growth rate data on Ti-6Al-4 V obtained from similar threshold tests are collated with data obtained at higher growth rates to describe a new equation for fatigue crack growth rate that may be more suitable for engineering application than currently available representations. The paper concludes with recommendations for future work related to both research as well as engineering application.

2 Intrinsic Threshold for Atmospheric Fatigue Crack Growth

A vast body of irrefutable fractographic evidence obtained under specially designed programmed load sequences confirms, that near-threshold crack growth rates exhibit significant load sequence sensitivity that cannot be explained by 'extrinsic' factors such as crack closure [20]. This effect recedes to vanishing proportions as growth rate increases into the Paris Regime. Early work revealed that the phenomenon does not appear to exist in high vacuum [21, 22]. This prompted the Brittle Micro Fracture (BMF) theory of near-threshold crack extension, whereby the crack tip suffers Mode I micro-fracture by surface embrittlement from hydrogen in moisture at room temperature and oxidation at elevated temperature [23]. Such 'embrittlement' has been shown to be associated with highly localized slip [24, 25], that would imply

[1] Both references describe details of the testing practice to determine intrinsic threshold. However, in [18], it is referred to as ΔK_{th}, while we now refer to it as K_{th} in order to differentiate it from the notation used in the literature that represents ΔK_{th} as the sum of intrinsic and extrinsic components.

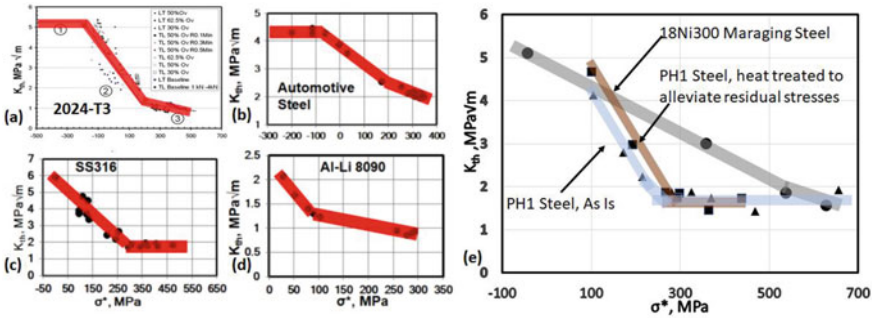

Fig. 1 Intrinsic threshold stress intensity, $\Delta K_{th,i}$, from experiments on 2024-T3 [18], automotive steel, stainless steel SS 316 and Al-Li alloy 8090 [19], and, from 3D printed high strength stainless steel, PH1 and 3D printed maraging steel 18Ni300 [27]

Mode II micro fracture. Therefore, by 'brittle' the connotation is merely about localized accelerated crack extension. Note that in the context of this work, whether it is by Mode I or II would be immaterial. Research leading up to this new understanding of variable amplitude fatigue is reviewed in [26].

If closure-free near-threshold crack growth rates are load sequence sensitive, it follows that the intrinsic component of ΔK_{th} cannot be treated as a material constant. If, however, one can relate the intrinsic component to a certain near-tip stress at the commencement of the rising load half-cycle, one can search for a relationship between them. An experimental procedure was developed to characterize intrinsic (closure free) component $\Delta K_{th,i}$ over a wide range of highly controlled and computable near-tip residual stress conditions (see Fig. 1). It was initially validated on 2024-T3 Al-alloy [18], then fine-tuned and demonstrated on a variety of materials [19] including additive manufactured materials [27].

The new experimental procedure utilizes the consequences of near-tip stress-strain hysteresis to 'set' controlled values of a certain near-tip residual stress, σ^*, through periodic application of precision controlled periodic overload/underload sequences, while at the same time decreasing ΔK with crack extension, with $P_{max} = \text{const}$, until threshold conditions conforming to 10^{-7} mm/cycle are reached. Test conditions may also include 'no overload' conditions, as the means to impose higher tensile values of σ^*. The magnitude of tensile overload is restricted to preclude the possibility of crack closure, whose absence is independently confirmed per ASTM E647. Also, crack extension during the periodic overloads constitutes a negligible fraction of baseline crack growth. The resultant threshold ΔK denoted as $\Delta K_{th,i}$ qualifies as 'intrinsic'. The absence of extrinsic component is confirmed by ensuring that K_{min} registered at threshold is well in excess of K_{op} measurement from unloading compliance made with most unconservative settings.

A fully automated test procedure permits determination of the $\Delta K_{th,i}$ *versus* σ^* relationship from a limited number of test coupons [18, 19]. As shown in Figs. 1a–e, test data from a variety of materials tested suggest a unique relationship between

$\Delta K_{th,i}$ and σ^* [18, 19, 27]. The wide range of possible cycle-sequence sensitive variation in $\Delta K_{th,i}$ points to its potential in determining residual fatigue life under service loading conditions in the HCF/VHCF range. These findings underscore limitations of prevailing standard testing practice.

It is important to note, that near-tip residual stress, σ^*, is sensitive to cyclic inelastic response well within the *cyclic* plastic zone, virtually, a crack-tip response. It is not synonymous and in fact, has little in common with 'residual stress' inferred by the well-known Wheeler [28] and Willenborg [29] crack growth retardation models that refer to the compressive residual stress caused by the stretched *monotonic* plastic zone after a tensile overload. Also, it is unrelated to the distributed residual stress that can occur by material processing [30, 31]. These 'macroscopic' residual stress distributions will affect crack closure as the crack wake will develop within their region of influence. However, the crack tip stress response will be the consequence of superposed action of such residual stress combined with that of actual cycle-by-cycle loading. This is illustrated by the $\Delta K_{th,i}$ *versus* σ^* relationships seen for AM specimens from PH1 steel, that were tested with and without heat treatment to remove residual stress (Fig. 1e). We can see a small but noticeable parallel shift in the relationship, but at higher σ^*, the two data sets merge into a flat (almost constant value), suggesting that AM-related residual stress in the material had little effect on lowest $\Delta K_{th,i}$. This may be the consequence of 'flattening out' of the monotonic near-tip stress *versus* K-curve, or, due to a certain 'saturation' in the effect of σ^* on $\Delta K_{th,i}$. Interestingly, a similar flattening of response at the lower bound is also seen in test data from the other stainless steel, SS 316 that was tested (Fig. 1c).

3 Near-Tip Stress Response and Intrinsic Threshold Stress Intensity, $\Delta K_{th,i}$

The connection between near-threshold fatigue crack growth and crack-tip diffusion kinetics has been highlighted in early work [32, 33]. The unique relationship between $\Delta K_{th,i}$ and σ^* underscores the obvious influence of instantaneous near-tip stress on diffusion kinetics, and consequently of the effect of K_{max} and particularly, of load history, two key aspects overlooked in early work that have a crucial bearing on engineering application.

Consideration of stress very close to the crack tip requires what may be referred to as a Linear Hysteretic Fracture Mechanics or LHFM approach in order to account for cycle-sequence sensitivity of near-tip stress to applied K-history. Equations associated with Linear Elastic Fracture Mechanics (LEFM) ignore near-tip cyclic inelastic response. LHFM overcomes this shortcoming by describing near-tip cyclic stress-strain hysteretic response even if K-values may conform to Linear-Elastic considerations. In the process, near-tip local *stress* history can be rendered as a function of applied stress intensity history given by equations whose description is forthcoming.

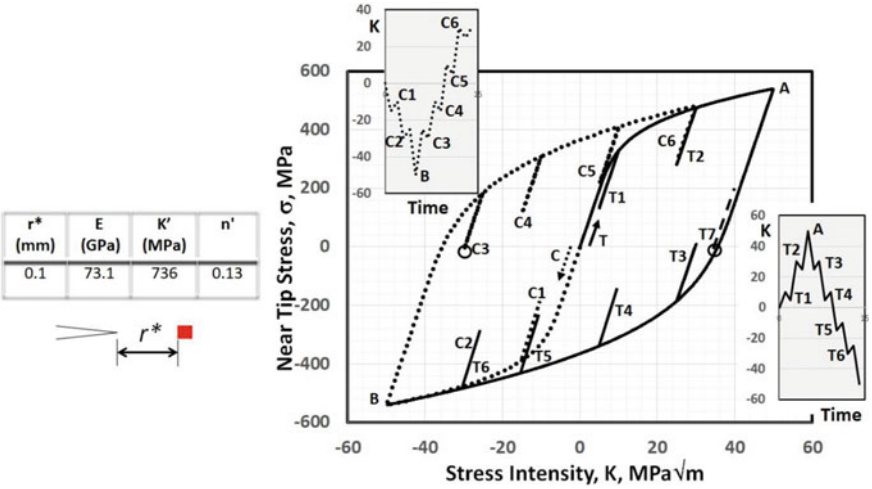

Fig. 2 Linear Hysteretic Fracture Mechanics (LHFM) representation of near-tip stress response to a complex tension-compression applied stress-intensity history. Computations made assuming fully open crack and using the constants as listed in table and (1)–(3). Variation in minimum near-tip stress in embedded cycles, σ^* should be viewed against associated variation in $\Delta K_{\text{th,i}}$ in Fig. 1a

Rendering σ^* at $K_{\min}$ as a unique function of K-history leaves *strain* response irrelevant to near-threshold fatigue even if it may retain its 'mechanistic' significance from considerations of crack closure, crack-tip blunting, etc.

Figure 2 explains the framework connecting cyclic stress–strain properties, applied load history, near-tip stress response to the applied load history including σ^* at the commencement of embedded load cycles of near-threshold magnitude and the experimentally established relationship between σ^* and intrinsic threshold stress intensity, $\Delta K_{\text{th,i}}$. The data and calculations are for 2024-T3 Al-alloy, but the same framework would be applicable for any other metallic material exhibiting strain hardening properties. The figure shows variation of near-tip stress, σ, computed for two sequences of applied stress intensity, K, for the case of a fully open fatigue crack and at a distance r^*. It is assumed that the crack wake will not close even in compression, a situation that is generally attempted to be reproduced in tests with compression—compression pre-cracking [6, 7] and in cyclic R-curve experiments [9, 10]. Near-tip response is plotted for two applied K-sequences. One sequence commenced in the tensile direction, while the other marked with the dotted line, did so in the compressive direction. The two sequences include a tensile and compressive overload marked as A and B respectively. These together form an envelope of near-tip stress response that effectively determines potential variation of σ^* for any given position of an embedded near-threshold load cycle. The material constants shown in the figure and the $\Delta K_{\text{th,i}}$ *versus* σ^* data points were obtained on 5 mm thick C(T) specimens cut from 2024-T3 [18]. These, together with the three equations below were adequate to compute the graph of σ *versus* K sequence shown:

$$K_1 = \sqrt{2\pi r^* E\sigma_1[\frac{\sigma_1}{E} + \left(\frac{\sigma_1}{K'}\right)^{\frac{1}{n'}}]} \quad (1)$$

$$K_1 - K_2 = \sqrt{2\pi r^* E(\sigma_1 - \sigma_2)[\frac{\sigma_1 - \sigma_2}{E} + 2\left(\frac{\sigma_1 - \sigma_2}{2K'}\right)^{\frac{1}{n'}}]} \quad (2)$$

$$K_3 - K_2 = \sqrt{2\pi r^* E(\sigma_3 - \sigma_2)[\frac{\sigma_3 - \sigma_2}{E} + 2\left(\frac{\sigma_3 - \sigma_2}{2K'}\right)^{\frac{1}{n'}}]} \quad (3)$$

where K_1 represents starting K-excursion from zero and following the monotonic material response, while K_2 and K_3 are the subsequent applied K-values assumed to be following the cyclic stress-strain response, associated with reversed strain and σ_1, σ_2, σ_3, are the associated near-tip stresses, E is Young's modulus, K' is the cyclic strength coefficient, n' is the cyclic strain hardening exponent and r^* is the distance from the crack tip at which local stress, σ is computed.

Note that each equation represents an excursion, whose sign would need to be inverted in the case of initial compressive excursion (the dotted line in Fig. 2). The solution of (1) determines σ_1. Similarly, solving (2) determines σ_2, while σ_3 is determined by solving (3).

The interruptions T1–T6 and C1–C6 are of equal magnitude and set to 5 MPa·m$^{1/2}$ to match the highest $\Delta K_{th,i}$ seen in the $\Delta K_{th,i}$ versus σ^* relationship for this material (Fig. 1a). The σ^* value corresponds to the minimum K-value in each of the 5 MPa·m$^{1/2}$ excursions seen. Three sets of near-threshold cycles have such minima at −30, −15, 5 and 25 MPa·m$^{1/2}$, respectively. Of these, σ^* for two, namely, C1, C2 can be computed from (1) alone. For T1–T6, σ^* requires solution of (1), (2). Estimation of σ^* for C3–C6 requires solution of (1)–(3).

The computed σ^* values are suggestive of the corresponding $\Delta K_{th,i}$ value as seen from the $\Delta K_{th,i}$ *versus* σ^* plot in Fig. 1a. The relationship between $\Delta K_{th,i}$ and σ^* being unique, *it does not matter,* what was the associated applied stress intensity. What mattered, was the LHFM-driven near-tip stress response to the applied K-sequence as estimated from (1)–(3). Note however, that the computations shown are assuming $r^* = 0.1$ mm. At this distance from the crack tip, elastic unloading over 5 MPa·m$^{1/2}$ induces a local stress change of approximately 100 MPa. This is about 35% less than at $r^* = 0.035$ mm that was used in [18]. Therefore, the $\Delta K_{th,i}$ *versus* σ^* relationship in the figure cannot be directly related to the σ *versus* K plot shown. There will be a horizontal shift in the $\Delta K_{th,i}$ *versus* σ^* relationship induced by the difference in σ^* due to elastic unloading and also a small vertical shift due to enhanced response to overloads A, B. Trends however, will remain unchanged.

Excursions T3–T6 will see the influence of overload A followed by the unloading to their respective minima. Likewise, C3–C6 will see the consequence of compressive overload B followed by tensile reloading.

Note that the four sets of three *identical* applied stress-intensity excursions, i.e., (C2, C3, T6), (C1, C4, T5), (T1, T4, C5), and (T2, T3, C6) will see vastly *different*

near-tip stress at the commencement of the rising load excursion. As a consequence, they will see vastly different $\Delta K_{th,i}$ values in atmospheric fatigue (refer to Fig. 1a). On the contrary, vastly *different* cycle pairs (C2, T6), (C1, T5), (C5, T1) and (C6, T2) end up with *minor deviation* in σ^* because of the manner in which their load history is different. These will therefore see correspondingly *similar* $\Delta K_{th,i}$ values. Note also, that cycles C3 and T3 are vastly different in terms of applied mean stress intensity, yet, σ^* in the two are not as vastly different as between identical applied cycles, e.g., C1, C4. These differences cannot be discerned by LEFM analysis. Application of LHFM to cycle-by-cycle stress-K analysis brings out the observed differences, with the added promise of opening up the possibility of modeling near-threshold variable amplitude fatigue crack growth.

Test conditions enforced by prevailing standard practice maintaining either stress ratio, R, or, K_{max} constant essentially restricts σ^* to a narrow band without necessarily freezing the extrinsic component. These two parameters have little bearing on thresholds experienced under load sequences of engineering importance. Compelling evidence in this regard emerges from a cursory comparison of load cycle C3 ($K_{max} = -25$ MPa·m$^{1/2}$) with a hypothetical load cycle T7 with K_{max} of 40 MPa·m$^{1/2}$. One of these cycles is in compression, the other in tension and separated by a difference of 65 MPa·m$^{1/2}$. Nevertheless, both will see the same $\Delta K_{th,i}$. If estimated ΔK_{th} for the two cycles does differ as it is quite likely to, the difference may *only* be attributable to the *extrinsic* fraction of ΔK_{th}.

The envelope formed by the near-tip stress response to tension-compression K-history is limited by the stress associated with highest overload and underload. The lower bounding curve in this case indicates the lowest possible σ^* at any given applied K_{min}. It determines σ^* for any load cycle 'standing' on the lower bound. The envelope illustrates the potential variation in σ^* depending on applied load history. Obviously, this margin will be controlled by strain hardening exponent, n', and the magnitude of extreme variations in loading. For the sequences in the figure, the margin of potential variation in σ^* for identical applied cycle in terms of K_{max} and K_{min} is of the order of 400 MPa. Judging from the $\Delta K_{th,i}$ *versus* σ^* relationship, this can induce significant load-history dependent variation in $\Delta K_{th,i}$. Thus, cycles C3, C4 will see lower $\Delta K_{th,i}$ values thanks to the compressive overload B, while cycles T3, T4 will see higher $\Delta K_{th,i}$ than cycles T1, T2, thanks to the overload A. This is a direct consequence of near-tip cyclic stress-strain hysteresis. It has nothing to do with crack closure, in fact, crack closure would inhibit such hysteretic response.

With increase in the magnitude of interruptions T1–T6, C1–C6, the minimum stresses in these cycles will approach the lower bound of the outer loop, reducing the variation in σ^* within each set. Simultaneously, as ΔK during these cycles is large enough to cause greater crack extension, closer to the Paris Regime (>10^{-4} mm/cycle), the associated mechanism change in crack extension will render any remaining variation irrelevant, and also effectively render LHFM considerations redundant.

The near-tip stress *versus* applied stress-intensity plot can assist in re-interpreting available test data to understand material response to the test procedures followed in compression-compression pre-cracking and from cyclic R-curve testing. Both these

strictly speaking, involve variable amplitude loading. In order to determine the $\Delta K_{th,i}$ fraction from ΔK_{th} estimated using these methods, one would need to model σ^* as a function of the applied load history in the course of compression-compression pre-cracking and cyclic *R*-curve testing.

4 Incorporation of $\Delta K_{th,i}$ into the Crack Growth Rate Equation

To be of value in engineering application, the crack growth rate equation should correctly describe crack extension during an applied load cycle that may vary by as much as seven orders of magnitude. The gradual transition of crack growth rates from threshold conditions to a magnitude, where threshold resistance ceases to be relevant needs to be adequately described by the crack growth rate equation. Judging from Fig. 3 and assuming fatigue crack extension occurs during the rising load half-cycle, the first point of interest in the load cycle is K_{op}. At K_{op}, the crack-tip 'does not know' by how much K will increase beyond this point. However, because σ^* is known, so is K_{th} that represents the incremental K required for the crack to extend by 10^{-7} mm. One may assume that this crack extension is the direct consequence of crack-tip surface diffusion kinetics associated with the rising magnitude of near-tip stress, combined with incremental crack-tip deformation.

$\Delta K_{th,i}$ can vary significantly in atmospheric fatigue depending on load history, K_{max}, etc. However, this being a crack-tip surface diffusion kinetics driven phenomenon, its significance will diminish with increasing contribution of crack extension by competing processes induced by the mechanics of crack tip response and associated crack growth once K exceeds K_{op}. Thus, whilst crack extension at 10^{-6} mm/cycle will be almost certainly influenced by $\Delta K_{th,i}$, it is unlikely crack extension at 10^{-3} mm/cycle will see the effect of $\Delta K_{th,i}$, irrespective, of whether $\Delta K_{th,i}$ for the given load cycle is small or large. At this point, it may not be appropriate to assume that da/dN is driven by the difference, $\Delta K_{eff} - \Delta K_{th,i}$.

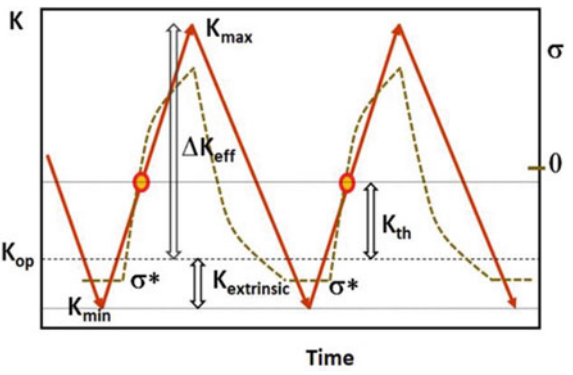

Fig. 3 Schematic variation of K and near-tip stress, σ, (broken line) in a load cycle, illustrating crack tip response to incremental loading; note flat near-tip stress response until applied incremental K exceeds extrinsic component of threshold; σ^* in turn determines the further incremental K, required for the onset of fatigue crack extension; hence there is the correlation of $\Delta K_{th,i}$ with σ^*

As K progressively increases beyond $K_{op} + \Delta K_{th,i}$, the significance of the $\Delta K_{th,i}$ component must be seen to progressively diminish as crack extension will be increasingly driven by a different mechanism altogether and increasingly sensitive only to ΔK_{eff}. This is particularly important, given the relationship between $\Delta K_{th,i}$ and σ^*. With increasing ΔK, while incremental near-tip stress towards K_{max} is attenuated by inelasticity, elastic unloading over twice the yield stress over the same ΔK will inevitably lead to lower σ^* and increasing $\Delta K_{th,i}$ over the next loading half-cycle! This is illustrated by Fig. 4a and by the broken line in Fig. 4b. Theoretically, $\Delta K_{th,i}$ in the Paris Regime will approach the highest possible values in the $\Delta K_{th,i}$ versus σ^* relationship. The receding significance of instantaneous $\Delta K_{th,i}$ in the face of rising ΔK may be accounted for by a certain effective threshold stress intensity, Δ denoted as $K_{th,eff}$ as described by the following equation valid over the range $\Delta K_{th,i} < \Delta K_{eff} < \Delta K^*_{eff}$:

$$K_{th,eff} = \Delta K_{th,i} \left[\frac{\left(\Delta K^*_{eff} - \Delta K_{eff}\right)}{\left(\Delta K^*_{eff} - \Delta K_{th,i}\right)} \right]^p \tag{4}$$

where, ΔK^*_{eff} is ΔK_{eff} associated with a growth rate of 10^{-3} mm/cycle and p is a constant, assumed for brevity to be unity. The form of this equation meets boundary conditions associated with both threshold as well as with the total disappearance of near-threshold response at $\Delta K_{eff} \geq \Delta K^*_{eff}$.

One may expect that ΔK^*_{eff}, being associated with the Paris Regime, will always exceed $\Delta K_{th,i}$. Actual value of p is likely to be determined by the competition of the two crack extension mechanisms involved. Determination of a more suitable value of p can be the subject of future work. However, judging from forthcoming empirical evidence, $p = 1$ appears reasonable.

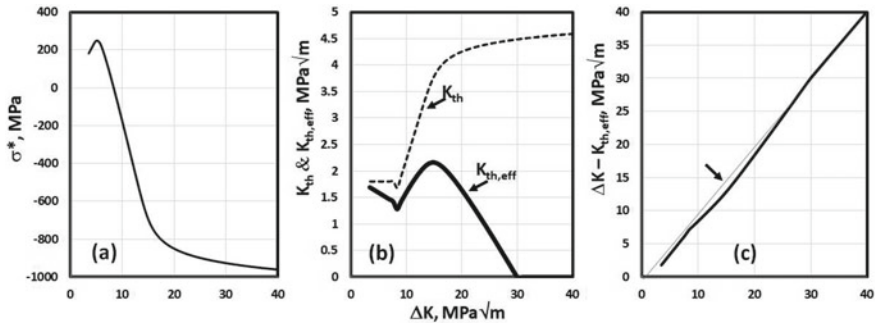

Fig. 4 Transformations of near-threshold response for Ti-6Al-4 V at $R = 0.3$: **a** computed near tip residual stress as a function of applied ΔK; **b** variation in $\Delta K_{th,i}$ with applied ΔK per (**a**) and $K_{th,eff}$ corrected for 'proximity of Paris Regime'; **c** kink indicated by arrow is due to the variation in $K_{th,eff}$. This may explain local deviation in da/dN data from expected log-linear relationship. Note that extrinsic component of ΔK_{th} is ignored *in these computations*

$\Delta K_{\text{th,i}}$ is computed as a dependent variable of ΔK_{eff} and associated $K_{\max}$ from the $\Delta K_{\text{th,i}}$ *versus* σ^* relationships as shown in Fig. 1. Under constant amplitude loading, the computed value of $\Delta K_{\text{th,i}}$ will be valid for a given stress ratio and known crack closure. Under near threshold conditions defined by the condition: $\Delta K_{\text{eff}} < \Delta K^*_{eff}$, crack growth rate will be influenced by $K_{\text{th,eff}}$. At $\Delta K_{\text{eff}} \geq \Delta K^*_{eff}$, $K_{\text{th,eff}} = 0$, i.e. at the other end, as $K_{\max}$ approaches K_c, increasing contribution of quasi-static component from local fracture by micro-void coalescence, strain localization across brittle constituents, etc. will accelerate growth. An equation that describes this entire range of growth rate may be assumed to take the form:

$$\frac{da}{dN} = C\left[\Delta K_{eff} - K_{th,eff}\right]^m \frac{1}{\left(1 - \frac{K_{max}}{K_c}\right)^q}, \Delta K_{eff} < \Delta K^*_{eff} \tag{5}$$

$$\frac{da}{dN} = C\left[\Delta K_{eff}\right]^m \frac{1}{\left(1 - \frac{K_{max}}{K_c}\right)^q}, \Delta K_{eff} \geq \Delta K^*_{eff} \tag{6}$$

where, K_c is the fracture toughness and q is a constant assumed for brevity to be unity. The correction of da/dN to account for $K_{\max} \rightarrow K_c$ is the same as that adopted widely in the literature. Equation (6) is essentially the same as (5) with the exception that $K_{\text{th,eff}} = 0$.

Note that (5) is limited to da/d$N \geq 10^{-7}$ mm/cycle. As engineering practice constantly pushes the demands on durability and residual crack growth life to higher cycle counts, $\Delta K_{\text{th,i}}$ will arguably also require reconsideration in terms of associated da/dN. For engineering purposes, one may extend $\Delta K_{\text{th,i}}$ at 10^{-7} down to 10^{-9} mm/cycle by correction of its value given the slope of da/dN curve at 10^{-7} mm/cycle.

We now proceed to summarise the procedure to determine the material constants in (5).

5 Material Constants and Validation

Obviously, a number of material constants are involved in forming an equation that attempts to describe variation of crack growth rate over seven orders of magnitude. Particularly so, when the 'origin' of the da/dN curve corresponding to threshold da/dN of 10^{-7} mm/cycle is itself highly sensitive to $\sigma^*.\sigma^*$ in turn is determined using constants that describe the cyclic stress-strain curve. Near-threshold crack growth rates will depend on $\Delta K_{\text{th,i}}$ as well as the emerging dominance of the Paris regime parameters C and m. Finally, the addition of quasi-static component from the proximity of fracture will accelerate growth rate as $K_{\max}$ approaches K_c.

Computation of near-tip stress response leading to the characterization of the $\Delta K_{\text{th,i}}$ *versus* σ^* relationship requires constants defining the cyclic stress-strain curve

of the material, namely, Young's modulus, E, cyclic strength coefficient, K', and cyclic strain hardening exponent, n' (see Fig. 2).

A realistic evaluation of the new framework involves an attempt to correlate experimental data over the entire range of associated crack growth rates, i.e., from 10^{-7} to 10^{-1} mm/cycle. Such a correlation can be assessed by plotting data in the log-log scale as $\frac{da}{dN}\left(1-\frac{K_{max}}{K_c}\right)$ against $\Delta K_{eff}-K_{th,eff}$. A good fit would be indicated by a linear fit with slope, m, and intercept C.

Experimental data obtained on Ti-6Al-4 V in the course of this data were consolidated using the above framework. All the required tests were performed at BISS Labs on a BISS 25 kN high performance servo-hydraulic test system permitting test frequency of up to 250 Hz. The tests were performed on 5 mm thick, 50 mm wide C(T) specimens, with test frequency set to 100 Hz to ensure amplitude error less than 1%. Two of the specimens were tested to determine $\Delta K_{\text{th,i}}$ values under a wide range of σ^*. The crack growth curves from these tests appear as Fig. 5.

The test procedure to characterize the $\Delta K_{\text{th,i}}$ versus σ^* relationship is described in detail elsewhere [18, 19, 27]. The sets of transient data covering a reasonably wide range of growth rate are consolidated as da/dN *versus* ΔK in Fig. 6. Given the nature of the transients involving cycling at $P_{\max}$ = const and steadily increasing $P_{\min}$ to impose receding ΔK, the stress ratio associated with individual data points invariably increases with reducing crack growth rate, reaching up to values in excess of $R = 0.8$. Also shown in Fig. 6 are data from a single constant amplitude test performed at stress ratio $R = 0.3$ and assumed to involve little or no crack closure. For the same reason, ΔK may be treated as ΔK_{eff} for these data.

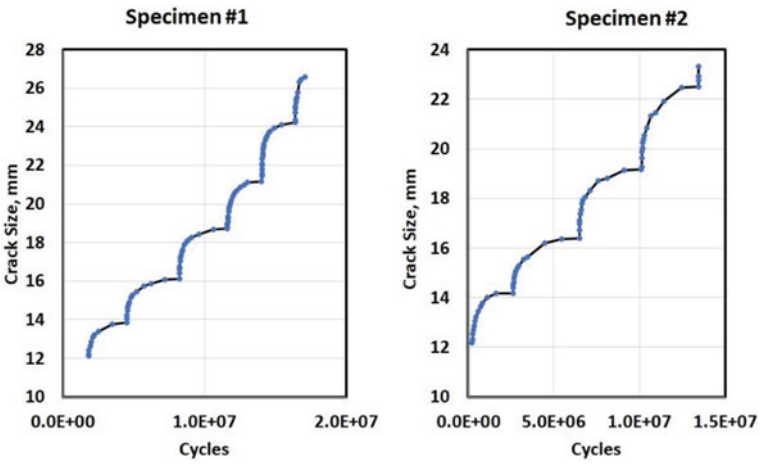

Fig. 5 Crack growth curves registered during tests on two specimens to characterize $\Delta K_{\text{th,i}}$ as a function of σ^*. Each segment on the curve corresponds to a regime of receding ΔK with $P_{\max}$ = const and possible periodic overload/underload sequence to 'set' required σ^*. Transient crack growth rate points from these curves appear as circles in Fig. 6

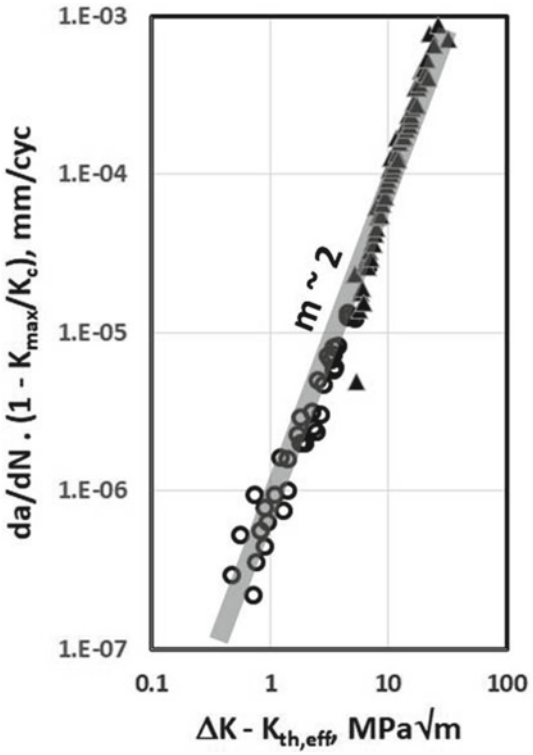

Fig. 6 Crack growth rate data from a single test on Ti-6Al-4 V at $R = 0.3$ (triangles) plotted along with transient da/dN data (circles) from the threshold tests to characterize $\Delta K_{\text{th,i}}$ *versus* σ^*; closure at $R = 0.3$ was ignored, as was in the transient data points all of which occurred at $R > 0.5$

The data in Fig. 6 are plotted as $\frac{da}{dN}\left(1 - \frac{K_{max}}{K_c}\right)$ against $\Delta K - K_{th,eff}$. Also shown in the figure is a trend line suggesting a slope $m = 2$ over the data range.

6 Discussion

The discovery of crack closure was a turning point in understanding stress ratio and load interaction effects in fatigue crack growth. Establishment of the unique relationship between $\Delta K_{\text{th,i}}$ and σ^* may serve as the next turning point by explaining why significant load interaction effects will persist even in the absence of crack closure, and why, the significance of these effects increases disproportionately into near-threshold fatigue, that dominates in the HCF and VHCF domains.

By drawing the line between propagating and non-propagating cracks, thresholds effectively determine fatigue limit. In doing so, the new understanding also provides a fundamental explanation as to why fatigue limit diminishes with mean stress, a phenomenon known (albeit unexplained) for more than 150 years from the pioneering work of Wöhler and Bauschinger [34].

The new procedure to determine the relationship between $\Delta K_{th,i}$ and σ^* suggests more conservative estimates of $\Delta K_{th,i}$ than would follow from conventional testing practice. To cite an example of consequences for engineering application to naturally forming cracks, given the estimates obtained on Ti-6Al-4 V, it would follow that the potential minimum size of cracks that can propagate at a given applied stress level would be less than half the size expected from the lowest ΔK_{th} estimates from conventional testing practice. This, given the square root dependence of K on crack size.

The $\Delta K_{th,i}$ *versus* σ^* relationship appears to lay to rest misunderstandings caused by prevailing testing practices to characterize fatigue thresholds, that resulted in attempts to relate ΔK_{th} to K_{max}, R-ratio, etc.,. Obviously, given a certain partial pressure of active species and rate of loading, the degree of BMF in a single rising load half cycle would be determined by the extent of their surface diffusion. The associated diffusion kinetics at a given temperature will be moderated by a certain instantaneous near-tip hydrostatic or biaxial stress as it increases from that, at the commencement of the rising load half cycle, i.e., from σ^*. For this reason, $\Delta K_{th,i}$ correlates with near-tip stress at the commencement of the rising half of the load cycle, rather than at K_{max}. Strictly speaking, this stress should not be referred to as 'residual' because by 'residual' one would imply stress at no load. However, the two would be synonymous, if $K_{min} \leq K_{op}$, as near-tip stress response can be assumed to cease below K_{op}.

It has for long been wrongly assumed, that by accounting for crack closure and other shielding effects, laboratory constant amplitude crack growth rate data can be extended to variable-amplitude loading. While closure does indeed go a long way in bridging the gap, its ability to do so becomes increasingly diluted in the near-threshold region leading down to threshold. This gap extends to a three order of magnitude variation in crack growth rate, where instantaneous $\Delta K_{th,i}$ comes into play. Closure can at best account for the extrinsic component of ΔK_{th}. The intrinsic component is uniquely related to near-tip residual stress, a parameter that like closure, is also sensitive to crack tip mechanics, but in ways that are very different from crack closure. Unlike crack closure, near-tip residual stress is cycle-sequence sensitive. Unlike crack closure, it can exhibit cycle-to-cycle bi-directional variation and do so, even without requiring crack extension. While crack closure is largely wake driven, near-tip stress variation requires an open crack.

The form of the modified (5) for da/dN accounts for the manner in which growth rate transits from threshold into the Paris regime. Further, the relationship between $\Delta K_{th,i}$ and σ^* combined with the treatment of $\Delta K_{th,i}$ as a cycle-sequence sensitive variable in the equation opens up the possibility of modeling variable-amplitude fatigue from its very early stages. Thus, variable-amplitude fatigue crack growth can be modeled as a consequence of the combined action of crack closure and crack-tip blunting on the one hand and on the other, by the effect of these on σ^* on a cycle-by-cycle basis. Such a 'tri mechanism' or 'TriM' model was successfully applied to model residual crack propagation lives in the range from 5 to 20 million cycles for 2024-T3 alloy under an extended duration transport aircraft load spectrum [35]. A fractographic study of the failures obtained revealed significant load sequence

sensitive variations in fatigue crack extension during the large fraction of smaller load cycles. These were adequately modeled by correcting $\Delta K_{th,i}$ over these cycles as a function of load history. There are hardly any data in the literature reflecting attempts to model residual life, exceeding even a million cycles, suggesting limitations posed by the lack of threshold data suitable for engineering application.

Unlike closure that develops early and persists throughout the crack growth process and is rather independent of the mechanisms that drive crack extension, intrinsic threshold fades into vanishing proportions as da/dN exceeds 10^{-4} mm/cycle. For this reason, both load interaction effects as well as environment related effects affected by $\Delta K_{th,i}$ will fade away with increasing growth rate. The latter was clearly brought out in early experiments by Bradshaw and Wheeler on the influence of test frequency and partial pressure of moisture on crack growth rates [36]. These highlighted the increasing effect of both test frequency and partial pressure of moisture with decreasing crack growth rate. It follows that if growth rates below the Paris regime are involved, prevailing approaches to laboratory data generation and modeling are limited in their ability to come up with residual life estimates of value to engineering practice. Moreover, given the vast difference in the physics behind crack closure and near threshold response, one cannot hope to 'fudge' the effect of the latter through distorted simulation of the former.

Load interaction effects have also been modeled by simulating mean stress variation in the cyclic plastic zone using a cumulative damage approach [37]. However, such an approach, just as also, the two-parameter approach [14] do not focus on the phenomenon in question, namely, the influence of near-tip stress on threshold response. They are faulted in wrongly assuming that the effect persists across the entire range of growth rates.

Most of fatigue life is exhausted in the early stages of fatigue crack growth. As nondestructive inspection technologies improve, smaller fatigue cracks can be detected to permit increased service life between inspections. The potential for induction of additive manufactured components in safety critical applications can benefit greatly from the ability to estimate the residual life assuming pre-existing defects associated with the 3D printing process. All these imply a rising demand for capability to estimate residual crack growth life in the HCF and VHCF regimes. Obviously, this is less likely to materialize without the ability to model $\Delta K_{th,i}$ variation along with other load interaction mechanisms such as closure. Analytical modeling of $\Delta K_{th,i}$ under variable-amplitude loading, combined with that of crack closure appears to be a potentially rewarding area of future research.

Discovery of the close connection between near-threshold fatigue crack growth behavior and near-tip residual stress raises new questions and opens new avenues in fatigue research of direct application value. An important new avenue of fundamental research is the search for an analytical connection between partial pressure of active species such as moisture in air and oxygen at high temperature, rate of loading (or frequency) and the relationship between $\Delta K_{th,i}$ and σ^*. One would expect a lateral shift in this relationship, whose model would significantly reduce the cost of future testing effort. An even more significant impact of engineering value would be the

development of engineered materials with improved resistance to surface diffusion of active species.

The new findings are also likely to impact a new interpretation of near-threshold region of sustained load cracking. Thus, it is likely that if service loading involves hold-time at an intermediate load level, one would have to consider the hysteretic variation in near-tip stress depending on whether such hold time occurs on the rising or falling half of a major load cycle.

From the standpoint of immediate application, an important question relates to the definition of r^*. In previous work, the goal was to select a value that provides the best correlation between $\Delta K_{th,i}$ and σ^*. It is not clear whether r^* thus selected will also deliver the best estimates of variable amplitude fatigue crack growth life, when cycle-by-cycle correction of $\Delta K_{th,i}$ is resorted to as a function of σ^*, computed at a given r^* for a given service load sequence. Another relates to the choice of cyclic-stress strain curve. K' and n' in this study were based on tests on smooth specimens. However, they are applied to a point ahead of the crack tip that is likely to see the effect of constraint, where K' and n' are likely to be different. Strictly speaking, r^* should be zero. However, analysis treats the crack tip to be a singularity, that in itself, is an approximation. Notwithstanding this contradiction, the consistent and reproducible relationship between $\Delta K_{th,i}$ and σ^*, seen in all the materials that were tested testifies to its uniqueness and reproducibility. It also suggests the apparent irrelevance of K_{max} and stress ratio that have served testing practice for all these years.

Finally, naturally forming small cracks will be sensitive to local phenomena as induced by microstructure such as grain size, grain boundary orientation and local mechanical property variations [38], that go beyond the scope of this study. The important question is whether such cracks will grow, or, get arrested. It now emerges, that in atmospheric fatigue, in addition to the three threshold states highlighted by Miller, instantaneous K_{th} as affected by loading conditions including load history plays a major role in controlling the fate of naturally forming small cracks that eventually determines durability.

7 Conclusions

(1). $\Delta K_{th,i}$, the intrinsic component of ΔK_{th}, is sensitive to a certain, computable, near-tip residual stress, σ^*, whose variation can be analytically described for a given load history, based on a material's cyclic-stress strain response. This enables accounting for significant load history effect on K_{th}, that hitherto appears to have been wrongly considered to be a material constant.

(2). Experiments on Ti-6Al-4 V test coupons show variations in K_{th} between 1.25 and 4.3 MPa·m$^{1/2}$, in what appears to be a unique relationship with σ^*. This trend and nature of relationship is similar to that, observed on several other materials that showed a variation up to a factor of five.

(3). An equation is proposed for crack growth rate that accounts for variations in $\Delta K_{th,i}$ in the transient region between threshold and the Paris regime. This equation appears to show good correlation of near-threshold crack growth rates obtained from tests on Ti-6Al-4 V test specimens. It can be used to account for effects of both load ratio as well as load history in engineering estimates of residual fatigue life extended into the HCF and VHCF regimes.

(4). The unique relationship between $\Delta K_{th,i}$ and σ^* appears to represent a scientific explanation for the residual stress effect on naturally forming small cracks growing in the absence of closure.

Acknowledgements The author is grateful to Air Force Research Laboratories (AFRL), WPAFB-OH, USA and University of Dayton, for the provision of Ti-6Al-4V C(T) test specimens. The tests were carefully performed by Meghanathan.

References

1. ASTM E647–15e1, *Standard Test Method for Measurement of Fatigue Crack Growth Rates* (ASTM International, West Conshohocken, PA, 2015). www.astm.org
2. W. Elber, in *Damage Tolerance in Aircraft Structures, ASTM STP 486* (ASTM International, West Conshohocken, PA, 1971), p. 230
3. R.O. Ritchie, D.L. Davidson, B.L. Boyce, J.P. Campbell, O. Roder, Fatigue Fract. Eng. Mater. Struct. **22**, 621 (1999)
4. A.K. Vasudevan, S. Suresh, Metall. Mater. Trans. A. **13**, 2271 (1982)
5. S. Suresh, G.F. Zamiski, R.O. Ritchie, Metall. Trans. A **12**, 1435 (1981)
6. J.C. Newman, J. Schneider, A. Daniel, D. McKnight, Int. J. Fatigue **27**, 1432 (2005)
7. J.C. Newman, Y. Yamada, Int. J. Fatigue **32**, 879 (2010)
8. S.W. Smith, B. R. Seshadri, J.A. Newman, in *15th International Symposium on ASTM/ESIS Symposium on Fatigue and Fracture Mechanics*, May 20–22, 2015, Anaheim, CA (2015)
9. K. Tanaka, Y. Akiniwa, Eng. Fract. Mech. **30**(6), 863 (1988)
10. J. Maierhofer, S. Kolitsch, R. Pippan, H. Gänser, M. Madia, U. Zerbst, Eng. Fract. Mech. **198**, 45 (2018)
11. L. Lawson, E.Y. Chen, M. Meshii, Int. J. Fatigue **21**, S15 (1999)
12. D.A. Taylor, *Compendium of Fatigue Thresholds and Growth Rates* (Engineering Materials Advisory Services Ltd., West Midlands, UK, 1985)
13. B.L. Boyce, R.O. Ritchie, Eng. Fract. Mech. **68**, 129 (2001)
14. A.K. Vasudevan, K. Sadananda, N. Louat, Scr. Metall. **28**, 65 (1993)
15. K.J. Miller, Int J. Fatigue **23**, S277 (2001)
16. A.K. Vasudevan, K. Sadananda, N. Louat, Mater. Sci. Eng. **A188**, 1 (1994)
17. A.K. Vasudevan, K. Sadananda, Int. J. Fatigue **21**, S263 (1999)
18. R. Sunder, Mater. Perform. Charact. (An ASTM J.) **4**(2), 105 (2015)
19. R. Sunder, R. Koraddi, C. Vishwas, Mater. Perform. Charact. J. Am. Soc. Test. Mater. (2020). https://doi.org/10.1520/MPC20190223
20. R. Sunder, Int J. Fatigue **27**, 1494 (2005)
21. R. Sunder, W.J. Porter, N.E. Ashbaugh, Fatigue Fract. Eng. Mater. Struct. **26**, 1 (2003)
22. N.E. Ashbaugh, W.J. Porter, A.H. Rosenberger, R. Sunder, in *Proceedings of the Fatigue 2002*, Stockholm, June 2–7, EMAS (2002)
23. R. Sunder, Fatigue Fract. Eng. Mater. Struct. **28**(3), 289 (2005)

24. Y. Ro, S.R. Agnew, R.P. Gangloff, Metall. Mater. Trans. **A39A**, 1449 (2008)
25. Y. Murakami, T. Kanezaki, Y. Mine, S. Matsuoka, Metall. Mater. Trans. A. **39**, 1327 (2008)
26. R. Sunder, J. ASTM Int. **9**(1), JAI103940 (2012). ASTM Special Technical Publication. **1546**, 20 (2012)
27. R. Sunder, R. Koraddi, A. Gorunov, in *Structural Integrity of Additive Manufactured Materials and Parts*, ed. by N. Shamsaei, M. Seifi (ASTM International, West Conshohocken, PA, 2020), p. 188
28. O.E. Wheeler, ASME J. Basic Eng. **94**, 181 (1972)
29. J. Willenborg, R.H. Engle, H.A. Wood, Report No. AFFDL-TM-71-1 FBR, WPAFB, OH (1971)
30. M.R. Hill, J.E. Van Dalen, M.B. Prime, Press. Vessel. Pip. Div. **6**, 251 (2011)
31. A. Diana, D.A., Lados, D. Apelian, J. Keith Donald, Int. J. Fatigue **29**, 687 (2007)
32. C.Q. Bowles, Report No. LR-270, Delft Univ. of Technology, Delft, The Netherlands (1978)
33. J. Petit, G. Henaff, C. Sarrazin-Baudoux, ASTM Spec. Tech. **1372**. American Society for Testing and Materials, West Conshohocken, PA (2000)
34. A. Anon, Engineering **4**, 160 (1867)
35. R. Sunder, in *Lecture Notes in Mechanical Engineering*, ed. by R.V. Prakash et al. (Eds.) (Springer Nature Singapore, Singapore, 2020). https://doi.org/10.1007/978-981-13-8767-8_1
36. F.J. Bradshaw, C. Wheeler, Int. J. Fract. Mech. **6**, 255 (1969)
37. S. Mikheevsky, G. Glinka, Int. J. Fatigue **31**, 1828 (2009)
38. K.J. Miller, ASTM STP 1296 Am. Soc. Test. Mater. **267** (1997)

Effect of Pitch Difference and Root Radius on Anti-Loosening Performance of Bolt Nut Connections

Ryo Kawano, Biao Wang, Nao-Aki Noda, Yoshikazu Sano, Xi Liu, Yuto Inui, and Bei -fen Siew

Abstract Bolt nut connections are widely used in the industry. To ensure the safety of structures, both good anti-loosening performance and high fatigue are needed. In previous studies, it has been proven that by enlarging the root radii of bolt nut connections or introducing a pitch difference between the bolt and the nut, the fatigue life can be improved significantly. Based on this, in this study, the anti-loosening performance of the root enlarged bolt nut connections are studied. The prevailing torque and the loosening process of M16 bolt nut connections are simulated by FEM analysis. It is found that even though the anti-loosening performance of the bolt nut connections decreases, introducing suitable pitch differences improves the anti-loosening performance compared to a common bolt nut connection.

Keywords Anti-loosening performance · Root radius · Pitch difference · Prevailing torque

1 Introduction

Bolt nut connections are one of the essential elements used in the industry. When subjected to impacts or dynamic loads, fatigue failure or self-loosening of bolted joints may happen and even leading to a disaster. The fatigue life of bolted joints can be improved by changing materials, using different manufacturing methods or special after effect to deal with the bolts and nuts, or changing the geometry of the threads [1–5]. There are many pieces of research on the anti-loosening of bolted joints. Prevailing torque is a commonly used method to prevent self-loosening of bolted joints. Nylon inserted nuts can generate a prevailing torque to resist loosening, but shows little loosening resistance after several repetitive usages [6]. Table 1 shows the prevailing torques of different anti-loosening nuts that can be obtained from the

R. Kawano (✉) · B. Wang · N.-A. Noda · Y. Sano · X. Liu · Y. Inui · B. . Siew
Mechanical Engineering Department, Kyusyu Institute of Technology, 1-1 Sensuicho, Tobata, Kitakyushu, Fukuoka 804-8550, Japan
e-mail: kawano.ryo621@mail.kyoutech.jp

I. A. Parinov et al. (eds.), *Physics and Mechanics of New Materials and Their Applications*, Springer Proceedings in Materials 10,
https://doi.org/10.1007/978-3-030-76481-4_31

Table 1 Prevailing torque of different M16 anti-loosening nuts from different companies

Nut type	Prevailing torque (N·m)	
	Screwing in	Screwing out
U-Nut (Fuji Seimitsu Co., Ltd)	3.0	1.5
Precision Lock Nut (Nikki Trading Corp.)	6.0	4.5
V-Nut (COMWELL Fujisawa Co., Ltd.)	2.8	1.5
Nylon nut (NISHI SEIKO Co., Ltd)	16.0	4.5
flange nut (Osaka Forming Co., Ltd)	9.6	4.5

market. Wakabayashi designed a nut pair named Hard Lock, which has witnessed the success of Japan Shinkansen for several decades [7].

To ensure the safety of structures under complex working environment, both good anti-loosening performance and high fatigue strength are needed. However, there are few pieces of research on improving fatigue strength and anti-loosening performance at the same time. In the authors' previous studies, it has been found that when introducing a pitch difference between the bolt and the nut, both fatigue life and anti-loosening performance were improved [8–10].

In this study, based on the previous researches on pitch difference, the effect of root radius on pitch difference bolt nut connections is studied. When increasing the root radii of bolt nut connections, the stress concentration factor will reduce. Thus, fatigue life and fatigue strength can be improved. Moreover, the anti-loosening performance can also be expected according to the FEM analysis.

2 Fatigue Experiments and Analysis

2.1 Specimen

For a common high strength Japanese Industrial Standards (JIS B1181 1xd), the height of the M16 nut is 16 mm. In this study, the height of the nuts is 16 mm. Figure 1 shows the sketch of an M16 bolt nut connection used in this study. For a common coarse thread bolt nut connection, both the pitch of the bolt and the nut are 2000 μm. The clearance between the thread of the bolt and the nut in the axial direction is 72 μm. In this study, to obtain a better anti-loosening performance and higher fatigue life of the bolt nut connections, the pitch of the nut is α larger than that of the bolt. In this study, the pitch difference α is chosen as 0, 15, and 33 μm. Owing to the existence of chamfer at two ends of the nut, the outer sides thread of the nut does not contact with the bolt.

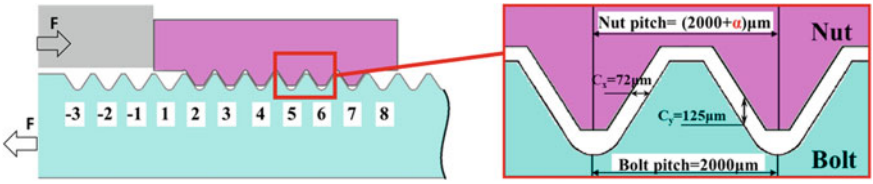

Fig. 1 Schematic illustration for a bolt nut connection

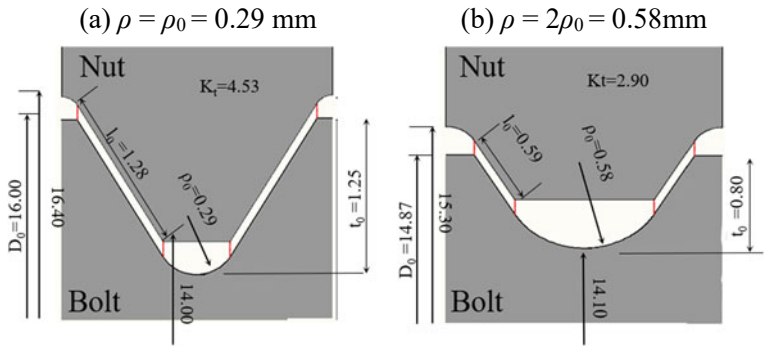

Fig. 2 Schematic illustration for special bolt nut connections having pitch difference

For a common JIS M16 bolt, the bolt root radius is $\rho_0 = 0.29$ mm. Previous studies have proven that fatigue strength can be enhanced by decrease of stress concentration [9, 11]. Therefore, the fatigue limit of a bolt nut connection can be improved by enlarging the root radius of the bolt. Two kinds of bolt root radii $\rho = \rho_0 = 0.29$ mm, $\rho = 2\rho_0 = 0.58$ mm, as shown in Fig. 2, are introduced in this study. To examine the improvement of fatigue strength with respect to ordinary bolts and nuts, here we consider the stress concentration factor Kt of a round bar with a circumferential 60° notch since detailed studies are available [12, 13]. When enlarging the root radius from $\rho = \rho_0$ to $\rho = 2\rho_0$, the stress concentration factor will reduce significantly, from Kt = 4.53 ($\rho = \rho_0$) to Kt = 2.90 ($\rho = 2\rho_0$).

2.2 *Fatigue Experimental Results and FEM Analytical Results*

The materials used for the bolt and the nut are SCM435 and S45C, respectively, and the stress–strain relationships for the two materials are shown in Table 2. A 40-ton servo fatigue testing machine is used in this test, and the frequency of the loading is 10 Hz. The fatigue limit was set at repetitive stress of 2×106 cycles. In the fatigue

Table 2 Material properties of bolt and nut

	Elastic modulus (GPa)	Poisson's ratio	Yield strength (MPa)	Tensile strength (MPa)
SCM435 (Bolt)	206	0.3	800	1200
S45C (Nut)	206	0.3	530	980

experiments, the mean load along the axial direction was set as 30 kN, and the stress amplitude was set from 8.5 to 22.6 kN.

From Fig. 3, it can be seen that the fatigue life for bolt nut connections increases with the increasing of pitch difference and then decrease. It should be noted that, for M16, even the fatigue life of $\alpha = 33$ μm is shorter compared to that of when $\alpha = 15$ μm, it is still much longer than the common bolt connections.

Figure 4 shows the S–N curve for common bolt nut connections and bolt nut connections with enlarged root radius and pitch difference.

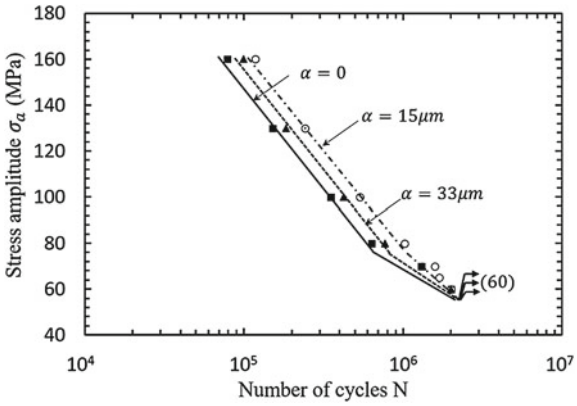

Fig. 3 S–N curve for the bolt-nut with the pitch difference of $\alpha = 0$ μm, $\alpha = 15$ μm, and $\alpha = 33$ μm, when the radius of the roots $\rho = \rho_0$

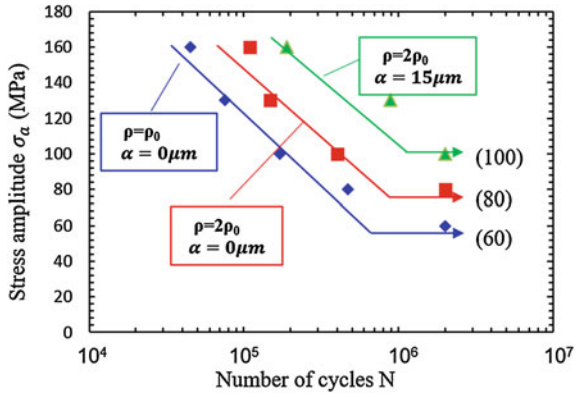

Fig. 4 S–N curve for different bolt root radii and pitch differences

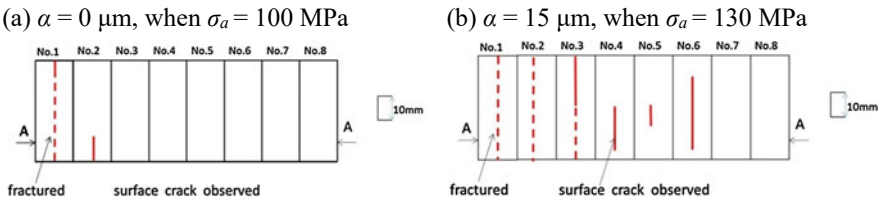

Fig. 5 Crack position observed from the surface of the specimen

As it can be seen from Fig. 4, when the root radius of the bolt is $2\rho_0$, the fatigue life of the bolt is about 2.2 times longer than of a normal bolt. Meanwhile, the fatigue limit of the bolt is increased by 30% from 60 to 80 MPa. In the case of $\rho = 2\rho_0$, the fatigue life of the bolt joints with a pitch difference of $\alpha = 15$ μm is about 2.4 times longer than of bolt joints without pitch difference. Moreover, when $\alpha = 15$ μm, the fatigue limit reaches about 100 MPa, and it has been improved by 30% with respect to $\alpha = 0$ μm. The fatigue life and fatigue limit at $\alpha = 15$ μm, $\rho = 2\rho_0$ are 2.2 times and 65% higher than those at $\alpha = 0$ μm, $\rho = \rho_0$, respectively.

Figure 5 shows the crack locations under the stress amplitude of 100 MPa when $\alpha = 0$ μm and under the stress amplitude 130 MPa, when $\alpha = 15$ μm. From Fig. 5a, cracks can be seen only at No. 1 and No. 2 threads since the pitch difference do not exist. From Fig. 5b, the final fracture can be seen at No. 2 and No. 3 threads also when $\alpha = 15$ μm. However, the cracks also can be seen between No. 3 and No. 6 threads due to the pitch difference. The pitch difference causes higher stress at both ends of the bolt, and the maximum stress appears at No. 6 thread. Therefore, crack occurs at No. 6 thread first, then crack occurs from right to left one by one, and final fracture occurs between No. 2 and No. 3 thread as explained in [14].

To figure out the reason for the crack differences for the bolt nut connections with and without pitch differences, the stresses at the bolt roots are analyzed by FE analysis. The boundary conditions are shown in Fig. 1, the left side of the clamped body is fixed, and the bolt head subjects to an axial tensile load F. The stresses of the bolt roots were simulated by elastoplastic analysis, using the FEM axis-symmetric model. When cyclic axial force F = 30 ± 14.1 kN, the corresponding mean stress and stress amplitude at the bolt roots are 213 MPa and 100 MPa, respectively. The simulation results are shown in the form of a durability diagram.

Figure 6 shows the stress amplitude and mean stress at each root of the bolt with different root radii. From Fig. 6a, it can be seen that when there is no pitch difference, the maximum mean stress and stress amplitude occurs at the No. 2 root, and this coincides with the experimental result as shown in Fig. 5a. Moreover, by increasing the bolt root radius, the stress amplitude decreases significantly at each root, and the stress amplitude at No. 2 root at $\rho = 2\rho_0$ is 30% smaller than that of $\rho = \rho_0$. Figure 6b shows the simulation results under different root radius with a pitch difference of $\alpha = 15$ μm. It can be seen that when there is a pitch difference between the bolt and nut, the maximum stress amplitude and the maximum mean stress occurs at the root of No. 6 and No. 7 thread, respectively, rather than occurs at the root of the

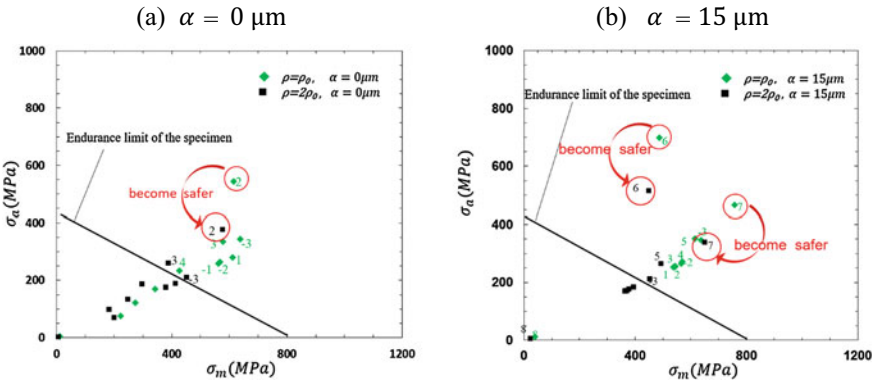

Fig. 6 Endurance limit diagram for different root radii and pitch difference

No. 2 thread. By comparing the results with the cracks in the experiment in Fig. 5b, it can be seen that the simulation results are in good agreement with the experimental results. Therefore, it can be assumed that the first crack occurs at No. 6 threads, then the crack happens from right to left one by one, and the failure happens between No. 2 and No. 3 thread eventually. Moreover, the mean stresses and the stress amplitudes at No. 6 thread and No. 7 thread decreased significantly as well when increasing the root radii from $\rho = \rho_0$ to $\rho = 2\rho_0$.

3 Loosening Experiment

3.1 Prevailing Torque

For a common bolt nut connection, the pitch of the bolt and the nut is the same, which means before the nut contacts the clamped body, there will no inner force occur between the bolt and the nut. However, with increasing the pitch difference of a bolt nut connection, a torque will occur before the nut contact with the clamped body. The torque is the so-called prevailing torque T_p, which is commonly used for anti-loosening [15].

3.2 Loosening Experiment Results

The loosening experimental device used is based on NAS3350 (National Aerospace Standard). The bolt nut connection is subjected to a transverse loading, which is perpendicular to the bolt axis loosening experiment. The frequency of the load is 30 Hz. If the vibration cycles are over 30,000, which is the specified life of the bolt

Table 3 Position, where prevailing torque occurs, and the contacted number between the nut and the bolt

Pitch difference, α	Sample	Whether the nut drops or not?	Cycles for dropping	Cycles for start loosening	Prevailing torque (N·m)	Axial force (kN)
0	No. 1	Yes	751	–	0	24
	No. 2		876	–		
15	No. 3		813	–	0	24
	No. 4		1,528	–		
33	No. 5	No	30,000	21,000	30	20
	No. 6		30,000	30,000		

nut connection, one can think the anti-loosening performance of the connection is good enough. Therefore, the experiments stop at a loading cycle of 30,000 if the nut does not drop. For all the bolt nut connections, the nuts are tightened under the same torque of 70 N·m. The experimental results are shown in Table 3.

From the results, we can see that when the pitch difference is 0 or 15 μm, the nut drops while the vibration numbers are nearly 1000 cycles. That is to say, when increasing the pitch difference from 0 to15 μm, for which pitch difference, there will be no prevailing torque in the tightening process, the loosening performance of the bolt nut connection almost remains the same. However, for $\alpha = 33$ μm, the nut does not drop before 30,000 cycles of vibration. Meanwhile, the axial force decreases from 24 to 20 kN, which means the clamping ability decreased by about 16.7%, which is acceptable for the actual application. When the pitch difference reaches a value, a prevailing torque will occur in the tightening process; along with the increase of the pitch difference, the axial force will decrease. Therefore, considering both anti-loosening performance and clamping ability, $\alpha = 33$ μm can be regarded as the most suitable pitch difference for anti-loosening.

3.3 FEM Results of the Anti-loosening Analysis

In the loosening experiments mentioned above, the transverse load changes over time. Thus, it is hard to simulate this loosening process. The Junker test is the commonly used method to evaluate the anti-loosening performances of threaded fasteners. In this paper, a simplified Junker test FE model shown in Fig. 7 is used to evaluate the anti-loosening performance of root radius enlarged bolt nut connection with and without pitch differencesV.

The material of the moveable plate is set as SCM435 in this analysis. The bolt head is fixed, and the surface at the bolt head side of the moveable plate cannot move in the axial direction; the cyclic displacement is±0.4 mm. When using MoS2 as the oil lubrication, the under-head coefficient μ_w between the moveable plate and

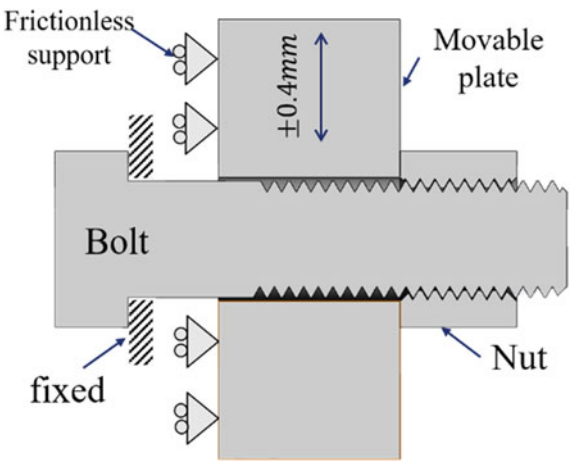

Fig. 7 Sketch of Junker loosening test model

the nut is between 0.16 and 0.18, and the thread friction coefficient μ_s is between 0.11 and 0.14 [16]. In this simulation, the under-head coefficient μ_w and the thread friction coefficient μ_s are set as $\mu_w = 0.17$ and$\mu_s = 0.12$, respectively. Bilinear elastic–plastic stress–strain relations are applied instead of multi-linear relations to save the calculation time. The Newton–Raphson approach is used to solve nonlinear problems. The elements number and the nodes number for $\rho = \rho_0$, $\alpha = 0$ μm are about 2.6 × 104 and 8.4 × 104, respectively. In these FE analyses, the nuts are tightened to 25% of the yield load of$F = F_{25\%}$; thus, the tightening clamp load is 28.8 kN. The prevailing torque for $\rho = \rho_0$, $\alpha = 33$ μm and $\rho = 2\rho_0$, $\alpha = 33$ μm are 39.1 N·m and 19.3 N·m, respectively.

From Fig. 8, it can be seen that for $\rho = \rho_0$, $\alpha = 0$ μm; $\rho = \rho_0$, $\alpha = 33$ μm; $\rho = 2\rho_0$, $\alpha = 0$ μm and $\rho = 2\rho_0$, $\alpha = 33$ μm, the average residual clamp load is 42.5%, 93.3%, 29.8%, and 71.7%, respectively. The residual clamp load for $\rho = \rho_0$, $\alpha = 0$ μm is 12.2% larger than that of $\rho = 2\rho_0$, $\alpha = 0$ μm, compared to the initial clamp load, this indicates that the anti-loosening performance for the bolt nut connections will decrease, when increasing the root radius from $\rho = \rho_0$ to $\rho = 2\rho_0$. The residual clamp load for $\rho = 2\rho_0$, $\alpha = 0$ μm is 41.9% smaller than that of $\rho = 2\rho_0$, $\alpha = 33$ μm, compared to the initial clamp load, this indicates that the anti-loosening performance for the bolt nut connections can be increased, when introducing a pitch difference of $\alpha = 33$ μm between the bolt and the nut.

Moreover, the residual clamp load for $\rho = 2\rho_0$, $\alpha = 33$ μm is 29.2% larger than that of $\rho = \rho_0$, $\alpha = 0$ μm, compared to the initial clamp load. Thus, we can make a conclusion that the anti-loosening performance of the bolt nut connections could be increased by introducing a large pitch difference between the bolt and the nut even the root radius is enlarged at the same time.

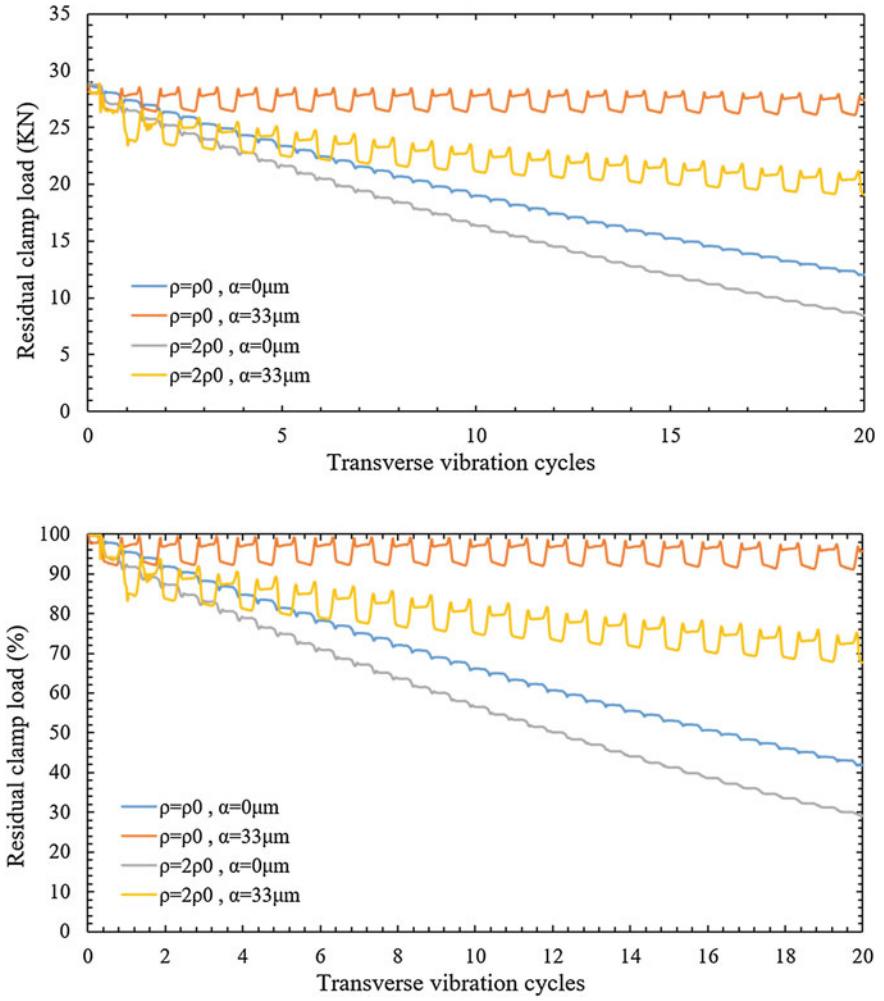

Fig. 8 Residual clamp load and its percentage after 20 cycles of vibration

4 Conclusions

In this study, the influence of the pitch difference on anti-loosening performance and fatigue life and the bolt root radius on fatigue life are analyzed by experiments and FEM analysis. Three kinds of pitch differences and bolt root radii for M16 bolt nut connections are used in this study. The conclusions can be summarized as follows:

(1) For M16 bolt nut connections, both fatigue life and anti-loosening performance can be improved by increasing the root radius from $\rho = \rho_0$ to $\rho = 2\rho_0$ and introducing a pitch difference of $\alpha = 33$ μm, between the bolt and the nut.

(2) The fatigue life can be improved by introducing a pitch difference between the bolt and the nut. Moreover, both the fatigue and fatigue limit can be improved by enlarging the root radius. The fatigue life and fatigue limit at $\alpha = 15$ μm, $\rho = 2\rho_0$ are 2.2 times longer and 65% higher than those at $\alpha = 0$ μm, $\rho = \rho_0$, respectively.
(3) When the pitch difference is large enough, a prevailing torque will occur, and the anti-loosening performance becomes quite good, when the pitch difference is large.

References

1. A.I. Yakushev. Effect of Manufacturing Technology and Basic Thread Parameters on the Strength of Threaded Connections. Department of Scientific and Industrial Research by Pergamon (1964)
2. K. Maruyama, Trans. Japan Soc. Mech. Eng. **41**(348), 2292 (1975) (in Japanese)
3. S.I. Nishida, C. Urashima, H. Tamasaki, Eur. Struct. Integrity Soc. **22**, 215 (1997)
4. M. Amiri, M.M. Khonsari, J. Fail. Anal. Prev. **13**(2), 183 (2013)
5. X. Shen, L. Lu, D. Zeng, M. Zhang, Eng. Struct. **210**, 110359 (2020)
6. N. Sase, S. Koga, K. Nishioka, H. Fujii, J. Mater. Process. Technol. **56**(1–4), 321 (1996)
7. K. Wakabayashi, Hard Lock Nut. Japan Patent. Hard Lock Kogyo. 195236 (2002)
8. X. Chen, N.A. Noda, W.M. Abdel, A. Yuichiro, Y. Sano, Y. Takase, G. Fekete, Acta Polytechnica Hungarica. **12**(8), 61 (2015)
9. N.A. Noda, X. Chen, Y. Sano, M.A. Wahab, H. Maruyama, R. Fujisawa, Y. Takase, Mater. Des. **96**, 476 (2016)
10. X. Chen, N.A. Noda, M.A. Wahab, Y. Sano, H. Maruyama, H. Wang, R. Fujisawa, Y. Takase, J. Chine Soc. Mech. Eng. **37**(1), 11 (2016)
11. H.A. Ly, H. Inoue, Y. Irie, J. Solid Mech. Mater. Eng. **6**(4), 299 (2012)
12. A.M. El-Batahgy, Mater. Lett. **21**(5–6), 415 (1994)
13. X. Chen, N.A. Noda, M.A. Wahab, Y.I. Akaishi, Y. Sano, Y. Takase, G. Fekete, Acta Polytechnica Hungarica. **12**, 61 (2015)
14. N.A. Noda, Y. Takase, Int. J. Fatigue **28**, 151 (2006)
15. W. Eccles, I. Sherrington, R.D. Arnell, Proceedings of the Institution of Mechanical Engineers. Part C: J. Mech. Eng. Sci. **224**(2), 483 (2010)
16. K.S. Udagawa. J. Japan Res. Inst. Screw Threads Fasteners **13**(5), 165 (1982) (in Japanese).

Effect of Shaft's Rigidity and Motor Torque on Interfacial Slip for Shrink-Fitted Bimetallic Work Roll

Rahimah Abdul Rafar, Nao-Aki Noda, Hiroyuki Tsurumaru, Yoshikazu Sano, and Yasushi Takase

Abstract The bimetallic work rolls are widely used in the roughing stands of hot rolling stand mills. The rolling rolls are classified into two types; one is a single-solid type, and the other is a shrink-fitted construction type consisting of a sleeve and a shaft. Regarding the shrink-fitted type, the interfacial slip occurs and causes damage between the shaft and the shrink-fitted sleeve. In this paper, by changing the shaft material from rigid body to elastic body, the FEM simulation is performed to realize the interfacial slip. The effect of the shaft deformation on the interfacial slip is clarified as well as the effects of the motor torque in relation to the slippage zone along the interface.

Keywords Bimetallic work roll · Rolling roll · Shrink-fitting · Interfacial slip · Motor torque · Sleeve · Shaft

1 Introduction

Among rolling rolls used in steel industries, for rolling rolls with a body diameter exceeding 1000 mm [1] and the rolling roll for large H-section steel rolls [2], a sleeve assembly type structure in which the shaft was shrink-fitted into the hollow sleeve were tried to be used and some of them were practically and successfully used (see Fig. 1). The circumferential slippage sometimes occurs due to the excessive rotational torque even though it was designed that the resistance torque at the interface is larger than the motor torque. Therefore, it is required to clarify the cause of the sleeve slippage.

The authors previously clarified that in the case of free rolling conditions, the sleeve moves relative to the rigid shaft at the shrink-fitted surface with respect to the roll rotation [3]. Next, the behavior of the interfacial slip that occurs in the shrink-fitted rolling roll is brought closer to the actual rolling conditions by applying the driving torque, and the factors including the shrink-fitting conditions and the stress

R. A. Rafar (✉) · N.-A. Noda · H. Tsurumaru · Y. Sano · Y. Takase
Mechanical Engineering Department, Kyushu Institute of Technology, 1-1 Sensuicho, Tobata, Kitakyushu 804-8550, Japan

I. A. Parinov et al. (eds.), *Physics and Mechanics of New Materials and Their Applications*, Springer Proceedings in Materials 10,
https://doi.org/10.1007/978-3-030-76481-4_32

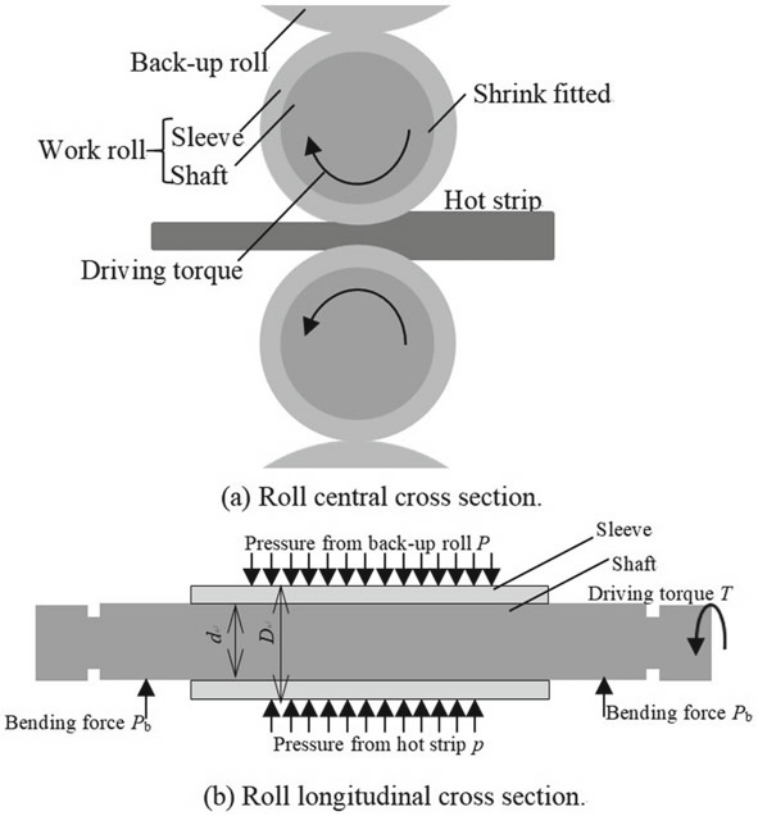

Fig. 1 Schematic illustration for real hot strip rolling roll. **a** Roll central cross section. **b** Roll longitudinal cross section

of the sleeve inner surface were also considered [4]. In the previous simulation, to clarify the amount of slippage, the rigid shaft was assumed and the displacement on the rigid body was fixed which made it easier to consider the movement of the elastic sleeve with respect to the rigid shaft. By using a rigid body for a shaft part, the mechanism of the sleeve circumferential movement could be clarified quantitatively.

In the actual roll problem, it is necessary to consider not only the sleeve but also the elastic deformation of the shaft, and the relative displacement of these two elastic body causes interfacial slip. Therefore, to get closer to the actual rolling conditions, the FEM analysis is performed to investigate the effect of elastic deformation of the shaft on the interfacial slip by changing the shaft part from a rigid body to an elastic body (steel) under the condition that motor torque is applied. Therefore, in this paper, by using numerical simulation that reproduces the actual rolling, the effects of rolling conditions will be discussed to deepen the consideration of interfacial slip.

2 Numerical Simulation Method for Interfacial Slip

The phenomenon of sleeve slip in our research up until now is referred to as the interfacial creep that follows an example in the field of rolling bearings. From this paper, it will be referred as non-uniform interface slip (also called non-uniform slip) according to the example of sleeve assembly type roll in the rolling field. In other words, as a factor of sleeve slip, in addition to overall slip due to the driving torque, a non-uniform slip is newly considered.

Figure 1 shows a schematic diagram during the rolling of the sleeve assembly type roll used in four stage rolling mill that is focused in this study. Figure 1a shows the central cross-section view of the rolling roll, and Fig. 1 b shows the longitudinal cross-section of the rolling roll. In the sleeve roll shown in Fig. 1, the steel shaft is assembled to the steel sleeve by shrink-fitting, and the sleeve is required to have both high abrasion resistance and high fracture toughness. Generally, the outer layer is made of wear resistance materials such as high-speed steel or high-chromium steel, and the inner layer is made of composite sleeve made of alloy steel.

Figure 2 shows the numerical simulation model used in this study in the relation to the actual roll. The rotation of the roll is expressed by the circumferential load transfer on the roll surface without rotating the roll [3]. Figure 2a shows a rotation of the two-dimensional real roll. Figure 2b is a model in which the entire shaft is made rigid as in the previous papers [3, 4]. As shown in Fig. 2c, a small rigid body is introduced at the center of the shaft to restrain the displacement and rotation of the center of the roll, and the elastic deformation of the sleeve and shaft is considered. In this analysis, the rigid body size at the center has been confirmed does not affect

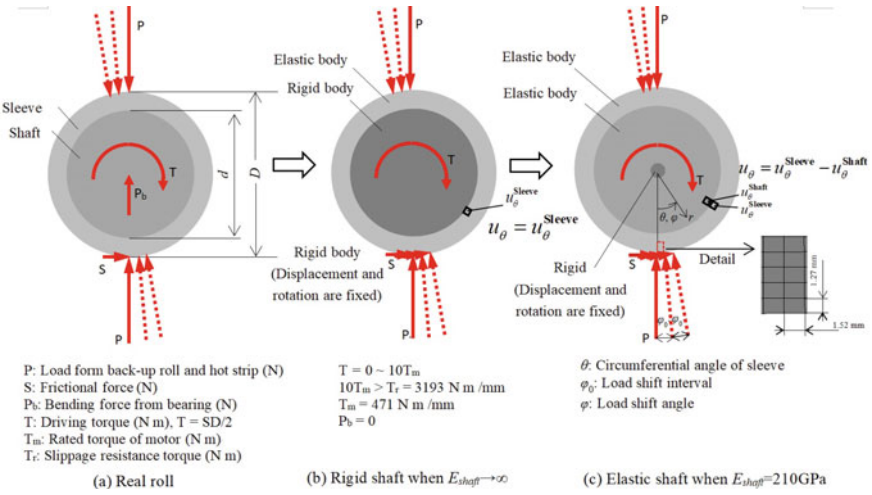

(a) Real roll (b) Rigid shaft when $E_{shaft} \to \infty$ (c) Elastic shaft when E_{shaft}=210GPa

Fig. 2 Modelling for interfacial slip. **a** Real roll. **b** Rigid shaft when Eshaft → ∞. **c** Elastic shaft when Eshaft = 210GPa

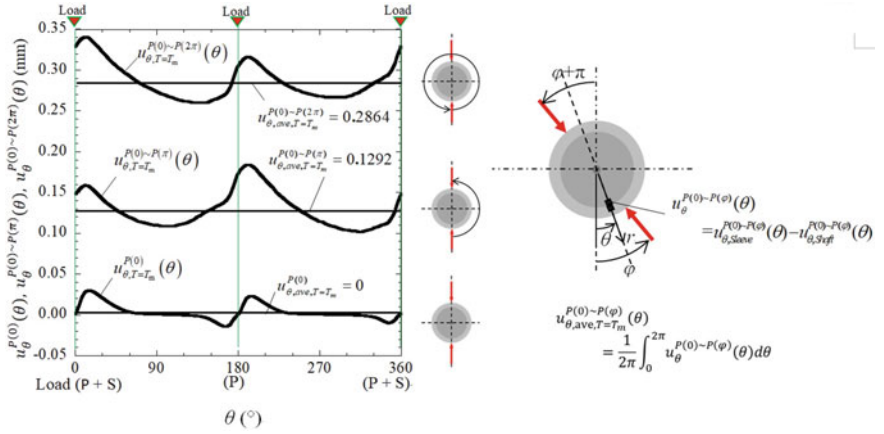

Fig. 3 Displacement due to initial load P(0) and displacements due to load shifting P(0) ~ P(π) and P(0) ~ P(2π) under T = Tm and Eshaft = 210 GPa

the result and the diameter is set to be 8 mm. The load transfer range is set to be φ = 4° in consideration of computational time without loosening the analysis accuracy.

The load on the roll used for the analysis of interfacial slip is the compressive force P from the backup roll to the sleeve, the rolling reaction force P from the rolled material to the sleeve, the frictional force (shear force), and the driving torque T from the motor to the shaft. Under stable rotation, the shaft driving torque T should be balanced.

with the torque due to the friction force S from the strips as T = SD/2 (see Fig. 3a). Let P = P0 be the standard reaction force. The bending force Pb of the shaft can be ignored since it is smaller than the reaction force P0. The effect of shaft torque T on the interfacial slip was also considered in the previous study [4]. Here by using the conditions from the previous paper, the frictional force (shear force) S = 1346 N·m/mm was obtained from the motor torque T = Tm = 471 N·m/mm [4]. The quadrilateral element is used for mesh division, and the total is 4.6 × 104.

The relative displacement in the circumferential direction between the sleeve and shaft is defined as u_θ. The displacement of the inner surface of the sleeve at an angle θ while the load moves from an angle φ = 0° to φ (at the same time there is a load from φ = π to (π + φ)) is expressed as $u_\theta^{P(0)\sim P(\varphi)}(\theta)$. In this study, since the sleeve and shaft are elastic body, the phase difference occurs between the sleeve and shaft parts as the roll is rotated (load transfer). Thus, the relative displacement u_θ between the elastic shaft and elastic sleeve on the shrink-fitted surface can be expressed as $u_\theta^{P(0)\sim P(\varphi)}(\theta) = u_{\theta,\text{Sleeve}}^{P(0)\sim P(\varphi)}(\theta) - u_{\theta,\text{Shaft}}^{P(0)\sim P(\varphi)}(\theta)$ that is defined as the interfacial slip on the shrink fitted surface.

The external force P = 13,270 N/mm is used, which is the load from the backup roll to the sleeve and the reaction concentrated load from the strip to the sleeve. The shrink-fitting ratio δ/d = 0.5 × 10–3, obtained by dividing the shrink fit allowance δ by the inner diameter d, is used in this analysis. The friction coefficient between the

sleeve and the shaft is $\mu = 0.3$. In this paper, the Finite Element Method (FEM) is used for the numerical analysis of the sleeve assembly type roll as shown in Fig. 2.

3 Numerical Simulation Results of Interfacial Slip

3.1 *Definition and Behavior of Relative Displacement of Elastic Shaft*

The circumferential displacement of the sleeve interface, when the load transfer P(0) to P(φ) is expressed as $u_{\theta}^{P(0)\sim P(\varphi)}(\theta)$. The notation $u_{\theta}^{P(0)\sim P(\varphi)}(\theta)$ means the displacement $u_{\theta}(\theta)$ at θ, when the pair of the loads are applied at $\varphi = 0$ to φ (at the same time, there is a load from $\varphi = \pi$ to $(\pi + \varphi)$ [3].

Figure 3 shows the displacement of$u_{\theta}^{P(0)}(\theta)$, $u_{\theta}^{P(0)\sim P(\pi)}(\theta)$ and$u_{\theta}^{P(0)\sim P(2\pi)}(\theta)$, when the load is moving to $\varphi = 0$, $\varphi = \pi$ and $\varphi = 2\pi$. At initial load $\varphi = 0°$, the absolute value of the displacement near both sides of the load position, on which the shear forces are applied ($\theta = 0°$), acts differently, and the absolute value of the displacement is larger on the positive direction of the shear force ($\theta > 0°$), $|u_{\theta,T=T_m}^{P(\varphi)}(-\theta)| < |u_{\theta,T=T_m}^{P(\varphi)}(+\theta)|$.

Figure 4a shows the behaviour of the sleeve displacement, which is expressed by the relationship between the average displacement $u_{\theta,ave.}^{P(0)\sim P(\varphi)}$ and the load rotation angle φ of the T = Tm elastic shaft and T = Tm rigid shaft as the load is rotated twice. The average value increases almost linearly as the load moves regardless of whether

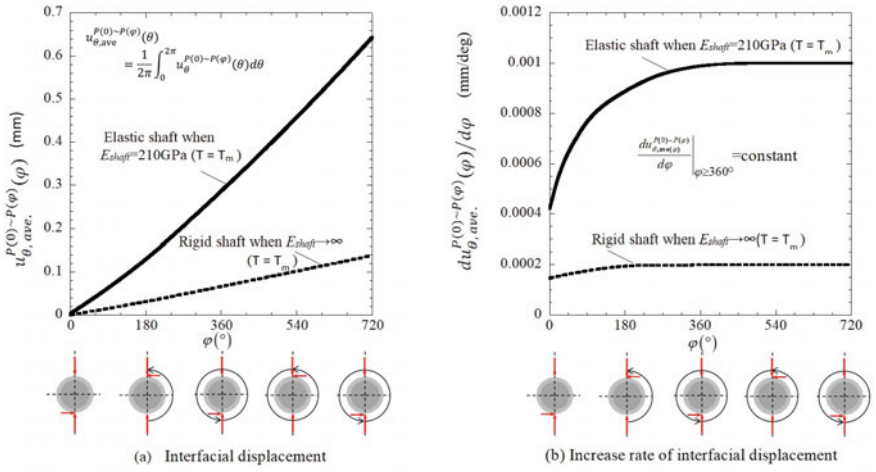

Fig. 4 Interfacial displacement and increase rate of interfacial displacement for rigid shaft (T = Tm) and elastic shaft when Eshaft = 210 GPa. **a** Interfacial displacement. **b** Increase rate of interfacial displacement

it is an elastic shaft or a rigid shaft. In particular, the changes can be considered as linear, when $\varphi = 2\pi \sim 4\pi$. Therefore, as shown in Fig. 4b, the interface slip is quantitatively evaluated by observing the increase rate of interfacial displacement $\mathrm{du}_{\theta}^{\mathrm{P(0)\sim P(\varphi)}}(\varphi)/\mathrm{d}\varphi\Big|_{\varphi\geq 2\pi}$ after one rotation. As shown in Fig. 4b, the displacement increasing rate $\mathrm{du}_{\theta}^{\mathrm{P(0)\sim P(\varphi)}}(\varphi)/\mathrm{d}\varphi\Big|_{\varphi\geq 2\pi}$ of the elastic shaft body is nearly four times larger than rigid shaft body. In addition, it is clearly shown that the displacement increasing rate after one rotation of the load ($\varphi = 2\pi$) becomes constant.

3.2 *Consideration of Slip Area by Introducing an Elastic Shaft*

In the previous report, the effect of torque on the interface slip generation mechanism was considered form the relationship between the shear stress $\tau_{r\theta}$ and the frictional stress $\mu\sigma_r$ at the interface [4]. Specifically, (i) there exist a slip area on the shrink fitted surface (stress quasi-equilibrium area called $\tau_{r\theta} \cong |\mu\sigma_r|$), (ii) the displacement remains around the slip (residual displacement), (iii) the average displacement of the interface increases with increasing of the load transfer (roll rotation); it has been observed. Figure 5 shows a comparison of the slip areas after one rotation of the load. It has been confirmed that the slip area does not changed after one rotation of the load. Figure 5a shows the slip area of the elastic shaft after one load rotation, which is shown in relation of the shear stress distribution $\tau_{r\theta,\mathrm{T=T_m}}$ and frictional stress $\mu\sigma_{r,\mathrm{T=T_m}}$. Figure 5b shows the slip area and the stress distribution of the rigid shaft

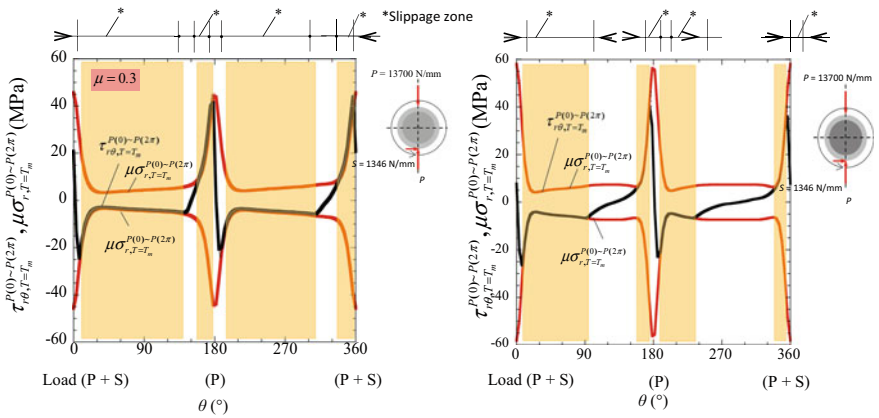

Fig. 5 Comparison of the slippage zone* for **a** the elastic shaft Eshaft = 210 GPa and **b** the rigid shaft, both under the loading shift P(0) ~ P(2π) and μ = 0.3

body. By considering the FEM accuracy, the region satisfying $\tau_{r\theta} \cong |\mu\sigma_r|$ within the error ±1 MPa is defined as the slippage area. From Fig. 5a and b, the slippage area can be observed on both sides of the load positions $\theta = 0$ and $\theta = \pi$. The slippage area after one load rotation of elastic shaftV body is almost twice larger than rigid shaft body. This causes the average displacement to increase, as shown in Fig. 4. This is because, under the action of the rolling load P, the rigid shaft does not deform, while the elastic shaft will undergo deformation.

4 Effect of Motor Torque and Rolling Load on Elastic Shaft

The motor torque applied to the roll has been considered based on the motor torque Tm per roll. In this chapter, the cases of the rolling load P = P0, 2P0, 3P0 applied for each motor torque T = Tm (reference torque), T = 2 Tm and T = 3 Tm are considered. Here, we consider the cases from the standard rolling conditions: T = Tm, P = P0 to the state of T = 3Tm, P = 3P0 with the assumption of the rolling problem. Figure 6 shows the.

increase rate of interfacial displacement for each motor torque and rolling load. As shown in Fig. 6, the solid line implied that the displacement increasing rate is increases at an accelerating rate as the torque T and the rolling load P increase. The break line in Fig. 6 shows the case of the load is fixed when the motor torque is varied [3]. As an example, if P = P0, T = Tm to P = P0, T = 3Tm that is the load P is fixed and the motor torque is three times of Tm, the displacement increasing rate will be 10 times from T = Tm, P = P0. When the motor torque is fixed at T = Tm and the load is three times of P0, the displacement increasing rate is 16 times

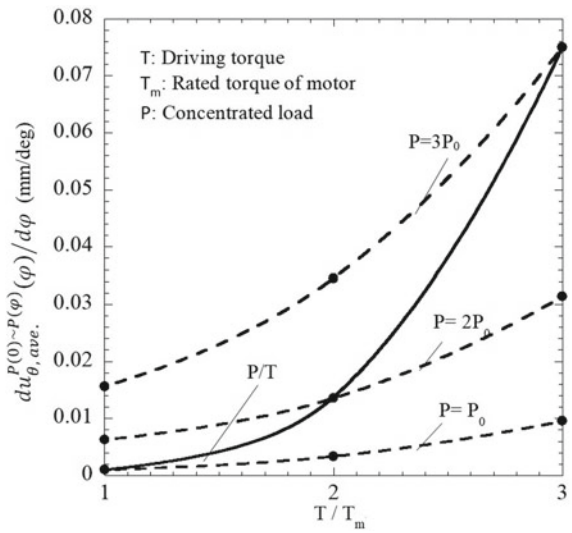

Fig. 6 Increase rate of interface displacement vs. T/Tm when $\varphi = 2\pi$ and P = P0, P = 2P0, P = 3P0, Eshaft = 210 GPa

higher than T = Tm, P = P0. The observation explained that the effect of the load increase is greater than the effect of the motor torque increase. Under the actual rolling conditions, the increase in rolling load P and the increase in the motor torque T are in a proportional relationship. Therefore, increasing both P and T significantly affects the displacement increasing rate. For example, comparing P = P0, T = Tm and P = 3 P0, T = 3 Tm, the displacement increasing rate is as high as 70 times.

5 Conclusion

In this study, the behavior of the sleeve slip that occurs in the sleeve assembly type roll was numerically simulated in consideration of the elastic deformation of the shaft as well as the sleeve according to the actual roll. The discussion on the interfacial slip and the displacement increasing rate are summarized as follows:

By changing from a rigid shaft to an elastic shaft (steel), the interfacial displacement u_θ is accelerated, and the displacement increasing rate increases about 5 times as the motor torque and load position increase (Fig. 4).

The effect of interfacial slip by the elastic shaft can be explained by introducing the concept of "slippage area" where the frictional stress is equal to shear stress. The slippage area of the elastic shaft is bigger than rigid shaft.

Under the conditions of T = Tm ~ 3Tm and P = P0 ~ 3P0, the effect on the displacement increasing rate is larger, and the slip increases as the load condition increases.

References

1. H. Shimoda, S. Onodera, K. Hori, O. Dohi, Trans. Japan Soc. Mech. Eng. **32**, 689 (1966)
2. H. Takigawa, K. Hashimoto, G. konno, S. Uchida, Camp-ISIJ, **16**, 1150 (2003)
3. H. Sakai, N.-A. Noda, Y. Sano, Y. Takase, G. Zhang, Testu-to-Hagane **105**, 411 (2019)
4. H. Sakai, N.A. Noda, Y. Sano, G. Zhang, Y. Takase, Tetsu-to-Hagane **105**, 1126 (2019)

Effect of the Residual Stress to the Fatigue Failure of the Bimetallic Work Roll in 4-High Rolling Mill

Mohd Radzi Aridi, Nao-Aki Noda, Yoshikazu Sano, Kakeru Takata, and Sun Zifeng

Abstract In this chapter, the finite element method (FEM) simulation is performed to study the generated stress when the rolling roll is used in the 4-high rolling mill. In order to study the effect of the residual stress, the heating treatment of the work roll is considered before the rolling process. By using the 3D model, we focus on the fatigue failure near the boundary layer, where the work roll received load from the backup roll and the rolled steel. The fatigue failure is discussed focusing on several critical points inside of the work roll. Results of the generated rolling stress are compared between the superposition method and the finite element method (FEM) analysis.

Keywords Hot rolling · Finite element method (FEM) · Residual stress · Bimetallic work roll

1 Introduction

In hot rolling of steel, bimetallic work rolls have been widely used to replace the conventional single material rolls in order to improve wear resistance, surface resistance, and heat crack resistance of the work rolls [1]. High fracture toughness is required at the roll center while high wear resistance and heat resistance are required at the roll surface. Bimetallic work rolls are manufactured by the centrifugal casting method, in which high-speed steel (HSS) is used as the outer layer and ductile casting iron (DCI) is used as the inner layer [2]. During the centrifugal casting process, minor defects and abnormal microstructures may contribute to the delamination phenomena, occurring near the boundary layer due to the repeated rolling loads [3]. Since the outer layer is repeatedly received many load repetitions exceeding 10^7 times, which corresponds to the total life of the roll, the boundary layer and the inner layer are the main parts focused on the roll life service.

The previous works have systematically studied the residual stress generated in the roll manufacturing process and related to the internal strength inside of the bimetallic

M. R. Aridi (✉) · N.-A. Noda · Y. Sano · K. Takata · S. Zifeng
Department of Mechanical Engineering, Kyushu Institute of Technology, Kitakyushu-shi 804-8550, Fukuoka, Japan

I. A. Parinov et al. (eds.), *Physics and Mechanics of New Materials and Their Applications*, Springer Proceedings in Materials 10,
https://doi.org/10.1007/978-3-030-76481-4_33

roll [4]. This study showed that the appropriate compressive residual stress is useful at the roll surface to prevent damage such as thermal cracks and the tensile residual stress at the center is required to be low as possible to avoid internal fracture.

Fatigue fracture of the internal roll, occurring during rolling, has been studied in [1], but there is no details on the relationship with the stress due to rolling. Therefore, in this paper, it has become possible to simulate the residual stress distribution from the quenching and tempering heating treatment by using the software MSC Marc/Mentat 2012. Then, the 4-high rolling mill simulation will consider the generated residual stress from the heating treatment as the initial condition. Therefore, the effect of the residual stress on the rolling can be studied. In this paper, we study the difference between the superposition method and the FEM analysis method. The risk of internal fatigue fracture between these two methods can be clarified using the stress amplitude *versus* mean stress diagram by focusing on some critical points.

2 Method of FEM Analysis

Figure 1 shows the three-dimensional model of 4-high rolling mill. The internal stress of the work roll can be generated when it receives the rolling force from the backup roll and the rolled steel. Table 1 shows the material properties of high-chrome steel for backup roll, HSS for the work roll's outer layer, and DCI for the work roll's inner layer.

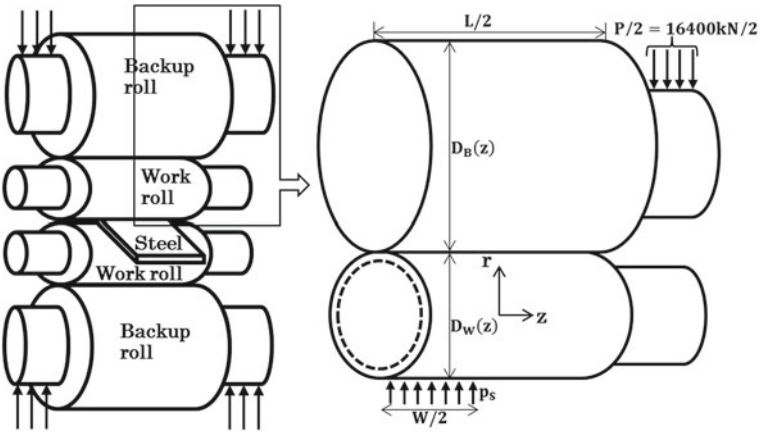

Fig. 1. 3D model of 4-high rolling mill

Table 1 Material properties of the rolls

Property	HSS	DCI	Backup roll
Tensile strength (MPa)	1575	415	1575
Young's modulus (GPa)	230	174	210
Yield strength (MPa)	1270	410	–
Poisson's ratio	0.3	0.28	0.3
Density $\left(\mathrm{kg/m^3}\right)$	7600	7300	7800

3 Effect of Residual Stress on the Stress Inside the Bimetallic Work Roll During Rolling Analysis

The fatigue fracture treated in this study occurs inside the roll and near the boundary layer of the work roll [3]. Therefore, we will pay attention to the internal stress σ_r on the boundary $r = 270\text{mm}$, to obtain the target result of fatigue fracture, which has not been studied so far. In this section, we study the difference of the rolling analysis between the superposition method and the finite element method (FEM) as shown in Fig. 2.

It is important to consider the position, where the maximum stress amplitude occurs, which controls the fatigue inside the roll. Figure 3 shows the stress distribution σ_r along z-direction on the boundary $r = 270\text{mm}$ for both superposition method and FEM analysis. It is found that the maximum stress amplitude on the boundary occurs from the rolled steel side as shown in Fig. 3, when $z = 0$.

Maximum amplitude stress can be found at the center, when $(r, z) = (270\text{mm}, 0)$ for both methods. For superposition method, the maximum stress amplitude is $\sigma_a^{\max} = 608\text{MPa}$, where the maximum tensile stress $\sigma_r = 118\text{MPa}$, and the maximum compressive stress $\sigma_r = -490\text{MPa}$. For FEM analysis, the maximum stress amplitude $\sigma_a^{\max} = 465\text{MPa}$, where the maximum tensile stress $\sigma_r = 118\text{MPa}$, and the maximum compressive stress $\sigma_r = -347\text{MPa}$. For the next safety evaluation study, this maximum amplitude stress position $(r, z) = (270\text{mm}, 0)$ is represented

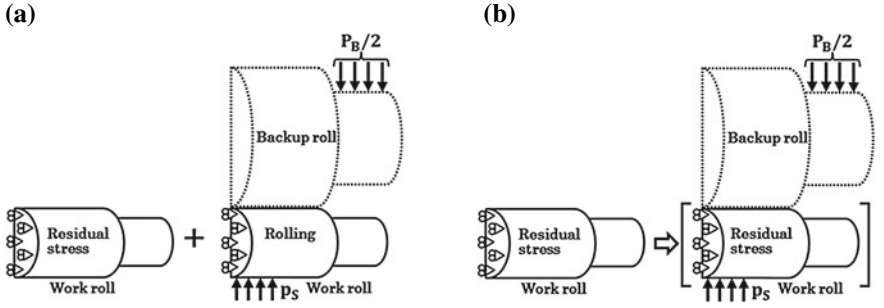

Fig. 2 **a** Superposition method, **b** FEM analysis

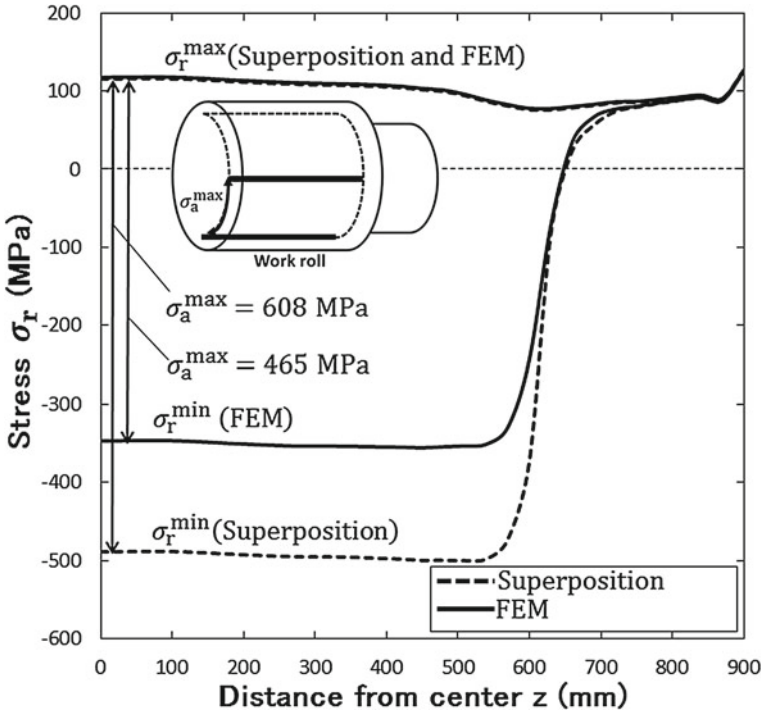

Fig. 3 Maximum and minimum stresses σ_r on the boundary $r = 270$ mm of the work roll

by point $B^{(\text{Superposition})}$ for the superposition method and point $B^{(\text{FEM})}$ for the FEM analysis.

Figure 4 shows the stress amplitude *versus* mean stress diagram for a large compression field [5, 6]. The safety factor is SF = 0.95 at point $B^{(\text{Superposition})}$, and SF = 1.09 at point $B^{(\text{FEM})}$. It is clear that point $B^{(\text{Superposition})}$ is more dangerous than point $B^{(\text{FEM})}$.

4 Conclusion

In this paper, the FEM simulation of 4-high rolling mill is performed to study the effect of the residual stress on the rolling stress. The following conclusions can be obtained:

(i) We clarified the severe area for fatigue fracture of internal stress during rolling near the boundary, when $z = 0$, based on the force received from the rolled steel side. Specifically, large stress amplitude occurs at the boundary part, where $(r, z) = (270\text{mm}, 0)$ at points $B^{(\text{Superposition})}$ and $B^{(\text{FEM})}$.

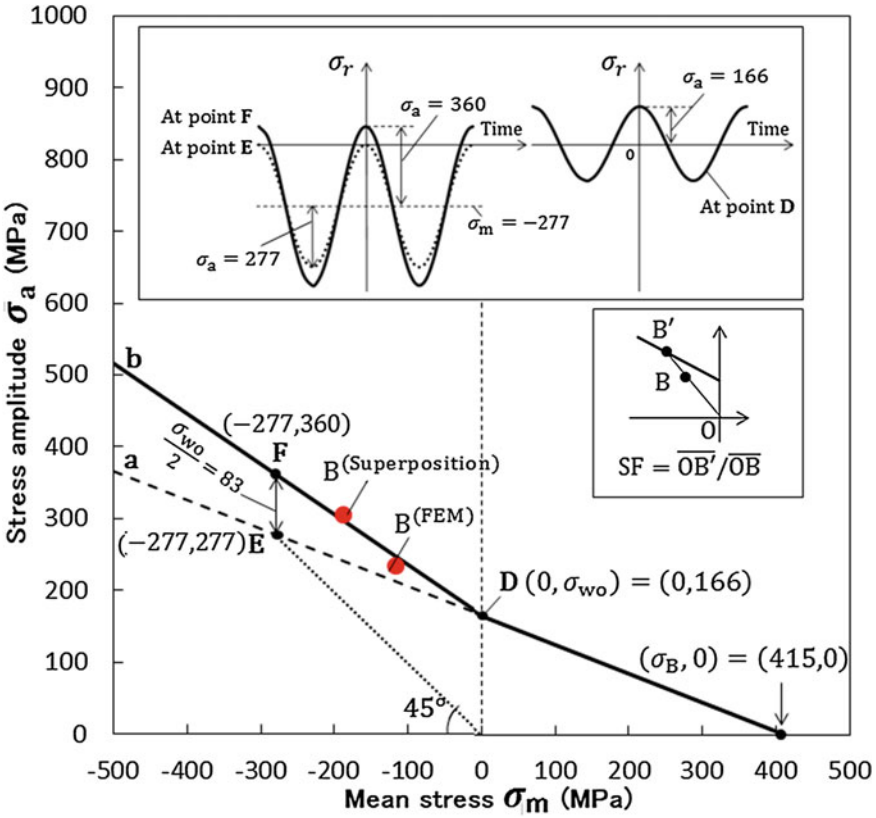

Fig. 4 Stress amplitude *versus* mean stress diagram

(ii) For fatigue evaluation, the stress amplitude *versus* mean stress can be used as a reference. Results in Fig. 4 showed that point $B^{(Superposition)}$ (SF = 0.95) is more dangerous than point $B^{(FEM)}$ (SF = 1.09).

References

1. Y. Sano, J. Jpn. Soc. Technol. Plast. **44**, 48 (2003). (In Japanese)
2. Y. Sano, T. Hattori, M. Haga, ISIJ Int. **32**, 1194 (1992)
3. Y. Sano, K. Kimura, Tetsu-to-Hagane **73**, 1154 (1987). (In Japanese)
4. N.A. Noda, Y. Sano, M.R. Aridi, K. Tsuboi, N. Oda, Metals **8**, 952 (2018)
5. H. Nishitani, N. Yamashita, Collect. Pap. Japan. Mech. **32**, 1456 (1966). (In Japanese)
6. S. Hamada, Y. Sakoda, D. Sasaki, M. Ueda, H. Noguchi, Soc. Mater. Sci. **9**, 790 (2011). (In Japanese)

Cost and Quality Analysis of the Use of Steel Fiber on Rigid Pavement with Laboratory Experimental Method

Risma Marleno, Fajar Romadhon, Gede Sarya, and Hari Susanto

Abstract This study aims to find and compare the cost and quality of the use of steel fiber (dramix) and iron wire mesh in the rigid pavement. The method used in this study is a laboratory experiment. The study results that steel fiber costs less and is more economic than reinforcing steel in rigid pavement. The cost of the 1 m^3 of concrete with reinforcing iron wire mesh m8 is equal to Rp. 2.138.34326. At the same time, the cost of a concrete with mixture of 10% steel fiber (dramix) is equal to Rp. 1.798.08900. So, there is cost savings of Rp. 340.25426 for 1 m^3. The mixing of steel fiber in concrete has through 28 days greater compressive strength than the ordinary concrete mix with value of compressive strength equal to $f_{c'} =$ 29.07 MPa. At the same time, concretes with the mix of steel fiber (dramix) have more compressive strength that varies as follows: $f_{c'} = 29.34$ MPa at 10% of dramix, $f_{c'} = 29.38$ MPa at 15% of dramix, $f_{c'} = 29.41$ MPa at 20% of dramix, and $f_{c'} =$ 29.58 MPa at 30% of dramix. In flexural strength test, the concrete with iron wiremesh m8 results flexural strength $f_{c'} = 4.978$ MPa. At the same time, a concrete with the mix of steel fiber (dramix) has more flexural strength that varies as follows: $f_{c'} =$ 5.173 MPa at 10% of dramix, $f_{c'} = 5.316$ MPa at 15% of dramix, $f_{c'} = 5.458$ MPa at 20% of dramix, and $f_{c'} = 5.707$ MPa at 30% of dramix.

Keywords Steel fiber · Dramix · Wire mesh · Rigid pavement

1 Introduction

Indonesia as a developing country is still using concrete in its construction. Concrete construction has several advantages over other constructions [1–3]. By applying various innovations to one or more components of the concrete structure, it will greatly affect the cost savings and improve quality of concrete construction, ultimately the innovation can be applied to all concrete constructions in Indonesia. The

R. Marleno (✉) · F. Romadhon · G. Sarya · H. Susanto
Master of Civil Engineering, University of 17 Agustus 1945 Surabaya Indonesia, Surabaya, Indonesia

I. A. Parinov et al. (eds.), *Physics and Mechanics of New Materials and Their Applications*, Springer Proceedings in Materials 10,
https://doi.org/10.1007/978-3-030-76481-4_34

current innovation in concrete technology in many developed country is the mixture of steel fiber in the concrete construction [4–6].

In Indonesia, research on steel fibrous concrete has been conducted as both material testing and form of specimens and structural testing [7–9]. However, results of several studies conducted in Indonesia show that the research is only limited to natural steel fiber, which has not been proven and tested for its quality and characteristics. In this study the authors will test steel fibrous concrete and also test supporting materials using steel fibers that have been proven and produced by dramix regarding its mechanical features and characteristics.

2 Problem Formulation

(i) To find out and compare the cost difference between steel fibers (dramix) and wire mesh used in concrete mixtures;
(ii) to find out the compressive strength ($f_{c'}$) of the concrete mixture by using steel fibers (dramix) .
(iii) to compare the flexural strength of concrete with the mix of steel fibers (dramix) and the corresponding value for concrete with wire mesh.

3 Research Methods

3.1 JMF Preparation (Job Mix Formula)

In this study we use JMF (Job Mix Formula) that already exists (see Table 1).

3.2 Test Specimen

It was manufactured the test cylindrical specimen with a diameter of 15 cm and height of 30 cm. Testing was carried out on 28th day (see Table 2).

Table 1 Composition of 1 m^3 Concrete $f_{c'} = 29.5$ MPa

No.	Material	Total	Unit
1	PC	448	kg
2	Pasir	667	kg
3	Koral	1000	kg
4	Air	215	liter
Total weight		2.330	kg

Source www.sentosamortar.com

Table 2 Number of test specimens

Volume Fraction	Normal	10%	15%	20%	30%	Wire mesh	Total
Compres-sive Strength	N.1	DSF.10.A	DSF.15.A	DSF.20.A	DSF.30.A		20
	N.2	DSF.10.B	DSF.15.B	DSF.20.B	DSF.30.B		
	N.3	DSF.10.C	DSF.15.C	DSF.20.C	DSF.30.C		
	N.4	DSF.10.D	DSF.15.D	DSF.20.D	DSF.30.D		
Flexural Strength	N.1	N.10	N.15	N.20	N.30	W.1	6

Table 3 Material composition for 1 m^3

No	Material	Unit	Concrete	Concrete	Concrete	Concrete	Concrete
			Normal	Dramix, 10%	Dramix, 15%	Dramix, 20%	Dramix, 30%
			N	DSF 10	DSF 15	DSF 20	DSF
1	Cement	kg	448				
2	Sand	kg	667				
3	Coral	kg	1000				
4	Water	liter	215				
5	Dramix	kg	–	10	11	12	13

Source www.signalreadymix.com

4 Data Analysis and Discussion

4.1 Results of Calculation of Mixed Plan (Job Mix Formula)

In this study, the calculation of the composition of concrete mixtures used in the manufacture of test specimens is referred to SNI 7394: 2008 [10–13] concerning concrete mixes for every 1 m^3. The achieved quality of concrete is defined by value of $f_{c'} = 29.5$ MPa or corresponds to the quality of concrete K-350. Each option consists of 4 specimens with the addition of wire mesh m8 or steel fiber (dramix) with a fraction of 10%, 15%, 20% and 30% for test beam specimens. The material composition/mixture of concrete is presented in Table 3.

The material requirements for manufacture of test cylindrical and beam samples with a section size of 15 × 30 cm^2 are present in Tables 4 and 5, respectively.

4.2 Volume Weight

From Table 6, it can be identified that there is a decrease in volume weight

Table 4 Material composition of 1 cylindrical specimen

No	Material	Unit	Concrete	Concrete	Concrete	Concrete	Concrete
			Normal	Dramix, 10%	Dramix, 15%	Dramix, 20%	Dramix, 30%
			N	DSF 10	DSF 15	DSF 20	DSF 30
1	Cement	kg	2.3				
2	Sand	kg	3.5				
3	Coral	kg	5.2				
4	Water	liter	1.1				
5	Dramix	kg	–	0.058	0.061	0.064	0.070

Source Research on steel fiber mixture (dramix)

Table 5 Material composition of 1 beam

No	Material	Unit	Conc-rete	Concrete	Concrete	Concrete	Concrete	Concrete
			Normal	Dramix, 10%	Dramix, 15%	Dramix, 20%	Dramix, 30%	Wire mesh
			N	DSF 10	DSF 15	DSF 20	DSF 30	
1	Cement	kg	6					
2	Sand	kg	9					
3	Coral	kg	13.5					
4	Water	liter	2.9					
5	Dramix	kg	–	0.058	0.061	0.064	0.070	–
6	Wire mesh	kg	–	–	–	–	–	0.65

Source Research on steel fiber mixture (dramix)

Table 6 Volume weight of concrete sampless with added steel fibers (dramix)

No.	Steel Fiber (Dramix)	Average weight (kg)	Volume weight (kg/m^3)
1	0%	12.72	2399.623
2	10%	12.70	2397.264
3	15%	12.71	2399.151
4	20%	12.73	2401.982
5	30%	12.74	2404.341

Source Processed data

(2397.264 kg/m^3) for the test specimen with 10% of steel fibers (dramix) . It is the lowest value than for the normal concrete or other samples. It leads from Fig. 1.

Similarly, for the beam test samples the highest volume weight (3317.037 kg/m^3) attains at 30% of steel fiber (dramix) , see Table 7 and Fig. 2.

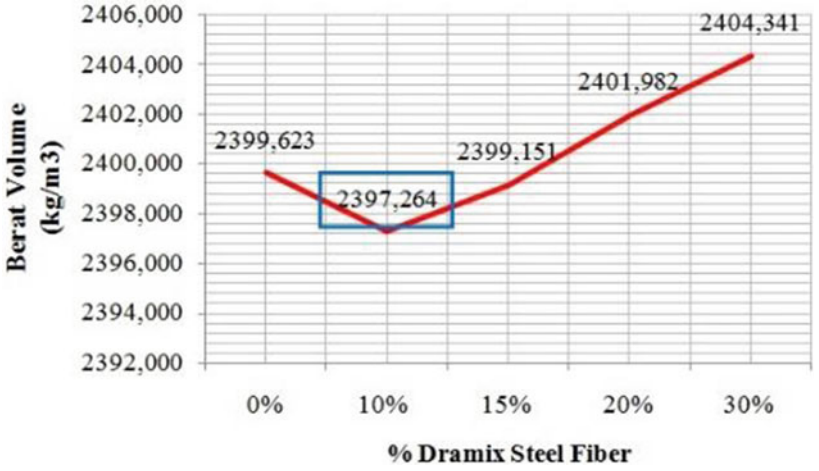

Fig. 1 Volume weight of cylindrical test samples

Table 7 Volume weight of unit of beam test specimen

No	Material type	Weight (kg)	Volume weight (kg/m^3)
1	Normal	44.46	3293.333
2	Wire mesh	44.54	3299.259
3	Steel Fiber, 10%	44.52	3297.778
4	Steel Fiber, 15%	44.59	3302.963
5	Steel Fiber, 20%	44.66	3308.148
6	Steel Fiber, 30%	44.78	3317.037

Source Processed data

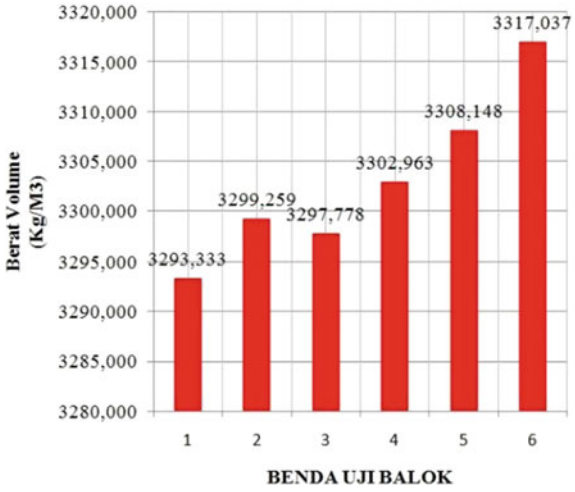

Fig. 2 Volume weight of beam test specimen: (1) Normal; (2) Wire mesh; (3) Steel Fiber (Dramix) , 10%; (4) Steel Fiber (Dramix) , 15%; (5) Steel Fiber (Dramix) , 20%; (6) Steel Fiber (Dramix) , 30%

4.3 Compressive Strength Test

The compressive strength results are presented in Table 8 and Figs. 3, 4, 5, 6, 7, and 8.

Based on the results of the samples 1 – 5 above, it can be identified the compressive strength ratio of concrete according to the steel fiber (dramix) content (see Fig. 8).

Table 8 Recapitulation of compressive strength results

No.	Dramix Steel Fiber	Specimen weight (kg)	Load *P* (kN)	Compressive strength after 28 days (MPa)	Average compressive strength (MPa)
1	0	12.74	519.40	29.41	29.07
2		12.69	515.90	29.21	
3		12.74	517.90	29.32	
4		12.69	500.80	28.35	
1	10	12.74	517.90	28.60	29.34
2		12.69	523.80	29.66	
3		12.69	525.60	29.76	
4		12.69	505.20	29.32	
1	15	12.73	522.50	28.61	29.38
2		12.69	523.50	29.64	
3		12.69	524.50	29,70	
4		12.74	505.30	29.58	
1	20	12.74	518.50	29.36	29.41
2		12.69	520.30	29.46	
3		12.74	518.50	29.36	
4		12.74	519.90	29.44	

Source Data processed

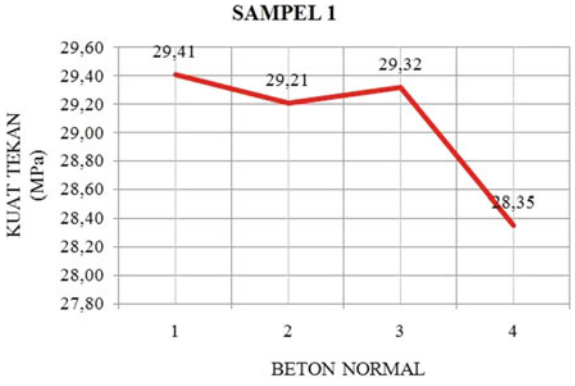

Fig. 3 Compressive strength for normal concrete

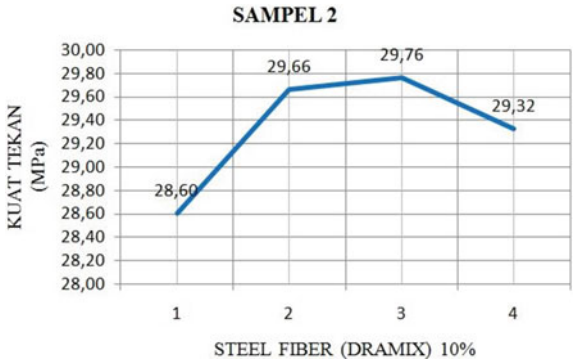

Fig. 4 Compressive strength for 10% of steel fiber (dramix)

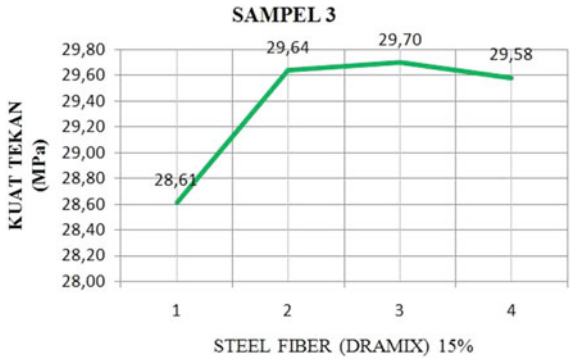

Fig. 5 Compressive strength for 15% of steel fiber (dramix)

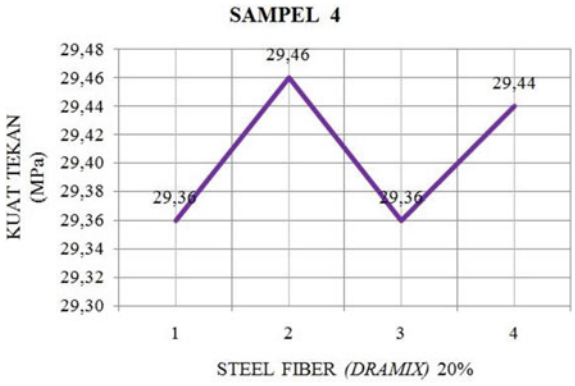

Fig. 6 Compressive strength for 20% of steel fiber (dramix)

Based on the plot data, we can find out the ratio of compressive strength of concrete according to the steel fiber (dramix) content. The highest compressive strength has the sample 5 with 30% steel fiber (dramix) Fig. 9.

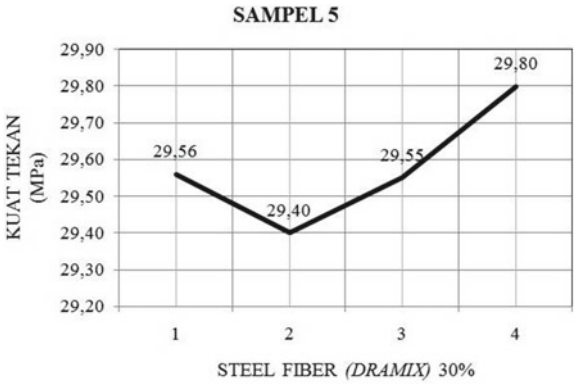

Fig. 7 Compressive strength for 30% of steel fiber (dramix)

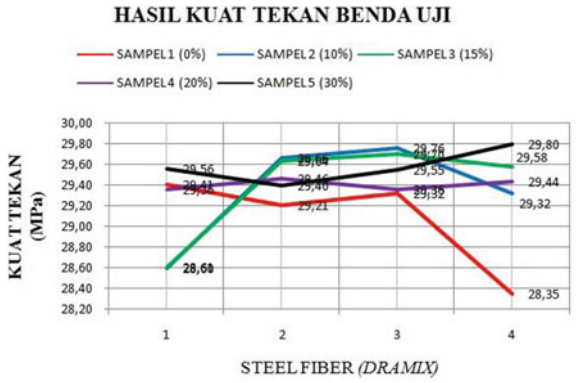

Fig. 8 Compressive strength for cylindrical test specimen

From the results of the compressive strength obtained from all test specimens, then it can be indified the most optimum addition of steel fibers (dramix) by drawing a perpendicular line to the planned compressive strength of $f_{c'} = 29.05$ MPa.

Moreover, based on the graph data, the lowest addition of steel fiber (dramix) equal to 10% can achieve compressive strength of $f_{c'} = 29.32$ MPa. The more fraction of steel fibers (dramix) , added to the concrete mix, leads to the higher compressive strength value of the concrete.

4.4 Flexural Strength Test

The results of the concrete flexural strength are present in Table 9 and Fig. 10. From the concrete flexural strength test, it can be concluded that the concrete containing a steel fiber (dramix) mixture has a greater flexural strength than a concrete sample containing a mixture of wire mesh m8 or normal concrete.

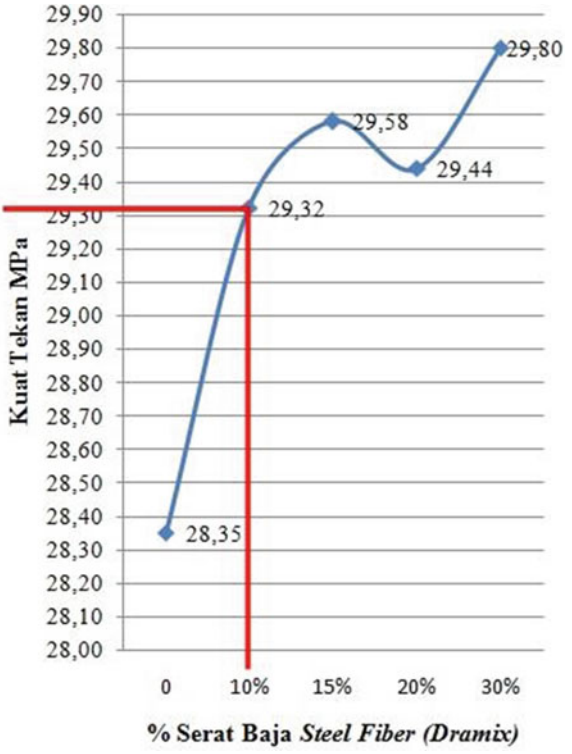

Fig. 9 Optimum and economical point graph of compressive strength with the addition of steel fibers (dramix)

Table 9 Flexural strength results for concrete after 28 days

No.	Material type	Weight (kg)	Average size			Load *P*	Flexural strength
			Wide (mm)	Height (mm)	Length (mm)	(MPa)	(MPa)
1	Normal	44.46	150.00	150.00	600.00	Normal	44.46
2	Wire mesh	44.54	150.00	150.00	600.00	Wire mesh	44.54
3	Dramix, 10%	44.52	150.00	150.00	600.00	Dramix, 10%	44.52
4	Dramix, 15%	44.59	150.00	150.00	600.00	Dramix, 15%	44.59
5	Dramix, 20%	44.66	150.00	150.00	600.00	Dramix, 20%	44.66
6	Dramix, 30%	44.78	150.00	150.00	600.00	Dramix, 30%	44.78

Source Data Processed

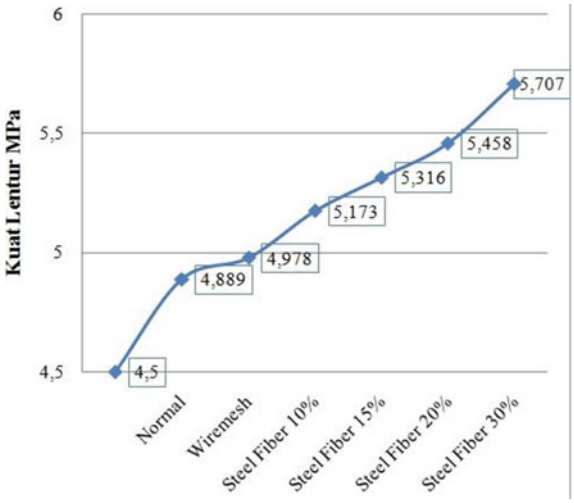

Fig. 10 Graph of concrete flexural test result

4.5 Cost Calculation Analysis

According to Table 10, it can be concluded that the rigid pavement using steel fibers is cheaper than using wire mesh m8 reinforcing steel.

Calculation of wire mesh and reinforcing steel in rigid pavement is present in Table 11 for 1 m^3 of concrete.

Table 10 Budget Plan

No.	URAIAN	PERHITUNGAN					KUANTITAS	SAT.	HARGA SATUAN (Rp)	JUMLAH (Rp)
		p		l		t				
A	SERAT BAJA	5.00	x	3.00	x	0.20	3.00	m3	Rp 1,798,089.00	Rp 5,394,267.00
	STEEL FIBER (DRAMIX)									
1	Perkerasan Beton Semen									
	Dengan Serat Baja *Steel Fiber*									
	(Dramix)									
	Jumlah Sub A									Rp 5,394,267.00
B	*WIREMESH M-8*									
1	Pekerjaan Beton Semen	5.00	x	3.00	x	0.20	3.00	m3	Rp 1,468,089.00	Rp 4,404,267.00
2	Pembesian Deking						7.41	kg	Rp 17,758.00	Rp 131,586.78
	(dudukan) *Wiremesh*									
3	*Wiremesh*						82.42	kg	Rp 22,800.00	Rp 1,879,176.00
	(M8 ukran 5,4x2,1/15x15)									
	Jumlah Sub B									Rp 6,415,029.78

Source: Data processed

Table 11 Budget plan for 1 m^3 of concrete

No.	URAIAN	KUANTITAS	SAT.	HARGA SATUAN (Rp)	JUMLAH (Rp)
A	SERAT BAJA	1.00	m3	Rp 1,798,089.00	Rp 1,798,089.00
	STEEL FIBER (DRAMIX)				
1	Perkerasan Beton Semen				
	Dengan Serat Baja *Steel Fiber*				
	(Dramix)				
	Jumlah Sub A				Rp 1,798,089.00
B	*WIREMESH M-8*				
1	Pekerjaan Beton Semen	1.00	m3	Rp 1,468,089.00	Rp 1,468,089.00
2	Pembesian Deking	2.47	kg	Rp 17,758.00	Rp 43,862.26
	(dudukan) *Wiremesh*				
3	*Wiremesh M-8*	27.47	kg	Rp 22,800.00	Rp 626,392.00
	(M8 ukran 5,4x2,1/15x15)				
	Jumlah Sub B				Rp 2,138,343.26

Source: Data processed

5 Conclusion

Based on the discussion in this study, the conclusions can be drawn as follows:

1. Steel fiber (dramix) is cheaper and more economical than wire mesh reinforcement in rigid pavement. 1 m^3 of concrete with iron reinforcement by wire mesh m8 costs Rp. 2,138,343.26. However, at the addition of the 10% of steel fibers (dramix) , the cost decreases to Rp. 1,798,089.00, defining a cost savings equal to Rp. 340,254.26 per 1 m^3.

2. The addition of steel fibers (dramix) in concrete mixes has increased compressive strength after 28 days compared with normal concrete mixes with compressive strength value of $f_{c'} = 29.07$ MPa. For the concrete with the added 10% content of steel fibers (dramix) , it reaches $f_{c'} = 29.34$ MPa; for 15%, it achieves $f_{c'} = 29.38$ MPa; for 20%, it achieves $f_{c'} = 29.41$ MPa; and for 30%, it achieves $f_{c'} = 29.58$ MPa. The addition of steel fibers (dramix) at an optimum level of 10% produces an average concrete compressive strength equal to $f_{c'} = 29.34$ MPa.

3. In flexural strength test, concrete with wire mesh m8 reinforcement produces a flexural strength of $f_{c'} = 4.978$ MPa. At the same time, flexural strength test of concrete with the addition of steel fibers (dramix) with 10% content reaches $f_{c'} = 5.173$ Mpa; for 15%, it achieves $f_{c'} = 5.316$ MPa; for 20%, it achieves $f_{c'} = 5.458$ MPa; and for 30%, it achieves $f_{c'} = 5.707$ MPa.

References

1. B. Witjaksana, Penambahan Fibre Steel Pada Campuran Beton **1**(2), 209 (2016) (In Indonesian)
2. Lirawati, Teknologi **1**(31), 39 (2018) (In Indonesian)
3. E.Y. Fachrurrozi, A. Kurniawandy, Pengaruh Penambahan Serat Baja Terhadap Sifat Mekanis Beton Normal **1** (2003) (In Indonesian)
4. F.S. Sustika Pratiwi, P. Hakas, Semesta Tek **19**(1), 55 (2016) (In Indonesian)
5. R.I. Abdul Azis, P. Herman, Studi Tarik Belah Beton Dengan Penambahan Dramix Steel Fiber (2016) (In Indonesian)
6. E.R. Nur Rohmad, Agus Setiya Budi. J. Soc. Sci. **81**, 51 (2016) (In Indonesian)
7. I.M. Kader, I Made Suardana. Wahana Tek. Sipil **23**(2), 56 (2018). ((In Indonesian))
8. T.P.G.A. Perbandingan Kekuatan Beton Dengan Campuran Dramix Steel Fiber Dan Tulangan Wiremesh Pada Rigid Pavement (2019) (In Indonesian)
9. W. Dwi Nuur Musyaffa, Sholihin As'ad, P*engaruh Dosis Dan Aspek Rasio Serat Baja Terhadap Kuat Tekan Dan Modulus Elastisitas Pada Beton Normal Dan Beton Mutu Tinggi*, 427 (2015) (In Indonesian).
10. Dirjend Cipta Karya DPU, Jakarta Direktorat Penyelid. Masal. Bangunan **7** 130 (1971) (In Indonesian)
11. SNI 4431. 2011, Cara Uji Kuat Lentur Beton Normal Dengan Dua Titik Pembebanan, Badan Standarisasi Nasional, Badan Standar Nas. Indones **16** (2011) (In Indonesian)
12. SNI 03-1974-1990, Metode Pengujian Kuat Tekan Beton, Badan Standarisasi Nasional, Badan Stand. Nas. Indones (1990) (In Indonesian)
13. Diklat Perkerasan Kaku, Konsep Dasar dan Konstruksi Perkerasan Kaku, Kepala Pusat Pendidikan dan Pelatihan Jalan, Perumahan, Permukiman, dan Pengembangan Infrastruktur Wilayah **51** (2017) (In Indonesian)

Applications of Advanced Materials

Analysis of the Ultrasonic Guided Wave Sensitivity to the Bone Structure for Osteoporosis Diagnostics

Evgeny Glushkov, Natalia Glushkova, Olga Ermolenko, and Alexey Tatarinov

Abstract In the last decades, Quantitative Ultrasound (QUS) has become a widespread method of examining human bones to assess their current state and detect developing osteoporosis. This is mostly based on empirical experimental data, while theoretical (computer) simulation of wave processes in bones and bone-like structures (so-called phantoms) provides an insight into the guided wave regularities in such structures. A parametric study reveals the influence of various factors that could be used in osteoporosis diagnostics as signs of latent bone degradation. The present work gives examples of such a case study using the Green's matrix-based semi-analytical model for guided wave excitation and propagation in elastic multilayered waveguides mimicking typical property variations in real bones covered by a soft tissue.

Keywords Bone phantoms · Guided waves · Green's matrix · Modal excitability · Time–frequency scalograms

1 Introduction

In recent years, in the field of diagnosis and prevention of osteoporosis, there has been an increase in interest in determining the condition of compact bone tissue being the main supporting element of the skeleton, which quality determines the risk of atraumatic bone fractures in osteoporosis. Quantitative Ultrasound (QUS) is a promising tool for diagnosing the risk of osteoporotic fractures since the ultrasound propagation parameters reflect the material properties of the compact bone tissue [1, 2]. Ultrasonometers have such advantages over X-ray densitometry as the absence of ionizing radiation, compactness, and lower cost. Understanding the dependence of

E. Glushkov (✉) · N. Glushkova · O. Ermolenko
Institute for Mathematics, Mechanics and Informatics, Kuban State University, Krasnodar, Russia
e-mail: evg@math.kubsu.ru

A. Tatarinov
Riga Technical University, Riga, Latvia

I. A. Parinov et al. (eds.), *Physics and Mechanics of New Materials and Their Applications*, Springer Proceedings in Materials 10,
https://doi.org/10.1007/978-3-030-76481-4_35

the guided wave (GW) propagation and structural frequency response on the factors related to the state of the bone can reveal hidden signs of osteoporosis, improving its diagnostics [3–11].

The present work is focused on the simulation of the dynamic response and ultrasonic guided waves piezoelectrically generated in samples mimicking real bones (phantoms) in order to identify signs predicting osteoporosis. Here we use the analytically-based computer model [12] that has also been developing for the ultrasonic inspection of composite materials in the framework of Structural Health Monitoring (SHM) technologies [13, 14]. The experimental and numerical results obtained for the phantoms under consideration are analyzed and discussed.

2 Bone Structure, Phantoms

In general, tubular bones are inhomogeneous cylindrical waveguides of variable thickness. Since the ultrasonometry is usually carried out at their middle part, where the thickness varies insufficiently, in the theoretical modeling, the bones are customarily considered as elastic waveguides of a constant cross-section. As an example, Fig. 1, which is copied from Ref. [10], shows a typical cross-section of a bone radius (left) and the dependence of its elastic properties on the transverse coordinate (right). The latter is illustrated by a simplified distribution of the elastic modulus C_{11} varying with the distance from the periosteum to endosteum for healthy and osteoporotic conditions. Their decrease with depth is because, inside, the bone becomes more and more spongy.

Outside, the bone is covered by a layer of soft tissue, and inside is the bone marrow. Both these materials are jelly-like substances typically modeled by viscous acoustic fluid. However, they still transmit shear waves. Therefore, in the numerical examples below, we also model them by an elastic medium with low transversal wave velocity, which Poisson's ratio is close to 0.5.

The bone ultrasonometry is based on the guided wave generation and registration by piezoelectric transducers applied to the guide's surface, i.e., to the soft tissue.

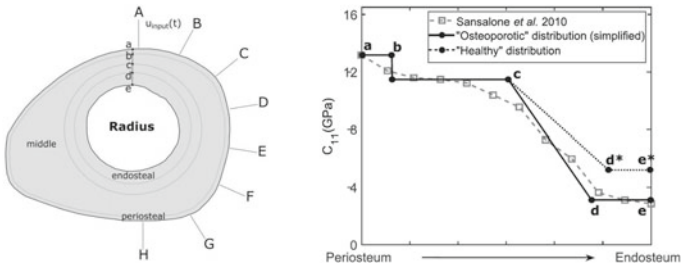

Fig. 1 Typical cross-section of a tubular bone (left) and a simplified distribution of elastic moduli with the transverse coordinate (right) [10]

The frequency response and dispersion properties of the traveling waves propagating from the source to sensors in most are due to the specific bone's layering under the soft tissue. To study the effect of bone thickness and elastic properties on wave characteristics, a wide range of bone samples is required, which is difficult to provide in practice. Therefore, experimental and theoretical studies are usually performed with artificial guides mimicking the wave properties of real bones, so-called, phantoms [6, 8].

To account for the cylindrical form of tubular bones, the phantoms are often fabricated in the form of layered pipes. However, it is unnecessary, because the response of the bone's wall to a localized surface loading is similar to that of an elastic plate, and comparative measurements show that laminate plates with properly chosen effective elastic properties can provide the same waveguide properties. For example, Minonzio et al. [6] have demonstrated that a non-absorbing free plate model can predict guided modes measured in bone-mimicking phantoms of circular cross-sections. Such a replacement of tubular waveguides by plates is widely used in research, for example, in developing a theoretical base for the guided wave structural health monitoring (GW SHM) of industrial pipelines [15].

One of the most popular is a bi-layer phantom mimicking a cortical bone covered with soft tissue (Fig. 2). Moreover, the tissue is often modeled by a fluid layer, which, nevertheless, allows obtaining substantive results. For example, using such a fluid–solid model, nonlinear grid-search inversion has been developed to estimate the thickness and elastic velocities of long cortical bones [16]. Single-layer phantoms without any soft covering but of more complex anisotropic [17] or porous [11] material properties are also used for the goal functions of the inverse problem. The objective functions are usually constructed as discrepancies between the experimentally obtained dispersion curves and those theoretically generated for the selected phantoms.

To account for the bone structure in more detail, we also use M-layered phantoms (M is the number of sublayers). The soft tissue is as in the bi-layer model, but the bone itself is divided into sublayers, and a layer of bone marrow can also be added (Fig. 3).

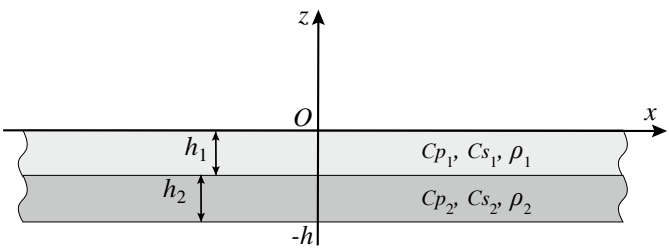

Fig. 2 Bi-layer phantom: soft tissue of thickness h_1 above a cortical bone of thickness h_2; the material properties are specified by body wave velocities c_p and c_s, and density ρ shown in the two first lines of Table 1

Table 1 Material parameters

Material	c_p, km/s	c_s, km/s	ρ, $\times 10^3$ kg/m^3	ν
ST: soft tissue	1.550	0.369	1.06	0.47
B1: periosteum	2.700	1.226	1.19	0.37
B2: middle bone	2.086	0.886	1.14	0.39
B3: endosteum	1.867	0.640	1.09	0.39
BM: bone marrow	1.550	0.369	1.06	0.47

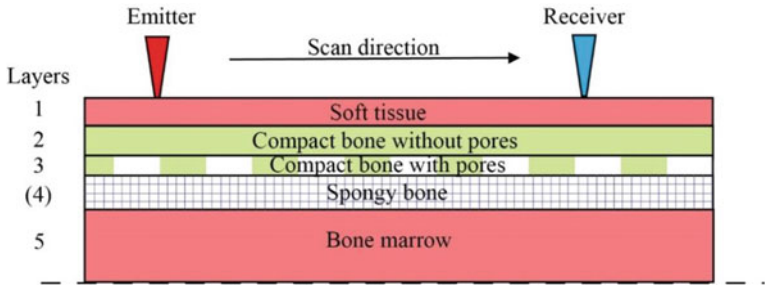

Fig. 3 Multilayered phantom

3 Experimental Measurements

The GW measurements at phantoms make it possible to evaluate the waveform patterns depending on the bone's weakening and soft tissue thickness. In this section, we give an example of such measurements carried out at Riga Technical University. The experimental setup and the measurement scheme are shown in Fig. 4. The soft tissue was simulated by a plastic layer with a thickness of $h_1 = 5$ mm, 2 mm, and 0 mm, and the layer of polymethyl methacrylate (also known as acrylic resin or plexiglass) with a thickness of $h_2 = 3$ mm were taken to mimic a cortical bone. Its

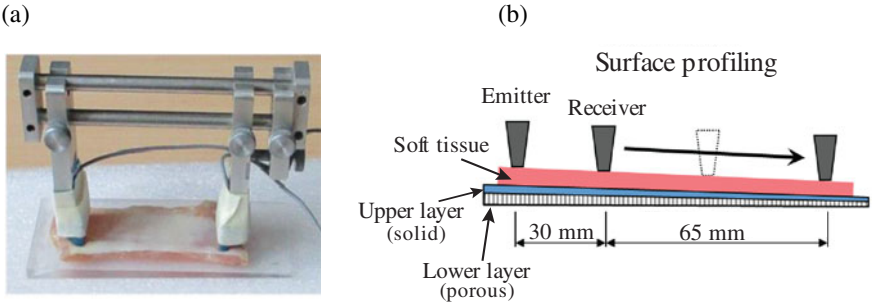

Fig. 4 Experimental setup (**a**), and measurement scheme (**b**)

developing weakening was provided by a set of holes imitating porosity, drilled from the bottom to half thickness, removing 10% or 35% of the material volume. The material properties of these layers are shown in the two first lines of Table 1 (*ST* and *B1*).

The materials in Table 1 are isotropic, while the bones, generally say, are anisotropic waveguides with different elastic properties along and across the bone axis. Such transversely isotropic materials are specified by five independent elastic moduli. To estimate the effect of anisotropy compared to material *B1*, the phantom with an anisotropic cortical bone layer (*BA*) was also considered in the numerical examples. Its elastic constants and density were taken as follows:

$C_{11} = 16.04$ GPa, $C_{22} = 13.17$ GPa, $C_{12} = 6.60$ GPa, $C_{44} = 3.62$ GPa, $C_{55} = 3.75$ GPa;

$C_{33} = C_{22}$, $C_{13} = C_{12}$, $C_{66} = C_{55}$, $C_{23} = C_{22} - 2C_{44}$, $\rho = 1850$ kg/m^3.

They yield body wave velocities close to those in material *B1*, but different from each other for the axial and transversal directions: $c_\mathrm{p} = 2.94$ km/s, $c_\mathrm{s} = 1.42$ km/s and $c_\mathrm{p} = 2.67$ km/s, $c_\mathrm{s} = 1.40$ km/s, respectively.

Figure 5 shows the measurement results obtained for nine bi-layer specimens: three options for the soft coating thickness: $h_1 = 5$ mm, 2 mm, and 0 mm (rows of subplots from top to bottom), and three choices of the bone substrate with 0%, 15%, and 35% porosity (columns from left to right). Each of the top subplots displays a time–space waveform profile composed of normalized signals $v_j(t) = u_z(x_j, 0, t)/\max|u_z|$ recorded at receiving points x_j, spaced 2.5 mm apart, starting at a distance of 30 mm from the emitter. The signals are arranged upwards, so the ordinate indicates the distance from the emitter. The abscissa is for the sampling time, the digits on the axis are the numbers of the time points. To give an idea of the signal patterns, the lower subplots show their enlarged view for the lines marked in red (20th grading step, 80 mm from the emitter).

The differences in the wave patterns in Fig. 5 make it visually evident the presence of changes in the samples' structure. However, it is not easy to interpret their meaning based on the unprocessed measurement data. Therefore, signal-processing algorithms and mathematical modeling are used to extract and study such GW characteristics as arrival times, dispersion curves, frequency response spectra, time–frequency representations, and others providing an insight into the wave processes.

4 Mathematical Framework

In modern research, the most popular numerical simulation tool is the finite element method (FEM) implemented in standard commercial packages. However, the same as in the experimental measurements, it cannot give an insight into the wave structure without post-processing. Therefore, for simulating the displacement field $\boldsymbol{u}(\boldsymbol{x}, t)$ generated in a multilayered waveguide by a given source $\boldsymbol{q}$, we traditionally use

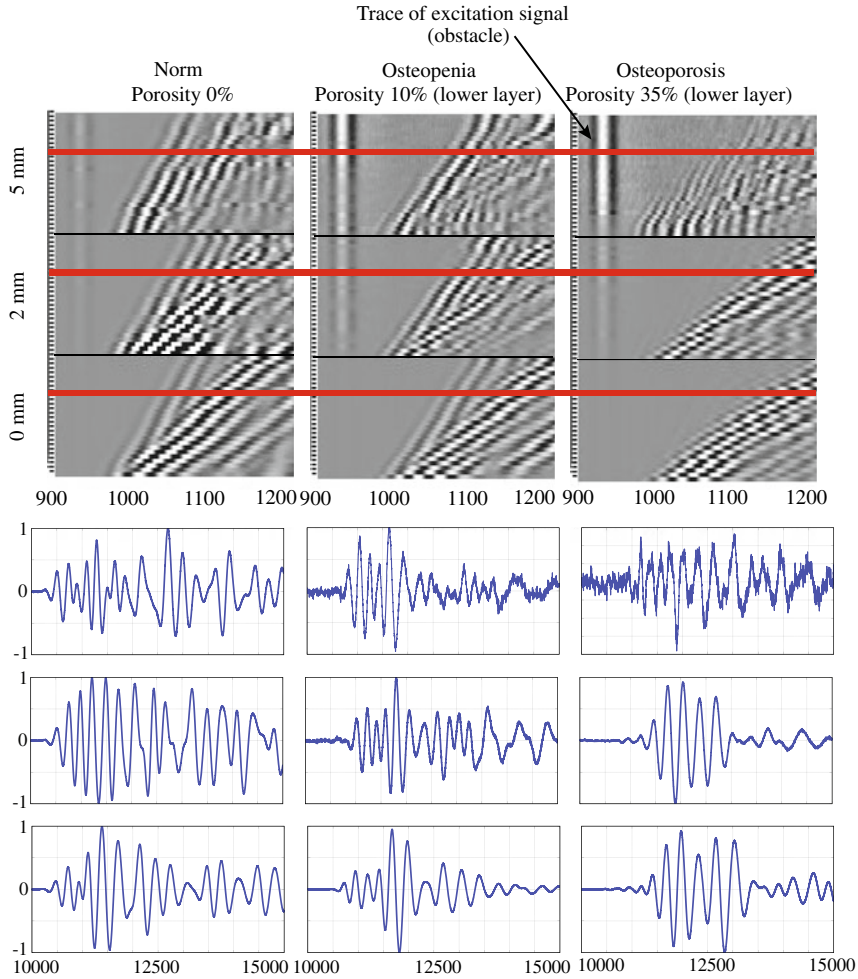

Fig. 5 Examples of 2D time–space waveform profiles at 100 kHz (top) and normalized signals (bottom) for the 20th profiling step marked by horizontal red lines; subplot rows are for the soft tissue of 5 mm, 2 mm, and 0 mm thick; the columns are for the second layer porosity of 0, 10, and 35%

a semi-analytical approach based on the explicit integral and asymptotic representations. A detailed description of deriving these representations can be found in Ref. [12] and papers cited therein.

The transient field is represented via its frequency spectrum $\boldsymbol{u}(\boldsymbol{x}, \omega)$ as the inverse Fourier integral in the frequency domain:

$$\boldsymbol{u}(\boldsymbol{x}, t) = \frac{1}{2\pi} \int_{-\infty}^{+\infty} \boldsymbol{u}(\boldsymbol{x}, \omega) e^{-i\omega t} d\omega. \tag{1}$$

In turn, the spectrum $\boldsymbol{u}(\boldsymbol{x}, \omega)$ (i.e., the complex amplitude $\boldsymbol{u} = (u_x, u_z)$ of the in-plane steady-state oscillations $\boldsymbol{u}e^{-i\omega t}$) is represented as a convolution of the structure's Green's matrix $k(x, z)$ with the surface load $\boldsymbol{q}$, or, alternatively, in terms of the path inverse Fourier-transform integral of their Fourier symbols $K(\alpha, z) = F_x[k]$ and $\boldsymbol{Q}(\alpha) = F_x[\boldsymbol{q}]$:

$$\mathbf{u}(\mathbf{x}, \omega) = \int_{\Omega} k(x - \zeta, z) \boldsymbol{q}(\zeta) d\zeta = \frac{1}{2\pi} \int_{\Gamma} K(\alpha, z) \boldsymbol{Q}(\alpha) e^{-i\alpha x} d\alpha. \tag{2}$$

Here F_x is the Fourier transform operator with respect to the horizontal coordinate x, Ω is the load application area (contact area of the piezoelectric actuator), $\omega = 2\pi f$ is the angular frequency, f is frequency, and $\boldsymbol{x} = (x, z)$. In the 2D case considered, the matrix $k = (\boldsymbol{k}_1 \,|\, \boldsymbol{k}_2)$ is of size 2×2. Its columns $\boldsymbol{k}_j$ are the solution vectors corresponding to the surface point loads $\boldsymbol{q} = \delta(x)\boldsymbol{i}_j$, $j = 1, 2$, applied along the basic coordinate vectors $\boldsymbol{i}_1 = (1, 0)$ and $\boldsymbol{i}_2 = (0, 1)$; δ is Dirac's delta function. In the numerical examples below, the action of a piezoactuator on the bone phantom is simulated by a vertical point load $\boldsymbol{q} = (0, \delta)$; thus, the integrand in Eq. (2) is the second column of matrix K. Moreover, only element K_{22} is required to simulate the frequency spectra $v_j(\omega)$ of the signals $v_j(t) = u_z(x_j, 0, t)$ registered by a receiver.

Applying the residue technique to the path integral in Eq. (2) gives the source-generated GWs as residues from the poles ζ_n of the matrix K elements:

$$\begin{aligned} &\boldsymbol{u}(x, z) = \sum_{n=1}^{N} \mathbf{a}_n(z) e^{i\zeta_n x} \left[1 + O\left(e^{-\mathrm{Im}\zeta_{N+1} x}\right)\right], \quad |\zeta_n| x \gg 1 \\ &\boldsymbol{a}_n = -i \,\mathrm{res} K(\alpha, z)|_{\alpha=-\zeta_n} \boldsymbol{Q}(-\zeta_n). \end{aligned} \tag{3}$$

Here N is the number of terms retained in the expansion; it includes the contribution of all real poles and, possibly, several complex ones close to the real axis. Each term describes the guided wave specified by the wavenumber ζ_n and the amplitude vector $\boldsymbol{a}_n$. The poles $\pm\,\zeta_n$ are zeros of the common denominator Δ of the matrix K elements, arranged in ascending order of the imaginary parts (Im $\zeta_{n+1} \geq$ Im ζ_n). They are roots of the characteristic equation:

$$\Delta(\alpha, f) = 0 \Longrightarrow \alpha = \zeta_n(f) \tag{4}$$

that coincides with the GW dispersion equation derived in the framework of usual modal analysis. Written as a function of frequency, the roots $\alpha = \zeta_n(f)$ are dispersion curves in the frequency-wavenumber plane. Consequently, $c_n = \omega/\mathrm{Re}\ \zeta_n$, $v_n = \mathrm{d}\omega/\mathrm{d}(\mathrm{Re}\ \zeta_n)$, and $s_n = \mathrm{Re}\ \zeta_n\ /\omega$ are GWs' phase velocities,

group velocities, and slownesses. The imaginary parts specify the damping decrements $\delta_n = 2\pi \mathrm{Im}\ \zeta_n / \mathrm{Re}\ \zeta_n$.

5 Numerical Case Studies

The Green's matrix-based representations above allow a fast parametrical study of wave processes in multilayered phantoms. The results presented in this section aim to clarify the effects of phantom structure on the GW characteristics in order to assess the manifestation of diagnostic signs.

5.1 Dispersion Curves and Guided Wave Excitability

First, we have analyzed the change in dispersion curve patterns depending on the model complexity. Besides the basic bi-layer model *ST/B1*, $h_1 = h_2 = 3$ mm, the dispersion curves for three-layered phantoms with an added underlying half-space ($h_3 = \infty$) or thick layer ($h_3 = 10$ mm) of the bone marrow (*BM*) was also calculated. Moreover, we considered a laminate sandwich with a thick middle layer of bone marrow ($M = 5$) and a bi-layer phantom with the anisotropic bone layer (*BA*) instead of *B1*.

Those studies have shown that the bone marrow accounting leads to the emergence of additional dispersion curves, associated with the new GWs propagating at the *B1/BM* interface and in the underlying *BM* layer. This results in a considerable complication of the dispersion curve patterns. At the same time, the calculated surface wave fields change slightly. This seeming contradiction can be explained, if we consider not only the dispersion curves themselves but also the excitability of the related GWs.

The excitability is determined by the amplitude factors $\boldsymbol{a}_n$ in expansion (3), which depend on both the guide's structure (via ***resK***) and the wave source (via $\boldsymbol{Q}$). This is the main advantage of the Green's matrix-based expansions compared with the modal analysis, not accounting for the source characteristics. The modal analysis technique also provides the normal mode eigenforms $\boldsymbol{a}_n(z)$, but only to the constant factor accuracy. In contrast, the GW amplitudes in Eq. (3) are uniquely determined by the source and structure.

The GW amplitudes, specified by the residues ***resK***, vary in a vast range; so that some dispersion curves or their parts do not visibly contribute to the total wave field. Figure 6 demonstrates how the modal excitability varies with frequency. The left subplot depicts the dispersion curves calculated for the basic bi-layer phantom *ST/B1*, $h_1 = h_2 = 3$ mm as the roots of Eq. (4). We plot the slowness curves $s_n(f)$ because they do not grow to infinity with f increase as is typical for the traditionally displayed wavenumber curves $\zeta_n(f)$. The right subplot shows the frequency spectra of the out-of-plane amplitude $|a_z(f)|$ of the corresponding GW modes. One can see

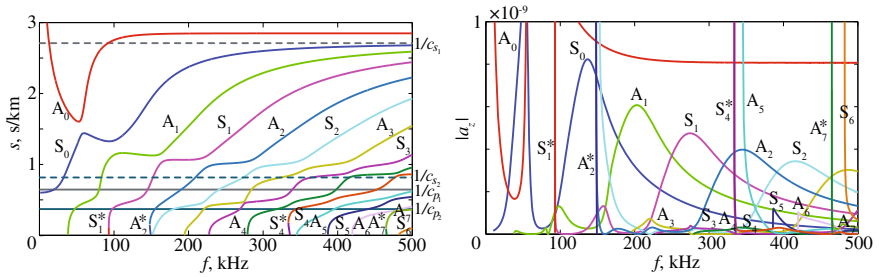

Fig. 6 Slowness dispersion curves $s_n(f)$ (left) and the amplitudes $|a_z|$ of the related GWs generated by the point- source in the bi-layer phantom *ST/B1*

that every higher mode gives a peak contribution at a certain frequency and then monotonous decreases. As a consequence, each GW appreciably contributes to the total field only in a certain limited frequency range.

The GW excitability can be seen after post-processing of the experimentally obtained wave profiles. For example, the 2D time–space discrete Fourier transform applied to the data displayed in Fig. 5 should yield scalogram images that draw patterns similar to that in Fig. 6 (left). The difference is that the curves associated with small-amplitude GWs should hardly be distinguishable on such post-processed images. In the mathematical model, the application of the Fourier transform F_{tx} to the signals $u_z(x, 0, t)$ is nothing but the Fourier symbol $U_z(\alpha,\omega) = K_{22}(\alpha,0,\omega)Q_z(\alpha)$ of the time-harmonic solution. Therefore, with the point source ($Q_z = 1$), the images of the K_{22} element in the frequency-slowness plane (f, s) should exhibit the same patterns as the post-processed images. As an example, Figs. 7, 8, and 9 show a series of such images for different phantoms; they depict $|K_{22}|$ multiplied by ω. This factor is added to balance the image by suppressing too high K_{22} magnitudes at low frequencies.

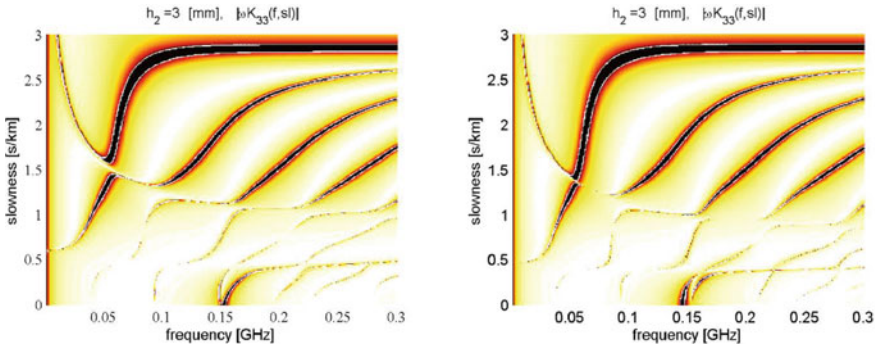

Fig. 7 Magnitude of Green's matrix element $\omega|K_{22}|$ in the frequency-slowness plane (f, s) for the bi-layer phantoms *ST/B1* (left) and *ST/BA* with the anisotropic bone model (right)

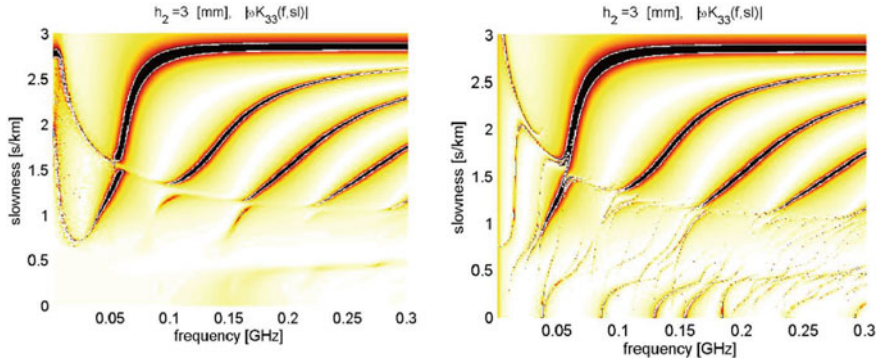

Fig. 8 Same as in Fig. 7, but for the M-layer structures demonstrating the influence of bone marrow (*BM*): *ST/B1/BM* half-space ($M = 3$, $h_3 = \infty$, left), and *ST/B1/BM/B1/ST* sandwich ($M = 5$, $h_3 =$ 10 mm, right)

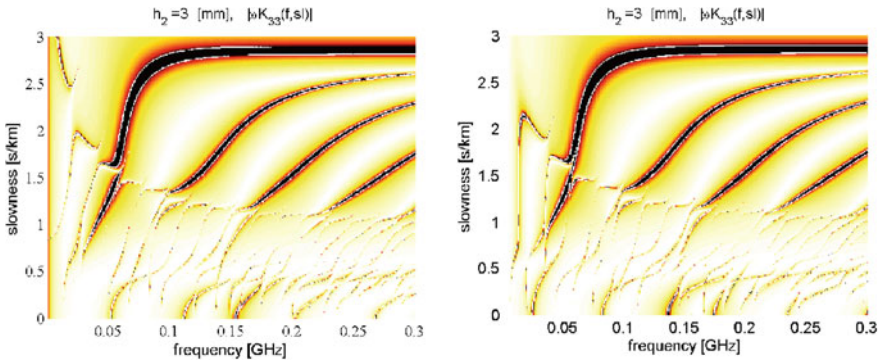

Fig. 9 Same as in Figs. 7, but for the 3-layer phantoms *ST/B1/BM* with a thick *BM* sublayer (h_3 = 10 mm) with a free (left) and clamped (right) bottom side

Comparison of Fig. 7 (left) with the curves in Fig. 6 (left) shows that while the dispersion curves are drawn very clear at the top of the figure, they are poorly visible at the bottom. It means that the corresponding GWs are badly excitable in this zone (approximately for $s_n < 1$ s/km, i.e. for the high phase velocity waves with $c_n >$ 1 km/s), except the backward A2 mode at the cut-off frequency $f = 150$ kHz. The right subplot of Fig. 7 demonstrates that accounting for the bone anisotropy insufficiently changes the dispersion properties and excitability of the generated wave modes. The assessment of the influence of the guide's structure variation on the manifestation of diagnostic signs is quite possible to study with isotropic models.

The images of Figs. 8 and 9 illustrate how accounting for the bone marrow (*BM*) can alter the patterns of excitable GWs. The general conclusion is that such a complication of the theoretical model does not add anything significant to the bi-layer phantom because the upper parts of these images, indicating the main excitable

GWs, remain very similar to those in Fig. 7. All essential differences are only in the lower parts, where many new modes emerge, or they all entirely disappear in the case of the underlying *BM* half-space (Fig. 8, left). But all these modes are poorly excitable and cannot make a significant contribution to the total wavefield measured in experiments.

Thus, the two-layer part of the guide (soft tissue/bone) is responsible for the general dispersion curve pattern of the main excitable GWs.

5.2 Bi-layer Phantom: Effect of Layer Thickness Ratio

Given the above conclusion, it is worth considering how the GW measurements on the bi-layer phantoms might depend on its thickness ratio. Figure 10 gives an example of such an analysis with a series of bi-layer samples *ST/B1* of the same total thickness $h_1 + h_2 = 6$ mm but various h_1 and h_2. The wavefields are generated by the vertical point source $\boldsymbol{q} = (0, \delta(x))p(t)$ with the Hann-windowed driving pulse at the central frequency $f_c = 200$ kHz and the window half-width $d = 50$ kHz:

$$p(t) = \frac{\pi cos\omega_c sindt}{t\left(\pi^2 - d^2t^2\right)}$$

The left-hand column of subplots in Fig. 10 display theoretical dispersion curves calculated as the real roots of the characteristic Eq. (4) for bi-layer phantoms with *ST* coating of thickness $h_1 = 6, 4, 3, 2$, and 0 (mm) and *B1* substrate of thickness $h_2 = 0$, 2, 3, 4, and 6 (mm), respectively. In the first and last cases, the bilayer degenerates into a homogeneous ($M = 1$) soft or hard layer. The middle column of subplots is for the transient signals received at a distance of 80 mm from the emitter. They are calculated using representation (3) and transform (1). The right-hand images are their time-frequency scalograms obtained after the wavelet-transform post-processing with a Gabor kernel Ψ_g [18]:

$$(Wu)(a,b) = \frac{1}{\sqrt{a}} \int_{-\infty}^{+\infty} u(t) \overline{\Psi_g\left(\frac{t-b}{a}\right)} dt,$$

$$\Psi_g = \frac{1}{\sqrt[4]{\pi}} \sqrt{\frac{\omega_o}{\gamma}} \exp\left[-\frac{(\omega_o/\gamma)^2}{2} t^2 + i\omega_0 t\right].$$

Parameter a is responsible here for the frequency, and b is for the time ($a = f_c/f$, $b = n\Delta t$, $\gamma = \pi\sqrt{2/ln2}$, $\omega_0 = 2\pi f_c$).

The comparison of the dispersion curves shows that with an increase in the thickness of the harder lower layer, the number of curves in the considered range becomes smaller, and their shape gradually changes. However, the location of the main spot on the time–frequency images indicates approximately the same arrival time of the

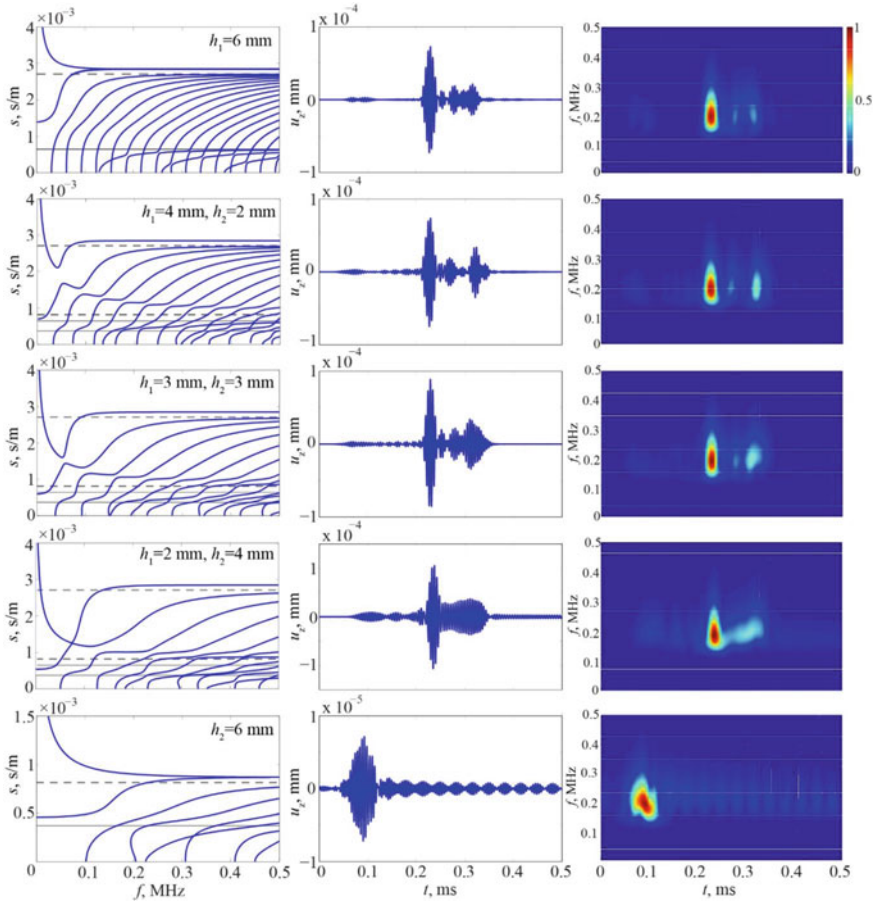

Fig. 10 Simulation of 200 kHz signals emitted and received in the bi-layer phantoms *ST/B1* of the total thickness $h_1 + h_2 = 6$ mm but various h_1 and h_2; theoretical dispersion curves (left), signals received at $x = 80$ mm (middle), and their time-frequency scalograms (right)

dominating wave packet in all cases, except for the last one, when it arrives much faster. This means that in bi-layer phantoms, the same arrival time is determined only by the presence of soft coating, regardless of its thickness and specific patterns of theoretical dispersion curves. And only in the absence of a soft coating, the group velocity of the primary wave packet changes sharply.

In the first four cases, the guide structure variation leads to changes in the transient-signal foreshocks and aftershocks, reflected in the shape variation of weak blurs before and after the principal spot in the time–frequency images. However, it seems not easy to use these variations as diagnostic indicators, also like the arrival time and the dispersion curves of measured (excitable) GWs.

5.3 Degradation of Cortical Bone

Osteoporotic bone degradation is manifested in the weakening of strength properties in the inner part. Therefore, it is natural to identify its signs by analyzing changes in the wave pattern with a gradual variation in the bone properties starting from the basic bi-layer model *ST/B1*. Since the optimal central frequency is not known in advance, in these numerical studies, we used a delta-like source pulse $p(t) = \delta(t)$ generating broadband signals. The time-frequency scalograms of such signals were calculated for the phantoms with the same *ST* coating of thickness $h_1 = 3$ mm and the same total thickness $h = 6$ mm, but with the increasing complexity of the bone structure. Figure 11 gives examples of such scalograms for the signals registered at distances of $x = 40$ mm and 80 mm with the three specimens:

$M = 2$, $h_1 = 3$ mm, $h_2 = 3$ mm (*ST/B1*);
$M = 3$, $h_1 = 3$ mm, $h_2 = 1.5$ mm, $h_3 = 1.5$ mm (*ST/B1/B2*);
$M = 4$, $h_1 = 3$ mm, $h_2 = 1.5$ mm, $h_3 = 0.75$ mm, $h_4 = 0.75$ mm (*ST/B1/B2/B3*).

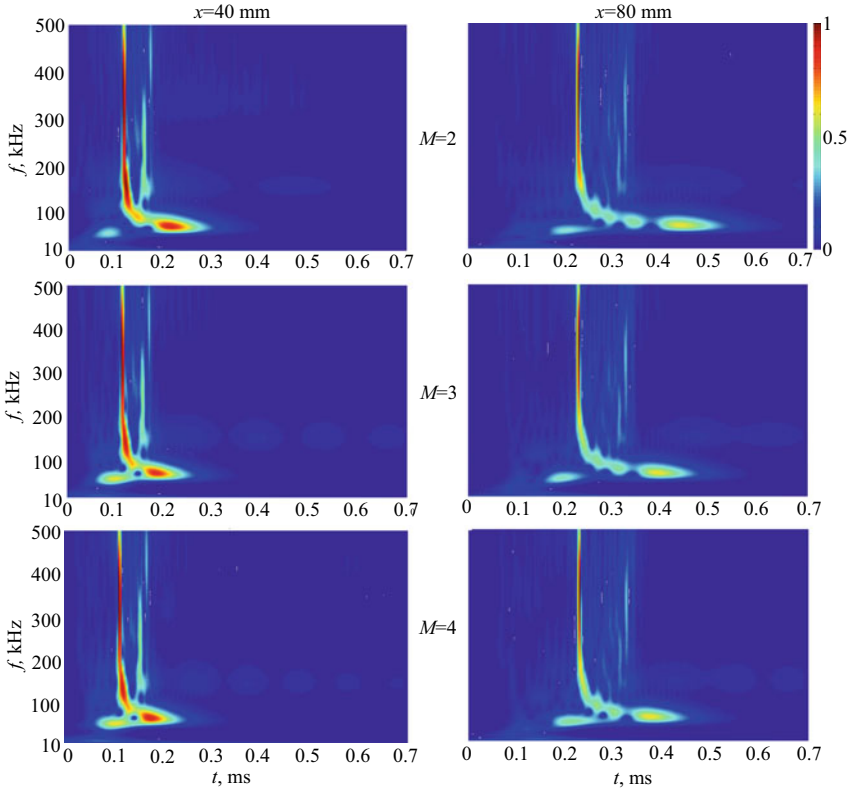

Fig. 11 Time-frequency scalograms of broadband signals calculated for the samples *ST/B1*, *ST/B1/B2*, and *ST/B1/B2/B3* (top-down) at distances of $x = 40$ mm and 80 mm (left–right)

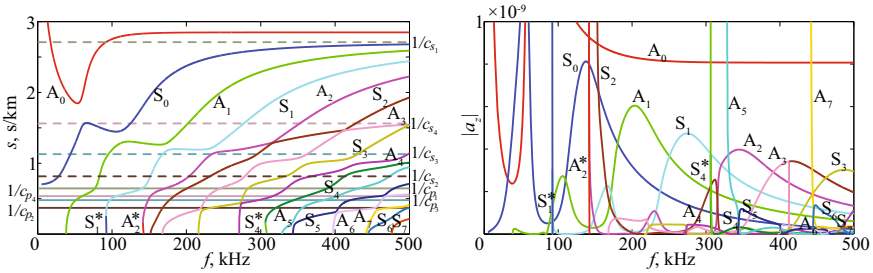

Fig. 12 Slowness dispersion curves $s_n(f)$ (left) and the amplitudes $|a_z|$ of the related GWs generated by the point- source in the four-layer phantom *ST/B1/B2/B3*

Comparison of the left and right images allows tracing the change with distance in the duration and frequency spectrum of the incoming GW packets. However, as in the previous examples in Fig. 10, the variation of bone structure does not noticeably affect the spots in these images, both the spots of the principal packets, and much weaker foreshocks and aftershocks.

At the same time, a more detailed study might reveal some diagnostic indicators even in small pattern variations. For example, the increase in the size of the speck appearing in the upper left image at $t < 0.1$ ms and f around 40 kHz looks potentially useful. In the last left-bottom image, it significantly swells, merging with the main spots.

Also interesting are chains of barely distinguishable oval spots behind the primary packet, stretching over the entire time range at a level of about 150 kHz. They indicate prolonged oscillations at this resonance frequency. It may be a thickness resonance or a zero-group velocity (ZGV) mode [19]. As the bone degenerates, the size of these spots decreases, i.e., the beat period of these oscillations shortens, which could be detected instrumentally.

It remains to add that the patterns of dispersion curves and modal excitability calculated for the four-layer phantom *ST/B1/B2/B3* (Fig. 12) also change little compared to those for the basic bi-layer phantom (Fig. 6). The most promising here are resonance peaks at the cut-off and ZGV frequencies. They are well detected by laser Doppler vibrometers (LDV) and are already used to fast estimate the plates' thickness and effective elastic properties [20, 21]. With multilayered waveguide structures, ZGV resonances are manifested as multiple peaks [22, 23]. Theoretically, it gives a chance to develop a QUS inspection method of the inner bone structure and monitor its gradual changes by detecting the number and frequencies of such multiple resonance peaks.

6 Conclusions

1. The analytically-based computer model earlier developed for ultrasonic SHM inspection of composite materials has been adapted and applied to the simulation of guided wave excitation and propagation in multilayered phantoms mimicking waveguide properties of tubular bones. The model provides a fast case study of the registered guided wave signals accounting for the emitter and guide's structure.
2. The patterns of theoretical dispersion curves are of little use because only excitable GWs contribute to the registered wavefields. Scalogram images of the corresponding Green's matrix elements are much more informative and should be used instead.
3. Accounting for the bone marrow layer in the computer model has not a significant effect on excitable GWs.
4. Time–frequency wavelet analysis has shown that the arrival time of the principal wave packet insensitive to changes in the ratio of thicknesses of soft and bone tissues and changes in the phantom's structure mimicking osteoporotic bone degradation. Such changes are reflected in variations of weak spots in the time-frequency scalograms related to non-principal foreshocks and aftershocks.
5. Thickness and ZGV resonances are well LDV detectable and, thus, of potential interest as a diagnostic indicator.

Acknowledgements The work is supported by the Russian Science Foundation (project No. 17-11-01191).

References

1. A. Tatarinov, N. Sarvazyan, A. Sarvazyan, Ultrasonics **43**, 672 (2005)
2. P. Moilanen et al., Ultrasound in Med. & Biol. **32**(5), 709 (2006)
3. P. Pisani, World. J. Radiol. **5**(11), 398 (2013)
4. V. Kilappa, K. Xu, P. Moilanen, Ultrasound Med. Biol **39**(7), 1223 (2013)
5. A. Tatarinov, V. Egorov, N. Sarvazyan, A. Sarvazyan, Ultrasonics **54**(5), 1162 (2014)
6. J.G. Minonzio, J. Foiret, P. Moilanen, J. Acoust. Soc. Am. **137**(1), 98 (2015)
7. D. Hans, S. Baim, J Clin Densitom **20**(3), 322 (2017)
8. K. Kassou, Y. Remram, P. Laugier, J.G. Minonzio, Ultrasonics **81**, 1 (2017)
9. K.I. Lee, S.W. Yoon, J. Biomech **55**, 147 (2017)
10. D. Pereira, G. Haïat, J. Fernandes, P. Belanger, J. Acoust. Soc. Am. **145**(1), 121 (2019)
11. J. Schneider, G. Iori, D. Ramiandrisoa, Arch. Osteoporos **14**(1), 21 (2019)
12. E. Glushkov, N. Glushkova, A. Eremin, J. Acoust. Soc. Am. **129**(5), 2923 (2011)
13. A. Raghavan, C.E.S. Cesnik, Shock Vib. Diagn. **2**, 91 (2007)
14. V. Giurgiutiu, *Structural Health Monitoring with Piezoelectric Wafer Active Sensors*. Academic Press/Elsevier: Cambridge, MA, 747 p. (2008).
15. M.J.S. Lowe et al., J. Acoust. Soc. Am. **112**(6), 2612 (2002)
16. J.-G. Minonzioa et al., Bone **116**, 111 (2018)
17. T. Tran, M.D. Sacchi, D. Ta, Ann. Biomed. Eng. **47**(11), 2178 (2019)

18. K. Kishimoto et al., J. Appl. Mech. **62**, 841 (1995)
19. C. Prada, O. Balogun, T.W. Murray. *Appl. Phys. Lett*. **87** 194109 (2005)
20. C. Prada, D. Clorennec, D. Royer, J. Acoust. Soc. Am **124**, 203 (2008)
21. C. Grünsteidl et al., Ultrasonics **65**, 1 (2016)
22. S. Karous et al., Can. J. Phys. **97**(10), 1064 (2019)
23. E.V. Glushkov, N.V. Glushkova, *J. Sound. Vibr*., **500**, 116023 (2021)

Finite Element Modeling of a Lensotome Tip with Piezoelectric Drive

A. N. Soloviev, A. N. Epikhin, N. I. Glushko, O. N. Lesnyak, and A. A. Solovieva

Abstract In the work mathematical and computer modeling the operation instrument, which is used in the operation to replace the lens are carried out. The tip of a lensotome, which is a hollow cylinder that vibrates axially is considered. Oscillations are excited by a piezoelectric element. A modal analysis of the structure is carried out, the frequencies of resonance, antiresonance and the coefficient of electromechanical coupling (CEMC) are found. An analysis of the values of this coefficient and natural modes of vibration allows us to select the operating frequency of the instrument, at which there is an effective conversion of electrical energy into mechanical and intensive movement of the lensotome tip end, which acts on the tissue of the lens during its fracture.

Keywords Lensotome · Lens · Piezoelectric element · FEM · CEMC · Vibration mode

1 Introduction

The operation to replace the lens (Fig. 1) can be conditionally divided into two stages: (i) the removal of natural lens, and (ii) the placement of an artificial lens in the capsular bag.

In Fig. 2, the diagrams of the lensotome device for the fracture and removal of the amorphous substance of the lens (patent [1]) are presented.

Figure 2 a shows the general scheme of interaction between the device and the apparatus. Figure 2 b demonstrates the device in longitudinal section, pneumatic version. In the figures, the numbers indicate: 1—lens, 2—eye, 3—inner tube of the handpiece, 4—handpiece, 5—drive, 6—handle, 7—lensotome device, 8—apparatus,

A. N. Soloviev (✉) · N. I. Glushko · O. N. Lesnyak · A. A. Solovieva
Department of Theoretical and Applied Mechanics, Don State Technical University, Rostov-on-Don, Russia

A. N. Epikhin
Department of Ophthalmology, Rostov State Medical University, Rostov-on-Don, Russia

I. A. Parinov et al. (eds.), *Physics and Mechanics of New Materials and Their Applications*, Springer Proceedings in Materials 10,
https://doi.org/10.1007/978-3-030-76481-4_36

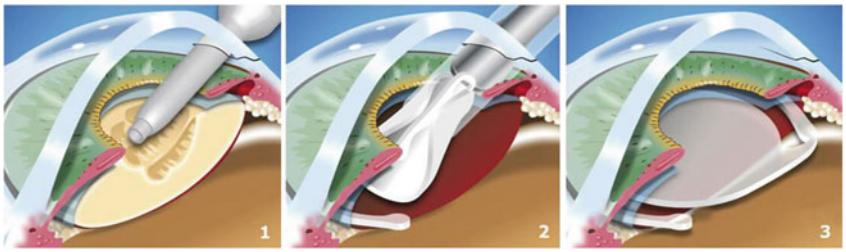

Fig. 1 Stages of the lens replacement surgery: (1) removal of clouded lens (phacoemulsification); (2) installing an artificial lens instead of removed lens; (3) Implantation of IOL

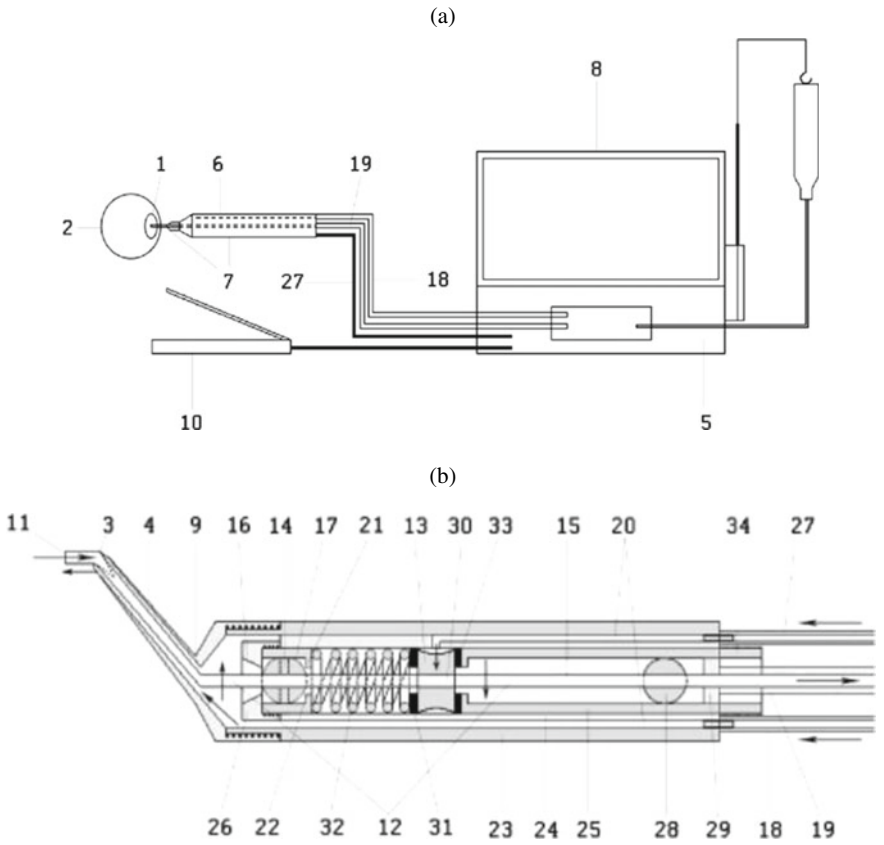

Fig. 2 **a** Lensotome schematic, **b** Lensotome element section

9—outer tube of the handpiece, 10—pedal remote control, 11—sharp cutting edge of the inner tube of the handpiece, 12—lever, 13—connecting rod, 14—support, point of rotation of the lever, 15—central suction tube of the handle, 16—guide groove, 17—front end cap of the handle, 18—irrigation hose, 19—suction hose, 20—channels and grooves, 21—cylindrical groove, 22—cylindrical groove opening, 23—outer handle tube, 24—middle handle tube, 25—inner handle tube, 26—guide sleeve, 27—air pneumatic hose or electric drive cable, 28—rear support, 29—absorbing ring, 30—connecting rod hole, 31—pressure washer, 32—pressure spring, 33—rubber gasket, 34—concentric holder. In the figures, arrows indicate the directions of movement of compressed air, irrigation and aspiration flows, and counter movements of the inner tube (3) of the tip (4) and the central aspiration tube (15) of the handle.

The method of fracture and removal of the pathologically altered and/or localized lens (1) of the eye (2) consists in the priority mechanical action of the pointed end of the movable internal aspiration tube (3) of the tip (4), movable by drive (5) placed outside or in/on the handle (6) of the device (7), indirectly connected to the device (8) and accompanying vacuum removal of the fractured substance through it by the aspiration system of the device (8). By this, there is a parallel replenishment of the volumes of the eye chambers (2) and the capsule sac of the lens (1) by a balanced solution, supplied through the second outer tube (9) of the tip (4) by the irrigation system of the device (8). For this, the necessary parameters of pressure levels, flow rates of liquids and vacuum in irrigation and aspiration systems, direction, speed and amplitude of the impact of the sharp end of the internal aspiration tube (3) of the tip (4) are preliminary set by the processor unit of the device (8). These procedures are activated and changed during the operation by a pedal stationary control panel (10). The operation is characterized by the mechanical fracture of the lens (1), carried out by lever-power cutting (vectopotential lensectomy) by using the specially sharpened and molded sharp edge (11) of the distal end of the inner cutting-aspirating tube-cutter (3) of the tip (4). By this, the force, amplitude, speed and direction are created by the lever (12) with the connecting rod (13) driven by the engine (5), which are united by the design of the device (7), namely the lens cutter.

In this case, cutting is performed due to the movements:

(i) with a given amplitude from 10 to 1 thousand microns, optimally from 50 to 500 microns, and a speed from 1 thousand to 1 million cuts/min, optimally from 3 to 300 thousand cuts/min, under the influence of a transversely swinging central suction tube (15) of the handle (6) of the movable element;

(ii) of the connecting rod (13), located transversely to the tube (15), and driven in different options by a compressed air or an electromagnetic field, or an electromechanical pusher;

(iii) in the direction specified at choice: circular clockwise or counterclockwise; linear-semicircular with deviations from top to bottom, vertically or diagonally; linear reciprocating vertical or horizontal, or diagonal movements; all types of the movements can be supplemented by abrupt reciprocating in the direction to the eye (2) movements of the support (14) along the longitudinal axis of the handle (6), and in the acceleration—deceleration mode;

(iv) with an amplitude of deviations and an impact force set at choice, which are found by two parameters: (a) by the value of the decentration of the through longitudinal hole of the connecting rod (13), through which the central aspiration tube (15) of the handle (6) passes, and (b) by the ratio of the lengths of the short and long arms of the lever (12), which can be changed by lengthening or shortening the long arm with help of longitudinal translational-return displacements of the connecting rod (13) and change on the required amplitude of deviations of the cutting edge (11) of the inner tube (3) of the tip (4) in the range from 10 to 1 thousand microns, optimally from 50 to 500 microns, and change the impact load.

2 The Continuum Formulation of the Problem

A device for a lensotome tip with a piezoelectric drive is proposed (see Fig. 3a). It consists of elastic piezoelectric pads and contacts with the acoustic medium. The linear equations of the theory of elasticity and electroelasticity, taking into account the

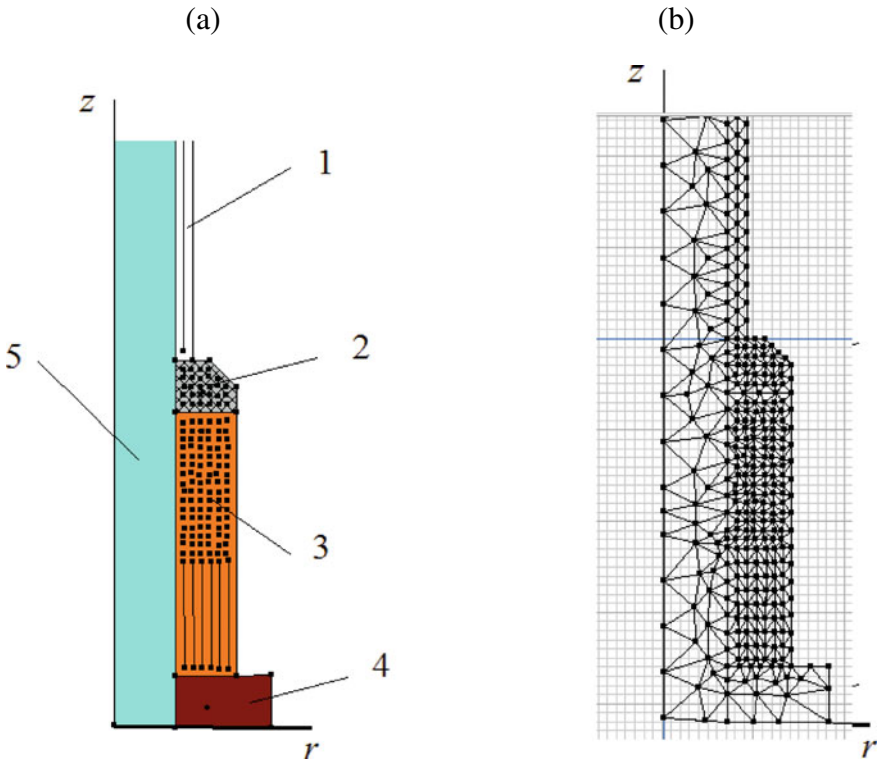

Fig. 3 Fragment of the tip: **a** elements, **b** finite element partition

dissipation of energy adopted in the ACELAN and ANSYS packages [2, 3], as well as the equations of motion of liquid and gaseous media in the acoustic approximation [4], are used as a continual model in this section.

For piezoelectric solid, we have:

$$\rho\ddot{u}_i + \alpha\rho\dot{u}_i - \sigma_{ij,j} = f_i; \quad D_{i,i} = 0, \tag{1}$$

$$\sigma_{ij} = c_{ijkl}(\varepsilon_{kl} + \beta\dot{\varepsilon}_{kl}) - e_{ijk}E_k; \quad D_i + \varsigma_d\dot{D}_i = e_{ikl}(\varepsilon_{kl} + \varsigma_d\dot{\varepsilon}_{kl}) + {}_{ik}\, E_k, \tag{2}$$

$$\varepsilon_{kl} = (u_{k,l} + u_{l,k})/2; \quad E_k = -\varphi_{,k}. \tag{3}$$

where ρ is the density of the material; u_i are the components of the vector-function of displacements; σ_{ij} are the components of the tensor of mechanical stresses; f_i are the components of the density vector of mass forces; D_i are the components of the electric induction vector; c_{ijkl} are the components of the tensor of the fourth rank of elastic moduli; e_{ijk} are the components of the tensor of piezomodules of the third rank; ε_{ij} are the strain tensor components; E_i are the components of the vector of the electric field strength; φ is the electric potential; $\ni_{\text{ij}}$ are the components of the second rank tensor of dielectric permittivity; α, β, ς_d are non-negative damping factors (in ANSYS $\varsigma_d = 0$).

For an elastic solid, we have:

$$\rho\ddot{u}_i + \alpha\rho\dot{u}_i - \sigma_{ij,j} = f_i; \tag{4}$$

$$\sigma_{ij} = c_{ijkl}(\varepsilon_{kl} + \beta\dot{\varepsilon}_{kl}); \tag{5}$$

$$\varepsilon_{kl} = (u_{k,l} + u_{l,k})/2. \tag{6}$$

Finally, the piezoelectric device can be loaded on working acoustic media $\Omega_j = \Omega_{al}$; $l = 1, 2..., N_a$; $j = l + N_p + N_e$. For these regions, we will use the equations of acoustics taking into account linear dissipative effects:

$$\frac{1}{\rho_j c_j^2}\dot{p} + \nabla \cdot \mathbf{v} = 0; \quad \mathbf{v} = \nabla\psi, \tag{7}$$

$$\rho_j\dot{\mathbf{v}} = \nabla \cdot \sigma; \quad \boldsymbol{\sigma} = -p\mathbf{I} + b\nabla\mathbf{v}, \tag{8}$$

where ρ_j is the equilibrium value of the density; c_j is the speed of sound; and b_j is the dissipative coefficient for the medium $\Omega_j = \Omega_{em}$; p is the sound pressure; $\mathbf{v}$ is the velocity vector; ψ is the potential of speeds; σ is the stress tensor; I is the unit tensor.

In the static case, there are no terms with the time derivative, in the modal analysis, in addition, there are no volume forces, and in the harmonic analysis, the replacements are made:

$$\dot{a} \rightarrow i\omega a \ \ and \ \ \ddot{a} \rightarrow -\omega^2 a$$

When defining mechanical boundary conditions, the body boundary is represented as a union of non-intersecting regions $S = S_u \cup S_t \cup S_{ut}$, on which the following conditions are performed:

(i) the condition of fixing the boundary or given displacements:

$$u_i \mid s_u = u_i^0, \tag{9}$$

(ii) the condition of force action, at which the components of the vector of mechanical stresses are given as

$$t_i = \sigma_{ij} n_j \mid S_t = p_i, \tag{10}$$

(iii) the condition of smooth contact with an absolutely rigid body, namely the equality to zero of normal displacements and shear stresses:

$$u_n = u_i n_i \mid S_{ut} = 0, \ \ldots \ t_\tau^{(k)} = \sigma_{ij} n_j \tau_i^{(k)} \mid S_{ut} = 0. \tag{11}$$

Condition (11) is also posed on the axis of symmetry when solving the axisymmetric problem.

When solving the problem of modal analysis, all boundary conditions are homogeneous (equal to zero).

The conditions of joining (continuity of certain quantities) during the transition to the FE model are performed automatically, so we will not dwell on them in detail.

Electrical boundary conditions are given in a set of regions $S = \bigcup_{m=1}^{M} S_{E_m} \cup S_D$, in which the following conditions are steted:

(i) the condition on metallized surfaces (electrodes), when a known electric potential is written as

$$\varphi|_{S_{E_m}} = \varphi_m^0 = const, \tag{12}$$

(ii) the condition on non-electroded parts of the boundary, when, with a certain degree of accuracy, the normal component of the electric induction vector can be considered equal to zero:

$$D_n \mid_{S_D} = D_i n_i \mid_{S_D} D_n^e \ \ (= 0). \tag{13}$$

Condition (13) is also posed on the axis of symmetry, when solving the axisymmetric problem.

To formulate the boundary conditions for the acoustic medium, we assume that the acoustic medium fills a volume Ω_w with a boundary $S_w = \partial$. Let us break S_w into four parts: $S_w = S_{wf} \cup S_{wc} \cup S_{wi} \cup S_{ws}$. We will assume that the boundary surface S_{wf} is free, S_{wc} is a rigid wall, S_{wi} is a section with a given impedance condition, and S_{ws} is a part of the boundary in contact with a deformable solid (elastic or piezoelectric). In this case, we have the following boundary conditions:

$$v_i = 0, \quad \mathbf{x} \in S_{wc}; \tag{14}$$

$$n_{wk}\sigma_{wkm} = 0, \quad \mathbf{x} \in S_{wf}; \quad n_{wk}\sigma_{wkm} = -Zv_m, \quad \mathbf{x} \in S_{wi}; \tag{15}$$

$$n_{wk}\sigma_{wkm} = n_{wk}\sigma_{skm}, \quad v_m = \dot{u}_m, \quad \mathbf{x} \in S_{ws}, \tag{16}$$

where n_{wk} are the vector components of the external in respect to the volume Ω_w of the unit normal to S_w; Z is the boundary impedance S_{wi}; σ_{skm} and u_m are the components of the stress tensor and the displacement vector of the deformable solid.

3 Finite Element Approximation in ACELAN

To solve dynamic problems of acoustoelectroelasticity, we will use the FEM in the classical Lagrangian formulation. A sufficiently complete and consistent presentation of the FEM for piezoelectrics and its implementation in the ACELAN software is presented in [3, 5].

Below, according to [3], the FE formulation of the tasks considered in the research is given. In the transition from the continual formulation to the FE, a consistent discretization of geometric regions is performed, namely partitioning into finite elements (triangulation) with a certain set of geometric points being nodes, in the result of which the boundary-value problem (1–16) with the help of representation (17) is reduced to a system of ordinary differential Eqs. (18). So

$$\mathbf{u}(\mathbf{x}, t) = \mathbf{N}_u^T(\mathbf{x}) \cdot \mathbf{U}(t); \ \varphi(\mathbf{x}, t) = \mathbf{N}_\varphi^T \cdot \Phi(t); \ \psi(\mathbf{x}, t) = \mathbf{N}_\psi^T(\mathbf{x}) \cdot \mathbf{\Psi}(t), \tag{17}$$

where $\mathbf{x}$ are the spatial coordinates; t is the time; $\mathbf{N}_u^T$ is the matrix of form functions for the displacement field $u = (u_1, u_2, u_3)$;$\mathbf{N}_\phi^T$, $\mathbf{N}_\psi^T$ are the row vectors of the shape functions for the fields of the electric potential φ and the velocity potential in the acoustic medium ψ; $U(t)$, $\Phi(t)$,$\mathbf{\Psi}(t)$ are the global vectors of the corresponding nodal degrees of freedom.

It is essential that the approximations (17) are specified in those regions, where there are corresponding physical fields, and can differ for different finite elements.

The FEM approximation (17) of generalized formulations of dynamic problems (3–8), including the main principal and natural boundary conditions, is reduced to a system of ordinary differential equations with respect to the nodal unknowns $\mathbf{a} = \lfloor \mathbf{U}, \mathbf{\Phi}, \mathbf{\Psi} \rfloor^T$:

$$\mathbf{M} \cdot \ddot{\mathbf{a}} + \mathbf{C} \cdot \dot{\mathbf{a}} + \mathbf{K} \cdot \mathbf{a} = \mathbf{F}, \tag{18}$$

where the global matrices $\mathbf{M}$, $\mathbf{C}$, $\mathbf{K}$, which, by analogy with the FEM for elastic media, can be called the matrices of mass, damping, stiffness, and the column of the right-hand terms have a block structure of the form:

$$\begin{gathered}
\mathbf{M} = \begin{pmatrix} \mathbf{M}_{uu} & 0 & \tilde{\mathbf{R}}_{u\psi} \\ 0 & 0 & 0 \\ \tilde{\mathbf{R}}^T_{u\psi} & 0 & -\mathbf{M}_{\psi\psi} \end{pmatrix}, \mathbf{C} = \begin{pmatrix} \mathbf{C}_{uu} & 0 & \mathbf{R}_{u\psi} \\ \varsigma_{\mathrm{d}} \mathbf{K}^T_{u\varphi} & 0 & 0 \\ \mathbf{R}^T_{u\psi} & 0 & -\mathbf{C}_{\psi\psi} \end{pmatrix}, \\
\mathbf{K} = \begin{pmatrix} \mathbf{K}_{uu} & \mathbf{K}_{u\varphi} & 0 \\ \mathbf{K}^T_{u\varphi} & -\mathbf{K}_{\varphi\varphi} & 0 \\ 0 & 0 & -\mathbf{K}_{\psi\psi} \end{pmatrix}, \mathbf{F} = \begin{Bmatrix} \mathbf{F}_u \\ \mathbf{F}_\varphi + \varsigma_{\mathrm{d}} \dot{\mathbf{F}}_\varphi \\ 0 \end{Bmatrix},
\end{gathered} \tag{19}$$

relatively unknown vector: $\mathbf{a} = [\mathbf{U}, \mathbf{\Phi}, \mathbf{\Psi}]^T$,

where the FE matrices of mass $\mathbf{M}_{uu}$, damping $\mathbf{C}_{uu}$, and stiffness $\mathbf{K}_{uu}$ in (19) are the same as in structural analysis. These matrices are symmetric and non-negatively defined, and $\mathbf{M}_{uu} > 0$. The matrices $\mathbf{K}_{u\phi}$ and $\mathbf{K}_{\phi\phi}$ are determined by the piezoelectric effect and reflect the piezoelectric and dielectric properties, respectively, and $\mathbf{K}_{\phi\phi}$ is symmetric and non-negatively defined $\mathbf{K}_{\phi\phi} \geq 0$ (here, the inequalities $\mathbf{B} > 0$ or $\mathbf{B} \geq 0$ mean that the matrix $\mathbf{B}$ is positive definite or semi-definite, respectively). The vectors $\mathbf{F}_u$ and $\mathbf{F}_\phi$ are formed as a result of taking into account mechanical and electrical influences. Matrices $\mathbf{M}_{\psi\psi}$, $\mathbf{K}_{\psi\psi}$, $\tilde{\mathbf{R}}_{u\psi}$, $\mathbf{R}_{u\psi}$, $\mathbf{C}_{\psi\psi}$ are conditioned by the acoustic environment. The matrices $\mathbf{M}$, $\mathbf{C}$ and $\mathbf{K}$ are obtained in the result of the ensemble process of the local matrices of all finite elements.

As can be seen from (1–6), the simplest models of attenuation are adopted in the FE software ANSYS and ACELAN. At the same time, in ANSYS, in piezoelectric, damping is taken into account only through elastic properties, namely a submatrix $\mathbf{C}_{uu}$, which, in accordance with the method of accounting for Rayleigh damping, can be represented as

$$\mathbf{C}_{uu} = \sum\nolimits_j (\alpha_j \mathbf{M}_{uuj} + \beta_j \mathbf{K}_{uuj}), \tag{20}$$

where α_j and β_j are the attenuation coefficients; $\mathbf{M}_{uuj}$ and $\mathbf{K}_{uuj}$ are the structural FE matrices of masses and stiffness of the j-th subtitle, respectively, and the remaining submatrices included in (18, 19) are described in [4, 5].

When considering ideal materials, the resonance region is inaccessible for investigation, since the amplitudes of various quantities tend to infinity. However, for the practice of using constructions, the numerical values of these quantities are extremely important, for example, the amplitudes of mechanical stresses that determine the strength of constructions at resonance. Various kinds of energy losses in real material define the final values of these quantities. In the region of low and medium frequencies, mechanical energy losses make the greatest contribution in solids. For a quantitative description of this type of energy loss, the concept of mechanical figure of merit of the material is introduced Q_M.

Let us define the width of the resonance curve $\Delta\omega$ as the difference between the frequencies, corresponding to the half power level at the resonance frequency ω_0. Then the quality factor is defined as

$$\Delta\omega = \frac{\omega}{Q_M}. \tag{21}$$

In the FE software ANSYS and ACELAN, to describe the loss of mechanical energy, attenuation coefficients α, β are introduced, which, by assuming the same quality factor at the first two resonant frequencies f_{r1}, f_{r2}, are expressed in terms of the quality factor as follows:

$$\alpha = \frac{2\pi\, f_{r1}\, f_{r2}}{Q(f_{r1} + f_{r2})}, \quad \beta = \frac{1}{2\pi\, Q\,(f_{r1} + f_{r2})}. \tag{22}$$

A characteristic feature of the form of Eqs. (18), (19) in ACELAN and ANSYS software is the symmetry of the matrices **M** and **K** and their similar saddle structure. The latter means that the matrices **M** and **K**, after some simultaneous permutation of their rows and columns, take the following block forms:

$$\mathbf{A} = \begin{pmatrix} \mathbf{B} & \mathbf{H} \\ \mathbf{H}^T & -\mathbf{S} \end{pmatrix}; \quad \mathbf{B} = \mathbf{B}^T; \quad \mathbf{S} = \mathbf{S}^T \quad \mathbf{B} \geq 0; \quad \mathbf{S} \geq 0 \tag{23}$$

and the sizes of all blocks for matrices **M, K**, as well as for matrix **C**, are the same.

For steady-state oscillations, the constitutive equations are obtained by replacing

$$\mathbf{F}_u = \tilde{\mathbf{F}}_u(\mathbf{x})\ \exp(j\omega t); \quad \mathbf{F}_\phi = \tilde{\mathbf{F}}_\phi(\mathbf{x})\exp(j\omega t); \quad \mathbf{a} = \tilde{\mathbf{a}}(\mathbf{x})\exp(j\omega t). \tag{24}$$

They are described by the following system of linear algebraic equations (SLAE):

$$\mathbf{K}_c \cdot \tilde{\mathbf{a}} = \tilde{\mathbf{F}}_c; \quad \tilde{\mathbf{F}}_c = \left[\tilde{\mathbf{F}}_u, \quad \tilde{\mathbf{F}}_\varphi, \quad 0\right]^T \tag{25}$$

$$\mathbf{K}_c = \begin{pmatrix} \mathbf{K}_{uuc} & \mathbf{K}_{u\varphi} & \mathbf{K}_{u\psi c} \\ \mathbf{K}_{u\varphi}^T & -\mathbf{K}_{\varphi\varphi c} & 0 \\ \mathbf{K}_{u\psi c} & 0 & -\mathbf{K}_{\psi\psi c} \end{pmatrix} \tag{26}$$

$$\mathbf{K}_{\eta\eta c} = -\omega^2 \mathbf{M}_{\eta\eta} + i\omega \mathbf{C}_{\eta\eta} + \mathbf{K}_{\eta\eta}; \quad \eta = u, \ \psi,$$

$$\mathbf{K}_{u\psi c} = -\omega^2 \tilde{\mathbf{R}}_{u\psi} + i\omega \mathbf{R}_{u\psi}; \mathbf{K}_{\phi\phi c} = \frac{1}{(1 + i\omega\zeta_d)} \mathbf{K}_{\phi\phi}$$

If we use real arithmetic, then problem (25) is a SLAE with respect to the vector of real and imaginary parts of the nodal degrees of freedom **a** with a matrix that does not have positive definiteness and a saddle structure.

In conclusion of this section, we note some features of modal analysis in ANSYS and ACELAN software. This analysis is designed to find natural or resonant frequencies of elastic bodies or frequencies of electrical resonances and antiresonances for piezoelectric bodies. The frequencies of electrical resonances $f_{ri} = \omega_{ri}/(2\pi)$ and antiresonances $f_{ai} = \omega_{ai}/(2\pi)$ are the most important characteristics of piezoelectric devices, and are also important when performing non-stationary analysis, for example, to determine the damping factors. These frequencies are the natural frequencies of piezoelectric devices and are calculated without taking into account the effects of damping and interaction with acoustic media. Thus, these frequencies can be determined from the FEM in the result of performing modal analysis from the solution of the generalized eigenvalue problems obtained from (25, 26) with the form (without taking into account acoustic media):

$$\mathbf{K} \cdot \mathbf{a} = \omega^2 \mathbf{M} \cdot \mathbf{a} \tag{32}$$

$$\mathbf{M} = \begin{pmatrix} \mathbf{M}_{uu} & 0 \\ 0 & 0 \end{pmatrix}, \ \mathbf{K} = \begin{pmatrix} \mathbf{K}_{uu} & \mathbf{K}_{u\varphi} \\ \mathbf{K}_{u\varphi}^* & -\mathbf{K}_{\varphi\varphi} \end{pmatrix}, \ \mathbf{a} = \begin{Bmatrix} \mathbf{U} \\ \Phi \end{Bmatrix},$$

and the matrices $\mathbf{K}_{u\phi}$ and $\mathbf{K}_{\phi\phi}$ differ, when finding the frequencies of electrical resonances ω_k and when finding the frequencies of antiresonances.

In the result of modal analysis, the spectrum of natural frequencies and the corresponding natural vibration modes are found.

The finite element model of the lensotome tip is built in ACELAN packages, Fig. 3 shows an element of the half axial section of the tip (a) and a fragment of the finite element mesh (b). Figure 4 shows the interface of the ACELAN software, when calculating the steady-state oscillations of the lensotome tip under the action of the potential difference across the electrodes of the piezoelectric element.

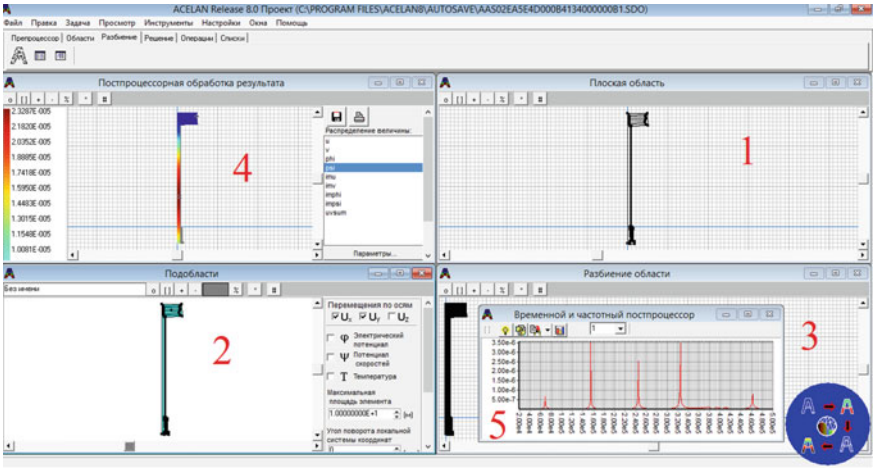

Fig. 4 Interface of ACELAN software

In Fig. 3a, numbers indicate: 1—tip tube (steel), 2—holder (steel), 3—annular piezoelectric element (PZT-4 piezoceramic), 4—stop (ebonite), 5—amorphous medium of the fractured lens (water).

In Fig. 4, digits mark the modules of the ACELAN software: 1—graphic editor, 2—selection of materials and their properties, 3—finite element partitioning, 4—postprocessor, 5—frequency response of the tip end axial displacement.

4 Lensotome Tip Vibration Analysis

When carrying out a numerical experiment, two cases were considered: in the first, the lower base of the stop (4) in Fig. 3 is free, in the second case, it is fixed along the normal. The outer and inner diameters of the tip tube (designated by 1 in Fig. 3) were 0.9 and 0.7 mm, respectively, the tube length was 2.5 mm, the outer radii of the holder and piezoelectric element (designated by 2 and 3 in Fig. 3) were 1.4 mm, and the heights were 0.6 and 3 mm, respectively, the outer radius and height of the stop (designated by 4 in Fig. 3) are 1.8 mmand 0.6 mm, respectively.

Table 1 shows the results of calculating the natural frequencies of resonance, f_r, and antiresonance, f_a, as well as the coefficient of electromechanical coupling (CEMS) K, which is calculated by the formula:

$$K = [1 - (f_r/f_a)^2]^{1/2} \tag{33}$$

for the case when the bottom surface of the stop is free.

No	f_r (kHz)	f_a (kHz)	K
1	68.404	68.780	0.104
2	154.792	156.508	–
3	244.678	249.670	0.199
4	323.260	341.218	0.320
5	369.393	374.583	–
6	399.674	430.761	0.373
7	459.590	493.021	0.362
8	531.069	536.079	–
9	549.127	551.201	–

As can be seen from Table 1, the value of CEMC of the first mode is relatively low and intense movements are observed both at the end of the tube and at the stop (Fig. 5).

The third vibration mode (Fig. 6) shows a value of CEMC twice as large as on the first mode, and moreover, the movement of the stop is not significant, but the oscillation amplitude of the tube end is quite large.

Although the fourth (Fig. 7) and sixth (Fig. 8) modes are characterized by large CEMCs, intense motions are not located at the tube end.

The seventh mode (Fig. 9) has a maximum amplitude at the end of the tube, it has a large value of CEMC, but its frequency is close to 500 kHz, which is ten times higher than that proposed in the patent [1].

In Figs. 10 and 11, the real and imaginary parts of the velocity potential in the acoustic medium on the third mode are presented, which characterize the wave motion of the fractured lens material.

Figures 12 and 13 show the amplitude frequency response (AFR) of the axial and radial displacements of the end of the tube. It should be noted that significant

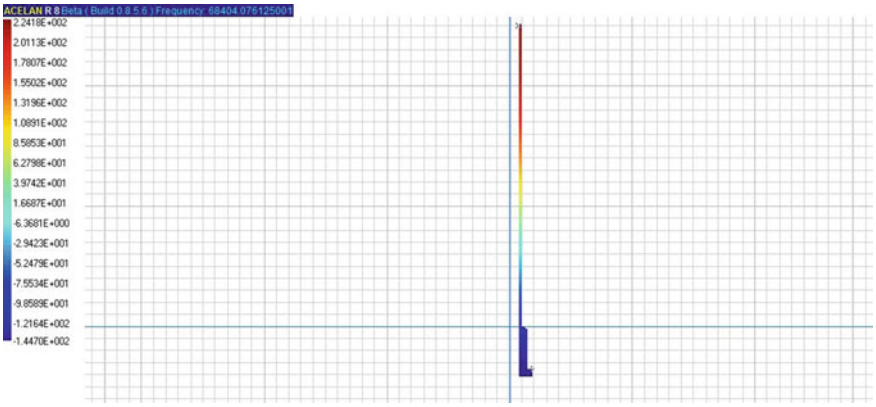

Fig. 5 First vibration mode (axial displacement distribution)

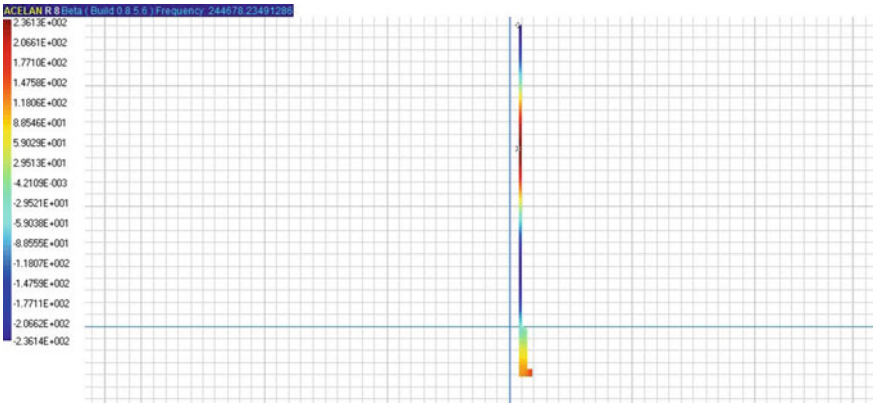

Fig. 6 Third vibration mode (axial displacement distribution)

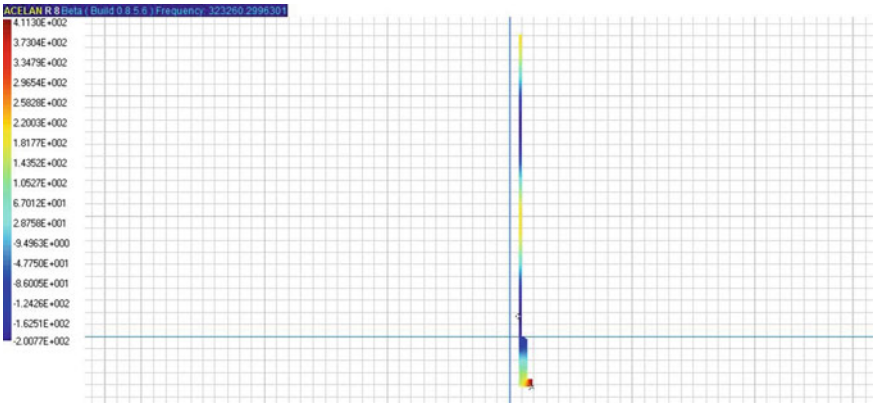

Fig. 7 Fourth vibration mode (axial displacement distribution)

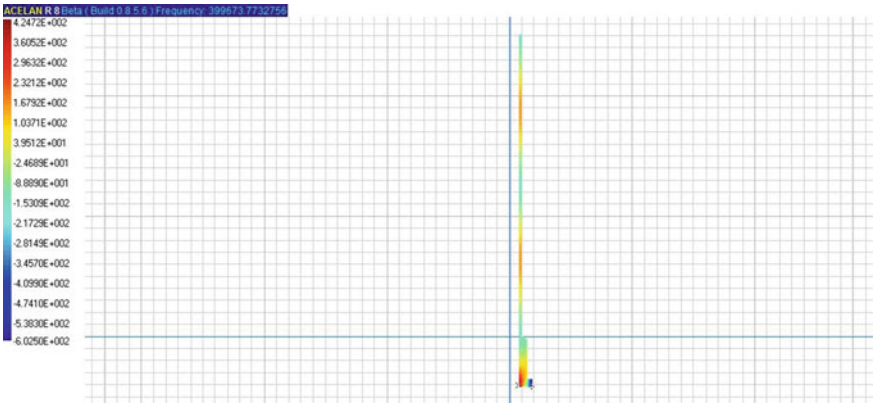

Fig. 8 Sixth vibration mode (axial displacement distribution)

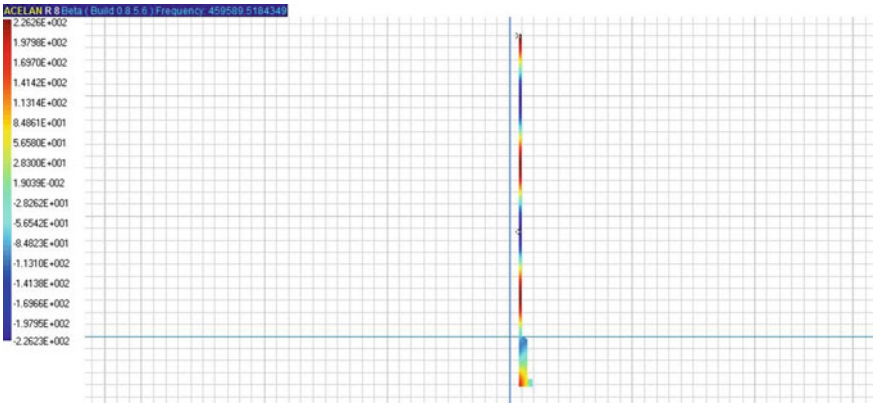

Fig. 9 Seventh vibration mode (axial displacement distribution)

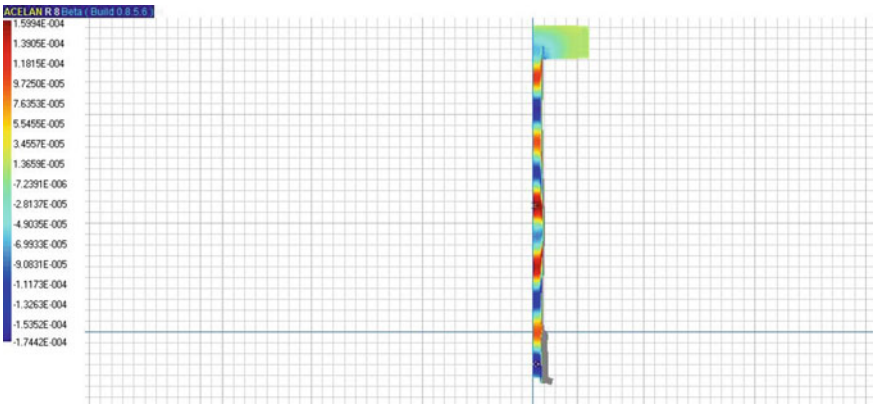

Fig. 10 Distribution of the real part of the velocity potential on the third vibration mode

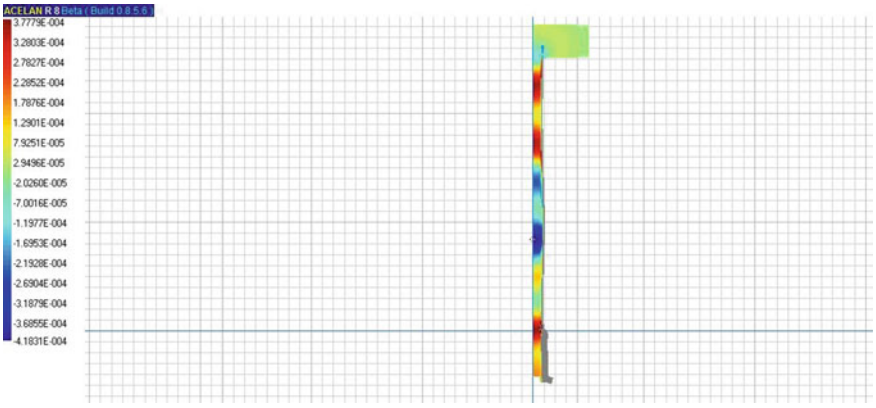

Fig. 11 Distribution of the imaginary part of the velocity potential on the third vibration mode

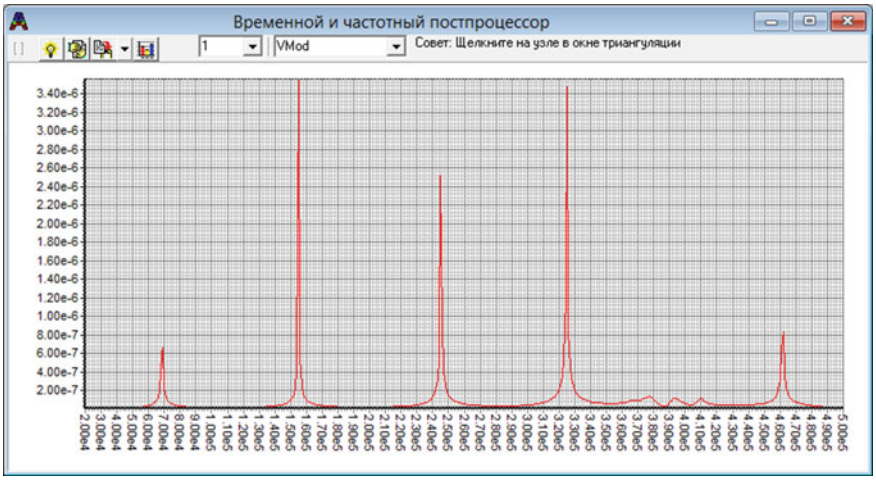

Fig. 12 AFR of axial displacement

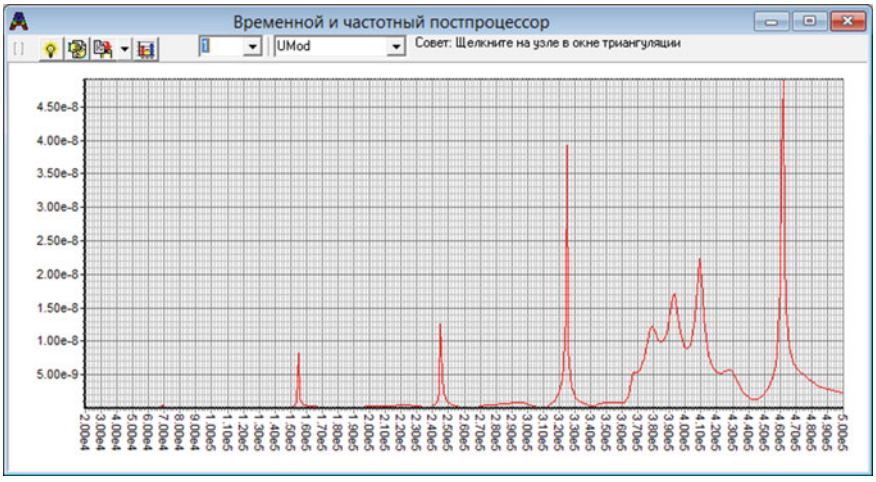

Fig. 13 AFR of axial displacement

radial oscillations are observed in the range from 370 to 430 kHz, with small axial vibrations; this motion feature can also be used.

Further, Table 2 and Figs. 14–21, present results for the fixed lower base of the stop similar to those described above.

No	f_r (kHz)	F_a (kHz)	K
1	43.121	44.818	0.273

(continued)

(continued)

No	f_r (kHz)	F_a (kHz)	K
2	116.163	122.521	0.318
3	174.758	176.811	–
4	256.195	256.324	–
5	344.396	347.294	–
6	418.244	435.785	0.281
7	469.217	494.458	0.315
8	512.675	524.227	–
9	542.291	550.078	–

Analysis of the CEMC values in Table 2, vibration modes and frequency response of axial and radial displacements of the upper end of the tool, shows that the first and second vibration modes satisfy both kinematic and energy conditions for the process of fracture by the end of the tube.

5 Conclusion

For the proposed model of the lensotome tip with a piezoelectric drive, a mathematical and finite element model is built for two cases of boundary conditions at the lower end of the tool: free end and rigid fixation. In the both cases, natural frequencies and CEMC are calculated and natural vibration modes are found. An analysis of these results shows that in the first case, the first mode is preferable, taking into account the restrictions on the frequency value; in the second case, the first and second modes are preferable. At the same time, the defined higher effective frequencies and vibration modes do not satisfy the limitation on the value of the operating frequency.

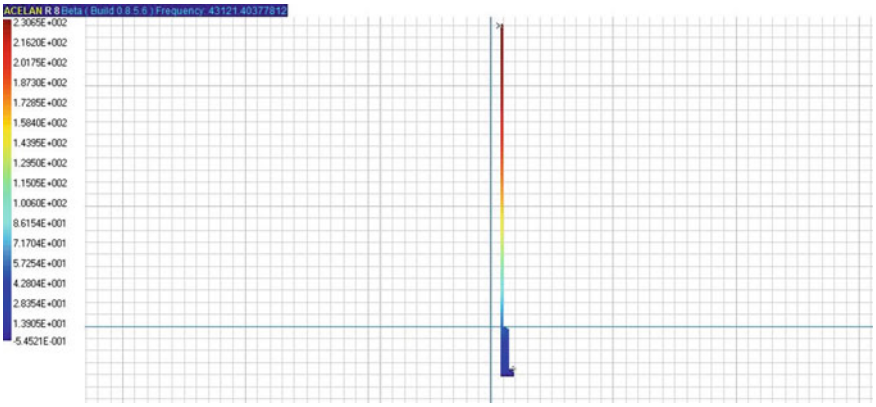

Fig. 14 First vibration mode (axial displacement distribution)

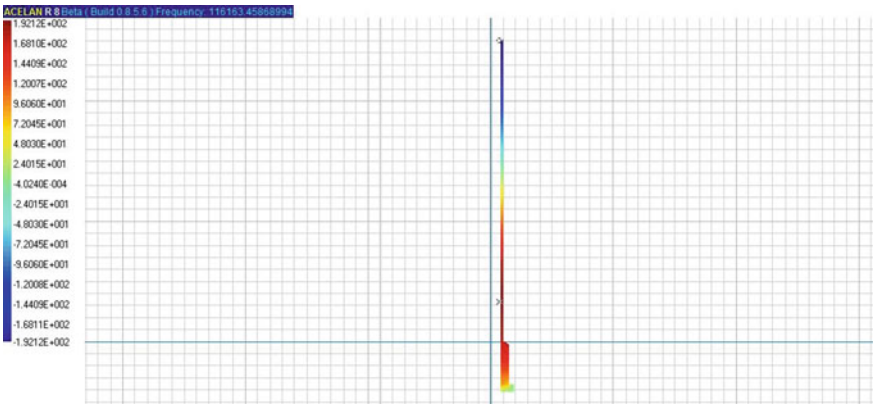

Fig. 15 Second vibration mode (axial displacement distribution)

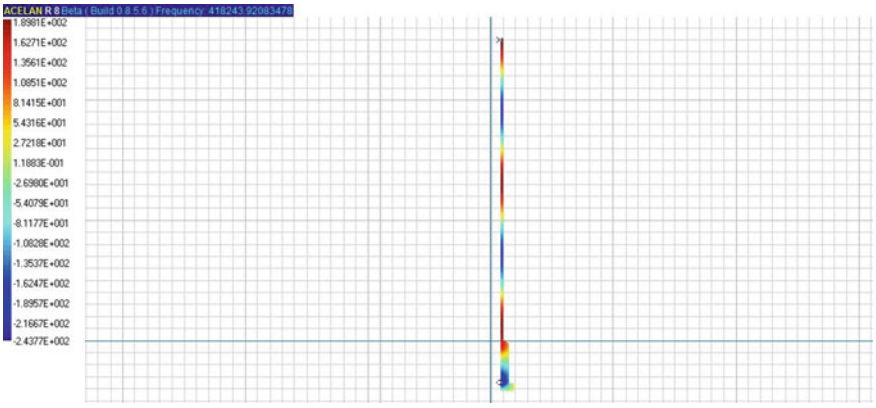

Fig. 16 Sixth vibration mode (axial displacement distribution)

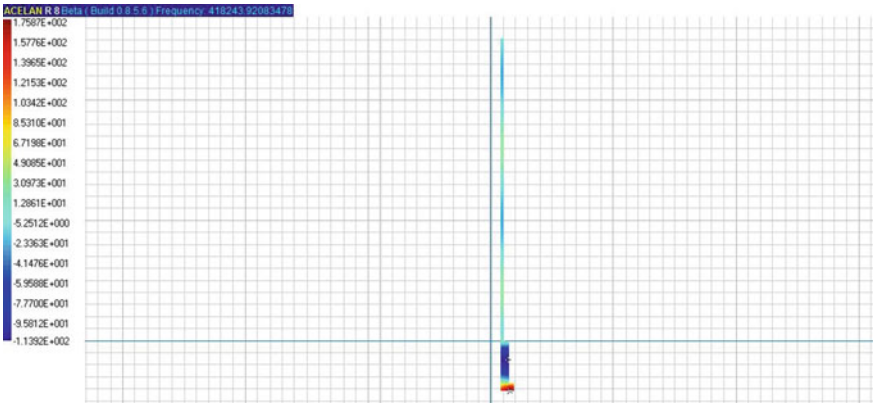

Fig. 17 Sixth vibration mode (radial displacement distribution)

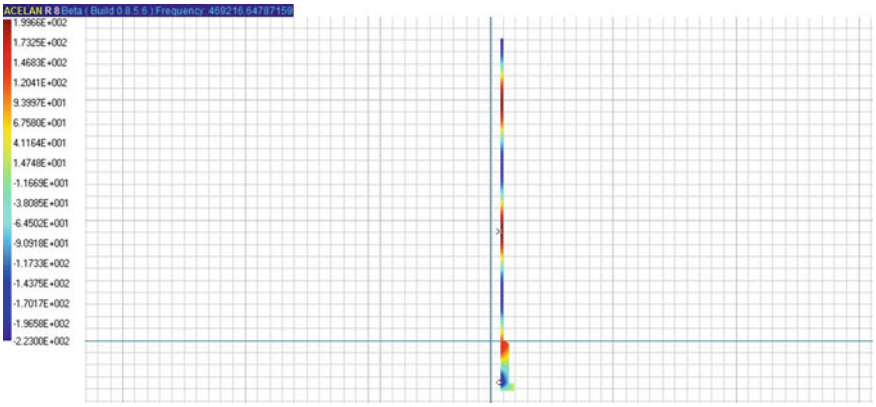

Fig. 18 Seventh vibration mode (axial displacement distribution)

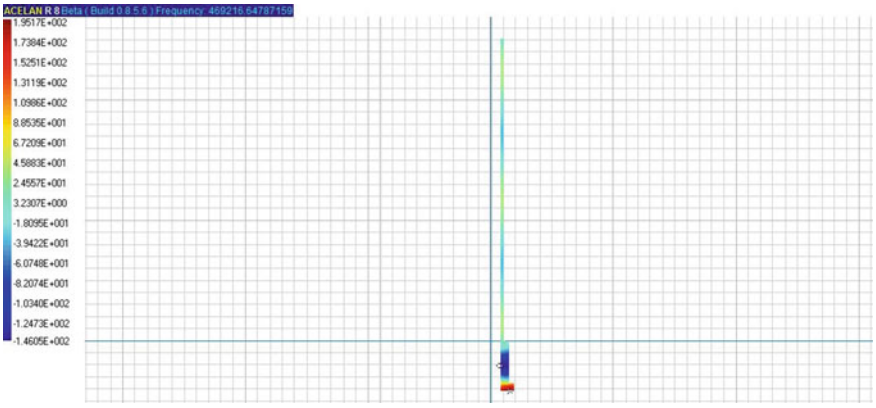

Fig. 19 Seventh vibration mode (radial displacement distribution)

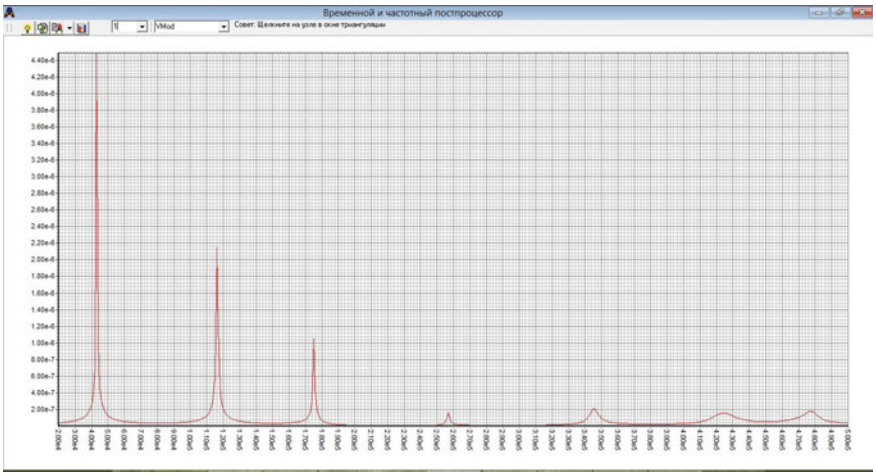

Fig. 20 AFR of axial displacement

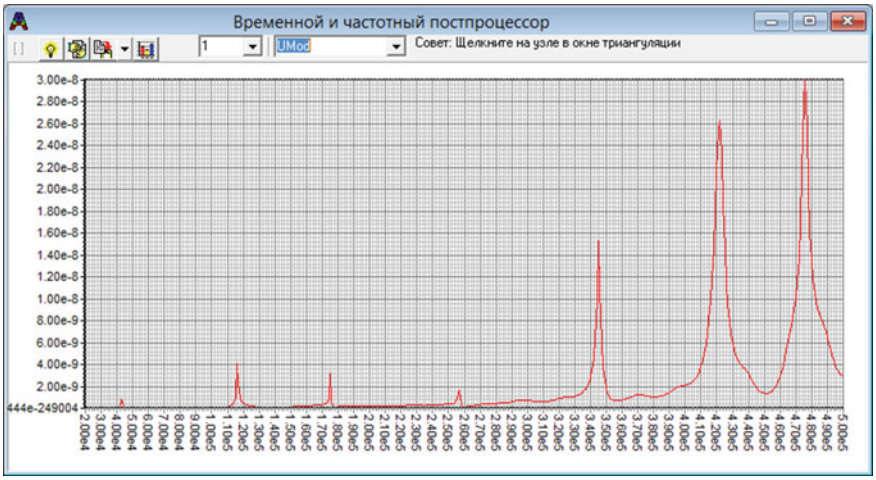

Fig. 21 AFR of the radial displacement

Acknowledgements This research was supported by the Government of Russian Federation (grant No. 14.Z50.31.0046)

References

1. A.N. Epikhin, The method of destruction and removal of the lens of the eye by lever-power cutting—vectopotential lensectomy—VPLEKT and a device for its implementation—lever-power lens cutter—vectopotential with a disposable lensotome. *RF Patent 2720822 from 2020.05.13* (In Russian) https://patents.google.com/patent/RU2720822C1/ru
2. A.V. Belokon, A.V. Nasedkin, A.N. Soloviev, J. Appl. Math. Mech. **66**(3), 491 (2002)
3. A.V. Nasedkin, *Wave fields in anisotropic elastic media with complicated properties and methods of finite element dynamic analysis.* DrSc Thesis (Physics and Mathematics). Rostov State University, Rostov-on-Don (2001), p. 271 (In Russian)
4. V.A. Krasilnikov, V.V. Krylov. *Introduction to Physical Acoustics* Science, Moscow (1984), p. 403 (In Russian).
5. A.N. Soloviev. *Direct and inverse problems for finite elastic and electroelastic bodies.* DrSc Thesis (Physics and Mathematics). Rostov State University, Rostov-on-Don, p. 296 (In Russian)

Modeling the Interaction of Elastic Haptic Parts of Two Intraocular Lenses Located in the Capsular Bag of the Lens

A. N. Soloviev, A. N. Epikhin, D. V. Krasnov, and O. N. Lesnyak

Abstract An intraocular lenses (IOLs) implanted in the eye is used to treat diseases such as cataracts or myopia. This chapter examines the problem of cataract healing while preserving the natural accommodation of the eye. The aim of this work is to model the system of IOLs, which has the possibility of accommodation, as well as the natural lens. The SpaceClaim CAD system was used for direct 3D modeling of an IOL with elastic haptic elements and the ANSYS Mechanical environment for creating a finite element mesh and a numerical model of deformations.

Keywords Cataract · Intraocular lenses · Mathematical modeling · FEM

1 Introduction

The intraocular lens (IOL) implanted into eye is used to treat diseases such as cataracts or myopia. One of the most common types of IOLs is a pseudophakic lens [1] . They are implanted during cataract surgery. A pseudophakic IOL provides the same function as a natural lens. The second type of IOL is a phakic IOL. The IOL is placed on top of the existing natural lens and is used in refractive surgery as a treatment for myopia [2]. Usually, IOL consist of a small plastic plate with side struts called haptics, which serve to hold the IOL in place in the eye's capsule bag [3]. IOLs were usually made from an inflexible material, although this was largely superseded by the use of flexible materials such as silicone and acrylic glass. Most IOLs introduced to date are fixed monofocal IOLs that provide a single focal length [4]. There are also types of IOLs, such as multifocal IOLs, which provide the patient with multi-focus vision, but this type of IOLs can create side effects in the form of reduced contrast

A. N. Soloviev (✉) · D. V. Krasnov · O. N. Lesnyak
Department of Theoretical and Applied Mechanics, Don State Technical University, Rostov-on-Don, Russia

A. N. Epikhin
Department of Ophthalmology, Rostov State Medical University, Rostov-on-Don, Russia

I. A. Parinov et al. (eds.), *Physics and Mechanics of New Materials and Their Applications*, Springer Proceedings in Materials 10,
https://doi.org/10.1007/978-3-030-76481-4_37

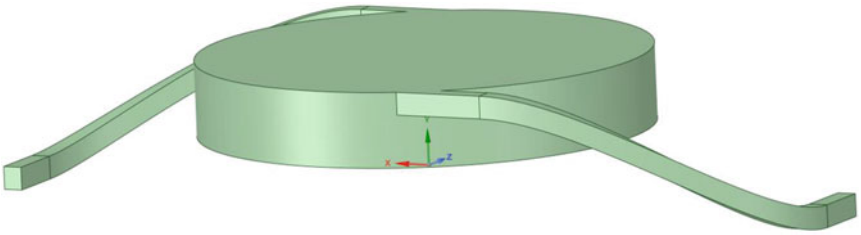

Fig. 1 CAD model of the lens

vision in the dark, as well as glare [5]. Adaptive IOLs that correct limited visual accommodation [6].

This chapter examines the problem of cataract healing while preserving the natural accommodation of the eye. The aim of this work is to model the system of IOL, which has the possibility of accommodation, as well as the natural lens. The SpaceClaim CAD system was used for direct 3D modeling of an IOL with elastic haptic elements (Fig. 1) and the ANSYS software for creating a finite element mesh and a numerical model of deformations.

2 The Continuum Formulation of the Problem

A shape of intraocular lenses is proposed (Fig. 1). The lenses are modeled in the frame of the theory of elasticity. The linear equations of the theory of elasticity, taking into account the dissipation of energy adopted in the ACELAN and ANSYS packages [7, 8], are used as a continual model in this section:

$$\rho\ddot{u}_i + \alpha\rho\dot{u}_i - \sigma_{ij,j} = f_i; \tag{1}$$

$$\sigma_{ij} = c_{ijkl}(\varepsilon_{kl} + \beta\dot{\varepsilon}_{kl}); \tag{2}$$

$$\varepsilon_{kl} = (u_{k,l} + u_{l,k})/2; \tag{3}$$

where ρ is the density of the material; u_i are the components of the vector-function of displacements; σ_{ij} are the components of the tensor of mechanical stresses; f_i are the components of the density vector of mass forces; c_{ijkl} are the components of the tensor of the fourth rank of elastic moduli; ε_{ij} are the strain tensor components; α, β, ς_d are the non-negative damping factors (in ANSYS $\varsigma_d = 0$).

When defining mechanical boundary conditions, the body boundary is represented as a union of non-intersecting regions $S = S_u \cup S_t \cup S_{ut}$, on which the following conditions are given:

i. the condition for fixing the boundary or specified displacements:

$$u_i|_{S_u} = u_i^0, \tag{4}$$

ii. the condition of force action, at which the components of the vector of mechanical stresses are given:

$$t_i = \sigma_{ij} n_j|_{S_t} = p_i, \tag{5}$$

iii. condition of smooth contact with an absolutely rigid body, namely the equality to zero of normal displacements and shear stresses:

$$u_n = u_i n_i|_{S_{ut}} = 0, \quad t_\tau^{(k)} = \sigma_{ij} n_j \tau_i^{(k)}|_{S_{ut}} = 0. \tag{6}$$

Condition (6) is also posed on the axis of symmetry, when solving the axisymmetric problem.

3 Finite Element Approximation in ANSYS

The main question that needs to be answered when calculating lens deformation is the relationship between the force on the haptic elements from the side of the capsular sac walls and the axial displacement of the lens. Therefore, in the computer model, the cylindrical surface (A) is fixed in the plane perpendicular to the axis, and the lower surfaces (B) of the haptic elements are fixed in the axial direction. The scheme and data of fastening are shown in Figs. 2–4.

A uniform pressure (0.4 MPa) acts on the haptic parts of the model, which corresponds to the interaction of the elastic haptic parts of two intraocular lenses located in the capsular sac of the lens. The loading scheme is shown in Fig. 5.

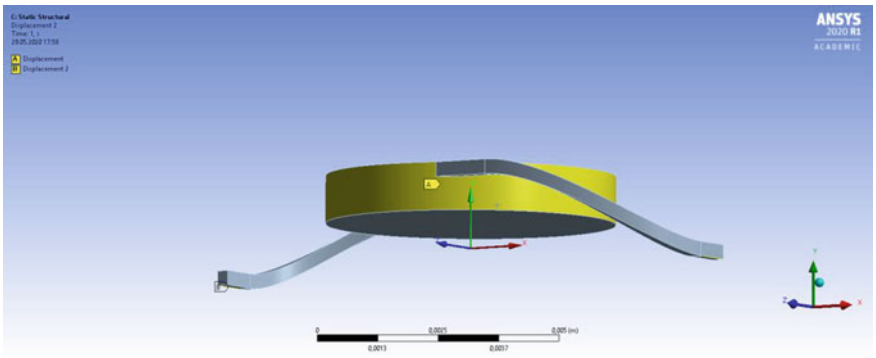

Fig. 2 Scheme of fixing the lens

Fig. 3 Data of displacement restrictions A

Scope	
Scoping Method	Geometry Selection
Geometry	1 Face
Definition	
Type	Displacement
Define By	Components
Coordinate System	Global Coordinate System
X Component	0, m (ramped)
Y Component	Free
Z Component	0, m (ramped)
Suppressed	No

Fig. 4 Data of displacement restrictions B

Details of "Displacement 2"

Scope	
Scoping Method	Geometry Selection
Geometry	2 Edges
Definition	
Type	Displacement
Define By	Components
Coordinate System	Global Coordinate System
X Component	Free
Y Component	0, m (ramped)
Z Component	Free
Suppressed	No

The finite element mesh is shown in Fig. 6, spatial hexagonal quadratic finite elements are used. The material of the lens and haptic parts was PMMA, Young's modulus was 2.69 GPa, and Poisson's ratio was 0.395.

4 Lens Deformation Analysis

A static analysis of the above structure is carried out and the components of the stress-strain state are determined. A series of experiments was carried out to determine the dimensions of the cross-section of the haptic parts. The distribution of the modulus of the displacement vector is shown in Fig. 7. The greatest displacement in the radial direction is obtained at the ends of the haptic parts.

Estimate of the structural strength of an artificial lens is carried out on the basis of von Mises stresses and equivalent deformations. Figure 8 shows the von Mises stress distribution. The greatest value of these stresses is observed at the boundaries of the haptic parts.

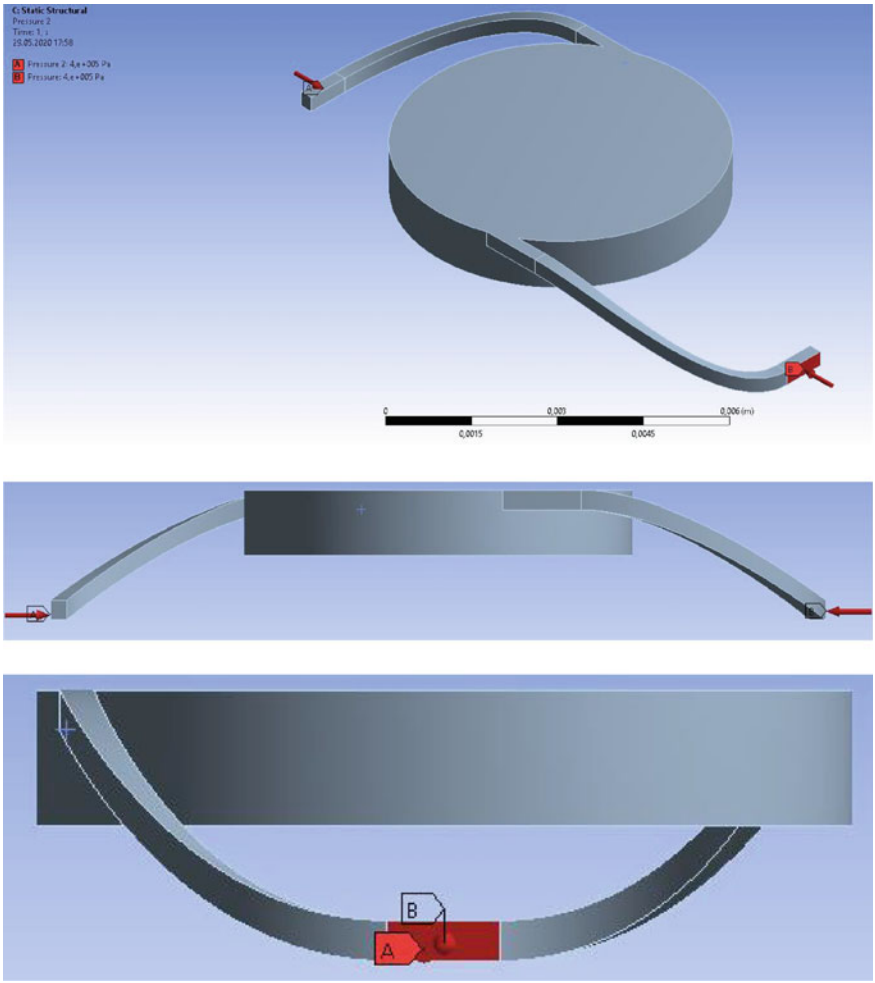

Fig. 5 Loading scheme

Distribution of equivalent deformation is presented in Fig. 9. Just like the von Mises stresses, the maximum equivalent deformation occurs at the boundaries of the haptic parts.

With radial deformation of the haptic parts, due to their shape, there is an axial displacement of the optical part of the lens. This axial movement allows the muscles of the capsular sac to accommodate vision. Figure 10 shows the distribution of the axial displacement of the lens.

An analysis of the results obtained shows that the considered geometric parameters of the design of artificial intraocular lenses satisfy the conditions for the strength of the rigidity of the haptic parts. In particular, at a pressure of 0.4 MPa on the haptic

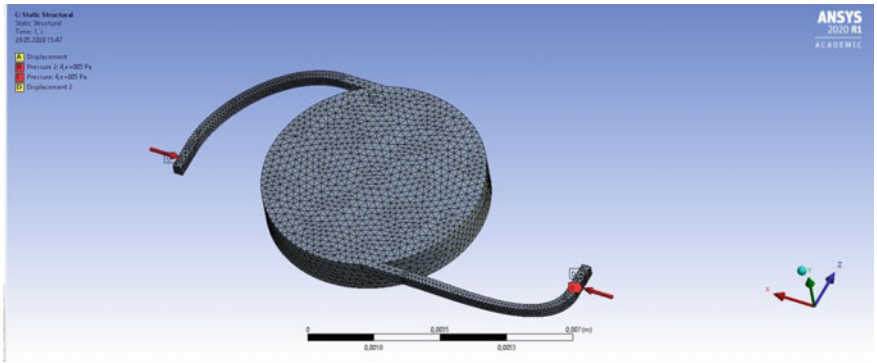

Fig. 6 Finite element mesh of the model

parts, the optical part receives an axial displacement of 1 mm, which meets the biological requirements.

5 Conclusion

A mathematical and finite element model of an artificial lens has been built. In this model, the effect of the walls of the capsular membrane of the lens on the haptic parts of the intraocular lens is analyzed.

This model reflects the distribution of strength in the anterior and posterior capsules, respectively. The strength data for comparison with our results was taken on the basis of literature data on the mechanical characteristics of the elements of the eye and the topography of the capsule sac. The lowest strength (1.0–2.2 g/mm^2) is characteristic of the central zone of the posterior capsule. With an increase in the diameter of the capsulorhexis, the tissue of the annular thickening zone with a higher modulus of elasticity is almost completely removed, which reduces stress. The equatorial vaults in contact with the intracapsular ring differ significantly in thickness from the central sections of the posterior capsule and have a higher modulus of elasticity, which should be taken into account when developing and choosing IOLs and the technique of their implantation.

A comparative analysis of the data on the elasticity modulus of human eye tissues made it possible to judge the relationship between the biomechanical characteristics of the main structural elements of the lens of the developed model in interaction with the entire apparatus. In the course of research, it was possible to find the geometric parameters of the design required for the movement of the lens and deformation of the haptic, similar to real data.

Summing up the preliminary results of the work of biomechanical studies of the eye and their clinical applications, it became clear that the study of theoretical and practical aspects of solving this problem of eye pathology, as well as the further

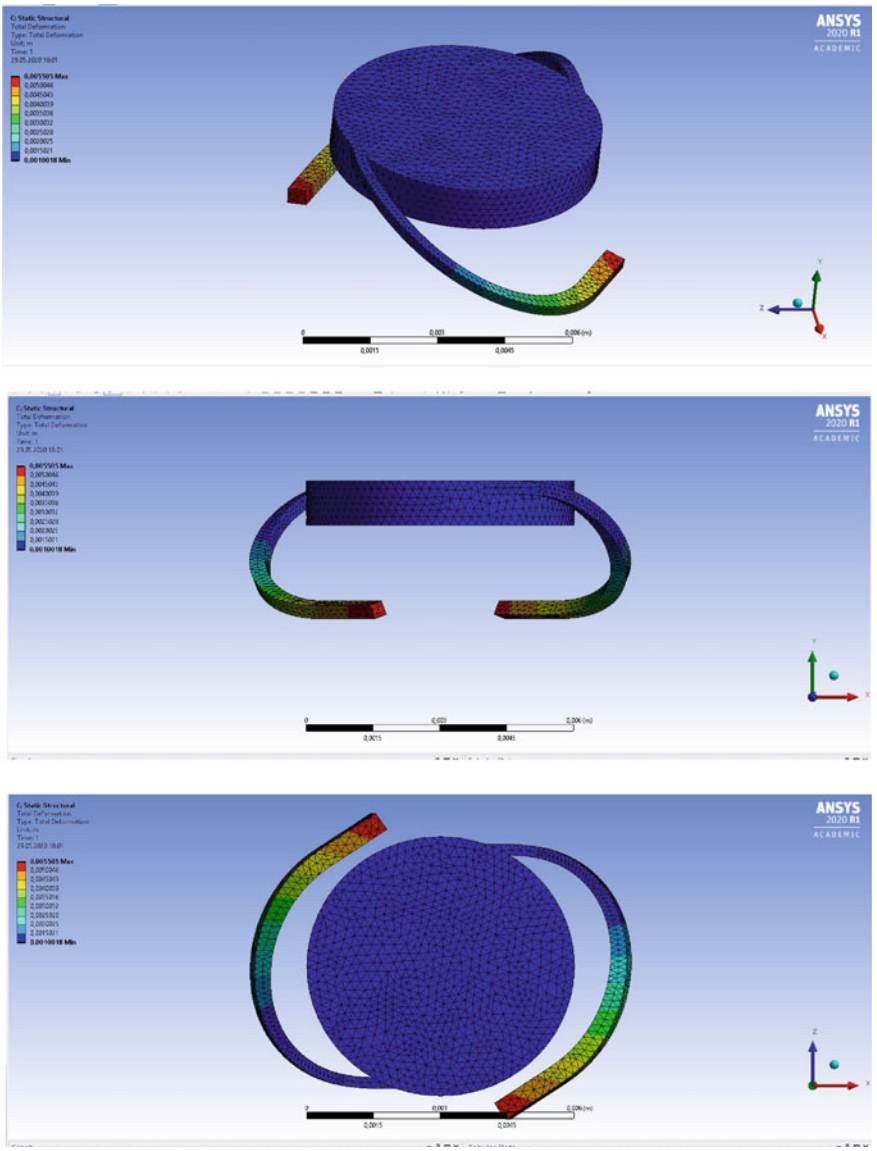

Fig. 7 Distribution of the modulus of the displacement vector

development of this direction, can be considered promising and useful, especially with the active cooperation of specialists in related scientific areas and employees of various medical practical centers.

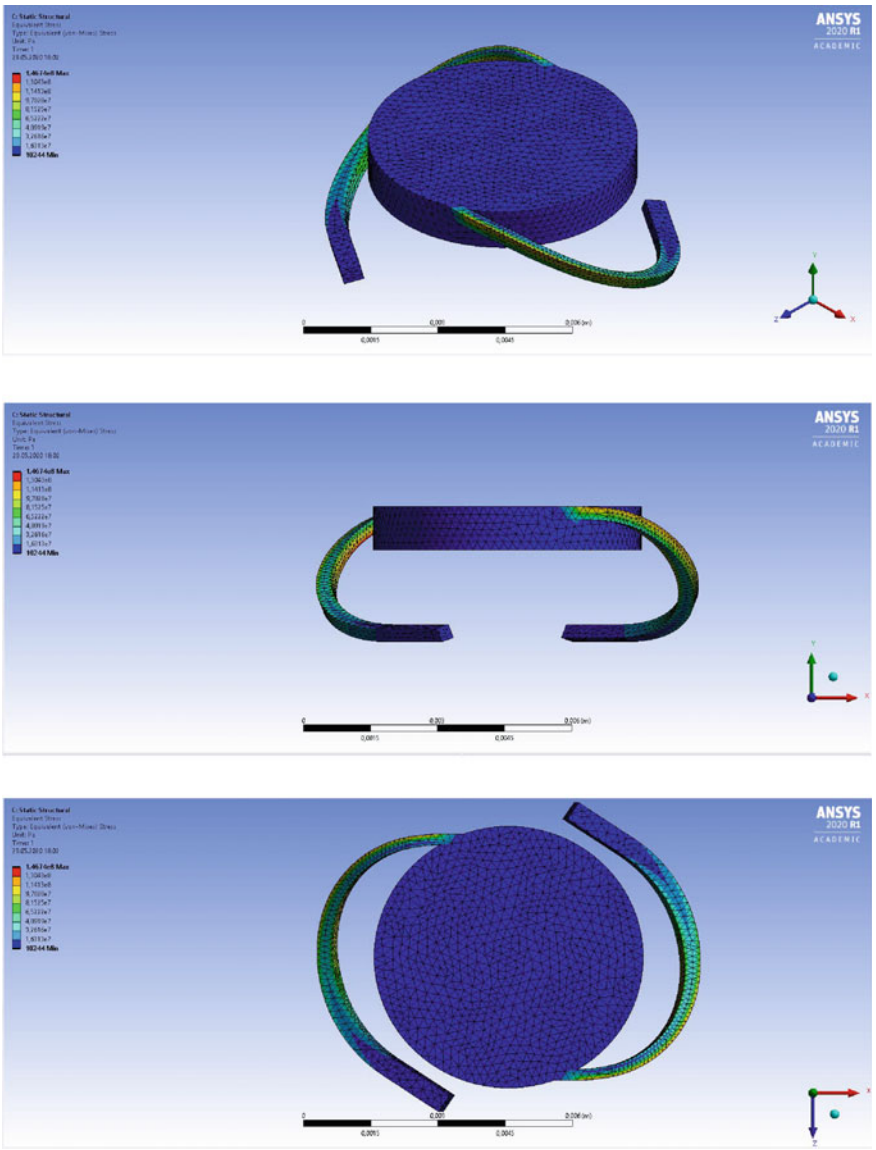

Fig. 8 Von Mises stress distribution

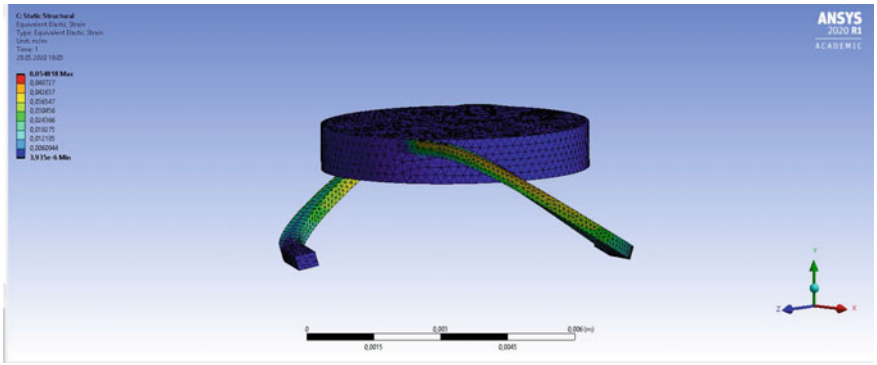

Fig. 9 Equivalent strain distribution

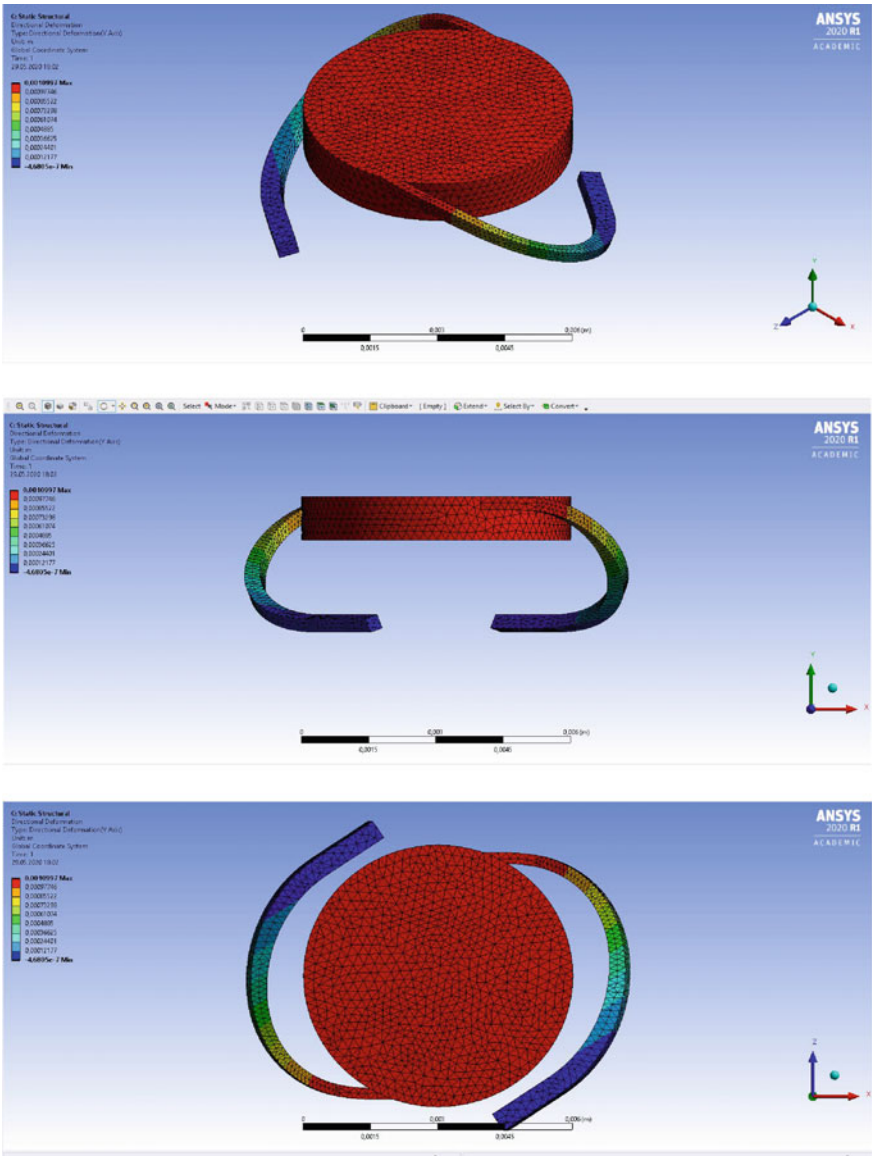

Fig. 10 The distribution of the axial displacement

Acknowledgements This research was supported by the Government of Russian Federation (grant no. 14.Z50.31.0046)

References

1. R. Trivedi, L. Werner, D. Apple et al., Eye **16**, 217 (2002)
2. J.L. Güell, M. Morral, D. Kook, T. Kohnen, J. Cataract Refract. Surg. **36**(11), 1976 (2010)
3. D. Sanders, J.A. Vukich, Cornea **25**(10), 1139 (2006)
4. S.R. de Silva, J.R. Evans, V. Kirthi, M. Ziaei, M. Leyland. The Cochrane Database of Systematic Reviews. **12**, CD003169. (2016)
5. D. Carson, W.E. Hill, X. Hong, M. Karakelle, Clin. Ophthalmol. **8**, 2105 (2014)
6. H. S. Ong, J. R. Evans, B. D. Allan. The Cochrane Database of Systematic Reviews. **5**, CD009667 (2014)
7. A.V. Belokon, A.V. Nasedkin, A.N. Soloviev, J. Appl. Math. Mech. **66**(3), 491 (2002)
8. A.V. Nasedkin. *Wave fields in anisotropic elastic media with complicated properties and methods of finite element dynamic analysis.* DrSc Thesis (Physics and Mathematics). Rostov State University, Rostov-on-Don. 271 p. (2001) (In Russian)

Comparison of MRI Image Segmentation Methods for Radiation-Induced Brain Edema After Radiotherapy for Patients with Intracranial Tumors

Chin-Shiuh Shieh, Chi-Ming Chou, Chen-Lin Kang, Chin-Dar Tseng, Chia-Chi Yen, Wei-Chun Lin, Pei-Ju Chao, Hsuan-Chih Hsu, Yu-Jie Huang, and Tsair-Fwu Lee

Abstract When patients receive stereotactic radiosurgery (SRS) treatment, more intracranial tumor cells usually need to be eliminated, and high radiation doses are required to improve tumor control rates. However, high doses can cause damage to the normal tissues around the intracranial tumor, resulting in normal tissues being unable to repair, and this leads to the complication of radiation-induced brain edema. This study examines the feasibility and relative effectiveness of three different image segmentation algorithms, as applied to the evaluation of hydrocephalus initiated by the radiative treatment of patients with intracranial tumors. We implemented three different segmentation algorithms to automate the tagging of brain edema regions, namely watershed transform segmentation, K-mean segmentation, and region growing segmentation. Two performance indices, Dice and Jaccard, were

C.-S. Shieh · C.-M. Chou · C.-D. Tseng · P.-J. Chao · T.-F. Lee (✉)
Department of Electronics Engineering, National Kaohsiung University of Science and Technology, Kaohsiung 80778, Taiwan
e-mail: tflee@nkust.edu.tw

C.-M. Chou · C.-D. Tseng · P.-J. Chao · T.-F. Lee
Medical Physics and Informatics Laboratory of Electronics Engineering, National Kaohsiung University of Science and Technology, Kaohsiung 80778, Taiwan

C.-L. Kang · P.-J. Chao · H.-C. Hsu · Y.-J. Huang
Department of Radiation Oncology, Kaohsiung Chang Gung Memorial Hospital, Chang Gung University College of Medicine, Kaohsiung 83342, Taiwan
e-mail: yjhuang@adm.cgmh.org.tw

C.-C. Yen · W.-C. Lin
Department of Orthopedic, Kaohsiung Municipal Min-Sheng Hospital, Kaohsiung, Taiwan

C.-C. Yen
Department of Nutrition, Institute of Biomedical Nutrition, Hung-Kuang University, Taichung, Taiwan

Department of Business Management, National Sun Yat-Sen University, Kaohsiung, Taiwan

T.-F. Lee
Department of Biomedical Engineering, Kaohsiung Medical University, Kaohsiung 80708, Taiwan

I. A. Parinov et al. (eds.), *Physics and Mechanics of New Materials and Their Applications*, Springer Proceedings in Materials 10,
https://doi.org/10.1007/978-3-030-76481-4_38

employed in our experiments. A performance index close to 1 is an indication of good correlation. Experimental results reveal that the region growing segmentation outperforms the other two. The region growing segmentation, K-mean segmentation, and watershed transform segmentation have Dice index values of 0.77, 0.72, and 0.71, respectively, and have Jaccard index values of 0.60, 0.56, and 0.55, respectively. Among the subjects of this comparative study, the region growing segmentation is superior in resembling the marking of brain edema suggested by expert clinicians.

Keywords Brain edema · Image segmentation · Intracranial tumors · Stereotactic radiosurgery (SRS)

1 Introduction

This study focused on the digitization of the complication of brain edema caused by radiation therapy in patients with intracranial tumors. Intracranial tumors are classified according to their primary tissues. The most common type is glioma, followed by astrocytoma, brainstem glioma, etc. [1]. The main methods of tumor treatment are surgical resection, radiotherapy, and chemotherapy. Radiotherapy uses the high-precision stereotactic radiosurgery (SRS) of Cyberknife M6 as the main treatment method, which is a real-time image monitoring system that has been proven to replace surgical brain tumor surgery [2, 3].

When patients receive SRS treatment, more intracranial tumor cells usually need to be eliminated and high radiation doses are required to improve tumor control rates. However, high doses can cause damage to the normal tissues around the intracranial tumor, which results in normal tissues being unable to repair [4–6]. This leads to the complication of radiation-induced brain edema. Most hospitals use magnetic resonance imaging (MRI) to check for complications of brain edema in patients with intracranial tumors, four months after radiotherapy. Because MRI images have excellent resolution for soft tissues, they have better localization of lesions. MRI images are divided into two types: longitudinal relaxation time (T_1) and transverse relaxation time (T_2) weighted images. In this study, the T_2-Flair high-intensity image (T_2 fluid attenuated inversion recovery) is used for the brain edema area, as it is more accurate than X-ray computed tomography (CT). It also provides much useful information for the diagnosis of tumors and brain edema [7]. In order to quantify the complications of radiation-induced brain edema in patients with intracranial tumors, this study used the T_2-Flair images and CT images displayed in MRI. Each set of images has different properties, and the two sets of images were imported into MIM vista software for fusion. The exported results were then analyzed.

At present, there is no complete standard numerical procedure for clinical diagnosis of the complications of radiation-induced brain edema. Clinical radiation oncologists make subjective judgments based on their own experience and cannot quantify the diagnostic records. This will lead to different areas of brain edema being identified by each physician, and there will be some differences in the evaluation of

the treatment plan system. As a result, uncertain information will not be useful for follow-up research and will not provide a reference base for new doctors. In this study, images were visualized so that the clinician could have a reference basis for the definition of brain edema complications. An algorithmic segmentation method was used to segment the image of the suspected brain edema area. The image results segmented by the algorithm were compared with the ground truth standard (GTS) drawn by the clinician to show the differences from earlier images. The purpose of this was to quantify the area of brain edema complications and assist the clinician in their judgment.

2 Research Method

Two sets of images with different properties of MRI (T_2-Flair brain edema images and CT images) were imported into MIM vista for fusion, and the exported results were analyzed. The treatment planning software Multiplan 5.1.3, equipped with Cyberknife M6, was used to export data of patients with intracranial tumors. Before treatment, the doctor observed the location of the patient's lesions in order to formulate a treatment plan. Patients were tracked for complications for 4 months after treatment.

T_2-Flair images and CT images are medical images with different properties. The slice thickness and pixel spacing are also different. Therefore, these two sets of images must be normalized by image registration before analyzing the relationship between the volume of radiation-induced brain edema described by clinicians and the algorithm for segmenting radiation-induced brain edema. The two sets of images used in this study were digital imaging and communications in medicine (DICOM) images and were imported into MIM software (MIM vista version 6.93 Cleveland, OH, US) for fusion as the original images for research. After the image fusion, the physician described the patient's brain edema GTS and transferred it to the digital image benchmark DICOM. The medical image specifications exported in this study are shown in Table 1. The flow chart of this research is shown in Fig. 1.

MIM vista was used to interpolate the CT and T_2-Flair images, once the images were aligned. The interpolated image provides a high image quality once enlarged, with no pixel discontinuity, but the outline of the image may become blurred [8]. Clinicians described the image area of the patients with radiation-induced brain edema. The DICOM technology was output as the benchmark value for this study.

This study uses bicubic interpolation to scale the image, as the resolution size of the digital medical image output in the radiotherapy planning system is different, and the image coordinate position is also inconsistent. The initial position of the image was weighted and averaged through the adjacent 16-pixel positions to obtain the new position coordinates, and the image resolution was uniformly corrected to 512×512 dpi. The treatment plan was planned by physicians and physicists based on CT images, with reference to other medical images.

Table 1 Medical imaging specifications

Category	Number of images	Slice thickness (mm)	Image resolution	Pixel spacing (mm)
CT image	429	1.25	512 × 512	[0.7422, 0.7422]
MRI (before treatment) image	156	1.00	512 × 512	[0.4688, 0.4688]
MRI (after treatment) T_2-flair image	22	5	320 × 320	[0.7188, 0.7188]
MRI and CT fusion	429	0.625	512 × 512	[0.7210, 0.7210]
CT image	429	1.25	512 × 512	[0.7422, 0.7422]

Abbreviations: CT—computed tomography; MRI—magnetic resonance imaging

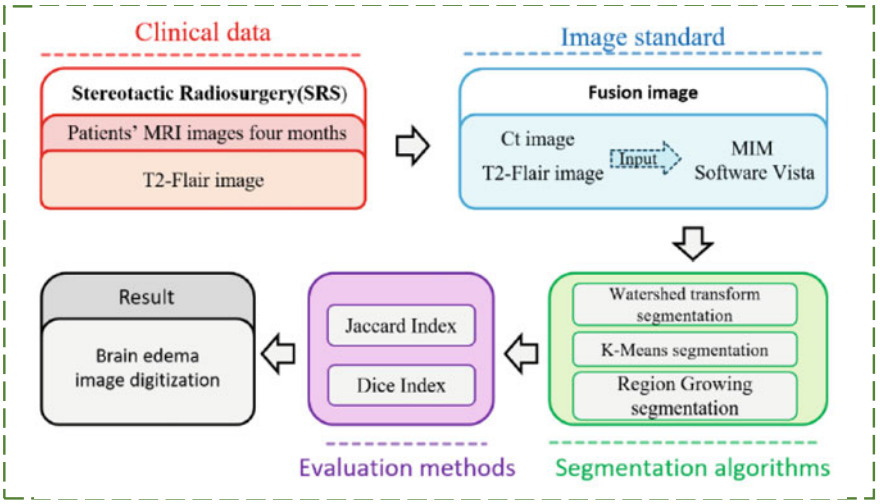

Fig. 1 Flow chart of MRI image segmentations. Abbreviations: CT— computed tomography; MRI— magnetic resonance imaging; GTS— ground truth standard

CT images were used as the standard value of the image in this study. Since medical images contain a lot of medical information, the coordinates of the affected part of the patient are included in the image coordinates. However, medical image information usually takes the actual size of 190 × 190 mm^2 as the standard value. Therefore, in the image processing, this needs to be converted to a resolution of 512 × 512 dpi, and the conversion between distance and pixel is done according to the pixel pitch. The inferred formula is shown as

$$\text{coordination in resolution system} = \left(\frac{\text{actual coordination}}{\text{pixel spacing}}\right) + \left(\frac{\text{size of resolution}}{2}\right) \tag{1}$$

Image filtering is usually designed as an odd-numbered square (3×3, 5×5), which is also called an image mask. It is mainly used to cover the pixels of the specified image in order to filter out unnecessary noise. Here, it is used to remove unnecessary noise from medical digital images and smooth the image. The low-pass filter is a common averaging mask in image processing. All the pixel values in the mask are added together and then averaged. The new value is written into the corresponding point pixel. The image filtering is shown as

$$p(x, y) = \frac{1}{9} \sum_{k=x-1}^{x+1} \sum_{l=y-1}^{y+1} f(k, l) \tag{2}$$

where $p(x, y)$ is the pixel position of the original image, and $f(k, l)$ is the pixel position of the filtered image.

The average value of gray-scale pixels of radiation-induced brain edema was used as the basis of the image feature extraction for the basic pixel feature of the statistical medical images. The probability of grayscale pixels appearing in the target area is shown as

$$P(r_i) = \frac{n(r_i)}{N} \tag{3}$$

where $P(r_i)$ is the probability that the pixel with the grayscale value r_i appears in the target area, $n(r_i)$ is the number of times for the grayscale value r_i appears in the target area, and N is the number of pixels in the entire target area.

The mean probability of gray scale is shown as

$$m = \frac{1}{n(r_i)} \sum_{i=0}^{L-1} r_i P(r_i) \tag{4}$$

where m is the mean probability of gray scale, L is the number of different grayscale values in the image area, and its range is 0, 1, 2, …, $L - 1$.

The information from the T_2-Flair image and the CT image were provided to the clinician to observe the soft tissue and bone hard tissue of the patient's lesion. After image alignment of the two images, the clinician used MIM vista to interpolate the T_2-Flair image and obtain image information equivalent to CT. The process is shown in Fig. 2.

Figure 2a shows the MRI image before treatment. The area circled by the red arrow is the area without brain edema before treatment. Figure 2b shows the MRI

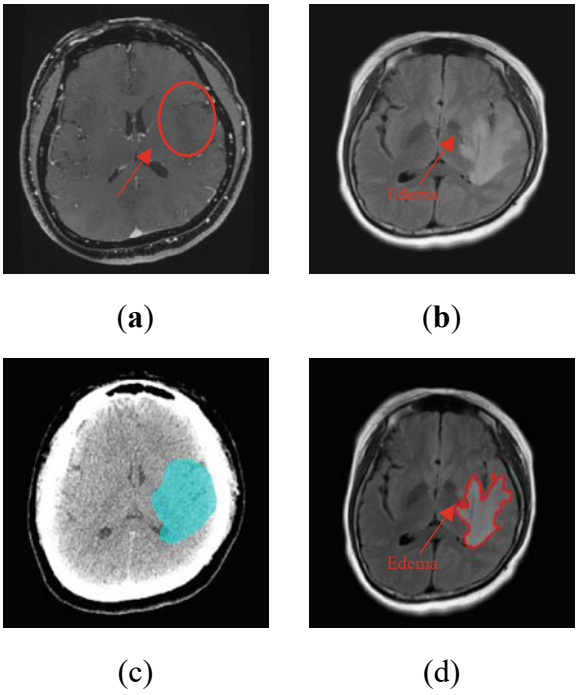

Fig. 2 The process of the algorithm to segment and extract MRI image of radiation-induced brain edema with CT image: **a** MRI image (before treatment, not found edema); **b** MRI-T_2 Flair image (after treatment); **c** edema GTS of CT; **d** edema algorithm segmentation (Abbreviations: CT—computed tomography, MRI—magnetic resonance imaging, GTS—ground truth standard)

image of the patient through 4 months after treatment. The arrow indicates the area, where the patient has suffered radiation-induced brain edema complications due to radiotherapy. Due to the different areas of image intensity after treatment, three algorithms: (i) region growth, (ii) watershed, and (iii) K-means clustering were applied to segment and extract image areas suspected of radiation-induced brain edema. Figure 2c shows the radiation-induced brain edema area drawn by the clinician on the CT images. The drawn area is also called the GTS. From Fig. 2d, it can be observed that the brain edema area after algorithm segmentation is smaller than that drawn by the clinician.

This research uses the following three algorithms:

(i) *Region Growing*

Region growing segmentation is a region-based image segmentation method, which is classified as a pixel-based image segmentation method. Because it involves the setting of initial seed points, the main goal of segmentation is to divide the image into regions and achieve the goal of segmentation by finding the boundaries between regions based on the discontinuities in the grayscale and color attributes. The concept of the algorithm region is as follows:

If R represents the entire range of an image, the purpose of image cutting is to cut R into n blocks [9]. R_i represents that an image is cut into i blocks. R_1, R_2, …, R_n must meet the following conditions:

(a) $\cup_{i=1}^{n} R_i = R$;
(b) R_i is a connected region, $i = 1, 2, \ldots, n$;
(c) $R_i \cap j =, i \neq j$;
(d) $P(R_i) = TRUE$ for $i = 1, 2, \ldots, n$;
(e) $P(R_i \cap R_j) = FALSE$ for any adjacent regions R_i and R_j.

$P(R_i)$ is a logical predicate defined at a point in the set. R_i and Ø are empty sets and R_i must meet the following requirements:

(a) the segmentation must be complete and each pixel must be in a region;
(b) the points in the area are required to be connected in some predefined way;
(c) these areas are indicated to be disjoint;
(d) the pixels in the segmented area must meet the corresponding attributes: for example, $P(R_i) =$ TRUE, if all pixels have the same grayscale in R_i for any adjacent region R_i and R_j.
(e) the meanings of the regions R_i and R_j in the predicate are different P.

Image processing uses the seed as the core to select pixels for image growth. The pixels around the seed are judged based on whether they have similar characteristics (grayscale values, joints, colors) to the seed. This is shown in the following equation:

$$|P - S| < 20\%[\max(R) - \min(R)] \tag{5}$$

Region growing segmentation represents the absolute value of pixel P and seed point S. The growth condition occurs, if the absolute value is less than 20% of the difference between the maximum strength value, max(R), and the minimum strength value, min(R), in the growth area; otherwise it will be stopped [10, 11].

(ii) *Watershed Transform Segmentation*

Watershed transform segmentation has good edge detection capabilities and can obtain the characteristics of a relatively concentrated catchment basin. This method has been widely used in image processing. However, the algorithm of watershed transform segmentation also has the problem of image over-segmentation while obtaining good edges. The basic steps of the algorithm of watershed transform segmentation are as follows:

(a) The Markers method is used for image pre-processing. The image gradient is calculated to obtain the area with the smaller gradient value as a catchment basin. In the process of obtaining the catchment basin, all pixels in the same catchment basin are obtained in eight directions.
(b) Water starts to be injected from the catchment basin area. The boundary pixels of the catchment basin area are judged in eight directions, to detect whether the pixels can be submerged. If the pixels of the catchment area are submerged, the image of the catchment basin and the boundary pixels of the catchment basin will be recalculated. When the water is submerged between the two catchment basins, the submerging is stopped. The pixel between the two catchment basins is a watershed.

(c) Step (b) is repeated until the water is submerged to a given height to obtain the watershed of all catchment basins [12]. The boundary point between the catchment basin images of the input image is the watershed, which represents the maximum point of the input image. Therefore, in order to obtain the edge information of the image, the gradient image is usually used as the input image. The gradient operation of the image is shown as

$$G(x,y) = \text{grad} f(x,y) = \left\{[f(x,y)-f(x-1,y)]^2[f(x,y)-f(x,y-1)]^2\right\}^{0.5} \tag{6}$$

where $f(x, y)$ is the original image, and grad{ } is the gradient operation [13].

(iii) *K-means Segmentation*

K-means segmentation is the most classic partition-based clustering method. It is also one of the top ten classic data mining algorithms. The basic structure of the K-means segmentation is to cluster K points in the space as the center. The objects closest to them are classified. Through the iterative method, the value of each cluster center is updated successively until the best clustering result is obtained. K-means segmentation aims to specify the number of subgroups k, and minimize the sum of variation within k groups. The calculation of the cluster Ck is defined by the formulae:

$$\text{W(Ck)} = \sum_{X_{i \in Ck}} (X_i - uk)^2 \tag{7}$$

where X_i is the data point in the cluster Ck, and uk is the center point specified by the average value of the data points in the cluster Ck. The total within-cluster variation is used to measure the compactness of the cluster. The operation of total within-cluster variation is defined as

$$\text{Total within} - \text{cluster variation} = \sum_{i=1}^{k} W(Ck) = \sum_{i=1}^{k} \sum_{X_i \in Ck} (X_i - uk)^2 \tag{8}$$

The smaller the value, the better the compactness.

Assuming that the sample set was divided into K categories, the algorithm is described as follows:

(a) the initial center of the Kth category must be appropriately selected;
(b) in the Kth iteration, for any sample, the distance to the Kth center is calculated, and the sample is classified into the category of the center with the shortest distance;
(c) the center value of the category is updated using the mean value method;
(d) for all cluster of K centers, after updating using the iterative method of (b) and (c), the iteration is ended, if its value remains unchanged; otherwise the iteration is continued.

The biggest advantage of this algorithm is its simplicity and speed. The key to the algorithm is the selection of the initial center and the distance equation [14].

Matlab surface reconstruction and volume reconstruction are used to evaluate the similarity between the GTS brain edema volume and the algorithm segmentation of the brain edema area in a three-dimensional (3D) model. The evaluation indicators are Dice and Jaccard. The surface reconstruction method uses the unevenness or features of the contour of the object to cut the image into triangles or polygons and merge the continuous surfaces. The merged continuous faces are stacked together in a progressively curved connection. The volume reconstruction stacks all points on the contour of the image plane slice in order to form a 3D image. The interpolation method is used to make up for the shortcomings of insufficient cut surface, based on the characteristics of each contour.

The Dice indicator is also called the overlap index. It is the most frequently validated medical volume segmentation index and is often used to calculate the similarity measure between the *GTS* volume and the segmentation algorithms volume (R) of the brain edema. The Dice index is defined as

$$\text{Dice Index} = \frac{2|(R \cap GTS)|}{|R| + |GTS|} \tag{9}$$

When the ratio is equal to 1.00, it represents the best condition for the volume correlation between *GTS* and R [15].

Jaccard and Dice indicators are used to calculate the *GTS* and segmentation algorithms of the brain edema volume to compare and verify the statistics of the similarity and diversity of the brain edema volume sample sets. The Jaccard index has the form:

$$\text{Jaccard Index} = \frac{|(R \cap GTS)|}{|(R \cup GTS)|} \tag{10}$$

When the ratio is equal to 1.00, it represents the best condition for the volume correlation and segmentation performance between *GTS* and R [16].

3 Results

The segmentation algorithms were used to segment the 2D image of the radiation-induced brain edema. Figure 3 shows (a) the region growing segmentation, (b) the watershed transform segmentation, and (c) the K-means segmentation. Figure 3 is divided into four parts to show the process of image segmentation: Original image includes Step 1, Step 2, and Step 3. Step 1 is the initial segmentation step of the algorithm, Step 2 is the radiation-induced brain edema image to be segmented by the segmentation algorithm, and Step 3 is the extraction feature of the edema image. The region growing segmentation algorithm gives the seed of the initial position of the image to expand the pixels in eight directions. The seed divides the radiation-induced

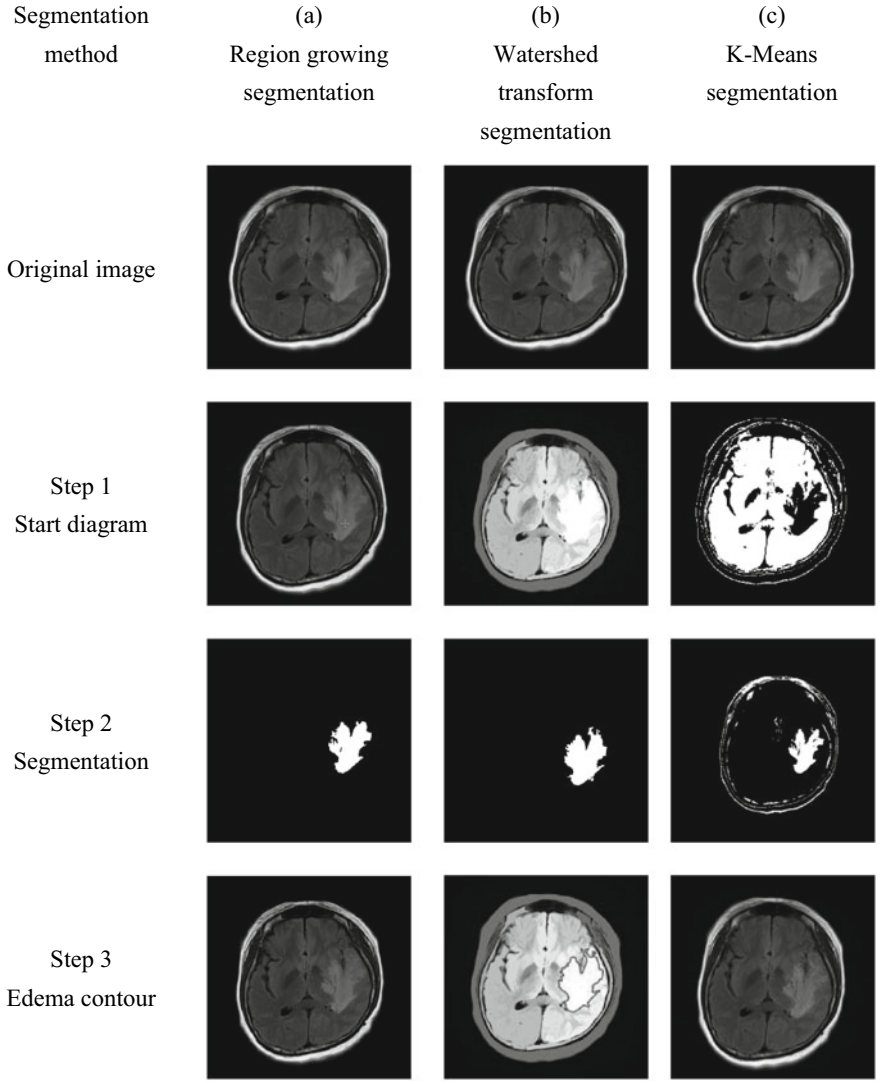

Fig. 3. 2D images by using algorithm segmentation for radiation-induced brain edema after MRI: **a** region growing segmentation **b** watershed transform segmentation **c** K-means segmentation. Abbreviations: MRI— magnetic resonance imaging

brain edema area image based on the similarity, intensity, color, texture, and other information of adjacent pixels [16, 17].

Watershed transform segmentation is a region segmentation method. The principle of this segmentation image is the use of different segmentation criteria between the spatial pixels. The application process requires pre-processing of the image, which includes thresholding, edge detection, etc. to obtain image markers. By using

pre-processing, the disadvantages of the spatial relationship of the pixels will be ignored. After 3D image reconstruction, over-segmentation often occurs in watershed transform segmentation.

The following is the four-part process. The first row is the original image. The second row is the image of Step 1, which is the initial segmentation of the algorithm. The third row is Step 2, which is the segmentation image of the radiation-induced brain edema. The fourth row is Step 3, which is the resulting image of feature extraction of the edema.

Figure 4 contains three algorithms for segmentation. The 3D reconstructions of the head are displayed in different directions. The red regions indicate GTS, whilst the yellow regions indicate the result of each algorithm segmentation [18]. Figure 4a is region growing segmentation, which shows very little over segmentation in its positive and side images. However, there is a slight over segmentation in the rear

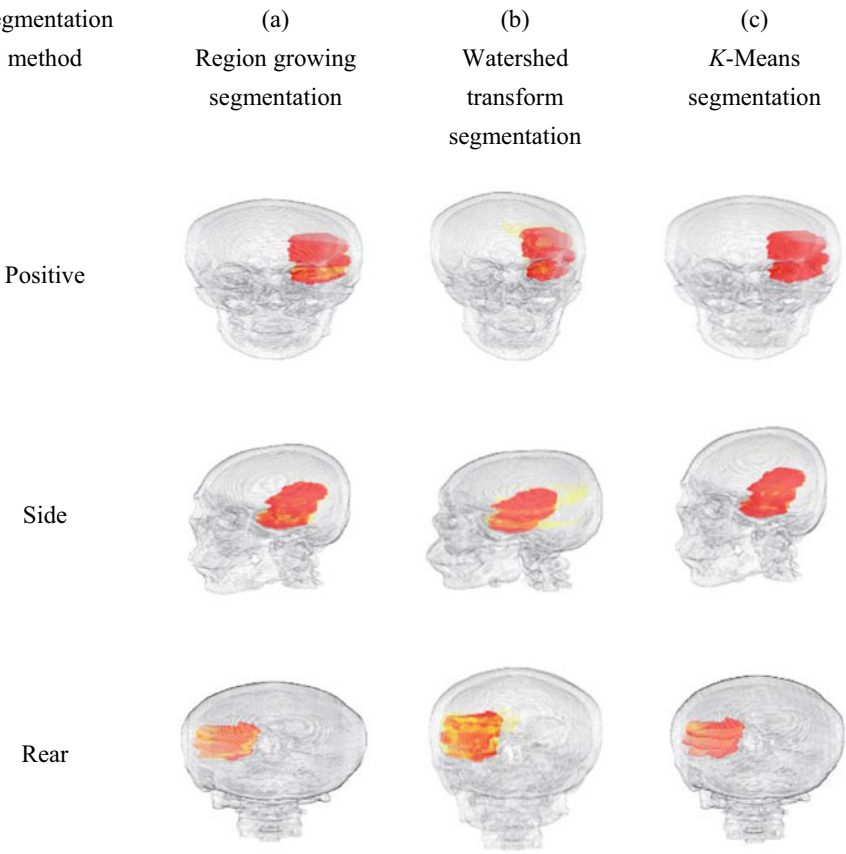

Fig. 4. 3D reconstruction images for three algorithms: Red regions indicate GTS and yellow regions indicate the result of each algorithm segmentation. Abbreviations: CT— computed tomography; MRI— magnetic resonance imaging

image. Figure 4b is watershed transform segmentation. In the side image, it can be clearly seen that the yellow block is the over-segmented area. Figure 4c is K-means segmentation, which divides the MRI image into K objects as the initial clustering center. The most similar categories are assigned according to the similarity of the objects. Similarity is the distance between pixels and cluster centers and refers to the square of the absolute deviation between them. Deviations usually include color, brightness, texture, position, and weighted combinations. This algorithm segmentation can ensure convergence, but it is not the best solution. The initial graph of this study is divided into 7 cluster categories. Radiation-induced brain edema is one of the categories. The feature extraction method is used to extract the area of radiation-induced brain edema [19].

Whether or not there is a similarity correlation analysis between the algorithm segmentation volume and the GTS volume of brain edema, it is necessary to provide index meaning with specific data. Therefore, the Dice index and Jaccard index are used as indicators of similarity. The closer the values of the Dice and Jaccard indexes are to 1.00, the better the correlation between the segmented volume of the algorithm and GTS of the brain edema [20]. As shown in Fig. 5, the regional growing algorithm segmentation is the best, with Dice and Jaccard indexes of 0.77 and 0.63, respectively. However, there is no difference between K-means segmentation and watershed transform segmentation results. In terms of correlation, the difference between the Dice and Jaccard indexes is only in the region of 0.01.

In Table 2, the volume of the watershed transform segmentation is 79 cm^3, which is higher than the other two algorithms. However, the watershed transform segmentation

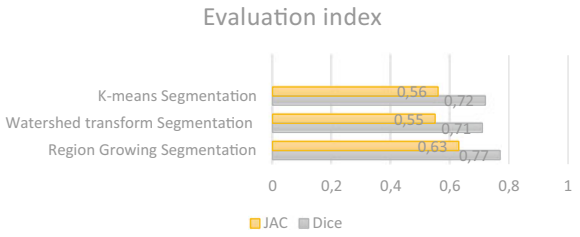

Fig. 5 Index evaluation result of three segmentations algorithms; Dice and JAC of region growing segmentation is better than the other 2 algorithms

Table 2 Three algorithms and edema segmentation evaluation. Abbreviations: GTS—ground truth standard

Evaluation parameter index	Region growing segmentation	Watershed transform segmentation	K-means segmentation
GTS (cm^3)	87.41	87.41	87.41
Algorithm segmentation (cm^3)	74.47	79	55.24
Algorithm and GTS overlap (cm^3)	61.03	59.26	50.97
Dice index	0.77	0.71	0.72
Jaccard index	0.63	0.55	0.56

Table 3 Dice and Jaccard index increased significantly after the optimization. Abbreviations: GTS— ground truth standard

Evaluation parameter index	Watershed transform segmentation	Optimization parameter
GTS (cm^3)	87.41	87.41
Dice index	0.71	0.77
Jaccard index	0.55	0.64

has over segmentation, so its performance in terms of the Dice index and the Jaccard index is poor.

Figure 2c and d show that the results of GTS and algorithm segmentation are not completely similar. The differences will be especially more obvious in medical images of different layers, and clinicians will draw a wider range of areas that may have radiation-induced brain edema. However, the algorithm used in this study divides the brain edema area into smaller ranges, which will cause the evaluated Dice and Jaccard index to be unsatisfactory.

Some optimized methods are used, such as the contour edge expansion of algorithm segmentation, so that the result of the segmentation algorithm approaches GTS. Due to the over segmentation of the watershed transform segmentation, the image layer is algorithmically optimized to solve the problem of over segmentation. The optimized indexes are close to the level of the regional growing algorithm, which means that different types of optimization algorithms can be used to make the segmentation result closer to GTS [13, 21, 22], as shown in Table 3.

M. Omran et al. proposed a new method for image clustering using particle swarm optimization (PSO). The purpose of PSO is to simultaneously minimize the quantization error and the distance within the cluster, and maximize the distance between the clusters. They further compared PSO with K-means segmentation, fuzzy *C*-means, and a genetic algorithm (GA). Generally, PSO produces better results than the other algorithms; the use of the distance between and within clusters making the segmentation performance better [23].

Yang et al. respectively proposed concepts based on GA, ant colony optimization, harmony search algorithms, and PSO, adjusting a series of parameters and designing an effective fitness function in order to provide good image segmentation quality. The optimization progress can be improved in the preliminary stage of the optimization results [24].

In future research, artificial intelligence will be used to optimize the algorithm segmentation and compare the brain edema area determined by clinicians. The construction and processing of image samples during brain edema training will be discussed in depth. The segmentation results of the algorithm used can predict a good level, similar to GTS. It can help clinicians to quantify the suspected brain edema complication areas.

4 Conclusion

In this study, we explored the lack of standard numerical procedures for brain edema complications. In order to make a reference base for clinicians to quantify the complications of radiation-induced brain edema, three algorithms were used to segment the medical images of patients with radiation-induced brain edema. The results of the algorithm segmentation were compared with the standard GTS, described by the clinician, to establish the difference in the volume of complications.

The region growing segmentation algorithm is an image segmentation method that segments connected regions with the same characteristics in the image. This method also guarantees better edge information. Its advantages are simple and easy to implement, but the space and time complexity is higher. Therefore, it has higher requirements for segmentation of images. The results of this study show that it is easy to form image holes and image over-segmentation with the region growing segmentation algorithm.

The principle of the watershed transform segmentation algorithm is to use different segmentation criteria between the spatial pixels of the image to segment the image. The application process requires pre-processing of the image, such as thresholding, edge detection, etc., to obtain image markers. Because of its good edge detection capabilities and its ability to obtain a relatively concentrated collection basin, it has been widely used in image processing and in the field of image segmentation. After 3D image reconstruction, the watershed transform segmentation faces the problem of image over-segmentation, while obtaining good edges.

The results of GTS and algorithm segmentation are not completely similar in different layers of medical images. Usually, clinicians will draw a wider area for the possible range of the radiation-induced brain edema, which leads to the poor Dice coefficient and Jaccard coefficient values that we evaluated. Therefore, some optimized methods are used to expand the contour edge of the algorithm segmentation so that the result of the algorithm segmentation is closer to the result of the GTS. The watershed transform segmentation algorithm has over-segmentation. However, the Dice and Jaccard values of the over-segmented image layer are significantly increased after the algorithm is optimized. The performance is similar to the result of region growing segmentation algorithm, which means that different types of optimization algorithms make the algorithm segmentation result closer to GTS.

The study found that the segmentation result of the region growing algorithm for the imaging of radiation-induced brain edema complications is the most similar to GTS, based on the two volume correlation evaluation indicators of Dice and Jaccard. Therefore, it can be used as an automatic segmentation of clinical brain edema complications. The results of this research allow clinicians to describe the complications of brain edema with supporting references. Therefore, in the future, we will use artificial intelligence algorithm segmentation to obtain a large amount of clinical experience to improve the problem of inaccurate segmentation results due to the small area of the algorithm segmentation.

Acknowledgements We thank Yi-Kuan Tseng for the statistical technical supports. This study was supported financially, in part, by grants from MOST109-2221-E-992-011-MY2.

Conflicts of Interest The authors declare no conflicts of interest. Part of this results was presented in an abstract form at the 6th Continental Congress of Dermatology.

Ethical Statement Institutional Review Board (IRB) approval was obtained from the Chang Gung Memorial Hospital IRB (approval number: 201701596B0), and the requirement for informed consent was waived given the retrospective nature of the study.

References

1. A.W. Jensen, P.D. Brown, B.E. Pollock, S.L. Stafford, M.J. Link, Y.I. Garces, R.L. Foote, D.A. Gorman, P.J. Schomberg, Int. J. Radiat. Oncol. Biol. Phys. **62**, 32 (2005)
2. M. Schell, *Report of Task Group 42 Radiation Therapy Committee: June*. AAPM Report No. 54 (1995)
3. J.H. Suh, N. Engl. J. Med. **362**, 1119 (2010)
4. J.M. Butler, S.R. Rapp, E.G. Shaw, Curr. Treat. Options Oncol. **7**, 517 (2006)
5. L.M. DeAngelis, N. Engl. J. Med. **344**, 114 (2001)
6. H.S. Sharma, J. Westman, F. Nyberg, *Progress in Brain Research*, vol. 115 (Elsevier, Amsterdam, 1998), p. 351
7. M. Watanabe, R. Tanaka, N. Takeda, Neuroradiology **34**, 463 (1992)
8. C.L. Zitnick, S.B. Kang, M. Uyttendaele, S. Winder, R. Szeliski, ACM Trans. Graph. (TOG) **23**, 600 (2004)
9. H.-D. Cheng, X.H. Jiang, Y. Sun, J. Wang, Pattern Recognit. **34**, 2259 (2001)
10. L.G. Ugarriza, E. Saber, S.R. Vantaram, V. Amuso, M. Shaw, R. Bhaskar, IEEE Trans. Image Process. **18**, 2275 (2009)
11. X. Xu, S. Xu, L. Jin, E. Song, Pattern Recognit. Lett. **32**, 956 (2011)
12. A.P. Mangan, R.T. Whitaker, IEEE Trans. Vis. Comput. Graph. **5**, 308 (1999)
13. A. Schenk, G. Prause, H.-O. Peitgen, *Proceedings of International Conference on Medical Image Computing and Computer-Assisted Intervention* (2000), p. 186
14. S. Äyrämö, T. Kärkkäinen, *Reports of the Department of Mathematical Information Technology. Series C, Software Engineering and Computational Intelligence* (2006)
15. J. Bertels, T. Eelbode, M. Berman, D. Vandermeulen, F. Maes, R. Bisschops, M.B. Blaschko, *Proceedings of International Conference on Medical Image Computing and Computer-Assisted Intervention* (2019), p. 92
16. J.C. Yue, M.K. Clayton, F.C. Lin, Biometrics **57**, 743 (2001)
17. H.-Y. Jiang, Y.-P. Si, X.-G. Luo, J. Northeast. Univ. Nat. Sci. **27**, 398 (2006)
18. M. Tabb, N. Ahuja, IEEE Trans. Image Process. **6**, 642 (1997)
19. H. Ng, S. Ong, K. Foong, P. Goh, W. Nowinski, *Proceedings of 2006 IEEE Southwest Symposium on Image Analysis and Interpretation* (2006), p. 61
20. Q. Dou, L. Yu, H. Chen, Y. Jin, X. Yang, J. Qin, P.-A. Heng, Med. Image Anal. **41**, 40 (2017)
21. W. Tao, H. Jin, L. Liu, Pattern Recognit. Lett. **28**, 788 (2007)
22. M. Omran, A.P. Engelbrecht, A. Salman, Int. J. Pattern Recognit. Artif. Intell. **19**, 297 (2005)
23. M. Omran, A.P. Engelbrecht, A. Salman, *Recent Advances in Simulated Evolution and Learning* (World Scientific, Singapore, 2004), p. 347
24. A. Kaveh, S. Talatahari, Comput. Struct. **87**, 267 (2009)

Reconstruction of the Optical Acoustic Signal for Visualization of Biological Tissues

Denis A. Kravchuk and Irina B. Starchenko

Abstract One of the most important applications of optoacoustics is the visualization of oxygenation, hemoglobin concentration, and monitoring. The paper presents the results of processing an acoustic signal obtained as a result of thermoelastic expansion under the influence of an ND: YAG laser with a duration of 84 ns on an aqueous solution using a modified back projection algorithm based on a combined wavelet for high-frequency optoacoustic tomography. The results show that the above wavelet-based back projection algorithm effectively improves the resolution and contrast of reconstruction images under conditions of strong background noise. It is shown that the method can be used in optoacoustic signal reconstruction to obtain images of biological tissues. The paper presents a modified reverse projection algorithm based on a combined wavelet for high-frequency optoacoustic tomography. The given wavelet-based back projection algorithm will improve the resolution and contrast images during reconstruction under strong background noise. The aqueous solution was irradiated with nanosecond laser pulses, and acoustic waves were formed in the result of thermoelastic expansion of the irradiated volume. The model liquid was exposed to a laser with a constant intensity. The results of the experimentally obtained and restored acoustic signals formed as a result of ND: YAG laser exposure were presented with an optoacoustic effect in an aqueous solution. Signal processing was performed using the reverse projection algorithm. A method for processing the acoustic signal based on the reverse filtering method is proposed, which showed that the modified algorithm can significantly improve the quality of the reconstructed image.

Keywords Laser · Diagnostics · Optoacoustic · Reconstructed

D. A. Kravchuk (✉)
Southern Federal University, Taganrog, Russia
e-mail: kravchukda@sfedu.ru

I. B. Starchenko
Parametrika LCC, Taganrog, Russia

I. A. Parinov et al. (eds.), *Physics and Mechanics of New Materials and Their Applications*, Springer Proceedings in Materials 10,
https://doi.org/10.1007/978-3-030-76481-4_39

1 Introduction

The most commonly used methods for determining optical properties require invasive procedures and in vitro autonomous work methods based on attenuation using spectrophotometry, reflection coefficient, fluorescence spectroscopy, Raman spectroscopy, and optoacoustics [1]. In vivo studies using a combination of optoacoustics and carbon nanoparticles were performed [2–5] and it was demonstrated an increase in image contrast [6].

Optoacoustic tomography combines the advantages of both pure optical imaging and ultrasound imaging, which can provide high resolution and high optical contrast imaging of tissues [6–10]. The basic idea of optoacoustic tomography is that the tissue is irradiated with nanosecond laser pulses, the absorbed energy leads to thermoelastic expansion and subsequent reduction of the irradiated volume, which generates acoustic waves that can be detected by highly sensitive sensors around the tissue. The amplitude and profile of acoustic signals carry spatial information about the distribution of light absorption by the tissue, which is often associated with its structure, physiological and pathological changes, since tissues in different physiological conditions have different light absorption coefficients [1].

Most of the results presented to date are qualitative, and there are no quantitative in vivo studies. The purpose of this work is a quantitative study of the characteristics of an optoacoustic signal in model liquid biological media.

The reverse filtering method, based on the configuration of scanning with rotation, is applied. It is a classical algorithm for reconstructing a cross-sectional image. Optoacoustic signals with pressure $P_r(t)$ were obtained by deconvolution of the recorded acoustic signal $P_{d0}(t)$, emanating from a point absorption source, with a fast inverse Fourier transform.

To extract weak acoustic signals, a focused transducer with a large aperture was used that can give us a good signal-to-noise ratio [11, 12]. Examples of approximate recovery methods include a multi-element phase-controlled technique [11, 12], a deconvolution algorithm [13], a weighted delay and summation method [14], an optimal statistical approach [15] and a Radon transform in the far-field approximation [16], reconstruction algorithms for various detection geometries [17, 18]. The FBP method with reverse filtering, based on a rotation scan configuration, is a classic algorithm for reconstructing a cross-section image. The quality of the restored image is mainly determined by the choice of various filters, such as Ramachandran and Lakshminarayanan RL, Shepp and Logan SL, Modi-SL and Kwoh-Reed, etc., Gibbs phenomena appearing in the after filter can cause the image to blur. Therefore, it is of great practical importance to find a new filtering method with better filtering and noise suppression.

2 Research Method

To obtain data for visualization based on the optoacoustic effect, the tissue is irradiated with a laser pulse at time $t = 0$. In response to the laser pulse, an acoustic wave field with pressure p is generated in the tissue. The function $p(r, t)$ describes the field of the pressure wave, thermoacoustically induced, at time $t \geq 0$ at the point r.

Suppose that the analytic wavelet function $\Psi(t)$ obeys the following conditions:

$$\Psi(t) \in L^1(R, dt) \cap L^2(R, dt). \tag{1}$$

$$\Psi(\omega) \in L^1\left[R\backslash\{0\}, \frac{d\omega}{|\omega|}\right] \cap L^2\left[R\backslash\{0\}, \frac{d\omega}{|\omega|}\right], \tag{2}$$

where $L^1(R)$ and $L^2(R)$ denote two functions of space; $\Psi(\omega)$ is the Fourier transform of the wavelet function $\Psi(t)$, and $\Psi(\omega) = 0$ when $\omega < 0$. Consider an arbitrary function $f(t) = L^2(R, dt)$, its wavelet transform of the original wavelet function $\Psi(t)$, defined as [19, 20]

$$W_f(b, a) = \frac{1}{a}\int_{-\infty}^{\infty} f(t)\overline{\Psi}\left[\frac{t-b}{a}\right]dt. \tag{3}$$

Then we can obtain the expression [7]:

$$\frac{1}{C_\Psi}\int_0^{+\infty} W_f(b, a)\frac{da}{a} = f(b) + iH[f(b)], \tag{4}$$

in the boundary conditions:

$$C_\Psi = \int_0^{+\infty} \frac{\Psi_R(\omega)}{\omega}d\omega < \infty, \quad C_\Psi \neq 0, \tag{5}$$

where $\overline{\Psi}(t)$ is the conjugate function of t; $\Psi_R(\omega)$ is the real part of $\Psi(\omega)$; $H[f(b)]$ is the Hilbert transform of $f(t)$.

Projections of the optical absorption distribution can be reconstructed using an inverse filtering algorithm [8, 9]:

$$\iint_{|r|=ct} A(r)ds = \frac{4\pi C_p kt}{\beta r_p} IFFT\left(\frac{P_{dt}(\omega)W(\omega)}{P_{d0}(\omega)}\right), \tag{6}$$

where filter $W(\omega)$ is the key to restoring the optoacoustic image. Theoretically, the reconstructed algorithm based on the inverse Radon transform needs a filter ω to be equal, which is the ideal copy of the Hilbert filter with infinite bandwidth. However, according to the Paley-Wiener theorem, it cannot be implemented in practice. In addition, the classical filter can cause strong Gibbs phenomena and has poor anti-noise ability, so the quality of the restored image is unsatisfactory. Induced optoacoustic signals with pressure $P_r(t)$ can be obtained directly by deconvolution of the registered acoustic signal $P_{d0}(t)$ coming from a point absorption source, with a fast inverse Fourier transform:

$$P_r(t) = IFFT\left(\frac{P_{dt}(\omega)}{P_{d0}(\omega)}\right), \tag{7}$$

so we can rewrite formula (6) as

$$\begin{aligned}\oiint_{|r|=ct} A(r)ds &= \frac{4\pi C_p kt}{\beta r_p} \cdot IFFT\left(\frac{P_{dt}(\omega)W(\omega)}{P_{d0}(\omega)}\right) * IFFT[W(\omega)] \\ &= \frac{4\pi C_p kt}{\beta r_p} P_r(t) * \left(-\frac{1}{2\pi^2 t^2}\right), t \neq 0 \\ &= \frac{2C_p kt}{\beta r_p} \cdot H\left[\frac{\partial}{\partial t} P_r(t)\right],\end{aligned} \tag{8}$$

where

$$f(t) = \frac{\partial}{\partial t} P_r(t), \tag{9}$$

Then according to the theorem in formula (4), we get

$$\oiint_{|r|=ct} A(r)ds = \frac{2\pi C_p kt}{\beta r_p} \cdot \mathrm{Im}\left[\frac{1}{C_\Psi}\int_0^\infty F_p(t,a)\frac{da}{a}\right], \tag{10}$$

where

$$F_b(b,a) = -\frac{1}{a^2}\int_{-\infty}^{\infty} P_r(t) \cdot \Psi'\left(\frac{t-b}{a}\right)dt, \tag{11}$$

$\Psi'(t)$ is the differential of the wavelet function t and "*" denotes convolution.

3 Results and Discussion

It can be seen from the expressions that the operation of convolution of projected data can be replaced by a wavelet transform. The frequency spectrum of an acoustic signal ranges from a few megahertz to tens of megahertz. We choose the modified Morlet wavelet as the parent wavelet, and then the combined wavelet can be obtained as follows:

$$g(t) = \Psi_m(t) \sum_{k=1}^{n} \exp[2\pi j(f_L - f_m + k\Delta f)t], \quad k = 0, 1, ..., n \tag{12}$$

where

$$\Psi_m(t) = [\cos mt + i \sin mt] \cdot \exp\left[-\frac{1}{2}\left(\frac{\sqrt{2}\sigma m}{2\pi r}\right)^2\right], \tag{13}$$

$g(t)$ is the combinational wavelet; $\Psi_m(t)$ is the mother wavelet; f_m is the central frequency $\Psi_m(t)$; f_L is the lower frequency limit of $g(t)$; Δf is the range of the central frequency of the combined wavelets, so the upper limit frequency of $g(t)$ is: $f_{\mathrm{H}} = f_{\mathrm{L}} - f_{\mathrm{m}} + n\Delta f$. The correction period can be ignored when $\left[\pi\tau/\sqrt{2}\sigma\right]^2$ is high enough [7].

Figure 1 shows the acoustic signal obtained experimentally on the Limo laser [10–12].

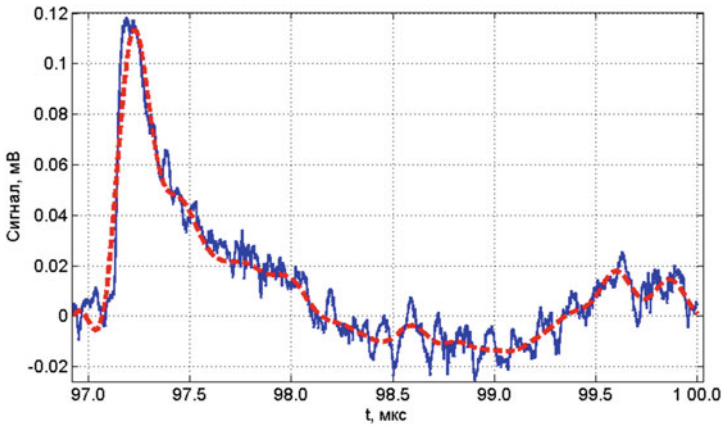

Fig. 1 Acoustic signal formed in the result of the optoacoustic effect (dotted line presents the restored acoustic signal formed in the result of the optoacoustic effect)

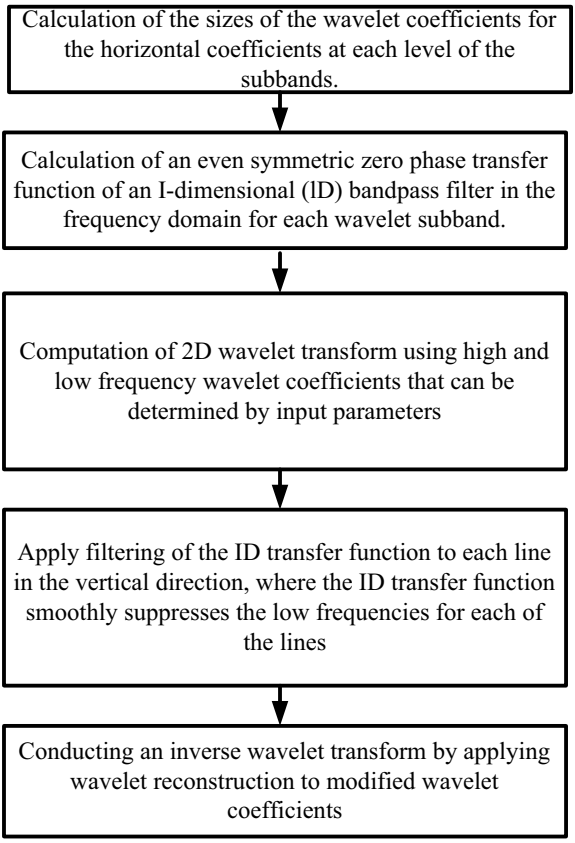

Fig. 2 Algorithm of removing the horizontal stripes

Another important interference in image formation can be the appearance of horizontal interference in the image. These errors in the image can be removed using a method based on a two-dimensional discrete wavelet transform or using a filter.

The algorithm shown in Fig. 2 can be used to remove horizontal interference in the image and is performed as follows:

4 Conclusion

The acoustic signal shown in Fig. 1 is obtained in the result of exposure to ND:YAG laser on an aqueous solution using the Limo installation [22, 23, 25, 26]. The duration of the laser pulse was 84 ns. Figure 1 (dotted line) shows the restored signal after the reverse filtering algorithm. Recently, the wavelet transform, which combines the best characteristics of time and frequency methods, such as Fourier transform methods, is rapidly becoming a new approach to signal processing and biomedical image

reconstruction. The paper presents a modified reverse projection algorithm based on a combined wavelet for high-frequency optoacoustic tomography. The results show that the given wavelet-based reverse projection algorithm effectively improves the resolution and contrast of reconstruction images under the condition of strong background noise. The method can potentially be used as a method for high-noise optoacoustic signal reconstruction for tissue diagnostics [27, 28].

References

1. R.G.M. Kolkman et al., Phys. Med. Biol. **49**(20), 4745 (2004)
2. D.V. Orda-Zhigulina, I.B. Starchenko, Inženernyj Vestnik Dona. **22**, 4–1 (2012). ((In Russian))
3. D.A. Kravchuk, I.B. Starchenko, Appl. Phys. **4**, 89 (2018)
4. D.A. Kravchuk, I.B. Starchenko, J. Phys. Conf. Ser. **1353**, 12088 (2019)
5. D.A. Kravchuk, K.A. Voronina. J Biomedical Photonics & Engineering (J-BPE). **6**(1), 010307 (2020)
6. C. Li, G. Ku et al., Phys. Med. Biol. **49**, 1329 (2004)
7. A.B. Karpiouk, et al. J. Biomed. Opt. SPIE-Intl Soc Optical Eng. **13**(5), 054061 (2008)
8. L. V. Wang, et al. in *Proceeding of the 2nd IEEE International Symposium on Biomedical Imaging: Macro to Nano* (2004)
9. Y. Su et al., J. Phys. D. Appl. Phys. **38**(15), 2640 (2005)
10. X. Wang, et al. Nat. Biotechnol. (2003)
11. G.J. Diebold, A.C. Beveridge, T.J. Hamilton, J. Acoust. Soc. Am. **112**(5), 1780 (2002)
12. D. Xing, et al.*Physics in Medicine & Biology.* **49** (2004)
13. Y. Wang et al., Phys. Med. Biol. **49**(14), 3117 (2004)
14. C.G.A. Hoelen, F.F.M. de Mul, Appl. Opt. The Optical Society **39**(31), 5872 (2000)
15. Y.V. Zhulina, Appl. Opt. The Optical Society. **39**(32), 5971 (2000)
16. R.A. Kruger et al., Med. Phys. **22**(10), 1605 (1995)
17. M. Xu, L.V. Wang, IEEE Trans. Med. Imaging. **21**(7), 814 (2002)
18. Y. Xu, M. Xu, L.V. Wang, IEEE Trans. Med. Imaging. **21**(7), 829 (2002)
19. A. Boukhamla, H.F. Merouani, H. Sissaoui, Evol. Syst. Springer Verlag. **7**(3), 197 (2016)
20. L. Zeng, et al. Med. Phys. John Wiley and Sons Ltd. **34**(2), 556 (2007)
21. H. Yoshida et al., Phys. Med. Biol. **48**(22), 3735 (2003)
22. I.B. Starchenko, D.A. Kravchuk, I.A. Kirichenko, Medical Engeneering. **5**, 4 (2017)
23. D.A. Kravchuk. *2019* in*Proceeding of the International Siberian Conference on Control and Communications, SIBCON 2019 - Proceedings. Institute of Electrical and Electronics Engineers Inc.,* 2019
24. I. Starchenko, D. Kravchuk, I. Kirichenko. Biomedical Engeneering. *(NY).* **51**(5), 308 (2018)
25. D.A. Kravchuk, D.V. Orda-Zhigulina, Biomedical Photonics. **8**(3), 11 (2019)
26. D.A. Kravchuk. Nauchnoe Priborostroenie. **29**(4), 119 (2019) (In Russian)
27. D.A. Kravchuk Biomedical Photonics. Russian Photodynamic Association, **7**(3), 36 (2018) (In Russian)
28. D.A. Kravchuk, K.A. Voronina, Appl. Phys. **5**, 93 (2019)

Modeling the Cantilever Type PEG with Proof Mass and Active Pinching by Using the Porous Piezoceramics with Effective Properties

Arkadiy Soloviev, Ivan Parinov, and Alexander Cherpakov

Abstract It is considered an energy harvesting device. The results of numerical simulation of the output parameters of a cantilever type piezoelectric generator (PEG) with a proof mass and an active base are presented. The piezogenerator uses two types of piezoelectric elements: (i) bimorph piezoelectric elements and (ii) cylindrical piezoelectric elements. Piezoelectric elements with effective properties for different porosities of the one type of piezoelectrics were used in the simulation. The results of modal and harmonic calculations of oscillations of a piezoelectric generator are presented. The analysis of output voltage and power on the bimorph and piezoelectric elements of the active base is carried out. Its efficiency was determined when using piezoelements with effective properties of various porosities.

Keywords Energy harvesting · Piezoelectric generator (PEG) · Cantilever type · Bimorph piezoelectric elements · Cylindrical piezoelectric elements · Proof mass · Active pinching · Modeling · Porous piezoceramic · Effective properties

1 Introduction

The tasks of developing energy harvesting devices and ensuring energy supply for transport, the residential sector and the operability of mobile devices are relevant at the present time. They show the need for the development of autonomous power sources that will provide renewable electricity for the devices necessary for life.

A. Soloviev
Department of Theoretical and Applied Mechanics, Don State Technical University, Rostov-on-Don, Russia

A. Soloviev · I. Parinov · A. Cherpakov (✉)
I. I. Vorovich Mathematics, Mechanics and Computer Sciences Institute, Southern Federal University, Rostov-on-Don, Russia
e-mail: alex837@yandex.ru

A. Cherpakov
Department of Information Systems in Construction, Don State Technical University, Rostov-on-Don, Russia

I. A. Parinov et al. (eds.), *Physics and Mechanics of New Materials and Their Applications*, Springer Proceedings in Materials 10,
https://doi.org/10.1007/978-3-030-76481-4_40

Today, the use of piezoelectric generators is actual for several classes of devices, such as: small-sized wireless electronics devices with a long service life, low-power built-in and wireless communication devices (for example, phones, walkie-talkies), household electrical appliances and electronics (for example, an electronic clock), as well as sensors and tracking systems operating in certain climatic zones or places inaccessible to humans, various generators for lighting and alarm systems [1–3].

Batteries are one of the types of electrical energy supply. The batteries in the form of chemically active elements have been actively used for over 100 years and are currently applied in almost all types of mobile devices. The development of the electric battery market is now at its peak. However, the use of electrochemical batteries face difficulties: (i) the electric element, in particular, may be renewable, but its service life is limited; (ii) the leakage currents cause the consuming the battery power even when there is no demand from device; (iii) extreme environmental conditions can lead to battery failure and shutdown of the entire system [4]. Moreover, the need for maintenance and replacement of electrochemical power supplies requires additional costs [5]. From this viewpoint, the type of transmission and storage of energy can be replaced in the near future with a newer one.

In environment, vibration is present in all types of constructions, both natural and artificial. Converting mechanical vibrations into electrical energy is an important issue. One of the types of generators are piezoelectric converters of mechanical energy into electrical one. This type of transducer is called piezoelectric generators (PEGs) . Basic information about PEGs, as well as the problems arising at the stages of development of energy storage devices, were presented in overview papers [6–9], as well as in fundamental monographs [10, 11].

Piezo-generators began to be considered relatively recently, and did not appear on the wide market due to their low power generation capacity. They convert electrical energy from mechanical vibrations based on the direct piezoelectric effect. These generators have been widely studied as an inexpensive and efficient alternative for low level energy harvesting. The shape, location and orientation of the electrodes relative to the crystal axes determine the type of oscillations and their intensity [12].

The use of power generators has been considered in many works. The examples of applications of power generators can be found in several works. For instance, the generation of energy from moving cars for the organization of motion sensors on the road has been considered in [13]. The system for providing wireless sensors for monitoring health has been considered in [14]. The power supplies for unmanned aerial vehicles have been presented in [15, 16].

The known cantilever type PEG, taken as a prototype, which contains a cantilever beam made of elastic material, on which piezoelectric elements are glued on one side (unimorph), or on both sides (bimorph), one end of which is fixed at a pinching, and a proof mass is fixed at the free end [16]. The proof mass converts the input external acceleration into an effective inertial force that deflects the cantilever beam, which causes an increase in mechanical stress in the piezoelectric layer of the cantilever, converting it into additional usful power.

Depending on different applications, various types of PEGs have been created, in which the direct piezoelectric effect is used when excited in the sensitive element as rule by longitudinal (d_{33}) [17–20] or bending (d_{31}) [21–25] oscillations.

The problem of evaluating the efficiency of the used and developed piezoelectric materials can be considered on an example of works [26, 27]. They present methods for measuring their output characteristics, as well as the parameters of piezomaterials with new electric-physical and mechanical properties.

In several works of the authors, experimental and theoretical approaches to the study of PEGs have been presented [28–34]. The effectiveness of these approaches is shown by close results od comparison with experimental ones.

The application of modeling taking into account effective piezomodules can clarify the output technical parameters of power generation devices. Approaches to analytical and numerical studies of mixed two-phase piezo-composites are described in [35, 36]. They revealed a significant dependence of the values of effective material properties on the size and number of pores, their disposition in respect to inclusions and the type of connectivity. The method of effective modules in combination with the finite element solution of homogenization problems and modeling of representative volumes makes it possible to fully take into account the internal structure of the piezocomposite, types of connectivity, as well as the shapes and sizes of inclusions or pores [37, 38].

2 Research Method

2.1 Continuous Formulation of the Problem

The main purpose of this work is to study the PEG output parameters when using piezoelectric ceramics of a certain type with various effective moduli.

A piezoelectric device for generating and converting mechanical energy into electrical energy is a composite elastic and electroelastic body. Certain constituent parts of the structure, and the body as a whole, can perform small amplitude oscillations in a moving coordinate system. The simplest form of organizing the movement of a construction is its vibration along a straight path. Optimal sources of vibration can be supplied through two points of the structure, namely the pinching of the PEG and the proof mass on the substrate plate of the construction. In this case, additional fastening conditions can be determined, and in the design model, the calculated load on these elements can be additionally described. Rectilinear movement in the direction of the y-axis of the construction can be specified by the law $y(t)$ or is caused by the action of the force $F(t)$. The construction of a mathematical model of the PEG device can be presented on the basis of the initial-boundary value problem of the linear theory of electroelasticity [39].

In this work, we use the linear equations of the theory of elasticity and electroelasticity, taking into account the energy dissipation adopted in the ANSYS software

[39], as well as the equations of motion of liquid and gaseous media in the acoustic approximation [40].

For a piezoelectric medium, the mathematical formulation of the problem is described in the form of the following equations:

$$\rho\ddot{u}_i + \alpha\rho\dot{u}_i - \sigma_{ijj} = f_i; \quad D_{i,i} = 0; \tag{1}$$

$$\sigma_{ij} = c_{ijkl}(\varepsilon_{kl} + \beta\dot{\varepsilon}_{kl}) - e_{ijk}E_k; \quad D_i + \varsigma_d\dot{D}_i = e_{ikl}(\varepsilon_{kl} + \varsigma_d\dot{\varepsilon}_{kl}) + \ni_{ik}\, E_k; \tag{2}$$

$$\varepsilon_{kl} = (u_{kl} + u_{lk})/2; \quad E_k = \varphi_k, \tag{3}$$

where ρ is the density of the material; u_i are the components of the vector-function of displacements; σ_{ij} are the components of the tensor of mechanical stresses; f_i are the components of the density vector of mass forces; $D_{i,i}$ are the components of the electric induction vector; c_{ijkl} are the components of the fourth rank tensor of elastic moduli; e_{ikl} are the components of the third rank tensor of piezomodules; ε_{kl} are the strain tensor components; E_k are the components of the vector of the electric field strength; φ_k is the electric potential; $\ni_{ik}$ are the components of the second rank tensor of dielectric permittivity; α, β, ς_d are non-negative damping factors (in ANSYS, $\varsigma_d = 0$).

For an elastic medium, the mathematical formulation of the problem is described in the form:

$$\rho\ddot{u}_i + \alpha\rho\dot{u}_i - \sigma_{ijj} = f_i; \tag{4}$$

$$\sigma_{ij} = c_{ijkl}(\varepsilon_{kl} + \beta\dot{\varepsilon}_{kl}); \tag{5}$$

$$\varepsilon_{kl} = (u_{kl} + u_{lk})/2; \tag{6}$$

To solve the problem, it is required to set additional boundary conditions.

To solve dynamic problems of acoustoelectroelasticity, we will use the FEM in the classical Lagrangian formulation. An example of the implementation of studies and calculations of the finite element method (FEM) for piezoelectrics, as well as composite solids have been presented in [41].

The finite element formulation of the problem can be presented on the example of work [39]. In the transition from the continuous formulation to the FE, a coordinated discretization of geometric regions is performed, namely a partitioning into finite elements (triangulation) with a certain set of geometric points being nodes, in the result of which problem (1)–(6) can be represented as

$$u(x,t) = N_u^T(x)U(t); \varphi(x,t) = N_\varphi^T(x)\Phi(t); \psi(x,t) = N_\psi^T(x)\Psi(t); \tag{7}$$

where x is the vector of spatial coordinates; t is the time; N_u^T is the matrix of form functions for the displacement field: $u = (u_1, u_2, u_3)$; N_φ^T, N_ψ^T are the row vectors of the shape functions for the fields of the electric potential φ and the velocity potential in the acoustic mediumψ; $U(t)$, $\Phi(t)$, $\Psi(t)$ are the global vectors of the corresponding nodal degrees of freedom.

An approximation of the FEM (7) for generalized statements of dynamic problems (1)–(6), including boundary conditions, is reduced to a system of ordinary differential equations with respect to the nodal unknowns $a = [U, \Phi, \Psi]^T$:

$$M\ddot{a} + C\dot{a} + Ka = F$$

where the global matrices M, C, K for elastic medium are, respectively, the matrices of mass, damping, stiffness.

3 Results and Discussion

3.1 Description of the Model

PEG modeling is carried out in the finite element software ANSYS. A model of a cantilever-type configuration PEG is considered. At the pinching of the PEG console there are cylindrical-shape piezoelectric transducers. A piezoelectric cantilever-type converter of mechanical energy into electrical one contains a cantilever beam made of elastic material, on which piezoelectric elements are attached from both sides (bimorph). One end of the cantilever beam is fixed to the pinching. A proof mass is located at the free end. Four piezoelectric elements are additionally installed at the pinching, two at the top and two at the bottom in respect to the beam, having opposite directions of the polarization vector. The planes of their electrodes are pressed by means of the base elements to the conductive layers of thin elastic pads metallized on one side.

Thin symmetrical piezoelectric elements (PEs) are polarized in thicknessand glued to the pinching of console. The geometric dimensions of the PEG are shown in Fig. 1b. The dimension characteristics of the PEG elements are presented in Table 1, the properties of the elements are shown in Table 2. Table 3 shows the material properties of the PE piezoplates and piezocylinders from porous ceramics with the dimension characteristics presented in Table 1. The electrical scheme of the PEG connection with an active load is shown in Fig. 1. The block diagram of the PEG construction is shown in Fig. 2.

2–substrate; 3–proof mass; 4–place of PEG fixing (B is the movable pinching); 5–piezoelectric cylinders.

The piezoceramic material is presented in [42, 43]. An analogue of ceramics with such properties is the piezoceramic material PZT-4. The results of calculating the effective moduli of three-phase piezo-composites with inclusions and pores are

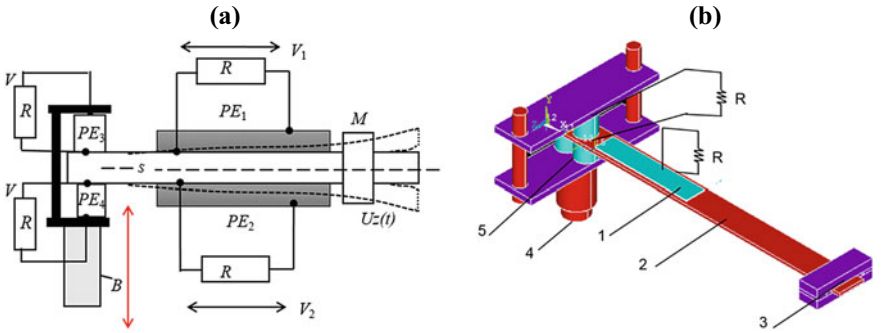

Fig. 1 **a** Electric scheme of PEG under active load; **b** location of electrical load on model

Table 1 Dimension characteristics of PEG elements

Piezoelements			Piezo cylinder	
l_p, mm	b_p, mm	h_p, mm	R, mm	H, mm
50	10	0.45	10	10
Substrate			Connected mass	
l, mm	b, mm	h, mm	M, g	l_m, mm
160	13.2	1.5	17.6	146.5

Table 2 Mechanical properties of the structural materials

No	Element of PEG	Material	ρ, kg/m^3	$E \times 10^{11}$, Pa	ν
1	Pinching	Duralumin	2800	0.33	0.33
2	Substrate	Duralumin	2800	0.33	0.33
3	Connected mass	Steel	7700	2.1	0.33

Table 3 Material properties of the porous composite

% of porosity	0	10	20	30	40	50	60	70	80
ρ, kg/m^3	7500	6750	6000	5250	4500	3750	3000	2250	1500
$c_{11}^{E\,\mathrm{eff}}$, 10^{10}, N/m^2	13.9	11.56	9.25	6.85	5.05	3.34	2.07	1.26	0.68
$c_{12}^{E\,\mathrm{eff}}$, 10^{10}, N/m^2	7.78	6.15	4.66	3.14	2.10	1.16	0.62	0.28	0.13
$c_{13}^{E\,\mathrm{eff}}$, 10^{10}, N/m^2	7.43	5.82	4.25	2.82	1.87	1.06	0.52	0.24	0.1
$c_{33}^{E\,\mathrm{eff}}$, 10^{10}, N/m^2	11.5	9.53	7.23	5.42	3.91	2.72	1.63	0.91	0.47
$c_{44}^{E\,\mathrm{eff}}$, 10^{10}, N/m^2	2.56	2.23	1.83	1.44	1.10	0.74	0.44	0.23	0.1
e_{33}^{eff}, C/m^2	15.1	13.38	11.37	9.59	7.68	5.93	3.93	2.30	1.25
e_{31}^{eff}, C/m^2	−5.2	−4.23	−3.14	−2.07	−1.32	−0.75	−0.43	−0.21	−0.1
e_{15}^{eff}, C/m^2	12.7	10.96	8.96	6.91	5.00	3.30	1.95	1.00	0.44
$\kappa_{11}^{S\,\mathrm{eff}}/\varepsilon_0$	730	663	582	509	439	349	263	191	122
$\kappa_{33}^{S\,\mathrm{eff}}/\varepsilon_0$	635	567	492	413	345	270	199	130	75

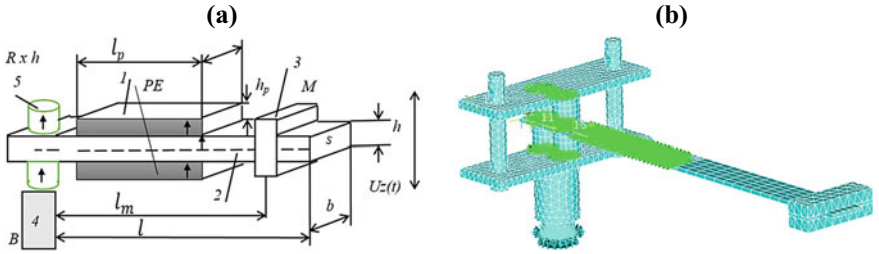

Fig. 2 Structure **a** and FE **b** scheme of PEG with proof mass: 1–piezoelectric element

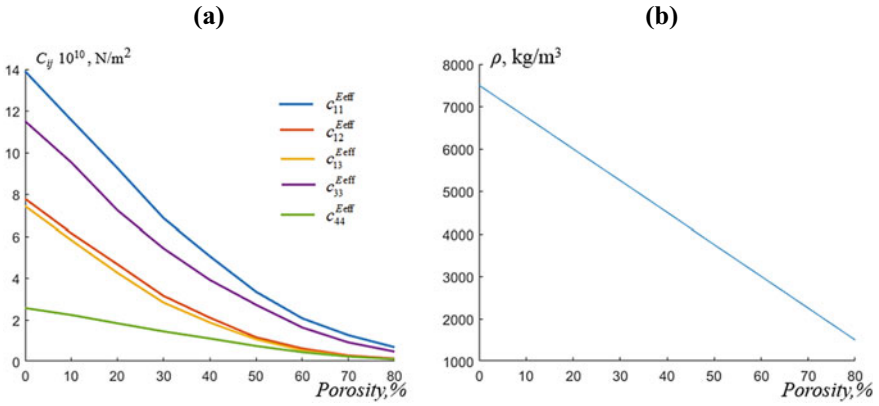

Fig. 3 Dependence of elastic stiffness moduli, and density of piezoelectric ceramics on different values of porosity

shown in Table 3 [43]. The calculations were carried out for representative volumes with a 3–0 connectivity type without additional restrictions on the location of the granules. Ceramic PZT-4 was chosen as the main material (first column of Table 3). For various percentages of porosity from 10 to 80% with a step of 10%, calculations of the effective properties of a porous composite material are given (see Table 3).

Figure 3 shows the dependencies of the effective elastic stiffness moduli $c_{\alpha\beta}^{E}$ of porosity. Moreover, Fig. 3b shows the dependence of piezoceramic material density on the porosity. This material for different values of porosity was used in the following calculations.

3.2 FE Modeling

The first part of the numerical experiment was to find the natural frequencies and natural forms of the PEG. The simulation was carried out with an active load of piezoelectric elements, $R = 1000\ \Omega$. The fixed mass was located at a distance equal

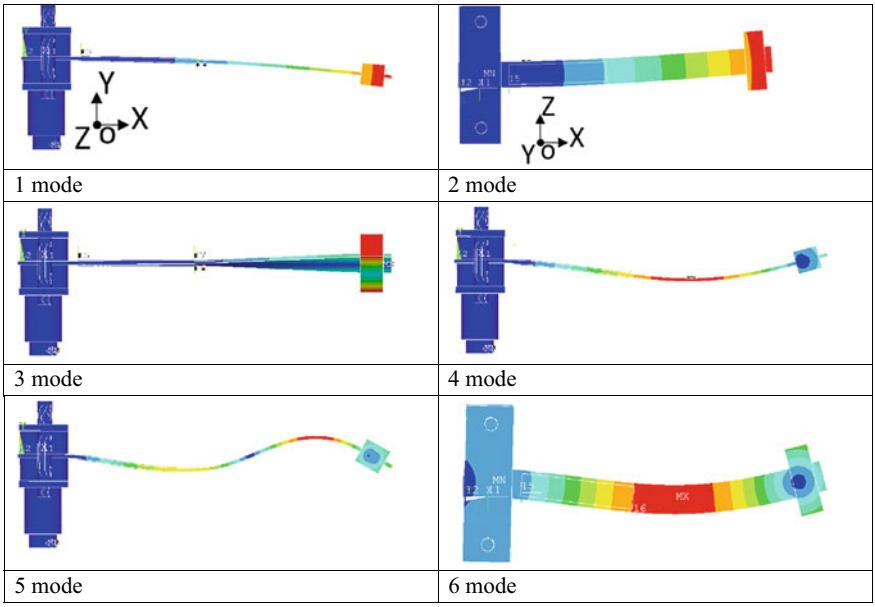

Fig. 4 Eigen-modes of PEG

to 146.5 mm. Figure 4 shows the first 6 modes of natural vibrations calculated in the ANSYS software. A model with 0% porosity was considered as a basic model (for comparison). The first vibration mode had a frequency of 37.8 Hz, and a flexural mode in respect to the x-axis. The first 4 vibration modes were in the range up to 382.5 Hz. Vibration modes 5 and 6 had frequencies above 1000 Hz, respectively, 1058.7 and 1318.7 Hz. The most effective modes can be the 1st ($\omega_1 = 37.8$ Hz), 4th ($\omega_4 = 382.5$ Hz) and 5th ($\omega_5 = 1058.7$ Hz) vibration modes due to bending modes in respect to the x-axis axis. In the Oxy-plane, at the lowest stiffness of the PEG cantilever, they form the 1st, 2nd and 3rd bending vibration modes. The 2nd and 6th vibration modes are flexural ones in respect to the x-axis in the plane of the highest cantilever rigidity. They form in this plane the 1st and 2nd vibration modes, respectively. The third natural mode of PEG vibration is torsional one in respect to the x-axis.

3.3 Research Results

The calculation results of harmonic oscillations in the ANSYS software are presented below. The calculations took into account the magnitude of the acceleration applied to the entire structure in the frequency range from 1 to 600 Hz, equal to 0.01 m/s^2. Table 4 shows the results of calculations of the dependence of the natural frequencies of the

Table 4 Dependence of the natural frequencies of the generator on the porosity of the piezoelectric elements

No *i*-th mode	Porosity of ceramic, %								
	0	10	20	30	40	50	60	70	80
	ω_i (porosity)								
Mode 1	37.8	37.2	36.5	35.7	34.9	33.9	32.9	32.1	31.4
Mode 2	136.3	134.4	131.8	128.8	125.8	122.1	117.7	112.7	104.9
Mode 3	295.4	294.3	292.9	291.1	289.4	287.4	285.0	283.0	280.7
Mode 4	382.5	382.1	380.9	378.9	376.9	374.2	371.1	368.2	364.6
Mode 5	1058.7	1063.1	1066.3	1068.2	1070.4	1071.3	1071.4	1072.4	1071.2
Mode 6	1318.7	1321.3	1319.7	1315.7	1308.6	1294.6	1267.5	1223.6	1152.2

generator on the porosity of the piezoelectric elements. The graphical dependence of the absolute and relative values of the natural frequencies of various vibration modes is shown in Fig. 5a, b. Analysis shows that the frequency of the first vibration mode, depending on the porosity, decreases at its value of 80% by more than 15%. The frequency of the second vibration mode drops to 23% at a porosity of 80%. The frequencies of the third and subsequent vibration modes vary within 5%. The most effective vibration mode is the first flexural vibration frequency.

Figures 6 and 7 show the results for the output voltage *U versus* the frequency of harmonic excitation of the construction. The results in Figs. 6 and 7 correspond to

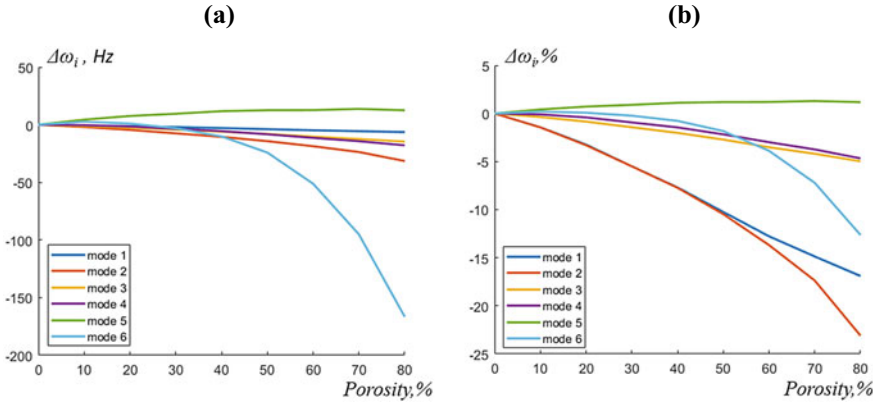

Fig. 5 Relative and absolute dependence of the natural frequencies of the generator on the porosity of the bimorph and piezocylinders

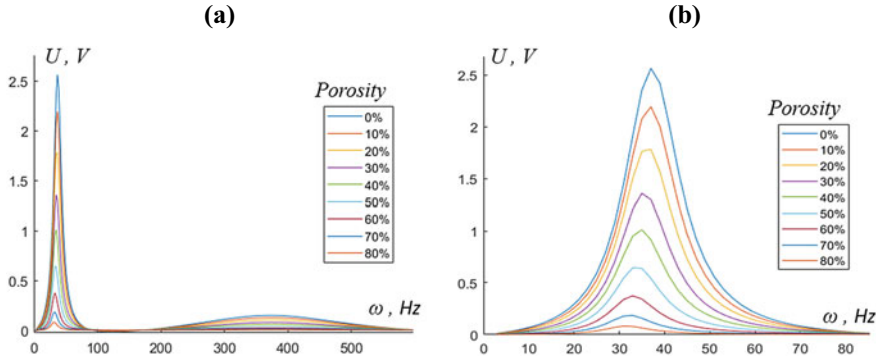

Fig. 6 Output values of voltage on the bimorph plates located on the PEG cantilever substrate *vs* the frequency of harmonic excitation: **a** frequency range from 0 to 600 Hz; **b** frequency range from 0 to 80 Hz

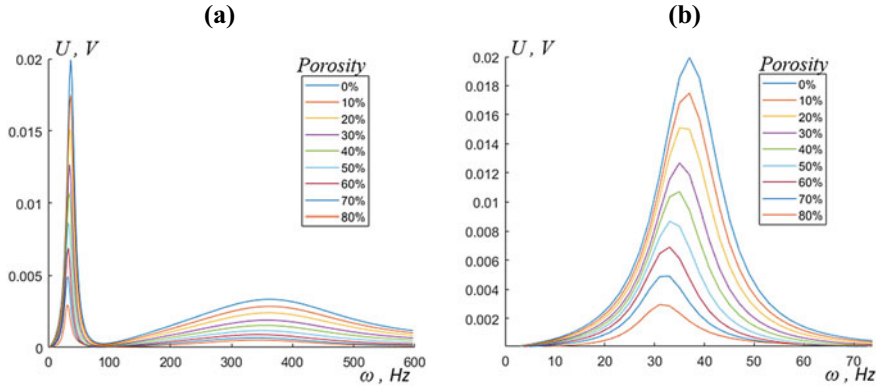

Fig. 7 Output values of the voltage on the plates of the PEG piezocylinders from the frequency of harmonic excitation: **a** frequency range from 0 to 600 Hz; **b** frequency range from 0 to 70 Hz

the values on the bimorph plates, located on the PEG cantilever substrate, and on the PEG piezocylinders, respectively. The analysis shows that the first vibration mode is the most productive for all parameters of ceramic porosity. The voltage amplitude at resonance for 0% porosity reaches 2.55 V at the first resonance frequency of 37 Hz. With a porosity of 80%, the voltage amplitude at the first resonance frequency of 31 Hz is 0.0822 V. That is 31 times less than with a porosity of 0%. The shift of the oscillation frequency of the generator for the first mode of bending vibrations from 37 to 31 Hz is recorded. The calculated output power at 1st resonance for the bimorph with a porosity of 0% was 6500 μW, and with a porosity of 80%, it was 6.75 μW. This reduces the effective output power by more than 950 times. At the same time, for piezoelectric elements of cylindrical shape located at the pinching of the cantilever, the output voltage at 0% porosity was 0.0199 V and 0.0029 V at

80% porosity. The difference between them was equal to 6.8 times. In this case, the output power for a porosity of 0% was 0.39 μW and with a porosity of 80%, it was 0.00841 μW, respectively. The ratio of these values was equal to 47 times.

4 Conclusion

Modeling of oscillations of a cantilever-type PEG with active pinching, which had piezoelements with effective properties of piezoelectric ceramics of a certain porosity, has been carried out. Modeling was carried out in the FE ANSYS software. During the simulation, the porosity of the piezoelements varied from 0 to 80%. Modal and harmonic analysis of the computations was carried out. Six vibration modes were calculated. The most effective modes were 1 and 3, which had bending modes of vibration in the plane of the least stiffness. The analysis showed that when comparing the output characteristics of the ceramic material with a porosity of 0% and 80%, the output voltage of the structure decreased by 31 times, while the output power at a load of 1000 Ω decreased by more than 950 times. Piezoelectric elements of cylindrical configuration at the pinching of PEG were more effective in comparison. When comparing the output characteristics for these ceramic constructions, in the construction with a porosity of 0% and 80%, the voltage changed by 6.8 times, while the power changed by 47 times, respectively.

Acknowledgements The study was financially supported by the Russian Science Foundation (Grant No. 21-19-00423).

References

1. Y. Tianchen, Ya. Jian, S. Ruigang, L. Xiaowei, Smart Mater. Struct. **23** (2014)
2. M. Grudén et al. IET wirel. Sens. Syst. **4**(2) (2014)
3. F.K. Shaikh, Sh. Zeadally, Renew. Sustain. Rev. **55** (2016)
4. D.E. Tiliute, Electr. Electr. Eng. **76**(4) (2007)
5. R. Caliò, U.B. Rongala, D. Camboni, et al. Piezoelectric energy harvesting solutions. Sensors **14** (2014)
6. A. Erturk, D.J. Inman, *Piezoelectric Energy Harvesting* (Wiley, Hoboken, 2011)
7. S.R. Anton, Multifunctional Piezoelectric Energy Harvesting Concepts. Ph.D. thesis, Virginia Polytechnic Institute and State University. Blackburn, Virginia, USA, p. 190 (2011)
8. A. Badel, D. Guyomar, E. Lefeuvre, C. Richard, J. Intelligent Material Syst. Structures **16**(10) (2005)
9. A.V.Cherpakov, V.A.Chebanenko, I.A. Parinov, S.-H. Chang, M. A. Jani, in *Proceedings of the International symposium Physics of Lead-free Piezoactive and Relative Materials* (Analysis of current state and prospects of development), LFPM-2016, Russia, vol. 2 (2016)
10. D. Guyomar, M. Lallart, Micromachines **2**(2) (2011)

11. S. Shevtsov, A.N. Soloviev, I.A. Parinov, A.V. Cherpakov, V.A. Chebanenko, *Piezoelectric Actuators and Generators for Energy Harvesting–Research and Development.* Series: Innovation and Discovery in Russian Science and Engineering (Springer Cham, Switzerland, 2018), p. 182
12. K.A. Cook-Chennault, N. Thambi, A.M. Sastry, Smart Mater. Struct. **17**, 43001 (2008)
13. G. Anastasi, M. Conti, M. Di Francesco, A. Passarella, Ad. Hoc. Networks. 7, 537 (2009)
14. M. Zhy, S. Edkins, Proc. Eng. **25** (2011).
15. A. Erturk, J.M. Renno, D.J. Inman, J. Intell. Mat. Syst. Struct. **20**, 529 (2009)
16. A. Abdelkefi, M. Ghommem, Theoret. Appl. Mech. Lett. **3**, 052004 (2013)
17. S. Shevtsov, V. Akopyan, E. Rozhkov, V. Chebanenko, C.-C. Yang, C.-Y. Jenny Lee, C.-X. Kuo, in *Advanced Materials—Manufacturing, Physics, Mechanics and Applications*, ed. by I. A. Parinov, S.-H. Chang, V.Yu. Topolov, vol. 175 (Springer, Heidelberg, New York, Dordrecht, London, 2016), p. 534
18. A.N. Soloviev, V.A. Chebanenko, I.A. Parinov, in *Analysis and Modelling of Advanced Structures and Smart Systems***.** Series: Advanced Structured Materials, ed. by H. Altenbach, E. Carrera, G. Kulikov (Springer Nature, Singapore, 2018), p. 227
19. S. Zhao, A. Erturk, Sens. Actuators, A Phys. **214**, 58 (2014)
20. J. Wang, Z. Shi, Z. Han, J. Intell. Mater. Syst. Struct. **24**(13), 1626 (2013)
21. A.N.Soloviev, I.A. Parinov, A.V.Cherpakov, V.A.Chebanenko, E.V.Rozhkov, L.V.Duong, in *Advances in Structural Integrity*. Springer—Proceedings of SICE-2016, Series: Mechanical Engineering, ed. by R.V. Prakash, V. Jayaram, A. Saxena, (2018), p. 291
22. V.A. Akopyan, Yu. N. Zakharov, I.A. Parinov, E.V. Rozhkov, S.N. Shevtsov, V.A. Chebanenko, in *Nano- and Piezoelectric Technologies, Materials and Devices*, ed. by I.A. Parinov (Nova Science Publishers, New York, 2013), p. 261
23. V.A. Akopyan, I.A. Parinov, Yu.N. Zakharov, V.A. Chebanenko, E.V. Rozhkov, in *Advanced Materials—Studies and Applications*, ed. by I.A. Parinov, S.H. Chang, S. Theerakulpisut (Nova Science Publishers: New York, 2015), p. 417
24. A. Erturk, D. J. Inman, Smart Mater. Struct. **18**(2), 025009 (2009)
25. N.E. Dutoit, B.L. Wardle, S.G. Kim, Integr. Ferroelectr. **71**(1) (2005)
26. A.A. Gusev, E.G. Avvakumov, V.P. Isupov, L.A. Reznichenko, I.A. Verbenko, A.I. Miller, A.V. Cherpakov, in *Piezoelectric Materials and Devices*, ed. by I.A. Parinov (Nova Science Publishers, New York, 2011), p. 189
27. S. Khasbulatov, A. Cherpakov, I. Parinov, et al. J. Adv. Dielectr. 10(4), 2050012 (2020)
28. A.N. Soloviev, I.A. Parinov, A.V. Cherpakov, V.A. Chebanenko, E.V. Rozhkov, Mater. Phys. Mech. **37**(2), 168 (2018)
29. A.N. Soloviev, I.A. Parinov, A.V. Cherpakov, Yu.A. Chaika, E.V. Rozhkov, Mater. Phys. Mech. **37**(2), 192 (2018)
30. T.V. Polyakova, A.V. Cherpakov, I.A. Parinov, M.N. Grigoryan, IOP Conf. Ser.: Mater. Sci. Eng. **913**(2), 022014 (2020)
31. V.A. Chebanenko, I.V. Zhilyaev, A.N. Soloviev, A.V. Cherpakov, I.A. Parinov, J. Adv. Dielectr. **10**(1–2), 2060016 (2020)
32. A.N. Soloviev, V.A. Chebanenko, I.V. Zhilyaev, A.V. Cherpakov, I.A. Parinov, Mater. Phys. Mech. **44**(1), 94 (2020)
33. A.V. Cherpakov, Y.A. Kokareva, IOP Conf. Ser.: Mater. Sci. Eng. **698**(6), 066020 (2019)
34. A.V. Cherpakov, I.A. Parinov, A.N. Soloviev, E.V. Rozhkov, in *Advanced Materials—Proceedings of the International Conference on "Physics and Mechanics of New Materials and Their Applications", PHENMA 2018*, Springer Proceedings in Physics, ed. by I.A. Parinov, S.-H. Chang, Y.-H. Kim, vol. 224 (Springer Nature, Cham, Switzerland, 2019), p. 593
35. C.R. Bowen, H. Kara, Mater. Chem. Phys. **75**, 45 (2002)
36. M.L. Dunn, M. Taya, J. Am. Ceram. Soc. **76**, 1697 (1993)
37. S. Iyer, T.A. Venkatesh, Int. J. Solid. Struct. **51** (2014)
38. G. Iovane, A.V. Nasedkin, Mater. Phys. Mech. **42** (2019)
39. A.V. Nasedkin, *Finite-element Modeling of Piezoelectric Generators from Highly Porous Piezoceramics.* Kiev, IGM NAN Ukraine (2011)

40. V.A. Krasilnikov, V.V. Krylov. *Introduction to Physical Acoustics.* (Science, Moscow, 1984), p. 403
41. A.V. Belokon', A.V. Nasedkin, A.N. Solov'yev, J Appl. Math. and Mech. **66**(3) (2002)
42. A.V. Nasedkin, P.A. Oganesyan, A.N. Soloviev, ZAMM Zeitschrift fur Angewandte Mathematik und Mechanik **101**(3), e202000129 (2021)
43. A.V. Nasedkin, in *Advanced Materials—Studies and Applications*, ed. by I.A. Parinov, S.H. Chang, S. Theerakulpisut (Nova Science Publishers, New York, 2015)

A Scissor Mechanism Shear Mode Piezoelectric Energy Harvester for Windmill

Tejkaran Narolia, Vijay K. Gupta, and Ivan A. Parinov

Abstract In this work, a shear mode excitation of the piezoelectric material has been suggested to harvest wind energy. A scissor mechanism with a scotch-yoke mechanism is used to convert the rotary motion of the wind turbine to linear vibration of the PZT patches. The input spring force is modified through a scissor mechanism. To calculate the average electric power, an analytical model has been formulated and simulated. Through analytical simulation, various parameters such as stiffness of springs, wind velocity, scissor angle, the thickness of the PZT patches, and length of the PZT patches are analyzed with the generated power. Maximum power of 242.4 W is calculated at a wind speed of 9 m/s from the harvester.

Keywords Energy harvesting · Shear mode · Piezoelectric material · Scissor mechanism · Windmill

1 Introduction

Day per day consumption of conventional sources of energy and emission of harmful elements affects the humans and other creatures' life, motivate scientists to an alternative. The piezoelectric material can be the best alternative to replace them by harvesting the energy from the wind or water. Most of the devices run on batteries and consume low power, such as sensor nodes, actuators, wireless communication systems, structural health monitoring systems etc. [1]. Frequently replacement of batteries in these devices becomes a tough and tedious task [2]. Continuous improvement in the design and working efficiency of the piezo-based energy harvester or micro power generator leads the application to supply the power to a small sensor and actuator uninterruptedly by harnessing the waste ambient energy.

T. Narolia (✉) · V. K. Gupta
Department of Mechanical Engineering, PDPM Indian Institute of Information Technology Design and Manufacturing, Jabalpur, India

I. A. Parinov
Southern Federal University, Rostov-on-Don, Russia

I. A. Parinov et al. (eds.), *Physics and Mechanics of New Materials and Their Applications*, Springer Proceedings in Materials 10,
https://doi.org/10.1007/978-3-030-76481-4_41

Conversion of the kinetic energy of the ambient wind or water flow into electricity through a piezoelectric medium is one of the best ways. Different modes of piezoelectric energy harvesters have been designed and developed by researchers having a simple design, low cost, easy fabrication, and high density of energy [3]. Bending (d_{31}), compression (d_{33}), and shear (d_{15}) are the basic modes of piezoelectric material that have been used to harvest the energy. In d_{31} mode, the PZT patch is mount on an elastic substrate and strained in a longitudinal direction by a force at the tip of the substrate with an electrode in the poling direction while in d_{33} mode, direct compressive or tensile forces are applied on the PZT material [4]. A shear elastic deformation has been used to harvest the energy in shear mode [5]. Nechibvute et al. [6] suggested and fabricated an energy harvester with an unimorph PZT cantilever. An analytical model was formulated and verified with the experimental results. At the resonance frequency, approximate power of 24.5 μW was calculated experimentally. A cantilevered (galloping type) PZT energy harvester was developed by Sirohi et al. [7] for wind energy harvesting through galloping action. The harvester consists of a bimorph piezo-sheet mounted on a substrate. Experimentally and analytically it was observed that the maximum power of 1.14 mW was calculated from the prototype at a wind velocity of 4.69 m/s by galloping vibration. Mineto et al. [8] proposed a transverse mode piezoelectric generator using the Euler-Bernoulli beam theory. Maximum power of 6.5 mW has been harvested from the harvester. Khameneifar et al. [9] presented an energy harvester based on the rotary. Unimorph PZT cantilevers have been used and excited by the gravity force of tip mass during rotation to strained the piezoelectric material. At an angular speed of 138 rad/s, the maximum amount of power of 6.4 mW was recorded. Xie et al. [10] presented rotary type energy harvester consists of inner and outer annular rings. Piezoelectric patches are mounted inside of the stationary ring and every piezo-patch magnet is fitted on the PZT-patches while on the outer periphery of the inner ring, the magnetic sinusoidal repulsive force produces during the rotation. At a speed of 30 m/s of the inner ring, the maximum power of 5274.8 w is calculated from the numerical simulation. Wind energy from the duct of heating, ventilation pipe, and air conditioning tube was studied by Weinstein et al. [11] with the help of cantilever piezoelectric beam harvester. The blowing air yielding the vibration in the beam and approximated 3 mW power is yielded with 5 m/s speed of air. Zhang et al. [12] proposed a piezo energy generator based on rotary motion. A high deflection in the piezoelectric (PVDF) has been induced by the impact of the turntable. Simulation results showed that the power of 2566.4 μW was obtained at a wind speed of 14 m/s. Tao et al. [13] designed and developed a wind energy harvester extracting the wind energy and converting it into electricity by the piezoelectric material. Simulating the numerical model, it has been found that power up to 150 W is estimated at a wind speed of 7.2 m/s. A parallel plate piezoelectric rotary energy harvester was presented by Narolia et al. [14] to harvest the energy from the rotary motion. A mathematical model has been formulated it was observed that the power of 1.3572 W recorded from the simulation. An octo generator was suggested by Viet et al. [15] to harvest the wind power through piezoelectric material; an analytical model allowed one to calculate a power of 5 kW for the device at a tidal speed of 1.75 m/s in ocean. Narolia et al. [16] designed and

developed a rotary-type energy harvester to harvest the kinetic energy in the form of rotation. Finite element and experiment results were validated analytically and found that the harvester is enabled to power a small power sensor. Narolia et al. [17] proposed an attractive magnetic force-based energy harvester. The magnitude of the magnetic force was magnified through the leverage system at the piezo-patches to strain them and an estimated power of 31.1432 W was found from the simulation. An experimental study showed that the shear mode (d_{15}) can generate power of a high amount as compare to d_{31} mode and d_{33} mode [18]. Wang and Liu [5] developed a shear mode of piezo energy generator based on the fluctuating pressure water. It was observed the power of 0.45nW with the help of an experiment at pressure frequency of 45Hz with 20.8kPa amplitude. A shear mode (d_{15}) cantilever type piezo-energy harvester was presented by Zhou et al. [19] to harvest the energy. It was estimated an approximate 16 mW power at 3 MΩ external loads. Zheng et al. [20] presented a bimorph piezo energy harvester that worked on shear mode (d_{15}) using Timoshenko beam theory. An analytical model was developed and showed that the results are agreed with the FEM calculation. Based on the Timoshenko beam theory, energy harvester with shear mode (d_{15}) was presented by Malakooti and Sodano [21]. A cantilever PZT sandwich beam was excited by the base vibration to induce shear strain; it was found that energy harvested at d_{15} mode was approximately 50 % more than the energy harvested at d_{33} mode. Narolia et al. [22] designed a rotary plate shear mode piezoelectric energy harvester. A numerical model is formulated to find out the power and validate with FEM results. The maximum power of 358.44 W was calculated at 600 rpm with sizes of 200 mm × 200 mm × 50 mm and 158 piezoelectric patches. Data of [23] showed that the magnitude of d_{15} is greater than the values of d_{31} and $d_{33.}$ Hence, we can apply the shear mode of excitations of piezoelectric material to capture the power with the rotary motion with a simple structure design.

In this chapter, a new design of shear (d_{15}) mode piezoelectric energy harvester is proposed to generate the energy from wind. Angular motion of the input shaft of the wind turbine is converted into reciprocating motion of the sliding rods to exert a magnified force on the piezo patches through scissor mechanism. A mathematical model has been formulated to obtain the power, and effect of various designed parameters on the power are investigated to prove the simplicity of the harvester.

2 Design and Modeling of Harvester

The working principle of the proposed generator is illustrated in Fig. 1. The major parts of the device are a windmill, scotch-yoke mechanism, four piezoelectric patches with two scissor jacks, and two springs (spring constant k_s). The rotary motion of the input shaft is converted into reciprocating motion through a scotch-yoke mechanism (Fig. 2) [24]. A sliding pair of slotted rods is fixed to the frame and cylinder is attached to the wheel stating a sliding motion normal to the shaft axis. Angular motion of the shaft (ω, rad/s) displaced the end of the slotted rod from the starting point in time t on distance $Z_s = Y\sin\omega t$.

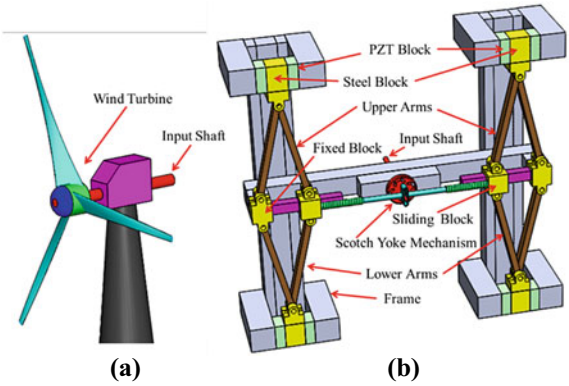

Fig. 1 **a** Simple configuration of wind turbine and **b** scissor mechanism energy harvester

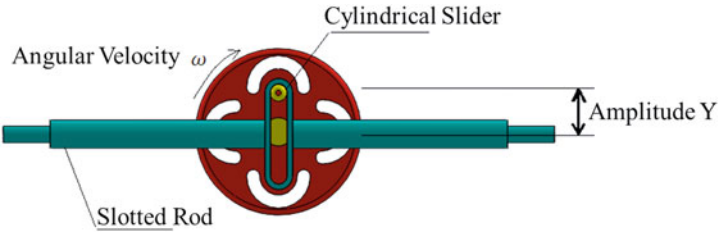

Fig. 2 Schematic view cotch-yoke mechanism

The mechanism to increasing the input force, shown in Fig. 3a, consists of two lower and two upper arms of the same length. Upper arms are hinged to stationary and moving blocks separately to make turning pair while other ends of arms hinged together with steel block to form self-turning pair. The material and cross-section of

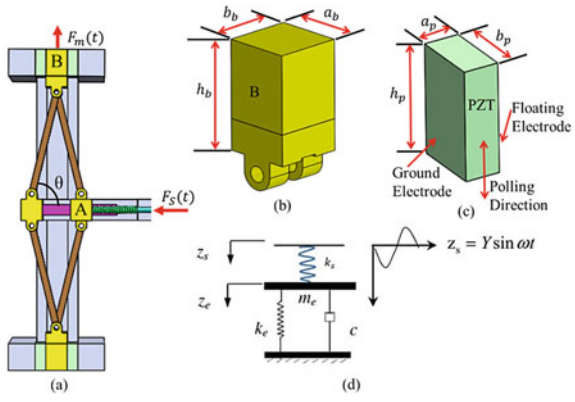

Fig. 3 **a** Scissor jack mechanism; **b** the equivalent mass-spring-damped model

the arms are steel and square with side $s = 10$mm, respectively. The length of arms is assumed equal to $l = 150$mm.

A block of steel of dimensions $a_b b_b h_b$ with shear modulus $G_{s,}$ is fixed on both sides by piezoelectric patches of dimensions $a_p b_p h_p$ and shear modulus G_p. Similar configuration used for lower arms. The rotation of the input shaft exerts a force $F_s(t)$ at a point A to scissor mechanism via springs, which increases by tanθ (θ = scissor mechanism angle) times at the point B on the PZT bar. The shear force on the piezoelectric bar induces the strain and then the electric power.

In analytical model of the harvester, we consider that the arms of the mechanism are made of rigid material having no strain and assume a single-degree-spring-mass-damped system, depicted in Fig. 3b [25, 26].

The equivalent mass of the sliding block can be calculated as

$$m_e = \left[\left(2hd + \frac{\pi}{4}d^2\right)b_s o + l_s(b_s o h_s o - b_s i h_s i)\right]\rho_s, \tag{1}$$

where $h = 20$mm, is the height and $d = 20$mm, is the diameter of an extruded portion of sliding block $l_s = 50$mm, $b_{so} = 40$ mm and $h_{so} = 40$mm, is the length, width, and height of the sliding block, respectively;$b_{si} = 20$mm, $h_{si} = 20$mm, is the width and height of the slot inside the sliding block and ρ_s is the material density of the sliding block.

The increased force at point B induces the shear deformation into the block and PZT patches; the spring stiffness, k_e, caused by the block and PZT patch, shown in Fig. 3b, can be calculated as [27]

$$k_e = \frac{k_b k_p}{(k_b + k_p)}, k_b = \frac{G_s h_b b_b}{(tan\theta^2 a_b)}, k_p = \frac{G_p h_p b_p}{(tan\theta^2 a_p)} \tag{2}$$

where , G_p, k_p, G_s, k_b are the shear moduli and spring constants of the piezoelectric patch and steel block, respectively.

The equivalent damping coefficient, c, can be determined as a sum of electrical and mechanical damping coefficients, in accordance with Fig. 3b:

$$c = c_e + c_m. \tag{3}$$

The electrical damping coefficient, c_e, due to conversion of work into electricity [28], can be given as [29]:

$$c_e = \tan\theta^2 d_{15}^2 k_e^2 / \left(\pi^2 c_v f\right), \tag{4}$$

where, d_{15} is the piezoelectric strain coefficient; c_v is the electric capacitance of the piezoelectric patch; f is the natural frequency of the system.

With electrical damping, there is viscous air friction on the steel block, when the vibration takes place, and inherently internal structure damping force [30], then a

mechanical damping coefficient can be expressed as

$$c_m = 2\zeta\sqrt{k_b m_e}, \tag{5}$$

where ζ is the ratio of damping.

After calculation of the value of mass m_e, spring constant k_e and coefficient of damping c, the displacement of the mass m_e can be expressed using Newton's second law as

$$m_e\ddot{z}_e + c\dot{z}_e + k_e z_e = (z_s - z_e)k_s, \tag{6}$$

where z_s is the displacement of slotted rod; z_e is the displacement of equivalent mass m_e.

As we know, the displacement of the slotted rod can be defined as $z_s = Y\sin\omega t$. Therefore, (6) can be written as

$$m_e\ddot{z}_e + c\dot{z}_e + (k_e + k_s)z_e = z_s k_s = k_s Y\sin\omega t, \tag{7}$$

The above expression could be considered as describing a single-spring-mass system with an equivalent sinusoidal force subjected to damping:

$$m_e\ddot{z}_e + c\dot{z}_e + kz_e = F\sin\omega t, \tag{8}$$

where $k = k_e + k_s$ and $F = k_s Y$. The displacement of the equivalent mass m_e can be obtained as [31]

$$z_e(t) = A\sin(\omega t - \phi), \tag{9}$$

where A is the highest amplitude of $z_e(t)$, ϕ is the phase angle given as

$$A = \frac{F}{\sqrt{(k - m_e\omega^2)^2 + (c\omega)^2}}, tan\phi = \frac{c\omega}{k - m_e\omega^2}. \tag{10}$$

Hence the displacement $z(t)$, can be expressed as

$$z(t) = z_s(t) - z_e(t). \tag{11}$$

The applied increased force $F_m(t)$, on each of the piezoelectric patch can be calculated as

$$F_m(t) = \tan\theta[k_s(z_s(t) - z_e(t)) - c\dot{z}_e(t)]/2 = \tan\theta F_s(t)/2, \tag{12}$$

The periodic surface charge, voltage, and current from the piezoelectric patches can be given as [4]

$$Q(t) = d_{15} F_m(t) = d_{33} \tan\theta [k_s(z_s(t) - z_e(t)) - c\dot{z}_e(t)]/2, \tag{13a}$$

$$V(t) = d_{15} \tan\theta [k_s(z_s(t) - z_e(t)) - c\dot{z}_e(t)]/2c_v, \tag{13b}$$

$$I(t) = d_{15} \tan\theta [k_s(\dot{z}_s(t) - \dot{z}_e(t)) - c\ddot{z}_e(t)]/2, \tag{13c}$$

where c_v is the electric capacitance of the PZT material given as [13]

$$c_v = c_v^{'} h_p b_p 0.0001/(0.010.01 a_p). \tag{14}$$

The electrical power generated by every PZT bar of the harvester is given as

$$P_e(t) = V(t) I(t), \tag{15}$$

$$P_e(t) = d_{15}^2 (\tan\theta)^2 [k_s(z_s(t) - z_e(t)) - c\dot{z}_e(t)][k_s(\dot{z}_s(t) - \dot{z}_e(t)) - c\ddot{z}_e(t)]/4c_v. \tag{16}$$

In this generator, there are eight piezoelectric patches included, hence the power, produced by the PZT, would be:

$$P_T(t) = 2d_{15}^2 (\tan\theta)^2 [k_s(z_s(t) - z_e(t)) - c\dot{z}_e(t)][k_s(\dot{z}_s(t) - \dot{z}_e(t)) - c\ddot{z}_e(t)]/c_v. \tag{17}$$

The root mean square value of the produced electric power during time from 0 to t could be expressed as

$$P_T^{rms} = 2\sqrt{\frac{1}{\tau} \int_0^{\tau} P_e^2(t) dt}. \tag{18}$$

Once the mathematical model is formulated, the voltage and current generated from the piezoelectric patches can be calculated and subsequently the root mean square value of the power.

Let the sliding blocks, stationary blocks, and springs are made of steel while the piezoelectric patches are manufactured of PZT-5H (lead zirconate titanate). Dimensions of PZT patches with material properties and dimension of scissor mechanism with steel properties are listed in Tables 1 and 2, respectively. An aerodynamic based model of wind turbine has been used to convert the wind energy into mechanical energy and consequently into electricity with the help of an energy harvesting device. Mechanical power, P_m, from the wind turbine can be calculated as [32]

Table 1 Material properties and dimensions of PZT-5H

K_{33}	d_{15}(C/N)	G_p(N /m^2)	a_p(mm)	b_p(mm)	h_p(mm)
0.78	7.41×10^{-10}	20.38×10^9	1–10	20	20-300
c_v'	0.375 for the PZT bar having dimensions of a_p= 0.01 m, h_p = 0.01 m, a_p = 0.0001 m [36]				

Table 2 Dimensions and properties of the material of the scissor jack device

G_s(N /m^2)	ρ_s(kg/m^3)	a_b(mm)	b_b(mm)	h_b(mm)	ζ	θ(degree)
80.76×10^9	8050	20	20	20-300	0.0017	70–80

$$P_m = \frac{1}{2}\rho\pi R^2 v_W^3 C_P(\lambda), \tag{19}$$

where ρ= 1.225kg/m^3 is the air density at NTP, R is the radius of the turbine (m); v_W is the wind velocity (m/s), $C_P(\lambda)$ is the turbine's power coefficient, λ(Tip-Speed Ratio)= $\frac{R\omega}{v_W}$.

The power coefficient C_P can be calculated empirically with the help of λ and can be given as [33]

$$C_P(\lambda) = 0.73\left(\frac{151}{\lambda} - 13.65\right)e^{\left(\frac{-18.4}{\lambda}+0.055\right)}. \tag{20}$$

As the input torque, T, the total resistive torque, T_R, dominates; due to the generator and drive train, the blades of the wind turbine (horizontal-axis) start to rotate. The speed of the wind when both the torque becomes equal is known as the cut-in speed. The cut-in speed can be calculated by standard blade elementary theory [34] and expressed as

$$U_C = \left(\frac{2T_R}{N\rho R^3 I_{cp}}\right)^{1/2}, \tag{21}$$

here U_C is the cut-in speed, T_{Rmax} is the resistive torque ($k_s Y^2$), N is the number of blades, ρ is the air density, and I_{cp} is the chord-pitch integral.

It is observed from (21), that cut-in speed is directly proportional to T_R. Hence, in the area of low wind velocity, to harvest the energy, the low value of T_R is necessary. Cut-in speed can be reduced by rising the radius and the number of blades for T_R (same resistive torque).

3 Effect of Various Parameters on Harvested Power

After getting the relation for RMS of electric power from turbine rotation, the performance of the harvester has been determined. Design parameters such as the spring stiffness, scissor angle, eccentricity, rotation of the turbine, PZT thickness, and length and width of the PZT on power the output were studied. We consider a wind turbine having three blades and 1 m blade tip radius for this purpose. The mechanical power from the wind turbine is calculated by the empirical formula, given by (19), for various resistive torque. An optimized design of the harvester has been proposed after studied various parameters of the harvester.

3.1 Effect of Stiffness of Spring

From the mathematical formulation, it is observed that the energy harvesting from the device mainly depends on the eccentricity of the scotch yoke mechanism and the stiffness of the spring. Fig. 4 shows the pattern of influence of the stiffness of spring,k_s, on the output electric power at wind speed ranging from 5 to 9 m/s, corresponding to the scissor jack angle of 80°, thickness, length and width of the PZT bar as 10 mm 100 mm, and 20 mm, respectively. From Fig. 4, it was found that electric power rises nonlinearly with an increase in the stiffness of spring, and after 100 kN/mm stiffness the power starts to decrease. At 9 m/s of the wind speed, the maximum RMS of the power of 242.4 W was obtained at 0.1 MN/s. Simultaneously, the eccentricity of the scotch-yoke mechanism decreases with increasing the stiffness of the spring as shown in Fig. 5, to maintain the constant resistive torque. It has been observed from Fig. 5, that, if we increase the spring stiffness then there is decreasing

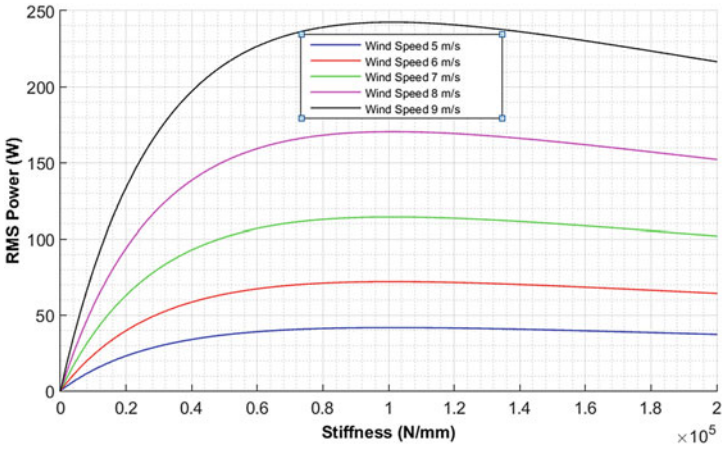

Fig. 4 Variation in RMS of electric power with spring stiffness

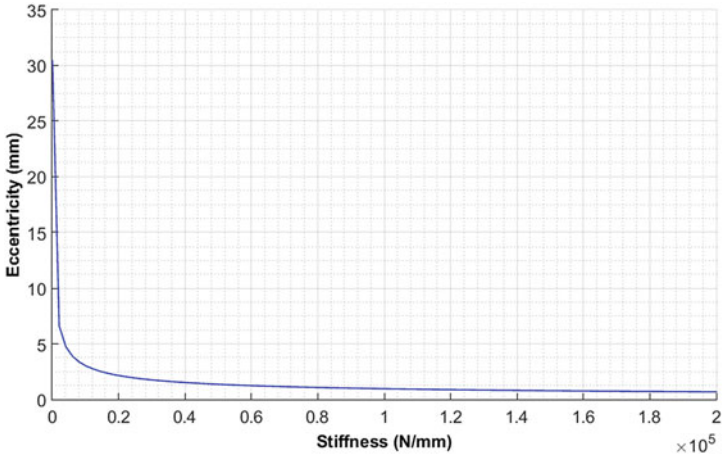

Fig. 5 Variation in spring force and eccentricity with spring stiffness

in the magnitude of Y, and simultaneously magnitude of the applied force on the PZT patches increases. Finding shows that a higher the spring stiffness, lower the eccentricity to make a constant resistive torque getting higher efficiency of the device

3.2 Effect of Speed of Input Shaft

How the angular velocity of the input shaft affects the electric power is given in Fig. 6. The angular speed of the shaft is proportional to the wind speed, as the wind velocity

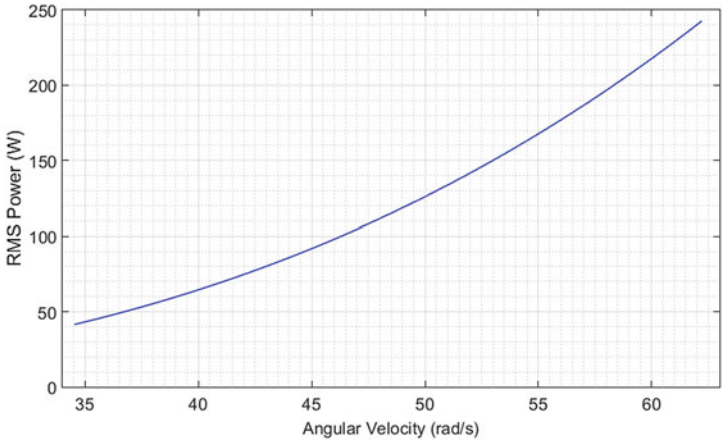

Fig. 6 Effects of angular velocity on RMS of electric power

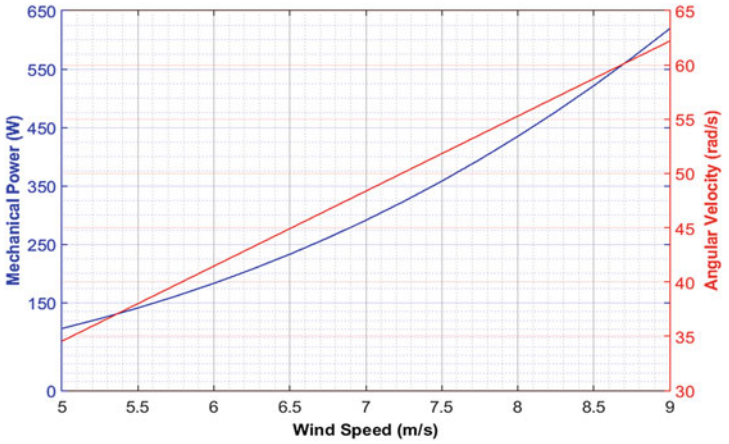

Fig. 7 Effects of wind speed on mechanical power and angular speed

increases the angular speed of the shaft increases linearly. Power output varies non-linearly with increasing the wind speed as depicted in Fig. 6. The length, width, and thickness of PZT patches, spring stiffness with scissor angle of 80° are selected as 100 mm, 20 mm, 10 mm and 100 kN/m, respectively. It is observed that the power increases non-linearly from 041.58W to 242.4W with the increase in angular speed from 034.55rad/s to 62.19rad/s. This variation can be interpreted as, the angular speed increase reduces the time period of the applied force, and simultaneously the kinetic energy of the harvester increases subsequently more electrical power generated.

As it is known, the higher mechanical power can be captured from the wind, if the power coefficient C_P is greater. Assuming the ratio of tip-speed, $\lambda = 6.91$, the highest magnitude of the power coefficient $C_P = 0.44$ is determined from (20). Using (19) and (20) with the above values, the variation in mechanical power P_m with angular speed ω can be shown in Fig. 7.

Windmill starts to rotate only when the wind speed dominates the cut-in speed value. Cut-in speed can be calculated using (21) for a particular wind turbine at resistive torque. It was found that the cut-in speed for a windmill with three blades having a radius of 1m, on the base of the chord-pitch integral from Ref. [35], is equal to 7.5m/s, for $T_R = 1$Nm. Wood [36] found that this estimated value of cut-in speed is approximate double, hence the actual value of cut-in speed is approximate 4m/s. Hence, the wind speed selected in this work ranges between 5m/s to 9m/s to evaluate the efficiency of the harvester as shown in Fig. 7.

In Fig. 7, the plot of mechanical power shows that the power P_m varies from 106.13 W to 618.99 W at optimal tip speed ratio during the variation in the wind. From Figs. 6 and 7, it is observed that the mechanical power (P_m) from the windmill constantly higher than the electrical power from the harvester at a particular rotation.

3.3 *Effect of Scissor Jack Angle*

Figure 8 shows the variation in RMS of electric power with the tangent of the scissor angle $\tan\theta$. From (13b), (13c) and (16) the generated power is proportional to the square of the tangent of scissor angle. It has been noted that a small increment of scissor angle gives high power output but after 80° of scissor angle, the power drastically decreases and becomes zero at 90°. It is shown from (2) and (4) that spring constant decreases with increasing the angle while the electrical damping coefficient increase that leads to decreasing the output power.

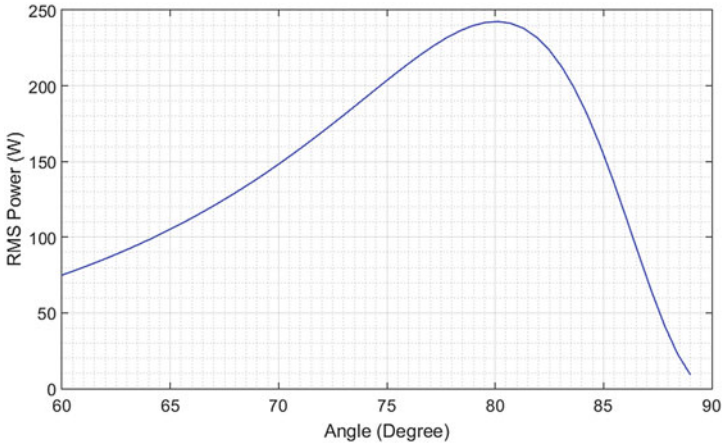

Fig. 8 Mechanical power *versus* scissor jack angle

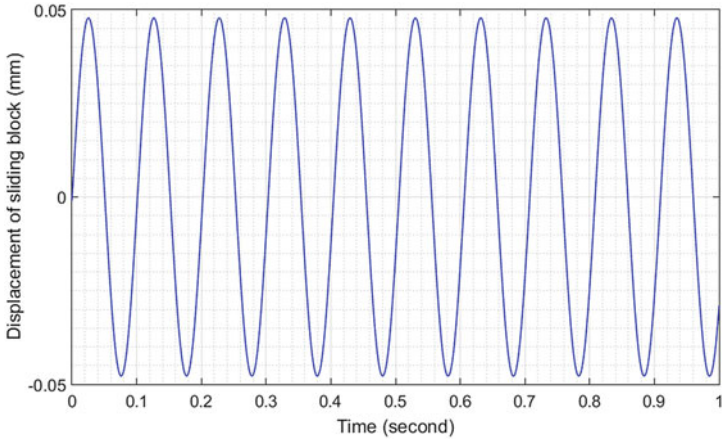

Fig. 9 Displacement of sliding block *versus* time

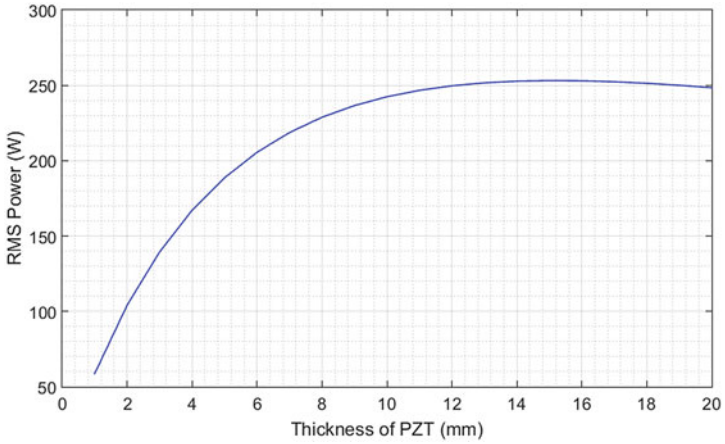

Fig. 10 RMS of generated power *versus* thickness of PZT bars

The displacement of the mass m_e with time is shown in Fig. 9. The maximum displacement of the mass, recorded by using analytical simulation is equal to 0.04724 mm, when the scissor angle is $\theta = 80°$, spring stiffness = 100 kN/m, angular velocity = 62 rad/s and eccentricity = 0.009 mm. In Fig. 9, the maximum displacement equal to 0.04724 mm is sufficient to use an 80° scissor angle in actual design to make the harvester sustainable.

3.4 Effect of Thickness of PZT Bar

As the piezopatch thickness varies, the electric power increases up to 16 mm and after this limit power starts to be reduced as is shown in Fig. 10. The following parameters to simulate the model are considered: angular velocity $\omega = 62$ rad/s, spring stiffness $k_s = 100$ kN/m, scissor angle, $\theta = 80°$, length of PZT = 100 mm, and width of PZT = 20 mm. The effect of the thickness on the electrical power can be explained with the help of (13b) and shows that the RMS of power is proportional to the thickness of the PZT patches, but from (2), an increasing the thickness of PZT decreases the spring constant, and the resultant effect of thickness is shown in Fig. 10.

3.5 Effect of Length of PZT Bar

Figure 11, depicts the variation in RMS of the electrical power with the length and width of the PZT patches. In this case, $\omega = 62$ rad/s, spring stiffness $k_s = 100$ kN/m, scissor angle $\theta = 80°$ and thickness of PZT bar = 10 mm was fixed for the analysis. It can be observed that the RMS value of the power increases first and then decreases,

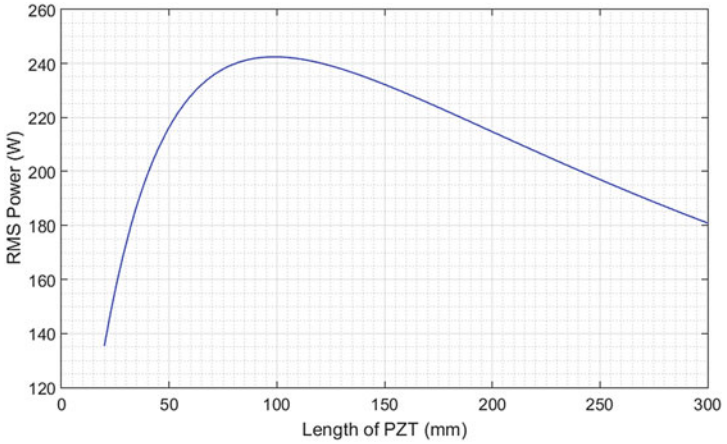

Fig. 11 Variation in RMS of electric power with length of PZT bars

when the length of the piezoelectric patches varies from 20 to 300 mm; the highest output power is obtained at 100 mm length of PZT. From (13b) and (16), it can be interpreted that with an increase in the length of the PZT, the electric capacity c_v increases, that leads to a decreasing in the electric voltage. The maximum stress, induced into the PZT patch at the peak load as much as low to the yield point of the piezoelectric material [37], hence the theoretical analysis results are convincible.

4 Conclusion

A piezoelectric energy harvester, based on the shear mode scissor mechanism, on a wind turbine is designed. The input force through scotch yoke mechanisms is increased through the scissor mechanism on piezoelectric patches to straining and generating electric power. Mathematical modeling has been performed to calculate the power, and analytical simulation is carried out to study the effect of parameters on the power. The results from the simulation showed that the optimum value of the power can be obtained at $a_p = 16\text{mm}, b_p = 20\text{mm}, h_p = 100\text{mm}, k_s = 100\frac{\text{kN}}{\text{m}}, \omega = 62\frac{\text{rad}}{\text{s}}, \theta = 80$, eccentricity , $y = 0.009\text{mm}$

and the wind velocity of 9 m/s, the RMS of generated power reaches up to 242.4 W, which is not sufficient to meet the energy requirement of average households (2 kW) [38]. In practice, it is proposed that a larger dimension of the harvester and/or large radius of the wind turbine rotor blade may be useful to meet the required energy for the household appliances.

Acknowledgment The authors highly acknowledge the director, PDPM Indian Institute of Information Technology Design and Manufacturing Jabalpur for providing facilities and permitted for publishing this research. IAP thanks RFBR for grant No. 19-08-00365.

References

1. W. Wang, F. Ismail, F. Golnaraghi, IEEE Trans. FUZZY Syst. **12**, 710 (2004)
2. M. Bhardwaj, T. Garnett, A.P. Chandrakasan, ICC 2001. IEEE Int. Conf. **3**, 785 (2001)
3. T. Hehn, Y. Manoli, Circ. Piezoelectr. Energy Harvest. **38**, 204 (2015)
4. D.J. Leo, *Engineering Analysis of Smart Material Systems* (Wiley, 2007), p. 576
5. D.-A. Wang, N.-Z. Liu, Sensors Actuators. A Phys. **167**, 449 (2011)
6. A. Nechibvute, A.R. Akande, P.V.C. Luhanga, Pertanika. J. Sci. Technol. **19**, 259 (2011)
7. J. Sirohi, R. Mahadik. J. Vib. Acoust. **134**, 011009 (2011)
8. A.T. Mineto, M.P. Souza Braun, H.A. Navarro, P.S. Varoto, Dincon'10 (2010), p. 599
9. F. Khameneifar, S. Arzanpour, M. Moallem, IEEE/ASME Trans. Mechatronics. **18**, 1527 (2013)
10. X.D. Xie, Q. Wang, N. Wu, Int. J. Eng. Sci. **77**, 71 (2014)
11. L.A. Weinstein, M.R. Cacan, P.M. So, P.K. Wright, Smart Mater. Struct. **21**, 045003 (2012)
12. J. Zhang et al., Sensors Actuators. A Phys. **262**, 123 (2017)
13. J.X. Tao, N.V. Viet, A. Carpinteri, Q. Wang, Eng. Struct. **133**, 74 (2017)
14. T. Narolia, V.K. Gupta, Parinov, in Advanced Springer Proceedings in Materials, ed. by I.A. Parinov, S.H. Chang, B. Long. vol 6. (Springer Nature Switzerland 2020), pp 503–511
15. N.V. Viet, M. Al-Qutayri, K.M. Liew, Q. Wang, Appl. Ocean Res. **64**, 128 (2017)
16. T. Narolia, V.K. Gupta, I.A. Parinov, Design and experimental study of rotary-type energy harvester. J. Intell. Mater. Syst. Struct. **31**, 1594 (2020)
17. T. Narolia, V.K. Gupta, I.A. Parinov, in *Advanced Materials—Proceedings of the International Conference on "Physics and Mechanics of New Materials and Their Applications", PHENMA 2018, Springer Proceedings in Physics*, ed. by I.A. Parinov, S.-H. Chang, Y.-H. Kim, vol. 224 (Springer Nature, Cham, Switzerland, 2019), p. 603
18. L. Edery-azulay, H. Abramovich, Compos. Struct. **64**, 443 (2004)
19. L. Zhou et al., Sens. Actuators A Phys. **179**, 185 (2012)
20. X. Zheng et al., IEEE/ASME Trans. Mech. **20**(2), 728 (2015)
21. M.H. Malakooti, H.A. Sodano, Smart Mater. Struct. **24**(5), 055005 (2015)
22. T. Narolia, V.K. Gupta, I.A. Parinov, J. Adv. Dielectr. **10**(3), 2050008 (2020)
23. T. Rodig, A. Schonecker, G. Gerlach, J. Am. Ceram. Soc. **93**(4), 901 (2010)
24. Scotch Yoke, https://en.wikipedia.org/wiki/Scotch_yoke.
25. N.V. Viet, X.D. Xie, K.M. Liew, N. Banthia, Q. Wang, Energy **112**, 1219 (2016)
26. S.O. Oyadiji, S. Qi, R. Shuttleworth, in *Engineering Asst Lifecycle Management*, ed. by A. Koronios, J. Mathew, (Springer, London, 2010), p. 697
27. R.D. Blevins, R. Plunkett, J. Appl. Mech. **47**, 461 (1980)
28. P.D. Mitcheson, E.M. Yeatman, G.K. Rao, A.S. Holmes, T.C. Green, Proc. IEEE. **96**, 1457 (2008)
29. X.D. Xie, Q. Wang, Energy. **86**, 385 (2015)
30. J. Woodhouse, J. Sound Vib. **215**, 547 (1998)
31. S.R. Singiresu, *Mechanical Vibrations*, 5th edn. (Pearson, London, 2011), p. 1084
32. T. Burton, *Wind Energy Handbook* (Wiley, Hoboken, 1947), p. 780
33. J.G. Slootweg, S.W.H. de Haan, H. Polinder, W.L. Kling, IEEE Power Eng. Rev. **22**, 56 (2002)
34. P.D. Clausen, D.H. Wood, Wind Eng. **24**, 189 (2000)
35. N. Wu, Q. Wang, X. Xie, Wind energy harvesting with a piezoelectric harvester. Smart Mater. Struct. **22**(9), 095023 (2013)
36. D.H. Wood, Wind Eng. **25**, 249 (2001)
37. K.V. Allamraju, S. Korla, Mater. Today Proc. **4**, 126 (2017)
38. https://en.wikipedia.org/wiki/Domestic_energy_consumption

Wind Energy Harvesting from Artificial Grass by Using Micro Fibre Composite

Rakesh Kumar Haldkar and Ivan A. Parinov

Abstract Energy harvesting technologies from ambient sources are the most interesting area of researchers nowadays because everyone is looking for an alternative to these conventional power sources. Ambient energy is extracted from thermal energy, solar energy, electromagnetic waves and vibration energy sources. The vibration energy is found a great presence nowadays. Micro Fiber Composite (MFC) is used to convert mechanical energy to electrical energy and vice versa. The various applications of MFC are available in the field of sensors and actuators. In this work, artificial grass is designed to harvest wind energy. The different structures of cantilever beams are designed. MFC is attached to the cantilever beam and converts the wind energy to electrical energy. The Finite Element analysis has been performed using ANSYS Multiphysics to analyze the electrical and mechanical properties. One artificial grass with proof mass gives the 0.0123 W.

Keywords Energy harvesting · Wind energy · Micro Fiber Composite (MFC) · Cantilever beam

1 Introduction

Energy harvesting is a very interesting area of research in recent times. The depletion in conventional non-renewable energy sources has made researchers look into new and alternate sources of energy. It was the early 1990s, and while the integration of electronics into everyday devices was underway, the revolutions that would become wireless communication and global networking were only beginning [1–4]. Lots of research are conducted in past years to improve the efficiency of piezoelectric energy harvesters. The researchers have tried several materials, different structures and various analyses are carried out to provide the best alternative solutions [5–11]. The most common structure of this technique is the cantilever beam having piezoelectric material is attached to it however, researchers have also developed

R. K. Haldkar (✉) · I. A. Parinov
Southern Federal University, Rostov-on-Don, Russia

I. A. Parinov et al. (eds.), *Physics and Mechanics of New Materials and Their Applications*, Springer Proceedings in Materials 10,
https://doi.org/10.1007/978-3-030-76481-4_42

various new designs for improving the efficiency of the cantilever [12–17]. In this paper, artificial grass is designed to convert wind energy to electrical energy. For the artificial grass, a cantilever structure is considered. The different designs of the cantilever beam are proposed with the proof mass. The cantilever beam consists of active materials and passive materials. MFC is the active and duralumin passive material, respectively. The artificial grasses are implant in 1 feet^2 area.

2 Energy Harvester Designs

The concept of power generation by artificial grass is shown in Fig. 1. Each energy harvester consists of passive cantilever beams, active MFC patches, and electronic circuits. The wind strikes with these cantilevers, the cantilevers deform, and wind energy is converted into electrical energy. The length of the passive cantilever is equal to 120 mm, width is 20 mm and thickness is 0.5 mm. The dimensions of the active MFC have a length of 28 mm, a width of 14 mm and thickness 0.3 mm. The proof mass length of 20 mm, width of 40 mm, and thickness of 0.5 mm are considered as shown in Fig. 2. The passive and active material properties are listed in Table 1.

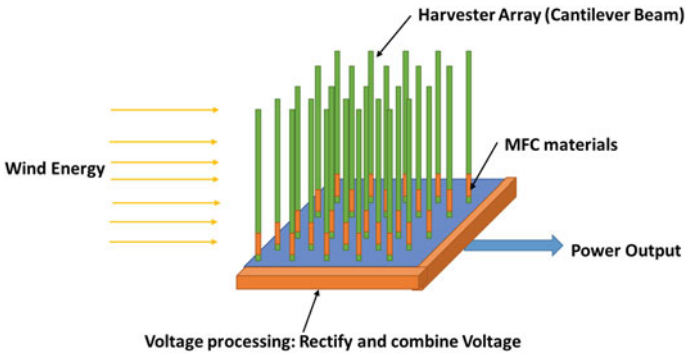

Fig. 1 Energy harvester

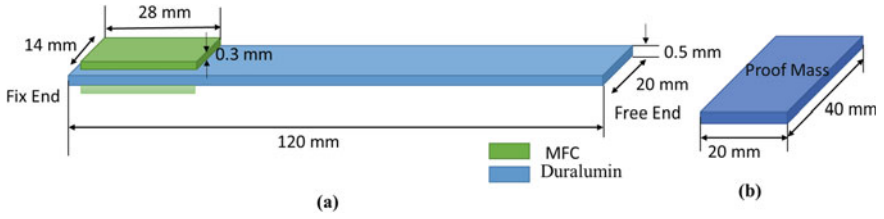

Fig. 2 MFC cantilever bimorph

Table 1 Materials properties

No	Energy harvester elements	Material	ρ, kg/m^3	E, Pa	ν
1	Passive material	Duralumin	2800	0.33×10^{11}	0.33
2	Active material	MFC	[18]		0.31
3	Proof mass	Metal (Steel)	7700	2.1×10^{11}	0.33
4	Active electrical load	Resistor (Ω)	100,000	–	–

3 FEA Modelling of the Cantilever Beam

CAD model of the cantilever with proof mass is shown in Fig. 3. MFC is glued to the fixed end and created the bimorph beam as shown in Fig. 3a. Figure 3b shows the second CAD model, the proof mass is attached at the free end. MFC material has meshed with SOLID226 and SOLID186 used for duralumin meshing. FEA analysis is carried out in the three models; (i) bimorph cantilever beam, (ii) bimorph cantilever beam with a steel proof mass and (iii) bimorph cantilever beam with a duralumin proof mass. Mesh independency test is carried out for all the above cases.

Modal analysis is carried out with above the three cases and natural frequency is summarized in Table 2 and mode shape is shown in Fig. 4.

Nan Wu et al. developed the periodical pressure variation on the downstream side of the cantilever beam. The equivalent dynamic force $P(t)$, scattered per unit length on the cantilever beam from the crosswind with the vortex shedding, is defined as [19]

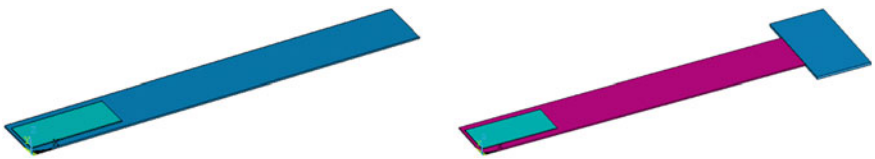

(a) **(b)**

Fig. 3 Cantilever beam with MFC patches: **a** without proof mass, **b** with proof mass

Table 2 Natural frequency at different design

No	Design	Natural frequency (Hz)	Deflection (m)
1	MFC bimorph cantilever beam without proof mass	30.75	1×10^{-3}
2	MFC bimorph cantilever beam with the steel proof mass	19.19	4×10^{-3}
3	MFC bimorph cantilever beam with the duralumin proof mass	29.88	1.5×10^{-3}

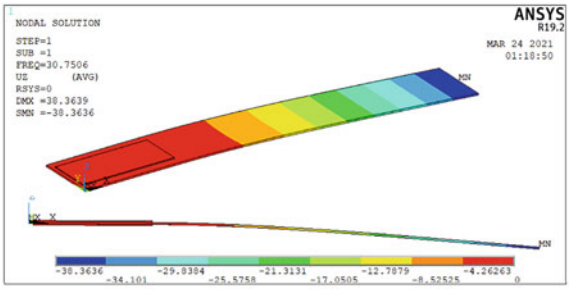

(a) without proof mass

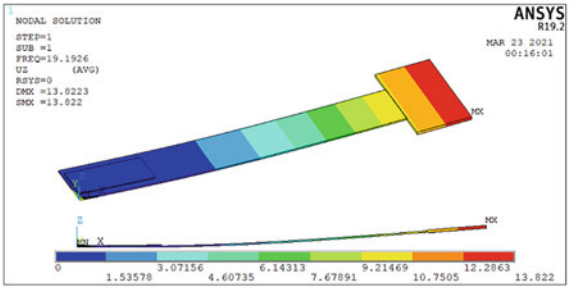

(b) with steel proof mass

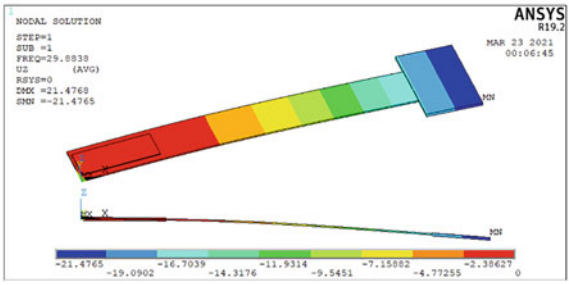

(c) with duralumin proof mass

Fig. 4 First mode shape of the bimorph cantilever beam. **a** without proof mass, **b** with steel proof mass, **c** with duralumin proof mass

$$P(t) = \frac{\rho_A \times v^2}{2} \times b \times \mu L \times \sin \omega_s t \tag{1}$$

$$\omega_s = \frac{2\pi \times v \times st}{b} \tag{2}$$

where v is the wind velocity, ρ_A is the air mass density; μ_L is the crosswind force coefficient, set as 0.6 for a rectangular beam cross-section; ω_s is the vortex shedding frequency; b is the width of the MFC patches and cantilever.

4 Results and Discussion

The wind velocity in normal conditions, varies from 1 to 8 m/s. The wind is strike to cantilever with above velocity and get deflected. The pressure exerted on the cantilever beam due to the above velocity range varies from 0.1 to 5 Pa. This pressure range is applied to the cantilever energy harvester models to find out the deflection and voltage. The pressure 1 Pa is applied to the above three energy harvesters and harmonic analysis is carried out. The maximum deflection is equal to 1.5×10^{-3} m and obtained at the natural frequency of 29.88 Hz in the case of duralumin proof mass shown in Fig. 5b and results are summarized in Table 2.

According to the wind flow, the pressure is employed on the cantilever beam. When the wind velocity increases, the exerted pressure also increases on the cantilever beam. The cantilever beam gets deflection when the pressure exerted on it and the results are shown in Fig. 6. When applied pressure increases, the cantilever beam deflects more. As compare with two designs with proof mass, the duralumin proof mass gives more deflection compared to steel proof mass. Figure 7 shows the relationship between the deflection and the output voltage of the cantilever with proof

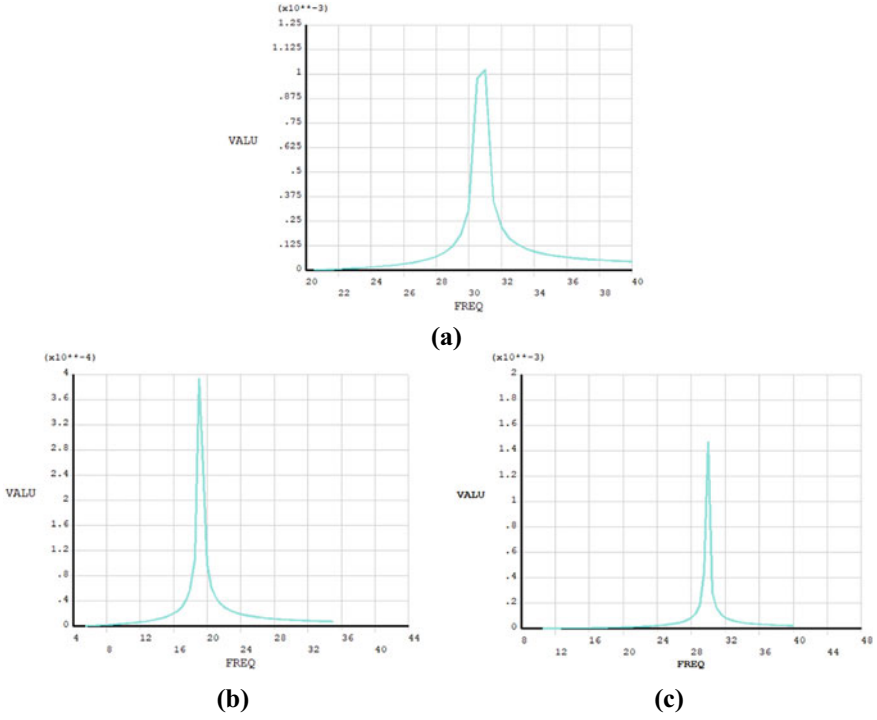

Fig. 5 Frequency versus deflection: **a** without proof mass, **b** with steel proof mass, **c** with duralumin proof mass

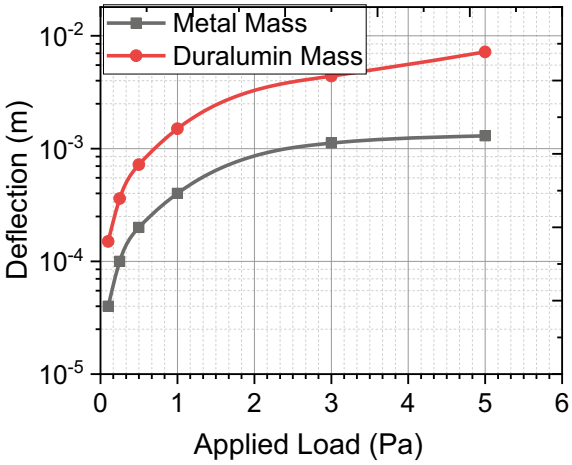

Fig. 6 Deflection versus applied load

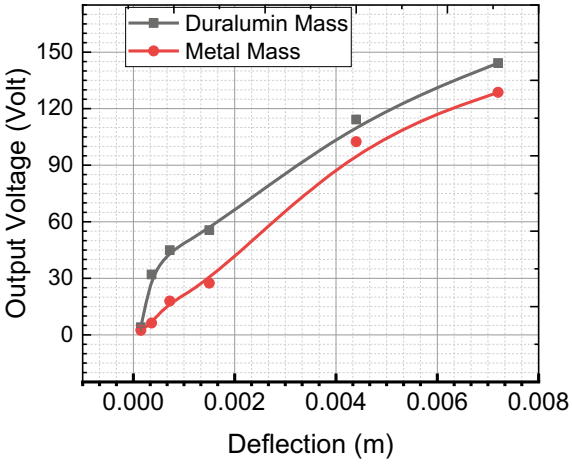

Fig. 7 Deflection versus voltage

mass. The applied pressure on the cantilever varies from 0.1 to 5 Pa and found out the output voltage. Duralumin proof mass gives the higher voltage as compared to the steel proof mass. In further analysis, cantilever energy harvester with duralumin proof mass is considered for artificial grass.

The wind pressure of 1 Pa, applied to the one cantilever of artificial grass, is found the 55.56 V as shown in Fig. 8 and an output current is 2.20×10^{-4} A. The power, generated by one cantilever of artificial grass, is about 0.0123 W. The number of 1050 (7×150) grass cantilevers are mounted on the area of 1 Feet^2. Then the total power generated is about 12.915 W.

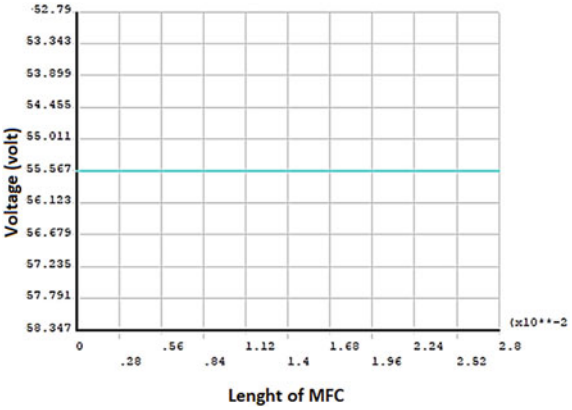

Fig. 8 Output voltage at the wind pressure of 1 Pa

5 Conclusion

The artificial grass is composed of a cantilever beam with MFC materials, a proof mass, and an electrical resistance. MFC cantilever beams are designed based on the finite element method. The finite element analysis software ANSYS is used to calculate the relationship between the deflection and output voltage of the MFC. Results show that the natural frequencies of the cantilever energy harvester with the duralumin proof mass is 29.88 Hz. The peak voltage of 44.99 V takes place at 1 Pa wind pressure. The one artificial grass harvest energy of about 0.0123 W and total output power is 12.95 W. This power can be utilized for running the MEMS devices.

Acknowledgements Research was financially supported by Southern Federal University, grant No. VnGr-07/2020-04-IM (Ministry of Science and Higher Education of the Russian Federation).

References

1. H.J. Song, Y.-T. Choi, N.M. Wereley, A.S. Purekar, J. Intell. Mater. Syst. Struct. **21**(6), 647 (2010)
2. S.R. Anton, H.A. Sodano, Smart Mater. Struct **16**(3), 1 (2007)
3. S. Roundy, P.K. Wright, Smart Mater. Struct. **13**(5), 1131 (2004)
4. H.S. Kim, J. Kim, J. Kim, Int. J. Precis. Eng. Manuf. **12**(6), 1129 (2011)
5. A.M. Khalatkar, R. Kumar, R. Haldkar, D. Jhodkar, *Arduino-Based Tuned Electromagnetic Shaker Using Relay for MEMS Cantilever Beam* (Springer, Singapore, 2019)
6. A. Khalatkar, V.K. Gupta, R. Haldkar, SPIE Smart Nano-Micro Mater. Devices **8204**, 82042G (2011)
7. A.M. Khalatkar, R.H. Haldkar, V.K. Gupta, in*Proceedingof the 2nd International Conference on Mechanical, Material Engineering (ICMME 2014), November 2223, 2014, Shiyan, Hubei, China*, 4212 (2014), pp. 110116
8. S. Ju, S.H. Chae, Y. Choi, C. Ji, Sens. Actuators, A **226**, 126 (2015)
9. S. Orrego et al., Appl. Energy **194**, 212 (2017)

10. G. Fei, G. Liu, B.L. Chung, H.H. Chan, B.L. Chung, H.H. Chan, Appl. Phys. Lett. **115**(3), 033901 (2019)
11. M. Safaei, H.A. Sodano, S.R. Anton, Smart Mater. Struct. **28**(11), 113001 (2019)
12. T. Narolia, V.K. Gupta, I.A. Parinov, J. Intell. Mater. Syst. Struct. **31**(13), 1594 (2020)
13. C.Q.G. Muñoz, G.Z. Alcalde, F.P.G. Márquez, Appl. Sci. **10**(17), 5951 (2020)
14. J. Liu et al., Microelec. Eng. **231**, 111333 (2020)
15. T. Shi, L. Zou, K.C.S. Kwok, Wind Energy, 1–13 (2021)
16. Z. Lai, S. Wang, L. Zhu, G. Zhang, J. Wang, K. Yang, Mechan. Syst. Signal Proc. **150**, 107212 (2021)
17. T. Narolia, V.K. Gupta, I.A. Parinov, in *Advanced Materials—Proceedings of the International Conference on "Physics and Mechanics of New Materials and Their Applications", PHENMA 2019*, Springer Proceedings in Materials, ed. by Ivan A. Parinov, Shun-Hsyung Chang, Banh Tien Long (Springer Nature, Cham, Switzerland, vol. 6, 2020), p. 503
18. *Macro Fiber Composite—MFC*, Smart Mater. **8** (2017) https://www.smart-material.com/media/Datasheets/MFC_V2.3-Web-full-brochure.pdf
19. N. Wu, Q. Wang, X. Xie, Smart Mater. Struct. **22**(9), 095023 (2013)

Absolute Stability of Control System for Deformation of Electromagnetoelastic Actuator Under Random Impacts in Nanoresearch

S. M. Afonin

Abstract The electromagnetoelastic actuator on the piezoelectric, piezomagnetic, electrostriction and magnetostriction effects is used in nanoresearch, nanotechnology, nanobiology and adaptive optics. The piezo-actuator is applied in nanotechnology and nanomechanics. The Yakubovich absolute stability criterion of the control system with the condition on the derivative for the hysteresis nonlinearity of the electromagnetoelastic actuator is used. This criterion with the condition on the derivative is development of the Popov absolute stability criterion. The stationary set of the control system for the electromagnetoelastic actuator with the hysteresis deformation is the segment of the straight line. This segment has the points of the intersection of the hysteresis partial loops and the straight line. The absolute stability conditions on the derivative for the control systems with the piezo-actuator at the longitudinal, transverse and shift piezo-effect are received. The condition of the absolute stability on the derivative for the control system for the deformation of the electromagnetoelastic actuator under random impacts in nanoresearch is obtained. For the Lyapunov stable control system this Yakubovich absolute stability criterion has the simplest representation of the result of the investigation of the absolute stability.

Keywords Absolute stability criterion · Control system · Electromagnetoelastic actuator · Piezo-actuator · Hysteresis deformation · Stationary set · Transfer function · Condition on derivative · Random impacts

1 Introduction

The use of an electromagnetoelastic actuator based on the piezoelectric, piezomagnetic, electrostriction, magnetostriction effects is promising in control systems for nanoresearch, nanotechnology, nanobiology, microsurgery and adaptive optics. In the control system, a piezo-actuator is used in scanning microscopy, astronomy for precision alignment, compensation for temperature, gravitational deformations,

S. M. Afonin (✉)
National Research University of Electronic Technology (MIET), Moscow, Russia
e-mail: eduems@mail.ru

I. A. Parinov et al. (eds.), *Physics and Mechanics of New Materials and Their Applications*, Springer Proceedings in Materials 10,
https://doi.org/10.1007/978-3-030-76481-4_43

atmospheric turbulence, focusing, and image stabilization [1–6]. The presence of the hysteresis deformation in an electromagnetoelastic actuator complicates the design of mechatronic systems for controlling its deformation. In contrast to the control system with unique characteristic of the actuator, for which the stability of the equilibrium position is investigated by using Lyapunov functions and Popov criterion, the stability of the deformation control system of an electromagnetoelastic actuator with hysteresis nonlinearity and a set of equilibrium positions is estimated using Yakubovich absolute stability criterion [5–12].

In this work, the condition for the absolute stability of the control system for an electromagnetoelastic actuator for nanoresearch and nanotechnology under deterministic and random influences is obtained. Many equilibrium positions are found in the control system of an electromagnetoelastic actuator for nanoresearch. The absolute stability of this system with respect to the mathematical expectations of the equilibrium positions of the control system of the electromagnetoelastic actuator is determined. The condition on the derivative of the nonlinear hysteresis characteristic of the electromagnetoelastic actuator is satisfied in the control system.

1.1 Research Purpose

The purpose of this paper is calculation of condition of the absolute stability on the derivative for the hysteresis nonlinearity of the electromagnetoelastic actuator under random impacts.

1.2 Research Scope Corresponding

In this work, we consider the following frameworks of the problem:

(i) condition of the absolute stability on the derivative for the hysteresis deformation of an electromagnetoelastic actuator under deterministic and random impacts;
(ii) applied theory of the absolute stability of the control system for the deformation of an electromagnetoelastic actuator under random impacts in nanoresearch;
(iii) calculation of transfer functions with distributed and lumped parameters for an electromagnetoelastic actuator;
(iv) determination of the hysteresis deformation function for an electromagnetoelastic actuator and the stationary set of the control system for its deformation;
(v) analytical and numerical calculation of the condition of the absolute stability on the derivative for the hysteresis deformation of the piezo-actuator under random impacts.

2 Research Method

The frequency method for studying the stability of the control systems on Yakubovich absolute stability criterion of system with the condition on the derivative for the hysteresis nonlinearity of the electromagnetoelastic actuator is used [8–12].

The problem of obtaining the condition of the absolute stability on the derivative for the control system for the deformation of the electromagnetoelastic actuator under random impacts in nanoresearch is solved using the frequency method on Yakubovich absolute stability criterion. For the Lyapunov stable control system this Yakubovich absolute stability criterion has the simplest representation of the result of the investigation of the absolute stability. The absolute stability conditions on the derivative for the control systems with the piezo-actuator at the longitudinal, transverse and shift piezo-effect under random impacts are received.

2.1 Transfer Function

The transfer function of an electromagnetoelastic actuator is determined by the joint solution of the electromagnetoelastic equation, wave equation, and boundary conditions.

The electromagnetoelasticity equation [2, 3, 5, 6, 13–28] has the form:

$$S_i = d_{mi}\Psi_m + s_{ij}^{\Psi}T_j, \tag{1}$$

where S_i is the relative displacement of the electromagnetoelastic actuator along i-axis; d_{mi} is the electromagnetoelastic module; Ψ_m is the electric or magnetic field strength along m-axis; s_{ij}^{Ψ} is the elastic compliance at $\Psi = \text{const}$; T_j is the mechanical stress along j-axis; $i,\ j = 1,\ 2,\ \ldots, 6, m,\ k = 1,\ 2,\ 3$ are the indexes.

The equation of the inverse piezoelectric effect [2, 3, 5, 6, 13, 14] has the form:

$$S_i = d_{mi}E_m + s_{ij}^{E}T_j, \tag{2}$$

where d_{mi} is the piezomodule; $E_m = u/\delta$ is the electric field strength along m-axis; u is the voltage on the piezo-actuator; δ is the thickness; s_{ij}^{E} is the elastic compliance at $E = \text{const}$.

The equation of the magnetostriction [3, 5, 6, 13, 14] has the form:

$$S_i = d_{mi}H_m + s_{ij}^{H}T_j, \tag{3}$$

where d_{mi} is the magnetostriction coefficient; H_m is the magnetic field strength along m-axis; s_{ij}^{H} is the elastic compliance at $H = \text{const}$.

For an electromagnetoelastic actuator with fixed first end and an elastic-inertial load at second end, the equation of the forces has the form:

$$T_j S_0 = -Md^2\xi(x,t)/dt^2 - C_e\xi(x,t), \tag{4}$$

where F is the external force applied to the actuator and M is the moved mass; C_e is the stiffness of the elastic load.

The Laplace transform for the wave equation of an electromagnetoelastic actuator at zero initial conditions has the form of a linear ordinary differential equation of the second order [5–7, 19–26]:

$$\frac{d^2\Xi(x,p)}{dx^2} - \gamma^2\Xi(x,p) = 0, \tag{5}$$

$$\gamma = p/c^{\Psi} + \alpha,$$

where $\Xi(x, p)$ is the Laplace transform of the displacement of an electromagnetoelastic actuator; x is the coordinate; p is the Laplace operator; γ is the wave propagation coefficient; c^{Ψ} is the speed of sound in an electromagnetoelastic actuator at $\Psi = \text{const}$; α is the attenuation coefficient, accounting for the damping of vibrations during wave propagation due to energy dissipation and heat loss.

From (1) and (4), the equation has the form:

$$\left.\frac{d\Xi(x,p)}{dx}\right|_{x=l} = d_{mi}\Psi_m(p) - \frac{s_{ij}^{\Psi}Mp^2\Xi(p)}{S_0} - \frac{s_{ij}^{\Psi}C_e\Xi(p)}{S_0}. \tag{6}$$

where l is length of an electromagnetoelastic actuator.

From here

$$\frac{\Xi(p)\gamma}{\text{th}(l\gamma)} + \frac{s_{ij}^{\Psi}Mp^2\Xi(p)}{S_0} + \frac{s_{ij}^{\Psi}C_e\Xi(p)}{S_0} = d_{mi}\Psi_m(p), \tag{7}$$
$$\Xi(p) = \Xi(l,p).$$

From (7), the transfer function of an electromagnetoelastic actuator has the form:

$$W_{\Psi}(p) = \frac{\Xi(p)}{\Psi_m(p)} = \frac{d_{mi}}{s_{ij}^{\Psi}Mp^2/S_0 + \gamma\,\text{cth}(l\gamma) + s_{ij}^{\Psi}C_e/S_0}. \tag{8}$$

From (7), the transfer functions with distributed parameters of an electromagnetoelastic actuator are obtained in the form:

$$W_\Psi(p) = \frac{\Xi(p)}{\Psi_m(p)} = \frac{d_{mi} l}{Mp^2 \Big/ C_{ij}^\Psi + l\gamma \operatorname{cth}(l\gamma) + C_e \Big/ C_{ij}^E}, \tag{9}$$

$$W_E(p) = \frac{\Xi(p)}{E_m(p)} = \frac{d_{mi} l}{Mp^2 \Big/ C_{ij}^E + l\gamma \operatorname{cth}(l\gamma) + C_e \Big/ C_{ij}^E},$$

$$W_U(p) = \frac{\Xi(p)}{U(p)} = \frac{d_{mi} l / \delta}{Mp^2 \Big/ C_{ij}^E + l\gamma \operatorname{cth}(l\gamma) + C_e \Big/ C_{ij}^E},$$

$$W_H(p) = \frac{\Xi(p)}{H(p)} = \frac{d_{mi} l}{Mp^2 \Big/ C_{ij}^H + l\gamma \operatorname{cth}(l\gamma) + C_e \Big/ C_{ij}^H}$$

$$C_{ij}^\Psi = S_0 \Big/ \left(s_{ij}^\Psi l\right),\ C_{ij}^E = S_0 \Big/ \left(s_{ij}^E l\right),\ C_{ij}^H = S_0 \Big/ \left(s_{ij}^H l\right).$$

where $C_{ij}^\Psi = S_0 \Big/ \left(s_{ij}^\Psi l\right)$ is stiffness of an electromagnetoelastic actuator.

From (9), taking into account two terms of the series obtained by expanding the hyperbolic cotangent, the transfer functions with lumped parameters of an electromagnetoelastic actuator with an elastic-inertial load are found in the form:

$$W_\Psi(p) = \frac{\Xi(p)}{\Psi_m(p)} = \frac{d_{mi} l}{\left(1 + C_e \Big/ C_{ij}^\Psi\right)\left(T_t^2 p + 2T_t \xi_t p + 1\right)}, \tag{10}$$

$$W_E(p) = \frac{\Xi(p)}{E_m(p)} = \frac{d_{mi} l}{\left(1 + C_e \Big/ C_{ij}^E\right)\left(T_t^2 p + 2T_t \xi_t p + 1\right)},$$

$$W_U(p) = \frac{\Xi(p)}{U(p)} = \frac{d_{mi} l / \delta}{\left(1 + C_e \Big/ C_{ij}^E\right)\left(T_t^2 p + 2T_t \xi_t p + 1\right)},$$

$$T_t = \sqrt{M \Big/ \left(C_{ij}^E + C_e\right)},\ \xi_t = \alpha l^2 C_{ij}^E \Big/ \left[3c^E \sqrt{M\left(C_{ij}^E + C_e\right)}\right],$$

$$W_H(p) = \frac{\Xi(p)}{H_m(p)} = \frac{d_{mi} l}{\left(1 + C_e \Big/ C_{ij}^H\right)\left(T_t^2 p + 2T_t \xi_t p + 1\right)}$$

$$T_t = \sqrt{M \Big/ \left(C_{ij}^H + C_e\right)},\ \xi_t = \alpha l^2 C_{ij}^H \Big/ \left[3c^H \sqrt{M\left(C_{ij}^H + C_e\right)}\right],$$

Consequently, the expression for the static displacement $\xi(l,\infty)$ of the piezo-actuator under the elastic-inertial load in the steady state has the form:

$$\xi(l,\infty) = \left(d_{mi}l/\delta\right)U_0/\left(1 + C_e/C_{ij}^E\right), \tag{11}$$

where U_0 is the voltage amplitude.

2.2 Hysteresis Deformation

The Preisach model is used to describe the hysteresis deformation of an electromagnetoelastic actuator [9–12, 18]. When considering the structure of the control system for this actuator, the transfer function $W(p)$ of the linear part of the control system and the hysteresis function S_i of an electromagnetoelastic actuator are applied.

The hysteresis deformation function of an electromagnetoelastic actuator for nanoresearch has the form:

$$\begin{aligned} S_i &= F\left[\Psi_m|_0^t, t, S_i(0), \operatorname{sign}\dot{\Psi}_m\right], \\ S_i &= F\left[E_m|_0^t, t, S_i(0), \operatorname{sign}\dot{E}_m\right], \\ S_i &= F\left[H_m|_0^t, t, S_i(0), \operatorname{sign}\dot{H}_m\right], \end{aligned} \tag{12}$$

where S_i the value of the hysteresis deformation with main and partial cycles depends on the electric or magnetic field strength in the interval $[0, t]$, on time t, on the initial value of the relative deformation and on the sign of the rate of change in the electric or magnetic field strength. To find the stationary set the control system of the actuator with the stable linear part of the control system on the plane, we draw the straight line L in Fig. 1, where $k = W(0)$ is the transfer coefficient or the value of the transfer function at $p \to 0$ for the linear part of the control system. The stationary set of points M of intersection of this straight line L with the hysteresis characteristic of the deformation is the selected line segment.

The straight line equation L has the form.

$$E_m + kS_i = 0. \tag{13}$$

Each point of the intersection of the hysteresis nonlinearity of deformation and the straight line L corresponds to the equilibrium position. Consider the projection of the stationary set of equilibrium positions on the x-axis, where $x = E_m/E_{m\,\max}$ is the coordinate for Fig. 1. Let us substitute the equation of the straight line (13) to the expression for the symmetric main hysteresis loop of the piezo actuator [9, 10] in the form:

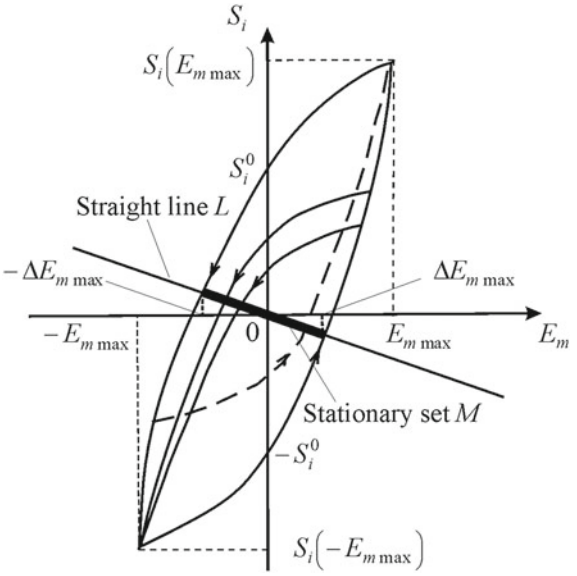

Fig. 1 Hysteresis characteristic of deformation piezo-actuator

$$S_i = d_{mi}E_m - \gamma_{mi}E_{m\max}\left(1 - \frac{E_m^2}{E_{m\max}^2}\right)^{n_{mi}} \operatorname{sign}\dot{E}_m, \tag{14}$$

where E_m is the amplitude of the electric field in the actuator in Fig. 1; $S_{i\max}$ is the maximum relative deformation of the piezo-actuator; $\gamma_{mi} = S_i^0 / E_{m\max}$ is the residual hysteresis; S_i^0 is the residual relative value of the static hysteresis characteristic at $E_m = 0$; n_{mi} is the power coefficient, determined by the shape of the hysteresis curve, for the PZT piezo-actuator this coefficient $n_{mi} = 1$.

Let us determine the relative width of the resting zone 2Δ for the control system of the deformation piezo-actuator with the symmetric main hysteresis loop. By substituting the value $E_m = E_{m\max}$ in (13), the equation has the form:

$$\Delta E_{m\max} + kS_i^+(\Delta E_{m\max}) = 0, \tag{15}$$

where Δ is the relative value of the electric field strength; $S_i^+(\Delta E_{m\max})$ is the value of the relative deformation on the ascending branch of the hysteresis characteristic at $\dot{E}_m > 0$ and $E_m = \Delta E_{m\max}$, $S_i^-(-\Delta E_{m\max})$ is the value of the relative deformation on the descending branch of the hysteresis characteristic at $\dot{E}_m < 0$ and $E_m = -\Delta E_{m\max}$ in Fig. 1. From (14) for the symmetric main hysteresis loop the equation is obtained in the form:

$$S_i^+(\Delta E_{m\max}) = d_{mi}\Delta E_{m\max} - \gamma_{mi}E_{m\max}\left(1 - \frac{(\Delta E_{m\max})^2}{E_{m\max}^2}\right). \tag{16}$$

In the result of transformation (16), the expression is received in the form:

$$S_i^+(\Delta E_{m\max}) = d_{mi}\Delta E_{m\max} - \gamma_{mi}E_{m\max}\left(1-\Delta^2\right). \tag{17}$$

By substituting expression (17) into Eq. (15), the expression is obtained in the form:

$$\Delta E_{m\max} + kE_{m\max}\left[d_{mi}\Delta - \gamma_{mi}\left(1-\Delta^2\right)\right] = 0. \tag{18}$$

After conversion (18), the expression has the form:

$$\Delta + k\left[d_{mi}\Delta - \gamma_{mi}\left(1-\Delta^2\right)\right] = 0. \tag{19}$$

From (19), the quadratic equation has the form:

$$\Delta^2 + \frac{(1+kd_{mi})}{k\gamma_{mi}}\Delta - 1 = 0. \tag{20}$$

The relative width of the rest zone 2Δ for the control system of the deformation piezo-actuator is obtained from (20) in the form:

$$2\Delta = -\frac{(1+kd_{mi})}{k\gamma_{mi}} + \sqrt{\frac{(1+kd_{mi})^2}{k^2\gamma_{mi}^2} + 4}. \tag{21}$$

For the asymmetric loop characteristic of the deformation piezo-actuator at the ascending branch of the hysteresis $\operatorname{sign}\dot{E}_n = +1$, residual hysteresis $\gamma_{mi} = \gamma_{mi}^+$ is obtained, at the descending branch of the hysteresis $\operatorname{sign}\dot{E}_n = -1$, residual hysteresis $\gamma_{mi} = \gamma_{mi}^-$ is received, where the superscripts are (+) for the ascending branch and (–) for the descending branch. Therefore, the relative width of the rest zone $\Delta^+ + \Delta^-$ for the control system deformation of the piezo-actuator has the form:

$$\begin{aligned}\Delta^+ + \Delta^- = &-\frac{(1+kd_{mi})}{2k}\left(\frac{1}{\gamma_{mi}^+} + \frac{1}{\gamma_{mi}^-}\right)\\ &+ \frac{1}{2}\sqrt{\frac{(1+kd_{mi})^2}{k^2\left(\gamma_{mi}^+\right)^2} + 4} + \frac{1}{2}\sqrt{\frac{(1+kd_{mi})^2}{k^2\left(\gamma_{mi}^-\right)^2} + 4}.\end{aligned} \tag{22}$$

The hysteresis nonlinearity function S_i of the electromagnetoelastic actuator is continuous. The minimum ν_{1mi}, and maximum ν_{2mi} values of the tangent of the angle of inclination to the hysteresis nonlinearity of deformation for the electromagnetoelastic actuator are obtained [9, 10] in the form:

$$\begin{aligned}&\nu_{1mi}, \nu_{2mi} \in [0,\ \nu_{mi}],\\ &\nu_{mi} = \max\left[dS_i/dE_m\right]\end{aligned} \tag{23}$$

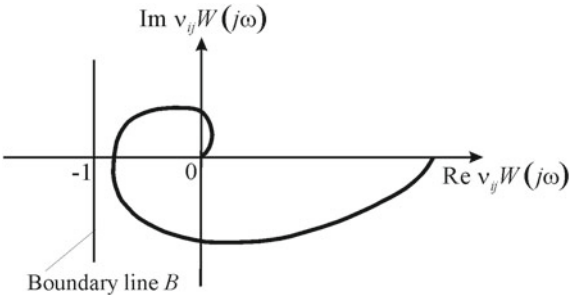

Fig. 2 Absolute stability condition for control system of electromagnetoelastic actuator deformation on complex plane

The values ν_{1mi} and ν_{2mi} are determined by the hysteresis characteristic of the deformation, measured at the maximum permissible field strength in the actuator, where the hysteresis loop of the actuator is bypassed counterclockwise.

For the piezo-actuator, the ratio of the tangents of the angle of inclination to the hysteresis nonlinearity of the piezo-actuator with longitudinal, transverse, shear piezoelectric effects is proportional to the ratio of the corresponding piezo-modules:

$$\nu_{33}{:}\nu_{31}{:}\nu_{15} = d_{33}{:}d_{31}{:}d_{15}. \tag{24}$$

2.3 Condition for Absolute Stability

From the Yakubovich criterion [8–12], which is a development of the Popov criterion, the condition for the absolute stability of the control system of the deformation of electromagnetoelastic actuator under deterministic influences is obtained. The condition for the absolute stability of the control system of the deformation electromagnetoelastic actuator under deterministic impacts in Fig. 2 at $\nu_{1mi} = 0$ and $\nu_{2mi} = \nu_{mi}$ [9–11] has the form:

$$\mathrm{Re}\nu_{mi}W(j\omega) \geq -1. \tag{25}$$

where j is the imaginary unit in the round brackets and ω is the frequency.

Let us consider the geometric interpretation of the absolute stability condition of the control system of electromagnetoelastic actuator deformation. Figure 2 shows the amplitude–phase frequency characteristic for the frequency transfer function on the complex plane with boundary line B in the form of the vertical line, passing through the point with coordinate (–1) on the real axis.

The amplitude-phase characteristic of an open-loop system must be located to the right of the vertical line B in the form $\mathrm{Re}\nu_{mi}W(j\omega) = -1$ for all values of $\omega \geq 0$. For the control system with the piezo-actuator made from PZT ceramic at deterministic

impacts the maximum value of the tangent of the angle of inclination to the hysteresis nonlinearity $\nu_{mi} = 1$ nm/V is obtained.

Let us find the condition of the absolute stability for the control system of the electromagnetoelastic actuator deformation under random impacts on the basis of the Yakubovich criterion [9–11]. The criterion of the absolute stability for the control system of the electromagnetoelastic actuator deformation with the hysteresis characteristic at $\nu_{1mi} = 0$ and $\nu_{2mi} = \nu_{mi}$ is written in the form (25).

For the absolute stability regarding mathematical expectations of the control system with the hysteresis deformation an electromagnetoelastic actuator under random impacts, acting upon by an external influence, containing the random component, we have.

$$\begin{aligned} &f(t) = m_f(t) + f^0(t), \\ &\left|m_f(t)\right| \le R_f \end{aligned} \tag{26}$$

where R_f is the upper bound for the modulus of the mathematical expectation m_f. It is sufficient, that for all values $\omega \ge 0$, the condition met

$$\mathrm{Re}\nu_{mi} W(j\omega) + 1 \ge 0 \tag{27}$$

and the derivative of the hysteresis deformation of the actuator satisfied the inequality:

$$0 < \frac{\partial m_{S_i}\left(m_{\Psi_m}, \sigma_{\Psi_m}\right)}{\partial m_{\Psi_m}} < \nu_{mi}. \tag{28}$$

Accordingly, using the method of statistical linearization, the derivative of the hysteresis deformation is obtained in the form:

$$\frac{\partial m_{S_i}}{\partial m_{\Psi_m}} = \frac{1}{2\sigma^2_{\Psi_m}} \int_{-\infty}^{+\infty} \left[S_i^+(\Psi_m) + S_i^-(\Psi_m)\right] \left(\Psi_m - m_{\Psi_m}\right) \frac{1}{\sigma_{\Psi_m}\sqrt{2\pi}} e^{-\frac{\left(\Psi_m - m_{\Psi_m}\right)^2}{2\sigma^2_{\Psi_m}}} d\Psi_m, \tag{29}$$

where $S_i^+(\Psi_m)$, $S_i^-(\Psi_m)$ are the ascending and descending curves of the hysteresis loop.

For an electromagnetoelastic actuator, the vertices of the main hysteresis loops are located on the initial curve in the form $S_i = F_1(\Psi_m)$. The maximum relative deformation of an electromagnetoelastic actuator is written in the form:

$$S_{i\,\max} = d_{mi\,\max} \Psi_{m\,\max}, \tag{30}$$

where $d_{mi\ \max}$ is the maximum value of the electromagnetoelastic module for each main hysteresis curve.

From (29), the expression for the derivative of the nonlinear relative deformation an electromagnetoelastic actuator is obtained in the form:

$$\frac{\partial m_{S_i}}{\partial m_{\Psi_m}} = \frac{1}{\sigma^2_{\Psi_m}} \int_{-\infty}^{+\infty} F_1(\Psi_m) \left(\Psi_m - m_{\Psi_m}\right) \frac{1}{\sigma_{\Psi_m}\sqrt{2\pi}} e^{-\frac{\left(\Psi_m - m_{\Psi_m}\right)^2}{2\sigma^2_{\Psi_m}}} d\Psi_m, \tag{31}$$

The initial curve of an electromagnetoelastic actuator [9–12] has the form:

$$F_1(\Psi_m) = d^0_{mi}\Psi_m + a_{mi}\Psi^3_m = d_{mi\ \max}\Psi_m, \tag{32}$$

therefore, the maximum value of the modulus is written in the form:

$$d_{mi\ \max} = d^0_{mi} + a_{mi}\Psi^2_m, \tag{33}$$

where d^0_{mi} is the initial value of the piezomodule, a_{mi} is the coefficient of the polynomial.

From (31) the derivative of the nonlinear characteristic is obtained in the form:

$$\frac{\partial m_{S_i}}{\partial m_{\Psi_m}} = \frac{1}{\sigma^2_{\Psi_m}} \int_{-\infty}^{+\infty} d_{mi\ \max}\Psi_m \left(\Psi_m - m_{\Psi_m}\right) \frac{1}{\sigma_{\Psi_m}\sqrt{2\pi}} e^{-\frac{\left(\Psi_m - m_{E\Psi_m}\right)^2}{2\sigma^2_{\Psi_m}}} d\Psi_m. \tag{34}$$

3 Results and Discussion

The Yakubovich absolute stability criterion has the simplest representation of the result of the investigation of the absolute stability for the control system deformation of an electromagnetoelastic actuator. For the control system with the hysteresis deformation of an electromagnetoelastic actuator under random impacts in nanoresearch, the condition of the absolute stability on the derivative is obtained.

The stationary set for the control system deformation of an electromagnetoelastic actuator is the segment of the straight line. The obtained condition of the absolute stability on the derivative for the control system deformation of an electromagnetoelastic actuator allows one to calculate the characteristics of the control system.

Using the method of statistical linearization, for $m_{\Psi_m} = 0$, the value of the partial derivative of the relative displacement of an electromagnetoelastic actuator on the field strength is obtained in the form:

$$\frac{\partial m_{S_i}}{\partial m_{\Psi_m}} = \frac{1}{\sigma^2_{\Psi_m}} \int\limits_{-\infty}^{+\infty} d_{mi\,\max} \Psi_m^2 \frac{1}{\sigma_{\Psi_m}\sqrt{2\pi}} e^{-\frac{\Psi_m^2}{2\sigma^2_{\Psi_m}}} d\Psi_m = d_{mi\,\max}, \quad (35)$$

$$0 < d_{mi\,\max} \leq \nu_{mi}$$

Similarly, for $m_{E_m} = 0$, the value of the partial derivative of the relative displacement of the piezo-actuator on the electric field strength has the form:

$$\frac{\partial m_{S_i}}{\partial m_{E_m}} = \frac{1}{\sigma^2_{E_m}} \int\limits_{-\infty}^{+\infty} d_{mi\,\max} E_m^2 \frac{1}{\sigma_{E_m}\sqrt{2\pi}} e^{-\frac{E_m^2}{2\sigma^2_{E_m}}} dE_m = d_{mi\,\max}. \quad (36)$$

Accordingly, from (35) for the control system with the hysteresis deformation of an electromagnetoelastic actuator under random impacts at $\nu_{1mi} = 0$ and $\nu_{2mi} = \nu_{mi}$, the condition of the absolute stability has the form:

$$\mathrm{Re}\,\nu_{mi} W(j\omega) = \mathrm{Re}\, d_{mi\,\max} W(j\omega) \geq -1. \quad (37)$$

For the control system with the piezo-actuator made from PZT ceramic at random impacts the maximum value of the tangent of the inclination angle to the hysteresis nonlinearity $\nu_{mi} = 1.7$ nm/V is obtained.

4 Conclusion

Applied theory of the absolute stability of the control system for the deformation of an electromagnetoelastic actuator under deterministic and random influences is obtained in nanoresearch. Condition of the absolute stability on the derivative is determined for the control system with the hysteresis deformation of an electromagnetoelastic actuator under deterministic and random impacts.

This work defines the transfer functions with distributed and lumped parameters of an electromagnetoelastic actuator. The hysteresis deformation function for an electromagnetoelastic actuator and the stationary set of the control system for its deformation are obtained. Analytical and numerical calculation of the conditions of the absolute stability for the piezo-actuator under random impacts are determined. The stationary set of points of intersection of the straight line with the hysteresis characteristic of the deformation is received.

References

1. J. Schultz, J. Ueda, H. Asada, *Cellular Actuators* (Butterworth-Heinemann Publisher, Oxford, 382 p. , 2017)
2. W.G. Cady, *Piezoelectricity*: *An Introduction to the Theory and Applications of Electromechancial Phenomena in Crystals* (McGraw-Hill Book Company, New York, London, 806 p., 1946)
3. W. Mason (ed.), *Physical Acoustics: Principles and Methods*, vol. 1. Part A. *Methods and Devices* (Academic Press, New York, 515 p., 1964)
4. K. Uchino, *Piezoelectric Actuator and Ultrasonic Motors* (Kluwer Academic Publisher, Boston, MA, 347 p., 1997)
5. S.M. Afonin, Structural-parametric model and transfer functions of electroelastic actuator for nano- and microdisplacement, in *Piezoelectrics and Nanomaterials*: *Fundamentals, developments and applications*, ed by I.A. Parinov (Nova Science Publishers Inc., New York, 225, 2015)
6. S.M. Afonin, A structural-parametric model of electroelastic actuator for nano- and microdisplacement of mechatronic system, in *Advances in Nanotechnology*, vol. 19, eds by Z. Bartul, J. Trenor (Nova Science Publishers Inc., New York, p. 259, 2017)
7. D. Zwillinger, *Handbook of Differential Equations.* Academic Press, Boston, 673 p. (1989).
8. V.A. Yakubovich, Eur. J. Control. **8**(3), 200 (2002)
9. S.M. Afonin, J. Comput. Syst. Sci. Int. **44**(2), 266 (2005)
10. S.M. Afonin, Dokl. Math. **74**(3), 943 (2006)
11. S.M. Afonin, J. Comput. Syst. Sci. Int. **47**(7), 111 (2008)
12. S.M. Afonin, Russ. Eng. Res. **28**(3), 203 (2008)
13. S.M. Afonin, Dokl. Phys. **53**(3), 137 (2008)
14. S.M. Afonin, Dokl. Math. **73**(2), 307 (2006)
15. S.M. Afonin, Russ. Eng. Res. **32**(7–8), 519 (2012)
16. S.M. Afonin, Russ. Eng. Res. **36**(6), 423 (2016)
17. S.M. Afonin, Mech. Solids **44**(6), 935 (2009)
18. A. Preisach, Z. Phys. **94**(5–6), 277 (1935)
19. S.M. Afonin, J. Comput. Syst. Sci. Int. **49**(1), 73 (2010)
20. S.M. Afonin, J. Comput. Syst. Sci. Int. **54**(3), 424 (2015)
21. S.M. Afonin, International. J. Phys. **5**(1), 9 (2017)
22. S.M. Afonin, Actuators. **7**(1), 1 (2018)
23. S.M. Afonin, Actuators. **8**(3), 1 (2019)
24. S.M. Afonin, Mech. Solids **49**(2), 196 (2014)
25. S.M. Afonin, International. J. Phys. **7**(2), 50 (2019)
26. S.M. Afonin, MOJ Ecology and Environmental Sciences. **3**(5), 306 (2018)
27. S.M. Afonin, Applied System. Innovation. **3**(4), 1 (2020)
28. H.S. Nalwa (Ed.), *Encyclopedia of Nanoscience and Nanotechnology*, 10 Vols (American Scientific Publishers, Los Angeles, 2004)

SAW Current Sensor with FeNi Film

G. Ya. Karapetyan, V. A. Kalinin, M. E. Kutepov, V. O. Kislitsin, and E. M. Kaidashev

Abstract Various designs of passive wireless surface acoustics wave (SAW) current sensors with a sensitive element in the form of a FeNi film or based on it are proposed and considered. Sensors with such films have a high sensitivity (the speed of the SAW changes 1/30000 when the current changes by 1 A) and therefore do not need magnetic cores and they can be installed directly on the conductive busbar.

Keywords SAW sensor · FeNi film · Interdigital transducer (IDT) · Parameter S_{11}

1 Introduction

In [1], magnetic field surface acoustics wave (SAW) sensors are described on the basis of changes of inductance in the gap in magnetic core, located around the current bar and also on the basis of changes in the capacitance of varicaps under the voltage induced in the coil wound on this magnetic core. Such sensors must have a magnetic circuit for their operation, which significantly increases the weight and dimensions of the sensor, as well as complicates its installation.

At the same time, such sensors are possible in which, under the influence of the magnetic field around the conductive bus, the changes of SAW speed are sufficient to detect the current in the bus at current in units of amperes. This becomes possible due to change of the SAW speed by magnetically sensitive films, deposited on the surface of the substrate, along which the SAW propagates under the action of elastic deformations, arising in the films owing to the magnetic field.

G. Ya. Karapetyan (✉) · M. E. Kutepov · E. M. Kaidashev
Laboratory of Nanomaterials, Southern Federal University, Rostov-on-Don, Russia
e-mail: gkarapetyan@sfedu.ru

V. A. Kalinin · V. O. Kislitsin
Scientific and Technical Center "Radio Engineering Devices and Systems" With Limited Liability, St. Petersburg, Russia

I. A. Parinov et al. (eds.), *Physics and Mechanics of New Materials and Their Applications*, Springer Proceedings in Materials 10,
https://doi.org/10.1007/978-3-030-76481-4_44

2 Current Sensor with Magnetically Sensitive FeNi Film

As shown in [2] for a magnetic field sensor based on FeNi films, the change in the SAW velocity is equal to $\Delta V/V = 0.0035\%$ (1/30000) for $LiNbO_3$ (*YX*/127°)-cut substrates, when the magnetic field strength changes by 10 Oe (current 1 A). The magnetic field strength near the busbar with current is defined as

$$\frac{4\pi\mu_0 aj}{4\pi} = \mu\ \mu_0\ a\ j\ =\ \mu\mu_0 a\frac{1}{ab} = \mu\mu_0\frac{1}{b}. \tag{1}$$

That is the magnetic field strength at the surface of the bus, $H = I/b$, where a is the thickness of the conductor, b is the width of the conductor, μ is a magnetic permeability, I is the current in the busbar.

In a flat conductor with a width of $b = 8$ cm and a thickness of $a = 5$ mm, at a current of $I = 10$ A, the magnetic field strength is $H = 10/0.08 = 125$ A/m $= 1.56$ Oe, and at a current of 100 A, $H = 15.6$ A/m. Calculations of the parameter S_{11} of the sensor in Fig. 1 show (see Fig. 2) that with a film length of 1000 SAW lengths at the central frequency, such a change in the SAW velocity is sufficient to noticeably change the frequencies of maxima and minima in the frequency dependence of parameter

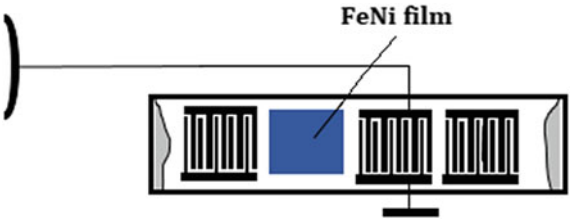

Fig. 1 Design of current sensor with FeNi film in acoustic channel

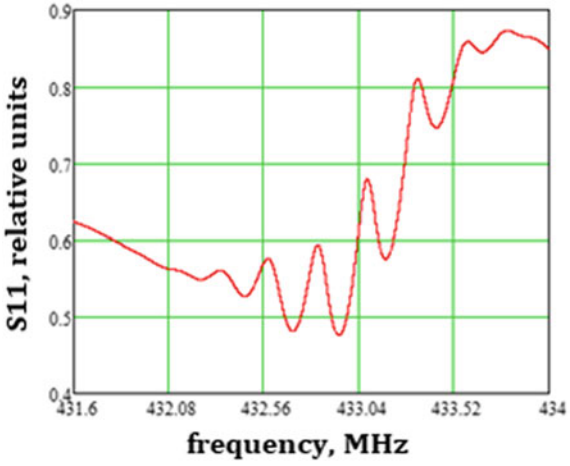

Fig. 2 Frequency dependence of parameter S_{11} for SAW sensor

S_{11}. The sensor is a delay line on surface acoustic waves, containing a receiving-transmitting interdigital transducer (IDT), exciting and receiving SAWs and reflective IDTs, located on both sides of it.

A magneto sensitive FeNi film is located between the receiving and transmitting IDT and one of the reflective IDTs, which, due to magnetostriction under the influence of a magnetic field, creates additional mechanical stresses on the substrate surface. It leads to a change in the SAWs velocity under the stresses. This, in turn, leads to a change in the frequency peaks on the frequency dependence of the parameter S_{11} (see Fig. 2). It is caused by that, the phase of the SAW, reflected from the reflective IDT, located at the site, where the SAW passes under the film, changes relative to the phase of the SAW reflected from the reflective IDT, located at the site, where the SAW passes on the free surface (see Fig. 1).

Figure 3 presents the change in the amplitude of the parameter S_{11} at a frequency of 433.29 MHz with a change in the magnetic field strength from 0 to 40 Oe. It corresponds to a change in the magnetic field induction from 0 to 0.004 T. In this case, the receiving-transmitting and reflecting IDTs are made thinned [3] and have 20 pairs of electrodes. Their lengths are equal to 340 and 260 SAW lengths at the central frequency, respectively. From this figure, it can be seen that the amplitude of the parameter S_{11} at a fixed frequency will change noticeably even at fields of 1–2 Oe, that corresponds to the current on the busbar equal to 10–20 A. Then this means that such a magnetic field sensor can be installed on the busbar without any magnetic wires, that will greatly simplify and reduce the cost of the magnetic field sensor (Fig. 4).

Figure 5 shows the reader circuit for a sensor that allows measuring an alternating magnetic field. The scheme works as follows. From the RF-generator with a frequency of 433.29 MHz (Fig. 5), which corresponds to the maximum of the parameter S_{11} at zero magnetic field, a signal is sent to the winding of the differential

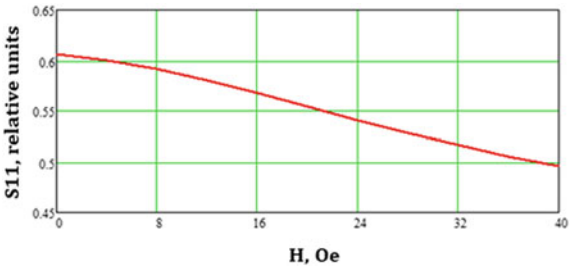

Fig. 3 Calculated dependence of the parameter S_{11} at a frequency of 433.49 MHz on the magnetic field. The length of the magnetically sensitive film is equal to 1000 SAW lengths at the central frequency

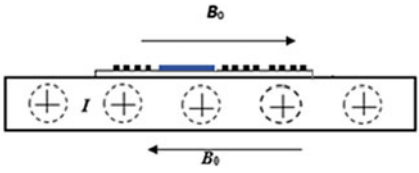

Fig. 4 Location of the current sensor with FeNi film on the busbar

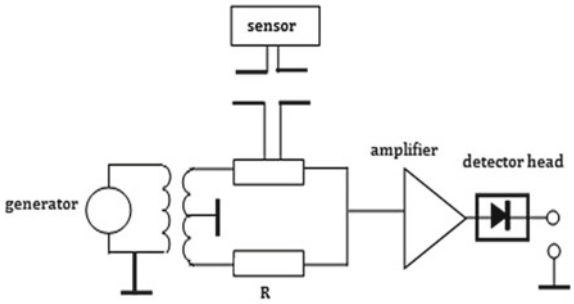

Fig. 5 Scheme of reader for sensor

transformer, and then goes to the secondary windings, and from them to the antenna and resistor *R*.

The antenna emits an electromagnetic signal in the direction of the sensor antenna under the action of an alternating magnetic field in accordance with Fig. 2. The sensor parameter S_{11} will change over time, which will cause the reader antenna impedance to change over time. This will lead to that the signals, supplied to the detector head, will not compensate each other and a signal will appear at the output of the detector head, the value of which will be the far greater than the parameter S_{11} of the sensor antenna changes. Therefore, an amplifier is needed to amplify the output signal, that increases the reading range. For example, at a frequency of 433 MHz, using two flat small-sized antennas, it was possible to obtain a signal amplitude at the reader output of about 20 mV using a 15 dB amplifier.

Since the dependence of the amplitude of the sensor parameter S_{11} depends almost linearly on the magnitude of magnetic field, a signal proportional to the change in the bus current will be observed at the output of the detector cooking. However, the change in the SAW speed does not depend on the sign of the magnetic field, a signal with double frequency will be observed at the output of the detector head. Therefore, at its output, it is necessary to provide either a frequency divider by 2, or a device that changes the polarity of the signal after each minimum of the signal. In this case, after each half-period, the sign of the signal will change and the original signal will be restored, i.e., the dependence of the current value in the bus on time, which can be used to judge current distortions in the network and measure current power and energy.

Such a reader is very suitable for measuring the current in the buses in the electrical cabinet, since the reading, formed by a continuous signal and all re-reflections from the walls of the cabinet, will not affect the current. The output of the reader will be a continuous time signal proportional to the current in the bus. In addition, the distance between the antennas in the cabinet can be made no more than 50 cm. It will significantly increase the signal at the output of the detector head and make it significantly higher than noise, that will improve the measurement accuracy. As follows from the reading method itself, when the frequency of the RF-generator corresponds to the maximum of the parameter S_{11}, the reference channel is not

needed, since the maximum voltage at the output of the detector head will correspond to the zero value of the bus current.

By installing the sensor, it is enough to select the frequency of the RF-generator so that the voltage amplitude at the output of the detector head is maximum. Then this frequency is fixed. Movement of the maximum of voltage output on detector head from this frequency will lead to a significant reduction of measurement accuracy. It is caused by that the amplitude of the output voltage of the detector head strongly depends on the position of the frequency maximum of the parameter S_{11} *versus* frequency of the RF-generator. Therefore, it is necessary that the frequency of the RF-generator always corresponds to the frequency of the maximum parameter S_{11}. But as the calculations show, it is necessary to measure temperature with an accuracy of 0.1 degrees, if lithium niobate substrates are used. However, there are no wireless temperature sensors with such an accuracy.

Therefore, it is necessary to use the ST-cut quartz substrate for sensors, in which the frequency goes away by only 0.14 MHz at a central frequency of 433 MHz when the temperature changes are equal to 100 °C. This means that if the temperature changes are by 5 °C, it does lead to a change in the measurement accuracy no more than a fraction of a percent. Therefore, a wireless sensor with a measurement accuracy of ± 2 °C is quite suitable for monitoring the frequency of the generator and will not lead to a decrease in the measurement accuracy. When using a quartz ST-cut substrate, the receiving-transmitting IDT will contain 340 pairs, and the reflecting IDT – 260 pairs of electrodes, in contrast to the lithium niobate substrate, since the square of the electromechanical coupling coefficient for quartz is almost 30 times less than that of lithium niobate and there is no need to thin out the IDT.

3 Conclusion

The presented research allows one to make the following conclusions:

1. The designs of magnetic field sensors based on magnetically sensitive films are proposed, allowing one to use sensors without magnetic cores, that will significantly simplify and reduce the cost of the current sensor.
2. The proposed single-frequency method of reading information of the deliverer is only suitable for quartz substrates ST-cut. It is caused by that the frequency drift at temperature measurement accuracy is ± 2°, but the frequency maximum of the parameter S_{11} is impossible to foresee. Therefore, the upper frequency limit for such sensors is limited by 1 GHz, and also there is no need for a reference channel.

Acknowledgements This research work is supported by Southern Federal University research project No.07/2020-06-MM.

References

1. V.O. Kislitsyn, V.A. Kalinin, G. Ya. Karapetyan, V.F. Kataev, N.V. Ermolaeva, Vestnik of National Res. Nucl. Univ. (MIFI), **9**(2), 177 (2020) (In Russian)
2. J. Tong, Y. Wang, S. Wang, W. Wang, Y. Jia, X. Liu, Appl. Sci. **7**, 755 (2017)
3. D. Morgan, *Surface Acoustic Wave Filters With Applications to Electronic Communications and Signal Processing* (Academic Press, Elsevier, 2007).

About Monitoring of the Medium State by the Parameters of the Surface Wave

Igor Andjikovich, Valery Kalinchuk, Irina Michailova, and Andrey Sedov

Abstract A method of low-frequency continuous monitoring of the stress-strain state of the construction is proposed, based on the analysis of the parameters of the surface wave field created by the shock effect, through the use of acceleration sensors (accelerometers) and ferroelectric strain sensors. The latter are made using thin-film technology and are ultra-miniature broadband dynamic strain sensors of the generator type. The possibilities of using sensors in stress state monitoring systems are discussed. To process the recorded signal, a special method is used based on the use of optimal orthogonal decompositions of the signal in the basis, adaptively tuned on the training sample. A series of experiments have been carried out to demonstrate the high efficiency of the method.

Keywords Non-destructive testing · Accelerometer · Films sensor · Low-frequency continuous monitoring · Surface wave field · Bi-spectral method

1 Introduction

The possibility of non-destructive testing of the stress-strain state (SSS) of structures, defects in various mechanical objects is relevant, which determines the need to create new methods for monitoring the "health" of complex structures to increase the reliability of their operation and prevent emergencies. In connection with the modern development of the technology for the production of new materials and the increased requirements for the characteristics of parts and assemblies, it becomes necessary to create simple and effective methods of constant control (continuous monitoring) of the state of the object. The technique used for registering the state of a product, namely, internal stresses, dynamics of defects, especially in multi-element

I. Andjikovich
I. I. Vorovich Mathematics, Mechanics and Computer Sciences Institute, Southern Federal University, Rostov-on-Don, Russia

V. Kalinchuk (✉) · I. Michailova · A. Sedov
Southern Scientific Center of Russian Academy of Sciences, Rostov-on-Don, Russia
e-mail: vkalin415@mail.ru

I. A. Parinov et al. (eds.), *Physics and Mechanics of New Materials and Their Applications*, Springer Proceedings in Materials 10,
https://doi.org/10.1007/978-3-030-76481-4_45

design, by analyzing surface vibrations assumes the presence of a large number of control points in various nodes and structural elements [1–6]. The overwhelming majority of such systems use accelerometers [1–7]. However, in some cases, the use of accelerometers is impractical and often impossible. Especially when it comes to monitoring the integral parameters of the controlled object. In such cases, it is advisable to use strain gauges that allow obtaining "integral information" about the state of the object. Of considerable interest are miniature generator-type ferroelectric film sensors with a small intrinsic mass, a wide range of working bands at a relatively low cost [8, 9]. They are designed using thin-film technology and are a thin ferroelectric film deposited on a metal foil. Thus, an object was obtained that combines the high piezoelectric characteristics of ceramics with the high strength of the metal to mechanical stress. These sensors have shown high efficiency when used in systems for monitoring the state of bar structures [9–11]. In this work, we propose a system for monitoring the stress state of a structure based on the use of thin-film ferroelectric sensors. The object of monitoring is the wave field on the surface of a square-section aluminum rod subjected to a force applied in its center. The surface wave field is created by an impulse source located at one of the ends of the rod. Studies have shown that small changes in the load (5, 10, 20, 50 g) lead to a significant change in the wave field, both in amplitude and in phase characteristics. The complex nature of changes in the parameters of the wave process does not allow sufficient monitoring of their relationship with the deformation of the object. To establish a clearer connection between the wave field and the load, the bi-spectral method is used, which converts the signal coming from the sensor in the form of an amplitude-time diagram to a certain point in the recognition feature space. The studies carried out have shown the high sensitivity of the thin-film sensor in comparison with the accelerometer.

1.1 Research Purpose

The chapter investigates a system for monitoring the stress state of a structure based on the use of thin-film ferroelectric strain gauges and accelerometers. The object of monitoring is the wave field on the surface of an aluminum square beam.

1.2 Research Scope

At this study, we consider the following frameworks of the problem:

(i) a description of the experimental setup;
(ii) results of experimental studies;
(iii) bi-spectral method of processing the results;
(iv) 2-D presentation of structural stress monitoring results.

2 Research Method

To study the effectiveness of using various methods for controlling of the surface wave field parameters, a multifunctional measuring setup was created based on the use of an accelerometer and a generator-type ferroelectric film sensor (Fig. 1). The setup allows one to conduct research, compare signals and build amplitude-time diagrams with sensors of various types and, thereby, assess the change in the surface wave field. A comparative analysis of the operation of various types of sensors has been carried out. In the result of the research, comparative diagrams were built, on the basis of which the degree of sensitivity of strain sensors and accelerometers to be changed in the stress state was investigated.

2.1 Description of the Experimental Setup

The sensors are located on the surface of the square beam. The stress state in the structure was created due to the action of a massive body suspended on threads. For experimental studies was established measuring system composed of a highly sensitive accelerometer PCB ICP 352A60 and ADC ZetLab4400 (control acceleration of point), the original thin film sensor generating type and booster charge B & K 2026 (control displacement of point), 16-channel ADC L-Card E-14- 140 (the analog signal is converted into a digital file). A computer is used for its processing. The scheme of the experiment using a miniature film sensor and an accelerometer is shown in Fig. 2.

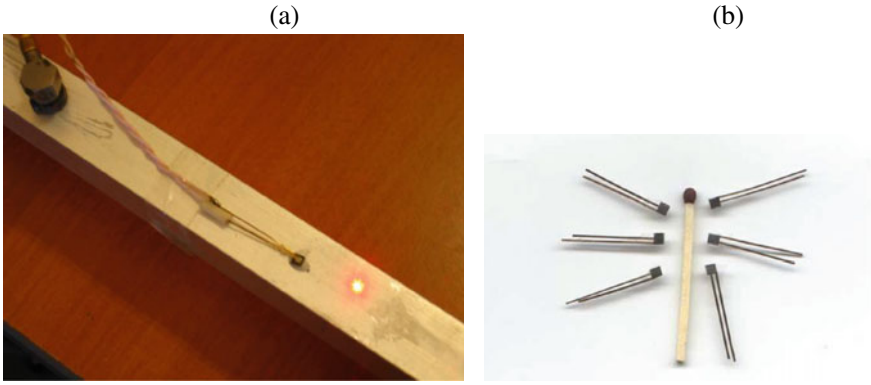

Fig. 1 **a** Accelerometer PCB ICP 352A60 (left) and original thin-film sensor (right), **b** thin-film sensors compared to a match [8–11]

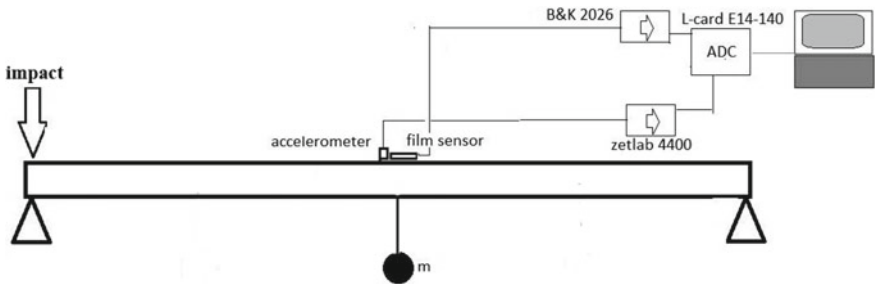

Fig. 2 Scheme of multifunctional experimental measuring system

2.2 Experimental Research Results

During the experiments, the excitation of oscillations in the model was carried out by an electromagnetic shock device. Thus, the impulse method of influencing the object was simulated. The signal taken from the strain sensor was amplified by a B&K 2026 charge amplifier and processed by an ADC. Figure 3 shows a typical amplitude-time diagram (ATD) of the acceleration of a point on the surface of the medium in the time interval 0.25 – 0.65 ms. Digits 1, 2, 3, 4, and 5 mark the curves corresponding to loads of 0.5 g, 10 g, 20 g, and 50 g. As follows from the graphs, the wave field has a complex multimode structure [12–14].

As follows from the graphs, a small change in the load leads to significant changes in both the amplitude and phase parameters of the surface waves. However, there is

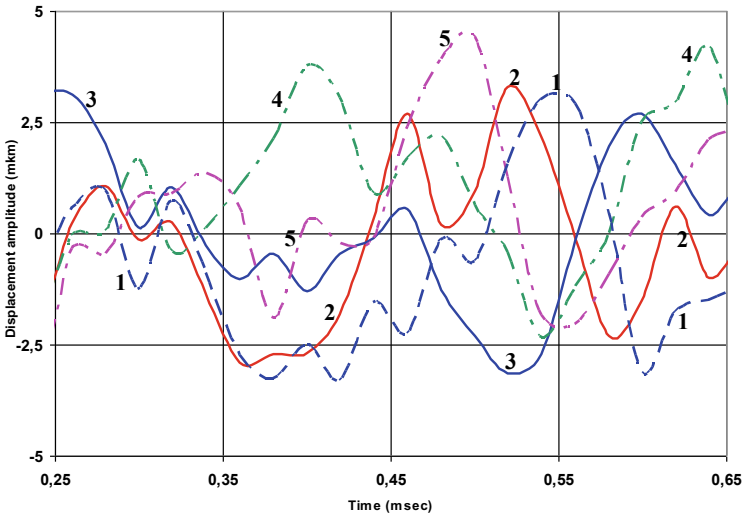

Fig. 3 ATD acceleration at a point on the surface of the medium at different values of the load. Digits 1, 2, 3, 4 and 5 correspond to the load of 0 g, 5 g, 10 g, 20 g and 50 g, respectively

no direct relationship between the amplitude-phase changes and the magnitude of the impact force on the beam.

Figure 4 shows a typical ATD of deformation at a point on the surface of the medium in the time range of 0.25 – 0.65 ms. Digits 1, 2, 3, 4 and 5 mark the curves corresponding to the load of 0 g, 0.5 g, 10 g, 20 g and 50 g. It can be seen that in this case a small change in the load leads to significant changes in amplitude, but small changes phase parameters of the wave field. A special feature of the film sensor is its high sensitivity to the low-frequency component of the field. It should be noted that due to the design features of the deformation sensor (Fig. 5a), namely, the absence of added mass, which is typical for a classical accelerometer (Fig. 5b), the ATD of the film sensor is more uniform, while as the ATD of the accelerometer is replete with various resonances.

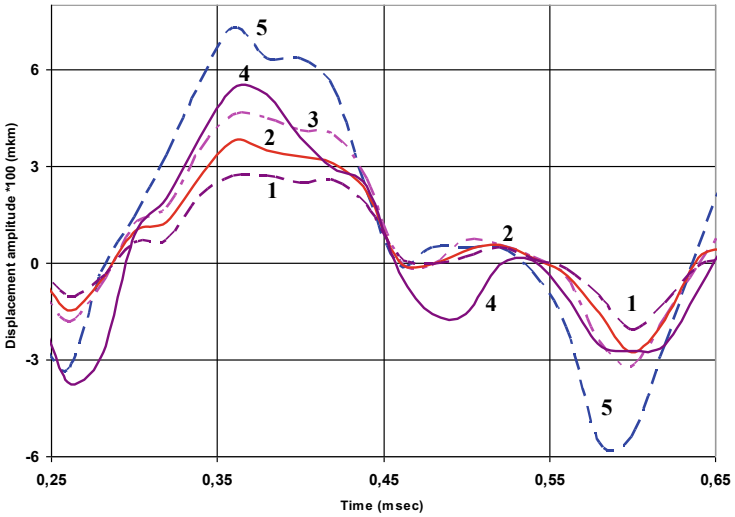

Fig. 4 ATD deformation at a point on the surface of the medium at different values of the load. Digits 1, 2, 3, 4 and 5 correspond to the load of 0 g, 5 g, 10 g, 20 g and 50 g, respectively

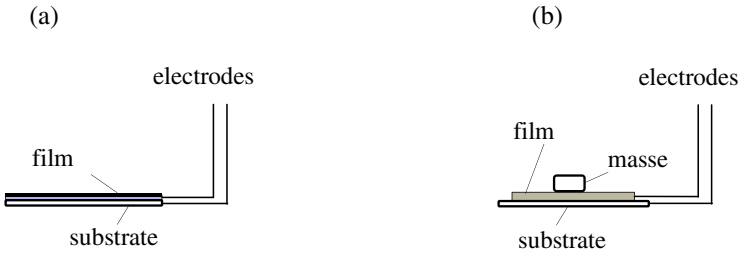

Fig. 5 Designs of deformation sensor (**a**) and piezoelectric accelerometer (**b**)

This may indicate a wider spectrum of influence of various vibration modes (more resonances) when controlled using accelerometers than measurements made by film sensors. Nevertheless, a certain correlation of the peaks is observed, which in many cases is sufficient to register even insignificant changes in the mechanical state of the system. It should be noted that the comparative tests carried out confirmed the anomalous sensitivity of the film sensors in the low frequency range. This makes it possible to register practically static deformation changes by the sensor, which, in contrast to traditional accelerometers, makes it indispensable for monitoring low-frequency and deformation overloads of structural elements.

Successful application of the proposed method for monitoring the SSS of the samples requires a certain mathematical processing of the recorded signal in order to more transparently visualize the parameters that determine the stress state. The most effective approaches to mathematical processing of the recorded signal include:

(i) traditional spectral approach;
(ii) approaches of correlation signal processing;
(iii) approaches, based on the use of artificial neural networks;
(iv) statistical approaches and models;
(v) wavelet transformation of signals;
(vi) optimal orthogonal decomposition of signals in the basis, adaptively tunable for the training sample.

In this work, the latter approach is used as one of the most promising ways. It has a number of advantages, the main one of which is the adaptive adjustment of the orthogonal basis, in accordance with the criteria for the best defect recognition**.**

3 Bi-spectral Method

To solve the problems of stress-strain state (SSS) diagnosis, we have used the method of image recognition [15–17]. The output measured value represents the scalar function of the response f(t), t ∈ [0, T_H] to the probing action F. The time interval T_H is sufficient for the stable detection of the emerging diagnosed states.

The training sample **f** is formed from separate graphs $f_i(t)$ obtained for various types of SSS in the construction, but for one type of probing non-destructive action F. Each graph $f_i(t)$ can be considered as a column-vector of real values $f_i = [f_{i1}, f_{i2}, f_{i3}, \ldots, f_{iN}]^T \in \mathbf{R}^N$ of response change in time. Discretization step Δt in time is selected in accordance with the discretization theorem [17].

Let n be the number of recognizable types of the defect in the construction. To each of the types, we associate a column-vector $f_i \in \mathbf{R}^N$. Then the test sample for n variations of the defect will be a matrix $\{f_1, f_2, f_3, \ldots, f_n\} \in \mathbf{R}^{N\times n}$. Initially, a set of vectors $\{f_1, f_2, f_3, \ldots, f_n\}$ is linearly dependent. This is due to the excessive dimensionality of the vectors $f_i \in R^N$, precision of the graph forms $f_i(t)$.

The construction of the diagnostic space state **D** is the finding an orthogonal transformation $X \in \mathbf{R}^{N\times m}$ of matrix $\mathbf{f} \in \mathbf{R}^{n\times N}$ into matrix $\mathbf{A} \in \mathbf{R}^{n\times m}$ of the

following form $\mathbf{A} = \mathbf{f}\mathrm{X}$, excluding excessive dimensionality $\mathbf{f}$. The matrix $\mathrm{X} = [\chi_1, \chi_2, \chi_3, \ldots, \chi_m]$ defines a linear subspace in $\mathbf{R}^N$.

At the same time, the vectors $\chi_1, \chi_2, \chi_3, \ldots, \chi_m$ form an orthonormal basis in $\mathbf{R}^N$ and for the matrix X, it is true that $\mathrm{X}^T\mathrm{X} = I_m$. Conventionally, the matrix X can be considered as a matrix of orthogonal compression of linear space $\mathbf{R}^N$ into the space $\mathbf{R}^m$. Using X, vectors $f_i \in \mathbf{R}^N$ of responses are transformed into images $A_i \in \mathbf{R}^m$, and $m < N$. In this case the investigated matrix of responses $\mathbf{f}$ transformed into the matrix of images $\mathbf{A} = [A_1, A_2, A_3, \ldots A_n]^T \in \mathbf{R}^{n\times m}$. In general, the orthogonal decomposition of the original vectors $f_i \in \mathbf{R}^N$ in the basis X can be represented as $f_i = \mathrm{X}A_i + A_0$, where A_0 is constant component of the transformation. The orthonormal basis $\chi_1, \chi_2, \chi_3, \ldots, \chi_m$ is adaptively adjustable and dependent on recognizable sample $\{f_1, f_2, f_3, \ldots, f_n\} \in \mathbf{R}^{N\times n}$. When determining the basis, a complex of optimization problems is solved:

1. The best reproducibility: $\left\|\mathbf{f} - \mathbf{A}\,\mathrm{X}^T - \mathbf{A}_0\right\|_2 \to min$, where $\mathbf{A}_0 \in \mathbf{R}^{n\times N}$ is the matrix of constant transform components, composed of the vectors A_0;
2. The orthonormality of the basis: $\left\|\mathrm{X}^T\mathrm{X} - I_m\right\|_2 \to min$;
3. The best distinguishability: $d^2(\mathbf{A}) = \frac{1}{m^2-m}\sum\limits_{\substack{i,j=1\\ i\neq j}}^{m}\left\|A_i - A_j\right\|_2 \to max$.

For the interpretation of diagnostic observability, the images $A_i = (a_{i1}, a_{i2}, ..., a_{im}) \in \mathbf{R}^m$ of the response functions $f_i(t)$ from the training sample of measurements, including all states of the object, diagnostics of which are necessary, are located in the diagnostic state space $\mathbf{D}$. In the space $\mathbf{D}$, the boundaries of the image clusters corresponding to each individual diagnosed state of the object are determined. For simplicity of the physical interpretation, we have realized the SSS-control of samples by images in two-dimensional feature space. As the two coordinates of image, we choose those that have the maximum spread. As investigation have shown, this dimension of feature space is sufficient for conducting qualitative diagnostics of the SSS of samples.

4 Results and Discussion

Figures 6, 7, and 8 show the results of constructing characteristic diagnostic spaces and the location of images for monitoring the stress-strain state of a beam using a film sensor (Fig. 7) and an accelerometer (Fig. 8) with separate mathematical processing of signals. Figure 6 shows the results of constructing diagnostic feature spaces during joint processing of signals received from the accelerometer (circles) and from the film sensor (asterisks). Each point in the graph corresponds to an experiment performed with a mass of 0 g (red), 5 g (blue), 10 g (green), 20 g (black) and 50 g (raspberry). As can be seen from the graphs, there is a certain scatter of readings. Moreover, it is larger for small values of mass, and less for large values of mass. However, the graphs demonstrate clear stress recognition when monitored with both an accelerometer and

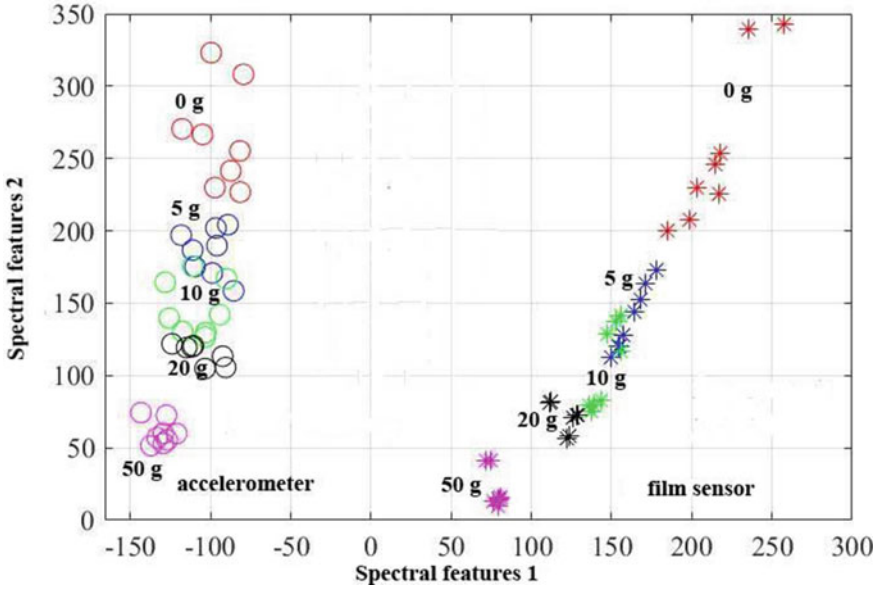

Fig. 6 Location of images in the recognition space for samples with different load weights

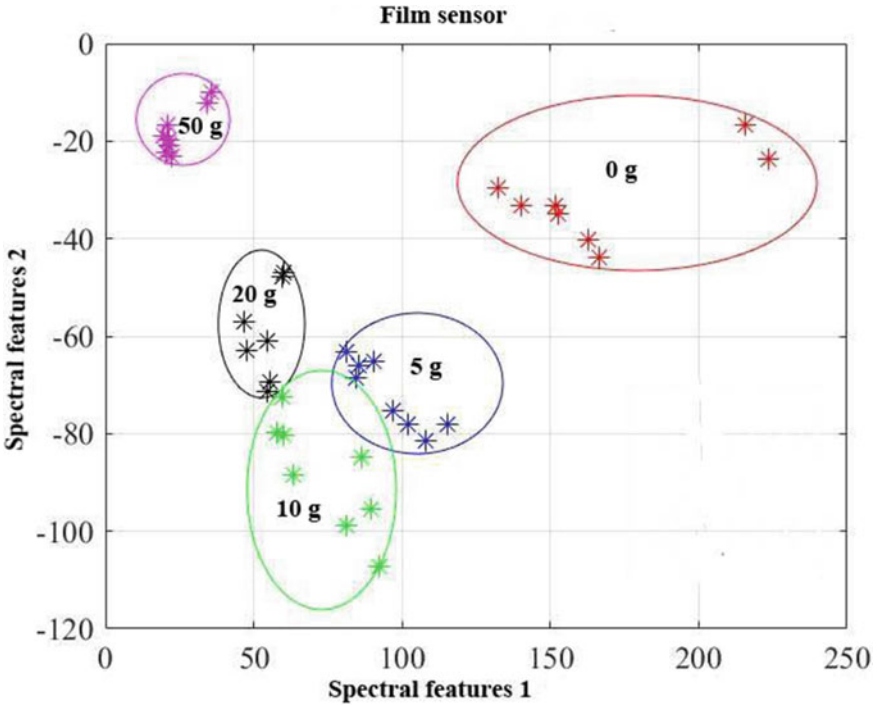

Fig. 7 Location of images in the space of recognition for samples with different load weights

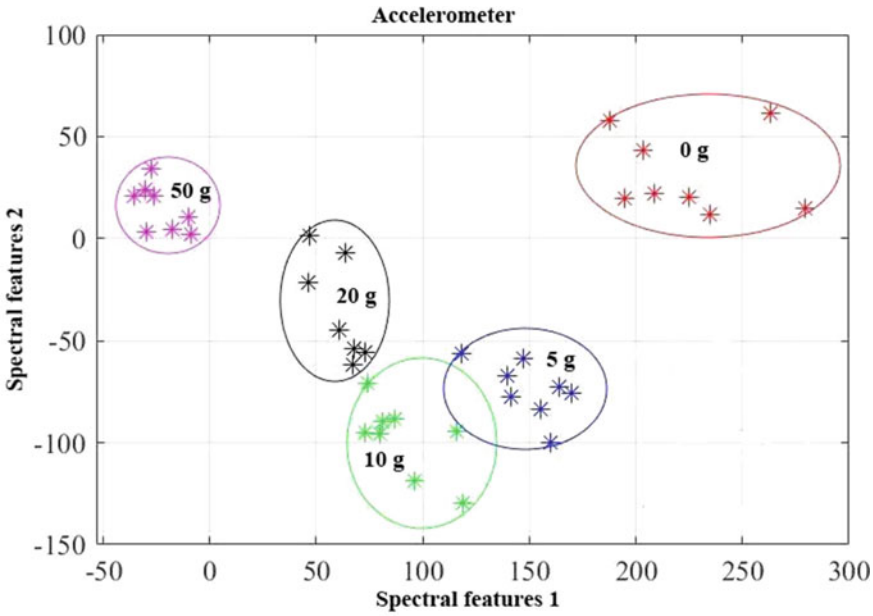

Fig. 8 Location of images in the space of recognition for samples with different load weights

a film sensor. In this case, the sensor demonstrates greater sensitivity to changes in the stress state by two spectral features, while the accelerometer is characterized by a change in only one spectral parameter.

The result of the location of the images in the diagnostic feature space for these samples is shown in Fig. 7. Here, clusters are shown for different values of the load in the case when the wave field is recorded by a film sensor. As can be seen from the figure, there is a clear distribution of images in the recognition space depending on the value of the mass. In this case, the dependence of the spread of images on the value of the load is observed. The largest scatter of images occurs in the case of an unstressed state, the smallest takes place at the maximum value of the mass. In this case, both spectral features are involved in recognition.

Figure 8 shows clusters for different values of the acting force in the case when the wave field is recorded by an accelerometer. As can be seen from the figure, in the case of the accelerometer, there is a clear distribution of patterns in the recognition space depending on the value of the mass. Similarly, to the previous one, there is a relationship between the scatter of images and the load value. The largest scatter of images occurs in the case of an unstressed state, the smallest takes place at the maximum value of the mass. In this case, both spectral features are involved in recognition. As can be seen from the figure, there is a clear distribution of images in the recognition space depending on the size of the load mass. This confirms the effectiveness, in terms of clustering, of the selected feature space. Studies have

shown that the specified dimension of the feature space is sufficient for high-quality diagnostics of samples.

5 Conclusion

A method of continuous monitoring of the SSS of objects is proposed, based on the control of changes of the surface wave field parameters. The method is implemented on a sample that is a square metal beam. SSS in a beam is created by the action of the weight of some massive object attached to the beam.

To establish a clearer connection between the wave field and the load, the bi-spectral method is used, which converts the signal coming from the sensor in the form of an amplitude-time diagram to a certain point in the recognition feature space.

The implementation of the method on a metal beam showed a high sensitivity of the method to changes in the stress-strain state of the beam.

The experiments carried out confirmed the high sensitivity of the film sensor to the low-frequency component of the recorded signal. Thus, the possibility of registration by the sensor of static deformation changes that are important for practice is realized, which, in contrast to traditional accelerometers, makes it indispensable for monitoring low-frequency and deformation overloads of structural elements.

Acknowledgements Research was financially supported by Southern Federal University, grant No. VnGr-07/2020-04-IM (Ministry of Science and Higher Education of the Russian Federation).

References

1. R.S. Sharpe (Ed.) *Research Techniques in Nondestructive Testing* (Academic Press, London and New York, 356 p., 1970)
2. C.C. Fuller, P.A. Nelson, S.J. Elliott, *Active Control of Vibration, Academic Press* (Harcourt Brace & Company Publishers, New York, USA, 1997)
3. A. Preumont, *Vibration Control of Active Structures: An Introduction* (Kluwer Academic Publishers, Norwell, MA, USA, 2002)
4. D.J. Inman, *Vibration with Control* (Wiley, West Sussex, England, 2006)
5. J.P. Amezquita-Sanchez, A. Dominguez-Gonzalez, R. Sedaghati, R.d.J. Romero-Troncoso, R.A. Osornio-Rios. Mech. Adv. Mater. Struct. **21**, 23 (2014)
6. Z. Zhao, Ceram. Int. **47**(4), 4389 (2021)
7. A.J. Fleming, R. Moheimani, *Piezoelectric Transducers for Vibration Control and Damping* (Springer-Verlag, London Limited, 2008)
8. S.V. Biryukov, Yu.I. Golovko, V.M. Mukhortov, Vl. M. Mukhortov, E.V. Sviridov, Meas. Tech. **35**(4), 455 (1992)
9. Yu.V. Esipov, V.M. Mukhortov, Tech. Phys. **54**(1), 78 (2009)
10. Yu.V. Esipov, V.M. Mukhortov, I.I. Poida, Russ. J. Nondestr. Test. **46**(7), 533 (2010)
11. Y.V. Esipov, S.V. Biryukov, S.I. Masychev, V.M. Mukhortov, Meas. Tech. **59**(4), 423 (2016)

12. T.I. Belyankova, V.V. Kalinchuk, Izvestiya Akademii Nauk. Mechanika Tverdogo Tela **6**, 83 (1994). ((in Russian))
13. T.I. Belyankova, V.V. Kalinchuk. Prikladnaya Matematika i Mechanika, 57(4), 123, (1993) (in Russian).
14. T.I. Belyankova, I.E. Andjikovich, D.N. Shejdakov, Vestnik Yuzhnogo Nauchnogo. Centra RAN **3**(3), 3 (2007) (in Russian)
15. O.V. Bocharova, A.V. Sedov, I.E. Andjikovich, V.V. Kalinchuk, Russ. J. Nondestr. Test. **52**(7), 377 (2016)
16. O.V. Bocharova, V.V. Kalinchuk, A.V. Sedov, I.E. Andjikovich, in *Proceedings of the 2015 International Conference on Physics and Mechanics of New Materials and Their Applications, devoted to 100-th Anniversary of the Southern Federal University*, eds. by I.A. Parinov, S.-H. Chang, V. Y. Topolov (Nova Science Publishers, New York, 2016)
17. O.V. Bocharova, I.E. Andjikovich, A.V. Sedov, V.V. Kalinchuk, Meas. Tech. **60**(9), 957 (2017)

Prospects for the Use of Hydroacoustic Tools Based on Nonlinear Interaction of Acoustic Waves in Underwater Archeology

I. A. Kirichenko and I. B. Starchenko

Abstract The shallow water environment is one of the most dynamic elements, including coastal zones subjected to rapid sedimentary flows and a significant focus for human activity throughout history. Coastal zones are characterized by shallow water, strong waves, strong currents and a large tidal range, as well as the presence of shallow gas, which can severely restrict the penetration of sound. As a result, such areas are rarely explored, that is unfortunate, since it is known that the land-sea transition areas are rich in archaeological features. Obtaining information about the bottom structure requires the use of tools that are used to emit an acoustic signal with a specific physical parameter, such as output power, signal frequency, and signal duration. Typical frequencies of such acoustic systems are in the range from 10 to 200 kHz. Currently, a new class of underwater acoustics equipment is being developed, namely active location hydroacoustic devices with parametric arrays and transducers. The narrow beam pattern of the parametric array allows to significantly increase the accuracy and angular resolution at short and medium distances of modern sonar devices, such as profilers. The absence of side lobes combined with a narrow directivity minimizes (often almost completely eliminates it) reverberation interference from the sea surface and bottom, which makes it possible to create precision sonar devices based on parametric arrays for marine archaeological work. In order to consider the parametric method of acoustic radiation formation, it is necessary to briefly consider the physical foundations of nonlinear acoustics, since many physical phenomena in the process of acoustic wave propagation cannot be described linearly. Such phenomena include cavitation, radiation force, and a number of others. Based on the results of a methodology for the evaluation of energy parameters of acoustic wave propagation, technical characteristics of profiler can be assessed, such as operating frequency range, the energy potential in the given hydrological conditions, the parameters of the transmitted signal, including the signal duration and sounding period, noise conditions, the acoustic properties of bottom sediments, which will

I. A. Kirichenko (✉)
Southern Federal University, Taganrog, Russia
e-mail: ikirichenko@sfedu.ru

I. B. Starchenko
Parametrika LCC, Taganrog, Russia

I. A. Parinov et al. (eds.), *Physics and Mechanics of New Materials and Their Applications*, Springer Proceedings in Materials 10,
https://doi.org/10.1007/978-3-030-76481-4_46

significantly expand the use of hydroacoustic tools in the interests of underwater archaeology.

Keywords Sea bottom · Stratification · Profiler · Parametric array · Directivity · Kepstrum

1 Introduction

Acoustic profilers are widely used as a tool for creating maps of the seabed, studying the structure of the upper layers of the seabed, as well as in the interests of underwater archaeology [1]. The mapping of the sea floor is almost always carried out with the help of acoustic systems. The use of optical and electromagnetic systems for this task is limited by the fact that optical and electromagnetic waves do not propagate under water deeper than 10–50 m due to the absorption of wave energy by the aquatic environment [2]. Modern systems for mapping the seabed often use a single operating frequency [3]. However, acoustic waves with different frequencies interact differently with the sea floor or objects. For example, high-frequency sonar can accurately measure the depth and register the topography of the upper edge of the seabed, giving almost no information about the structure of the bottom layers. The structure of bottom layers is better observed at lower frequencies, because of frequency dependence of sound absorption and, consequently, a decrease in the energy absorption of acoustic waves at lower frequency. Low-frequency sonars allow us to study the upper layers below the sea floor, the thickness of which usually reaches several tens of meters. Such acoustic systems allow us to determine the physical properties of the seabed and identify the geological layers below the seabed [4]. The structure of bottom sediments is determined by measuring the time elapsed since the receipt of acoustic energy reflections at the boundaries between layers with different acoustic properties.

2 Methods

Acoustic systems have been a major tool of oceanography and marine geology for many years. From a geological point of view, underwater acoustics can explore three distinct zones; surface, subsurface, and deep sedimentary layers. The cross-section of the seabed is usually a ratio between three zones, the depth of penetration: the surface of the seabed (less than 1 m), the surface layers (up to 100 m) and the deep layers (over 100 m) [5]. Obtaining information about these zones requires a variety of instrument design to emit an acoustic signal with a specific physical parameter, such as output power, frequency, and signal length. For example, single-beam echo sounders with a frequency range from 100 to 200 kHz are designed to obtain information about the topography of the seabed surface and determine the

exact depth. To ensure the penetration of acoustic waves into the surface layers of the seabed, it is necessary to use a low-frequency signal with high energy. Low-frequency systems with a frequency range from 10 to 20 kHz ensure the penetration of acoustic waves into surface layers of more than 10 m [6].

The function of the profiler is to record echoes from the interface between layers of sedimentary rocks, which correspond to differences in the acoustic impedance of the layers. Good horizontal resolution requires a very narrow-angle antenna directivity characteristic, which depends on the size of the antenna and the frequency of the acoustic waves. The use of parametric arrays in hydroacoustic equipment based on the nonlinear interaction of acoustic waves makes it possible to increase information content and accuracy in detecting underwater objects and determining the structure of the seabed due to the high directivity and low level of the side field.

With all the advantages of using nonlinear effects and hydroacoustic systems with a parametric radiation mode for profiling the bottom and bottom sediments, the disadvantage is the small area of the bottom surface, voiced by the radiating antenna of the profiler, which leads to the need to choose the method of viewing space and sensing modes of the parametric profiler with a vertical profiling scheme and taking into account critical angles [7].

To obtain a picture of the bottom structures in a parametric profiler, a survey method can be selected associated with the movement of the receiving-emitting antenna system of the profiler due to the movement of the antenna carrier. The movement of the carrier of the acoustic antenna system allows one to create a profile of the vertical cross-section of sedimentary structures, obtained as an image of the boundaries between layers. The scheme of scanning the bottom structures when the antenna carrier moves is shown in Fig. 1.

Simultaneous scanning of the beam pattern in the transverse plane of the radiating antenna system allows the band to be voiced on the bottom surface and provides penetration into the surface layers of the seabed.

3 Theory

In practical implementation, high efficiency in hydroacoustic systems with parametric antennas is achieved in the case of formation of highly directional radiation. The directivity pattern R_θ of such antenna in the parametric mode is well described by the expression [8]:

$$R_\theta = exp\left[-\frac{\left(\frac{k1+k2}{4}a \bullet \theta\right)^2}{6}\right] \tag{1}$$

where k_1, k_2 are wave numbers on the pump frequency, a is the array aperture, Θ is the opening angle.

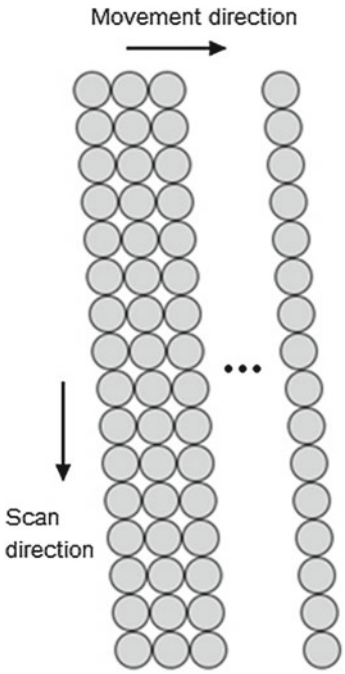

Fig. 1 Scanning when the antenna carrier moves

Theoretical consideration of the problem allows one to systematize the phenomena that determine the process of nonlinear interaction of acoustic waves, as well as to consider a number of hydrophysical inhomogeneities that have the greatest impact on the directivity of hydroacoustic systems with parametric antennas in real conditions.

As noted above, the directivity characteristic is one of the most important technical characteristics of a parametric antenna. The radiating antenna of the profiler is, as a rule, a multi-channel antenna array, while each of the channels is a line of individual piezoelectric elements. The distance between the acoustic axes of the elements is the same. Such antenna systems are called equidistant.

4 Cepstral Analysis of Echo Signals

In the case of a hydroacoustic remote sensing system operating in shallow water, the received echo signal is characterized by multiple re-reflections due to the small distance between the surface and the bottom. In addition, interference creates difficulties for analyzing and processing echoes from the layered structure when profiling bottom structures due to multiple re-reflections, as well as the effects of overlapping echo pulses. When a parametric array emits a probing pulse, it is reflected from two interfaces. If the distance between the interface boundaries exceeds half the spatial length of the emitted signal, then the echo pulses are distinguishable. In the case

when the spatial dimensions of the layer are such that the acoustic pulse completely overlaps the layer, the echo pulses are superimposed.

Recovering a signal that has been distorted both in frequency and time due to the effects of multiple re-reflections and noise is a common problem encountered in profiling bottom structures. In the vertical profiling scheme of bottom structures, the echo signal reflected in the opposite direction is processed. At the same time, the distance resolution when using a tonal probing pulse is determined by half of its duration [9].

When defining a filtering procedure to separate signals that have been non-additively combined, such as by multiplication or convolution, the components of the echo signal are usually more difficult to separate, and in many cases, it is impractical to use a linear system for the filtering procedure.

The essence of the used cepstral method is explained as follows. Let us have two almost identical signals, $S_1(t)$ and $S_2(t-\tau)$, delayed one relative to the other. The total signal $S(t)$ can be represented as [10]:

$$S(t) = S_1(t) + S_2(t-\tau) \tag{2}$$

In the result of the fast Fourier transform (FFT) and the corresponding z-transform, the total signal $S(\omega)$ will take the form, described by the expression [10]:

$$S(\omega) = S_1(\omega) + S_2(\omega)exp(-i\omega\tau) = S(z) \bullet S[1 + exp(-\omega\tau)] \tag{3}$$

The resulting product can be represented as a convolution of two-time functions described by an expression of the form [10]:

$$S(t) = S_1(t) \otimes S_2(t) \tag{4}$$

In this case, two-time domain functions are collapsed together, with one function representing a forward signal and the other a time-delayed signal. In the frequency domain, the Fourier transform of two functions is multiplied. Since the Fourier transform is not band-limited, the two functions occupy the same frequency band, and frequency-dependent filtering cannot be used to remove the unwanted function. Taking the logarithm of the multiplied functions and the inverse Fourier transform to the cepstral (time) domain results in functions that now intersect in a region or regions where both of their amplitudes are relatively small. In the cepstral region, normal filtering can be applied to remove what corresponds to the unwanted function. The required function, the transmitted signal, can be partially reconstructed by taking the Fourier transform of what remains in the cepstral region, exponentiating, and then the inverse Fourier transform. Later on, in the result of inverse Fourier transform from the resulting logarithm, a signal may be received, referred to as kepstrum.

The kepstrum of the received signal with (n) is determined as follows [10]:

$$C(n) = F^{-1}\{logF\{s(n)\}\} = F^{-1}\{logF\{S_1(n) \otimes S_2(n)\}\} = C_{S_1}(n) + C_{S_2}(n) \tag{5}$$

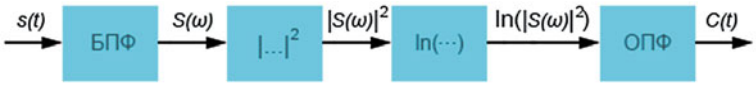

Fig. 2 Algorithm cepstral analysis

where $S_1(z)$ and $S_2(z)$ are the z-transformations of $S_1(n)$ and $S_2(n)$; $C_{S1}(n)$ and $C_{S2}(n)$ are the kepstrum of $S_1(n)$ and $S_2(n)$.

The algorithm of cepstral analysis of the total signal is shown in Fig. 2.

In practice, a power kepstrum is effective, if the wavelet and pulse sequence, whose convolution makes up the composite data, occupy different frequency ranges. Thus, it is proposed that the power kepstrum of the data sequence is the square of the inverse z-transform of the logarithm of the square magnitude of the z-transform for data sequence.

5 Results and Discussion

Figure 3a shows the theoretical expression of the directivity of the parametric array R_θ based on the Khokhlov–Zabolotskaya–Kuznetsov model [8], as well as the results of experimental studies of the directional properties of the parametric antenna, for which the wave numbers at the pump frequencies and the size of the pump transducer aperture corresponded to the values accepted for calculations according to the theoretical model. The results of experimental studies shown in Fig. 4b confirm the regularities of the formation of directional properties of a parametric antenna, described in detail in [8].

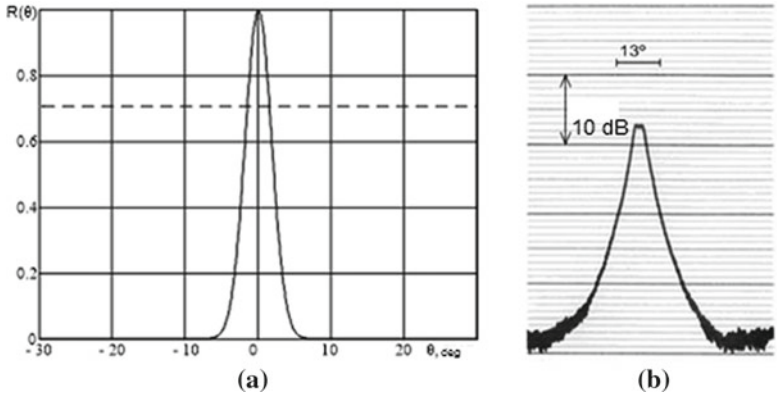

Fig. 3 Directional characteristics of a parametric radiating antenna: **a** theoretical; **b** experimental

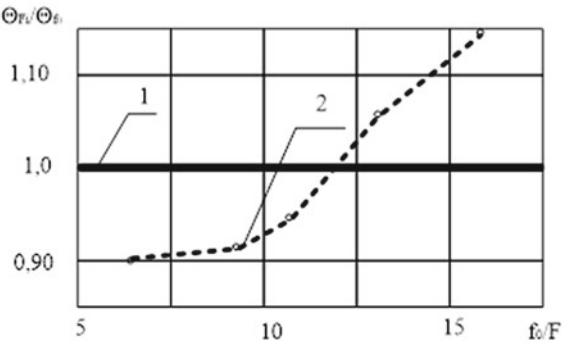

Fig. 4 Normalized dependence of the width of the directivity characteristic on the decrease in the difference frequency of the parametric antenna relative to the central frequency of the pump waves

Analysis of the results of theoretical studies of the formation of directional properties and experimental measurements of the directivity characteristics of the parametric anti-antenna allows us to determine the approximate range of changes in directional properties in real working conditions. In order to generalize the results of theoretical and experimental studies, obtained for various parametric antennas, we compared the normalized values of the width of the directivity pattern of the parametric array Θ_{Fi}/Θ_{f0} for the case of a decrease in the difference frequency F of the parametric antenna relative to the central frequency of the pump waves f_0 in the range f_0/F from 5 to 16. The obtained normalized dependences of the width of the directivity characteristic of the parametric antenna (1—theoretical dependence, 2—experimental dependence) are shown in Fig. 4.

Models describing the characteristics of a parametric array in the far zone are valid only in a certain range of parameter changes [8]. Since the region of nonlinear interaction is a three-dimensional antenna, when developing a parametric array, it is necessary to take into account the influence of hydrophysical inhomogeneities on the process of nonlinear interaction and the formation of its characteristics [11].

To test the possibility of using cepstral analysis of echo signals when profiling a layered structure using parametric arrays, as well as to select the optimal algorithm for calculating kepstrum, the following problems were experimentally investigated:

(i) dependence of the echo signal kepstrum on the delay time of the pulse reflected from the second boundary;
(ii) noise immunity of kepstrum.

It should be noted that the signals reflected from two interfaces were experimentally modeled, which also remain visually indistinguishable in the spectral region. Echo signals with different spatial overlap spectra were calculated.

Figure 5 shows the kepstrum of the echo signals when they are superimposed by 10 and 30%, respectively. The duration of the probing signal is 1 ms, the frequency of the generated wave is 10 kHz, the amplitude of the signal reflected from the first boundary was 15% of the amplitude of the reflection from the second boundary.

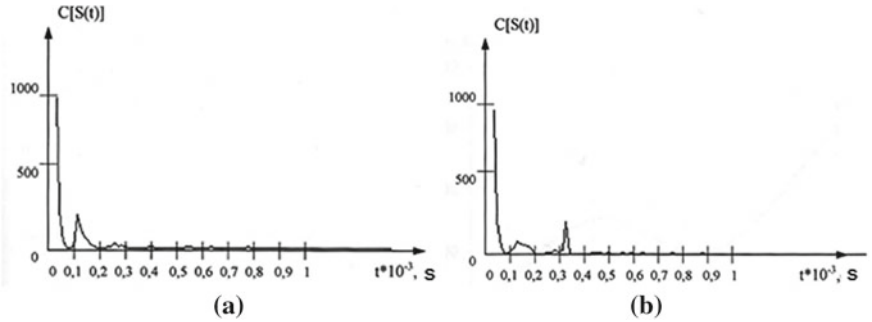

Fig. 5 Kepstrum of the echo signal at the pulse delay from the second boundary: **a** 10% of the theoretical duration of signal; **b** 30% of the signal duration

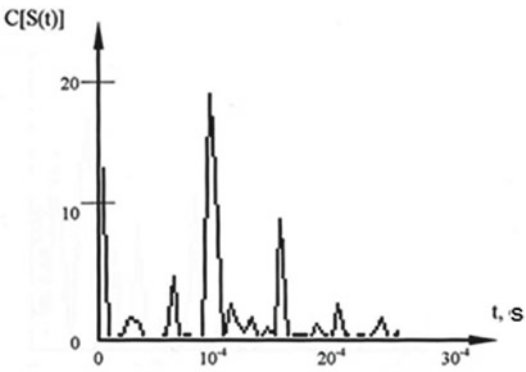

Fig. 6 Kepstrum of the echo signal at a signal-to-noise ratio equal to 2

Obtained kepstrum allow one to determine the position of the second border section. However, the width of the cepstral peak is not constant, which introduces an error in determining the boundaries.

To clarify the nature of the noise immunity of kepstrum a series of experiments were conducted. The signal-to-noise ratio is varied by changing the excitation amplitude. For each change in this ratio, the kepstrum of experimentally obtained echo pulses was calculated. Figure 6 shows the kepstrum of the echo signal ($t = 1$ ms, $F = 10$ kHz) with a signal-to-noise ratio equal to 2.

From Fig. 6, one can see the resolution of kepstrum in determining the time of arrival of the signal reflected from the second boundary section.

6 Conclusion

Analysis of the calculated and experimentally obtained dependences allows us to draw the following conclusions:

(i) the results of experimental studies confirm the regularities of the formation of directional properties of a parametric array;
(ii) the low-frequency echo pulse kepstrum allows one to uniquely determine the moment of arrival of the echo signal from the second interface when the ratio of the signal amplitude from the first boundary to the signal amplitude from the second boundary is less than 30 dB;
(iii) it is unambiguously possible to determine the moment of arrival of the echo signal from the second interface, when the ratio of the amplitude of the signal reflected from the second interface to the noise amplitude is greater than 2.

Based on the unique advantages of kepstrum in estimating time delay, the cepstral analysis method can be applied to the processing of echoes from a layered structure to increase the resolution over distance.

Acknowledgements The reported study was funded by RFBR and ASA according to the research project No. 19-52-40005.

References

1. T. Missiaen, D. Evangelinos, Ch. Claerhout, M. De Clercq, M. Pieters, I. Demerre, Geoarchaeology **33**(3), 386 (2017)
2. H. Medwin, C.S. Clay, *Fundamentals of Acoustical Oceanography* (Academic Press, New York, 1998)
3. R. Carbo, J. Acoust. Soc. Am. **101**, 227 (1997)
4. J. Yang, S. Khim, S. Woon, H. Meng, H. Yong, Jpn. J. Appl. Phys. **44**(9A), 6817 (2005)
5. W. Kuperman, F. Jensen (Ed.), *Acoustics of the ocean floor*. (Mir, Moscow, 1984), p. 454 (In Russian)
6. D. Ding, J. Acoust. Soc. Am. **115**, 35 (2004)
7. I. Kirichenko, I. Starchenko, J. Phys.: Conf. Ser. **1353**(1), 5 (2019)
8. B.K. Novikov, V.I. Timoshenko, *Parametric Arrays*. Leningrad, Sudostroenoe, p. 275 (1990) (In Russian)
9. W.D. Blair, J.E. Conte, T.R. Rice, IEEE Trans. Educ. **38**(3), 211 (1995)
10. A.V. Oppenheim, R.S. Schafer, IEEE Signal Process. Mag. **9**, 95 (2004)
11. I. Starchenko, I. Kirichenko, in *4th European Congress on Acoustics*, vol. 1415 (2005)

Space Time Block Code Based FBMC Advanced Underwater Image Communication Technology

Chin-Feng Lin, Chih-Chin Chuang, Shun-Hsyung Chang, Ivan A. Parinov, and Sergey N. Shevtsov

Abstract In the paper, a 2×4 space time block code (STBC) based filter bank multicarrier (FBMC)-low density parity check (LDPC) code underwater image communication technology (UICT) is proposed. The adaptive binary phase shift keying (BPSK) modulation and four offset quadrature amplitude modulation (4-OQAM), are integrated into the proposed UICT. The performances of bit error rates (BERs) and peak signal-to-noise ratios (PSNRs) of the proposed UICT with perfect channel estimation (PCE)(0%) are investigated. From these simulation results, we evaluate the performances of the proposed advanced UICT with a PCE.

Keywords Underwater image communication technology · 2×4 space time block code · Filter bank multicarrier · Low density parity check code · Peak signal-to-noise ratio

1 Introduction

Underwater image communication technology is an interesting research topic. Yoshida et al. [1] recorded 109 videos and 122 still-images of fish, diving birds and shrimp using underwater animal-borne video cameras in Lake Biwa, Japan. Threatened endemic fish, two types of alien fish, and bluegill sunfish were shown, and

C.-F. Lin (✉) · C.-C. Chuang
Department of Electrical Engineering, National Taiwan Ocean University, Keelung, Taiwan, ROC
e-mail: lcf1024@mail.ntou.edu.tw

S.-H. Chang
Department of Microelectronic Engineering, National Kaohsuing University of Science and Technology, Kaohsuing, Taiwan, ROC

I. A. Parinov
I. I. Vorovich Mathematics, Mechanics, and Computer Science Institute, Southern Federal University, Rostov-on-Don, Russia

S. N. Shevtsov
Aircraft Systems and Technologies Laboratory, South Center of Russian Academy of Science, Rostov-on-Don, Russia

I. A. Parinov et al. (eds.), *Physics and Mechanics of New Materials and Their Applications*, Springer Proceedings in Materials 10,
https://doi.org/10.1007/978-3-030-76481-4_47

clear evidence for the behavior of aquatic organisms under natural conditions was provided. Connor et al. [2] reviewed current algorithms, communication methods and designed concepts for underwater swarm robotics, and an acoustic modem, blue and green lights, WiFi, and Bluethooth underwater transmission schemes were integrated into this technology. An underwater camera is a common sensor used in underwater swarm robotics, and an underwater acoustic image modem is a required component of this camera. Fayaz et al. [3] discussed the restoration of distorted underwater images, and processed and restored them, demonstrating various techniques and methodologies, and illustrating hardware- and software-driven image-restoration techniques.

Ahmed et al. [4] proposed a filter orthogonal frequency-division multiplexing acoustic modem with turbo and polar codes, and explored the transmission performance of bit error rates (BERs) on *t*-distribution noise. The simulation results showed that the performance of the turbo code was superior to that of the polar code by 2 dB at a BER of 0.001. Xi et al. [5] proposed an improved proportionate normalized minimum-symbol error rate (SER) algorithm by using the minimum-SER criterion to derive the adaptive turbo equalizer update equation in deep-sea vertical acoustic transmission. The transmission range was approximately 10,500 m. A single-carrier, multiple-input–multiple-output (MIMO) underwater acoustic receiver scheme was investigated, and Turbo equalization (TEQ) with the sparse Bayesian learning algorithm for iterative channel estimation was integrated into the proposed MIMO-based underwater transmission scheme [6]. Moreover, a low-complexity space–time soft decision feedback equalizer (ST-SDFE) with successive soft interference cancelation was also proposed, and the proposed ST-SDFE TEQ significantly outperformed the low-complexity minimum mean square error TEQ in terms of the BER. Lin et al. [7, 8] proposed a filter bank multicarrier (FBMC)-based underwater acoustic multimedia transceiver with low-density parity-check (LDPC) channel coding. The adaptive binary phase shift keying (BPSK) modulation or offset quadrature amplitude modulation (OQAM), a power assignment mechanism, and a direct mapping transmission scheme were integrated into the proposed FBMC-based underwater acoustic multimedia transceiver.

In this paper, a 2 × 4 space time block code (STBC) based FBMC-LDPC code underwater image communication technology (UICT) is demonstrated.

2 Research Method

Figure 1 deplicts the proposed 2 × 4 STBC-based FBMC-LDPC UICT. The transmission performances of the proposed 2 × 4 STBC-based FBMC-LDPC UICT is discussed for image signals. The underwater channel model [9] with an underwater channel bandwidth of 3.9 kHz, a carrier central frequency of 11.5 kHz,, and a transmission distance of 1 km was adopted in the proposed UICT. The BER requirement of underwater transmission image signals is 10^{-4}, and the peak signal-to-noise ratios (PSNRs) (in dB) of the 2 × 4 STBC-based FBMC-LDPC UICT is demonstrated.

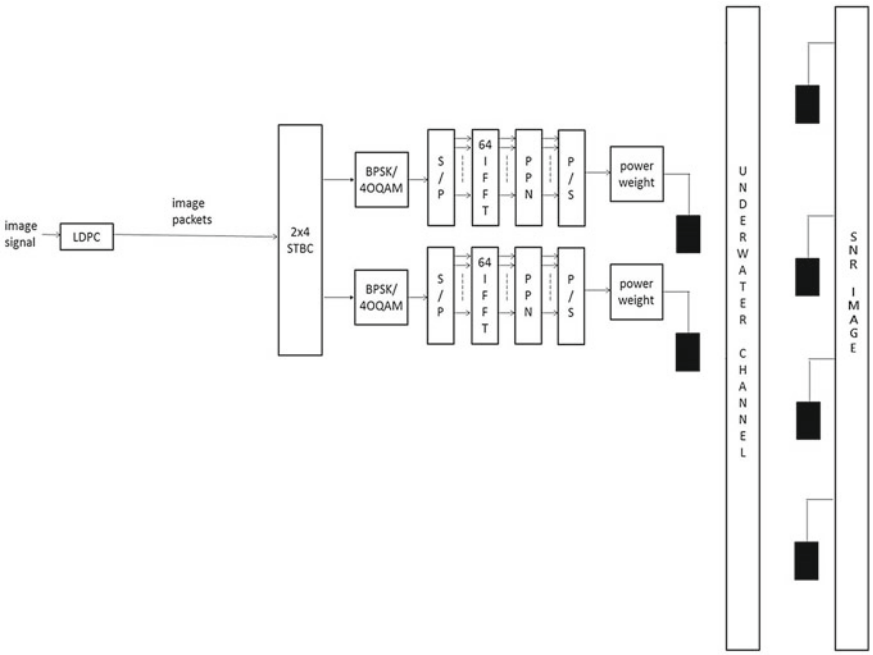

Fig. 1 Proposed 2 × 4 STBC-based FBMC-LDPC UICT

The image mean square error MSE (IMSE) of an $m \times n$ image signal is defined as follows:

$$IMSE = \frac{1}{mn} \sum_{i=0}^{m-1} \sum_{j=0}^{n-1} [O(i, j) - R(i, j)]^2 \tag{1}$$

where $O(i, j)$ is the matrix, containing the pixel values of the original image signal, and $R(i, j)$ is matrix containing the pixel values of the received image signal.

The PSNR is defined as follows:

$$PSNR = 10 \log_{10} \left(\frac{(Max(O(i, j))^2}{IMSE} \right) \tag{2}$$

The power-saving ratio of the 2 × 4 STBC-based FBMC-LDPC UICT is defined as follows:

$$PowerSaving = (1 - u) \times 100\ \% \tag{3}$$

u denote the transmission power weight, and u is less than or equal to one. The performances of BERs, PSNRs, and power-saving ratios of the proposed 2

× 4 STBC-based FBMC-LDPC UICT with PCE)(0%) are investigated. With the SNRs increased, the BERs are decreased. With the SNRs increased, the PSNRs are increased.

3 Simulation Results

Figure 2 shows that BER performances of the 2 × 4 STBC-based FBMC-LDPC UICT, using BPSK and 4-OQAM modulations, with PCE (0%), respectively. The colors 'red', and 'blue', in Figs. 2–4, denote the 2 × 4 STBC-based FBMC-LDPC UICT using BPSK and 4-OQAM modulations, respectively. Using the BPSK modulation with a PCE, for signal to noise ratios (SNRs) of 5.4516 dB, 6.2893 dB, and 7.3283 dB, respectively, with the corresponding BERs of the received image signals were 9.6×10^{-5}, 3.6×10^{-5}, and 8×10^{-6}. Using the 4-OQAM modulation with a PCE, for signal to noise ratios (SNRs) of 7.3283 dB, and 8.6967 dB, respectively, with the corresponding BERs of the received image signals were 1.84×10^{-4}, and 4×10^{-5}. With the SNRs increased, the BERs are decreased.

Figure 3 shows the PSNR performances of the 2 × 4 STBC FBMC-LDPC UICT, using BPSK and 4-OQAM modulation, respectively, with PCE. The underwater image signals received using the BPSK modulation with a PCE, for signal to noise

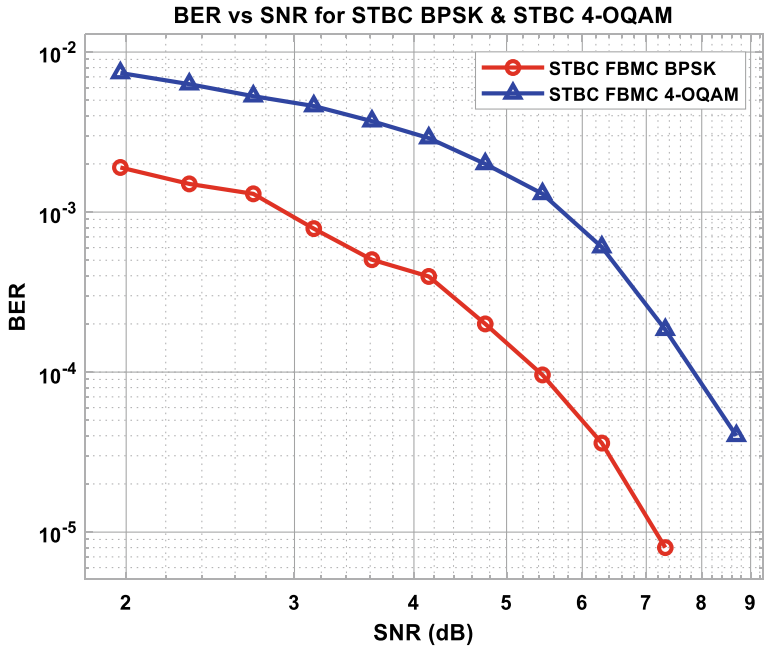

Fig. 2 BER performance of the 2 × 4 STBC FBMC-LDPC UICT with a PCE

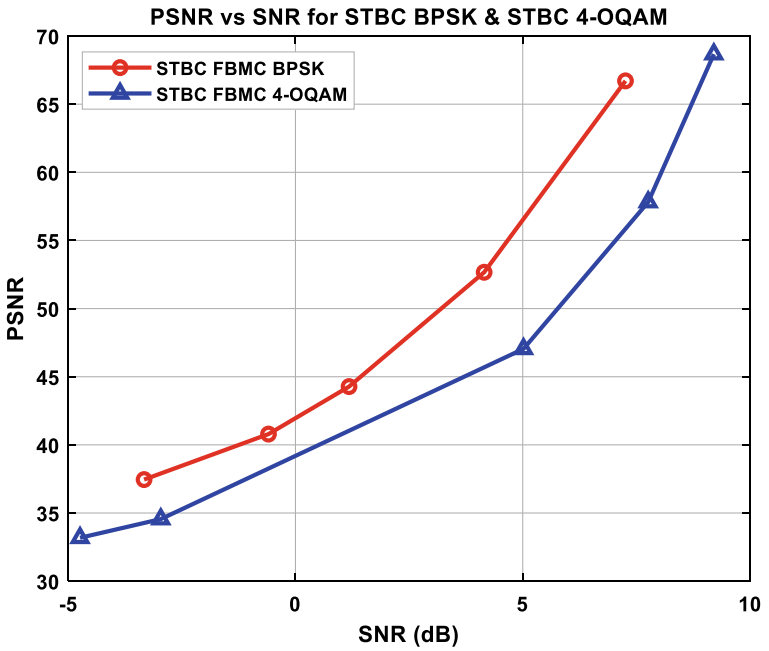

Fig. 3 PSNR performance of the 2 × 4 STBC FBMC-LDPC UICT with a PCE

ratios (SNRs) of 1.17 dB, and 4.15 dB, respectively, with the corresponding PSNRs of the received underwater image signals were 44.27 dB, and 52.66 dB. The underwater image signals, received using the 4-OQAM modulation with a PCE, for signal to noise ratios (SNRs) of 5.01 dB, and 7.75 dB, respectively, with the corresponding PSNRs of the received underwater image signals, were 47.04 dB, and 57.81 dB. Simulation results show that the BERs and PSNRs performances of the 2 × 4 STBC FBMC-LDPC UICT, using BPSK modulation, are better than that of the 2 × STBC FBMC-LDPC UICT, using 4-OQAM modulation.

Figure 4 demonstrates the power saving ratios of the 2 × 4 STBC FBMC-LDPC UICT with a BER of 10^{-4}, for PCE. The maximum acceptable transmission BER value for the underwater image signal is 10^{-4}. The underwater image signals received using the BPSK modulation for the SNRs of 7.98 dB, 8.77 dB, and 9.74 dB, with the corresponding power saving ratios of 45%, 54%, and 63%, respectively. The underwater image signals were received using the 4-OQAM modulation for the SNRs of 10.67 dB, 11.58 dB, and 12.69 dB, with the corresponding power saving ratios of 45%, 54%, and 63%, respectively. At the same power saving ratio, the SNRs of the BPSK modulation are lower than that of 4-OQAM modulation.

Figure 5 shows the original underwater image. Figure 6 illustrates that the underwater image signal received using BPSK modulation in the 2 × 4 STBC FBMC-LDPC UICT with a BER of 10^{-3}, for PCE, and the PSNR is 44.27 dB. Figure 7 illustrates that the Underwater image signal, received using BPSK modulation in the

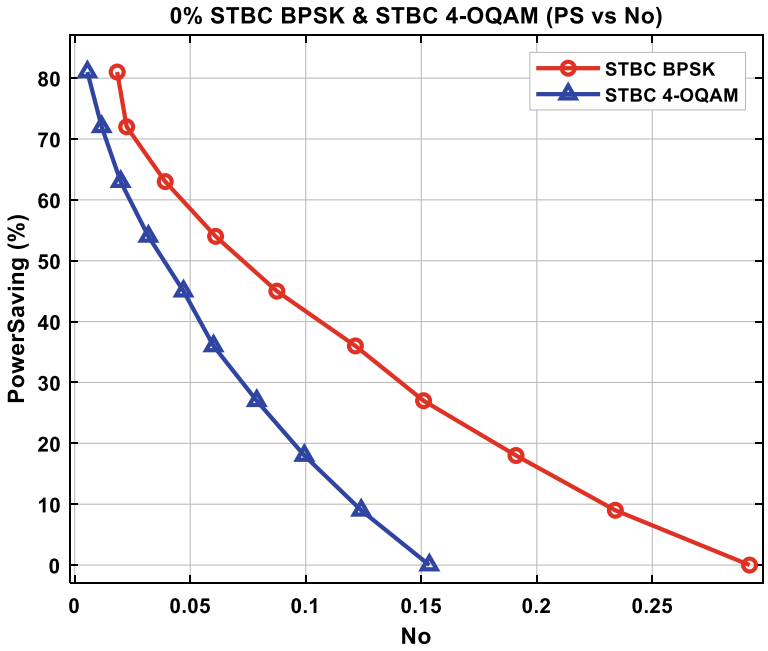

Fig. 4 Power saving ratios of the 2 × 4 STBC FBMC-LDPC UICT with a BER of 10^{-4}, for PCE

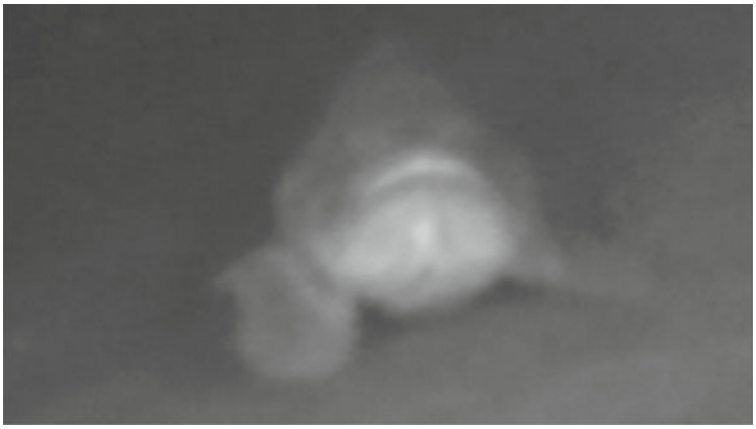

Fig. 5 Original underwater image

2 × 4 STBC FBMC-LDPC UICT with a BER of 10^{-4}, for PCE, and the PSNR, is 52.66 dB. The received underwater image signals are clear, and the 2 × 4 STBC FBMC-LDPC UICT can be applied to underwater acoustic image transmission.

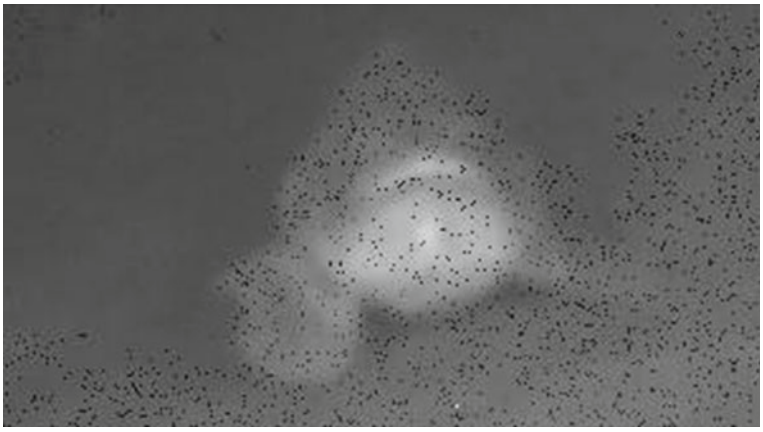

Fig. 6 Underwater image signal, received using BPSK modulation in the 2 × 4 STBC FBMC-LDPC UICT with a BER of 10^{-3}, for PCE, and the PSNR, is 44.27 dB

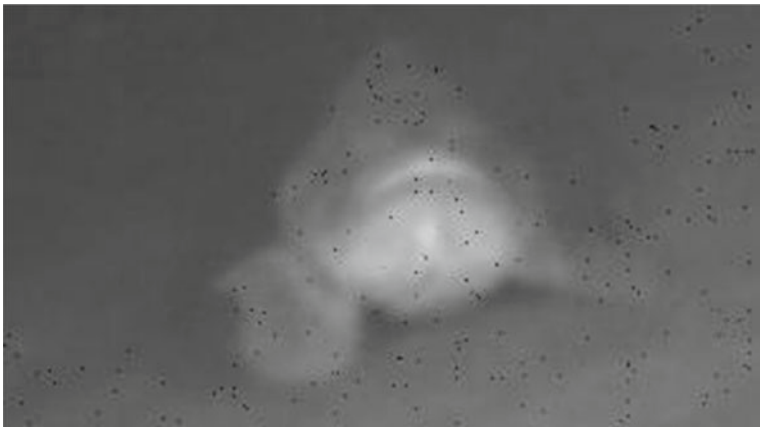

Fig. 7 Underwater image signal, received using BPSK modulation in the 2 × 4 STBC FBMC-LDPC UICT with a BER of 10^{-4}, for PCE, and the PSNR, is 52.66 dB

4 Conclusion

In this paper, a 2 × 4 STBC FBMC-LDPC UICT for underwater acoustic image signals was demonstrated. The BERs, PSNRs, and power saving performances of the 2 × 4 STBC FBMC-LDPC UICT, using BPSK and 4-OQAM modulations, with PCE, were explored. The BERs, PSNRs, and power saving performances of the 2 × 4 STBC FBMC-LDPC UICT using BPSK modulation is superior to the 2 × 4 STBC FBMC-LDPC UICT using 4-OQAM modulation. With SNR increased, the BERs performances are decreased. With SNR increased, the PSNRs performances

are increased. Power saving ratios of the 2×4 STBC FBMC-LDPC UICT with a BER of 10^{-4}, for PCE, are explored. Simulation results show that the proposed 2×4 STBC FBMC-LDPC UICT is suitable for underwater acoustic image transmission.

Acknowledgements The authors acknowledge the support of the grant from The Ministry of Science and Technology of Taiwan, under contract No. MOST 108-2221-E-992-026, and the valuable comments of the reviewers. IAP thanks Southern Federal University for grant No. VnGr-07/2020-04-IM.

References

1. A.Y. Makoto, Kumiko K.S. Totsu, M. Kohji, Ecol. Res. **35**, 1001 (2020)
2. C. Jack, C. Benjamin, A.J. Matthew, IEEE Sens. J. **21**(1), 153 (2021)
3. F. Sheezan, A.P. Shabir, G.J. Qureshi, V. Kumar, IET Image Process. **15**, 269 (2021)
4. S.A. Mustafa, M.S. Shahida, Y.A. Yasin, S.M. Gismalla, F.L. Abdullah, Y.A. Jawhar, B. Mohammed, ETRI J. **1** (2020)
5. J. Xi, S. Yan, L. Xu, C. Hou, IEEE J. Oceanic Eng. **46**(1), 338 (2021)
6. X. Qin, F. Qu, Y.R. Zheng, IEEE J. Oceanic Eng. **46**(1), 326 (2021)
7. C.F. Lin, Y.T. Hung, H.W. Lu, S.H. Chang, I.A. Parinov, S.N. Shevtsov, J. Mar. Sci. Technol. **26**(3), 327 (2018)
8. C.F. Lin, T.J. Su, H.K. Chang, C.K. Lee, S.H. Chang, I.A. Parinov, S. Shevtsov, Appl. Sci. **10**, 233 (2020)
9. J. Zhang, Y.R. Zheng, C. Xiao,in *Proceedings of the MIT/IEEE Ocean International Conference* (IEEE Publishers, Piscataway, USA, 2008)

Parametric Modeling of High-Rise Objects with Complex Configuration by Forming the Description of Their External Shaping

Galina Kravchenko, Elena Trufanova, Ol'ga Shilyaeva, Alexander Cherpakov, and Ivan Parinov

Abstract An algorithm for creating an information model based on a numerical experiment to study the formation of the surface of object by using an analytical functional modeling is proposed. The surface of a high-rise building object is formed by a straight generatrix of a movable axoid. Two models of high-rise buildings are considered. Information model is developed using digital technology and the finite element method. The method of analyzing the dynamic characteristics and stress-strain state of the frame elements of a parametric architecture object allows one to assess the dynamic properties of buildings.

Keywords Information model · Parametric modeling · Numerical experiment · Analytical functional · High-rise building · Stress-strain state · Parametric architecture

1 Introduction

Parametric modeling in the design of unique buildings and structures determines the geometric shape of the object by introducing the parameters of the model components and the relationships between these components [1]. A mathematical model is formed

G. Kravchenko · E. Trufanova
Department of Mechanical Engineering, Don State Technical University, 344000 Rostov-on-Don, Russia
e-mail: Galina.907@mail.ru

E. Trufanova
e-mail: El.Trufanova@mail.ru

A. Cherpakov (✉) · I. Parinov
I. I. Vorovich Mathematics, Mechanics, and Computer Science Institute, Southern Federal University, 344090 Rostov-on-Don, Russia
e-mail: alex837@yandex.ru

O. Shilyaeva · A. Cherpakov
Department of Information Systems in Construction, Don State Technical University, 344000 Rostov-on-Don, Russia

I. A. Parinov et al. (eds.), *Physics and Mechanics of New Materials and Their Applications*, Springer Proceedings in Materials 10,
https://doi.org/10.1007/978-3-030-76481-4_48

with certain characteristics, by varying which it is possible to change the configuration of the building [2]. When specifying linear equations, algebraic curves, splines and applying approximation processing, computer visualization, a surface of a complex architectural shape is created. The parameterization in 3D modeling allows for ideal non-linear shape designs [3]. The parametric method allows us to describe a certain set of object shapes by geometrical representation of the mathematical relationship. It is possible to change the shaping of the model by varying the parameters present in the mathematical models [4].

In [5], Patrick Schumacher reveals many elements of subsystems and parameters in architecture. Differentiation in a system means change in other systems. All major parameters of the architectural model, environment and observer parameters should be included in the system. Therefore, it is necessary to make all the forms compliant, "harmonizing" them with neighboring forms, to use interconnected structures that pass into each other. The ability to change leads to the achievement of the main goal, namely the creation of diversity and complexity of any social objects [6]. Schumacher created a new way of working with architectural forms. This is a kind of theoretical matrix into which other architectors can write their parameters [7]. Parametricism is based on the analysis of many components, which as a result turns into an algorithm [8]. This is a complex equation, substituting various data into which the future concept of the building is formed. Schumacher designates parametricism as a new epoch-making architectural style, which has a special look at the fundamental aspects of building the sphere of social life, corresponding to the new paradigm.

The introduction of building technology based on 3D printers requires the development of software to control industrial robots. It is necessary to expand the ability to print volumetric rigid complex structures from stable materials of any size. The software includes print parameters and strategies for different types of 3D printed lines, as straight or curved lines require different adjustments. The technology is more economical and scalable. This method allows us to create 3D objects of parametric architecture of almost any size and shape.

The difference between parametric modeling and two-dimensional or three-dimensional modeling is that the model is set by mathematical equations in the form of changing functions. Digital technologies develop this design method, combining CAD and numerical methods in the form of a single system, realizing the mathematical description of the design of a digital analogue of an object [3]. The use of modeling complexes is presented in a number of works for various conditionally simple types of structures [9–19]. The use of software and computing systems allows us to design buildings of complex architectural shapes and to study the stress-strain state of objects on the basis of finite element analysis. Examples of the works are presented in monographs [20, 21].

The aim of this study is to develop and analyze an information model of an object with complex configuration, which has a certain parametric description of the external shaping.

2 Materials and Methods

The object of research is the building of parametric architecture. An epicycloid cylinder, or an epicycloid straight cylindrical surface [22, 23], is used to build an information model of an object of parametric architecture.

The surface is formed by a straight generatrix of a movable axoid that is a cylinder with a radius r, which rolls without sliding along the outer surface with a radius R and is described by the equations:

$$x = x(u, \varphi) = (R + r)cos\varphi - rcos(1 + n)\varphi;$$

$$y = y(u, \varphi) = (R + r)sin\varphi - rsin(1 + n)\varphi,$$

$$z = u,$$

where $n = R/r$;

φ is the angle counted from the fixed x-axis in the rolling direction to the straight line connecting the center O of the fixed cylinder with a certain point into which the line of tangency of two axoid-cylinders is projected. For an integer value of the parameter n, the cylindrical surface does not intersect itself (see Fig. 1).

The SAPFIR software has a built-in function for specifying a line and surface [24]. The parameter n affects the number of "petals" of the model. Figure 1 shows surfaces for the parameter value $n = 5$, $n = 2$, respectively. The model in Fig. 2a has dimensions 35 × 35m^2 in plan, the model in Fig. 2b has sizes 35 × 25m^2.

When the mathematical parameters are varied, the height of the object remains constant, the dimensions in the plan and the shaping of the model change. To create a finite element scheme, the information model was exported to SP LIRA [25].

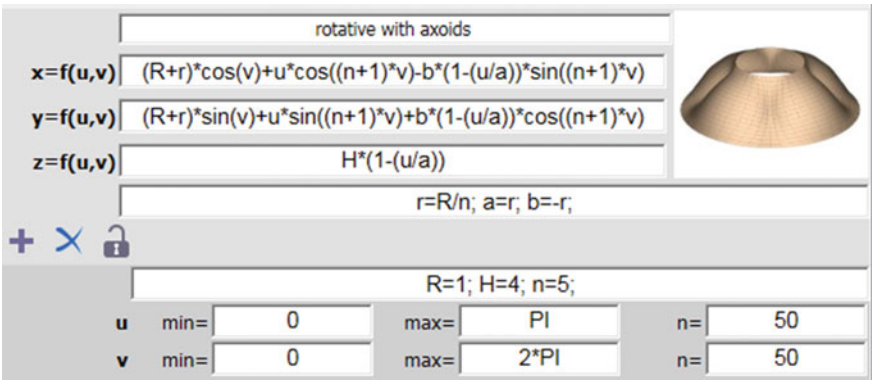

Fig. 1 Setting the surface "Epicycloid cylinder" in SAPPHIRE software

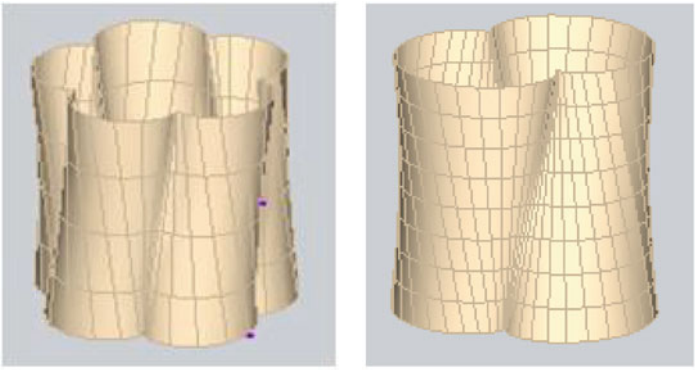

Fig. 2 Variation of the parameter *n*: **a** five petals of the model; **b** two petals

The spatial slab-rod system of the projected building is made with a load-bearing monolithic reinforced concrete structural frame made of concrete of class B35. The projected building has 75.6 m height. The number of floors is 25, the height of a typical floor is 3 m.

Spatial rigidity is ensured by the joint work of the bearing walls of the stiffening diaphragm, columns and horizontal floor disks. The placement of the stiffening core in the form of the walls of the staircase and elevator assembly in the central part of the building made it possible to exclude significant torsional vibrations. The stiffness core provides rigidity and stability both during the construction period and during the operation of the building.

The arrangement of the columns is made so that the outer row follows the shape of the object surface. The inner row takes the form of a vicious circle (Fig. 3). The

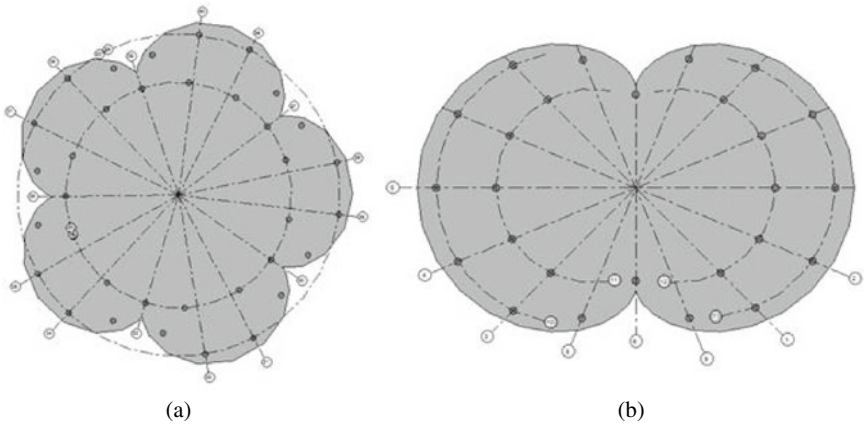

Fig. 3 Arrangement of columns: **a** the first model; **b** second model

minimum distance between the columns is not less than 2.5 for the organization of an easy passage. The cross-section of the columns is taken to be round, the diameter of the basement columns and from the 1st to the 12th floor is 600 mm, from the 13th to the 25th floor is 500 mm.

Since the building is twisted by 16.5°, each subsequent slab must be rotated on 0.635° around its axis relative to the previous slab, with the exception of the underground part of the building. The slab of the first floor will not rotate relative to the foundation slab in order to ensure the joining of the slab and the walls of the basement.

The columns of each subsequent floor are installed in relation to the previous one with an eccentricity along the axis corresponding to the twisting of the building surface. The arrangement of the bearing columns is carried out in such a way that the cantilever light of the slab does not exceed 1500 mm.

To increase the contact area of two adjacent columns, the device of capitals is performed, the diameter of which is 100 mm larger than the diameter of the corresponding column. The capital thickness is 275 mm. The upper part of the capital protrudes beyond the column, providing a constructive transition to the horizontal floor slab.

Slabs, walls and diaphragms were introduced using the Kirgoff–Mindlin medium thickness slab hypothesis [26]. Conjugation of columns with floors uses the "kinematic" hypothesis, which improves the accuracy of the approximation of the solution in the vicinity of the slab-column connection.

To model the slab grillage, floor and roof slabs, walls and stiffening diaphragms, universal triangular and quadrangular shell elements with 6° of freedom in the node were used. The columns in the design model are taken into account by universal spatial rods with 6° degrees of freedom at the node.

When calculating the parameters of free vibrations, the soil foundation of the building was not specified [27]. Parametric foundations approximately take into account the rigidity and do not take into account the significant inertial properties of soils. In this case, the vibration modes, obtained taking into account the compliance of the parametric base, move to the beginning of the spectrum, where "false" forms appear [28]. Such a distortion of the spectrum of natural frequencies is aimed at reducing the dynamic effects on the building structure [29]. When using an absolutely rigid foundation, the dynamic effects on the topside increase, which leads to a safety margin of the system [30]. The design model of an object with different parameters is shown in Fig. 4.

The algorithmic method for studying the rational surface of an object of parametric architecture requires determining the dynamic characteristics and stress-strain state of the building frame elements.

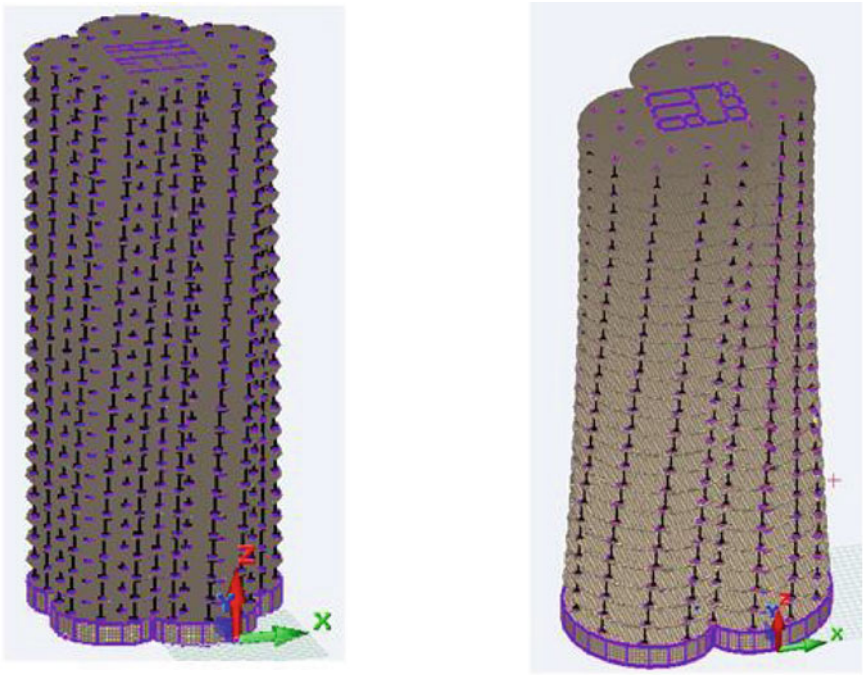

(a) (b)

Fig. 4 Design model of the object: **a** the first variation at $n = 5$; **b** second variation with $n = 2$

3 Results

The finite element analysis of an architecture object is a step-by-step implementation of three stages: preprocessing, calculation and post-processing. At the first stage, a finite element scheme is created, the boundary conditions of the problem, loading conditions, material properties and geometric characteristics of the frame elements are set. The stage of performing the calculation involves solving a system of linear algebraic equations of the finite element method. At the last stage, the analysis of the calculation results and the stress-strain state of the object is carried out.

A modal analysis was carried out, on the basis of which the forms, frequencies and periods of natural vibrations of the building frame were obtained. The first three modes of vibration reflect all possible variants of the dynamic response of the structure; therefore, high frequencies can be neglected.

For the first model, the natural frequencies change from 0.6 Hz to 0.98 Hz, respectively, with a subsequent increase by 250%. The periods of natural oscillations vary from 1.66 s to 1.02 s (Fig. 5).

For the second model, the natural frequencies vary from 0.58 Hz to 1.13 Hz, respectively, with a subsequent increase by 200% (Fig. 6). The periods of natural oscillations vary from 1.41 s to 0.88 s (Fig. 4).

(a) (b) (c)

Fig. 5 Forms of vibrations of the first model: **a** 1st form; **b** 2nd form; **c** 3rd form

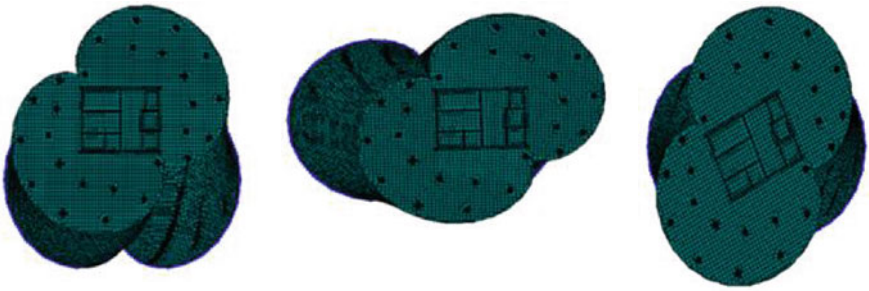

(a) (b) (c)

Fig. 6 Forms of vibrations second model: **a** 1st form; **b** 2nd form; **c** 3rd form

The frequencies and periods of the first ten forms of natural vibrations of the frameworks of the two building models are shown in the plots (see Fig. 7). The results of the dynamic calculation show that the first and second modes of vibration are translational, while the third is torsional. A comprehensive analysis of the dynamic

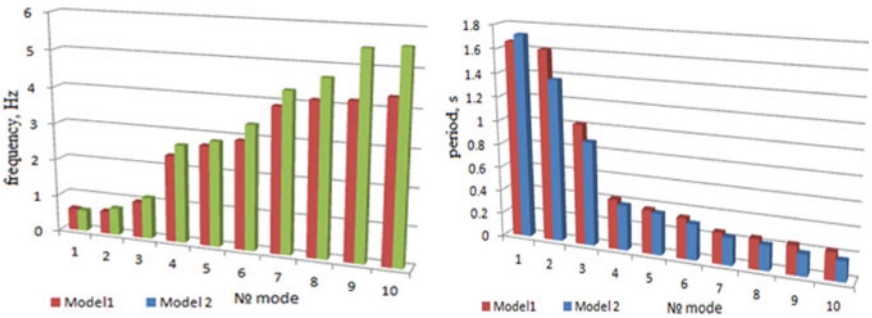

(a) (b)

Fig. 7 Results of modal analysis: **a** natural frequencies; **b** periods of oscillation

characteristics allows us to conclude that in the first model, the contribution of the fundamental vibration mode is the best [31].

The calculation of the stress-strain state of the object of parametric architecture is carried out taking into account the pulsation component of the wind load. When modeling the pile field, it is proposed to use pliable rods with a stiffness corresponding to the average settlement of the pile foundation. The proposed approach to modeling the compliance of the pile foundation makes it possible to correctly determine the bending forces and correctly calculate the reinforcement of the foundation slab, while the standard uniform settlement of the pile field does not take into account these forces and uneven deformations [32]. The displacements of the nodes of the finite element scheme in the global coordinate system X, Y, Z (Fig. 8) and the forces in the load-bearing elements of the frame (Table 1) were obtained.

The maximum longitudinal force in the column of the first model was 4700 kN, and for the second model 5184 kN. For the first variant of modeling the object of

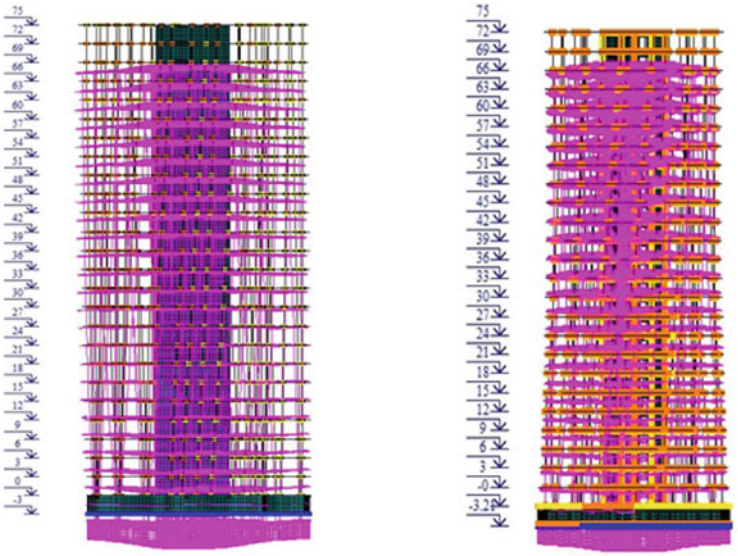

(a) (b)

Fig. 8 Deformed building frame diagram: **a** 1st model; **b** 2nd model

Table 1 Maximum values of forces in load-bearing structures

Frame model	Supporting element	M_x, kN	M_y, kN	Q_x, kN/m	Q_y, kN/m
Model 1	Cover plate	129	129	391	349
	Base plate	3370	3450	4640	3740
Model 2	Cover plate	135	166	551	543
	Base plate	3100	2660	1810	2010

parametric architecture, the following values of the stress-strain state were obtained [33]. The deflection of the cover plate is 11.9 mm. The settlement of the foundation slab reaches 13.2 mm. The maximum horizontal displacements of the upper point of the frame in the X-direction are 19.2 mm, and in the Y-direction are equal to 14.8 mm. The calculation results do not exceed the standard maximum permissible values.

For the second variant of forming an epicycloidal cylindrical surface, the results of calculating the building frame by the finite element method in SP LIRA are as follows: (i) vertical displacements of the covering slab are 15.4 mm; (ii) foundation slab settlement reaches 11.0 mm; (iii) the maximum horizontal displacements of the frame in the X-direction are 29.2 mm, and in the Y-direction are equal to 16 mm. The components of the stress-strain state correspond to the standard values.

The analysis of slab grillage settlement has been carried out. The relative settlement for the points of the design scheme, located along the X-axis (the geometric center of the slab corresponds to the $X = 17.5$ m), is shown in Fig. 9.

To select a rational option for shaping the object of parametric architecture, a comparison of the calculation results for the first and second finite element model of the building is carried out. The maximum deflections of the covering slabs differ by 23%, horizontal displacements differ by 34%. The analysis of these results allows us to conclude that the elements of the frame of the first model of the formation of the analytical surface are less susceptible to the main influences, taking into account the pulsating component of the wind load.

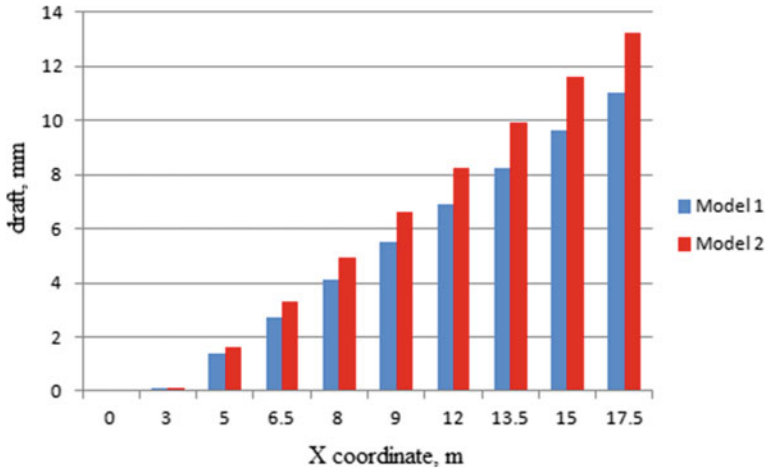

Fig. 9 Draft of slab grillage

4 Discussion

The use of the finite element method in the study of the stress-strain state of the elements of a parametric architecture object makes it possible to obtain an information model of a building, which is a system of finite elements. The design model abstracts the correspondence between the geometric parameters of the element and the finite element representation, therefore the design model is fundamentally different from the architectural one.

It should be noted that the geometric characteristics of the building frame elements are the same for the two models. Figure 10 shows the distribution of the geometric characteristics of the frame: columns are shown in yellow and blue, floor slabs are shown in blue, and stiffness diaphragms are shown in red.

In the result of studying the stress-strain state of the objects of parametric architecture by the finite element method, it can be concluded that the smallest stresses and displacements of individual structural elements are observed in the first model. The deformation model gives the clearest idea of the stress-strain state of a construction with a complex deformation.

The analysis of the displacement isofields of the nodes of the finite element scheme from the calculated combination of loads, taking into account the pulsation of the

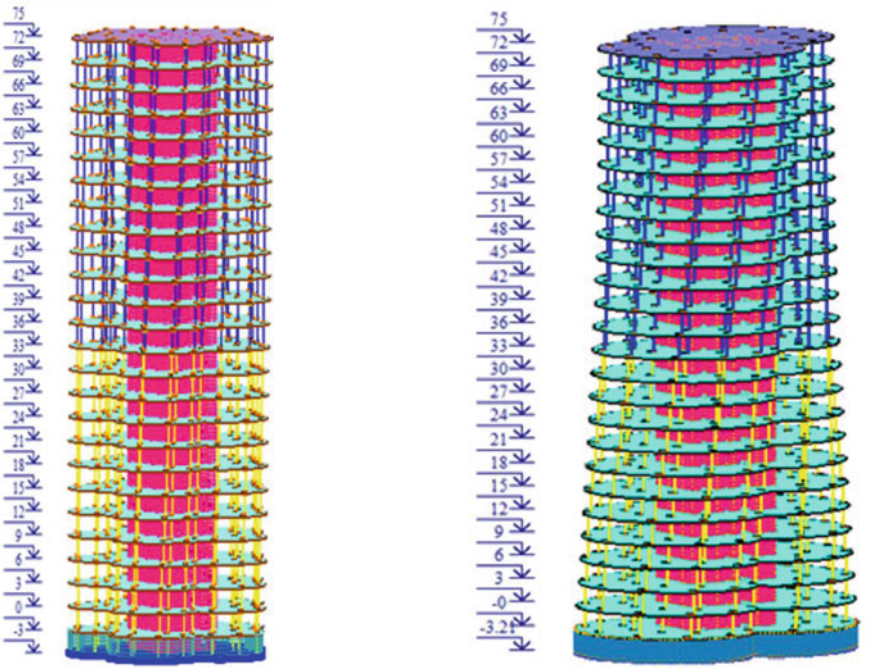

Fig. 10 Distribution of geometric characteristics: **a** first model; **b** second model

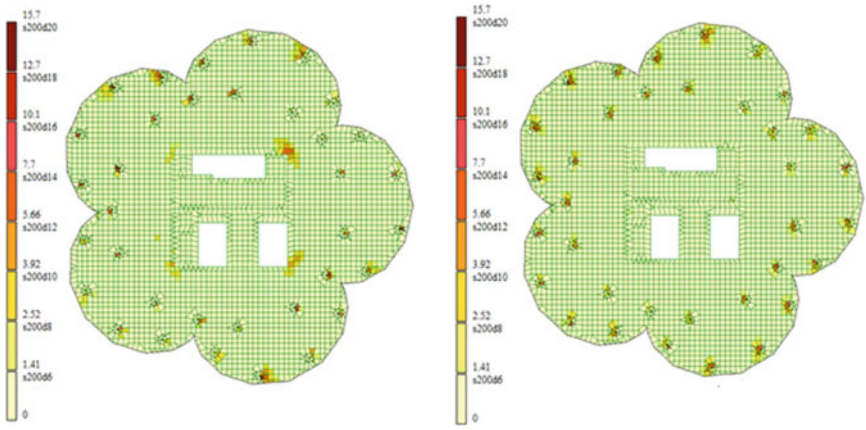

Fig. 11 Top reinforcement of the floor slab: **a** in the longitudinal direction; **b** in the transverse direction

wind, shows that the maximum displacements correspond to the upper tiers of the object. For a rational version of the analytical surface, the load-bearing elements of the building frame were reinforced [34]. Figure 11 shows the reinforcement of the floor slab.

When reinforcing the floor slab with reinforcement with a diameter of 12 mm with a step of 200 mm, taking into account additional reinforcement zones, the requirement for a minimum percentage of reinforcement of the supporting structures of the reinforced concrete frame is fulfilled. The resulting reinforcement of the supporting structures of the building frame does not violate the normative condition for limiting the maximum reinforcement of the constructions.

5 Conclusions

Two variants of the analytical surface of the epicycloid cylinder have been developed using the graphic editors Revit, AutoCad and technologies for converting graphic information. To assess the bearing capacity of the construction as a whole and its individual elements, including the purpose of materials and geometric characteristics of cross-sections, parameters of the geoengineering structure of the base, a finite element plate-bar model was constructed using the finite element method.

In SP LIRA, the modeling of static and dynamic effects in a 3D setting has been performed. A comprehensive analysis of the results of numerical modeling made it possible to choose a rational option not only for the structural solution of the building frame, but also for the shaping of the analytical surface of the object of parametric architecture based on software. With the advent of improved computer systems and

powerful computing programs, it became possible to work with complex parametric models.

The use of the algorithmic method when choosing a rational shaping of an object of a complex geometric shape makes it possible to accept the structural scheme of a building with minimal material costs for the construction of this object. Parametric architecture allows us to expand the scope of the finite element method and create unique high-rise and large-span buildings and structures.

The information model, developed using digital technologies according to the method of analyzing the dynamic characteristics and stress-strain state of the frame elements of the parametric architecture object, allows us to choose a rational analytical surface. For the development of information modeling of objects of parametric architecture, it is necessary to expand the library of finite elements of software systems.

Acknowledgements Research was financially supported by Southern Federal University, grant No. VnGr-07/2020-04-IM (Ministry of Science and Higher Education of the Russian Federation).

References

1. J. Wassim, *Parametric Design for Architecture* (Laurence King Publishing, London, 2013), p. 208
2. G.M. Kravchenko, E.V. Trufanova, IOP Conf. Ser.: Mater. Sci. Eng. **1083**, 012011 (2021)
3. G.M. Kravchenko, A.Yu. Manoilenko, V.V. Litovka, ESJ Eng. J.Don **2** (2018) (In Russian)
4. I.A. Mamieva, Struct. Mech. Eng. Constr. Build. **15**(4), 299
5. P. Schumacher. *Parametric Diagrammes.* http://www.patrikschumacher.com/Texts/ParametricDiagrammes.html
6. P. Schumacher. *AD Architectural Design—Digital Cities*, vol. 79, issue 4 (Wiley, London, 2008).
7. Z. Hadid, P. Schumacher, in *Educating Architects*, ed. by N. Spiller, N. Clear, vol. 295 (Thames and Hudson, London, 2013)
8. J. Barrallo, S. Sánchez-Beitia, in *Proceedings of Bridges 2011: Mathematics, Music, Art, Architecture, Culture,* vol. 65 (2011)
9. A.V. Cherpakov, O.V. Shilyaeva, M.N. Grigoryan, T.V. Polyakova, IOP Conf. Ser.: Mater. Sci. Eng. **698**(6), 066021 (2019)
10. N.M. Seleznev, O.V. Shilyaeva, Kuen, University News. North-Caucasian Region. Technical Sciences Series, vol. 3, issue 151 (2009), p. 10
11. A.A. Lyapin, N.M. Seleznev, O.V. Shilyaeva, Ecol. Bull. Sci. Centers Black Sea Econ. Cooperat. **2**, 45 (2008)
12. O.V. Shilyaeva, R.A. Khunagov, A.M. Blyagoz, New Technol. **3**, 149 (2012)
13. A. Cherpakov, I. Egorochkina, E. Shlyakhova, A. Kharitonov, A. Zarovny, S. Dobrohodskaya, MATEC Web Conf. 04009 (2017)
14. A.V. Cherpakov, E.A. Shlyakhova, I.O. Egorochkina, Y.A. Kokareva, Mater. Sci. Forum **931**, 373 (2018)
15. A.A. Krasnoshchekov, B.V. Sobol, A.N. Solov'ev, A.V. Cherpakov, Russ. J. Nondestr. Test. **47**(6), 412 (2011)
16. A.V. Cherpakov, A.N. Soloviev, V.V. Gricenko, O.U. Goncharov, Def. Sci. J. **66**(1), 44 (2016)
17. V.A. Akopyan, A.N. Solov'ev, A.V. Cherpakov, S.N. Shevtsov, Russ. J. Nondestr. Test. **49**(10), 579 (2013)

18. V. Akopyan, A. Soloviev, A. Cherpakov, *Mechanical Vibrations: Types, Testing and Analysis*, vol. 147 (2011).
19. M.N. Grigoryan, T.V. Polyakova, Ya.A. Kokareva, I.A. Parinov, A.V. Cherpakov. IOP Conf. Ser.: Mater. Sci. Eng. **1083**, 012016 (2021)
20. S.N. Shevtsov, A.N. Soloviev, I.A. Parinov, A.V. Cherpakov, V.A. Chebanenko, *Piezoelectric Actuators and Generators for Energy Harvesting* (Springer, Cham, Switzerland, 2018), p. 182
21. A.A. Lyapin, I.A. Parinov, N.I. Buravchuk, A.V. Cherpakov, O.V. Shilyaeva, O.V. Guryanova. *Improving Road Pavement Characteristics* (Springer, Cham, Switzerland, 2020), p. 238 (2020)
22. A.L Kheyfets., D. Galimov, I. Shleykov. In: *GraphiCon' 2001.* Nizhny Novgorod, 283 (2001) (In Russian)
23. S.N. Krivoshapko, V.N. Ivanov, *Encyclopedia of Analytical Surfaces* (Springer International Publishing, Switzerland, 2015), p. 752
24. G.L. Gbaguidi Aisse, Struct. Mech. Eng. Constr. Build. **15**(4), 308 (2019)
25. G.M. Kravchenko, E.V. Trufanova, IYu. Danileiko, V.A. Zabeyvorota, ESJ Eng. J. Don **1**, 11 (2019). ((In Russian))
26. K.-J. Batht, *Finite Element Procedures* (Prentice Hall, New Jersey, 1996), p. 10
27. R.W. Clough, J. Penzien, Computer & Structure, Inc. Berkeley. USA (2003), p. 752
28. S. Rezaeian, A. Der Kiureghian, Earthquake Eng. Struct. Dynam. **39**(10), 1155 (2010)
29. Z.I. Georisk, Assess. Manag. Risk Eng. Syst. Geo-hazards **7**(1), 37 (2013)
30. M.I. Kadomtsev, A.A. Lyapin, S.I. Timofeev, ESJ Eng. J. Don. **1**, 8 (2012). ((In Russian))
31. G.M. Kravchenko, E.V. Trufanova, E.V. Ladnaya, ESJ Eng. J. Don **1**, 9 (2017). ((In Russian))
32. G.M. Kravchenko, E.V. Trufanova, A.S. Osadchiy, A. Sazonova, Mater. Sci. Forum **974**, 535 (2020)
33. L.N. Panasyuk, G.M. Kravchenko, E.V. Trufanova, I.D. Tarba, L.G. Tsveiba, Constr. Arch. **7**(1), 34 (2019) (In Russian)
34. S.J. Medwadowski, A. La Samartin, Journal de l'Association Internationale pour la Coquille et Spatiale Structures **45(**1), 41 (2004)

Algorithmization of the System for Collecting and Processing Information on the Geometric Description of Three-Dimensional Object

O. V. Shilyaeva, A. V. Cherpakov, and I. A. Parinov

Abstract The paper describes an algorithm for restoring the three-dimensional (3D) geometric structure of an object in the form of its digital image based on the study of a set of two-dimensional images, as well as the algorithmization of the operation system for collecting information on a three-dimensional object.

Keywords 3D cloud of points · 2D cloud of points · algorithm · digital image · geometric structure · restoration

1 Introduction

The development of the use of digital technology in the surrounding human service systems is quite actual at the present time. The use of digital technologies makes it possible to visualize information about the surrounding world quite well. This requires specialized systems for data transmission and processing [1–3]. Currently, one of the directions of the further development of science is the creation of computer vision systems and object recognition in space. Modernization of this direction will allow in the future to optimize the processing time of information in the form of large arrays of data on the geometric representation of research objects [4, 5]. To date, a large number of different algorithms and approaches have been developed for solving problems of restoring the geometric description of an object to obtain discrete images [6–8]. In this chapter, the stereo images of the object under study, which have different projections, are analyzed. The applied approaches are based on

O. V. Shilyaeva · A. V. Cherpakov (✉)
Department of Information Systems in Construction, Don State Technical University, Rostov-on-Don 344000, Russia
e-mail: alex837@yandex.ru

O. V. Shilyaeva
e-mail: lejla-25@mail.ru

A. V. Cherpakov · I. A. Parinov
I. I. Vorovich Mathematics, Mechanics, and Computer Science Institute, Southern Federal University, Rostov-on-Don 344090, Russia

I. A. Parinov et al. (eds.), *Physics and Mechanics of New Materials and Their Applications*, Springer Proceedings in Materials 10,
https://doi.org/10.1007/978-3-030-76481-4_49

the use of different algorithms and mathematical methods, and each approach can have different ranges of accuracy and applicability [9–12]. Moreover, the algorithms in various degree require the availability of certain *a priori* data on the reconstructed geometric structure of the object and are entirely related to the parameters of the shooting cameras. The data of digital images on the investigated 3D objects will make it possible to solve in the future the problems of clustering, a schematic, concise description of objects.

At present, the researches on determining the spatial shapes of objects, the coordinates of an object with known location, building maps in unknown locations or space using a moving object, determining the movement of an object in 3D space are very relevant.

2 Problem Formulation

The purpose of this work is to develop algorithms for the system of collecting and processing information on the restoration of the geometric structure of a 3D object. The subject of this work is the description of algorithms for restoring the 3D geometric structure of an object in the form of its digital image based on the study of number its two-dimensional (2D) images, as well as the automatization of the operation of information collection system.

3 Algorithmization Procedure of Data Collection

To automatize the data collection on a 3D object, a system for collecting and storing information on the object has been developed. The system performs 3D reconstruction of the geometric structure of the object based on the analysis of digital raster photographs by using the following algorithm:

(i) data collection on the camera matrix and creation of the matrix of camera internal calibration;
(ii) photographing a set of 2D images;
(iii) image processing;
(iv) determination of key points on each image;
(v) comparison of key points between related images;
(vi) building a dilute cloud of the points in 3D space;
(vii) building a dense cloud of the points in 3D space;
(viii) construction of a polygonal mesh based on the dense point cloud.

The approach on the point reconstruction in 3D space is based on the following procedure. The position of the camera (rigid body) in space is described by three coordinates of the center of mass of the body and three Euler angles. Then the formula for coordinates is written as follows:

$$\begin{pmatrix} X \\ Y \\ Z \end{pmatrix} = R \begin{pmatrix} X_0 \\ Y_0 \\ Z_0 \end{pmatrix} + T \tag{1}$$

where R is the rotation matrix containing the angles, T is the center of mass of the object, X, Y, Z are the coordinates of a point in the current image, X_0, Y_0, Z_0 are the coordinates of the initial point of the object in the current coordinate system.

Due to the similarity of triangles, we can find the coordinates of the projection of a point on the image:

$$x' = \frac{X}{Z}; y' = \frac{Y}{Z} \tag{2}$$

Since this formula does not imply units of measurement, the first step is to translate the result into pixels. For this, the scale factors f_x and f_y, as well as the shear factors c_x and c_y, are taken, the geometric meaning of which is to select the center of the optical axis at $X = 0$, $Y = 0$, $Z = 1$, and in most cases the coefficients c_x and c_y coincide with the coordinates of the image center:

$$u = f_x x' + c_x; v = f_y y' + c_y \tag{3}$$

Homogeneous coordinates can be written as a projection matrix

$$w \cdot \begin{pmatrix} u \\ v \\ 1 \end{pmatrix} = P \begin{pmatrix} X \\ Y \\ Z \\ 1 \end{pmatrix} \tag{4}$$

where

$$P = K(R|T); K = \begin{pmatrix} f_x & 0 & c_x \\ 0 & f_y & c_y \\ 0 & 0 & 1 \end{pmatrix} \tag{5}$$

By calculation of homogeneous coordinates, it is important to take into account the fact that the third coordinate must always be equal to 1; for this, the matrix is multiplied by a coefficient w. Multiplying the coordinates of the point by the matrix P leads to obtaining a vector in homogeneous coordinates. Then, by solving the equation, the coefficient w is determined, which makes it possible to equate the last coordinate to 1, and the coordinates in pixels on the image are obtained at the output.

The object has some 3D points, there are points with known coordinates on the image, and each point corresponds to a point on a 3D object. Knowing these data, it is possible to solve the optimization problem. It requires calculation of the minimum of the error function by varying the matrices R, T to find the disposition of the object:

$$err(P) = \sum_i \left| \begin{pmatrix} u_i \\ v_i \end{pmatrix} - \begin{pmatrix} u_i^p \\ v_i^p \end{pmatrix} \right|^2 \tag{6}$$

After finding key points on each image and fixing a descriptor to each point, it is necessary to match the images using the *RANSAC* method by sampling of random matches and search their correct projection onto the image. The *RANSAC* method [13] is used as the most stable to dropped points.

The relationship of points between images can be stated thanks to the homography matrix used to transform coordinates for planar objects in space. To do this, we need to take a coordinate system on the plane itself. In this coordinate system, there will be new projection matrices that can always be recalculated. Now, the object coordinates will be (*X, Y,* 0, 1) instead of (*X, Y, Z,* 1):

$$\begin{pmatrix} u''w \\ v''w \\ w \end{pmatrix} = H \begin{pmatrix} u \\ v \\ 1 \end{pmatrix} \tag{7}$$

The matrix H is the homography transformation matrix. If the coordinates of the first image on the plane are known, then there is such a matrix, multiplying by which, we can obtain the coordinates on the second image.

Moreover, the transformation of the coordinates of the projection of one image to another is expressed using the fundamental matrix F:

$$(u_1, v_1, 1) F \begin{pmatrix} u_2 \\ v_2 \\ 1 \end{pmatrix} = 0 \tag{8}$$

The algorithm for transforming 2D coordinates *u, v* into 3D coordinates *X, Y, Z* is based on minimizing the reprojection error ε:

$$\varepsilon = \bar{m} - m = \begin{bmatrix} \bar{x} \\ \bar{y} \end{bmatrix} - \begin{bmatrix} u/w \\ v/w \end{bmatrix} \tag{9}$$

where $\bar{m}(\bar{x},\ \bar{y})$ is the projection of the point (*u, v*) with an error, which must be minimized. Representing the coordinates *u, v, w* in the form of the matrices of rotation, displacement and internal parameters of the camera, we obtain the transformation of the matrices:

$$\begin{bmatrix} u \\ v \\ w \end{bmatrix} = P \begin{bmatrix} X \\ 1 \end{bmatrix} = K R \begin{bmatrix} I_{33} & -C \end{bmatrix} \begin{bmatrix} X \\ 1 \end{bmatrix} \tag{10}$$

where X is a point with coordinates *X, Y, Z; C* is the center of the camera; matrices I and C represent the decomposition of the displacement matrix t.

It is necessary to minimize the reprojection error by solving nonlinear equations using the least squares method:

$$\min_{(R,C,X)} \left\| \begin{bmatrix} \bar{x} \\ \bar{y} \end{bmatrix} - \begin{bmatrix} u(R, C, X)/w(R, C, X) \\ v(R, C, X)/w(R, C, X) \end{bmatrix} \right\|^2 \tag{11}$$

By finding matrices *R, C* for all points on all images, it becomes possible to establish the initial position of a point in space.

Algorithms for restoring a three-dimensional geometric set of points of an object have been successfully implemented in several free software libraries, such as *OpenMVG* [14], *OpenMVS* [15], etc.

The performation system is split into several implementable algorithms in the form of files. The first implementable file is "*openMVG*_main_*SfMInit_ImageListing*". It is the input point into the restoration algorithm. The main functions of this stage are to initialize the existing images. The result of this application will be a *json*-file, containing images and extracted data about camera parameters.

The next step after the initialization of the images is to determine the key points in the image. This procedure is implemented in an application and called "*openMVG_main_ComputeFeatures*".

4 The Result of the Research

The result of the research is the formation of files for the list of key points and descriptors. The content of the file that stores key points consists of a list of coordinates of points on the image and their size in pixels.

After finding the key points, the next stage consists of their comparison. The "*openMVG_main_ComputeMatches*" application is responsible for the comparison.

After comparison of the key points of the images, the stage of solving the residuals of 2D projections into 3D coordinates begins. The solution is produced by the application "*openMVG_main_GlobalSfM*".

The system uses a global method of the image reconstruction algorithm, which takes into account all 2D projections at once, thus providing high accuracy compared to the incremental method. The result of this application is a 3D cloud of points in 3D space, obtained by converting 2D coordinates of projections into 3D ones, as well as determining the position of the camera.

Figure 1 shows an example of a 3D geometric reconstruction of a toy. By analyzing the images, unrecovered points were identified, as shown in Fig. 1. The algorithm provides for the removal of points as not having the necessary features, if the contrast shift does not exceed three hundredths.

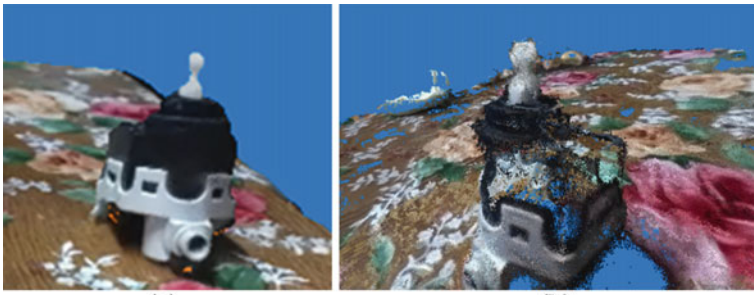

Fig. 1 Example of the result of 3D geometric reconstruction of toy: **a** the original object; **b** the reconstructed cloud of points of the object

5 Conclusion

Within the framework of the presented work, a system for collecting information on a 3D object was described. At the stage of analyzing the subject area and existing solutions, the necessary theoretical foundations, algorithms and mathematical models, software modules and libraries were presented, with the help of which a system for collecting information om a 3D object was implemented. The use of software libraries for data processing at the first stage shows the possibility of geometric description of the objects. The next stages of research can be clustering, data compression in the form of a vector description of an object, etc.

Acknowledgements Research was financially supported by Southern Federal University, grant No. VnGr-07/2020-04-IM (Ministry of Science and Higher Education of the Russian Federation).

References

1. O.V. Shilyaeva, A.V. Cherpakov, K.K. Kuralesin, D.S. Ilyina, Inzhenernyj Vestnik Dona, **1** (2019) (In Russian)
2. D.V. Yavna, V.V. Babenko, Inzhenernyj Vestnik Dona, **3** (2014) (In Russian)
3. R.Gonzalez, R. Woods, *Digital Image Processing* (Technosphere, Moscow, 2005), p. 1072 (In Russian)
4. V.I. Moshkin, A.A. Petrov, V.S. Titov, Yu.G. Yakushenkov, *Technical Vision of Robots.* Moscow, Engineering (1990), p. 272 (In Russian)
5. M.V. Polyakova, V.N. Krylov. Trans. Odessa Polytech. Univ. **1**(25), 98 (2006) (In Russian)
6. A.S. Nazarov, *Photogrammetry; Textbook for University Students.* (TetraSystems, Minsk, 2006), p. 368 (In Russian)
7. Z. Cui, Global Structure-from-Motion and Its Application, Simon Fraser University (2017), p. 82
8. M.I.A. Lourakis, A.A. Argyros, SBA: ACM Trans. Math. Softw. **36**(1), 2 (2009)
9. B. Triggs, P.F. McLauchlan, R.I. Hartley, A.W. Fitzgibbon, Bundle adjustment–a modern synthesis, in *Vision Algorithms*'99 (2000), p. 298

10. D.G. Lowe, Computer Science Department University of British Columbia Vancouver, B.C, Canada (2004), p. 28
11. N.T. Dung, Inzhenernyj Vestnik Dona **1** (2015) (In Russian)
12. E.V. Akindinova, D.I. Petrenko, Inzhenernyj Vestnik Dona **6** (2019) (In Russian)
13. A. Hast, J. Nysjö, Andrea Marchetti, J. WSCG. **21**(1), 21 (2013)
14. P. Moulon, P. Monasse, R. Marlet, Global Fusion of Relative Motions for Robust, Accurate and Scalable Structure from Motion, in *ICCV*, Sydney, Australia (2013), p. 9
15. P. Moulon, P. Monasse, R. Marlet, Adaptive Structure from Motion with a Contrario Model Estimation (2012), p. 257

Hybrid Immune Algorithms Application for Solving Unclear Optimisation Problems

Olga Purchina, Anna Poluyan, and Dmitry Fugarov

Abstract The main aim of the research is the development of effective methods and algorithms based on the hybrid principles functioning of the immune system and evolutionary search to determine a global optimal solution to optimisation problems. Artificial immune algorithms are characterised as diverse ones, extremely reliable and implicitly parallel. The integration of modified evolutionary algorithms and immune algorithms is proposed to be used for the solution of above problem. There is no exact method for the efficient solving unclear optimisation problems within the polynomial time. However, by determining close to optimal solutions within the reasonable time, the hybrid immune algorithm (HIA) is capable to offer multiple solutions, which provide compromise between several goals. Quite few researches have been focused on the optimisation of more than one goal and even fewer used to have distinctly considered diversity of solutions that plays fundamental role in good performance of any evolutionary calculation method.

Keywords optimisation problem · hybrid immune algorithm (HIA) · artificial immune algorithms · affinity · optimal solutions

1 Introduction

The existing application of artificial immune algorithms (AIA) for optimisation problems is usually studied as a competitive adaptive mechanism for the artificial neural networks, in which the adaptation mechanism becomes active in case of approaching threat followed with the further output accumulation. Artificial immune algorithms are also used to solve the problems connected with the anomalies identification and detection. This research studies the symbiosis of the artificial immune algorithms, based on the bionic search [1].

There are certain advantages of artificial immune algorithms to bionic search systems as the follows: wide variety, high reliability, implicit parallelism. At the

O. Purchina · A. Poluyan · D. Fugarov (✉)
Don State Technical University, Rostov-on-Don, Russia
e-mail: ddf_1@mail.ru

I. A. Parinov et al. (eds.), *Physics and Mechanics of New Materials and Their Applications*, Springer Proceedings in Materials 10,
https://doi.org/10.1007/978-3-030-76481-4_50

same time there are some disadvantages of AIA: training complexity, difficulties by choosing offspring for cloning and mutation, multiplicity of initial parameters at the start of functioning algorithm, determination of parent chromosomes to form offsprings, etc.

2 Research Method

There should be considered the problem how to find the optimal flow of the minimum cost of the transport network, which is an essential direction in the research of artificial intelligence systems [2].

The parameters of the constructing process of the abilities of access to transport streams are distinguished and the model for the representation of input information is formed on its basis, as well as mathematical model with ill-caused conditions and quality indicators of the obtained solution. The parameters mentioned above are just preconditions and an appropriate algorithm for solving problems of the given type is built or selected on its basis [3].

The minimum cost flow problem is formed in the following way:

$$F \cong \sum_{(ij)\in U} \sum_{(ij)\in U} \sum_{(ij)\in U} c_{ij} x_{ij} \to \min \tag{1}$$

$$\sum_{(ij)\in U} x_{ij} - \sum_{(i,j)\in U} x_{jk} = \begin{cases} -r, \ j = \alpha \\ 0, \ j \neq \alpha, \beta \\ r, \ j = \beta \end{cases} \tag{2}$$

$$0 \leq p_{ij} \leq x_{ij} \leq l_{ij} \tag{3}$$

where l_{ij} is the upper limit of the flow; p_{ij} is the lower limit of the flow; c_{ij} is the unclear cost flow unit delivery; $\cong$ is the unclear equality operation; r is the flow no exceeding set data.

The main idea of HIA is to obtain multiplicity of quasi-optimal solutions (population) with the help of fast probabilistic algorithm and then to create evolution based on the bionic algorithms (BA) and/or artificial immune algorithms (AIA).

In the process of initial population forming, sets of alternative solutions are obtained by cloning solutions, based on heuristic algorithms, and certain number of antibodies is introduced, too. The formation process is going continuously until the average suitability of the population is close to the initial one, that means stability of the network [4]. New antibodies are introduced in case of unstable network. Antibodies are evolving through cloning selection theory that consists of solutions search in the space. The given approach allows one to maintain the population diversity.

The optimal population quantity can be calculated with the formula:

$$N_{t+1} = N_t e^{r\left(1-\frac{N_t}{K}\right)} \tag{4}$$

where N_t is the population quantity; $r = \text{const}$ is the population growth rate, with values of $0 < r < 2$ from the best range for the population existence within the system; K is the definite population quantity at which the actual reproduction rate is reduced in the result of competition so that the population as a whole can only restore its quantity in each generation [5].

The work algorithm of HIA can be represented in the following way:

1. Population formation and estimation of the optimal population quantity.
2. Entering the cycle, when the condition is fulfilled:
   - (2.1) determination of the target function values for each chromosome and the average value of the target function of the entire population and also the danger signals for the antibodies;
   - (2.2) sampling (n, %) or quality n of the best individuals to clone. The quality of clones is connected with affinity;
   - (2.3) the implementation of modified genetic operators is carried out in the process of adaptation and regulation;
   - (2.4) the mutation operator based on the golden section is done, at the same time it can be adjusted gradually;
   - (2.5) random generation of certain quantity of antibodies, which are added to the population;
   - (2.6) determination of the target function values to obtain offspring chromosomes, selection of the percentage of best specified chromosomes and addition them to the population with determination of the danger signals;
     - (2.6.1) the danger zone is determined, dangerous signals are calculated for each antibody and then antibodies concentration is adjusted through its danger signals;
     - (2.6.2) cloning is performed, a crossing-over operator generates clones' groups, a certain quantity duplicates from random antibodies, and then a mutation operator for each clone is performed keeping the parent antibody;
     - (2.6.3) the antibody with high availability is selected, which then placed in the danger zone of the parent antibody and antibodies with higher availability than the parent antibody are found from outside the danger zone of the parent antibody;
     - (2.6.4) the randomly generated antibodies are added, adjusting the population quantity, recalculating the danger signals of all antibodies with following removing antibodies with zero concentration;
   - (2.7) chromosomes that do not match the specified conditions are removed from the population.

3. Checking the condition of the stop of calculation procedure; if the condition is not fulfilled, then pass to point (2.1), otherwise output of the obtained optimal (quasi-optimal) solution and pass to item 4.
4. Analysis of the obtained results.
5. End of the algorithm

3 Results and Discussion

The alternative adaptation allows one to intellectualise the control of work algorithm for solving the optimisation problem (here genetic algorithm). The given approach makes it possible to set specific control alternatives, depending on the algorithm of solving the optimisation problem [6]. The adaptation change realised through decreasing/increasing the number of conditions corresponding to each alternative, gives the control over the inertia of the immune response.

In above algorithm, an antibody is subjected to selection, if it satisfies the condition:

$$f(Ab_i) \geq 98\% CSel \tag{5}$$

where $CSel = \frac{\sum_{i-1}^{n} f(Ab_i)}{n}$.

The convergence between antibodies and antigens is strongly coupled with those ones which are suitable solutions to the problem [7]. This is expressed in terms of a convergence (Ab_i) and a normalised function representation $f(Ab_i)$.

The convergence Ab_i is calculated as [8]

$$affinity(Ab_i) = \begin{cases} \frac{f(Ab_i) - f\min}{f\max - f\min}, & P = \max f(x), \\ 1 - \frac{f(Ab_i) - f\min}{f\max - f\min}, & p = \min f(x), \end{cases} \tag{6}$$

where $f(Ab_i)$ is the antibody function, $f_{\min}$ is the minimal meaning of population, $f_{\max}$ is the maximal meaning of population.

After AIA obtainment, the danger signals, based on changes of the adaptive environment, may lead to an immune response [9]. Actually the danger signals create a danger zone around themselves and immune cells inside this zone will be activated to participate in the immune response.

Since antigens are invisible for the optimisation problem, it might be assumed that each antibody is a peak; at the same time, the area around the peak is a danger zone.

The danger zone is expressed as

$$D(Ab_i) = \left\{ Ab_i \middle| dis\left(Ab_i, Ab_j\right) < r_{danger} \right\},$$

where r_{danger} is the danger zone radius, its meaning corresponds to the peak size.

A danger signal can be interpreted as the received information on the values of target function (a number of "unfavourable" decisions falling into the danger zone). As a result, those solutions are stimulated which fall into the danger zone. Taking into account this idea, a danger signal can be defined as an identifier in the user's interests. It brings to conclusion that it is possible to imagine various scenarios, in which a danger signal could be useful.

In such a way through the selection theory combination for cloning and danger signals, it is possible to model the biological immune mechanism more suitably and precisely. All individuals in the population are combined into a network, which improves similarity of the population in the process of constant evolution.

The antibody concentration is dynamic and dependent on the antibody danger signal and the convergence between antibody and antigen. These two factors are the general reasons for the dynamic changes of antibody concentration.

$\alpha \in [0, 1]$ is the initial concentration set for the prior population. The antibody concentration decreases down to 0, when a danger signal comes, otherwise the concentration increases up to 1. The antibodies concentration in the population in the danger zone reflects the condition of the whole population for the optimisation task and provides the population diversity. The following shutdown criteria for the operation of the HIA are the main termination conditions:

i. the specified quantity of algorithm generations has been reached;
ii. the current solution time is longer than the specified one;
iii. the specific exactness of the solution ε is achieved, that is within several iterations the difference in the values of the objective function is equal to or less than the specific value of ε.

4 Conclusion

The given research represents a hybrid immune algorithm to solve the problem of finding the minimum cost of the optimal flow of transport network, which is a symbiosis of the modified genetic and immune algorithms and operators allowing us to control the adaptation parameters by executing the algorithm, taking into account the influence of possible changes in the boundary conditions.

The approach to the formation and regulation of the population size becomes distinctive feature, which has shown its effectiveness for solving this type of problem. As a result, a formula for the optimal calculation of the number of the population was proposed, the algorithm maintains a good diversity of the population, it has fewer errors, allows one to reduce the search area for affordable solutions and to obtain optimal results within reasonable time. In the given approach each generation of a population consists of two parts. It contains antibodies with memory of the previous generation while the other contains randomly added new antibodies. Antibodies with high convergence after mutation operation are found mainly in the vicinity of the parental antibody. After the cloning operation, the convergence of the population is higher than in the previous generation. Antibodies with greater convergence can

change the adaptive environment and then generate danger signals. The process of the generation increases, if antibodies with low convergence cannot leave the danger zone, their concentration decreases down to 0 after that they are going to be removed.

Highly convergent antibodies will be preserved in memory due to unchanged conditions. In this mechanism, antibodies in the memory of the population generally have high convergence. This will be ensured by adding new random antibodies to each generation not from the danger zone memorised by antibodies [10]. Thus they will develop a new search location and ultimately the algorithm will find all the peaks in the evolution process.

References

1. Y.O. Chernyshev et al., J. Theor. Appl. Inf. Technol. **81**(3), 466 (2015)
2. AYu. Poluyan et al., J. Phys. Conf. Ser. **1333**, (2019)
3. D.D. Fugarov, Y.Y. Gerasimenko et al., J. Phys. Conf. Ser. **1118**, (2018)
4. AYu. Poluyan et al., J. Phys. Conf. Ser. **1333**, (2019)
5. D.D. Fugarov et al., J. Phys. Conf. Ser. **1333**, (2019)
6. A.Y. Poluyan et al., J. Phys. Conf. Ser. **1015**, (2018)
7. KYu. Solomentsev et al., J. Phys. Conf. Ser. **1015**, (2018)
8. Y. Gerasimenko et al. *Advances in Intelligent Systems and Computing*, **1259**, (2021) p. 471
9. Y.O. Chernyshev et al., J. Theor. Appl. Inf. Technol. **80**(1), 13 (2015)
10. D. A. Onyshko, et al. E3S Web Conf. **164**, 03030 (2020)

Index

I. A. Parinov et al. (eds.), *Physics and Mechanics of New Materials and Their Applications*, Springer Proceedings in Materials 10,
https://doi.org/10.1007/978-3-030-76481-4